



UNIVERSITAT^{DE}
BARCELONA

**Fluid flow evolution in the Alpine-related basement
and sedimentary cover structures in the Southern
Pyrenees: an integrated structural, petrographic
and geochemical approach**

José Daniel Muñoz López



Aquesta tesi doctoral està subjecta a la llicència **Reconeixement 4.0. Espanya de Creative Commons.**

Esta tesis doctoral está sujeta a la licencia **Reconocimiento 4.0. España de Creative Commons.**

This doctoral thesis is licensed under the **Creative Commons Attribution 4.0. Spain License.**



UNIVERSITAT DE BARCELONA

Facultat de Ciències de la Terra

Departament de Mineralogia, Petrologia i Geologia Aplicada

Universitat de Barcelona

**Fluid flow evolution in the Alpine-related basement and
sedimentary cover structures in the Southern Pyrenees: an
integrated structural, petrographic and geochemical
approach**

PhD Thesis

José Daniel Muñoz López

2021



UNIVERSITAT DE
BARCELONA

Facultat de Ciències
de la Terra

**Fluid flow evolution in the Alpine-related basement and
sedimentary cover structures in the Southern Pyrenees: an
integrated structural, petrographic and geochemical
approach**

Memòria de tesi doctoral presentada per José Daniel Muñoz López per
optar al títol de doctor per la Universitat de Barcelona

Tesi realitzada dins el Programa de Doctorat de Ciències de la Terra
HDK09, sota la direcció de la Dra. Anna Travé i la Dra. Gemma Alías.

El doctorand

Les directores

J. Daniel Muñoz López

Anna Travé

Gemma Alías

Barcelona, juliol de 2021

A mis padres, a mis sobris, a mis hermanas y a mi abuela.

Gracias por ser y por estar. ¡Os quiero!

*“Perquè no hi ha res més que l'ara estricte
i el tornaveu repeteix les preguntes
que ens anem fent,
deixa que el vell prodigi
de viure es realitzi cada dia
tan plenament en tu
que et sentis sempre
generosament nou, dignament lliure.”*

Miquel Martí i Pol, Camí de les fonts (Peramola).

Esta tesis se ha llevado a cabo en el Departament de Mineralogia, Petrologia i Geologia Aplicada de la facultat de Ciències de la Terra, Universitat de Barcelona. La tesis ha sido financiada por los proyectos CGL2015-66335-C2-1-R y PGC2018-093903-B-C22 (Ministerio de Ciencia, Innovación y Universidades/Agencia Estatal de Investigación/Fondo Europeo de Desarrollo Regional, Unión Europea), el grupo consolidado de investigación “Geologia Sedimentària” (2017-SGR-824) y el programa FPI2016 (BES-2016-077214) del Ministerio de Economía y Competitividad.

Acknowledgements / Agradecimientos

Esta tesis representa un proceso continuo de aprendizaje y evolución en muchos sentidos. Me siento muy satisfecho de haber llegado hasta aquí y de haber superado todos los obstáculos que han ido surgiendo a lo largo de este corto, pero intenso recorrido. Ahora pienso en todas las cosas que cambiaría de la tesis, e incluso, en lo mucho que me gustaría empezar de cero con los conocimientos actuales. He aprendido a reconocer las cosas que para mí son más simples y las que me resultan más complejas, y es eso precisamente lo que ahora me llena de satisfacción.

Y por supuesto, todo esto no hubiera sido posible sin la ayuda de tantas personas que directa o indirectamente han contribuido al progreso de esta tesis.

Primer de tot, vull agrair a les meves directores, l'Anna i la Gemma, pel seu paper fonamental en el desenvolupament d'aquesta tesi, la vostra expertesa i saviesa m'han fet arribar fins aquí.

Anna, de tu he après i continuo aprenent moltíssimes coses, m'has anat guiant quan ho he necessitat. Crec que reuneixes totes les característiques que ha de tenir un bon investigador, la teva disposició per rebre i donar noves idees i la teva capacitat de solucionar ràpidament qualsevol problema, han fet avançar aquesta tesi i m'han fet millorar cada dia. Gràcies per la teva disposició e implicació en tot moment i per obrir-me les portes de casa teva durant l'inici de les campanyes de camp al Pirineu.

Gemma, definitivament tens un do per a l'ensenyament i la transferència de coneixement, m'has fet entendre fàcilment tot allò que semblava difícil. Encara que per diverses raons no hem pogut treballar tot el que m'hagués agradat, m'has fet espavilar en molts sentits, m'has anat guiant quan ho he necessitat i les teves contribucions també han estat essencials per haver arribat fins aquí.

També vull agrair a tot el grup de Geologia sedimentària i especialment a la Irene y al David, per participar de manera activa en el desenvolupament d'aquesta tesi i per tota l'ajuda rebuda durant tot aquest temps. També al Juandi, el Telm, el Luis, l'Enrique y la Eli, per la seva disponibilitat per resoldre qualsevol dubte en tot moment, per les xerrades, els cafès i les cerveses, i en definitiva, per haver fet tan agradable la meva estada a la Universitat de Barcelona. Gràcies Juandi pels teus consells i el teu interès en el desenvolupament d'aquesta tesi. Gràcies Telm per ajudar-me sempre que ho he necessitat i per les teves correccions per millorar el meu Català.

A Antonio Benedicto, por su entera disposición para colaborar con el grupo, por todos los consejos, las explicaciones y el buen ambiente durante las campañas de campo.

Al Jaume Vergés, per les seves correccions tan detallades que han millorat moltíssim els treballs de la zona de Bóixols, pels seus mapes i talls i per la seva bona disponibilitat en tot moment.

A tot el departament de Mineralogia, Petrologia i Geologia Aplicada i en particular, a la nostra secció de Petrologia i Geoquímica. Gràcies sobretot a les persones que encara no he anomenat i que han estat més a prop durant aquest anys: a la Meri, al Ramón Salas i a la Montse Liesa.

A la comissió de doctorat de la facultat de Ciències de la Terra i a la comissió de seguiment d'aquesta tesi, el Dr. Albert Soler Gil, la Dra. Montserrat Torne i el Dr. Joan Francesc Piniella.

Al nuevo “comando becaris”: Vito, Xiaolong, Gabriel, Oriol y Baoqin (“Paco Mojito”). Vaya grupo! Hemos conseguido encajar muy bien a pesar de ser todos tan diferentes. Gracias por todos los momentos de risas, los planes, las discusiones, las escapadas, las cervezas y las bromas. Habéis aliviado mis momentos más tensos sobre todo al final de la tesis. To the other Chinese visitors: Pei and Jun, for all those funny moments that we shared together, I have a lot of good memories!

A mis primeros compañeros de despacho: Ari, David, Sergi Esteve, Sergi Valenzuela, Nelson, Nicholas Nardini, por todos los momentos agradables que hemos compartido y por todas las discusiones sobre cualquier tema. Gracias en especial a ti, Ari, por todo el buen rollo que has transmitido en el despacho y por todos los consejos y ayuda que he recibido de ti durante estos cuatro años.

Al equipo técnico y científico de todos los laboratorios con los que he trabajado y colaborado. En primer lugar, a Jordi Illa, del laboratorio de Petrología del departamento y a Dolors, Fadoua, Montse y Vicenç, del servei de làmina prima. Gracias a todos por la preparación de muestras y de láminas delgadas y por intentar tener las muestras terminadas para el momento en que las necesitaba.

A Joaquim Perona por su disponibilidad y amabilidad durante los análisis de isótopos estables.

A Marta Rejas del LabGEOTOP de Geosciences Barcelona, no sólo por realizar los análisis de ICP-MS sino también por su rápida respuesta a cualquier duda que me ha surgido durante los análisis.

A todo el equipo del CAI de Geocronología y Geoquímica isotópica de la Universidad Complutense de Madrid. Gracias especialmente a José Manuel Fuenlabrada “Chema” por su disponibilidad absoluta e implicación a la hora de realizar los análisis isotópicos de estroncio y de neodimio.

I also want to thank Cédric M. John from the Imperial College London for running the clumped isotope analysis and for his guidance during the integration and interpretation of results.

Thanks to Xavier Mangenot from the California Institute of Technology for his willingness to perform new clumped isotope analysis even though we could not manage to get results before the end of this thesis.

A Marga, Elisenda y Jordi Bàguena, por dar respuesta a todos los trámites burocráticos y administrativos.

A toda mi familia, principalmente a mis padres y hermanas, pilar fundamental de esta tesis. Gracias por vuestro apoyo incondicional, por entender mis ganas de explorar el mundo y por seguir estando ahí incluso en todas las temporadas que he estado fuera de casa.

Y, por último, pero no menos importante, quiero agradecer a todas las demás personas que forman parte de mi vida, a mis amigos de siempre, a mis amigos de algún lugar en concreto. He tenido la suerte de conocer a muchísimas personas durante este largo camino. Mi infancia entre Medellín y Euskadi, mi carrera en Bilbao, mi máster en Granada, mi estancia en París y mi doctorado en Barcelona..... ¡Qué afortunado me siento! En cada uno de estos lugares tengo el recuerdo y cariño de tantas personas, que sería imposible nombrarlas a todas.

Eskerrik asko guztioi (Jtxo) momentu oro nirekin egoteagatik eta nire bizitzaren parte garrantzitsua izateagatik.

¡A todos, a todos vosotros, GRACIAS! ESKERRIK ASKO!

TABLE OF CONTENTS

Abstract	1
Resum	5
1. INTRODUCTION	9
1.1. Fluid flow and deformation: State of the art	9
1.2. Problems to solve	14
1.3. Objectives.....	15
1.4. Working hypothesis and thesis overview.....	16
2. GEOLOGICAL SETTING	19
2.1. The Estamariu thrust, involving Paleozoic basement rocks from the Orri thrust sheet in the Axial Zone.....	21
2.2. The Sant Corneli-Bóixols anticline along the front of the Bóixols thrust sheet, involving Mesozoic-Cenozoic cover rocks from the Southern-Central Pyrenean Unit. .	23
3. METHODOLOGY	27
4. RESULTS	32
4.1. Studied domains.....	32
4.2. Petrographic features of host rocks	37
4.3. Structural analysis	41
4.4. Petrographic features of calcite cements.....	54
4.5. Geochemistry of calcite cements and host rocks.....	58
4.6. U-Pb geochronology of calcite cements.....	63
5. OVERALL DISCUSSION: SYNTHESIS OF THE MAIN RESULTS	66
5.1. Timing of deformation: fracture development and related tectonic setting	66
5.2. Fluid flow and deformation relationships in the two studied domains, along the Segre transect	72
5.3. Fluid flow and deformation relationships at regional scale.....	85
6. CONCLUDING REMARKS	91
REFERENCES	95
Annex	110
Article 1.....	110
Article 2.....	136
Article 3.....	162
Article 4.....	192
Supplementary data.....	240

ABSTRACT

This PhD thesis examines the fracture-fluid interactions across different compressional structures affecting both Paleozoic basement and Mesozoic-Cenozoic cover lithologies in the Southern Pyrenees in order to investigate the relationships between fluid flow and deformation. The studied structures, from two different domains, include the Estamariu thrust in the Pyrenean Axial Zone and the Sant Corneli-Bóixols anticline along the front of the Bóixols thrust sheet in the Southern-Central Pyrenees. These structures are very well exposed in the study area and could provide exceptional field analogues for the exploration of equivalent subsurface systems or for selection of potential storage sites in complex fold-and-thrust belts worldwide. The proposed methodology integrates field data with U-Pb dating and petrographic and geochemical ($\delta^{18}\text{O}$, $\delta^{13}\text{C}$, $^{87}\text{Sr}/^{86}\text{Sr}$, clumped isotopes and elemental composition) analyses of vein cements, fault rocks and host rocks present in the study area.

The Estamariu thrust resulted from a multistage late Paleozoic to Neogene tectonic evolution. Despite this thrust is known to be Variscan in origin, in the study area it places a Devonian pre-Variscan unit on top of a Stephano-Permian late to post-Variscan sequence, indicating that the structures within this thrust zone have to be post-Variscan. In this regard, the contractional structures found at the contact between Devonian and Stephano-Permian units have been attributed to the Alpine reactivation of the Estamariu thrust. This Alpine-related deformation is consistent with the transposition of the Variscan regional foliation within the main thrust zone and with the formation of a subsidiary thrust zone in the footwall of the Estamariu thrust. Other structures found in the study area, such as extensional fractures, shear bands and normal faults, postdate the reverse structures and have been attributed to the Neogene extension.

In the Sant Corneli-Bóixols anticline, the folded units involve Jurassic-mid Upper Cretaceous pre-compression and latest Cretaceous-Paleocene syn-orogenic sedimentary successions detached on Upper Triassic evaporites. Contrary to the Estamariu thrust, in the Sant Corneli-Bóixols anticline this PhD thesis provides the absolute age of deformation reporting 23 U-Pb dates measured in different sets of fracture-filling calcite cements. These U-Pb dates reveal Late Cretaceous to late Miocene age variations, which are coeval with growth strata deposition and Bóixols thrust sheet emplacement (dates from 71.2 ± 6.4 Ma to 56.9 ± 1.4 Ma), tectonic transport of the Bóixols thrust sheet above

the southern Pyrenean basal thrust (dates from 55.5 ± 1.2 Ma to 27.4 ± 0.9 Ma) and post-orogenic exhumation of the Sant Corneli-Bóixols anticline (dates younger than 20.8 ± 1.2 Ma).

Throughout this long-lived deformation history, the geochemical data of the successive calcite veins allow to analyze the relationships between fluid flow and deformation in the two studied domains. In the Estamariu thrust, the high $^{87}\text{Sr}/^{86}\text{Sr}$ ratios of the different calcite cements indicate the interaction between the vein-forming fluids and radiogenic Paleozoic basement rocks. The geochemical evolution from the earliest to the latest calcite cements also evidence a progressive change in the fluid regime and composition during successive compressional and extensional tectonic events. The progressive increase in precipitation temperatures, from 50 °C to around 210 °C, and enrichment in $\delta^{18}\text{O}_{\text{fluid}}$, from -6.4 to +12 ‰SMOW, in cements attributed to the Alpine compression to cements from the Neogene extension, is probably linked to a higher extent of fluid-rock interaction with basement rocks. By contrast, during the latest stages of the Neogene extension, the geochemistry of the youngest calcite cements evidence the percolation of cold meteoric fluids that indicates a more significant change in the fluid regime, from upward to downward fluid migration.

In the Sant Corneli-Bóixols anticline, the fluid origin and the extent of fluid-rock interaction varied in the several structural positions of the fold and according to the age and nature of their stratigraphy and the involved fracture networks. This evidences a compartmentalization of the fluid system. In the core of the anticline and in the lowest part of the synorogenic sequence from the footwall of the Bóixols thrust, the similar petrographic and geochemical features between successive calcite cements and host rocks indicate a closed fluid system, leading to high extent of fluid-rock interaction. This host-rock buffered fluid was likely derived from the surrounding Lower Cretaceous and Upper Cretaceous marine carbonates, respectively. Contrarily, along large faults, such as the Bóixols thrust, which affect the entire anticline and in the fold limbs, the fluid system was open. Large faults registered the upward migration of fluids in thermal and geochemical disequilibrium with surrounding host rocks, as attested by the light $\delta^{18}\text{O}$ values of their associated vein cements, down to -14 ‰VPDB, and the high temperature of precipitation, up to 120 °C. The fold limbs registered the infiltration of meteoric waters, corroborated by the low Sr contents and by the $\delta^{18}\text{O}$ and $\delta^{13}\text{C}$ values of the vein cements, from -8 to -

6 ‰VPDB and down to -10 ‰VPDB, respectively, which are typical values of meteoric carbonates.

In the fault zone of the Bóixols thrust, successive fracture systems and related calcite cements highlight an episodic evolution of the thrust zone. The presence of early extensional fractures and a chaotic breccia is consistent with the formation of dilatant fracturing within a process zone (around the fault tip) during initial fault growth, whereas the formation of the latest fracture system points to hybrid shear-dilatational failure during propagation of the Bóixols thrust. Similarly, the different structural and fluid flow histories in the footwall and hanging wall of the Bóixols thrust indicate a compartmentalization of the thrust zone. Clumped isotopes applied to vein cements from the footwall evidence a progressive increase in precipitation temperatures from 50 °C to 117 °C, approximately, and an enrichment in $\delta^{18}\text{O}_{\text{fluid}}$, from -1.8 to +5.5 ‰SMOW. This has been interpreted as a change in the fluid source from meteoric fluids to evolved meteoric fluids due to water-rock interaction at increasing depths and temperatures. Contrary to the footwall, clumped isotopes applied to vein cement from the hanging wall, which is the same cement found in the fault core, revealed temperatures around 95 °C and $\delta^{18}\text{O}_{\text{fluid}}$ up to +1.9 ‰SMOW. This has been interpreted as the migration of formation waters from the fault core and towards the hanging wall. Therefore, the Bóixols thrust likely acted as a transverse barrier, dividing the thrust zone into two separate fluid compartments, and a longitudinal drain for migration of fluids.

Altogether, the maximum temperatures and $\delta^{18}\text{O}_{\text{fluid}}$, up to 120 °C and +5.5 ‰VSMOW, obtained in the Sant Corneli-Bóixols anticline, implying 3-4 km depth and presence of formation waters, respectively, together with the $^{87}\text{Sr}/^{86}\text{Sr}$ ratios of the vein cements, within the range of values documented in the sedimentary cover, discard the transfer of fluids between the basement and the sedimentary cover in the Southern-Central Pyrenees. This indicates that the paleohydrological system in the Sant Corneli-Bóixols anticline was restricted to the Bóixols thrust sheet above the Upper Triassic detachment level. This evaporitic detachment likely acted as a lower fluid barrier, preventing the input of fluids from deeper parts of the belt, as interpreted in other areas of the Pyrenees and in other detached thrust systems as the Central Appalachians and Sierra Madre Oriental.

Finally, comparing the results obtained in both studied domains with those reported in previous contributions, this study assesses the fluid flow and deformation relationships at regional scale. On the one hand, this thesis highlights a common fluid flow behavior along

strike in the central-eastern part of the southern Pyrenees, where major faults acted as transfer zones for migration of fluid in thermal and geochemical disequilibrium with adjacent host rocks, whereas background fracturing recorded the presence of fluids that highly interacted with surrounding host rocks. Additionally, our data indicates that regardless of the fluid origin and the tectonic context, the fluids that have interacted with basement rocks have a higher $^{87}\text{Sr}/^{86}\text{Sr}$ ratio (> 0.710) than those that have circulated through the sedimentary cover (< 0.710). Lastly, extensional deformation structures in the eastern Pyrenees have acted as conduits for hydrothermal fluid migration in Neogene times similarly as in the northern part of the Catalan Coastal Ranges. These fluids likely interacted with basement rocks before ascending through fault zones and related fractures.

RESUM

Aquesta tesi examina les interaccions entre fracturació i fluids a diferents estructures compressives que afecten els materials del sòcol Paleozoic y de la cobertora Mesozoica-Cenozoica amb l'objectiu d'investigar les relacions entre migració de fluids i deformació a la Zona Sud-Pirinenca. Les estructures estudiades inclouen l'encavalcament d'Estamariu a la Zona Axial i l'anticlinal de Sant Corneli-Bóixols a la part frontal del mantell de Bóixols, Unitat Sud-Pirinenca Central. Aquestes estructures afloren excepcionalment a la zona d'estudi i podrien proporcionar anàlegs de camp per a l'exploració de sistemes subterranis equivalents o per a la selecció de possibles àrees d'emmagatzematge en cinturons de plects i encavalcament més complexos. Aquest estudi integra dades de camp amb datacions U-Pb i anàlisis petrogràfics i geoquímics ($\delta^{18}\text{O}$, $\delta^{13}\text{C}$, $^{87}\text{Sr}/^{86}\text{Sr}$, cumpled isotopes i composició elemental) de venes de calcita, roques de falla i encaixants presents a la zona d'estudi.

L'encavalcament d'Estamariu és el resultat d'una evolució tectònica que comprèn des del Paleozoic superior al Neogen. Tot i que aquest encavalcament té un origen varisc, a la zona d'estudi superposa una unitat devoniana (pre-varisca) a sobre d'una seqüència estefano-permiana (post-varisca), cosa que indica que les estructures presents dins de la zona de falla han de ser post-varisques. En aquest sentit, les estructures contractives trobades al contacte entre les unitats devoniana i estefano-permiana s'han atribuït a la reactivació alpina de l'encavalcament d'Estamariu. Aquesta deformació alpina va donar lloc a la transposició de la foliació regional varisca dins de la zona principal d'encavalcament i a la formació d'una zona de falla subsidiària al bloc inferior de l'encavalcament d'Estamariu. Altres estructures trobades a la zona d'estudi inclouen fractures extensionals i falles normals que postdaten les estructures inverses i, per tant, que s'han atribuït a l'extensió neògena.

A l'anticlinal de Sant Corneli-Bóixols, les unitats plegades impliquen materials pre-compressius del Juràssic-Cretaci superior i materials sinorogènics del Cretaci superior-Paleocè desenganxats en evaporites del Triàsic superior. A l'anticlinal de Sant Corneli-Bóixols, aquesta tesi proporciona l'edat absoluta de deformació amb 23 edats U-Pb mesurades en diferents ciments de calcita omplint les fractures. Aquestes dades revelen edats de deformació des del Cretaci superior fins al Miocè superior, que són coetànies amb la deposició de sediments sinorogènics i l'emplaçament del mantell de Bóixols (edats

de $71,2 \pm 6,4$ Ma a $56,9 \pm 1,4$ Ma), el transport tectònic del mantell de Bóixols per sobre de l'encavalcament basal sud-pirinenc (edats de $55,5 \pm 1,2$ Ma a $27,4 \pm 0,9$ Ma) i l'exhumació postorogènica de l'anticlinal de Sant Corneli-Bóixols (edats més joves de $20,8 \pm 1,2$ Ma).

Durant aquesta història de deformació, les dades geoquímiques de les successives venes de calcita permeten analitzar les relacions entre la migració de fluids i la deformació a les dues zones d'estudi. A l'encavalcament d'Estamariu, les relacions $^{87}\text{Sr}/^{86}\text{Sr}$ dels diferents ciments de calcita indiquen la interacció entre els fluids i les roques del sòcol Paleozoic. L'evolució geoquímica dels ciments de calcita també evidencia un canvi progressiu en el règim i la composició dels fluids durant successius episodis tectònics de compressió i extensió. L'augment progressiu de les temperatures de precipitació, de 50 °C a uns 210 °C, i l'enriquiment en $\delta^{18}\text{O}_{\text{fluid}}$, de $-6,4$ a $+12$ ‰SMOW, de ciments atribuïts a la compressió alpina a ciments de l'extensió neògena, probablement està relacionat amb un major grau d'interacció entre els fluids i les roques del sòcol. Per contra, durant les darreres etapes de l'extensió neògena, la geoquímica dels ciments de calcita més joves evidencia la percolació de fluids meteòrics, indicant així un canvi més significatiu en el règim de fluids, de migració ascendent a percolació de fluids.

A l'anticlinal de Sant Corneli-Bóixols, l'origen dels fluids i el grau d'interacció fluid-roca van variar en les diverses posicions estructurals del plec i segons l'edat i la naturalesa de la seva estratigrafia i les fractures relacionades. La qual cosa evidencia una compartimentació del sistema de fluids. Al nucli de l'anticlinal i a la part més baixa de la seqüència sinorogènica del bloc inferior del l'encavalcament de Bóixols, les característiques petrològiques i geoquímiques similars entre successius ciments de calcita i les seves roques encaixants indiquen un sistema tancat de fluids i un grau alt d'interacció fluid-roca. Aquests fluids probablement es deriven dels carbonats marins del Cretaci inferior i del Cretaci superior, respectivament. Contràriament, al llarg de grans falles, com l'encavalcament de Bóixols, que afecten tot l'anticlinal i als flancs del plec, el sistema de fluids estava obert. Les grans zones de falla van registrar la migració ascendent de fluids en desequilibri tèrmic i geoquímic amb les roques encaixants, com ho demostren els valors empobrits de $\delta^{18}\text{O}$ dels ciments associats, fins a -14 ‰VPDB, i l'alta temperatura de precipitació, fins a 120 °C. Els flancs del plec van registrar la infiltració d'aigües meteòriques, segons el baix contingut de Sr i els valors de $\delta^{18}\text{O}$ i $\delta^{13}\text{C}$ dels ciments, de -

8 a -6 ‰ VPDB i fins a -10 ‰ VPDB, respectivament, que són valors típics de carbonats meteòrics.

A la zona de falla de l'encavalcament de Bóixols, els successius sistemes de fractures i ciments de calcita relacionats indiquen una evolució episòdica de la zona de falla. La presència de fractures extensionals i d'una bretxa caòtica és consistent amb la formació de fractures dilatants durant el creixement inicial de la falla, mentre que la formació del darrer sistema de fractures apunta a una fracturació híbrida extensional i de cizalla durant la propagació de l'encavalcament de Bóixols. De la mateixa manera, les diferents històries estructurals i de migració de fluids al bloc inferior respecte al bloc superior de l'encavalcament de Bóixols indiquen una compartimentació de la zona de falla. Els clumped isòtops dels ciments de calcita del bloc inferior mostren un augment progressiu de les temperatures de precipitació de 50 °C a 117 °C, aproximadament, i un enriquiment en $\delta^{18}\text{O}_{\text{Fluid}}$, de -1,8 a +5,5 ‰ SMOW. Això s'ha interpretat com un canvi de fluids meteòrics a fluids meteorics evolucionats a causa de la interacció aigua-roca a profunditats i temperatures creixents. Contràriament al bloc inferior, els clumped isòtops aplicats als ciments del bloc superior, que és el mateix ciment que es troba al cor de falla, van revelar temperatures al voltant de 95 °C i $\delta^{18}\text{O}_{\text{Fluid}}$ fins a +1,9 ‰ SMOW. Això s'ha interpretat com la migració de les aigües de formació a través de la falla i cap al bloc superior. Per tant, l'encavalcament de Bóixols probablement va funcionar com un segell transversal, dividint la zona de falla en dos compartiments de fluids separats, i un conducte longitudinal per a la migració de fluids.

En conjunt, els màxims valors de temperatura i de $\delta^{18}\text{O}_{\text{fluid}}$, de 120 °C i de +5,5 ‰ VSMOW, obtinguts a l'anticlinal de Sant Corneli-Bóixols, impliquen profunditats de 3-4 km i la presència d'aigües de formació, respectivament. Aquests valors juntament amb les relacions $^{87}\text{Sr}/^{86}\text{Sr}$ dels ciments de calcita, dins del rang de valors documentats a la cobertura sedimentària, descarten la possible transferència de fluids entre el sòcol i la cobertura sedimentària a la Zona Sud-Pirinenca Central. Tot plegat, aquests resultats indiquen que el sistema paleohidrològic estava restringit al mantell de Bóixols per sobre del nivell de desenganxament del Triàsic superior. Aquest nivell evaporític probablement va actuar com un segell evitant l'entrada de fluids de parts més profundes de la serralada, tal com s'interpreta en altres zones del Pirineu i en altres sistemes d'encavalcaments com els Apalatxes centrals i la Sierra Madre Oriental.

Finalment, comparant els resultats obtinguts en els dos dominis estudiats amb els resultats reportats en altres contribucions prèvies, aquesta tesi analitza la relació entre migració de fluids i deformació a escala regional. D'una banda, aquesta tesi posa de manifest un comportament comú del flux de fluids al llarg de la part central-oriental de la Zona Sud-Pirinenca, on les falles principals van actuar com a zones de transferència per a la migració de fluids en desequilibri tèrmic i geoquímic amb roques encaixants, mentre que les fractures de escala menor van registrar la presència de fluids equilibrats amb els seus encaixants. A més, les nostres dades també indiquen que, independentment de l'origen del fluid i del context tectònic, els fluids que han interaccionat amb les roques del sòcol tenen una relació de $^{87}\text{Sr}/^{86}\text{Sr}$ ($> 0,710$) superior als fluids que han circulat per la cobertora sedimentària ($< 0,710$). D'altra banda, les estructures de deformació extensiva, tant al Pirineu oriental com a la part nord-est de la Cadena Costera Catalana, han actuat com a conductes per a la migració de fluids hidrotermals al Neogen i en l'actualitat. Aquests fluids probablement van interactuar amb les roques del sòcol abans d'ascendir a través de zones de falla i les fractures relacionades.

1. INTRODUCTION

1.1. Fluid flow and deformation: State of the art

Fluids play an important role on the Earth's crust as, on one hand, they transport solutes and distribute heat, controlling mineral and diagenetic reactions including precipitation and dissolution (Garven, 1989; Ferry and Dipple, 1991; Deming, 1994; Duddy et al., 1994; Putnis, 2002). On the other hand, fluids may change the effective stress in rocks, triggering the formation and reactivation of fractures (Sibson, 1995, 2003). All these fluid-related processes exert a major control on the development, evolution and preservation of fractured reservoirs in fold-and-thrust belts (Swennen et al., 2000; Baqués et al., 2020). In these settings, the risk of reservoir damage associated with diagenesis, and therefore the prediction of the reservoir quality, is still one of the main exploration challenges (Roure et al., 2005; Morad et al., 2010). Regarding to this, the paragenetic sequence found in fracture networks that developed during the polyphasic evolution of a mountain belt records successive events of fluid flow and fluid-rock interactions at very different P-T conditions and involves fluids from different origins (Roure et al., 2005; Travé et al., 2007; Cruset et al., 2018; Crognier et al., 2017; Beaudoin et al., 2020). The source and distribution of such migrating fluids in fold-and-thrust belts depend, among other factors, on the connectivity between different fluid reservoirs (Caine et al., 1996). This connectivity is in turn influenced by the hydraulic behavior of the deformation structures (fluid pathways) such as fault zones and fracture networks, and their evolution through time (Caine et al., 1996; Lefticariu et al., 2005; Evans et al., 2012; Evans and Fischer, 2012; Beaudoin et al., 2014). Poorly permeable pathways lead to dominantly closed fluid systems that remains significantly rock-buffered during progressive deformation (Henry et al., 1996; Lacroix et al., 2011). Contrarily, the increase in fracture density and connectivity, as well as the superposition of different fracture sets, may result in the formation of preferential pathways for fluid flow and the opening of the fluid system (Lefticariu et al., 2005; Fischer et al., 2009; Boutoux et al., 2014).

In this line, the diagenetic products (vein cements) developed during the evolution of a particular structure (fault or fold) are the integrated result of tectonic activity and the associated fluid flow event. However, these processes may not be directly analyzed at depth in active tectonic settings or in ancient structures that are not currently exposed at the Earth's surface. Therefore, exhumed fault zones and folds, and their associated vein

systems, provide field analogues to investigate the relationships between fluid flow and deformation in the upper crust and the effect that such migrating fluids have on surrounding host rocks (Barker, 2007; Cosgrove, 2015; Watkins et al., 2018). These relationships are summarized in the following lines.

Fluid flow and faulting relationships. In areas undergoing compressional regimes, the largest fluid fluxes, heat transport and mass transfer commonly occur along the main thrust faults and related fractures due to the loading induced by thrust sheets emplacement (Oliver, 1986; Muchez and Sintubin, 1998; Gudmundsson, 2001). This is evidenced by the common occurrence of complex mineral-filled fracture networks within numerous fault zones described in different worldwide tectonic settings (Gudmundsson, 1999; Gudmundsson et al., 2001; Kim et al., 2004; Breesch et al., 2009; Wiltschko et al., 2009; Agosta et al., 2010; Trincal et al., 2017; Lacroix et al., 2018). Contrarily, fluid rates are commonly very low in surrounding rock-matrix and in poorly connected fractures, resulting in rock-buffered fluid systems (Muchez and Sintubin, 1998; Gudmundsson et al., 2001). In some cases, the development of thrust faults may also inhibit vertical fluid transport inducing fluid overpressure, which in turn produces a reduction of effective stress causing rock failure and hydraulic fracturing (Hilgers et al., 2006; Sibson and Scott, 1998; Sibson, 2019). Whether a fault zone will constitute either a conduit or barrier for fluid flow depends, among many other factors, on the architecture of the fault zone and the permeability associated with the developed structures (Caine et al., 1996; Jolley et al., 2007). The architecture of a brittle fault zone consists of a fault core, where the main fault slip is accommodated, and a damage zone, containing subsidiary deformation around the core (Sibson, 1977; Faulkner et al., 2010). As the fault core usually consists of low-permeability fault rocks with insignificant fracture density and the damage zone mainly includes extensional fractures and faults, the fluid properties and permeability of a fault zone are conditioned by the spatial distribution and the internal composition of these two fault zone elements (Caine et al., 1996; Agosta et al., 2010). Additionally, the structural permeability of a fault is generally transient and could vary in time and space across and along the fault zone (Agosta et al., 2007; Barker, 2007).

Fluid flow and folding relationships. Folds are an important deformation feature that occur in worldwide compressional belts. Such structures have largely been a target for oil and gas exploration (Mitra, 1990), and in depleted oil fields, they depict important analogues for the appraisal of reservoir storage potential (Mitiku and Bauer, 2013).

The folding process commonly involves a multilayered sequence of rocks with different mechanical properties, thickness and competence contrast between layers (Barker, 2007; Vidal-Royo et al., 2013). These varying rock features control the folding mechanism and the distribution of structural damage (fracture networks) that develop within the folded strata (Fischer and Wilkerson, 2000; Chester, 2003; Shackleton et al., 2005; Barker, 2007; Laubach et al., 2009; Barker and Cox, 2011; Watkins et al., 2015; Casini et al., 2018). The folding process not only supplies the mean stress gradients and the fracture-induced permeability that triggers fluid flow (Roure et al., 2005; Casini et al., 2011; Cosgrove, 2015), but it is also responsible for the development of structural traps and reservoirs of economic interest (Mitra, 1990).

During the fold growth, the origin and distribution of fluids largely depend on the connectivity between different hydrostratigraphic units, which in turn is influenced by the formation of fold-related fractures (Lefticariu et al., 2005; Evans et al., 2012; Evans and Fischer, 2012; Beaudoin et al., 2014). Therefore, the nature and origin of fluids may continuously change in space and time at different stratigraphic and structural positions within the evolving fold and from the early-folding to the latest stages of folding (Travé et al., 2000; Beaudoin et al., 2011, 2015; Barbier et al., 2012; Evans and Fischer, 2012; Vandeginste et al., 2012; Cruset et al., 2016).

For the reasons explained above, integrated studies coupling the evolution of fracture networks and the origin of the related vein cements are key to constrain the fluid flow history of an area during orogenic growth (Roure 2005; Travé et al., 2007; Vandeginste et al., 2012; Beaudoin et al., 2015; Cruset et al., 2018). Integrating this information in well-exposed field analogues, such as those structures selected in the Pyrenees is crucial for the following reasons:

- (i) To recognize the fluid pathways in complex tectonic settings or in areas where outcrops are not available (Bergbauer and Pollard, 2004).
- (ii) To identify the timing and controlling factors of fluid flow and fluid-rock interactions in deformed rocks (Swennen et al., 2000; Ferket et al., 2003, 2006; Roure et al., 2005; Travé et al., 2007; Callot et al., 2013).
- (iii) To decipher the nature and origin of fluids that circulate through time and space during deformation, and the resulting diagenetic reactions (Crognier et al., 2017; Mangenot et al., 2017; Cantarero et al., 2018).

- (iv) To understand the transition between successive fluid flow regimes such as topography-driven infiltration of fluids, compaction-driven upflow or squeegee-type fluid migration (Baqués et al., 2012; Beaudoin et al., 2015).
- (v) To unravel when fluid migration occurs, when fractures act as seal or pathways and to assess the sealing capacity of different structures and host rocks involved in the evolution of foreland fold-and-thrust belts (Caine, 1996; Moretti et al., 2000; Vilasi et al., 2009; Breesch et al., 2009; Dewever et al., 2013; Ogata, 2014).
- (vi) To identify the reservoir properties such as porosity and permeability and the distribution of minerals, hydrocarbons and geothermal anomalies (Moretti, 1998; Labaume et al., 2000; Vilasi et al., 2006; Roure et al., 2010; Taillefer et al., 2017).

Therefore, even though the proposed research has a clear scientific character, covering multidisciplinary subjects such as structural geology, petrography, geochemistry and diagenesis, the obtained results will have direct implications in economic and strategic fields for the exploration of geological resources or selection of potential storage sites. For instance, for hydrocarbon recovery, mining, hydrology, geothermal energy, disposal of contaminated waste and CO₂ sequestration (Bachu, 2000; Cooper, 2007; Mitiku and Bauer, 2013; Alcalde et al., 2014; Sun et al., 2020; Benedicto et al., 2021).

Previous case studies over the world. Due to the economic and scientific reasons explained above, the interest in the interplay between deformation and fluid flow has significantly increased during recent years giving rise to many new studies that have tackled this topic in worldwide compressional, extensional and strike-slip tectonic settings. Some representative studies are from: the Ionian fold-and-thrust belt (Swennen et al., 2000; Van Geet et al., 2002; Vilasi et al., 2011), the Alps (Hausegger et al., 2010; Boutoux, 2014; Incerpi et al., 2017), the Apennines (Cello et al., 2001; Conti et al., 2010; Petracchini et al., 2012; Pizzati et al., 2018; Mozafari et al., 2019; Beaudoin et al., 2020), the Zagros (Morley et al., 2014), the Oman Mountains (Breesch et al., 2009; Balsamo et al., 2016; Mozafari et al., 2017), the Sicilian belt (Dewever et al., 2010; 2013), the Appalachians (Hilgers and Sidern, 2005; Evans et al., 2012), the Sierra Madre Oriental in Mexico (Lefticariu et al., 2005; Fischer et al., 2009; Fitz-Diaz et al., 2011), the Catalan Coastal Range (Travé et al., 1998; Cantarero et al., 2014, 2018, 2020; Baqués et al., 2010, 2012), the Tarim Basin, NW China (Li et al., 2010; Baqués et al., 2020) and the Rio Grande Rift, USA (Williams et al., 2015, 2017).

In the case of the Southern Pyrenees, the investigation of fluid flow linked to the evolution of Alpine-related compressional structures started in the early 90's (Grant et al., 1990; Banks et al., 1991; McCaig et al., 1995). These studies focused on fluid movement along the Gavarnie thrust and the Pic de Port Vieux thrust. However, extensive research deciphering fluid flow during the evolution of the Southern Pyrenean belt did not start until the late 90's during the pioneering work of Travé et al. (1997, 1998, 2000). These works focused on the early compressional deformation that affected the south Pyrenean foreland basin during the southward migration of the imbricated thrust-fold system. Afterwards, many other studies have tackled the relationships between deformation and fluid migration during the successive stages of the belt evolution. Some representative studies are from: the Ebro foreland basin (Travé et al., 2000), the Jaca and Ainsa basins (Travé et al., 1997, 1998; Lacroix et al., 2013, 2014, 2018; Crognier et al., 2018), the Sierras Exteriores (Beaudoin et al., 2015), the Cadí thrust sheet (Caja et al., 2006; Caja and Permanyer, 2008).

Most of the above-mentioned contributions focused on individual folds and thrusts from specific areas of the belt. An early attempt to constraint the evolution of fluids at different moments of the thrust front propagation is found in Travé et al. (2007).

In recent years, an increasing knowledge of fluid migration during the whole configuration of the south Pyrenean wedge has resulted from different national and international projects, promoted by the increasing global demand for raw materials and new energetic resources as well as by the search and definition of potential storage sites (management of contaminated/radioactive waste and CO₂, among others). Particularly, this PhD thesis has been carried out within the framework of two I + D national projects. The former has been accomplished during a three-year period between 2016 and 2019: "Flujo de fluidos durante la evolución de un orógeno: caracterización diagenética, hidrotermal y metamórfica con aplicación al almacenamiento de gas y exploración de minerales" (CGL2015-66335-C2-1-R). The latter started in 2019 and it is still ongoing: "Circulación de fluidos durante la evolución de cuencas invertidas y cinturones orogénicos: aplicación en el almacenamiento de CO₂" (PGC2018-093903-B-C22). Substantial advances in the comprehension of fluid flow and fluid-rock interactions have resulted from these two projects. The more remarkable results concern the evolution of the paleofluid system during configuration of a whole N-S section of the south-eastern Pyrenean fold-and-thrust belt (the Llobregat section) (PhD thesis of Cruset, 2019 and

related contributions: Crusset et al., 2016, 2018, 2020a,b) and the global to reservoir scale assessment of CO₂ storage potential (ongoing PhD thesis of Sun, 2021).

Additionally, another important advance in the understanding of the fluid flow-deformation relationships derived from the above-mentioned projects is the application of innovative analytical methods for first time in the Southern Pyrenees. These methods are the absolute dating of structures by means of U-Pb geochronology and the determination of temperature and composition of vein-forming fluids by clumped isotope thermometry. Due to the promising results obtained from these methodologies, this PhD thesis will expand the use of such procedures in the selected study area.

1.2. Problems to solve

Even though the Pyrenees have been the subject of multiple fluid flow studies in the last three decades, the good exposure of this belt and the availability of extensive regional data, offer the opportunity to explore new areas of study and to provide renewed knowledge on fluid flow behavior that may be exportable elsewhere to similar settings. Taking as a base the previous studies, this PhD thesis will expand the paleofluid analysis along the Segre section, at the transition between the basement and the sedimentary cover in the South-Central Pyrenees and will tackle specific questions with emphasis on the controls that different host rocks and structures (folds, fault zones and related fractures) have on the spatiotemporal evolution of the fluid system. Therefore, this thesis will examine the thrust zone evolution and its direct implications with the development of hydrological conduits and barriers along and across the thrust zone. It will also characterize the fluid flow regimes during successive reactivations of a long-lived thrust fault and the source, distribution and variation of fluids across a large-scale anticline and the effect that both, faults and folds, have on the compartmentalization of fluids. Additionally, this study will analyze the influence of basement rocks on the composition of fluids that circulated during deformation and will assess the possible transfer of fluids between the basement and the sedimentary cover. Finally, through a comparison of results obtained in the studied structures with those reported in previous contributions, this thesis will provide insights into fluid circulation at orogen scale.

1.3. Objectives

This PhD thesis examines the fluid flow behavior through time and space in different compressional structures (folds, fault zones and related fractures) developed and/or reactivated during the Alpine compression, and locally during the subsequent Neogene extension in the Southern-Central Pyrenees, along the Segre transect. Selected structures involve both Paleozoic basement and Mesozoic-Cenozoic cover lithologies and therefore, this study examines the influence of basement rocks on the composition of migrating fluids, the possible transfer of fluids between the Paleozoic basement and the sedimentary cover, and provides insights into the fluid flow at regional scale during the Neogene extension. Obtained results are then compared with other studies reporting fluid flow in other Pyrenean structures and other worldwide compressional belts.

In order to reach the main general objective, several specific objectives have been proposed:

- To constrain the successive deformation (fracturing) events occurred in each studied structure.
- To determine the absolute/relative timing of vein formation and therefore of fluid migration using geochronological data and/or crosscutting relationships.
- To decipher the origin and characteristics (temperature and composition) of fluids and the paleohydrological regime (open vs closed) associated with each deformation phase.
- To recognize the fluid pathways and the main factors controlling the migration of fluids during deformation (considering host rocks and fractures): implications for fluid compartmentalization and fracture-related permeability.
- To evaluate the spatial and temporal hydraulic behavior (conduit vs barrier) of a specific fault zone. To characterize the multiphase evolution and changes in the fluid regime during successive reactivations of a long-lived fault.
- To determine the spatiotemporal variation in the fluid flow behavior and the main factors controlling the fluid origin and regime at different structural positions of a large-scale fold.
- To assess the influence of Paleozoic rocks and Mesozoic-Cenozoic sedimentary units on the fluid chemistry during deformation.

- To assess the possible transfer of fluids between the basement and the sedimentary cover (whether there is connectivity or not from one system to the other).
- To compare the obtained results in the Segre transect (this thesis) with those reported in the Llobregat section in order to understand the lateral variations of fluid-deformations relationships in the Southern Pyrenees. In addition, to compare the obtained results with other studies performed in similar geological settings in order to provide insights into the evolution of fluids at worldwide scale.

1.4. Working hypothesis and thesis overview

Different types of rock deformation structures have distinct effects on fluid flow, acting as potential fluid seals or pathways (Moretti et al., 2002; Ferket et al., 2006; Barbier et al., 2012; Breesch et al., 2013; Dewever et al., 2013). These effects are generally transient in time, present strong spatial anisotropies and may change during successive episodes of cementation/sealing, dissolution/fracturing or during successive tectonic phases (Swennen et al., 2000; Roure et al., 2005; Arndt et al., 2014; Lacroix et al., 2018). Both, the hydraulic behavior of deformation structures and the nature of the involved lithologies play a key role in governing the origin, evolution and distribution of fluids in fold-and-thrust belts and related foreland basins (Travé et al., 1997; Breesch et al., 2009). In turn, the transport of fluids through rocks induces important diagenetic reactions at variable scales (Mangenot et al., 2018; Salomon et al., 2020). Thereby, understanding the relationships between deformation of rocks and mobilization of fluids is still a hot topic and a matter of intense research (Mangenot et al., 2018; Pagel et al., 2018; Humphrey et al., 2019; Salomon et al., 2020; Dimmen et al., 2020; Benedicto et al., 2021).

The structure of this PhD thesis consists of a summary of results and an overall discussion of four scientific articles published or submitted to international peer-reviewed journals indexed in the Science Citation Reports. Three of the four articles are already published in open access journals and the other one is under revision for publication. Besides, each paper deals with different structures at variable temporal and spatial scales and involving diverse rock units. The four articles are attached in the Annex of this manuscript and briefly summarized in this section:

- **Muñoz-López, D.**, Alías, G., Cruset, D., Cantarero, I., Jonh, C. M., and Travé, A., 2020: Influence of basement rocks on fluid evolution during multiphase deformation: the example of the Estamariu thrust in the Pyrenean Axial Zone, *Solid Earth*, 11,

2257–2281. <https://doi.org/10.5194/se-11-2257-2020>. Impact factor: 2.921. Position: Q1 (41/235) in *Geology* (2020).

In this contribution, the temporal and spatial relationships between deformation and fluid migration is documented in the Estamariu thrust, a long-lived Variscan thrust deforming basement rocks in the Pyrenean Axial Zone. This study focuses on two successive reactivations of the Estamariu thrust linked to the Alpine compression (Late Cretaceous to Oligocene) and the Neogene extension. Important aspects discussed in this paper are: (1) the relative timing of deformation and fluid migration and the changes in the fluid regime during regional compressional and subsequent extensional tectonic events; (2) the influence that basement rocks have on the composition of fluids that circulate during deformation. Finally, this study provides insights into the fluid flow at regional scale in the NE part of the Iberian Peninsula, where the presence of hydrothermal fluids has been reported from Neogene times to present.

- **Muñoz-López, D.**, Cruset, D., Cantarero, I., Benedicto, A., John, C. M., and Travé, A., 2020: Fluid dynamics in a thrust fault inferred from petrology and geochemistry of calcite veins: An example from the Southern Pyrenees, *Geofluids* 2020, 1-25. <https://doi.org/10.1155/2020/8815729>. Impact factor: 1.534. Position: Q2 (77/187) in *General Earth and Planetary Sciences* (2020).

This study examines the qualitative fault-related permeability and its control on fluid flow during the evolution of the Bóixols thrust, which has associated a well-exposed carbonate thrust zone in the Southern Pyrenees. This contribution assesses the origin, composition, and temperature of the vein-forming fluids as well as the timing of fluid migration in relation to the fracturing events, and discerns the fluid pathways, the extent of fluid-rock interaction, and the transfer of fluids (longitudinal vs transversal) within the thrust zone. Important aspects highlighted in this contribution are: (1) the transient fault-related structural permeability linked to the episodic evolution of the thrust zone; (2) the compartmentalization of fluids during thrusting; and, (3) the similarity in deformation processes and mechanisms linked to the evolution of fault zones in compressional and extensional contexts involving carbonate rocks.

- Nardini, N., **Muñoz-López, D.**, Cruset, D., Cantarero, I., Martín-Martín, J., Benedicto, A., Gomez-Rivas, E., John, C. M., and Travé, A., 2019: From early

contraction to post-folding fluid evolution in the frontal part of the Bóixols thrust sheet (Southern Pyrenees) as revealed by the texture and geochemistry of calcite cements, *Minerals*, 9(2), 117, doi:10.3390/min9020117. Impact factor: 2.380. Position: Q2 (90/235) in *Geology* (2020).

This contribution aims to understand fluid evolution in the successive fold-fracture systems of the frontal part of the Bóixols thrust sheet to decipher the fluid regime during the earliest stages of evolution of the South-Central Pyrenees, as it corresponds to the oldest emplaced allochthonous unit in the area. The analyzed structures include the southern limb of the Sant Corneli-Bóixols anticline and the footwall of the Bóixols thrust sheet. Important aspect discussed in this contribution are the evolution of fracture systems and the associated fluid flow regimes through time, during the overall evolution the Sant Corneli-Bóixols anticline along the front of the Bóixols thrust sheet.

- **Muñoz-López, D.**, Cruset, D., Vergés, J., Cantarero, I., Benedicto, A., Albert, R., Gerdes, A., Beranoaguirre, A., and Travé, A. (Submitted). Spatio-temporal variation of fluid flow behavior along a fold: the Sant Corneli-Bóixols anticline (Southern Pyrenees) from U-Pb dating and structural, petrographic and geochemical constraints. Submitted to *Marine and Petroleum Geology*. Impact factor: 3.790. Position: Q1 (22/235) in *Geology* (2020); Q1 (3/39) in *Economic Geology* (2020).

This study examines the fracture-fluid interactions across the Sant Corneli-Bóixols anticline in order to date and to investigate the relationships between fluid flow and a large scale fold evolution. Important aspects discussed in this paper are: (1) the absolute timing of vein formation, revealing important age variation from the Late Cretaceous to late Miocene; (2) the qualitative fracture-related permeability and the main factors controlling the scale of fluid flow and the extent of fluid-rock interaction; and, (3) the origin, distribution and variation of fluids across the several structural positions of the anticline. Additionally, this study assesses the possible transfer of fluids between the basement and the sedimentary cover in the South-Central Pyrenees and provides a conceptual model of fluid circulation in compressional structures detached along evaporitic units, which may act as a seal for the fluid system.

2. GEOLOGICAL SETTING

The Pyrenees constitute an asymmetric and doubly verging orogenic belt that resulted from the Alpine (Late Cretaceous to Miocene) convergence between the Iberian and European plates (Choukroune, 1989; Roure et al., 1989; Srivastava et al., 1990; Muñoz, 1992), causing the inversion of previous Mesozoic extensional basins and their incorporation into the thrust sheet stacking (Choukroune, 1989; Muñoz, 1992; Vergés and Fernandez, 2012). The Pyrenean structure consists of a central antiformal stack of basement-involved rocks from the Axial Zone, flanked by two oppositely verging fold-and-thrust belts and their associated Cenozoic Ebro and Aquitaine foreland basins (Muñoz et al., 1986; Muñoz, 1992) (Fig. 1a). The antiformal stack of the Axial Zone includes three main thrust sheets, which are, from upper to lower, Noguères, Orri and Rialp (Poblet, 1991; Muñoz, 1992; Saura and Teixell, 2006). This thrust imbrication involves a Paleozoic basement deformed by successive Variscan, Alpine and Neogene phases (Saura and Teixell, 2006), and an upper Carboniferous-Triassic cover (Roure, 1989; Muñoz, 1992). The southern fold-and-thrust belt includes a piggy-back imbrication of Mesozoic-Cenozoic cover thrust sheets that have been detached from the Paleozoic basement along Upper Triassic evaporites, and transported southwards over the autochthonous Ebro foreland basin (Fig. 1b) (Seguret and Daignières, 1986; Roure et al., 1989). In the Southern-central Pyrenees, these cover thrust sheets are, from north to south, the Bóixols thrust sheet, originated from the Late Cretaceous to Paleocene, the Montsec thrust sheet, emplaced during the Paleocene to late Ypresian, and the Serres Marginals thrust sheet, developed from Lutetian to Oligocene times (Roure et al., 1989; Vergés and Muñoz, 1990).

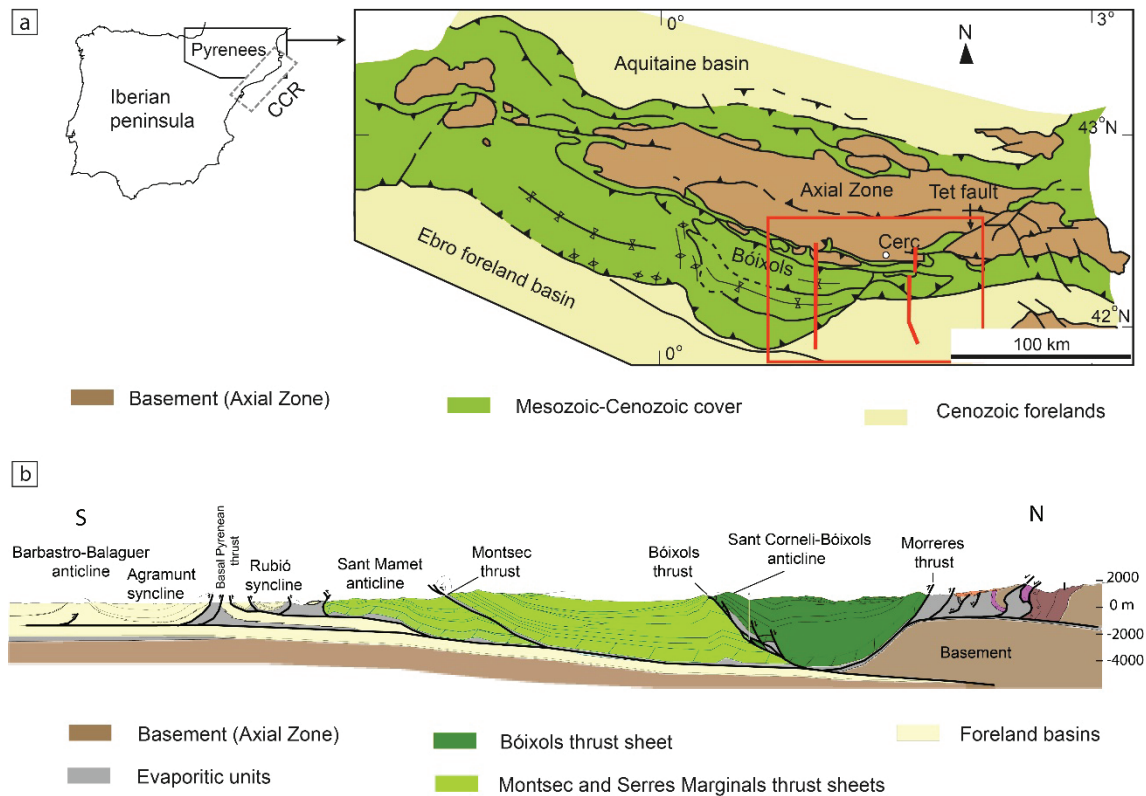


Fig. 1. a) Simplified geological map of the Pyrenees modified from Muñoz (2017) and its localization in the Iberian Peninsula. The red lines represent the trace of cross-section shown in b, and the red square represents the location of Fig. 2. b) Cross-section of the Southern-Central Pyrenees showing the main structural units. Modified from Vergés (1993).

This PhD thesis has been carried out in two different Pyrenean domains, where compressional structures (faults and folds), that developed and/or reactivated during the Alpine compression, are very well exposed and show evidence of synkinematic fracturing and fluid migration. These domains are located in a transect along the Segre River, in the Southern Pyrenees. This transect represents the link between the innermost (Paleozoic basement) and the outermost zones (sedimentary cover) of the Pyrenean belt and involves rocks ranging from the Cambro-Ordovician to the Neogene (Fig. 2). In the Pyrenean Axial Zone, the northern part of this transect, the main thrust faults generating the antiformal stack in the Paleozoic basement do not crop out or do not generate fault scarps, thus preventing the sampling of veins for further petrographic and geochemical analyses, which are the main focus of this PhD thesis. Therefore, the Estamariu thrust was selected because the structural deformation found in the thrust zone, and the age of the involved lithologies, yield relative timing constraints on the thrust evolution and provide the opportunity to sample for further analytical analyses. In the southern limit of this section, the Bóixols thrust sheet is very well exposed, showing the surficial expression of the Sant Corneli-Bóixols anticline along its front. This frontal anticline was selected due to the

excellent exposures of pre- and syn-orogenic rocks involving carbonate and clastic units and the preservation of pre-shortening fractures and syn-orogenic folding and fracturing. Therefore, due to the good quality of outcrops and diversity of structures preserved in the frontal anticline of the Bóixols thrust sheet, this fold will represent a big part of the work carried out in this PhD thesis. The selected structures of these two studied domains are described below (Fig. 2).

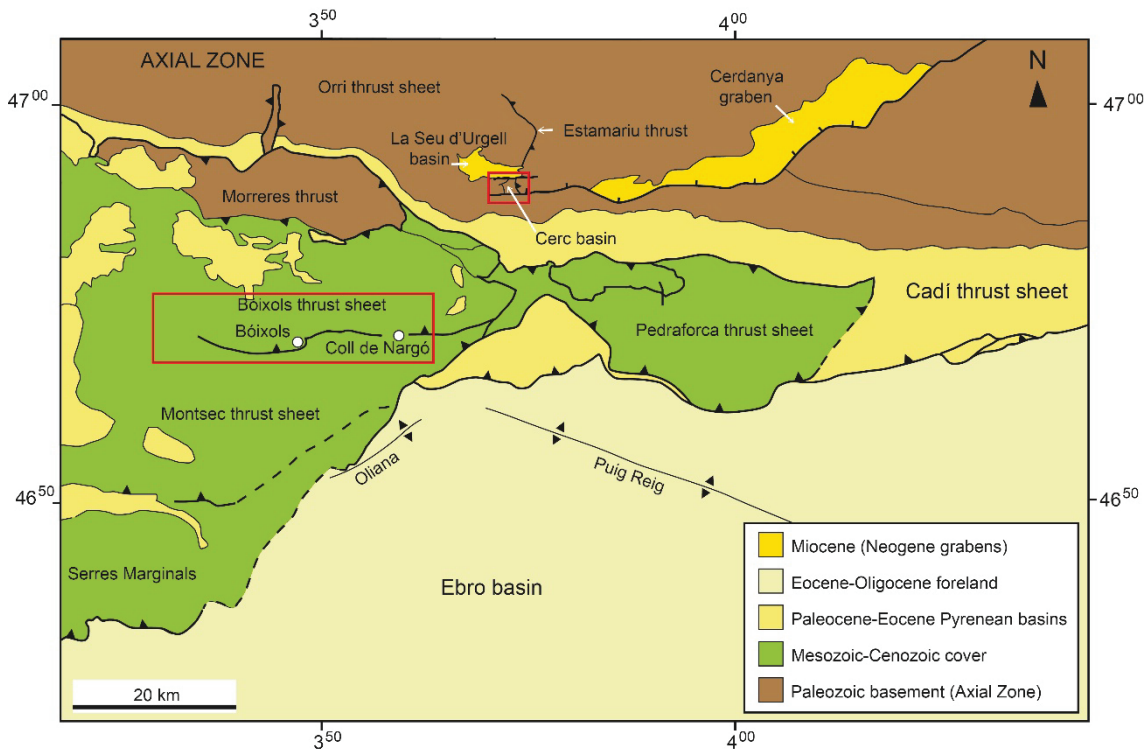


Fig. 2. Geological map of the study area located between the innermost (Paleozoic basement) and the outermost zones (Mesozoic-Cenozoic sedimentary cover) of the Pyrenean belt and involving rocks ranging from the Cambro-Ordovician to the Neogene. Red squares represent the studied structures, which corresponds to the Estamariu thrust and the frontal part of the Bóixols thrust sheet. Modified from Vergés (1993).

2.1. The Estamariu thrust, involving Paleozoic basement rocks from the Orri thrust sheet in the Axial Zone

In the eastern Axial Pyrenees, an E-W to ENE-WSW fault system developed during the Neogene extension (Roca and Guimerà, 1992; Roca, 1996; Vergés et al., 2002). The main fault, La Tet fault, has associated a set of E-W extensional basins such as La Cerdanya, Conflent, La Seu d'Urgell and the Cerc basins (Cabrera et al., 1988; Roca, 1996). The Cerc basin consists of a Stephano-Permian accumulation of volcanic rocks discordantly overlying Cambro-Ordovician materials. This Cerc basin is thrust in its eastern limit by the Estamariu thrust, whereas the northern and southern boundaries correspond to two

Neogene extensional faults, La Seu d'Urgell fault and the Ortedó fault, respectively (Hartevelt, 1970; Roca, 1996; Saura, 2004) (Fig. 3a, b). In the NW part of the Cerc basin, the limit between the Stephano-Permian unit and the Upper Ordovician sequence corresponds to a Stephano-Permian extensional fault formed coevally with the deposition of the volcanic sequence (Saura, 2004). This fault was reactivated during the latest stages of the Neogene extension (Saura, 2004) and is here referred as the Sant Antoni fault.

The Estamariu thrust is a basement-involved thrust fault originated during the Variscan orogeny with a minimum displacement of 27 km (Poblet, 1991). However, in its southwestern termination, it juxtaposes a Devonian sequence (the Rueda Formation) against a Stephano-Permian volcanic unit (the Erill Castell Formation) (Fig. 3). The Erill Castell Formation developed during the late to post-orogenic collapse of the Variscan belt (Martí, 1991, 1996; Ziegler, 1988; Lago et al., 2004). This evidences the reactivation of the Estamariu thrust during the subsequent Alpine orogeny (Poblet, 1991; Saura, 2004).

Rocks cropping out around the Estamariu thrust range from Upper Ordovician to Miocene (Fig. 3). However, due to the complex structural setting, the stratigraphic record is discontinuous and only Upper Ordovician, Devonian, Stephano-Permian and Neogene rocks are present in the study area. The basement lithologies consists of Upper Ordovician and Devonian metasedimentary rocks affected by multiscale folds and related pervasive axial plane regional foliation (Zwart, 1986; Bons, 1988; Casas et al., 1989; Cochelin et al., 2018). This deformation is linked to low-grade metamorphic conditions developed during the Variscan orogeny (Hartevelt, 1970; Poblet, 1991; Saura, 2004). The Upper Ordovician succession includes an alternation of shales, sandstones, conglomerates, quartzites and phyllites, and the Devonian sequence consists of an alternation of limestones and black slates (Rueda Formation) (Mey, 1967). The Stephano-Permian sequence developed during the late to post-orogenic extensional collapse of the Variscan belt and in the study area is represented by a volcanic and volcanoclastic unit (the Erill Castell Formation) (Mey et al., 1968; Martí, 1991), involving tuffs and ignimbrites at the base and andesites in the upper part (Martí, 1996; Saura and Teixell, 2006). Finally, the Neogene sequence is constituted of detrital and poorly lithified sediments, mainly shales, sandstones and conglomerates deposited during the Neogene extension associated with the opening of the NW Mediterranean Sea (Roca, 1996).

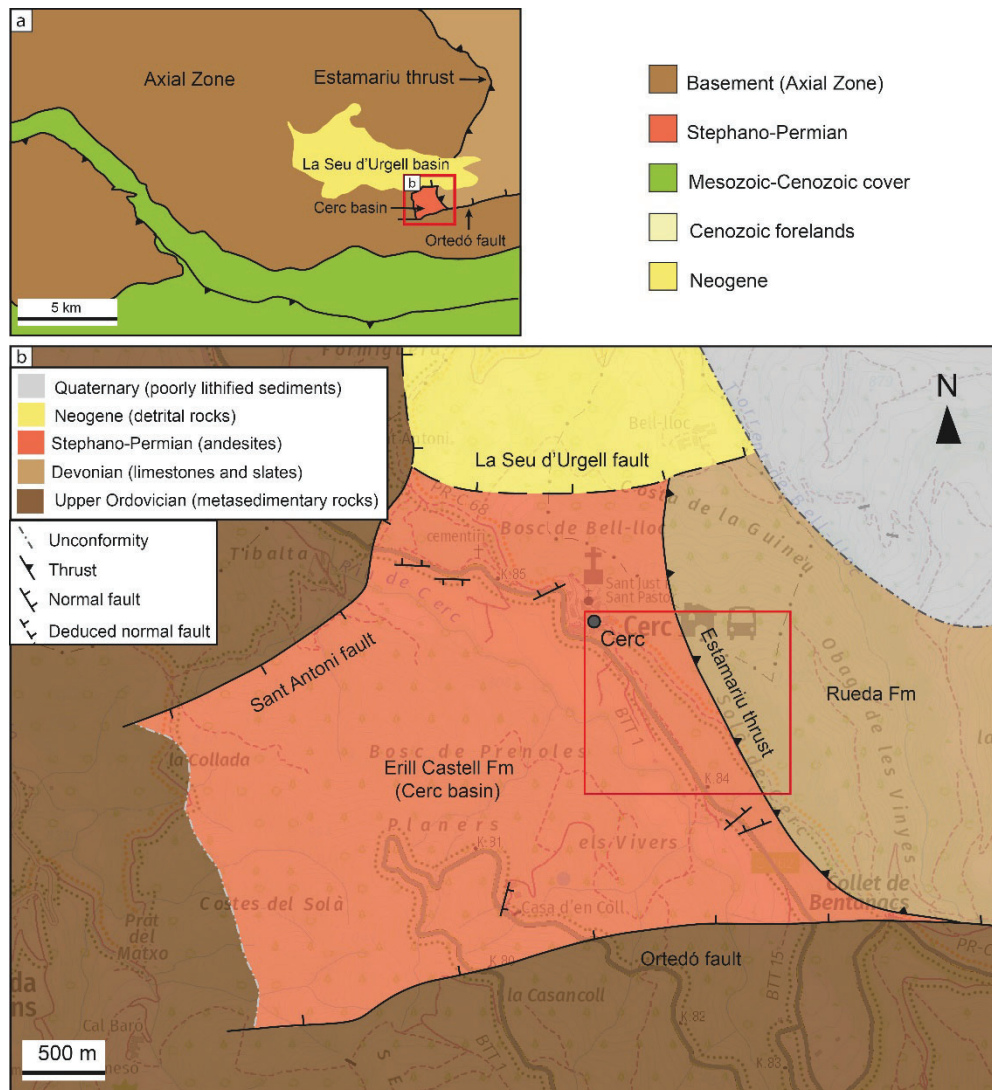


Fig. 3. Simplified geological map of the northern domain studied in this PhD thesis, which is related to the Estamariu thrust. a) Detail of the study area located within the Pyrenean Axial zone. b) Geological map of the Cerc basin (using own data and data from Saura (2004) with the Estamariu thrust located in its eastern termination and the Neogene extensional faults in the northern and southern limits. The red square indicates the location of the main outcrop.

2.2. The Sant Corneli-Bóixols anticline along the front of the Bóixols thrust sheet, involving Mesozoic-Cenozoic cover rocks from the Southern-Central Pyrenean Unit.

The Bóixols thrust sheet is the northernmost and oldest emplaced allochthonous unit in the Southern-Central Pyrenees. This thrust sheet represents the tectonic inversion of the Lower Cretaceous Organyà extensional basin (Berástegui et al., 1990; Vergés, 1993; Bond and McClay, 1995; Garcia-Senz, 2002). The basal thrust of the Bóixols thrust sheet has been interpreted as a footwall shortcut of the pre-existing Lower Cretaceous extensional fault (Mencos et al., 2011). The structure of the Bóixols thrust sheet is composite, formed by the large Santa Fe syncline and the two linked and south-verging

anticlines of Sant Corneli and Bóixols (the Sant Corneli-Bóixols anticline) (Fig. 4). The surficial expression of the Sant Corneli-Bóixols anticline crops out along more than 40 km showing a well-defined geometry in its central-western segment. This geometry is characterized by a gently dipping (around 40°) northern backlimb and a subvertical to overturned southern forelimb. During the inversion and growth of the Sant Corneli-Bóixols anticline, shortening direction has been determined as NNW-SSE, and thus slightly oblique to assumed E-W trending inverted normal fault (Tavani et al., 2011) conditioning the fracture orientation developed during the evolution of this frontal anticline (Shackleton et al., 2011; Tavani et al., 2011).

The Bóixols thrust along the forelimb of the Sant Corneli-Bóixols anticline is well preserved, near the village of Bóixols and in Abella de la Conca village (Fig. 4). Contrarily, around the Coll de Nargó locality, the Bóixols thrust is blind and sealed by syn-orogenic deposits and the southern limb of the Bóixols anticline is cut by decametric to kilometric subvertical strike-slip faults (Fig. 4). The northern limb of the anticline is cut by well-preserved large normal faults beautifully exposed when displacing Upper Cretaceous carbonate sequences in Montagut and Sant Joan localities. These different scale fractures record a significant part of the structural-fluid flow history of the Bóixols thrust sheet preserving both pre-shortening fractures and folding and fracturing during compression.

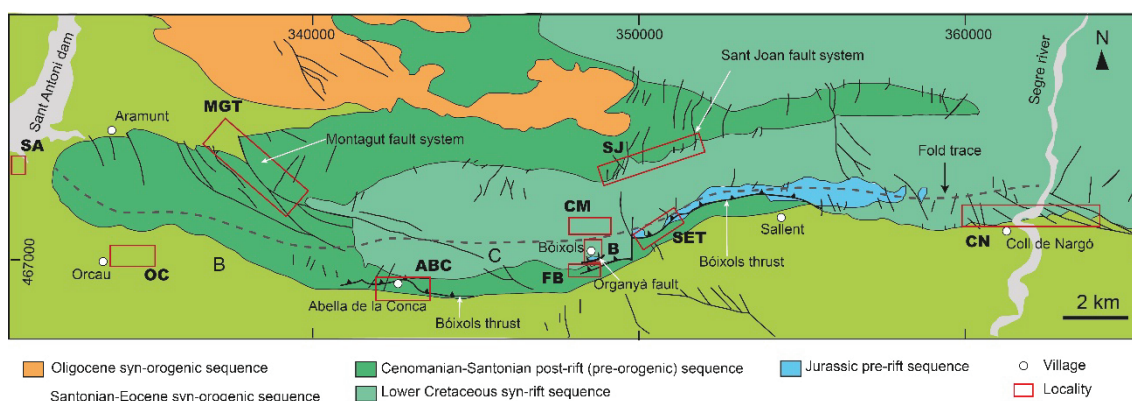


Fig. 4. Simplified geological map (Mencos, 2010; Tavani et al., 2011) of the Sant Corneli-Bóixols anticline, along the front of the Bóixols thrust sheet, showing the studied localities. Location in Fig. 2.

The complete stratigraphic record involved in the Sant Corneli-Bóixols anticline includes Upper Triassic to Upper Cretaceous pre-orogenic rocks and Upper Cretaceous to Paleocene syn-orogenic units (Simó, 1986; Berástegui et al., 1990; Mencos et al., 2015) (Fig. 5). The pre-orogenic sequence includes up to 5 km of pre-rift, syn-rift and post-rift

(pre-orogenic) rocks located in the hanging wall of the Bóixols thrust. The pre-rift sequence crops out discontinuously in the study area (only present next to the trace of the Bóixols thrust) and includes Upper Triassic shales and evaporites, which constitutes the main detachment level in the Pyrenees, and Jurassic dolomitic limestones and dolostones. The thickness of the pre-rift sequence is up to a few thousands of meters (Lanaja, 1987; Mencos et al., 2011). The syn-rift Lower Cretaceous sequence extensively crops out in the core of the anticline (Fig. 5) exhibiting syn-faulting deformation structures and syn-tectonic slump intervals (Tavani et al., 2011). This sequence ranges from a few meters and up to 4000 m thick, and includes an intercalation of basinal marls, marly limestones and limestones (i.e., the Lluçà Formation), whose lower part abruptly evolves to platform limestones (the Setcomelles Member) (Berástegui et al., 1990; Garcia-Senz, 2002).

The upper Cenomanian to lower Santonian post-rift (pre-orogenic) sequence is around 800 m thick and mainly consists of carbonate rocks divided in five sedimentary formations, which in the study area are known as the Santa Fe, the Reguard, the Congost, the Collada Gassó and the Sant Corneli Formations (Gallemí et al., 1982; Simó, 1986; Mencos, 2010).

The Upper Cretaceous to Paleocene syn-orogenic succession comprises three shallowing upward sequences grading from turbidites and marls into shallow marine, fluvial and continental deposits (Mey et al., 1968; Mencos, 2010). These sequences are located in the footwall of the Bóixols thrust and belong to the Vallcarga Formation and to the Areny and the Tremp Groups. The Vallcarga Formation (upper Santonian to middle Campanian) mainly consists of hemipelagic marls. The middle part of this formation consists of a slope-toe chaotic unit (i.e., the Puimanyons Member) developed due to the destabilization of the carbonate platform and characterized by growth faulting and olistostrome resulting from basin margin collapse during the growth of the Sant Corneli-Bóixols anticline (Simó, 1986; Bond and McClay, 1995). The Areny Group (late Campanian to Maastrichtian) deposited coevally with the Bóixols thrust and its related Sant Corneli-Bóixols anticline evolution (Bond and McClay, 1995; Mencos et al., 2011; Robert et al., 2018). This sequence mainly consists of shallow marine to coastal deposits. Finally, the Maastrichtian to Paleocene Tremp Group (i.e., Garumnian facies) includes alluvial, fluvial, lacustrine and carbonate deposits.

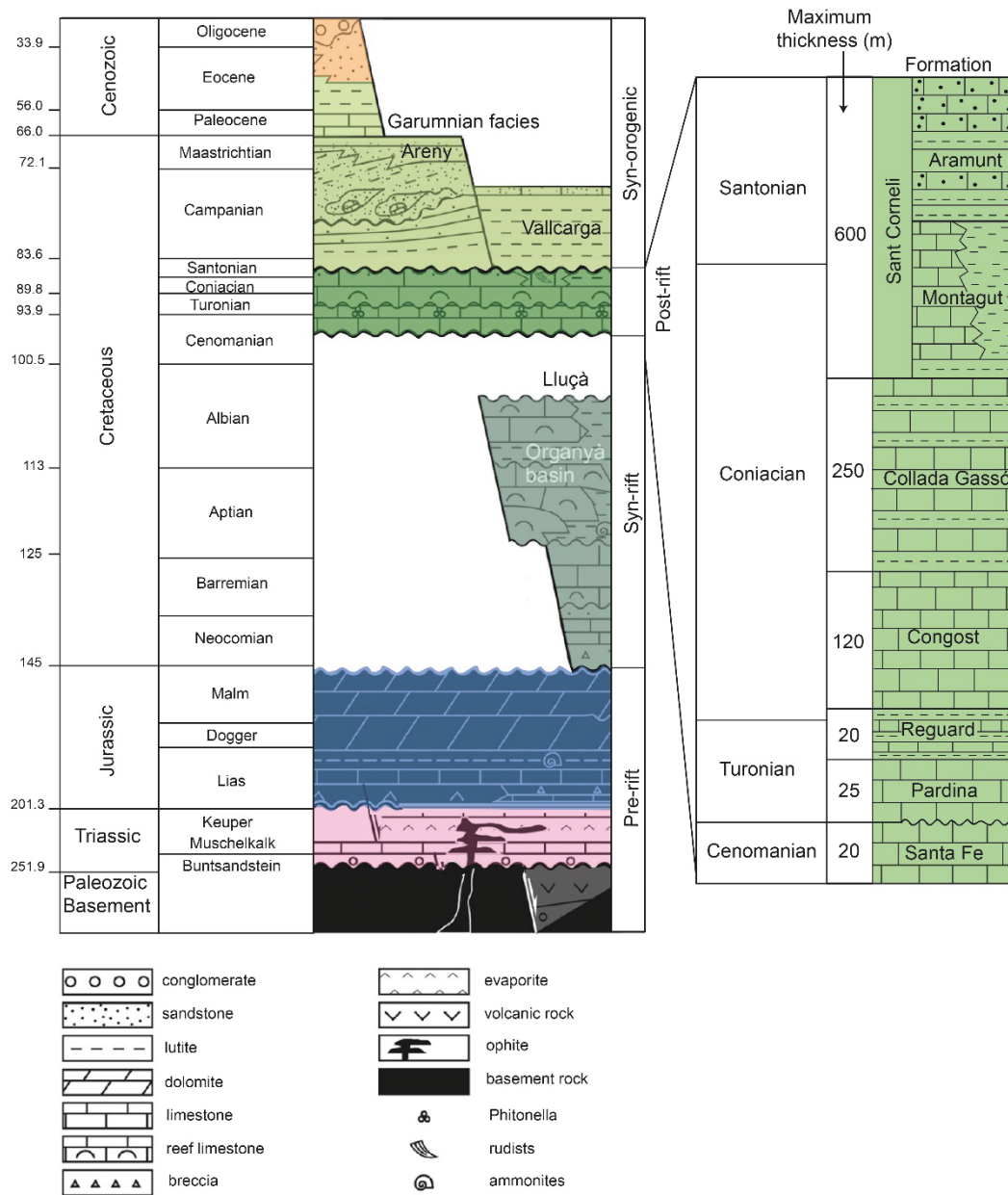


Fig. 5. Chronostratigraphic diagram displaying the main stratigraphic sequences found around the Sant Corneli-Bóixols anticline and their associated tectonic event (Mencos et al., 2015).

3. METHODOLOGY

The adopted approach, followed to reach the proposed objectives, includes field work (compilation of structural data and samples), petrographic observations under optical and cathodoluminescence (CL) microscopes, geochemical analyses (stable and radiogenic isotopes, clumped isotope thermometry, and elemental composition) and U-Pb geochronology. The initial research stage consisted in the creation of a bibliographic dataset, mainly including geological maps and cross-sections performed in the study area as well as compilation of similar studies carried out in the Pyrenees and in similar worldwide geological settings.

Extensive field work was carried out mainly during the early research stages (and also during synthesis of results and final discussions) in a Pyrenean transect located at the transition between the innermost and outermost zones of the belt, in order to select appropriate outcrops (structures) to apply the proposed methodology. In this study area, including the Estamariu thrust and the Bóixols thrust sheet, different outcrops were selected in order to characterize the entire fractures-fluid interactions in each selected structure. In each selected outcrop, fieldwork consisted of the characterization of the structural/stratigraphic setting and the timing relationships between different fracture networks (including extensional fractures, faults, etc) and stylolites. Data related to bedding orientation and dip were also collected. Representative samples of veins, fault rocks and host rocks were carefully oriented in the field (for their further reorientation in the lab, if needed) and sampled for the following petrographic and geochemical analyses. Hand samples collected in the field includes around 250 specimens.

The structural data were plotted in equal-area lower-hemisphere projections with the software Win-Tensor in order to establish different fracture sets according to their type, orientation, mineral infillings, and the relative/absolute age. These data were used to reconstruct the successive deformation and fracturing events occurred in the study area and to constrain their relation to the main regional tectonic phases reported in the Pyrenees.

Thin sections of samples were prepared and studied under a Zeiss Axiophot optical microscope and a cold cathodoluminescence (CL) microscope model 8200 Mk5-1 operating between 16–19 kV and 350 μ A gun current. Geochemical analyses consisted of carbon,

oxygen and strontium isotopes, clumped isotope thermometry, elemental composition, and U-Pb geochronology.

The U-Pb geochronology has been previously described in (Ring and Gerdes, 2016; Burisch et al., 2017). U-Pb ages were obtained with a laser ablation-inductively coupled plasma mass spectrometry (LA-ICPMS) at FIERCE (Frankfurt Isotope and Element Research Center, Goethe University), following a modified method of (Gerdes and Zeh, 2009, 2006). A Thermo Scientific Element XR sector field ICPMS was coupled to a RESOLUTION 193nm ArF excimer laser (COMPexPro 102) equipped with a two-volume ablation cell (Laurin Technic S155). Samples were firstly ablated in a helium atmosphere (300 mL/min) and then mixed in the ablation funnel with 1100 mL/min argon and 5 mL/min nitrogen. Signal strength at the ICP-MS was tuned for maximum sensitivity but keeping the oxide formation (monitored as $^{248}\text{ThO}/^{232}\text{Th}$) below 0.2% and low fractionation of the Th/U ratio. Static ablation used a spot size of 193 μm and a fluency of about 2 J/cm^2 at 12 Hz.

Data were obtained in fully automated mode overnight in two sequences of 598 analyses each one. Each analysis comprised 18 s of background acquisition, 18 s of sample ablation, and 25 s of washout. During 36 s of data acquisition, the signal of ^{206}Pb , ^{207}Pb , ^{208}Pb , ^{232}Th , and ^{238}U was detected by peak jumping in pulse-counting and analogue mode with a total integration time of ~0.1s, resulting in 360 mass scans. Each spot was pre-ablated with 8 laser pulses to remove surface contamination before analysis. Soda-lime glass NIST SRM-612 was used as primary reference material (spot size of 50 μm , 8 Hz) together with four carbonate reference materials, which were bracketed in between the analysis of samples.

Raw data were corrected offline with an in-house VBA spreadsheet program (Gerdes and Zeh, 2009, 2006). Following background correction, outliers ($\pm 2\sigma$) were rejected based on the time-resolved $^{207}\text{Pb}/^{206}\text{Pb}$, $^{208}\text{Pb}/^{206}\text{Pb}$, $^{206}\text{Pb}/^{238}\text{U}$, and $^{232}\text{Th}/^{238}\text{U}$ ratios. Such ratios were corrected for mass biases and drift over time, using NIST SRM-612. An additional matrix related offset was applied on the $^{206}\text{Pb}/^{238}\text{U}$ ratios (sequence 1: 21.5%, sequence 2: 19.6%) that was determined using WC-1 carbonate reference material (Roberts et al., 2017). The $^{206}\text{Pb}/^{238}\text{U}$ downhole-fractionation was estimated to be 3%, based on the common Pb corrected WC-1 analyses, and was applied to all carbonate analyses. Uncertainties for each isotopic ratio are the quadratic addition of the within run precision, counting statistic uncertainties, excess of scatter (calculated from NIST SRM-612) and

the excess of variance (calculated from WC-1) after drift correction (Horstwood et al., 2016). The systematic uncertainties considered are the decay constants uncertainties and the long-term reproducibility of the method (1.5%, 2σ , calculated from repeated measurements ($n = 7$) of ASH-15D between 2017 and 2019).

Carbonate reference materials were measured for quality control. Reference material B6 (41.86 ± 0.53 Ma and 42.12 ± 0.88 Ma) (Pagel et al., 2018) was measured in sequences 1 and 2, whereas reference material ASH-15D (2.907 ± 0.210 Ma) (Nuriel et al., 2021) was measured in sequence 1. Results on the secondary reference materials indicate an accuracy and repeatability of the method of about 1.5 to 2%. Data were displayed in Tera-Wasserburg plots, and ages were calculated as lower concordia-curve intercepts using the same algorithms as Isoplot 4.14 (Ludwig, 2012). All uncertainties are reported at the 2σ level.

The performed geochemical analyses consist of stable and radiogenic isotopes as well as the elemental composition of vein cements and host rocks. 190 samples were prepared for carbon and oxygen isotopes. Between 50 and 100 μm of each powdered sample was reacted with 100% phosphoric acid at 70 °C for 2 minutes. The resultant CO_2 was analyzed following the method of (McCrea, 1950) and using an automated Kiel Carbonate Device attached to a Thermal Ionization Mass Spectrometer Thermo Electron MAT-252 (Thermo Fisher Scientific). For calibration, the internal standard RC-1, traceable to the International Standard NBS-19, and the International Standard NBS-18 have been employed. Results are expressed in ‰ with respect to the Vienna Pee Dee Belemnite (VPDB). Standard deviation is ± 0.05 ‰ for $\delta^{18}\text{O}$ and ± 0.03 ‰ for $\delta^{13}\text{C}$.

Clumped isotope thermometry was applied to representative samples of calcite cements in order to determine the temperature and $\delta^{18}\text{O}_{\text{fluid}}$ in ‰ VSMOW of the vein-forming fluids. Around 2 – 3 mg aliquots of powdered calcite cements were measured with an automated line developed at Imperial College London (the Imperial Batch Extraction system, IBEX). Samples were dropped in 105% phosphoric acid at 90 °C and reacted for 30 minutes. The reactant CO_2 was separated with a poropak-Q column and transferred into the bellows of a Thermo Scientific MAT 253 mass spectrometer. The characterization of a single replicate consisted of 8 acquisitions in dual inlet mode with 7 cycles per acquisition. The total time of analysis per replicate is ~ 2 hours, and each sample was replicated at least 3 times. The post-acquisition processing was completed with a software for clumped isotope analyses (Easotope) (John and Bowen, 2016). During

phosphoric acid digestion, Δ_{47} values were corrected for isotope fractionation with a phosphoric acid correction of 0.069‰ at 90 °C for calcite (Guo et al., 2009). The data were also corrected for non-linearity applying the heated gas method (Huntington et al., 2009) and projected into the reference frame of Dennis et al. (2011). Carbonate $\delta^{18}\text{O}$ values were calculated with the acid fractionation factors of Kim and O’Neil (1997). Results were converted to temperatures applying the calibration method of Kluge et al. (2015). Calculated $\delta^{18}\text{O}_{\text{fluid}}$ values are expressed in ‰ with respect to the Vienna Standard Mean Ocean Water (VSMOW).

For $^{87}\text{Sr}/^{86}\text{Sr}$ ratios, 50 samples of powdered calcite cements and host rock have been analyzed. These samples have been dissolved in 5 mL of 10% acetic acid and then centrifuged. The supernatant was dried and dissolved in 1 mL of 1M HNO_3 . The solid residue, resulted after evaporation, was diluted in 3 mL of 3M HNO_3 and then loaded into chromatographic columns to separate the Rb-free Sr fraction, using SrResinTM (crown-ether (4,4’(5’)-di-t-butylcyclohexano-18-crown-6)) and 0.05M HNO_3 as eluent. After evaporation, samples were loaded onto a Re filament with 2 μL of Ta_2O_5 and 1 μL of 1 M phosphoric acid. Analyses of isotopic ratios have been performed in a TIMS-Phoenix mass spectrometer (Isotopx) according to a dynamic multicollection method, during 10 blocks of 16 cycles each one, maintaining a ^{88}Sr beam intensity of 3-V. Obtained ratios have been corrected for ^{87}Rb interferences and normalized with a $^{88}\text{Sr}/^{86}\text{Sr} = 0.1194$ reference value, aiming at correcting possible mass fractionation during sample loading and analysis. The isotopic standard NBS-987 has been analyzed 6 times, yielding an average value of 0.710243 ± 0.000009 (standard deviation, 2σ). NBS 987 data have been used to correct the sample ratios for standard drift from the certified value. The analytical error in the $^{87}\text{Sr}/^{86}\text{Sr}$ ratio was 0.01% (referred to two standard deviations). The internal precision is 0.000003. Sr procedural blanks were below 0.5 ng.

To determine the elemental composition of calcite cements and host rocks, 81 samples were analyzed employing a magnetic sector field Element XR (HR-ICP-MS, high resolution inductively coupled plasma-mass spectrometer, Thermo Fisher Scientific). In this case, the LR (low resolution) and the MR (medium resolution) have only been used. 100 mg of each powdered sample was firstly dried at 40 °C during 24h and then acid digested in closed polytetrafluoroethylene (PTFE) vessels with a combination of $\text{HNO}_3 + \text{HF} + \text{HClO}_4$ (2.5mL: 5mL: 2.5mL v/v). Samples have been evaporated and, to make a double evaporation, 1 mL of HNO_3 was added. Then, samples have been re-

dissolved and diluted with MilliQ water ($18.2 \text{ M}\Omega \text{ cm}^{-1}$) and 1 mL of HNO_3 in a 100 mL volume flask. A tuning solution of $1 \mu\text{g L}^{-1}$ Li, B, Na, K, Sc, Fe, Co, Cu, Ga, Y, Rh, In, Ba, Tl, U was employed to improve the sensitivity of the ICP-MS and 20 mg L^{-1} of a monoelemental solution of ^{115}In were used as internal standard. Reference materials are the BCS-CRM n° 393 (ECRM 752-1) limestone, JA-2 andesite and JB-3 basalt. Precision of results is expressed in terms of two standard deviations of a set of eight reference materials measurements (reference material JA-2). Accuracy (%) has been calculated employing the absolute value of the difference between the measured values obtained during the analysis and the certified values of a set of eight reference material analysis (reference material BCS-CRM n° 393 for major oxides and JA-2 for trace elements). The DL (detection limit) has been calculated as three times the standard deviation of the average of ten blanks.

The integration of the structural, petrographic, geochemical and geochronological analyses in each studied structure allowed constraining a structural and diagenetic framework that assesses the fluid migration and deformation relationships in different Alpine-related structures developed at different stages of the belt evolution. The correlation of the obtained field and analytical data with other structures developed both in the Pyrenees and in other worldwide fold-and-thrust belts have allowed to provide insights into the dynamic of fluid flow during deformation at regional scale.

4. RESULTS

4.1. Studied domains

The studied domains, the Estamariu thrust and the frontal anticline of the Bóixols thrust sheet, were selected to examine the evolution of fractures-fluid flow interactions in different Pyrenean structures. The Estamariu thrust has been selected to characterize the migration of fluids in a long-lived fault that involves basement rocks and that has been successively reactivated during different events of regional tectonism. The frontal part of the Bóixols thrust sheet has been selected to characterize the paleohydrological system in two different structures, in a well-exposed thrust displacing the southern limb of the Sant Corneli-Bóixols anticline, and in the whole structure of the Sant Corneli-Bóixols anticline, covering the different structural and stratigraphic positions of the fold.

In these two domains, the sampling localities were chosen according to their structural position, the involved lithologies and the quality of their associated outcrops. The Estamariu thrust has been studied in one locality. By contrast, the frontal anticline of the Bóixols thrust sheet has been studied in ten localities due to the good exposure of this fold along strike and considering its heterogeneous distribution of faults and fracture system (as it will be explained in the following sections). The main characteristics of these localities are described below.

The Cerc locality (C), which corresponds to the northern studied domain in this thesis, is located around the Cerc village (Fig. 6a, b). In this area, the NNW-SSE Estamariu thrust is well-exposed juxtaposing Devonian carbonates against Stephano-Permian andesites belonging to the Cerc basin. Additionally, in this area the Estamariu thrust predates E-W extensional faults such as the Ortedó fault and La Seu d'Urgell fault that have previously been attributed to the Neogene extension (Hartevelt, 1970; Roca, 1996; Saura, 2004).

The Bóixols locality (B) is located closed to the Bóixols village, next to the axial surface of the anticline (Fig. 7a). In this locality, the upper part of the main E-W early Cretaceous extensional fault has been preserved affecting Lower Cretaceous limestones and marls (the syn-rift sequence) in the hanging wall and Jurassic dolomitic limestones (the pre-rift succession) from the footwall (Berástegui et al., 1990; Garcia-Senz, 2002).

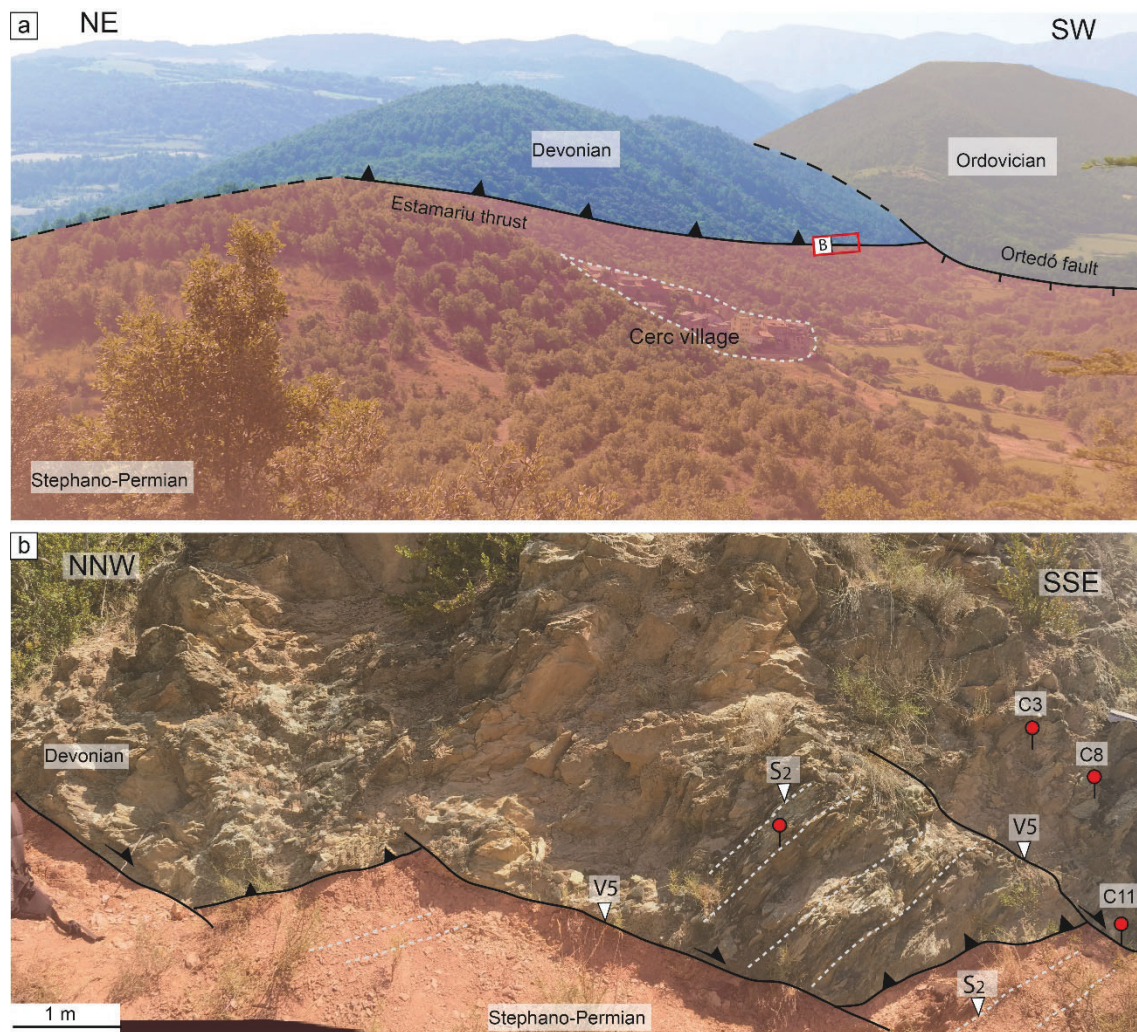


Fig. 6. Main outcrop of the Estamariu thrust in the Cerc locality (C). a) Panoramic view from the Sant Antoni hill showing the extensional Ortedó fault postdating the Estamariu thrust. b) Main outcrop showing the Estamariu thrust and the related thrust zone foliation developed in the Devonian hanging wall and in the Stephano-Permian footwall (S_2). The thrust is displaced by later shear fractures locally mineralized with calcite (V5).

The Cal Mestre locality (CM) is located 0.5 km to the northeast of the Bóixols village, in the core of the Bóixols anticline. In this area, the Lower Cretaceous limestones and marls from the syn-rift sequence are broadly exposed exhibiting a minimum thickness of 2500 m according to well data (Lanaja, 1987).

The Montagut (MGT) and the Sant Joan (SJ) localities are located in the northern limb of the Sant Corneli-Bóixols anticline, affecting Upper Cretaceous limestones from the post-rift (pre-orogenic) sequence. The structure of the Montagut locality consists of a relatively well exposed system of normal and strike-slip faults with a lateral continuity of several kilometers (Fig. 7b) (i.e., the Montagut fault system). The structure of the Sant Joan locality consists of two conjugate sets of strike-slip faults and a set of normal faults (Fig. 7c).

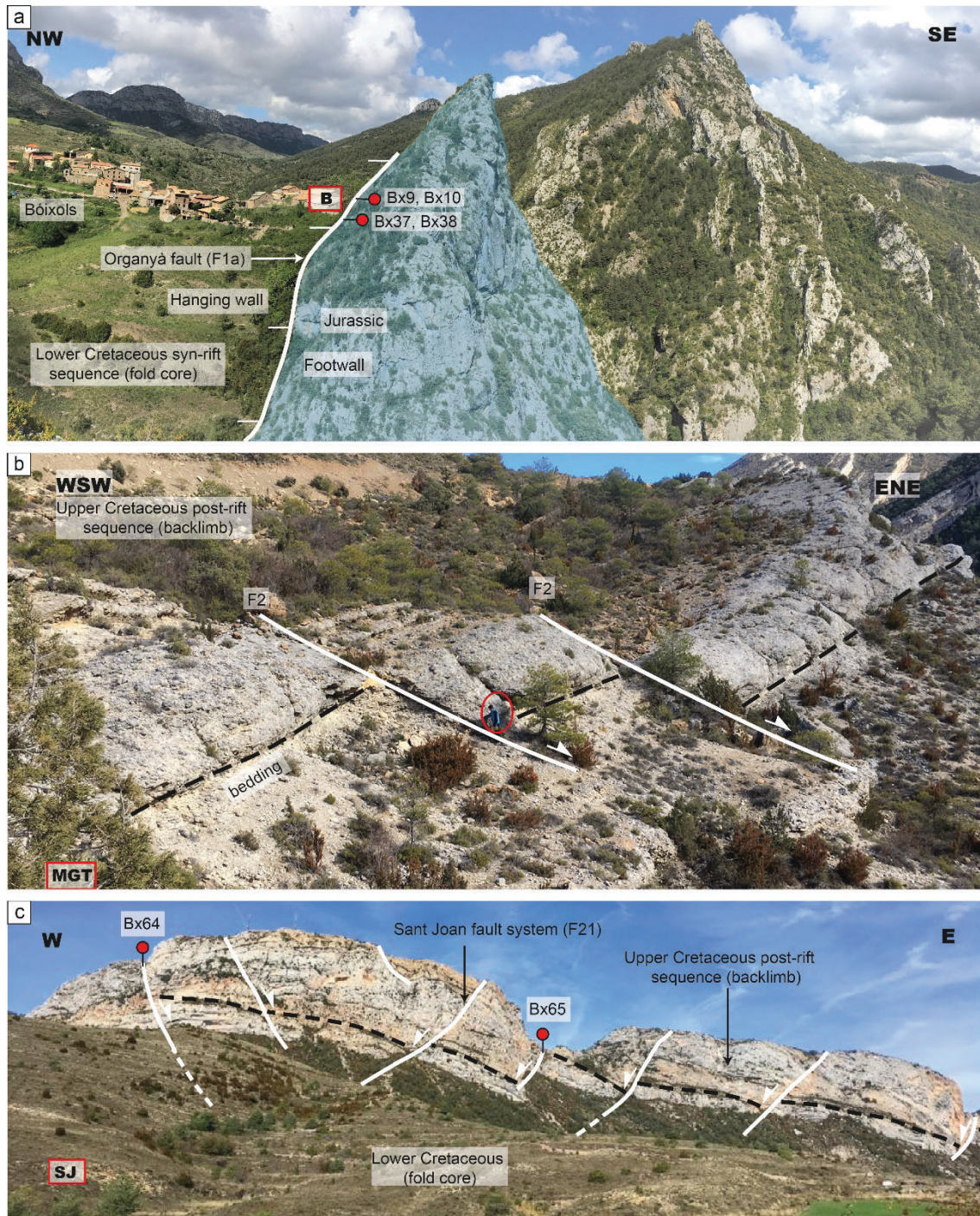


Fig. 7. Field images showing the main features of Bóixols, Montagut and Sant Joan localities. a) Bóixols locality (B) showing the main E-W extensional fault (the Organyà fault, F1a), which juxtaposes the Jurassic sequence (in the footwall) and the Lower Cretaceous unit (in the hanging wall). b) Montagut locality showing NNW-SSE extensional faults (F2) affecting the Upper Cretaceous sequence in the backlimb of the Sant Corneli-Bóixols anticline. c) Sant Joan locality showing the main NNE-SSW extensional faults (F21) also affecting the Upper Cretaceous sequence in the backlimb. Red circles indicate sample location.

The remaining localities are located along the frontal region of the Bóixols thrust sheet, and include fractures that cut pre-orogenic depositional units from the southern limb of the Sant Corneli-Bóixols anticline and syn-orogenic units deposited in the footwall of the Bóixols thrust sheet. The Bóixols thrust has been studied in Abella de la Conca (ABC),

Forat de Bóixols (FB) and Setcomelles (SET) localities (Figs 8a-c). In Abella de la Conca and Forat de Bóixols localities, the E-W trending and north-dipping Bóixols thrust offsets subvertical post-rift Upper Cretaceous limestones along the southern limb of the Sant Corneli-Bóixols anticline. The Abella de la Conca locality also includes a reduced Upper Cretaceous syn-orogenic sequence. The Forat de Bóixols locality, located 2 km southwest of the Bóixols village, preserves a good exposure that allows to study the evolution of fractures across the Bóixols thrust zone (Fig. 8b). In the Setcomelles locality, between Bóixols and Sallent villages, the Bóixols thrust is interpreted as a footwall shortcut of the previous Lower Cretaceous Organyà fault. In this area, Jurassic dolomitized limestones juxtapose against Upper Cretaceous limestones (Garcia-Senz, 2002) (Fig. 8c).

The Sant Antoni (SA), Orcau (OC) and Coll de Nargó (CN) localities are aligned along the footwall of the Bóixols thrust, involving Upper Cretaceous to Paleocene syn-orogenic sequences showing growth strata patterns (Garrido-Megías and Ríos, 1972; Vergés and Muñoz, 1990; Bond and McClay, 1995; Mencos et al., 2011; Tavani et al., 2017). The Sant Antoni locality, next to the Sant Antoni dam, comprises the lowest part of the syn-orogenic sequence integrated in the Vallcarga Formation. The Orcau locality, next to the Orcau village, constitutes the middle part of the syn-orogenic unit integrated in the Areny Group. Finally, the Coll de Nargó locality, near the Coll the Nargó village, involves the upper part of the syn-orogenic sequence integrated within the Garumnian facies from the Tremp Group. In this area, the Bóixols thrust is buried and the syn-orogenic deposits are deposited in angular discordance on the front of the anticline.

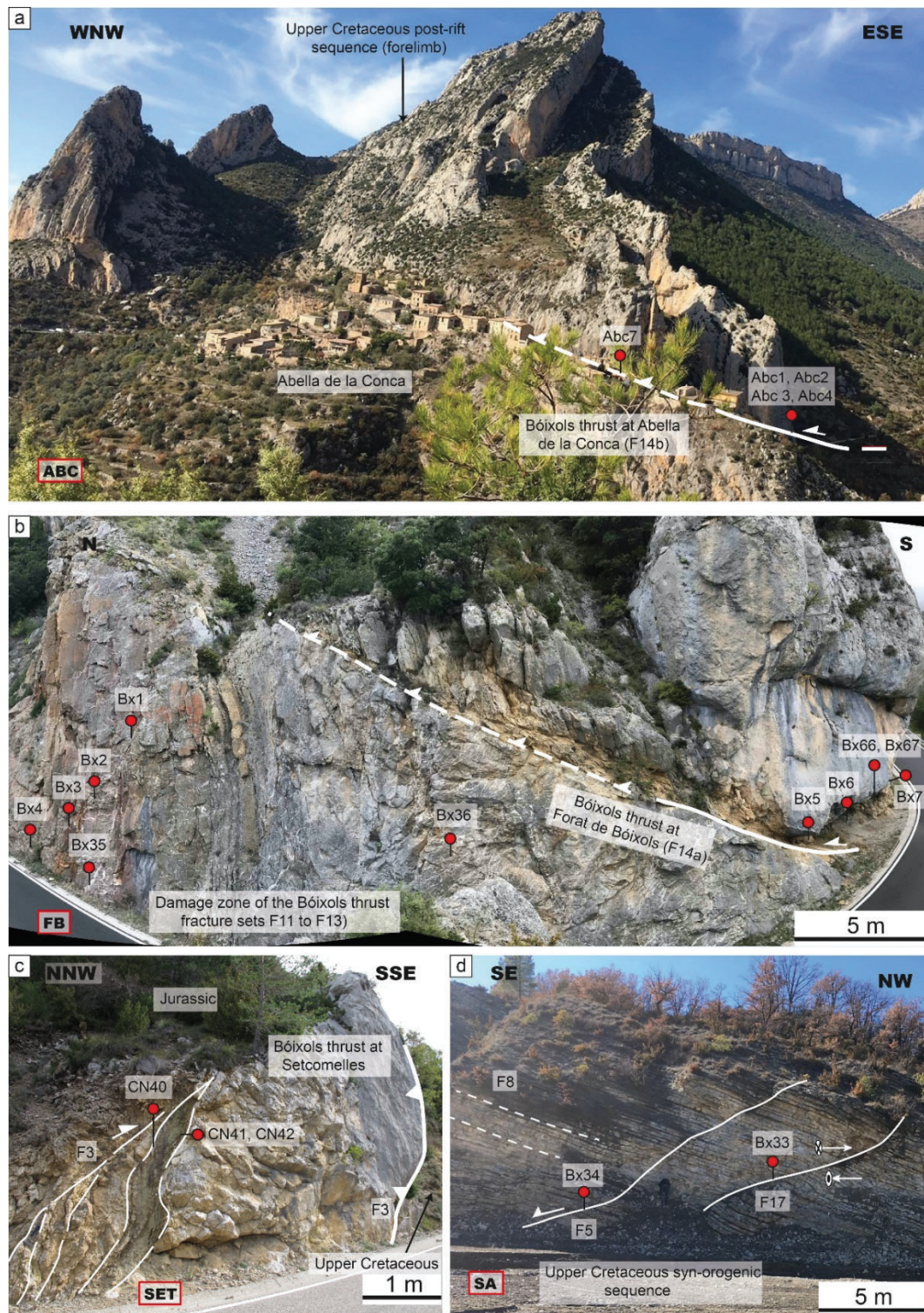


Fig. 8. Field images showing the main features of Abella de la Conca (ABC), Forat de Bóixols (FB), Setcomelles (SET) and Sant Antoni (SA) localities. a) The Bóixols thrust in the Abella de la Conca locality offsetting the steeply dipping Upper Cretaceous sequence located in the forelimb of the Sant Corneli-Bóixols anticline. b) The Bóixols thrust in the Forat de Bóixols locality showing a well exposed thrust zone that also displaces the southern limb of the anticline. c) The Bóixols thrust in the Setcomelles locality juxtaposing Jurassic dolomitized limestones in its hanging wall with Upper Cretaceous limestones in its footwall. d) Main structural features of Sant Antoni locality showing normal faults (F5b), bed-parallel slip surfaces (F8) and strike-slip faults (F17) affecting the base of the syn-orogenic sequence located in the footwall of the Bóixols thrust sheet. Red circles indicate sample location.

4.2. Petrographic features of host rocks

This section summarizes the main petrographic characteristics of the involved host rocks. The **Estamariu thrust** includes the Devonian Rueda Formation from the hanging wall and the Stephano-Permian Erill Castell Formation from the footwall. The Rueda Formation is characterized by a well-bedded alternation of dark to light grey limestones with subordinate dark grey shales. This unit is affected by a pervasive NNW-SSE regional foliation (S_1) concentrated in the pelitic intervals. Limestones are made up of encrinites, which consist of a bioclastic packstone formed essentially of crinoid stems (Fig. 9a) and characterized by dark to bright orange luminescence (Fig. 9b). Encrinites are affected by stylolites (e1) and veins (V0) that will be explained in the following section 4.3 (Fig. 9c).

In the footwall of the Estamariu thrust, the Erill Castell Formation comprises massive, dark greenish andesitic levels showing a rhythmic magmatic layering, which corresponds to a fluidal structure of the host rock. The local presence of pyroclastic and brecciated volcanoclastic levels is also ubiquitous, mainly in the lower part of this sequence. Andesites are characterized by a porphyritic texture (Fig. 9d, e) defined by a dark fine-grained spherulitic matrix partially devitrified, large zoned crystals of plagioclase up to 2–3 cm long, and less abundant biotite and hornblende. These mafic phenocrystals are systematically pseudomorphosed by clay minerals and frequently show evidence of oxidation and chloritization.

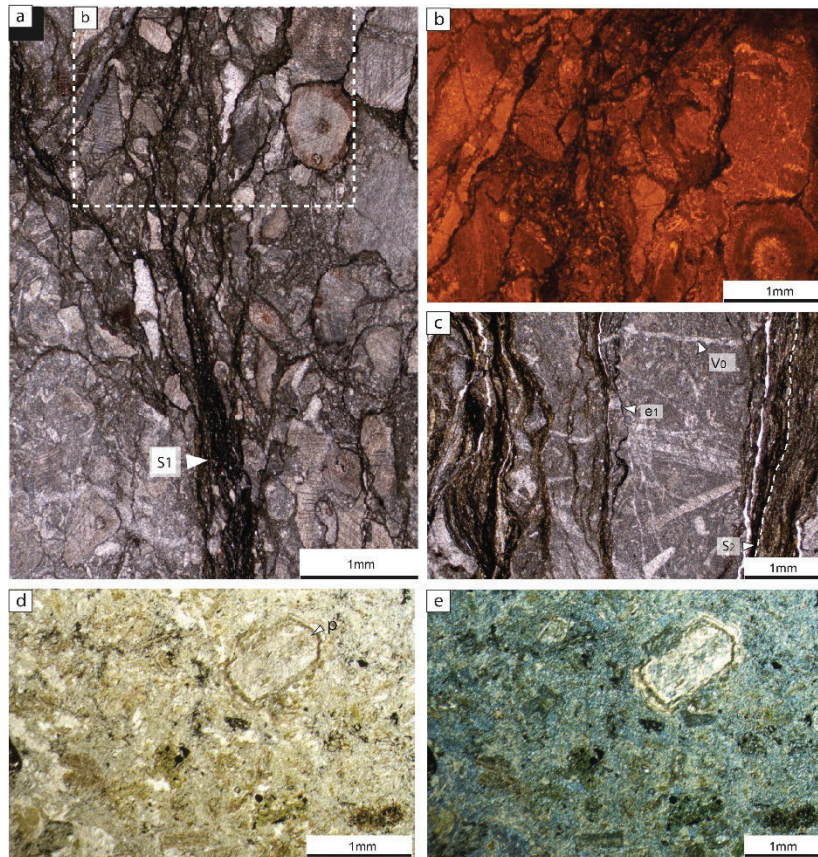


Fig. 9. Microphotographs showing the main petrographic characteristics of the studied host rocks in the Estamariu domain. a) and b) paired optical and CL microphotographs of encrinites from the Devonian Rueda Formation alternating with pelitic rich bands, where the regional foliation [S_1] is concentrated, and showing a dark orange luminescence. c) Encrinites affected by Veins V0 and stylolites e1. d) and e) Andesites from the Stephano-Permian Erill Castell Formation exhibiting a porphyritic texture with large plagioclase crystals [p].

In the **Sant Corneli-Bóixols anticline**, the syn-rift Lower Cretaceous Lluçà Formation, made up of mudstones with isolated sponge spicules and agglutinated foraminifera (Fig. 10a), features a dark brown to non-luminescence (Fig. 10b). The lower part of the Lluçà Fm (the Setcomelles Member) is formed of wackestones, locally packstones, made up of corals, red algae (*Agardhiellopsis cretacea*), echinoderms, bryozoans and foraminifera. The moldic porosity is filled with micrite sediment with a geopetal distribution, which indicates vadose environment, and the remanent intraparticle porosity is filled by calcite cement (Fig. 10c). The micrite matrix exhibits a brown to dark orange luminescence, whereas the intraparticle micrite sediment shows an orange luminescence and the cement has a non- to bright yellow zonation (Fig. 10d).

The Upper Cretaceous post-rift (pre-orogenic) sequence includes five sedimentary formations, which are known as the Santa Fe, the Reguard, the Congost, the Collada Gassó and the Sant Corneli Formations. The Santa Fe Fm. includes wackestones, locally

packstones with calcispheres and planktonic foraminifera. Under cathodoluminescence, it exhibits a very dark orange color. The Reguard Fm. consists of mudstones, locally wackestones, made up of foraminifera (mainly miliolids) and showing a dark brown luminescence. The Congost Fm. is made up of packstones, locally grainstones formed of bivalves, foraminifera, echinoderms, corals, bryozoans and partially to totally micritized components (i.e., peloids). The micritic matrix as well as the inter- and intraparticle calcite cement is dark brown to non-luminescent. The Collada Gassó Fm. is formed of grainstones made up of gastropods, bivalves, echinoids, corals, bryozoans, miliolids, peloids, and locally quartz grains (Fig. 10e). The inter- and intraparticle porosity is cemented by calcite cement, which exhibits a bright yellow luminescence, whereas the skeletal components display a dull to bright brown luminescence (Fig. 10f). The Sant Corneli Fm. is divided in two members (the Montagut Mb and the Aramunt Vell Mb). The Montagut Mb. consists of peloidal wackestones to packstones with abundant presence of rudists, miliolids, corals, equinoderms and local quartz detrital components. Under cathodoluminescence, these packstones exhibit a dark to bright brown color. The Aramunt Vell Mb. consists of bioclastic grainstones with variable quartz content and abundant presence of miliolids, bryozoans, equinoderms and bivalves. The interparticle calcite cement displays a dark orange luminescence.

The Upper Cretaceous to Paleocene syn-orogenic successions include the Vallcarga Formation, the Areny Group and the Tremp Group (Garumnian facies). The Vallcarga Formation consists of mudstones that are brown to non-luminescent (Figs 10g-h). The Areny Group, in the study localities, is composed of grainstones made up of peloids, local bryozoans and miliolids, and upward increasing detrital quartz content. The interparticle calcite cement is bright yellow luminescent. The Tremp Group (i.e., Garumnian facies) is constituted of fluvial-alluvial and lacustrine detrital and carbonate rocks. Detrital units include versicolored clays with abundant *Microcodium*, fine-grained sandstones and polymictic conglomerates. Carbonate units include red nodular mudstones, grey wackestones with charophytes and oncolytic packstones.

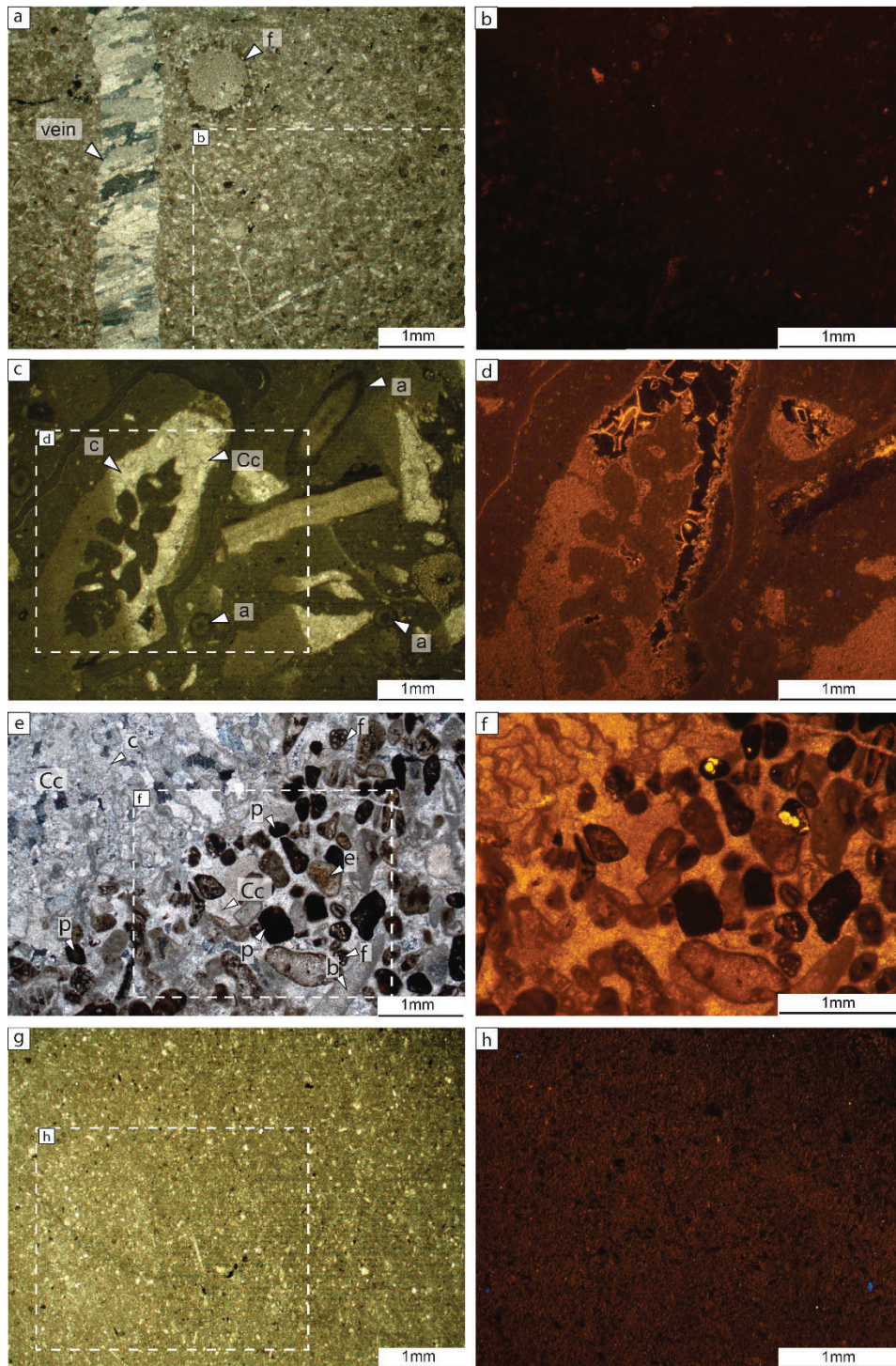


Fig. 10. Paired optical and CL microphotographs showing the main petrographic characteristics of the studied host rocks in the Bóixols domain. a) and b) Mudstones from the Lower Cretaceous Lluçà Fm. with an isolated agglutinated foraminifera [f] and featuring a dark brown luminescence. c) and d) Wackestones to packstones from the Lower Cretaceous Setcomelles Mb made up of corals [c], red algae [a], presence of micritic sediment filling moldic porosity with a geopetal distribution and calcite cement [Cc] filling the rest of the intraparticle porosity. The micritic matrix has a brown to dark orange luminescence, the intraparticle micrite sediment has an orange luminescent and the intraparticle cement is zoned, varying from a non-luminescence to bright yellow. e) and f) Grainstones from the Upper Cretaceous Collada Gassó, which are made of corals [c], foraminifers [f], bivalves [b], echinoids [e], and peloids [p], cemented by calcite [Cc] and showing a bright yellow luminescence. g) and h) Mudstones from the Vallcarga Fm. featuring a brown luminescence.

4.3. Structural analysis

The Estamariu thrust

The Estamariu thrust strikes N-S to NW-SE and dips between 40 and 70° towards the NE. It has a displacement of a few hundred meters and juxtaposes a Devonian alternation of limestones and shales in the hanging wall against Stephano-Permian andesites in the footwall (Poblet, 1991). The main slip plane is undulose and generates a 2 – 3 m thick thrust zone affecting both the hanging wall and footwall, but it is thicker in the hanging wall, up to 2.5 m thick. In the footwall the thrust zone is less than 1 m thick and has associated minor restricted thrust zones developed as subsidiary accommodation structures related to the main thrust fault. Most kinematic indicators, including S-C structures and slickenlines, indicate reverse displacement.

The mesostructures and microstructures observed in the Estamariu thrust are described below according to their structural position in relation to the thrust, that is, hanging wall, thrust zone and footwall (Fig. 11, 12). The relative timing of the different mesostructures and microstructures has been determined by means of crosscutting relationships and microstructural analysis.

In the hanging wall of the Estamariu thrust, Devonian rocks form a decametric anticline oriented NW-SE with a well-developed axial plane foliation (S_1) concentrated in the pelitic intervals. S_1 , which is oriented NNW-SSE, is a pervasive regional foliation dipping 30 to 55° towards the E and NE and is generally between 2 and 5 cm spaced. In the hinge of the anticline, bedding (S_0) dips gently towards the SE and forms a high angle with S_1 (Fig. 11b), whereas in its eastern limb, the regional foliation (S_1) dips steeper than S_0 . These geometric relationships between bedding and foliation have been used to determine the fold type at great scale (i.e., as it is shown in Fig. 11b).

Towards the main thrust plane the intensity of deformation progressively increases. This deformation consists of a penetrative thrust zone foliation (S_2), two generations of stylolites (e1, e2) and three generations of calcite veins (V0, V1a and V1b) (Fig. 12). These structures are described below in chronological order.

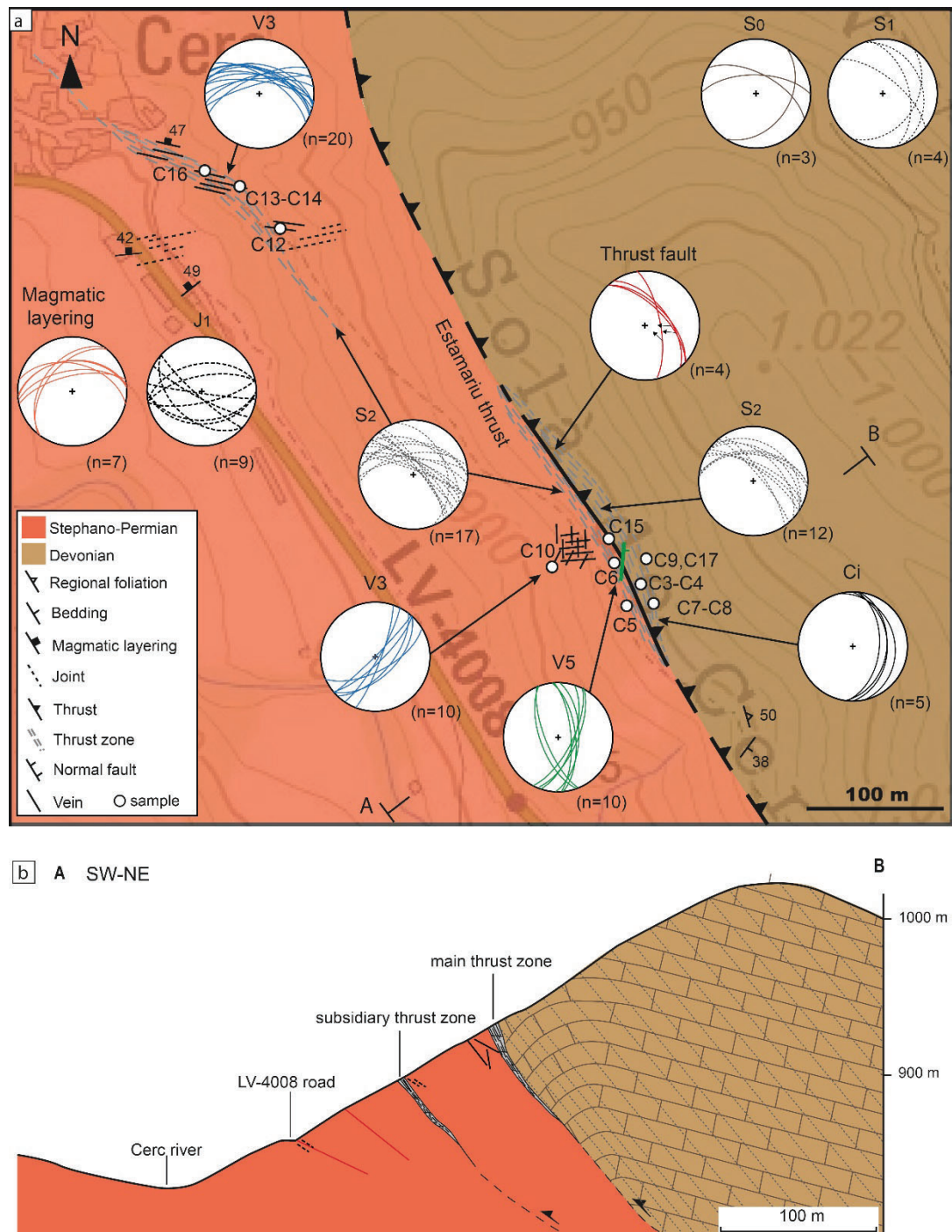


Fig. 11. (a) Geological map and (b) cross-section of the Estamaru thrust, which juxtaposes a Devonian unit against a Stephano-Permian sequence ($H=V$, no vertical exaggeration). Lower-hemisphere equal-area stereoplots of the Devonian bedding (S_0), regional foliation (S_1), thrust zone foliation affecting the hanging wall and footwall (S_2), magmatic layering and the different faults and veins observed in the study area are also included. Location of the study area in Fig. 3b.

The foliation within the thrust zone affecting the Devonian hanging wall (S_2) strikes NW-SE and dips $40 - 50^\circ$ NE, similar to the regional foliation (S_1), but it is more closely spaced, generally between 0.2 and 1 cm. This observation points to a progressive transposition of the regional foliation within the thrust zone during thrusting. At

mesoscale, S_2 has related shear surfaces (C_i) defining centimetric S-C-type structures, indicating again reverse kinematics.

Stylolites e1 have a wave-like shape and trend subparallel to the thrust zone foliation (S_2). When present, these stylolites are very systematic exhibiting a spacing of 1 – 2 mm. The first calcite vein generation (V_0), only observed at microscopic scale (Fig. 9c), corresponds to up to 1 cm long and less than 1 mm thick veins cemented by calcite. Veins V_0 and stylolites e1 are perpendicular between them and show ambiguous crosscutting relationships. These microstructures are concentrated into discontinuous fragments of the Devonian host rocks within the thrust zone. Calcite veins V_{1a} are the most abundant and crosscut the previous vein generation (V_0) as well as the stylolites e1 and are developed within S_2 surfaces. Stylolites e2, more abundant than stylolites e1, are up to 10 cm long and show spacing between 0.5 and 2 cm. These stylolites mainly correspond to sutured areas developed between the host rock and the calcite veins V_{1a} and between foliation surfaces S_2 .

Calcite veins V_{1b} , up to 1 cm long and less than one mm thick, were also identified at microscopic scale. These veins postdate the previous V_0 and V_{1a} generations and trend perpendicular to stylolites e2.

Towards the thrust slip plane, the thrust zone foliation S_2 is progressively more closely-spaced and stylolites e2 become more abundant (showing mm spacing) and exhibit ambiguous cross-cutting relationships with veins V_{1b} . The main slip surface corresponds to a discrete plane that contains calcite slickensides (veins V_2).

Deformation in the footwall is concentrated within the main thrust zone and subsidiary thrust zones and corresponds to the thrust zone foliation (S_2) and calcite veins V_3 (Fig. 12). This foliation (S_2) strikes NW-SE, dips towards the NE and is mm to cm spaced. Calcite veins V_3 are generally 1 – 2 cm thick and strike NW-SE. They are parallel or locally branch off cutting the S_2 planes in the subsidiary thrust zone.

In the footwall, outside the thrust zone, andesites are affected by E-W striking open joints (J_1) dipping indistinctively towards the north and south. These joints locally trend parallel to the magmatic layering (Fig. 12).

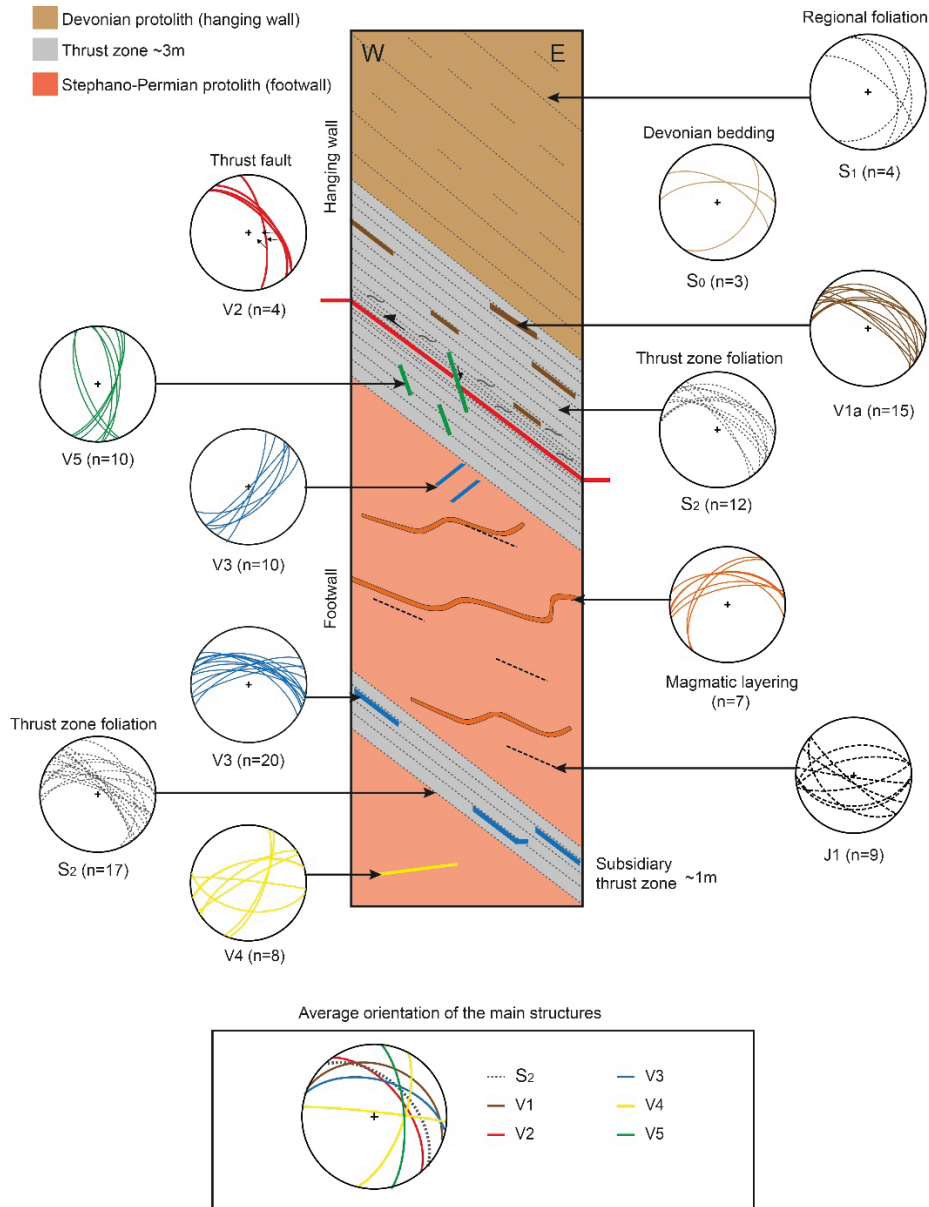


Fig. 12. Sketch showing the spatial distribution of mesoscale structures in the Estamariu thrust and lower hemisphere equal-area stereo-plots of the different mesostructures. The average orientation of the main structures is also provided.

Finally, as described above, the northern and southern limits of both the Cerc basin and the Estamariu thrust correspond to two Neogene extensional faults, La Seu d’Urgell and the Ortedó fault systems (Fig. 3b). These faults are subvertical or steeply dip towards the north. In the northern part, the slip plane of La Seu d’Urgell fault has not been observed and the limit between the Stephano-Permian rocks and the Neogene deposits is not well constrained due to the poor quality of the Neogene outcrops and the presence of Quaternary deposits. In the southern part, the Ortedó fault generates a several meter-thick dark greyish to brown fault zone, characterized by the presence of clay-rich incohesive fault rocks developed at the contact between Stephano-Permian and Upper Ordovician

rocks. Related to these main fault systems, mesoscale normal faults commonly affect the andesites within the Cerc basin. These faults are mainly E-W and locally NE-SW, are subvertical and dip indistinctly towards the N and S. Fault planes are locally mineralized with calcite cement (veins V4) and exhibit two striae set generations indicating dip-slip and strike-slip movements. On the other hand, the main Estamariu thrust zone is locally displaced by shear fractures and a later set of shear bands (Cn) both having an overall NNW-SSE to NNE-SSW strike (Fig. 12) that indicate a minor normal displacement. Shear fractures are locally mineralized with calcite (veins V5).

The Sant Corneli-Bóixols anticline

The folded sequence within the Sant Corneli-Bóixols anticline is affected by up to 23 fracture sets (F1 to F23) that include the main fault systems affecting the anticline (the Organyà fault, the Bóixols thrust, the Montagut fault system and the Sant Joan fault system) and the background deformation (centimetric to metric fractures). These fracture sets have been grouped according to fracture type, orientation, kinematics, crosscutting relationships and U-Pb geochronology of fracture-filling calcite cements. We use the term “fracture set” to include extensional (mode I) fractures and shear fractures (faults) (Bons et al., 2012) and we follow the classification of fault breccias of Woodcock and Mort (2008). All fracture sets are summarized in Fig. 13 and are described below in chronological order.

Fracture set F1 corresponds to E-W to WNW-ESE normal faults that have been attributed to the Early Cretaceous extension (Garcia-Senz, 2002). This fracture set includes the main extensional fault, the Organyà fault (F1a), preserved next to the axial surface of the anticline in the Bóixols locality. In this locality, the Organyà fault is subvertical or steeply dips towards the north and juxtaposes the Jurassic pre-rift sequence in its footwall with the Lower Cretaceous syn-rift sequence in its the hanging wall. Meter-scale normal faults (F1b), which dip 40° to 70° towards the NE and SW and only affect the Lower Cretaceous (syn-rift) Lluçà Formation in Cal Mestre locality, are also included in fracture set F1.

Fracture set F2 corresponds to a backlimb normal fault around the Montagut fault system. This metric fault strikes NNW-SSE and cuts the Upper Cretaceous pre-orogenic sequence in the backlimb of the anticline (Montagut locality). These faults exhibit subvertical striae sets and dip between 40° and 80° predominantly towards the SW.

F3 represents the main Bóixols thrust, which consists of an E-W trending and south verging reverse fault associated with the growth of the Sant Corneli-Bóixols anticline. Although most of the fault trace has been buried by syn-orogenic deposits, its frontal ramp crops out between Bóixols and Sallent villages (in Setcomelles locality) juxtaposing Jurassic rocks in its hanging wall with Upper Cretaceous carbonates in its footwall. The Bóixols thrust zone is around 15-meter-thick and contains a 2-meter-thick fault core characterized by a dark grey to greenish fine-grained foliated gouge featuring well-developed S-C structures. Kinematic indicators indicate reverse kinematics towards the S-SE.

F4 consists of two NW-SE and NE-SW conjugated and centimetric vein systems dipping between 50° and 80°. These veins have regular shapes and show extensional (mode I) openings ranging from 1 to 15 mm. F4 occurs in the Lower Cretaceous syn-rift sequence in Coll de Nargó locality. The orientation of the conjugated F4 sets is compatible with the shortening direction reported for the Bóixols thrust (F3) (Tavani et al., 2011).

F5 is constituted of meter-scale WNW-ESE extensional faults dipping between 40 and 80° towards the NE and SW. These faults, which exhibit subvertical striae sets indicating pure dip-slip kinematics, affect the syn-orogenic succession in the Sant Antoni locality (F5b).

F6 consists of meter-scale and steeply dipping vein systems found in several localities of the Sant Corneli-Bóixols anticline. F6a is mostly NE-SW and occurs in the backlimb of the anticline affecting the pre-orogenic sequence (Sant Joan locality). F6b includes two NW-SE and NE-SW conjugate vein sets, which consist of a reactivation of previous F4 fractures (Coll de Nargó locality), revealed by the presence of two calcite cements showing clear crosscutting relationships. F6c consists of two WNW-ESE and NNW-SSE vein sets affecting the syn-orogenic unit (Orcau locality).

F7 consists of a NNW-SSE vein set dipping between 70° and 85° towards the SW and NE. These veins are up to 1 meter long and show up to 1-centimeter extensional openings. F7 veins crosscut (postdate) the F6c fractures in the Orcau locality.

F8 consists of bed-parallel slip surfaces developed between well-bedded layers of marls and marly limestones in the syn-rift sequence (Cal Mestre locality) and the base of the syn-orogenic sequence (Sant Antoni and Abella de la Conca localities). These surfaces correspond to centimeter-thick and striated discrete planes cemented by calcite.

F9 consists of WNW-ESE right-lateral strike slip faults affecting pre-orogenic units in Montagut locality (decametric F9a faults) and Cal Mestre locality (metric F9b faults). In the Cal Mestre locality, these faults developed during the strike-slip reactivation of earlier F1b extensional faults due to their favorable orientation with respect to N-S to NNW-SSE shortening direction. This is evidenced by the presence of slicken lines and striae sets showing crosscutting relationships. F9b includes subordinate NNE-SSW left-lateral faults.

F10 consists of E-W to WSW-ENE centimetric and steeply dipping veins affecting the syn-orogenic sequence in Abella de la Conca locality. These veins are bed-perpendicular, up to 1 or 2 cm thick and show extensional (mode I) openings.

F11 to F13 consist of three vein sets differentiated by their orientation and crosscutting relationships between them. These sets exclusively occur in the damage zone of the Bóixols thrust in Forat de Bóixols locality (F14a). F14 consists of the E-W trending and south-verging Bóixols thrust dipping 15° to 30° towards the north in the Forat the Bóixols and in Abella de la Conca localities (F14a and F14b, respectively). In both localities, the Bóixols thrust displaces the vertical to overturned southern forelimb of the Sant Corneli-Bóixols anticline generating up to 7 m thick fault cores. The Bóixols thrust zone and the associated fracture networks (F11 to F13) in the Forat de Bóixols locality represent important structures of discussion in this PhD thesis and thereby, they will be described in detail at the end of this section.

F15 are E-W to WSW-ENE calcite veins oriented sub-perpendicular to the bedding strikes. These veins are up to 1 meter long and less than 1 centimeter thick and are present in the pre-orogenic unit (Cal Mestre locality) and in the syn-orogenic sequence (Orcau locality).

F16 corresponds to metric N-S to NW-SE and subordinated NE-SW conjugate calcite veins dipping between 60° and 85° . The occurrence of these veins (fracture intensity) increases towards F17 faults. F16 veins affect the syn-rift unit (Cal Mestre locality) and the lower and upper part of the syn-orogenic sequence (Abella de la Conca and Coll de Nargó localities, respectively).

F17 consists of N-S to NW-SE and less abundant NE-SW conjugate strike slip faults. This set includes decametric (F17a, F17b, F17d) and metric (F17c, F17e) faults that are mainly subvertical, regardless of the bedding dips, and that show displacements from a

few centimeters up to several meters. Deformation associated with F17 faults is either localized on discrete polished slip surfaces or accommodated along an up to 1 m thick fault core formed of brittle incohesive fault rocks. Sub-horizontal slickenlines present on the slip planes indicate pure strike-slip kinematics. F17 faults affect most of the studied units and are observed in all the structural positions of the anticline, that is, in the backlimb (Montagut and Sant Joan localities), in the fold core (Cal Mestre locality) and in the syn-orogenic sequence (Sant Antoni and Coll de Nargó localities).

F18 includes metric to decametric NNW-SSE extensional faults dipping 50° to 80° either towards the SW or NE and affecting the pre-orogenic sequence around the Montagut fault system (Montagut locality). Deformation associated with these faults is mainly localized in discrete slip planes exhibiting subvertical striae sets or in centimetric fault cores constituted of grey to reddish calcite-cemented breccias. F18 faults exhibit centimetric to metric displacements.

F19 consists of metric and steeply dipping NE-SW and NW-SE extensional faults deforming the syn-orogenic sequence in Abella de la Conca locality. Deformation associated with these faults is localized in discrete polished slip planes showing centimetric displacements.

F20a is constituted of WNW-ESE right-lateral strike slip reactivations of earlier developed faults (F9a) in the Montagut fault system (Montagut locality) as evidenced by the presence two different calcite cements. F20b corresponds to WSW-ENE calcite veins dipping between 60° and 80° towards the south. They are less than 1 meter long and occur in the syn-orogenic sequence (Orcau locality).

F21 corresponds to the Sant Joan fault system, which consists of metric to decametric NNE-SSW to NE-SW extensional faults dipping around 60° towards the NW and SE in Sant Joan locality. These faults present striae sets indicating dip-slip kinematics and are widely present offsetting the pre-orogenic Upper Cretaceous sequence in the backlimb of the anticline. Deformation associated with F21 faults is accommodated in discrete slip planes or in up to two-meter-thick fault cores that are constituted of calcite-cemented breccias.

F22 and F23 correspond to NNW-SSE to WNW-ESE normal faults and strike-slip faults developed as subsidiary metric slip planes around the Montagut fault system (Montagut locality).

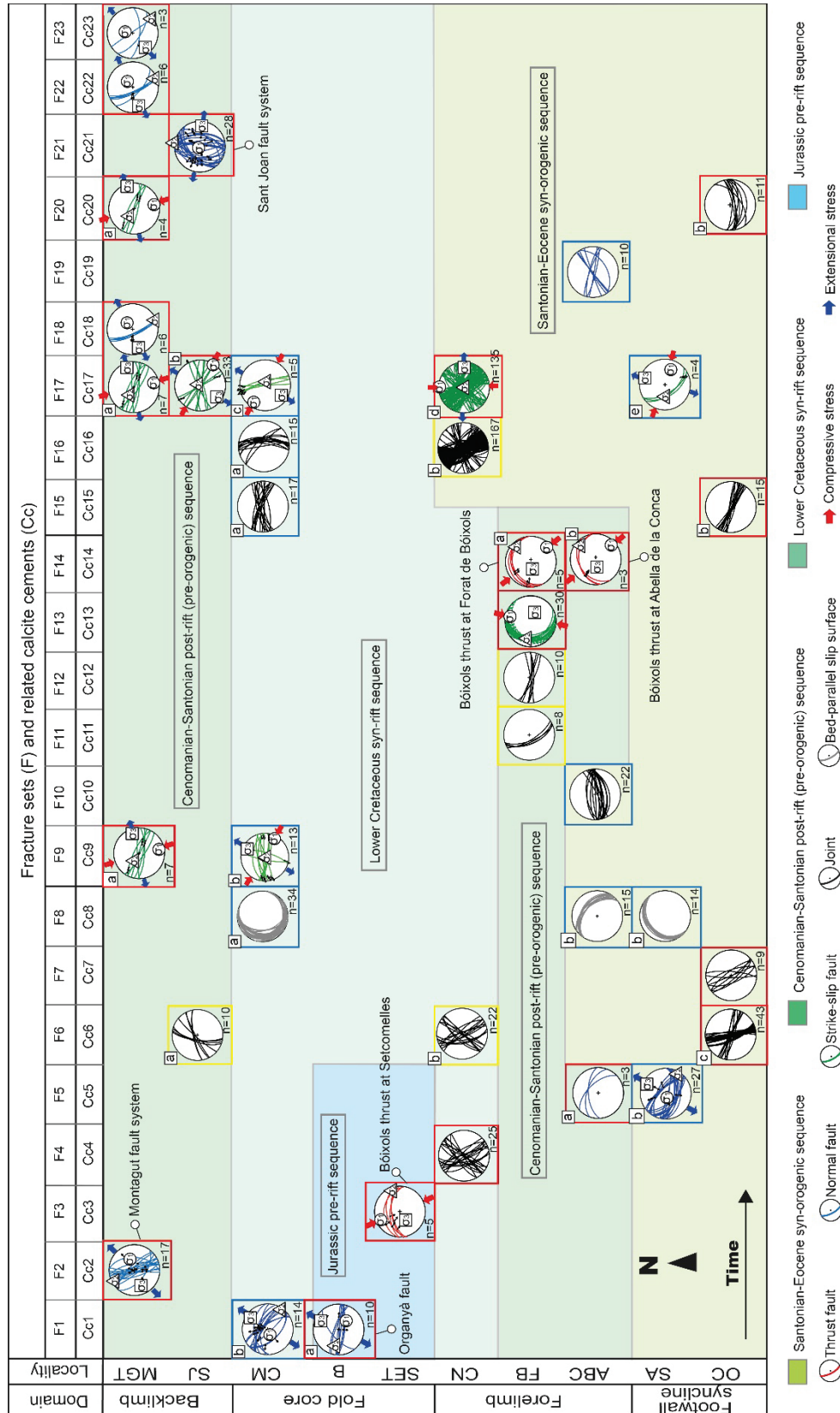


Fig. 13. Spatial and temporal distribution of fractures (F1 to F23) and related calcite cements (Cc1 to Cc23) within the Sant Corneli-Boixols anticline. The lower-hemisphere equal-area projections are arranged according to the structural position of the anticline, the study localities and the involved host rocks. Plots are also grouped in three geochemical groups (blue, red and yellow squares) that will be explained in the geochemical section.

The Bóixols thrust in the Forat de Bóixols locality

In the central part of the Sant Corneli-Bóixols anticline, the southern tilted limb is offset by the low-dipping and south-directed Bóixols thrust in Forat the Bóixols and Abella de la Conca localities). In the Forat de Bóixols locality, the Bóixols thrust is well exposed, exhibiting a complex calcite-filled fracture network (sets F11 to F14) developed in the thrust zone of this reverse fault. This thrust zone represents an exceptional field analogue to observe in a 300 m-long outcrop the variation in deformation mechanisms developed across a fault zone and their contribution as seal or conduit for fluids. In this locality, the Bóixols thrust juxtaposes the Upper Cretaceous Santa Fe Formation against the Collada Gassó Formation (Fig. 5).

The thrust zone exhibits a classical fault organization with a main slip plane, a fault core and two surrounding damage zones within the footwall and hanging wall, respectively (Fig. 14, 15). The slip plane locates immediately below the fault core, strikes E-W, dips between 15 and 30° N and has a displacement of several hundred meters juxtaposing the Cenomanian-Turonian sequence of the hanging wall against the Coniacian succession of the footwall. The fault core overlying the slip plane consists of a 2 to 7 m thick, light grey to yellowish foliated cataclasite. This foliated cataclasite is characterized by well-developed S-C shears forming sigmoidal lenses (imbricated lithons), a combination of host rock carbonate and calcite lenses within a fine-grained micritic matrix with abundant calcite cement. Imbricated lithons are bounded by well-developed pressure-dissolution seams or stylolites. S-C shears and stylolites strike ENE-WSW, compatible with the NNW-SSE shortening direction. Orange to reddish clay minerals concentrate along pressure-dissolution surfaces, and are locally scattered within the micritic matrix.

The transition from the fault core to the hanging wall damage zone is marked by discrete S-C sigmoidal shears without the development of foliated cataclasite, or by a discrete, discontinuous slip plane mineralized with calcite. Both, the footwall and hanging wall damage zones comprise multiple sets of systematically and randomly oriented calcite-cemented fractures (i.e., veins) developed at both sides of the fault core (Fig. 14, 15). Although in both cases there is a progressive increase in deformation and vein intensity from the protolith towards the fault core, the geometry of veins differ from one to another damage zone.

In the footwall damage zone, there are two areas showing different vein characteristics (Fig. 14a). The first area is around 30 m wide from the protolith and is characterized by three systematically oriented vein systems (F11 to F13) with clear crosscutting relationships between them (Fig. 14a-c). F11 consists of NNW-SSE extensional veins dipping between 50 and 70° to the SW. They are up to 1 – 2 m long and less than 2 cm thick. F12 is characterized by E-W extensional veins steeply dipping to the S-SW. These veins are several meters long and up to 5 cm thick. F13 consists of N-S and NE-SW *en échelon* conjugate sets of tension gashes (i.e., hybrid extensional-shear calcite veins) gently dipping towards the NW. These veins are centimetric-sized and have sigmoidal shapes. The second area observed in the footwall covers around 15 - 20 m between the first area and the fault core and is dominated by randomly oriented calcite veins defining a dilational mosaic to chaotic breccia.

By contrast, in the hanging wall, the damage zone is narrower, only concentrated in the 15 - 20 meters near the fault core (Fig. 14d), and it is defined by randomly oriented calcite veins defining an incipient crackle breccia (proto-breccia). Fracture density is lower than within the footwall damage zone.

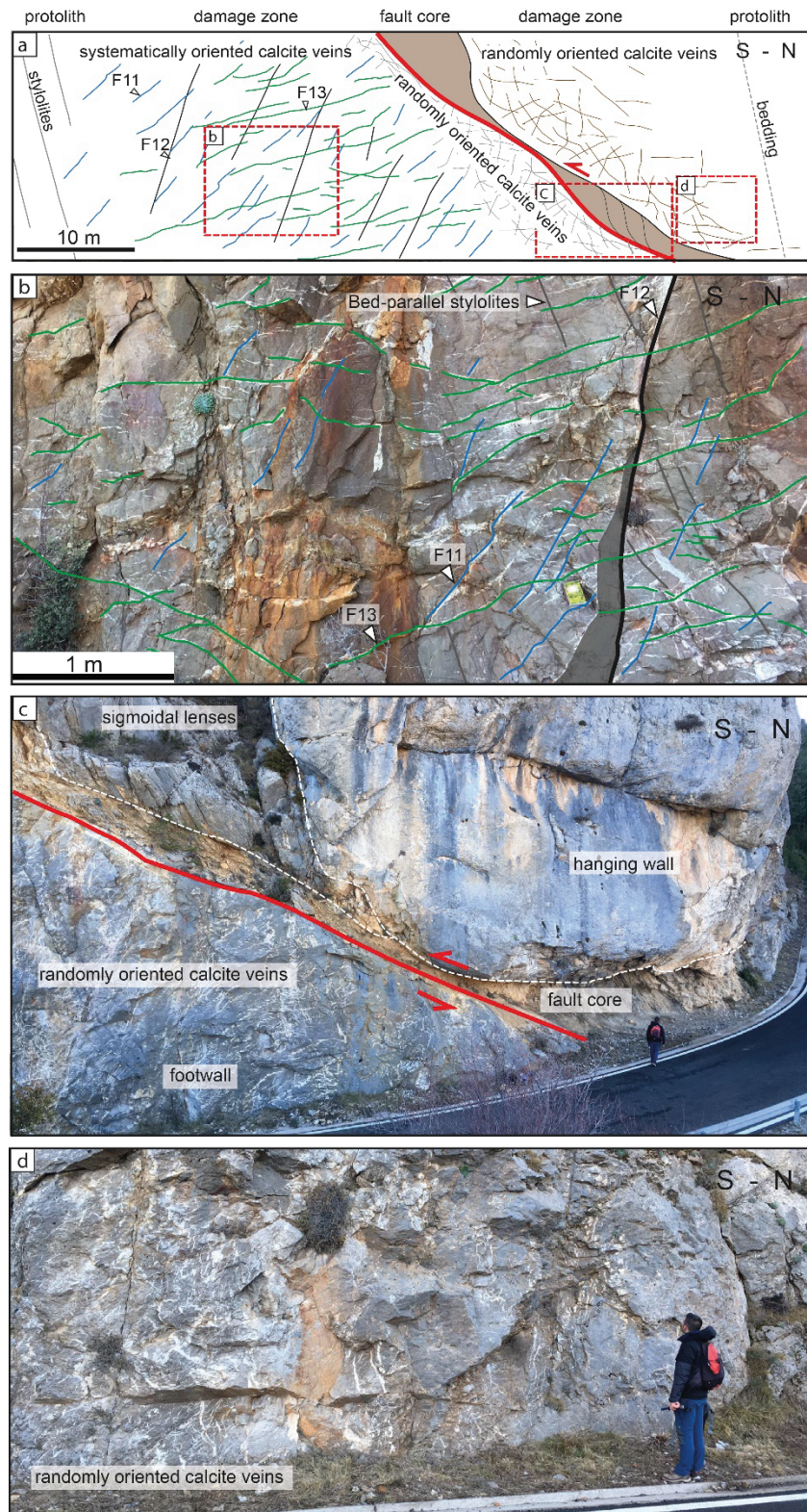


Fig. 14. (a) Sketch of the spatial distribution of veins within the outcrop. In the footwall, three systematically oriented vein systems (F11 to F13) (b) evolve to randomly oriented veins located next to the fault core (c). In the hanging wall, only randomly oriented veins are observed (d).

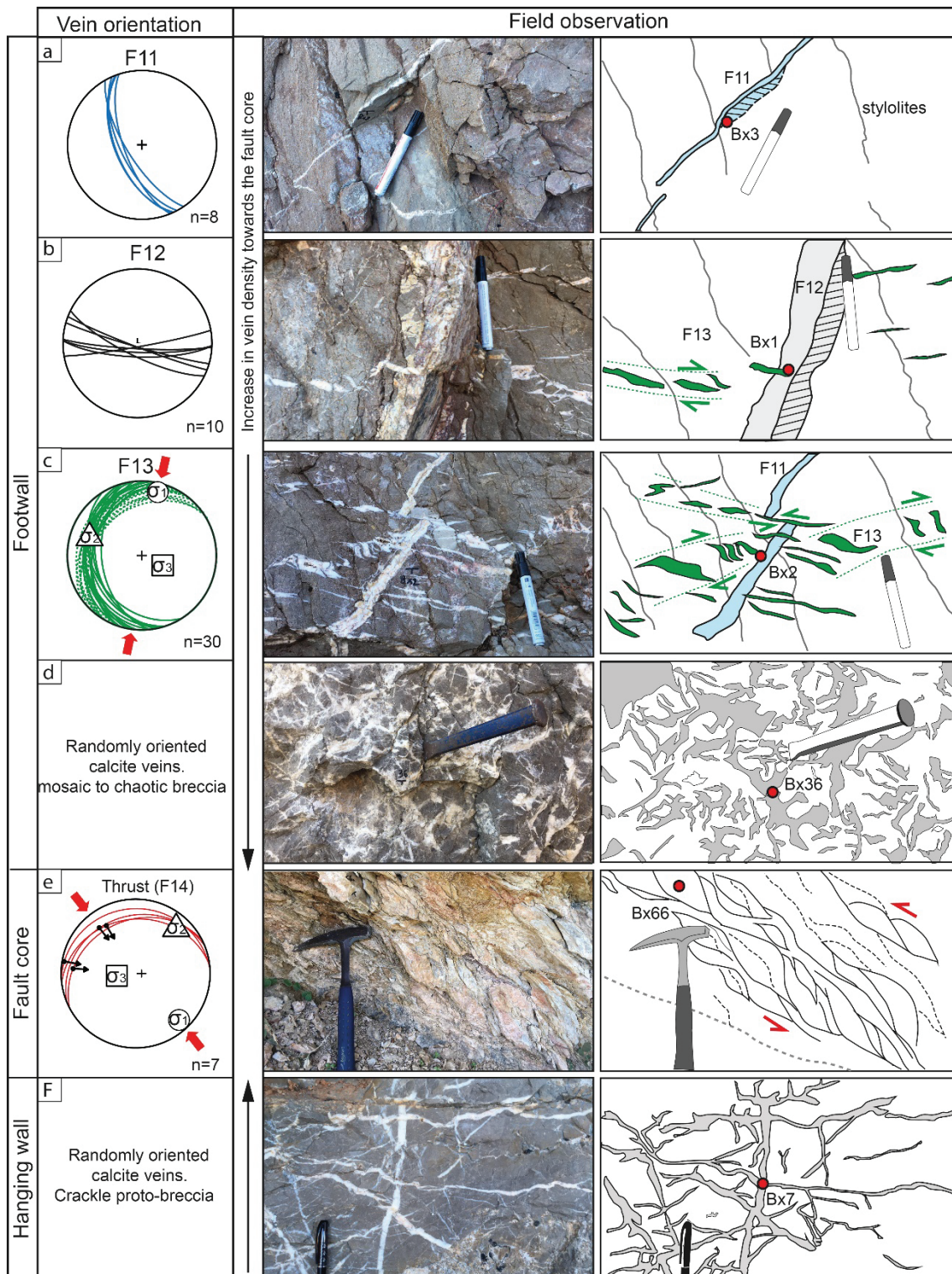


Fig. 15. Spatial distribution and crosscutting relationships between veins developed within the Bóixols thrust zone in Forat de Bóixols locality. Vein density increases towards the fault plane. In the footwall, three vein systems: F11, F12, F13 (a, b, c, respectively) evolve to randomly oriented veins (d) on approaching the fault core (e). In the hanging wall, only randomly oriented veins are observed, being more chaotic towards the fault plane (f). The red circles refer to sample location.

4.4. Petrographic features of calcite cements

The integrated use of crosscutting relationships as well as petrographic and geochemical analyses applied to vein cements have allowed us to characterize the whole paragenetic sequence in the Estamariu thrust and in the Sant Corneli-Bóixols anticline. In the Estamariu thrust, up to 7 calcite cements have been recognized in the different structures and microstructures. In the Sant Corneli-Bóixols anticline, 23 cements were found in the several fracture sets described in the last section. The petrographic description using conventional and cathodoluminescence (CL) microscopes of the successive vein cements from fractures is summarized in Tables 1-2 and Figs. 16-17.

Table 1. Main petrographic characteristics of the calcite cements found in the Estamariu thrust.

Calcite cement	Set	Locality	Cathodoluminescence	Main textural and petrographic features
Cc0	V0	C	Dark brown	Blocky to elongated blocky crystals (Fig. 16a).
Cc1a	V1a	C	Dark brown	Up to 3-4 mm anhedral and blocky crystals (Fig 16b-c).
Cc1b	V1b	C	Bright yellow	Up to 0.1 mm-sized blocky crystals.
Cc2	V2	C	Dull to bright orange	Up to 3 mm-sized blocky to elongated blocky crystals (Fig. 16d-e).
Cc3	V3	C	Dull orange to non-luminescent	Up to 3 mm-sized efibrous crystals, growing perpendicular to the fracture walls (Fig 16f-g).
Cc4	V4	C	Dark orange	Up to 2 mm-sized blocky to elongate blocky crystals.
Cc5	V5	C	Non-luminescent	Greyish microsparite.

Table 2. Main petrographic characteristics of the calcite cements in the Sant Corneli-Bóixols anticline.

Calcite cement	Set	Locality	Cathodoluminescence	Main textural and petrographic features
Cc1a	F1a	B	Dull brown to dark orange	Up to 3 – 4 mm elongate to fibrous crystals.
Cc1b	F1b	CM	Dark brown to non-luminescent	Up to 7 mm elongated to fibrous, locally blocky crystals.
Cc2	F2	MGT	Brown to dark yellow	0.4 to 1 mm-sized blocky crystals, local presence of thin twin planes.
Cc3	F3	SET	Brown	Up to 3-4 mm-sized elongated to fibrous crystals.
Cc4	F4	CN	Dull orange to non-luminescent	Up to 1.5 mm-sized elongated blocky crystals, growing perpendicular to the fracture walls, locally up to 4 mm anhedral to subhedral blocky crystals.
Cc5a	F5a	ABC	Dark brown to dark orange	Up to 2 mm-sized anhedral blocky crystals.
Cc5b	F5b	SA	Dark brown to non-luminescent	Up to 7 mm elongate to fibrous crystals.
Cc6a	F6a	SJ	Zoned bright orange to non-luminescent	0.5 to 5 mm long blocky to elongate blocky crystals (Figs 17a-b).
Cc6b	F6b	CN	Non-luminescent	Up to 4 mm elongated to fibrous crystals, locally up to 2 mm in blocky crystals.
Cc6c	F6c	OC	Dark to bright brown	Up to 5 mm blocky and up to 7 mm elongate crystals growing perpendicular to the fracture walls.
Cc7	F7	OC	Brown to dark orange	Up to 5-6 mm long blocky crystals.

Cc8	F8	CM SA ABC	Dark brown to non-luminescent	Up to 5 mm elongated to fibrous crystals arranged parallel to the fracture walls and parallel to bedding surfaces.
Cc9a	F9a	MGT	Dark orange	Up to 5 mm-sized blocky crystals.
Cc9b	F9b	CM	Dark brown	Up to 4 -5 mm-sized elongated to fibrous crystals.
Cc10	F10	ABC	Dark brown to non-luminescent	Up to 1 mm-sized blocky crystals with local thin twin planes and up to 5 mm-sized elongated crystals growing syntaxially.
Cc11	F11	FB	Dark- to bright orange	Up to 1 mm-sized blocky crystals locally displaying mechanical twinning and growing syntaxially (Figs 17c-d).
Cc12	F12	FB	Non-luminescent to bright orange concentric zonation	0.2 to 5 mm-sized blocky to elongated blocky crystals growing syntaxially (Figs 17c-d).
Cc13	F13	FB	Dull orange	Up to 0.5 mm-sized anhedral blocky to elongated blocky crystals.
Cc14a	F14a	FB	Dark brown	Up to 1 mm anhedral crystals.
Cc14b	F14b	ABC	Dark brown	Up to 2 mm anhedral to subhedral blocky crystals.
Cc15a	F15a	CM	Dark brown to non-luminescent	Up to 5 mm elongated to fibrous crystals, growing perpendicular to the fracture walls, and local up to 2 mm long anhedral blocky crystals (Figs 17e-f).
Cc15b	F15b	OC	Dark orange	Up to 3-4 mm blocky crystals.
Cc16a	F16a	CM	Non-luminescent	Up to 1 mm blocky crystals.
Cc16b	F16b	CN	Orange to bright yellow	Blocky and elongate blocky crystals ranging in size from 1 to 4 mm.
Cc17a	F17a	MGT	Brown to dark orange	Up to 1.5 mm long elongated blocky crystals.
Cc17b	F17b	SJ	Dull to bright yellow	Up to 6 mm elongated to fibrous crystals (Figs 15g-h).
Cc17c	F17c	CM	Dark to bright brown	Up to 3 mm elongated to fibrous crystals and up to 1 mm long blocky crystals.
Cc17d	F17d	CN	Dull to bright orange	Anhedral to subhedral blocky crystal ranging in size from 0.1 to 2 mm.
Cc17e	F17e	SA	Dark brown	Elongated to fibrous crystals ranging in size from 0.1 to 2 mm.
Cc18	F18	MGT	Dark brown	0.1 to 4 mm-sized elongated blocky crystals.
Cc19	F19	ABC	Dull brown	0.2 to 4 mm-sized crystals with a blocky texture.
Cc20a	F20a	MGT	Dark orange	Up to 4 mm-sized blocky to elongated blocky crystals.
Cc20b	F20b	OC	Dark to light brown	Up to 1 mm in size blocky crystals.
Cc21	F21	SJ	Bright brown to dark orange	0.1 to 1 mm-sized (locally up to 4 mm) blocky and inequigranular crystals.
Cc22	F22	MGT	Dark brown	Up to 2 mm-sized blocky crystals showing local twin planes.
Cc23	F23	MGT	Dark orange	Up to 8 mm-sized anhedral to subhedral crystals with a blocky texture.

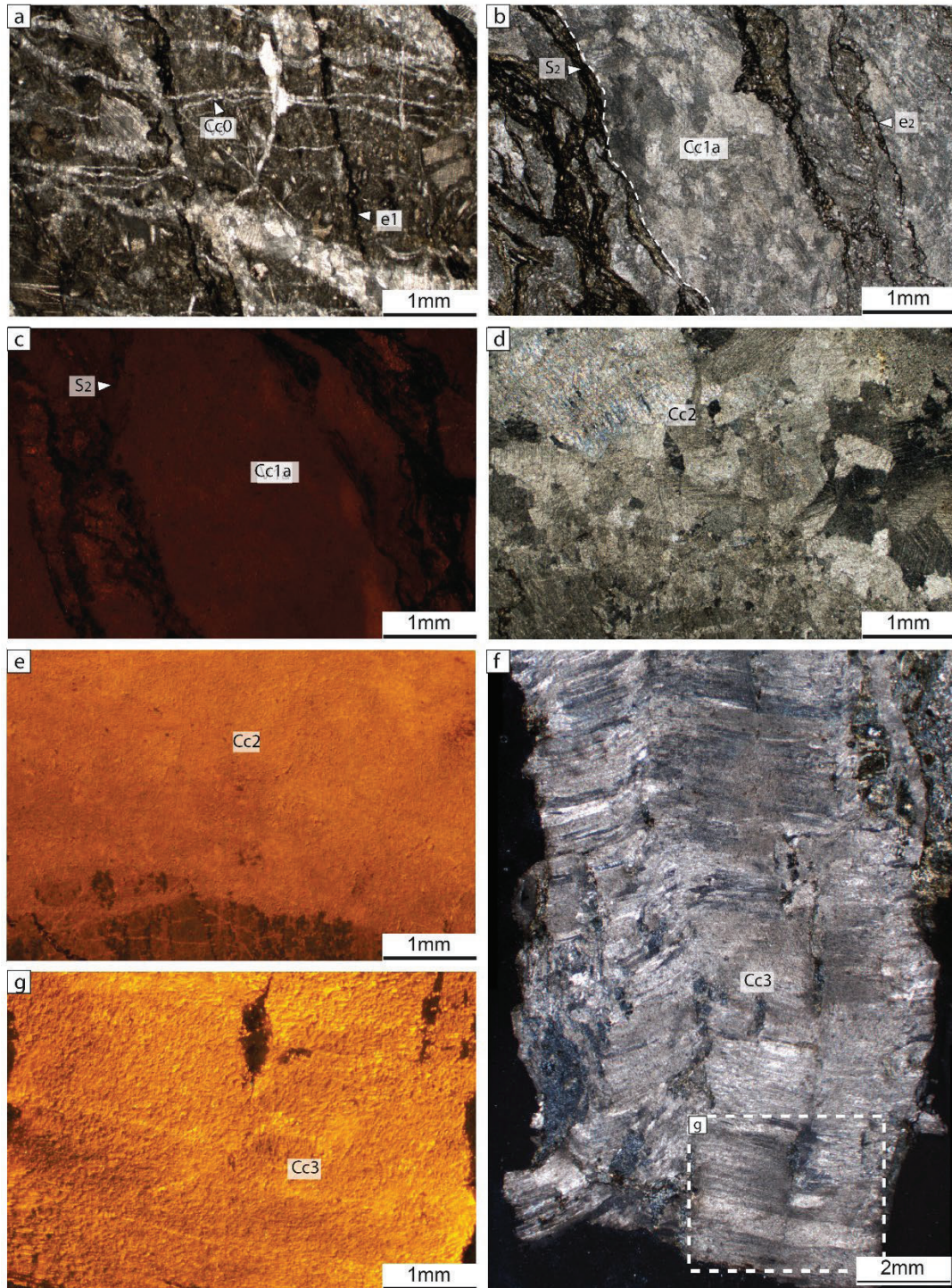


Fig. 16. Optical and CL microphotographs showing the main textural features of the studied calcite cements in the Estamariu thrust. (a) Stylolites e1 and calcite cement Cc0 affecting the Devonian encrinites from the hanging wall. (b) Cross-polarized light and (c) CL microphotographs of Cc1a concentrated between foliation surfaces S_2 . (d) Cross-polarized light and (e) CL microphotographs of calcite cement Cc2 located on the main thrust slip plane. (f) Cross-polarized light and (g) CL microphotographs of calcite cement Cc3 (V3), characterized by calcite fibers growing perpendicular to the vein walls.

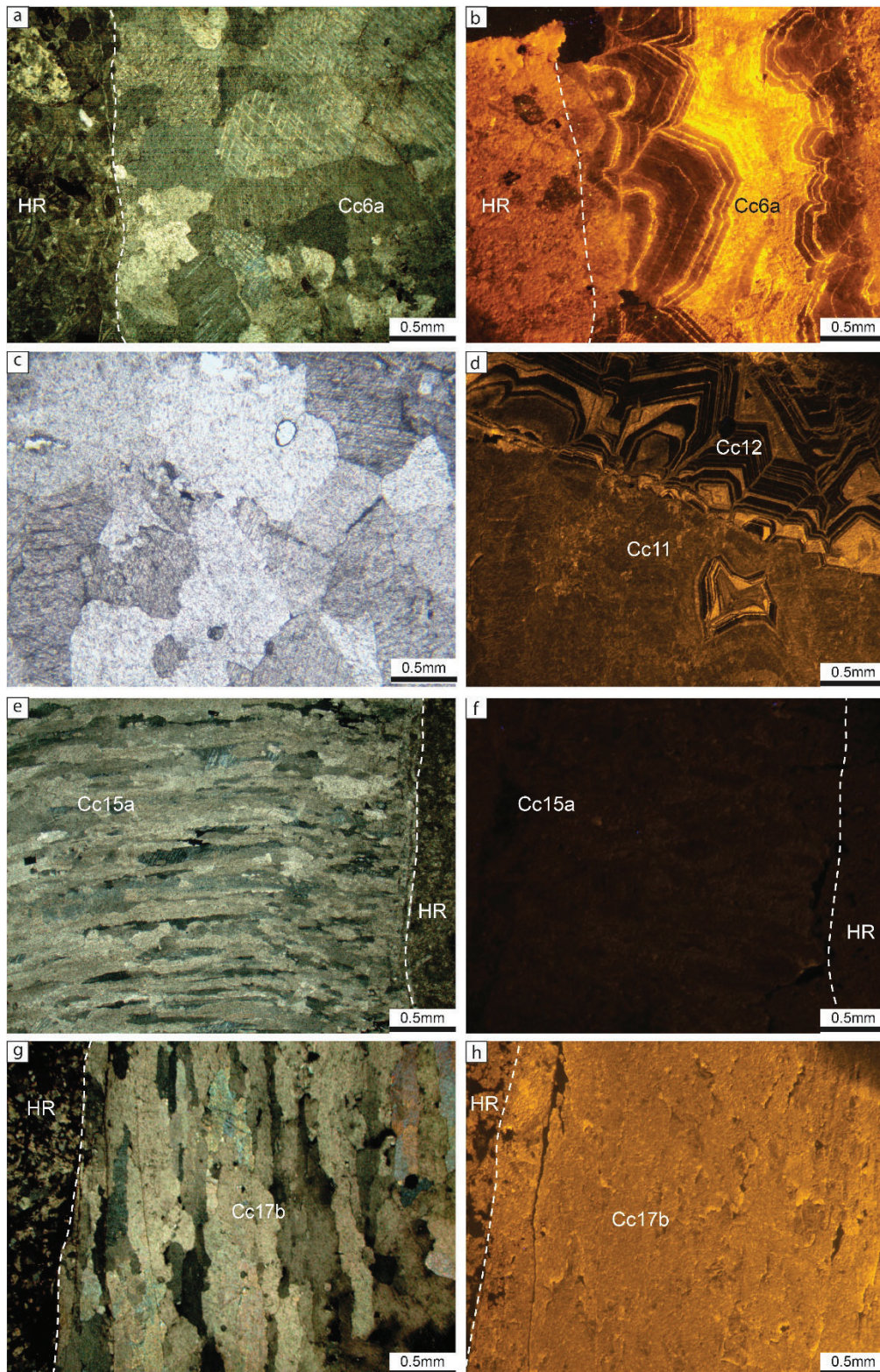


Fig. 17. Paired optical and CL microphotographs showing the main textural features of the studied calcite cements in the Sant Corneli-Bóixols anticline. (a) and (b) Cement Cc6a with a blocky texture and exhibiting a concentric zoned luminescence. (c) and (d) Cements Cc11 and Cc12 exhibiting a blocky texture and featuring a dark orange luminescence and a concentric zonation, respectively. (e) and (f) Cements Cc15a characterized by elongated to fibrous crystals arranged perpendicular to the vein walls and displaying a dark to non-luminescence. (g) and (h) Cement Cc17b with an elongated blocky texture and a dull yellow luminescence.

4.5. Geochemistry of calcite cements and host rocks

Stable ($\delta^{18}\text{O}$ and $\delta^{13}\text{C}$) and clumped isotopes, $^{87}\text{Sr}/^{86}\text{Sr}$ ratios and the elemental composition of the successive calcite vein generations and related host rocks are summarized in Figs 18-21. In order to discuss all the complexity of the geochemical data, the studied calcite cements have been assembled in three groups, according to similarities of the main geochemical features. Group 1 is only present in the Sant Corneli-Bóixols anticline, whereas group 2 and group 3 are present in both studied domains.

Group 1 calcites includes dark to non-luminescent calcite cements, similar to their adjacent marine host rocks, either the Lower Cretaceous marls of the Lluçà Formation or the Upper Cretaceous marls of the Vallcarga Formation. These cements also show $\delta^{13}\text{C}$ values and $^{87}\text{Sr}/^{86}\text{Sr}$ ratios similar to their adjacent host rocks, which are typical of marine carbonates (Figs 18, 20) (Veizer et al., 1999). They are also characterized by Sr contents between 600 and 5000 ppm, Mn contents lower than 200 ppm, REE contents lower than 20 ppm and Y/Ho ratios higher than 50 (Fig. 21). The $\delta^{18}\text{O}$ values of these cements are similar to or up to 5 ‰VPDB lighter than those values of their correspondent host rocks (Fig. 18). Group 1 cements are present in the core of the Sant Corneli-Bóixols anticline at Cal Mestre locality (Cc1b, Cc8, Cc9b, Cc15a, Cc16a and Cc17c) and in the lowest part of the syn-orogenic sequence from the footwall of the Bóixols thrust, this is, in Sant Antoni locality (Cc5b, Cc8 and Cc17e) and locally in Abella de la Conca locality (Cc10 and Cc19). The geochemistry of all these cements reflects in general the composition of their host carbonates.

Group 2 is characterized by calcite cements with the lightest $\delta^{18}\text{O}$ values, from -14 ‰VPDB to -8 ‰VPDB, which are up to 10 ‰VPDB lighter than their correspondent host rocks (Fig.18). These cements have $\delta^{13}\text{C}$ values between -12 ‰VPDB and +2 ‰VPDB, which may either be similar or lighter than those values of their adjacent host rocks (Fig. 18). Group 2 cements precipitated in large-scale faults and related fractures in the Estamariu thrust (Cc1a to Cc4) and in the Sant Corneli-Bóixols anticline (Cc1a, Cc2, Cc3, Cc4, Cc5a, Cc6c, Cc7, Cc9a, Cc13, Cc14a, Cc14b, Cc15b, Cc17a, Cc17b, Cc17d, Cc18, Cc20a, Cc20b, Cc21, Cc22 and Cc23). In the Estamariu thrust, group 2 cements yield $^{87}\text{Sr}/^{86}\text{Sr}$ between 0.713018 and 0.718294 (Fig. 20) and display low Sr contents (between 70 and 700 ppm), very high Mn contents (up to 8200 ppm), high REE contents (up to 900 ppm) and low Y/Ho ratios (Fig. 21). In the Sant Corneli-Bóixols anticline,

group 2 cements have $^{87}\text{Sr}/^{86}\text{Sr}$ ratios between 0.7074 and 0.7080 and exhibit low to intermediate Sr contents (between 300 and 2000 ppm), intermediate Mn contents (less than 700 ppm), low REE contents (less than 100 ppm) and intermediate Y/Ho ratios (between 40 and 80) (Fig. 21). Additionally, according to clumped isotopes, group 2 exhibits the highest temperature of precipitation and the heaviest $\delta^{18}\text{O}_{\text{fluid}}$ (Fig. 19). In the Estamariu thrust, these high values are up to 210 °C and up to +12 ‰SMOW, respectively, and in the Sant Corneli-Bóixols anticline, up to 120 °C and up to +5.5 ‰SMOW, respectively.

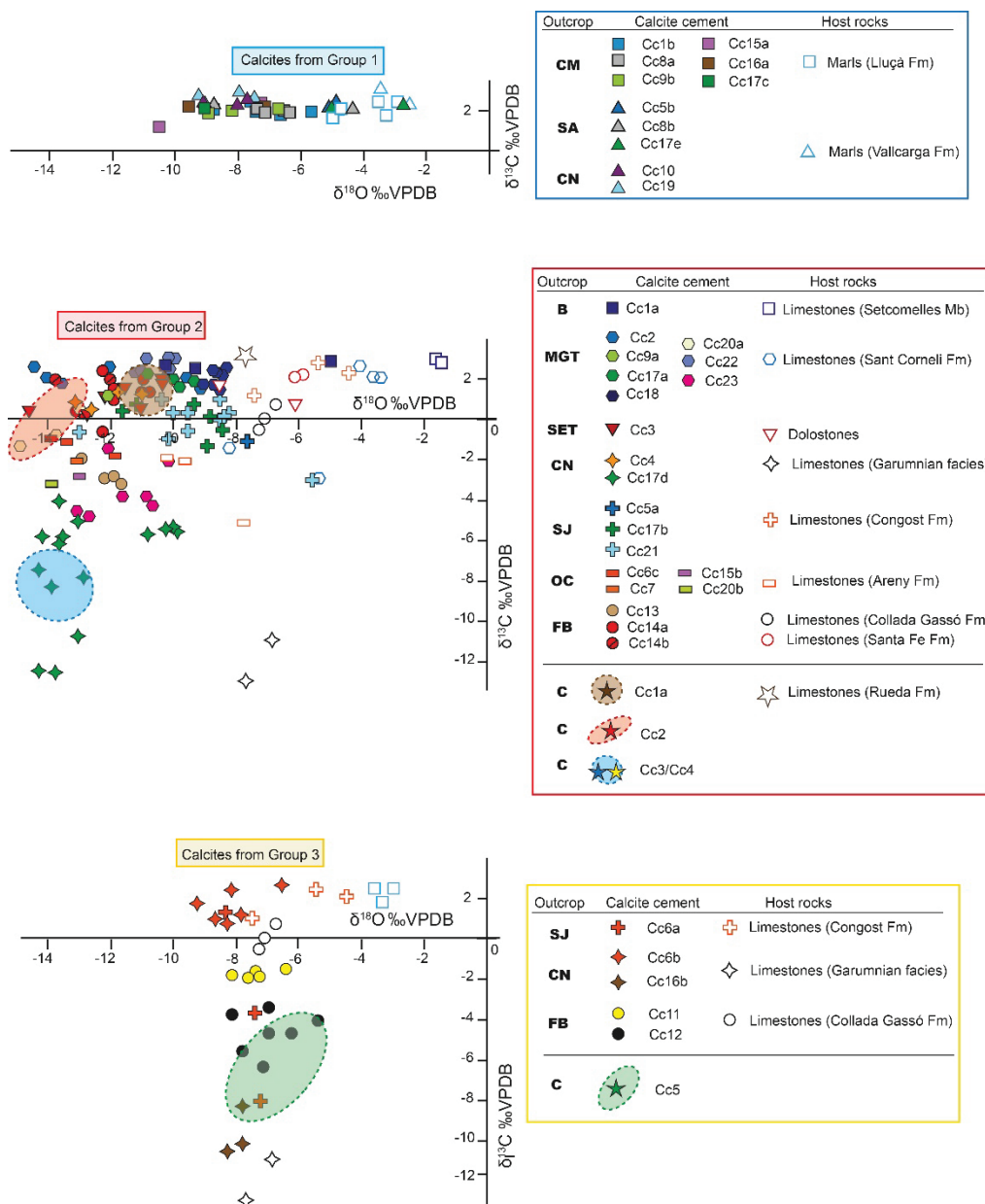


Fig. 18. Stable isotopic composition ($\delta^{18}\text{O}$ vs. $\delta^{13}\text{C}$) of the three groups of calcite cements and host rocks. Solid symbols refer to calcite cements and open symbols refer to their associated host rocks.

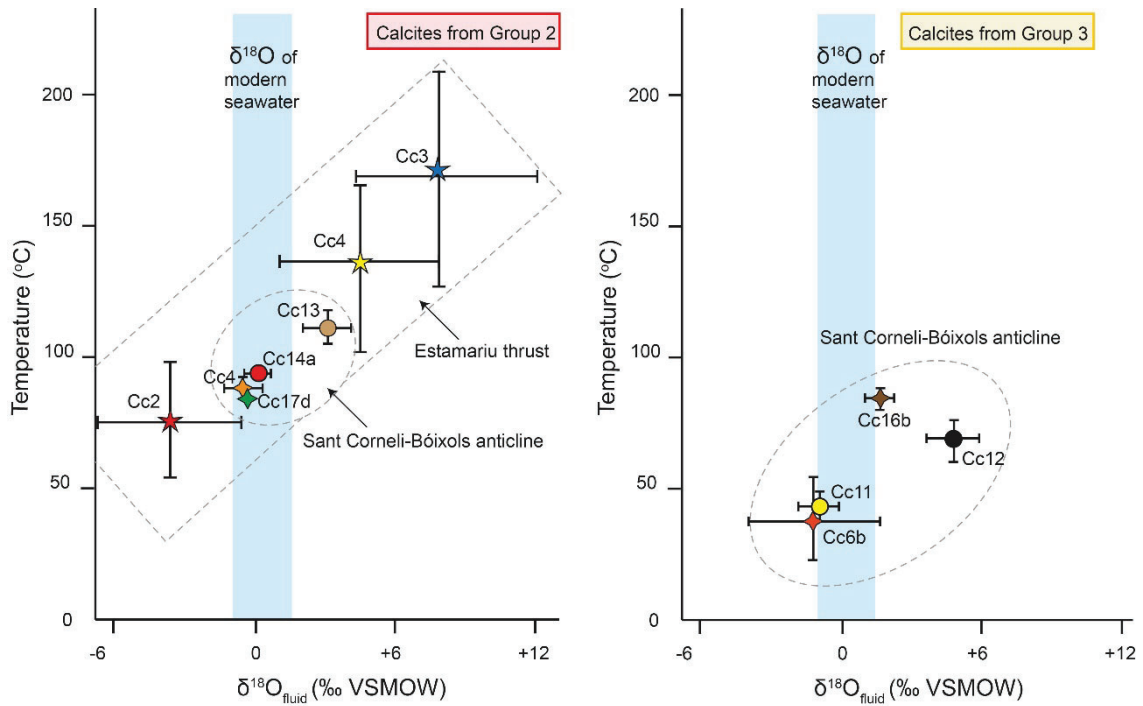


Fig. 19. Temperature (T) of precipitation and $\delta^{18}\text{O}_{\text{fluid}}$ obtained for representative calcite cements from the two studies domains. Legend of symbols in Fig. 18.

Group 3 calcites includes cements characterized by a narrow range of the $\delta^{18}\text{O}$ values, between -8 and -6 ‰ VPDB, and $\delta^{13}\text{C}$ -depleted values, between -10 and $+2$ ‰ VPDB, which are up to 10 ‰ VPDB lighter than their surrounding host rocks (Fig. 18). These cements display the lowest Sr contents (less than 500 ppm), intermediate Mn contents (up to 1400 ppm), Y/Ho ratios less than 60 (Fig. 21). Group 3 cements precipitated in fractures postdating the Estamariu thrust (Cc5 in Cerc locality) and in centimetric to metric-scale fractures in the backlimb (Cc6a in Sant Joan locality) and forelimb (Cc6b/Cc16b in Coll de Nargó locality and Cc11-Cc12 in Forat de Bóixols locality) of the Sant Corneli-Bóixols anticline. In the Estamariu thrust, group 3 cements yield $^{87}\text{Sr}/^{86}\text{Sr}$ of 0.716923 and REE contents between 70 and 110 ppm. In the Sant Corneli-Bóixols anticline, group 3 cements have low REE contents (lower than 40 ppm) and $^{87}\text{Sr}/^{86}\text{Sr}$ ratios between 0.7073 and 0.7077 , which are lower than values of their correspondent host rocks but within the range of Cretaceous carbonates (McArthur et al., 2012) (Fig. 20). Additionally, the temperature of precipitation and composition of the parent fluids has also been calculated for representative cements belonging to group 3. The measured temperature and $\delta^{18}\text{O}_{\text{fluid}}$ for Cc6b range between 25 and 57 °C and between -4.2 and $+1.6$ ‰ SMOW, respectively. The calculated T and $\delta^{18}\text{O}_{\text{fluid}}$ for Cc11 range from 42 to 51 °C and -1.8 to -0.1 ‰ SMOW, respectively. Cc12 exhibits T and $\delta^{18}\text{O}_{\text{fluid}}$ between

64 and 78 °C and between +3.7 and +5.9 ‰SMOW, respectively. Cc16b displays T and a $\delta^{18}\text{O}_{\text{fluid}}$ in the range of 80 to 90 °C and from +1 to +2 ‰SMOW.

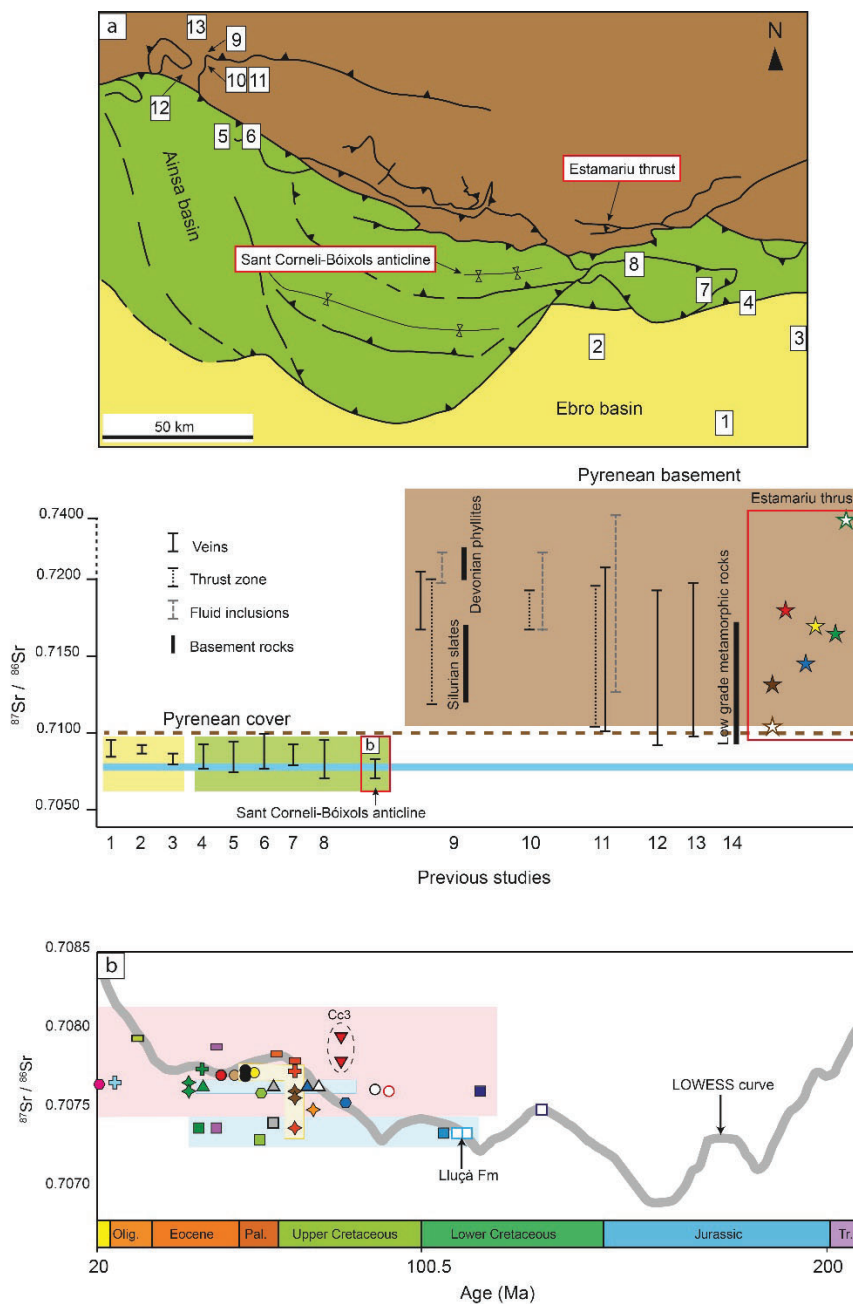


Fig 20. Simplified geological map of the South-Central Pyrenees showing the two studied domains and the location of previous studies where $^{87}\text{Sr}/^{86}\text{S}$ ratios have been carried out. a) $^{87}\text{Sr}/^{86}\text{S}$ ratios from this study compared to results from other structures involving either cover units (1-8) or basement rocks (9-14). The blue thick line refers to the $^{87}\text{Sr}/^{86}\text{Sr}$ range of Phanerozoic seawater and the dashed brown line represents the $^{87}\text{Sr}/^{86}\text{Sr}$ limit value between basement and cover structures. 1. El Guix anticline (Travé et al., 2000), 2. Puig Reig anticline (Cruset et al., 2016), 3. L'Escala thrust (Cruset et al., 2018), 4. Vallfogona thrust (Cruset et al., 2018), 5. Ainsa basin (Travé et al., 1997), 6. Ainsa-Bielsa area (McCaig et al., 1995), 7. Lower Pedraforca thrust (Cruset et al., 2020a), 8. Upper Pedraforca thrust (Cruset, 2019), 9. Gavarnie thrust (McCaig et al., 1995), 10. Pic de Port Vieux thrust (Banks et al., 1991), 11. Pic de Port Vieux thrust (McCaig et al., 2000b), 12. Plan de Larri thrust (McCaig et al., 1995), 13. La Glere shear zone (Wayne and McCaig, 1998). 14. Trois Seigneurs Massif (not in the map) (Bickle et al., 1988). b) $^{87}\text{Sr}/^{86}\text{S}$ ratios obtained in the Sant Corneli-Bóixols anticline as a function of the LOWESS curve that represents the $^{87}\text{Sr}/^{86}\text{S}$ ratios of seawater through time (McArthur et al., 2012). Legend of symbols in Fig. 18.

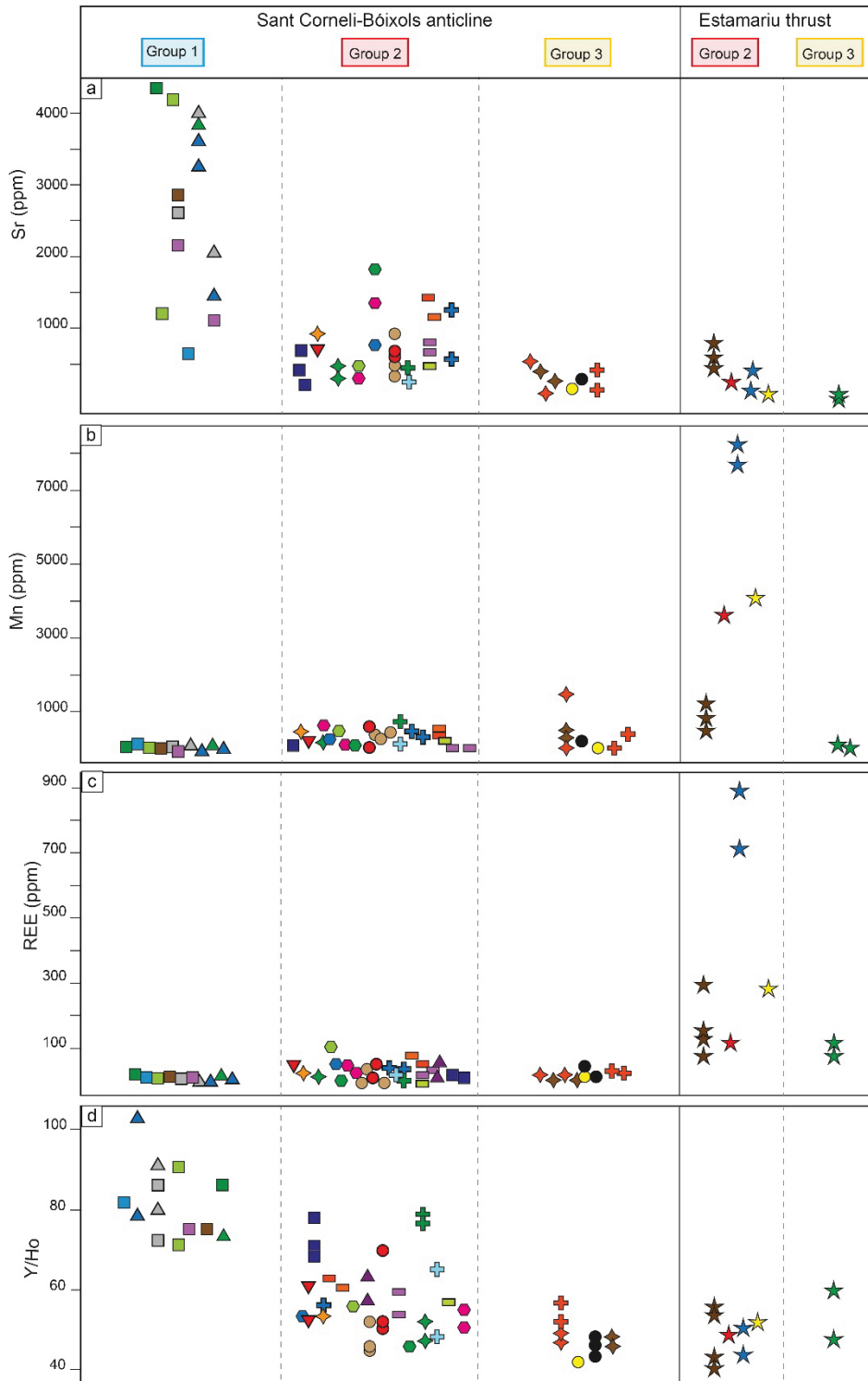


Fig. 21. Elemental composition of the three groups of calcites from the two studied domains. (a) Sr contents. (b) Mn contents. (c) Rare Earth Elements (REE) contents. (d) Y/Ho ratios. Legend of symbols in Fig. 18.

Additionally, another important aspect to highlight is that this study also attempted to provide other novel geochemical constraints based on the use of neodymium isotopes ($^{143}\text{Nd}/^{144}\text{Nd}$) as a tracer of the fluid origin. However, due to the general low Nd concentrations in most of the analyzed calcite cements, only two values could be

measured in samples from the Estamariu thrust. These samples correspond to the latests generation of calcite cement in the area (Cc5) and the andesite host rock from the footwall. Cc5 has a $^{143}\text{Nd}/^{144}\text{Nd}$ ratio of 0.512178, which is similar to the one of its footwall host rocks, which is 0.512196.

4.6. U-Pb geochronology of calcite cements

U-Pb ages were measured for different fracture-filling calcite cements that precipitated in the study area. However, U-Pb dating of calcite cements in the Estamariu thrust failed due to their high lead contents and low uranium contents. Therefore, the relative timing of the different structures and microstructures in this thrust has been determined by means of crosscutting relationships and microstructural analysis. Contrarily, in the Sant Corneli-Bóixols anticline 23 U-Pb ages were obtained (Table 3). These ages vary from Late Cretaceous (79.8 ± 1.2 Ma) to late Miocene (9.0 ± 4.6 Ma). Most of these dates were acquired for calcite cements from group 2 (18 out of 23), which precipitated along the Bóixols thrust, the Montagut fault system and other large faults and related fractures affecting the entire anticline. The other ages were measured in cements from group 1 (3 out of 23) and cements from group 3 (2 out of 23). These results together with eight previously published dates (Cruset et al., 2020b; Haines, 2008) provide a well constrained absolute timing of deformation in the frontal anticline of the Bóixols thrust sheet as summarized below.

The Bóixols thrust has been studied in Setcomelles, Forat de Bóixols and Abella de la Conca localities (F3, F14a and F14b, respectively). At Setcomelles, a previously reported date for the Bóixols thrust yielded a Late Cretaceous age (71.2 ± 6.4 Ma) (Haines, 2008), whereas the reported age at Forat de Bóixols was 55.5 ± 1.2 Ma (Cruset et al., 2020b). Both dates are older than the new U-Pb age reported in this study for the Bóixols thrust at Abella de la Conca (36.6 ± 7.9 Ma).

In the several faults that constitute the Montagut fault system we obtained 13 U-Pb dates. These present important age variations from the oldest one during the Late Cretaceous at 79.8 ± 1.2 Ma (for Cc2) to the youngest one during the late Miocene at 9 ± 4.6 Ma (for Cc23). This dataset has been completed with two previously published dates in the area, which also yielded early and middle Miocene ages at 18.5 ± 0.5 Ma and 12.7 ± 2.9 Ma (Cruset et al., 2020b). These results point to successive episodes of fault development and/or reactivation affecting the Upper Cretaceous Sant Corneli Formation at the

Montagut locality. In this locality, we report the formation and/or reactivation of normal faults during precipitation of calcite cements Cc2 (at 79.8 ± 1.2 Ma), Cc18 (at 48.8 ± 8.6 Ma to 43.9 ± 0.7 Ma), Cc22 (at 20.8 ± 1.2 Ma to 16.8 ± 0.2 Ma) and Cc23 (9 ± 4.6 Ma), which precipitated in fractures F2, F18, F22 and F23, respectively. Therefore, the calcite cement Cc2 yielded a Late Cretaceous date, which is: (i) the oldest obtained age in this contribution and, (ii) older than the first age documented for the Bóixols thrust (71.2 ± 6.4 Ma, Haines, 2008). Ages for the Organyà fault and other pre-shortening fractures were not obtained in this study.

In the same way, at the Montagut locality, we document the formation and/or reactivation of strike-slip faults during precipitation of calcite cements Cc9a (at 58.7 ± 1.1 Ma), Cc17a (at 45.5 ± 0.8 Ma to 37.8 ± 3.5 Ma) and Cc20a (at 27.6 ± 2.3 Ma), which precipitated in fractures F9a, F17a and F20a, respectively. The precipitation of calcite cement Cc17a in strike-slip faults during the Lutetian, coincides with the formation of similar strike-slip faults in other localities, according to the age of their related cements Cc17b at 43.4 ± 3 Ma (Sant Joan locality) and cement Cc17e at 45.7 ± 9.7 (Sant Antoni locality).

At the Sant Joan locality, we did not obtain ages for the Sant Joan fault system (F21). However, we measured two dates for calcite cement Cc6a (67.1 ± 2.2 Ma and 65.4 ± 1.3 Ma), which precipitated in metric fractures (F6) in this locality. The former age has a mean squared weighted deviate (MSWD) of 10.6 (Table 3). As this value is higher than 2, it could indicate a mixing of ages, an open system or an incomplete initial equilibration of the Pb isotopes (Rasbury and Cole, 2009).

Other obtained ages in the Sant Corneli-Bóixols anticline account for the background deformation represented by fracture systems at different scales and studied at distinct localities. In this line, we document the formation of layer-parallel slip surfaces at 61 ± 21.8 Ma, according to its associated calcite cement Cc8 at Abella de la Conca locality. Similarly, we also report the formation and/or reactivation of meter-scale fractures during the Late Cretaceous to Oligocene, according to precipitation of calcite cements Cc6b (at 67.9 ± 3.9 Ma), Cc10 (at 56.9 ± 1.4 Ma), Cc15a-Cc15b (at 44.7 ± 4 Ma to 43.9 ± 1 Ma) and Cc20b (at 27.4 ± 0.9 Ma). These cements precipitated in fractures F6b, F10, F15 and F20b, respectively.

Table 3. U-Pb ages obtained for the different calcite vein generations. Cc3 from Haines, 2008; Cc5b from Guillaume et al., 2008, and Cc6b, Cc14a, Cc15a, Cc17e, Cc22 and Cc23 from Cruset et al., 2020b.

Cc	Sample	F	Locality	Age (Ma)	$\pm 2\sigma$	MSWD	Upper intercept	Number of spots
Cc2	Mgt21a	F2	MGT	79.8	1.2	1.3	0.7982 \pm 0.1746	20
Cc3	-	F3	SET	71.2	6.4	-	-	-
Cc5a	Abc34	F5a	ABC	67	0.7	1.3	0.8227 \pm 0.0041	12
Cc5b	-	F5b	SA	69	-	-	-	-
Cc6a	Bx47a	F6a	SJ	67.1	2.2	10.6	0.8118 \pm 0.0160	20
Cc6a	Bx47	F6a	SJ	65.4	1.3	1.3	0.8157 \pm 0.0070	20
Cc6b	Cn38	F6b	CN	67.9	3.9	1	0.8364 \pm 0.0110	27
Cc8	Abc24	F8a	ABC	61.2	21.8	1.5	0.8415 \pm 0.038	25
Cc9a	Mgt35a	F9a	MGT	58.7	1.1	1	0.8213 \pm 0.0157	20
Cc10	Abc22	F10	ABC	56.9	1.4	1.3	0.8261 \pm 0.0239	20
Cc14a	Bx5	F14a	FB	55.5	1.2	1.3	0.8210 \pm 0.0065	24
Cc14b	Abc3	F14b	ABC	36.6	7.9	0.78	0.8055 \pm 0.0145	21
Cc15a	Bx16	F15a	CM	44.7	4	0.5	0.8483 \pm 0.0091	23
Cc15b	Bx26	F15b	OC	43.9	1	1.5	0.8446 \pm 0.0050	21
Cc17a	Mgt15	F17a	MGT	45.5	0.8	1.4	0.8341 \pm 0.0072	21
Cc17a	Mgt15a	F17a	MGT	42.1	2.6	1.4	0.8521 \pm 0.0102	20
Cc17a	Mgt20	F17a	MGT	37.8	3.5	1.2	0.8288 \pm 0.0043	19
Cc17b	Bx46	F17b	SJ	43.4	3	1	0.8232 \pm 0.0064	20
Cc17e	Bx33	F17e	SA	45.7	9.7	0.7	0.8417 \pm 0.0081	20
Cc18	Mgt24	F18	MGT	48.8	8.6	0.9	0.8449 \pm 0.0253	24
Cc18	Mgt21b	F18	MGT	45.3	2.5	0.4	0.8074 \pm 0.0568	20
Cc18	Mgt3	F18	MGT	43.9	0.7	1.2	0.7629 \pm 0.0598	20
Cc19	Abc32	F19	ABC	33.2	0.8	0.9	0.8219 \pm 0.0098	20
Cc20a	Mgt35b	F20a	MGT	27.6	2.3	0.5	0.8061 \pm 0.0438	21
Cc20b	Bx28	F20b	OC	27.4	0.9	1.3	0.8389 \pm 0.0074	20
Cc22	Mgt3	F22	MGT	20.8	1.2	1.2	0.8143 \pm 0.0059	18
Cc22	Mgt2	F22	MGT	18.1	0.5	1.3	0.8392 \pm 0.0087	9
Cc22	Mgt1	F22	MGT	16.8	0.2	1.6	0.8115 \pm 0.0815	15
Cc22	Mgt9	F22	MGT	18.5	0.5	1.4	0.8232 \pm 0.0092	27
Cc23	Mgt9	F23	MGT	12.7	2.9	0.9	0.8234 \pm 0.0039	23
Cc23	Mgt33	F23	MGT	9	4.6	0.4	0.8134 \pm 0.0025	21

5. OVERALL DISCUSSION: SYNTHESIS OF THE MAIN RESULTS

5.1. Timing of deformation: fracture development and related tectonic setting

Several approaches have been applied in this PhD thesis to determine the chronology of the studied structures. In the Estamariu thrust, U-Pb dating of the vein cements failed due to their high lead contents and low uranium contents and therefore, the relative timing of the different mesostructures and microstructures has been determined by means of crosscutting relationships and microstructural analysis. In the Sant Corneli-Bóixols anticline the timing of deformation has been constrained by means of U-Pb geochronology of the vein cements as well as field structural data and crosscutting relationships between fractures.

In **the Estamariu thrust**, the observed structures and microstructures have been attributed to three stages of regional deformation including Variscan and Alpine compressional phases and the subsequent Neogene extension. The Estamariu thrust is Variscan in origin (Poblet, 1991) but in the study area, it affects late to post-Variscan Stephano-Permian andesites, thus confirming its reactivation during the Alpine orogeny. Therefore, the structures that are attributed to the Variscan orogeny correspond to the background deformation that is only found in pre-Variscan (Devonian) rocks located in the hanging wall of the Estamariu thrust. This pre-Variscan sequence is affected by a decametric-scale anticline and pervasive axial plane regional foliation (S1). Therefore, these structures are considered as developed during the Variscan compression, contemporaneous with the main activity of the Estamariu thrust. Similar structures, multiscale folds and axial plane regional foliation, broadly developed during the main Variscan deformation phase in the Paleozoic metasedimentary rocks from the Pyrenean basement (Zwart, 1986; Bons, 1988; Cochelin et al., 2018). In addition, Veins V0 and stylolites e1 are only concentrated in the Devonian rocks of the hanging wall and therefore are interpreted as originating coevally, probably in Variscan times.

The structures that are strictly attributed to the Alpine reactivation of the Estamariu thrust are those structures indicating reverse kinematics or associated with a compressional stress, which are found within the thrust zone deformation at the contact between Devonian and Stephano-Permian units. Calcite veins V1a and V2 (and related cements Cc1a and Cc2), exclusively occurring within the Estamariu thrust zone, belong to this Alpine stage. Associated with this ongoing deformation and progressive shortening,

stylolites e2 developed as sutured areas between host rock and veins V1a and between foliation surfaces, coevally with the development of veins V1b, as denoted by their crosscutting relationships and orientations.

Other structures present in the study area, such as veins V3 to V5 and related cements Cc3 to Cc5, postdate the compressional deformation and are compatible with an extensional regime. Therefore, these structures have been attributed to the Neogene extension. Veins V3 precipitated in the subsidiary thrust zone developed in the footwall of the Estamariu thrust. These veins strike parallel to, and locally crosscut, the thrust zone foliation (S2) and are characterized by calcite fibers growing perpendicular to the vein walls and to the foliation surfaces (Fig. 16f), thus postdating the compressional deformation and evidencing their extensional character. Veins V4 precipitated in subvertical and E–W mesoscale faults affecting the Stephano-Permian andesites away from the thrust zone. The fault orientation and dip that bound the Cerc basin and postdate the Estamariu thrust as well as the two striae set generations observed on the fault planes are compatible with the Neogene extensional faults (Cabrera et al., 1988; Roca, 1996; Saura, 2004). Calcite cements Cc3 and Cc4, occluding veins V3 and V4, have a similar geochemical composition, supporting the idea that their precipitation occurred during the same tectonic event and associated with a similar fluid regime (i.e., although these cements precipitated in different structures, they are likely contemporaneous). Finally, veins V5 (and related cement Cc5) precipitated locally in shear fractures crosscutting and postdating the thrust-related deformation. These veins strike parallel to the shear bands (Cn) located in the main thrust zone, exhibiting normal slip kinematics, postdating the reverse structures, and therefore indicating reactivation of the Estamariu thrust during the Neogene extension.

In the **Sant Corneli-Bóixols anticline**, this PhD thesis provides a robust geochronological dataset that includes 23 U-Pb ages of fracture-filling calcite cements. This dataset coupled with field data and crosscutting relationships between fractures allow to constrain the absolute timing of fracturing and to characterize the evolution of deformation in the frontal part of the Bóixols thrust sheet. This evolution of deformation is interpreted to record the pre-shortening fractures, developed previously to 79.8 ± 1.2 Ma, and the syn-compression folding and fracturing linked to the emplacement of the Bóixols thrust sheet and growth of the Sant Corneli-Bóixols anticline along its front between 71.2 ± 6.4 and 56.9 ± 1.4 Ma. Our data also reveal the post-emplacement

deformation during tectonic transport of the Bóixols thrust sheet to the south over the basal thrust of the South-Central Pyrenean Unit, from 55.5 ± 1.2 to 27.4 ± 0.9 Ma, and the post-orogenic exhumation of the Bóixols structure, from 20.8 ± 1.2 to 9 ± 4.6 Ma.

In this line, the oldest obtained date (79.8 ± 1.2 Ma), in a backlimb small normal fault from the Montagut locality (F2), is younger than the base of the syntectonic strata along the southern limb of the Sant Corneli-Bóixols anticline. Ages for the Organyà fault (F1a) and other pre-shortening fractures (F1b) were not obtained in this study. However, this pre-shortening deformation consists of WNW-ESE normal faults that are consistent with the NNE-SSW extensional regime that predates the Pyrenean compression (Berástegui et al., 1990). On the other hand, the Organyà fault juxtaposes the Jurassic pre-rift sequence in its footwall with the Lower Cretaceous syn-rift sequence in its hanging wall and thereby, this fault has previously been associated with the Early Cretaceous extension (Berástegui et al., 1990; Garcia-Senz, 2002). Faults F1b only affect the Lower Cretaceous syn-rift Lluçà Formation, which exhibits syn-faulting sedimentary geometries. Therefore, normal faults F1b have been considered syn-sedimentary faults and also attributed to the Early Cretaceous extension (Tavani et al., 2011).

Dates ranging from 71.2 ± 6.4 to 56.9 ± 1.4 Ma (calcite cements Cc3 to Cc10) are coeval with growth strata deposition along the southern limb of the Sant Corneli-Bóixols anticline. Therefore, these ages, obtained for fracture sets F3 to F10, are interpreted to record the emplacement of the Bóixols thrust sheet and growth of the Sant Corneli-Bóixols anticline along its front during the Late Cretaceous to Paleocene (Fig. 13). This is consistent with previous estimates placing the emplacement of the Bóixols thrust sheet and its eastern equivalent structure, the Upper Pedraforca thrust sheet, from 70.6 ± 0.9 to 55.3 ± 0.5 Ma (Cruset et al., 2020b). Similarly, authigenic illite dating of the Bóixols thrust-related deformation in the Setcomelles locality (F3) yielded an age of 71.2 ± 6.4 Ma (Haines, 2008), which agrees with growth strata that set the onset of shortening at ca. 72 Ma (Puigdefàbregas and Souquet, 1986; Bond and McClay, 1995). Besides, we did not obtain age for the two conjugated fracture sets (F4). However, the orientation of these fractures are compatible with the shortening direction of the Bóixols thrust (F3), and the similar petrographic and geochemical features of calcite cements Cc3 and Cc4, which precipitated in F3 and F4, accounts for a synchronous development. Fracture set F6 postdates fractures F4, as evidenced by crosscutting relationships and by the younger U-Pb age of F6, which yielded 67.9 ± 3.9 to 65.4 ± 1.3 Ma. Similarly, fracture set F7

postdates fractures F6 but are characterized by a similar orientation, thus indicating that they developed under the same stress field. The orientation of both F6 and F7 coincides with the NNW-SSE to NNE-SSW orientation of fractures that have previously been interpreted as developed during the main folding stage in the western termination of the Sant Corneli-Bóixols anticline (Shackleton et al., 2011). Fractures F8 represents bed-parallel slip surfaces. Although the obtained age for the cement Cc8 has a large error (61.2 ± 21.8 Ma), the formation of these surfaces is compatible with flexural-slip folding, which in turn is attributed to growth of the of the Sant Corneli-Bóixols anticline during the Bóixols thrust sheet emplacement (Tavani et al., 2011, 2017). Fracture set F9 is characterized by the strike-slip reactivation of inherited extensional faults developed during the pre-shortening deformation in the Cal Mestre and Montagut localities (F1b and F2, respectively). This reactivation is supported by the presence of overprinting striae sets and slickenlines exhibiting dip-slip and strike-slip kinematics and by the coexistence of two calcite cements in the same fractures (Cc9a postdating Cc1b and Cc9b postdating Cc2). Finally, fracture set F10 yielded a U-Pb age of 56.9 ± 1.4 Ma that postdates the previous deformation. The E-W orientation of set F10 is parallel to the fold axis. Therefore, these fractures have been associated with local extension due to strata bending, as interpreted by Beaudoin et al., 2015 in the Pico del Aguila anticline in the Sierras Exteriores in the Central-Western Pyrenees.

Dates ranging from 55.5 ± 1.2 to 27.4 ± 0.9 Ma, obtained for fractures F14 to F20, are Post-Paleocene and postdate the syn-tectonic strata that fossilizes the Bóixols structure. Therefore, these ages are interpreted to record the tightening of the entire Bóixols thrust sheet including its frontal Sant Corneli-Bóixols anticline during Eocene and Oligocene times. The major structural elements of this post-emplacement deformation are represented by fractures with a constant orientation independently of the bedding dips, and by strike-slip faults (F17) and frontal thrusts (F14) offsetting the steeply dipping limbs of the Sant Corneli-Bóixols anticline. Therefore, all these fracture sets developed once the strata had already been folded, coeval with the tectonic transport of the Bóixols thrust sheet to the south over the basal thrust of the South-Central Pyrenean Unit during a period that is characterized by maximum shortening rates (Vergés et al., 2002; Grool et al., 2018; Cruset et al., 2020b). In this line, the obtained U-Pb date for the Bóixols thrust in the Forat de Bóixols locality (F14a) yielded an age of 55.5 ± 1.2 Ma. Fractures F11 to F13 exclusively occur in the fault zone of this Bóixols thrust and they are considered to

have developed during the same process of thrusting. The synchronicity between the Bóixols thrust in the Forat de Bóixols locality (F14a) and fractures F11 to F13 is further explained at the end of this section. In addition, the obtained U-Pb age for the Bóixols thrust in the Forat de Bóixols locality (F14a), differs by almost 20 million years from that obtained for this thrust in the Abella de la Conca locality (F14b, 36.6 ± 8.0 Ma). However, in both places, the Bóixols thrust has the same orientation and exhibit the same relation with respect to bedding dips (i.e., it displaces the steeply dipping southern limb of the Sant Corneli-Bóixols anticline). Therefore, the obtained time span could be explained by a long-lasting faulting history or by a later movement of the main thrust fault during the post-emplacment deformation. Fractures F15 have a similar orientation to WSW-ENE fractures F10 and are also subperpendicular to the bedding strike. However, the obtained U-Pb ages for cements Cc15a and Cc15b (44.7 ± 4.0 to 43.9 ± 1.0 Ma), postdating the age of cement Cc10, allowed us to discern distinct fracture systems and to attribute them to different deformation stages. Fractures F16 predate strike-slip faults F17, although they have a similar orientation. Fractures F16 are interpreted as a pre-slip stage of F17. On the other hand, the obtained ages for Cc17a, Cc17b and Cc17e, ranging between 45.7 ± 9.7 and 37.8 ± 3.5 Ma, are consistent with the formation of strike-slip faults F17 in the Lutetian, during the post-emplacment deformation. Faults F18 and F19 are extensional and their formation indicates a local extension perpendicular to the main Pyrenean shortening direction. Finally, the obtained U-Pb ages for fracture set F20, ranging from 27.6 ± 2.3 to 27.4 ± 1.0 Ma, mark the end of the post-emplacment deformation during the Oligocene.

Finally, ages ranging from 20.8 ± 1.2 to 9.0 ± 4.6 Ma, obtained for sets F21 to F23, are post-Oligocene. Sets F21 to F23 are represented by normal faults that displace already folded beds in the northern backlimb of the anticline (the Sant Joan fault system) and by subsidiary faults developed around the Montagut fault system (Montagut locality). As compressional deformation in the SE Pyrenees is estimated to have finished in the Oligocene (Vergés et al., 2002; Grool et al., 2018), such faults likely developed during the post-orogenic exhumation of the Bóixols thrust sheet and the Sant Corneli-Bóixols anticline along its front during the Miocene. This post-orogenic deformation has also been reported in the eastern equivalent of the Bóixols thrust, which corresponds to the Upper Pedraforca thrust sheet (Cruset et al., 2020b).

Fracturing and veining in the Bóixols thrust zone at Forat de Bóixols locality. The relationships between thrusting and fracturing in the Bóixols thrust zone at Forat de Bóixols locality is discussed in this section. In this respect, the main stress orientations responsible for the development of the Bóixols thrust have been calculated plotting the main plane orientation and related slickenlines (Fig. 15e). The estimated stress field shows a SSE transport direction, compatible with the N-S to NNW-SSE shortening direction reported in the Pyrenees (Choukroune, 1989; Muñoz, 1992; Tavani et al., 2011), and a vertical minimum principal stress ($\sigma_v = \sigma_3$), characteristic of compressional regimes (Sibson, 2004; 2017). Fracture sets F11 to F13, found in the Bóixols damage zone, are interpreted as developed during the thrust activity under the same compressional regime (Gudmundsson, 2001; García-Senz, 2002; Bense et al., 2013). The synchronicity between thrusting and fracturing is supported by the exclusive presence of fractures F11 to F13 in the damage zone as well as by the gradual increase in fracture density and slight change in strike when approaching the main slip plane. However, the steeply dipping orientation of F11 and F12 with respect to the subhorizontal σ_1 axis differs with theoretical models that describe the formation of flat-lying extensional fractures that open in the σ_3 vertical direction (i.e., oriented parallel to the σ_1 axis) (Sibson and Scott, 1998; Vermilye and Scholz, 1998; Sibson, 2003; 2017). Despite this apparent discrepancy, the presence of the same calcite cements (Cc11 and Cc12) in F11-F12 fractures and in the mosaic to chaotic breccia developed along the fault plane corroborates the synchronicity between thrusting and fracturing. In the case of conjugated fracture systems F13, their bisector angle indicates a subhorizontal σ_1 and a subvertical σ_3 , and therefore, their formation is compatible with the prevailing stress field associated with thrusting ($\sigma_v = \sigma_3$).

Two mechanisms, a local variation of the stress axes as well as high fluid pressure conditions, are invoked to explain the formation of the steeply dipping F11 and F12 fractures in relation to the low angle reverse fault (Enlow and Koons, 1998; Begbie and Craw, 2006; Upton et al., 2008). In the first case, the remote stress fields could have varied locally within a constant far-field compressional regime to become properly oriented for the development of these fractures (Wilkinson and Johnston, 1996; Vermilye and Scholz, 1998; Begbie and Craw, 2006). Such a local variation of the magnitude and orientation of the remote stress fields is attributed to the formation of a process zone at the front of the fault tip during thrust (slip plane) propagation (Scholz and Dawers, 1993; Vermilye and Scholz, 1998). This occurs, firstly, because the fault tip acts as a stress

concentrator amplifying the magnitude of the remote stress (Scholz and Dawers, 1993) and, secondly, because the main compressive stress (σ_1) exhibits different angles with the fault in compressive quadrants with respect to dilational quadrants in propagating faults (Scholz and Dawers, 1993; Vermilye and Scholz, 1998).

On the other hand, several observations indicate that the formation of fractures F11 to F13 occurred under high fluid pressure conditions. A hydraulic pressure mechanism may explain the high concentration of systematically oriented extensional (F11, F12) and extensional-shear (F13) veins, as well as the absence of any structural orientation of veins in the breccias (Dewever et al., 2013). Comparable fracture systems (systematic arrays of extensional and extensional-shear fractures) are expected to develop in compressional settings when the tensile overpressure condition is achieved, that is, when the pore fluid pressure exceeds the least compressive stress ($P_f > \sigma_3$) (Branquet et al., 1999; Sibson, 2004; 2017). Such a fluid pressure is common during the propagation of thrust faults in compressional regimes (Bitzer, 2001; Cox et al., 2001; Sibson, 2004; Hilgers et al., 2006) and is attributed to: (i) the constraint stress field around the fault tip may generate overpressure of a confined fluid (Bussolotto et al., 2015; Sibson, 1996) (ii) the low dip of thrusts prevents vertical flow (Sibson, 2003; 2019) and, (iii) because of sediment compaction induced by loading during thrust sheet emplacement (Sibson, 1996; Dewever et al., 2013).

5.2. Fluid flow and deformation relationships in the two studied domains, along the Segre transect

Change in the fluid regime during the evolution of a long-lived thrust fault: the example of the Estamariu thrust

The geochemical features of the successive vein cements that precipitated in the Estamariu thrust attest for the origin, evolution of regimes and characteristics of the fluids that circulated during deformation.

In the Estamariu thrust, the $^{87}\text{Sr}/^{86}\text{Sr}$ ratios of the different calcite cements (Cc1a to Cc5) are significantly higher radiogenic than ratios of Phanerozoic seawater (between 0.7070 and 0.7090). This has been interpreted as resulting from the interaction between the vein-forming fluids and Rb-rich and/or Sr-rich Paleozoic basement rocks such as those underlying the Estamariu thrust. However, the geochemical evolution through time from

cement Cc1a to Cc5 highlights the progressive change in the fluid regime and composition during successive compressional and extensional tectonic events.

Calcites Cc1a and Cc2 were attributed to the Alpine reactivation of the thrust. As these cements precipitated in the thrust zone during the same tectonic, they likely precipitated from the same migrating fluids. The temperature and the $\delta^{18}\text{O}_{\text{fluid}}$ of their parent fluids, calculated from clumped isotope thermometry of Cc2, range between 50 and 100°C and between -6.4 ‰SMOW and -0.3 ‰SMOW, respectively. These values are interpreted as the involvement of meteoric fluids that were probably heated at depth and enriched in radiogenic Sr during their flow and interaction with basement rocks (Fig. 22a). These fluids flowed preferentially along the thrust zone, as evidenced by the exclusive presence of calcites Cc1a and Cc2 in this area, likely due to the enhanced permeability associated with the thrust discontinuity (McCaig et al., 1995). In addition, Cc1a has $\delta^{13}\text{C}$ values between +0.91 and +2 ‰VPDB, which are similar to values of the Devonian marine limestones from the hanging wall (between +1.54 and +2.75 ‰VPDB). Likewise, the elemental composition of Cc1a follows a similar trend to that of its Devonian host, both having high Mg and Sr and low Mn contents with respect to the other calcite cements. These geochemical similarities indicate high fluid-rock interaction and buffering of the carbon and elemental composition of the precipitating fluid by the Devonian carbonates (Marshall, 1992). Calcite cement Cc2 has slightly lower $\delta^{13}\text{C}$, lower Mg and Sr and higher Mn contents with respect to both Cc1a and the Devonian host. This indicates a progressive increase in the extent of fluid-rock interaction from the thrust plane, where Cc2 precipitated, towards the hanging wall, where Cc1a is found.

Calcites Cc3 to Cc5 were attributed to the Neogene extension and their associated geochemistry characterizes the fluid system during this tectonic event. Cements Cc3 and Cc4 are characterized by heavier $\delta^{18}\text{O}_{\text{fluid}}$ (up to +12‰SMOW), within the range of metamorphic and/or formation fluids, and higher temperature of precipitation (up to 210°C) with respect to the previous cements (Cc1a and Cc2). Assuming a normal geothermal gradient of 30 °C/km, these temperatures would have been reached at a minimum depth of 3 – 5 km. However, these veins have never reached such a burial depth, since during the Neogene extension the studied structure acquired its current configuration (Saura, 2004) and was only buried under the Devonian sequence (hanging wall), which has a maximum thickness of several hundred meters (Mey, 1967). This assumption evidences the hydrothermal character of the circulating fluids, which

probably migrated rapid enough through newly formed and reactivated fault zones to maintain their high temperatures and to be in thermal disequilibrium with the surrounding rocks. Similarly, the high Mn content of Cc3 and Cc4 (around 7700-8300 and 4000 ppm, respectively), responsible of their bright luminescence, is consistent with hydrothermal waters (Pomerol, 1983; Pfeifer et al., 1988; Pratt and Force, 1991). On the other hand, the $\delta^{13}\text{C}$ -depleted values of these cements (around -8 ‰VPDB) are indicative of the influence of organic-derived carbon (Cerling, 1984; Vilasi et al., 2006). A plausible source for these low $\delta^{13}\text{C}$ values is the Silurian black shales that do not crop out in the study area but acted as the main detachment level during the Variscan compression, and locally during the Alpine compression in the Pyrenean Axial Zone (Mey, 1967). These black shales have significant organic carbon contents (TOC around 2.3%), and around the Gavarnie thrust, they exhibit syntectonic carbonate veins yielding $\delta^{13}\text{C}$ values between -8 and -2 ‰VPDB (McCaig et al., 1995). Thus, cements Cc3 and Cc4 precipitated from hydrothermal fluids derived from and/or equilibrated with basement rocks and expelled through fault zones during deformation (Fig. 22b). The continuous increase in precipitation temperatures and enrichment in $\delta^{18}\text{O}_{\text{fluid}}$ from calcite cements Cc1a and Cc2 (Alpine) to cements Cc3 and Cc4 (Neogene) is probably linked to longer residence times of the later fluids and a higher extent of fluid–rock interaction with basement rocks.

Finally, the isotopic signature of Cc5, ranging between -8.1‰VPDB and -5.7‰VPDB for $\delta^{18}\text{O}$ and between -8.2‰VPDB and -3.8‰VPDB for $\delta^{13}\text{C}$, falls within the range of meteoric carbonates (Veizer, 1992; Travé et al., 2007). The similar tendency in the elemental composition of this cement and the Stephano-Permian volcanic rocks, both having the highest Mg and Fe and the lowest Mn and Sr contents with respect to the other cements and host rocks, reveals significant fluid–rock interaction with the footwall rocks. The significant water–rock interaction is also demonstrated by the Nd isotopic composition of Cc5 (0.512178), yielding values similar to the volcanic host (0.512196). This fact indicates that this cement precipitated from percolation of meteoric fluids, the geochemistry of which was controlled by the volcanic host rock. Studies focused on infiltration of meteoric fluids and subsequent upflow along La Tet fault during the Neogene extension have shown that meteoric waters in the area infiltrate at high altitudes, around 2000 m, and low temperatures, around 5 °C (Krimissa et al., 1994; Taillefer et al., 2018). Therefore, during the latest stages of extension, the infiltration of meteoric fluids

likely indicates a more significant change in the fluid regime from upward migration of hydrothermal fluids to downward percolation of meteoric waters.

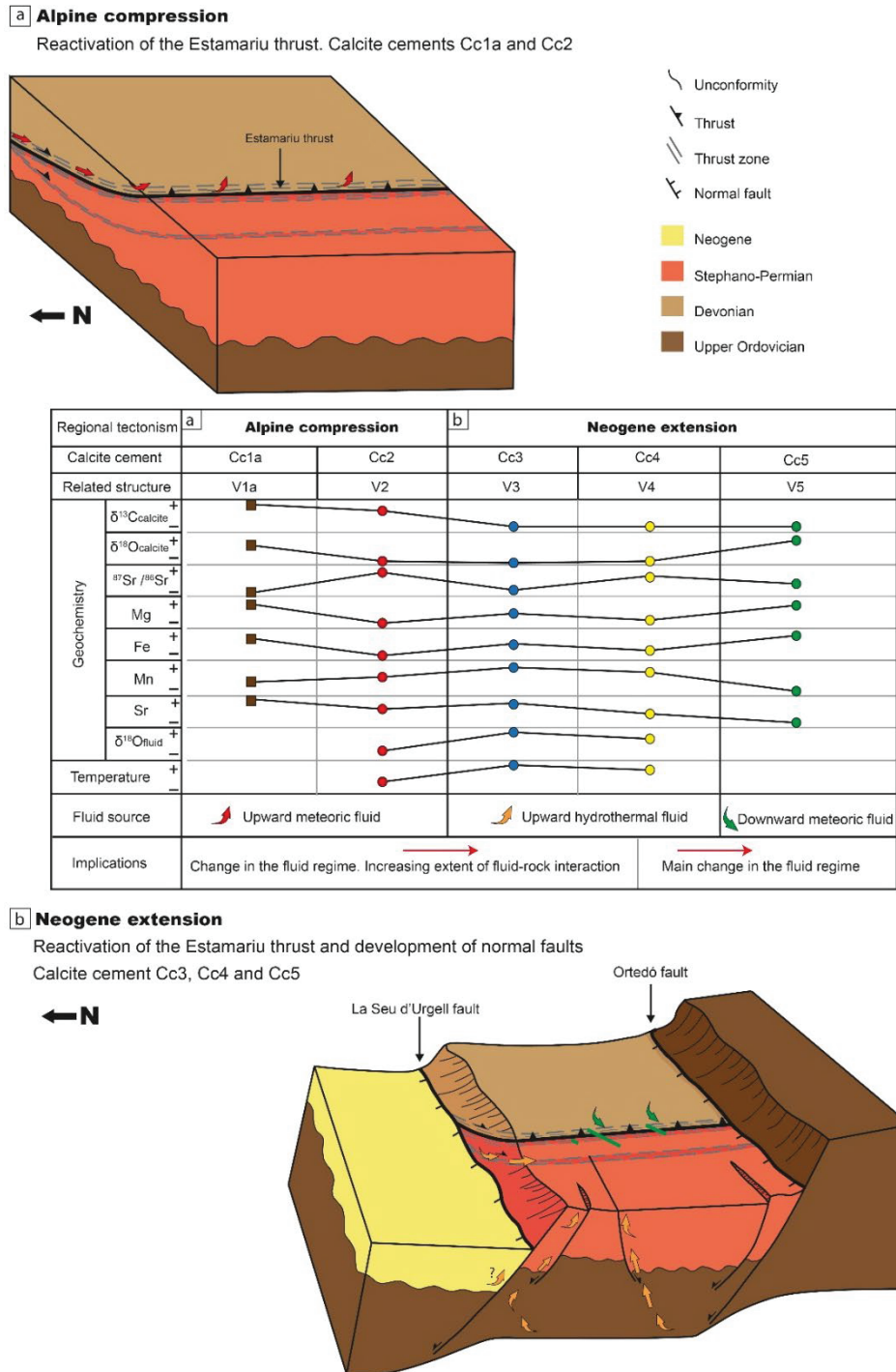


Fig. 22. Tectonic and geochemical evolution of the Estamariu thrust (not to scale) and relationships with the evolution of the fluid system. a) During the Alpine reactivation of the Estamariu thrust, a meteoric fluid (red arrows) interacted at depth with basement rocks and then migrated along the thrust zone and towards the hanging wall, precipitating cements Cc1a and Cc2, respectively. b) During the Neogene extension, basement-derived hydrothermal fluids (orange arrows) flowed upwards through newly formed and reactivated fault zones. This fluid precipitated calcite cements Cc3 and Cc4. Finally, during ongoing deformation, meteoric fluids (green arrows) percolated in the system and precipitated Cc5, revealing a main change in the fluid regime.

Origin, distribution and variation of fluids across a large fold: the example of the Sant Corneli-Bóixols anticline

This section discusses the source and spatial distribution of fluids across the distinct structural positions of the Sant Corneli-Bóixols anticline.

In the core of the Sant Corneli-Bóixols anticline and in the base of the syntectonic deposits in the footwall of the Bóixols thrust sheet (Cal Mestre and Sant Antoni localities, respectively) the calcite cements associated with successive episodes of fracturing and vein formation (i.e., group 1 of calcites) do not record significant changes in the fluid composition through time (Figs 18-21). Accordingly, all cements from this group have similar $\delta^{13}\text{C}$ values to their associated carbonate host rocks (Lluçà and Vallcarga Formations, respectively), which in turn yield typical marine values (Fig. 18) (Veizer et al., 1999). The $^{87}\text{Sr}/^{86}\text{Sr}$ ratios of the vein cements are similar to those ratios of local host rocks, which also reflect the composition of contemporaneous seawater (LOWESS curve in Fig. 20). Indeed, the low Mn content of calcites group 1 and correspondent host rocks, responsible for their dark to non-luminescence, together with their high Sr content and high Y/Ho ratios (Fig. 21) approaches the elemental composition of marine carbonates derived from well-oxygenated seawater (Popp et al., 1986). Therefore, the similar petrographic and geochemical features of all calcite cements and host rocks from Cal Mestre and Sant Antoni localities indicate very low water-rock ratios (i.e., diffusive flow) and precipitation of successive calcite cements in a closed/rock-buffered system during different fracturing events (Vandeginste et al., 2012; Boutoux et al., 2014; Hurai et al., 2015). A plausible source for this host rock-buffered fluid was the interstitial seawater trapped in the Lower Cretaceous and Upper Cretaceous marine carbonates present in Cal Mestre and Sant Antoni localities, respectively. Alternatively, the local host carbonates could have been the source for the successive calcite cements by means of pressure-resolution and/or diffusion processes (Oliver and Bons, 2001; Bons et al., 2012; Vandeginste et al., 2012; Toussaint et al., 2018; Salomon et al., 2020). In this scenario, the slight depletion in $\delta^{18}\text{O}$ values of calcites group 1, with respect to host rocks and typical marine values, likely indicate variation in fluid temperatures during different events of calcite cement precipitation. These varying conditions are expected during progressive deformation linked to the emplacement of the Bóixols thrust and growth of the Sant Corneli-Bóixols anticline.

Therefore, this host-rock buffered fluid from which calcites group 1 precipitated characterizes the paleohydrological system in the core of the Sant Corneli-Bóixols anticline and in the base of the syntectonic deposits along the southern flank of the fold (Fig. 23). In the core of the anticline (Cal Mestre locality), the Lower Cretaceous mudstones and marls from the Lluçà Formation have a minimum thickness of 2500 m (Lanaja, 1987). Due to the expected non-permeable character of this unit and its considerable thickness, the small-scale fractures (up to several meters long) occurring in this locality, likely represented poorly efficient conduits to connect different hydrostratigraphic reservoirs, thus preventing the input of external fluids. In the base of the syntectonic deposits (Sant Antoni locality), the Upper Cretaceous marine mudstones from the Vallcarga Formation were deposited during the early contraction and initial growth of the Sant Corneli-Bóixols anticline (Ardèvol et al., 2000). Therefore, the local origin of the fluids in this domain is consistent with the marine setting of deformation that likely affected recently deposited and poorly lithified sediments (Travé et al., 2007).

The geochemical data of calcite cements from group 2, precipitated in decametric to kilometric faults (the Bóixols thrust, the Montagut fault system, the Sant Joan fault system) and related fractures, evidence a very different scenario. These calcites display the most depleted $\delta^{18}\text{O}$ values, with respect to other cements, and exhibit up to 10 ‰VPDB lighter values than their adjacent host rocks (Fig. 18). This $\delta^{18}\text{O}$ -depletion, which indicates that the parent fluids were external, is linked to a relative high temperature of precipitation ($>80\text{ }^{\circ}\text{C}$ and up to $120\text{ }^{\circ}\text{C}$), according to results from clumped isotope thermometry. Indeed, the $\delta^{18}\text{O}_{\text{fluid}}$, between $+0.6$ and $+5.5$ ‰VSMOW, also obtained from clumped isotopes, indicates formation waters circulating through fault zones and related fractures during faulting. On the other hand, the scattered $\delta^{13}\text{C}$ values and $^{87}\text{Sr}/^{86}\text{Sr}$ ratios of these cements, as well as their variable enrichment in Mn content, and their differing luminescence characteristics could indicate that the formation fluids evolved from distinct fluid origins (marine, connate and/or meteoric) and that they interacted with different sedimentary units (Travé et al., 2007; Vandeginste et al., 2012). Similarly, the Y/Ho ratios of group 2 of cements indicate a variable degree of siliciclastic and marine influence (Fig. 21). As large-scale faults affect all stratigraphic sequences involved in the anticline, from Jurassic marine to Paleocene continental host rocks, such variation may result from the interaction between the vein-forming fluids and marine

(high Y/Ho ratio) or continental (low Y/Ho ratio) rocks (Bau and Dulski, 1994; Nardini et al., 2019).

In this line, strike-slip faults F17 from Coll de Nargó locality acted as transfer zones for the migration of deeper Late Cretaceous connate waters to shallower non-marine sediments of the Garumnian facies, where cement Cc17d was observed. Likewise, the Bóixols thrust in Forat de Bóixols locality (F14a) acted as an efficient conduits for the migration of deep formation waters. In both examples, fluids were in chemical, and probably in thermal disequilibrium with their adjacent host rocks but the $^{87}\text{Sr}/^{86}\text{Sr}$ values of their associated cements reflect the composition of Cretaceous carbonates. Therefore, these ascending fluids were likely expelled due to vertical compaction linked to thrust sheet emplacement and/or tectonic horizontal shortening (squeegee-type fluid flow) during continuous compression (Oliver, 1986; Roure et al., 2010; Vandeginste et al., 2012).

Therefore, heated formation waters from which calcites group 2 precipitated characterizes the fluid system associated with large-scale faults and related fractures. The development of these larger fracture systems facilitated the transference of fluids between different hydro-stratigraphic units decreasing the extent of interaction between fluids and host rocks. This indicates that the Bóixols thrust, the Montagut fault system, the Sant Joan fault system and other large faults and related fractures acted as efficient conduits for fluid migration during their formation at different stages of the deformation history.

Cements from group 3 precipitated in centimetric to metric scale fractures in the limbs of the Sant Corneli-Bóixols anticline. The isotopic signature of these cements, ranging between -8 and -6 ‰VPDB for $\delta^{18}\text{O}$ and between -10 and +2 ‰VPDB for $\delta^{13}\text{C}$, fall within the range of meteoric carbonates (Veizer, 1992; Travé et al., 2007; Pujalte et al., 2009), although with occasional marine influence evidenced by the positive $\delta^{13}\text{C}$ values of cements Cc6a and Cc6b (Fig. 18). The meteoric origin of cements from group 3 is supported by their $^{87}\text{Sr}/^{86}\text{Sr}$ ratios, which are lower than those values of their adjacent host rocks (Fig. 20), and by the elemental composition of these cements, yielding the lowest Sr contents with respect to other cements and host rocks. The low Y/Ho ratios, which indicates the influence of terrigenous sediments (Bau and Dulski, 1994), and the CL zonation of Cc6a and Cc12, which points to oxidizing-reducing fluctuations, are again characteristic features of the meteoric environment. At outcrop scale, clumped isotopes reveal a progressive increase in precipitation temperatures, from 40 °C to 80 °C (Forat de

Bóixols locality) and from 25 °C to 85 °C approximately (Coll de Nargó locality), as well as an enrichment in $\delta^{18}\text{O}_{\text{fluid}}$, from -1.8 to +5.9 ‰VSMOW and from -4.2 to +2 ‰VSMOW, respectively (Fig. 19). This fact indicates a continuous shift in the fluid composition, from meteoric fluids to evolved meteoric fluids due to water-rock interactions at increasing temperatures during deformation. Therefore, these geochemical features indicate that the fluid system associated with fractures F6a, F6b, F11, F12 and F16b was open to the input of meteoric fluids, which geochemistry was influenced by the surrounding host carbonates.

Therefore, meteoric waters from which calcites group 3 precipitated characterizes the fluid system in the limbs of the Sant Corneli-Bóixols anticline, where Forat the Bóixols, Coll de Nargó and Sant Joan localities are located (Fig. 23). Meteoric waters generally infiltrate at high structural reliefs such as the crestal domain of anticlines (Beaudoin et al., 2015; Cruset et al., 2016). However, in the Sant Corneli-Bóixols anticline meteoric fluid percolation was recorded in the fold limbs because most of the crestal domain was eroded synchronously with folding (Tavani et al., 2011). This interpretation is in line with the exclusive presence of calcites from group 3 in the forelimb (Coll de Nargó and Forat de Bóixols localities) and backlimb (Sant Joan locality) of the anticline. On the other hand, the geochemical and geochronological data of calcite cements Cc6a and Cc6b (both from group 3) set the initial infiltration of meteoric fluids at the Maastrichtian, during formation of fractures F6 at ca. 67 – 65 Ma. This fluid flow event coincides with the transition from marine to continental conditions, during the progressive uplift of the structure, coevally with sedimentation of the non-marine continental Garumnian facies (Trempl Group) from Late Maastrichtian to Paleocene (Plaziat et al., 1981; Garcés et al., 2020). This scenario of meteoric fluid infiltration during the main folding stage and during the change from marine to continental conditions have also been reported in other studies focused on the evolution of the fold-fluid system (Travé et al., 2007; Evans and Fischer, 2012; Beaudoin et al., 2015).

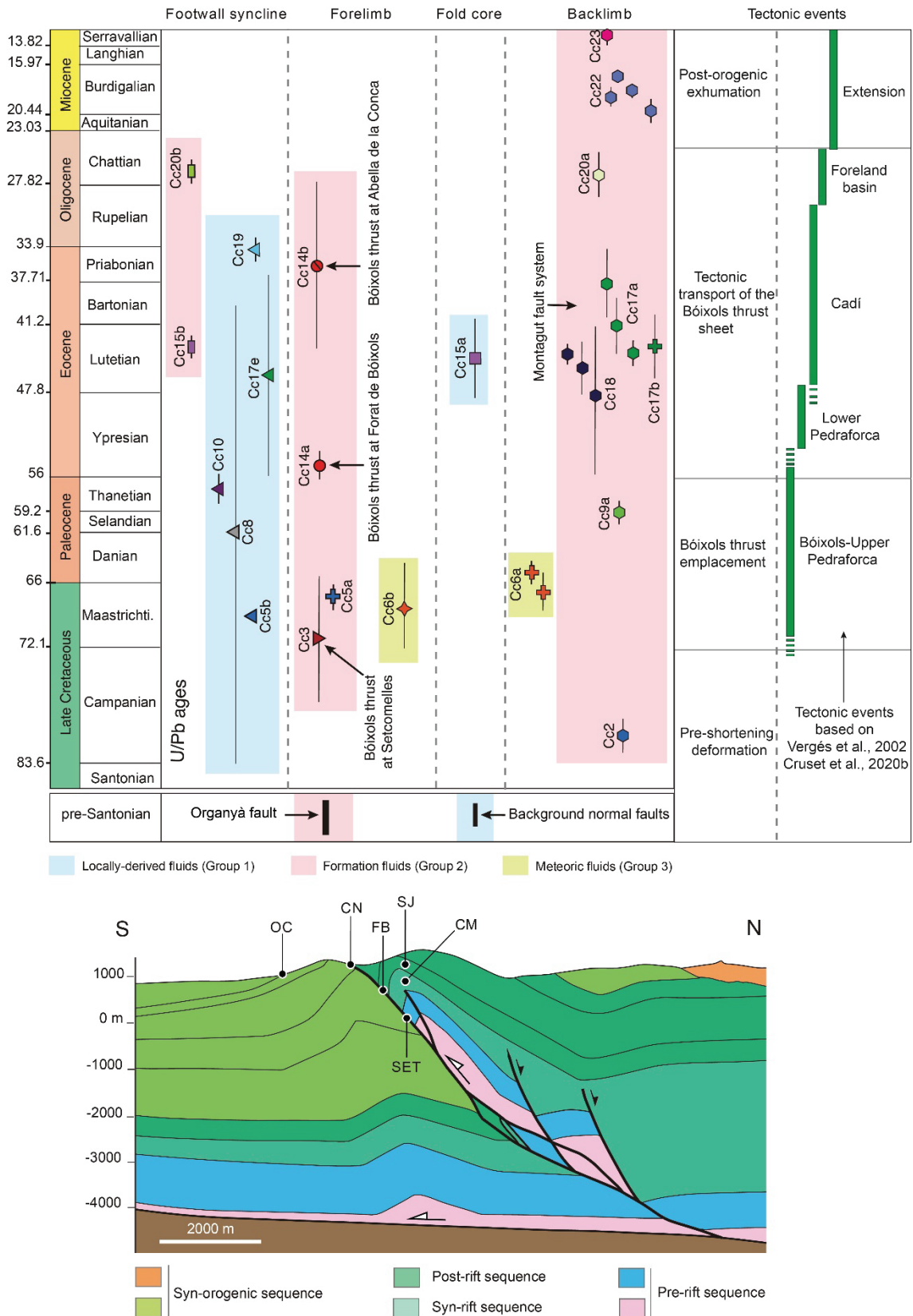


Fig. 23. Cross-section of the Sant Corneli-Bóixols anticline along the front of the Bóixols thrust sheet showing the spatial variation of fluids in the several structural positions of this fold and according to the studied localities (CM: Cal Mestre, SJ: Sant Joan, FB: Forat de Bóixols, SET: Setcomelles, CN: Coll de Nargó, OC: Orcau). The U-Pb ages of the different calcite vein generations and related tectonic events are also included. Cross-section modified from Vergés, 1993.

In conclusion, our data reveal that the fluid flow history varied at the several structural positions of the Sant Corneli-Bóixols anticline and according to the age and nature of their stratigraphy and the involved fracture networks. This indicates a compartmentalization of the fluid system (Fig. 23). Thus, in the core of the fold, at least around Cal Mestre locality, and in the base of the syn-tectonic deposits (Sant Joan locality), the fluid system was essentially stratified and locally derived from the Lower Cretaceous and Upper Cretaceous marine carbonates, revealing high extent of fluid-rock interaction. Contrarily, along large faults, affecting different parts of the anticline, and in the fold limbs, the paleohydrological system was open to the input of external fluids in geochemical and probably thermal disequilibrium with their adjacent host rocks. Large faults acted as conduits for the upward migration of formation waters from deeper regions of the Sant Corneli-Bóixols anticline, whereas the fold limbs registered the infiltration of meteoric waters (Fig. 23). Therefore, in the studied anticline, the scale, connectivity and distribution of the main fracture networks together with the involved stratigraphy were the main controls on the source and distribution of fluids, the degree of fluid-rock interactions and the scale of fluid migration during deformation.

Spatio-temporal hydraulic behavior of a carbonate thrust zone: The example of the Bóixols thrust

The scale, connectivity and distribution of fractures that developed during the evolution of the Bóixols thrust sheet and growth of the Sant Corneli-Bóixols anticline along its front strongly controlled the origin and distribution of fluids during deformation. Therefore, this section aims to reconstruct the evolution of a well-exposed thrust zone displacing the forelimb of the anticline (fault F14a and related fractures F11 to F13 in Forat de Bóixols locality), and to evaluate the qualitative hydraulic behavior of the fault.

In the Bóixols thrust zone, the successive deformation stages, associated with different fracture systems and related calcite veins, highlight an episodic evolution of the studied thrust. We interpret this evolution as resulting from an upward propagation of the fault tip leading to distributed deformation within the process zone before propagation of the fault (Reches and Lockner, 1994; Vermilye and Scholz, 1998; Labaume et al., 2004; Baqués et al., 2010). During initial fault growth, deformation at the fault tip, i.e., within the process zone, was likely dominated by concentration of dilatant (extensional)

fracturing, giving rise to fractures F11, F12 and the mosaic to chaotic breccia from the footwall. The cements that precipitated in such fractures (Cc11 and Cc12) belong to group 3 of calcites, and thereby, the fluid associated with this initial deformation stage was a meteoric fluid that infiltrated the system on high structural reliefs likely elevated during growth of the Sant Corneli-Bóixols anticline. These fluids migrated through diffuse deformation developed in the process zone before the growth and propagation of the thrust slip plane (Fig. 24a). During this initial stage of deformation the remote stress fields varied locally in the process zone, allowing for the formation of steeply dipping fractures (F11 and F12) (Fig. 24a, b).

Finally, the thrust slip plane propagated through the process zone. Frictional processes occurred along the thrust surface as well as the progressive weakening of the fault zone, which led to the formation of the foliated cataclasite, characterized by S-C shear fabric, pressure solution seams, calcite mineralization and carbonate fine-grained matrix. This micritic matrix is petrographically similar to that of the hanging wall protolith and displays comparable isotopic composition. These observations indicate that the cataclasite matrix derived from the hanging wall carbonates. During this period of thrust sheet emplacement, fractures F13 developed. We interpret that the orientation of these fractures represents the far-field stress regime unaltered by faulting (Fig. 24c). The calcite cement Cc13, precipitated in fractures F13, belong to group 3 of calcites and indicates the evolution of previous meteoric fluids into formation waters at increasing depths and temperatures during thrusting. Later, the thrust acted as a preferential pathway for fluids that only infiltrated in the hanging wall block as indicated by the presence of the same calcite cement (Cc14) along the thrust slip plane (F14), in the fault core and within the crackle proto-breccia from the hanging wall. This cement also belongs to group 3 of calcites and its geochemistry also indicates the presence of formation fluids that likely evolved from connate waters derived from Cretaceous carbonates. This last interpretation is deduced from the $\delta^{13}\text{C}$ and $^{87}\text{Sr}/^{86}\text{Sr}$ ratios of Cc14, which yield typical marine values.

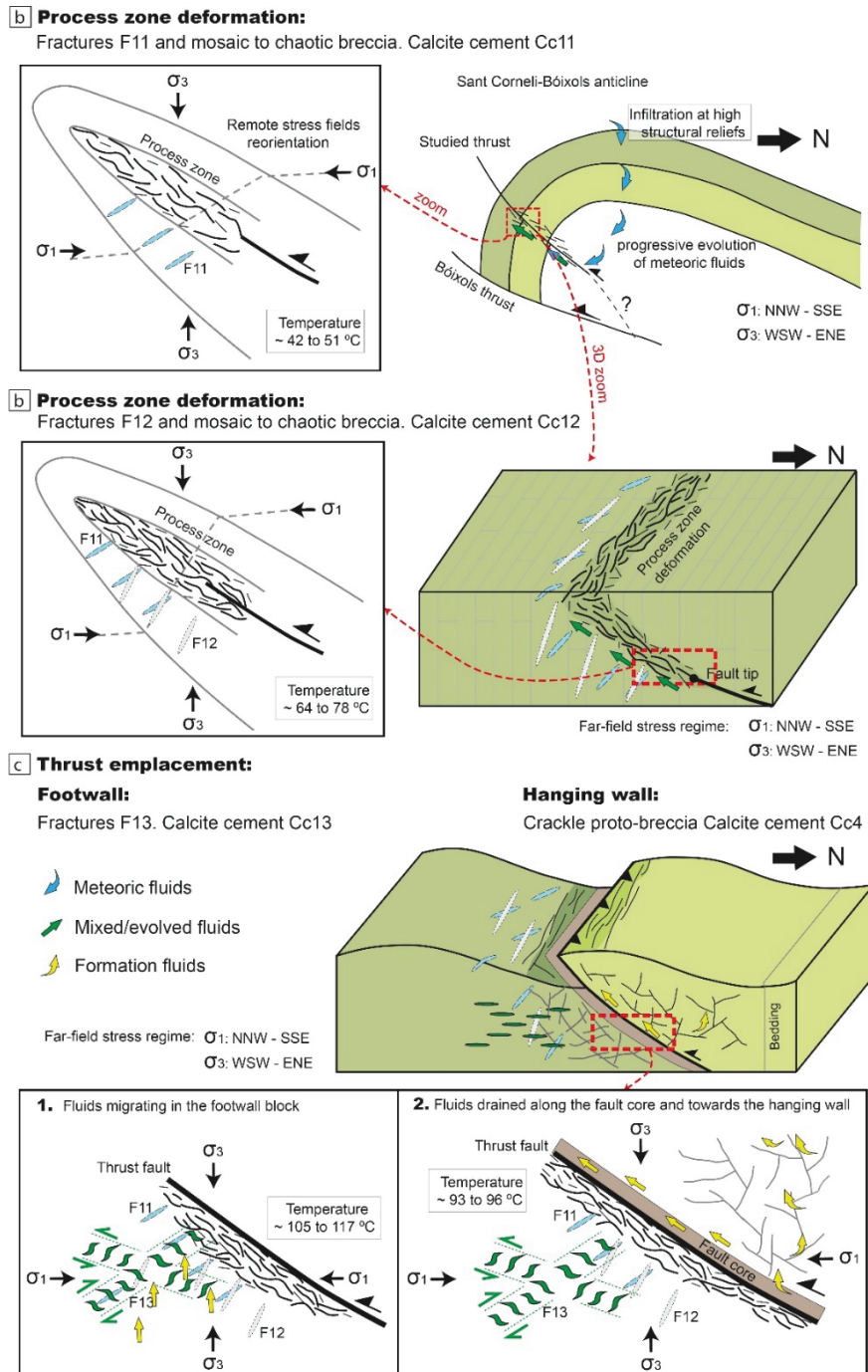


Fig. 24. Fluid flow model during the evolution of the Bóixols thrust in Forat de Bóixols locality (not to scale) showing the relationships among synkinematic fracture development, the stress state at each deformation phase and the involved fluid flow event. (a) During initial fault growth, deformation was concentrated in the process zone (around the fault tip) allowing the formation of fractures F11 and randomly oriented fractures (mosaic to chaotic breccia). During this episode, meteoric fluids infiltrated at high structural reliefs, warmed at depth and then migrated through diffused deformation around the fault tip. (b) During progressive deformation, new fractures develop and meteoric fluids evolved at increasing depths and temperatures. During these two initial fracturing events (F11-F12) the remote stress field varied locally within the process zone to generate steeply dipping fractures. (c) As the thrust developed, fractures F13 were formed in the footwall damage zone. The orientation of these fractures reflects the far-field stress regime unaltered by faulting. The fluid involved in this stage evidences the continuous increase in precipitation temperatures due to burial during thrust emplacement. From this stage, the thrust drained fluids that only infiltrated in the hanging wall. These fluids were likely expelled from underlying Cretaceous carbonates due to rock compaction during thrusting.

In conclusion, the petrology and geochemistry of the studied calcite cements indicate that the Bóixols thrust separates two compartments with different deformation and fluid flow patterns. It is therefore likely that the thrust acted as a transversal barrier for fluids migrating between the footwall and hanging wall. The barrier role of the thrust is attributed (i) to the poor permeability of the foliated cataclasite and its micritic carbonate matrix with concentration of clay minerals associated with pressure-solution surfaces, and (ii) to the non-porous character of the hanging wall carbonates (i.e., wackestones). In the latter case, although it has not been measured, the permeability is likely lower in the hanging wall wackestones with respect to the footwall grainstones. Therefore, the thrust acted as a transversal barrier and a longitudinal drain from fluids. On the other hand, the continuous formation of different fracture systems and related calcite cementation phases evidences that the structural permeability was transient and that successive episodes of fracturing added new pathways to fluids that were rapidly occluded by calcite precipitation and sealing (Agosta et al., 2007; Bense et al., 2013). The fact that the calcite cements Cc11 to Cc13 vary geochemically through time demonstrate that the fluid pathways and regime evolved due to successive events of fracture opening and calcite cementation. This change may result from a continuous shift in the fluid composition, due to the evolution of the meteoric waters, or from a progressive change in the fluid origin, from percolation of diluted meteoric waters to upflow of hotter formation fluids.

The interpreted evolution of the studied thrust zone is similar to models of fault evolution proposed in extensional settings during upward propagation of normal faults deforming carbonate rocks (Stewart and Hancock, 1988; 1990; Vermilye and Scholz, 1998; Labaume et al., 2004; Baqués et al., 2010; Bussolotto et al., 2015). Therefore, the comparison between these studies allows to provide insights into deformation processes and mechanisms related to propagation of faults in different geological settings. Interestingly, all these contributions reported an initial stage of fault nucleation related to the development of a process zone (in the fault tip) before individualization of the fault plane. This period was characterized by the formation of hydraulic extension fracturing and brecciation and the presence of a fluid in chemical equilibrium with the host rocks. Finally, the progressive deformation resulted in the propagation of the fault (slip plane) through the process zone and the circulation of external fluids along the main slip surfaces (i.e., longitudinal fluid migration). These studies also reported an evolution of the fracture connectivity, a continuous opening of the fluid regime, and a progressive change in the

fluid composition and origin during the evolution of the fault zone (Labaume et al., 2004; Baqués et al., 2010; Bussolotto et al., 2015). Therefore, this study also highlights the similarity in deformation processes and mechanisms linked to the evolution of fault zones in compressional and extensional regimes involving carbonate rocks.

5.3. Fluid flow and deformation relationships at regional scale

Influence of Paleozoic basement rocks on the $^{87}\text{Sr}/^{86}\text{Sr}$ ratios of the vein-forming fluids

This section assess the influence that basement rocks have on the chemistry of fluids that circulate during deformation comparing the data from the two studied domains in this PhD thesis with previous studies reporting fluid flow in the Pyrenees. This comparison evidences that fluids migrating through basement or cover units have a different geochemical signature that is recorded in the $^{87}\text{Sr}/^{86}\text{Sr}$ ratios of the resulting vein cements. In this line, in the Estamariu thrust, the analyzed calcite cements originated during successive compressional (Cc1 and Cc2) and extensional (Cc3 to Cc5) tectonic events, yielded high radiogenic $^{87}\text{Sr}/^{86}\text{Sr}$ ratios (from 0.713 to 0.718). This indicates that regardless of the origin of the fluids and the tectonic context, basement rocks have a significant influence on the fluid chemistry that is recorded in the high $^{87}\text{Sr}/^{86}\text{Sr}$ ratios (>0.710). These high radiogenic ratios are within the range of values reported in other synkinematic veins from the Pyrenean basement in the Gavarnie thrust, the Pic de Port Vieux, la Glere shear zone, the Trois Seigneurs Massif, among others (Fig. 20) (Wayne and McCaig, 1998; Bickle et al., 1988; Banks et al., 1991; McCaig et al., 1995; McCaig et al., 2000b). By contrast, the vein cements precipitated in the frontal anticline of the Bóixols thrust sheet yielded lower $^{87}\text{Sr}/^{86}\text{Sr}$ ratios (<0.710). These lower ratios are within the range of values reported for vein cements precipitated from fluids that have circulated through the Pyrenean Mesozoic–Cenozoic sedimentary cover in the El Guix and the Puig Reig anticlines, in the L'Escala, vallfogona, Upper and Lower Pedraforca thrusts and in the Ainsa basin (i.e., through younger rocks with a different radiogenic signature) (Fig. 20). Such lower values may be similar to Phanerozoic seawater values, evidencing interaction between the parent fluids and marine carbonate units, or they may be higher, evidencing interaction with siliciclastic rocks (Travé et al., 2007; Cruset et al., 2018).

Therefore, this limit value ($^{87}\text{Sr}/^{86}\text{Sr} = 0.710$) may be used to unravel the ultimate source of the fluids circulating during deformation and/or to examine the possible transfer of

fluids between the basement and the sedimentary cover in the Pyrenees and probably, in other worldwide deformed areas. For instance, a previous study, focused on fluid flow along the Gavarnie thrust in the central-western Axial Pyrenees, used this limit value ($^{87}\text{Sr}/^{86}\text{Sr} = 0.710$) to differentiate between the unaltered limestone protolith and the Cretaceous thrust-related carbonate mylonite affected by fluids carrying radiogenic Sr (McCaig et al., 1995). In addition, Williams et al. (2015) and Beaudoin et al. (2014) also attributed $^{87}\text{Sr}/^{86}\text{Sr}$ ratios > 0.710 to the input of basement-derived fluids in the Rio Grande rift and in the Bighorn Basin, USA, respectively.

In the same way, the different REE contents obtained in calcite cements from the two studied domains may also be indicative of fluids circulating either through the Paleozoic basement or the sedimentary cover. Indeed, the different calcite veins recognized in the Estamariu thrust exhibit enrichments in REE contents that may reach up to 900 ppm (Fig. 21c), which could indicate mobilization of REE elements from basement rocks. By contrast, calcite veins found in the Sant Corneli-Bóixols anticline show overall low REE contents, which may reach up to 100 ppm, but are generally lower than 40 ppm (Fig. 21c). This indicates that the REE concentrations may constitute a potential tracer of the origin of fluids derived from basement or cover lithologies.

Fluid flow along the south Pyrenean fold-and-thrust belt: evidence of basement-derived fluids?

This section analyses the scale of fluid flow in the Bóixols thrust sheet and in the Southern Pyrenees, and evaluates the possible transfer of fluids between the Paleozoic basement and the sedimentary cover.

The Bóixols thrust sheet corresponds to the uppermost and oldest emplaced structure of the southern-central Pyrenean cover thrust units. Therefore, the structural position of this thrust sheet, detached in Upper Triassic evaporites and above Lower Triassic detrital sediments of the Buntsandstein and the Paleozoic basement, allows to assess the possible transfer of external fluids derived from these three potential reservoirs. In a previous section, we concluded that advective fluid flow in the frontal anticline of the Bóixols thrust sheet was linked to the presence of major fault zones (including the Bóixols thrust) and associated fractures, which acted as preferential fluid flow pathways. Therefore, the geochemical signature of calcite cements precipitated in these fractures (group 2 calcites) provides evidence on the relative scale of fluid flow and the fluid circulation depth. Thus,

during precipitation of group 2 calcites, a maximum temperature of around 120 °C was obtained from clumped isotopes in calcites precipitated in fractures associated with the Bóixols thrust in Forat de Bóixols locality. Assuming a normal geothermal gradient of 30 °C/km (Travé et al., 2007), these temperatures would have been reached at 3-4 km depth. Considering the thickness of the Bóixols thrust sheet (around 5 km thick), such temperatures imply circulation of fluids along fault zones that were originated in the deeper regions of the sedimentary cover. Indeed, the $\delta^{18}\text{O}_{\text{fluid}}$ of this group of cements, yielding maximum values of +5.5 ‰ VSMOW, indicate the presence of formation waters, as has been explained before, and discard the input of basement-related fluids such water derived from and/or equilibrated with metamorphic rocks (Taylor, 1987). In the same way, the $^{87}\text{Sr}/^{86}\text{Sr}$ ratios of the vein cements documented in this study are (1) within the range of marine carbonates (LOWESS curve in Fig. 20), (2) within the range of synkinematic veins precipitated in the sedimentary cover (i.e., $^{87}\text{Sr}/^{86}\text{Sr} < 0.710$), and (3) significantly lower than values of cements precipitated from fluids that have interacted with Triassic evaporites or with Paleozoic basement rocks. All these observations indicate that the fluid system in the study area was restricted to the scale of the Bóixols thrust sheet and rule out the input of external fluids derived from the underlying Triassic detachment, from deeper cover units such as the Buntsandstein or from the Paleozoic basement. An exception arises for the cement precipitated in the Bóixols thrust-related deformation at the Setcomelles locality (Cc3), which exhibits the most radiogenic $^{87}\text{Sr}/^{86}\text{Sr}$ ratio in the Sant Corneli-Bóixols anticline, similar to Upper Triassic values (Fig. 20). Therefore, fluids derived from Upper Triassic evaporites acting as a main detachment of the Bóixols thrust sheet could have locally infiltrated the paleohydrological system, as has also been reported in other salt-detached Pyrenean structures (Travé et al., 2007; Lacroix et al., 2011; Crognier et al., 2018; Cruset et al., 2020a).

The results presented in this study also reveal that the Sant Corneli-Bóixols anticline shares a common fluid flow behavior with other worldwide compressional structures above evaporitic detachments. In these structures, the paleohydrological system only involves fluids sourced above the detachment levels, which may act as a lower boundary for the fluid system, preventing the input of fluids from deeper parts of the compressional belt. This fluid flow scenario in the Bóixols thrust sheet is similar to that of: 1) worldwide detachment folds (Beaudoin et al., 2014); 2) other south Pyrenean structures detached in Triassic and Eocene evaporitic units such as the Pico del Águila and El Guix anticlines

(Travé et al., 2000; Beaudoin et al., 2015), the Monte Perdido and Abocador thrusts (Lacroix et al., 2011; Cruset et al., 2018), and the Upper and Lower Pedraforca thrust sheets (Cruset; 2019; Cruset et al., 2020a); 3) other worldwide detached structures such as the Sierra Madre Oriental (Leticariu et al., 2005; Fischer et al., 2009) and the Central Appalachians (Evans et al., 2012).

On the other hand, in order to examine the lateral variation and scale of fluid flow in the Southern Pyrenees, we compare different paleohydrological studies performed along central-eastern part of the south Pyrenean wedge, this is, along the Segre transect (this thesis) and the Llobregat section (Cruset et al., 2018; 2020b) (Fig. 25). Our comparison reveals that the fluids migrating through upper thrust sheets, emplaced from Late Cretaceous to middle Eocene, reached maximum temperatures of 120 °C during the emplacement of the Bóixols thrust (Fig. 25). Similarly, in the Upper Pedraforca thrust sheet, which constitutes the eastern equivalent of the Bóixols structure, a maximum temperature of 100 °C has been reported (Cruset, 2019). In contrast, the fluids migrating through the Vallfogona thrust, which represents the frontal thrust fault of the Southeastern Pyrenees, reached maximum temperatures of around 150 °C (Cruset et al., 2018; Fig. 25).

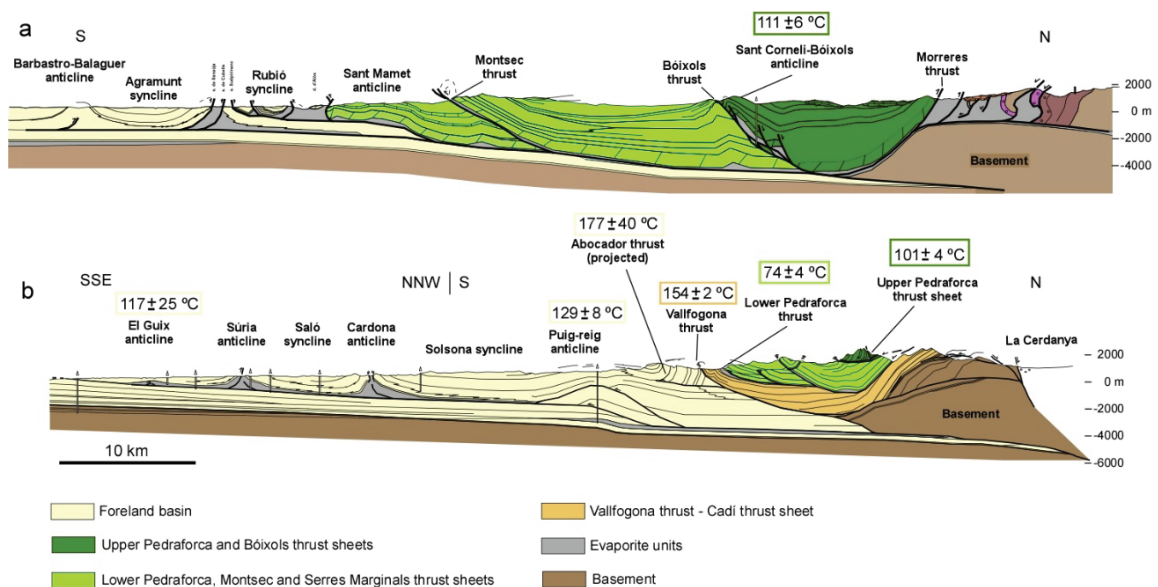


Fig. 25. Cross-sections along the central (a) and eastern (b) Southern Pyrenees (Vergés, 1993) showing the maximum temperatures obtained from clumped isotopes applied to syn-kinematic calcite veins precipitated in the main structural units. Location of cross-sections in Fig. 1a. Temperatures are from this work and from Cruset et al. (2018; 2020a).

Similar high temperatures have also been reported for the fluids circulating through the thrust faults affecting the sediments of the Ebro foreland basin. These high temperatures, which are ~180 °C for the Abocador thrust and ~130 °C for the Puig-reig anticline, could not have been reached by burial (Cruset et al., 2018). Therefore, the major thrust faults likely acted as preferential pathways for the upward migration of hot fluids circulating during compression. In the regions of the south Pyrenean cover thrust sheets that are only affected by background deformation, the geochemical composition of these hot fluids was modified as they interacted with surrounding host rocks and when moving away from the major thrust zones. Therefore, this background deformation was characterized by the migration of formation waters with high interaction with their surrounding host rocks. This highlights an overall common fluid flow behavior along strike in the central-eastern part of the southern Pyrenees, where major faults acted as transfer zones for migration of fluid in thermal and geochemical disequilibrium with adjacent host rocks, whereas background fracturing recorded the presence of rock-buffered and/or local fluids.

Fluid flow in the NE part of the Iberian Peninsula during the Neogene Extension

In the Estamariu thrust, the structural and geochemical data indicate that calcite cements Cc3 and Cc4 (veins V3 and V4, respectively) precipitated from hydrothermal fluids (temperatures up to 210 °C) that interacted at depth with basement rocks before ascending through newly formed and reactivated structures during the Neogene extension. These interpretations are consistent with the presence of several hydrothermal springs (temperatures of 29 to 73 °C) currently upwelling aligned along the La Tet fault (Krimissa et al., 1994; Taillefer et al., 2017, 2018), which is the main Neogene extensional fault in the Pyrenean Axial Zone. Several studies indicate the origin of these hot water springs as meteoric fluids infiltrated at high-elevated reliefs above 2000 m, warmed at great depths by normal geothermal gradients, and migrated upwards along permeability anisotropies related to fault zones (Taillefer et al., 2017, 2018). The $^{87}\text{Sr}/^{86}\text{Sr}$ ratios of these springs, ranging between 0.715 and 0.730 (Caballero et al., 2012), are within the range of values obtained in this study and also account for interaction between circulating fluids and basement lithologies. Studies based on numerical models suggest that the La Tet fault and the involved basement rocks are still permeable down to 3km of depth (Taillefer et al., 2017, 2018), although the fault has been dormant since the Mio-Pliocene (Goula et al., 1999). It has also been suggested that the footwall topography, which induces high hydraulic gradients and produces fluid advection, is the major factor controlling the

infiltration of meteoric fluids, the circulation depth, and the maximum temperature reached by the migrating fluids (Taillefer et al., 2017). A similar geological context and fluid regime evolution to those explained above are found in the Barcelona Plain and the Vallès Basin, located in the northeast part of the Catalan Coastal Range (CCR). Consequently, the comparison between the two geological contexts allows providing insights into the fluid circulation in extensional basins at regional scale (in the NE part of Iberia). In these locations of the CCR, the main fault system associated with the Neogene extension acted as a conduit for hydrothermal fluid circulation at temperatures between 130 and 150 °C during synkinematic periods (Cardellach et al., 2003; Cantarero et al., 2014) and is also responsible for the present-day circulation of hot water springs up to 70 °C (Fernández and Banda, 1990; Carmona et al., 2000). In both cases, fluids would have been topographically driven from elevated areas to great depths (Cantarero et al., 2014), where they circulated through basement rocks, acquiring high $^{87}\text{Sr}/^{86}\text{Sr}$ ratios (>0.712) and high temperatures (Cardellach et al., 2003) before ascending through fault discontinuities. However, in the Penedès basin, which corresponds to the southwestern termination of the Neogene structure in the CCR, basement lithologies do not crop out and the extensional faults only involve Neogene deposits filling the basin and a Mesozoic sedimentary substrate. In this location, the main fault system acted as a conduit for several episodes of meteoric fluids percolation during the Neogene extension, and evidence of hydrothermal fluid circulation has not been reported in the area (Travé et al., 1998; Travé and Calvet, 2001; Baqués et al., 2010, 2012). This fact agrees with previous studies that highlight the fact that hydrothermal activity, in particular the occurrence of hot water springs in the Pyrenees and in the CCR, is preferably concentrated in basement rocks, which constitute the elevated footwall of the main extensional fault systems (Taillefer et al., 2017; Carmona et al., 2000). All these observations indicate an open fluid system in the NE part of the Iberian Peninsula associated with the Neogene extensional deformation. This extensional fault system acted as a conduit for the circulation of hot fluids in Neogene times and does so in the present. This fault-controlled fluid flow could have been continuous through time or could be related to intermittent pulses. Fault control on upflowing of hot fluids along fault systems is a common process in different geological settings and has been reported in the Great Basin, USA (Nelson et al., 2006; Faulds et al., 2010), in the Western Turkey (Faulds et al., 2010), in the Southern Canadian Cordillera (Grasby and Hutcheon, 2001) and in the southern Tuscany, Italy (Liotta et al., 2010).

6. CONCLUDING REMARKS

Field and analytical data allowed to analyze the relationships between fluid flow and deformation in different Alpine-related basement and sedimentary cover structures in the Southern Pyrenees as summarized below.

1. Several approaches have been applied to determine the chronology of the studied structures. In the Estamariu thrust, U-Pb dating of the vein cements failed due to their high lead contents and low uranium contents and the relative timing of the different mesostructures and microstructures has been assessed using crosscutting relationships and microstructural analysis. The Estamariu thrust is known to be Variscan in origin, but in the study area, it places a Devonian pre-Variscan unit against a Stephanian-Permian late to post-Variscan sequence and the structures present within the thrust zone, affecting both sequences, are attributed to the Alpine compression and subsequent Neogene extension. During the Alpine compression, the reactivation of the thrust resulted in the transposition of the Variscan regional foliation within the thrust zone and in the formation of a subsidiary thrust zone affecting the andesites in the footwall. During the Neogene extension, the Estamariu thrust was likely reactivated and normal faults and shear fractures were developed.
2. In the Sant Corneli-Bóixols anticline, along the front of the Bóixols thrust sheet, 23 U-Pb dates measured in different sets of fracture-filling calcite cements constrain the absolute timing of deformation. These dates present important age variations from the oldest Late Cretaceous at 79.8 ± 1.2 Ma to the youngest late Miocene at 9 ± 4.6 Ma. The oldest date (79.8 ± 1.2 Ma), in a backlimb normal fault, is younger than the base of the syntectonic deposits along the southern flank of the Sant Corneli-Bóixols anticline. Ten ages ranging from 71.2 ± 6.4 to 56.9 ± 1.4 Ma (calcite cements Cc3 to Cc10) are coeval with growth strata deposition and Bóixols thrust sheet emplacement. Ages from 55.5 ± 1.2 to 27.4 ± 0.9 Ma (calcite cements Cc14a to Cc27b) precipitated in the frontal Bóixols thrust zone, at Forat de Bóixols and Abella de la Conca localities, in hundred-meters scale fractures with a constant orientation with respect to bedding regardless of dip, and in strike slip faults that offset the tilted limbs of the anticline. These ages are consistent with the tectonic transport of the Bóixols thrust sheet above the basal thrust of the South Pyrenean Unit. The youngest Miocene dates from $20.8 \pm$

1.2 to 9 ± 4.6 Ma (calcite cements Cc21 to Cc23) are partially coeval with the post-orogenic exhumation of the Sant Corneli-Bóixols anticline.

3. Seven fracture-filling calcite cements were identified in the Estamariu thrust and 23 calcite cements in the Sant Corneli-Bóixols anticline. All these cements were assembled in three groups according to similarities of the geochemical data. Group 1 is only present in the Sant Corneli-Bóixols anticline, whereas group 2 and group 3 are present in both studied domains:

- Group 1 includes calcites with similar petrographic and geochemical features with respect to their host carbonates (i.e., non-luminescent calcite cements with high Sr contents and $\delta^{13}\text{C}$ values and $^{87}\text{Sr}/^{86}\text{Sr}$ ratios typical of marine carbonates).
- Group 2 comprises calcites with the lightest $\delta^{18}\text{O}$ values, down to -14 ‰VPDB, the highest temperature of precipitation, up to 210 °C in the Estamariu thrust and up to 120 °C in the Sant Corneli-Bóixols anticline, and a trends towards high Mn contents.
- Group 3 includes calcites with $\delta^{18}\text{O}$ from -8 to -6 ‰VPDB, $\delta^{13}\text{C}$ down to -10 ‰VPDB and the lowest Sr contents.

4. Group 1 to group 3 calcites record the origin and distribution of the vein-forming fluids in the study area. In both studied domains, the major faults acted as preferential pathways for the upwards migration of fluids, whereas background fracturing registered the presence of fluids that highly interacted with their adjacent host rocks:

- In the core of the Sant Corneli-Bóixols anticline and in the lowest part of the syn-orogenic sequence from the footwall of the Bóixols thrust, group 1 cements indicate an essentially closed and locally derived fluid system.
- Along large faults such as the Estamariu thrust, the Bóixols thrust and other fault systems that occur in both studied domains, group 2 cements indicate an open fluid system evidencing that these large faults acted as conduits for the upward migration of fluids in thermal and geochemical disequilibrium with surrounding host rocks.
- In the youngest fractures developed in the Estamariu thrust and in fractures present in the limbs of the Sant Corneli-Bóixols anticline, group 3 cements indicate the presence of meteoric waters that likely infiltrated at high structural reliefs that were elevated during deformation.

5. The integrated field and analytical data in each studied structure assesses the relationships between fluid flow and deformation in different types of rock deformation structures:
- In the Estamariu thrust, the geochemical evolution of cements Cc1 to Cc5 highlights a progressive change in the fluid regime and composition during successive compressional and extensional tectonic events. The continuous increase in precipitation temperatures and enrichment in $\delta^{18}\text{O}_{\text{fluid}}$ from heated meteoric fluids (Cc1 and Cc2 during the Alpine compression) to hydrothermal fluids (Cc3 and Cc4 during the Neogene extension) is probably linked to higher extent of fluid-rock interaction with basement rocks during a longer time span. By contrast, during the latest stages of extension, the infiltration of cold meteoric fluids (Cc5) likely indicates a more significant change in the fluid regime, that is, from upward to downward fluid migration.
 - In the Sant Corneli-Bóixols anticline, the fluid origin and the extent of fluid-rock interaction varied in the several structural positions of the fold and according to the age and nature of their stratigraphy, evidencing a compartmentalization of the fluid system. In the core of the anticline, the rock-buffered fluids, likely locally derived from the adjacent Lower Cretaceous carbonates, indicates a high degree of fluid-rock interaction. Contrarily, along large faults such as the Bóixols thrust affecting the entire anticline, and in the fold limbs, the upwards migration of fluids and the percolation of meteoric waters, respectively, indicate an open system.
 - In the Bóixols thrust (at Forat de Bóixols locality), successive fracture systems and related calcite cements highlight an episodic evolution of the thrust zone, resulting from an upward migration of the fault tip (process zone development) before propagation of the thrust, and compartmentalization of the thrust fault zone, leading to different structural and fluid flow histories in the footwall and hanging wall. This evidences that the Bóixols thrust acted as a transverse barrier, dividing the thrust zone into two separate fluid compartments, and a longitudinal drain for migration of fluids.
6. The paleohydrological system in the Sant Corneli-Bóixols anticline was restricted to the Bóixols thrust sheet above the Upper Triassic detachment level. This evaporitic detachment likely acted as a lower fluid barrier, preventing the input of fluids from deeper parts of the belt, as interpreted in other areas of the Pyrenees and in other detached thrust systems as the Central Appalachians and Sierra Madre Oriental. The

maximum temperature of 120 °C and the maximum $\delta^{18}\text{O}_{\text{fluid}}$ of +5.5 ‰VSMOW obtained in the Sant Corneli-Bóixols anticline, implying 3-4 km depth and presence of formation waters, respectively, together with the $^{87}\text{Sr}/^{86}\text{Sr}$ ratios of the vein cements, within the range of values documented in the sedimentary cover, discard the transfer of fluids between the basement and the sedimentary cover.

7. This study also assesses the influence of basement rocks on the fluid chemistry during deformation in the Pyrenees and provides insights into the fluid regime in the NE part of the Iberian Peninsula. Our data indicates that regardless of the fluid origin and the tectonic context, the fluids that have interacted with basement rocks have a higher $^{87}\text{Sr}/^{86}\text{Sr}$ ratio (> 0.710) than those that have circulated through the sedimentary cover (< 0.710). On the other hand, extensional deformation structures in both the eastern Pyrenees and the northeastern part of the Catalan Coastal Ranges, have acted as conduits for hydrothermal fluid migration in Neogene times and in the present. These fluids likely interacted with basement rocks before ascending through fault zones and related structures.

REFERENCES

- Agosta, F., Alessandroni, M., Antonellini, M., Tondi, E., Giorgioni, M., 2010. From fractures to flow: A field-based quantitative analysis of an outcropping carbonate reservoir. *Tectonophysics* 490, 197–213
- Agosta, F., Prasad, M., Aydin, A., 2007. Physical properties of carbonate fault rocks, fucino basin (Central Italy): implications for fault seal in platform carbonates. *Geofluids* 7, 19–32
- Alcalde, J., Marzán, I., Saura, E., Martí, D., Ayarza, P., Juhlin, C., Pérez-Estaún, A., Carbonell, R., 2014. 3D geological characterization of the Hontomín CO₂ storage site, Spain: Multidisciplinary approach from seismic, well-log and regional data. *Tectonophysics* 627, 6–25. <https://doi.org/10.1016/j.tecto.2014.04.025>
- Ardevol, L., Klimowitz, J., Malagón, J., Nagtegaal, P.T.C., 2000. Depositional Sequence Response to Foreland Deformation in the Upper Cretaceous of the Southern Pyrenees, Spain. *Am. Assoc. Pet. Geol. Bull.* 84, 427–53. <https://doi.org/10.1306/C9EBCE55-1735-11D7-8645000102C1865D>
- Arndt, M., Virgo, S., Cox, S.F., Urai, J.L., 2014. Changes in fluid pathways in a calcite vein mesh (Natih Formation, Oman Mountains): insights from stable isotopes. *Geofluids* 14, 391–418
- Bachu, S., 2000. Sequestration of CO₂ in geological media: criteria and approach for site selection in response to climate change. *Energy Convers. Manag.* 41, 953–970. [https://doi.org/10.1016/S0196-8904\(99\)00149-1](https://doi.org/10.1016/S0196-8904(99)00149-1)
- Balsamo, F., Clemenzi, L., Storti, F., Mozafari, M., Solum, J., Swennen, R., Taberner, C., Tueckmantel, C., 2016. Anatomy and paleofluid evolution of laterally restricted extensional fault zones in the Jabal Qusaybah anticline, Salakh arch, Oman. *Geol. Soc. Am. Bull.* 128, 957–972. <https://doi.org/10.1130/B31317.1>
- Banks, D., Da Vies, G., Yardley, B.W., McCaig, A., Grant, N., 1991. The chemistry of brines from an Alpine thrust system in the Central Pyrenees: An application of fluid inclusion analysis to the study of fluid behaviour in orogenesis. *Geochim. Cosmochim. Acta* 55, 1021–1030. [https://doi.org/10.1016/0016-7037\(91\)90160-7](https://doi.org/10.1016/0016-7037(91)90160-7)
- Baqués, V., Travé, A., Benedicto, A., Labaume, P., Cantarero, I., 2010. Relationships between carbonate fault rocks and fluid flow regime during propagation of the Neogene extensional faults of the Penedès basin (Catalan Coastal Ranges, NE Spain). *J. Geochemical Explor.* 106, 24–33. <https://doi.org/10.1016/j.gexplo.2009.11.010>
- Baqués, V., Trave, A., Roca, E., Marin, M., Cantarero, I., 2012. Geofluid behaviour in successive extensional and compressional events: a case study from the southwestern end of the Valles-Penedes Fault (Catalan Coastal Ranges, NE Spain). *Pet. Geosci.* 18, 17–31. <https://doi.org/10.1144/1354-079311-017>
- Baqués, V., Ukar, E., Laubach, S.E., Forstner, S.R., Fall, A., 2020. Fracture, Dissolution, and Cementation Events in Ordovician Carbonate Reservoirs, Tarim Basin, NW China. *Geofluids* 2020, 1–28
- Barbier, M., Leprêtre, R., Callot, J.-P., Gasparini, M., Daniel, J.-M., Hamon, Y., Lacombe, O., Floquet, M., 2012. Impact of fracture stratigraphy on the paleo-hydrogeology of the Madison Limestone in two basement-involved folds in the Bighorn basin, (Wyoming, USA). *Tectonophysics* 576–577, 116–132
- Barker, S., 2007. Dynamics of fluid flow and fluid chemistry during crustal shortening. Ph.D. thesis, Res. Sch. Earth Sci. Aust. Natl. Univ. 238p.
- Barker, S.L.L., Cox, S.F., 2011. Evolution of fluid chemistry and fluid-flow pathways during folding and faulting: an example from Taemas, NSW, Australia. *Geol. Soc. London, Spec. Publ.* 359, 203–227
- Bau, M., Dulski, P., 1994. Evolution of the Yttrium-Holmium Systematics of Seawater Through Time. *Mineral. Mag.* 58A, 61–62. <https://doi.org/10.1180/minmag.1994.58A.1.35>

- Beaudoin, N., Bellahsen, N., Lacombe, O., Emmanuel, L., 2011. Fracture-controlled paleohydrogeology in a basement-cored, fault-related fold: Sheep Mountain Anticline, Wyoming, United States. *Geochemistry, Geophys. Geosystems* 12, 1–15. <https://doi.org/10.1029/2010GC003494>
- Beaudoin, N., Bellahsen, N., Lacombe, O., Emmanuel, L., Pironon, J., 2014. Crustal-scale fluid flow during the tectonic evolution of the Bighorn Basin (Wyoming, USA). *Basin Res.* 26, 403–435
- Beaudoin, N., Huyghe, D., Bellahsen, N., Lacombe, O., Emmanuel, L., Mouthereau, F., Ouanhnon, L., 2015. Fluid systems and fracture development during syn-depositional fold growth: An example from the Pico del Aguila anticline, Sierras Exteriores, southern Pyrenees, Spain. *J. Struct. Geol.* 70, 23–38
- Beaudoin, N.E., Labeur, A., Lacombe, O., Koehn, D., Billi, A., Hoareau, G., Boyce, A., John, C.M., Marchegiano, M., Roberts, N.M., Millar, I.L., Claverie, F., Pecheyran, C., Callot, J.-P., 2020. Regional-scale paleofluid system across the Tuscan Nappe–Umbria–Marche Apennine Ridge (northern Apennines) as revealed by mesostructural and isotopic analyses of stylolite–vein networks. *Solid Earth* 11, 1617–1641
- Begbie, M.J., Craw, D., 2006. Geometry and petrography of stockwork vein swarms, macraes mine, Otago Schist, New Zealand. *New Zeal. J. Geol. Geophys.* 49, 63–73. <https://doi.org/10.1080/00288306.2006.9515148>
- Benedicto, A., Abdelrazek, M., Ledru, P., Mackay, C., Kinar, D., 2021. Structural Controls of Uranium Mineralization in the Basement of the Athabasca Basin, Saskatchewan, Canada. *Geofluids* 2021
- Bense, V.F., Gleeson, T., Loveless, S.E., Bour, O., Scibek, J., 2013. Fault zone hydrogeology. *Earth-Science Rev.* 127, 171–192. <https://doi.org/10.1016/j.earscirev.2013.09.008>
- Berástegui, X., Garcia-Senz, J.M., Losantos, M., 1990. Tecto-sedimentary evolution of the Organya extensional basin (central south Pyrenean unit, Spain) during the Lower Cretaceous. *Bull. la Soc. Geol. Fr.* VI, 251–264
- Bergbauer, S., Pollard, D.D., 2004. A new conceptual fold-fracture model including prefolding joints, based on the Emigrant Gap anticline, Wyoming. *Bull. Geol. Soc. Am.* 116, 294–307. <https://doi.org/10.1130/B25225.1>
- Bickle, M.J., Wickham, S.M., Chapman, H.J., Taylor, H.P., 1988. A strontium, neodymium and oxygen isotope study of hydrothermal metamorphism and crustal anatexis in the Trois Seigneurs Massif, Pyrenees, France. *Contrib. to Mineral. Petrol.* 100, 399–417. <https://doi.org/10.1007/BF00371371>
- Bitzer, K., Travé, A., Carmona, J.M., 2001. Fluid flow processes at basin scale. *Acta Geol. Hisp.* 36, 1–20.
- Bond, R.M.G., McClay, K.R., 1995. Inversion of a Lower Cretaceous extensional basin, south central Pyrenees, Spain. *Geol. Soc. London, Spec. Publ.* 88, 415–431. <https://doi.org/10.1144/GSL.SP.1995.088.01.22>
- Bons, A., 1988. Intracrystalline deformation and slaty cleavage development in very low-grade slates from the Central Pyrenees, *Geologica Ultraiectina*.
- Bons, P.D., Elburg, M.A., Gomez-Rivas, E., 2012. A review of the formation of tectonic veins and their microstructures. *J. Struct. Geol.* 43, 33–62. <https://doi.org/10.1016/j.jsg.2012.07.005>
- Boutoux, A., Verlaguet, A., Bellahsen, N., Lacombe, O., Villemant, B., Caron, B., Martin, E., Assayag, N., Cartigny, P., 2014. Fluid systems above basement shear zones during inversion of pre-orogenic sedimentary basins (External Crystalline Massifs, Western Alps). *Lithos* 206–207, 435–453
- Branquet, Y., Cheilletz, A., Giuliani, G., Laumonier, B., Blanco, O., 1999. Fluidized hydrothermal breccia in dilatant faults during thrusting: the Colombian emerald deposits. *Geol. Soc. London, Spec. Publ.* 155, 183–195

- Breesch, L., Swennen, R., Vincent, B., 2009. Fluid flow reconstruction in hanging and footwall carbonates: Compartmentalization by Cenozoic reverse faulting in the Northern Oman Mountains (UAE). *Mar. Pet. Geol.* 26, 113–128. <https://doi.org/10.1016/j.marpetgeo.2007.10.004>
- Burisch, M., Gerdes, A., Walter, B.F., Neumann, U., Fettel, M., Markl, G., 2017. Methane and the origin of five-element veins: Mineralogy, age, fluid inclusion chemistry and ore forming processes in the Odenwald, SW Germany. *Ore Geol. Rev.* 81, 42–61. <https://doi.org/10.1016/j.oregeorev.2016.10.033>
- Bussolotto, M., Benedicto, A., Moen-Maurel, L., Invernizzi, C., 2015. Fault deformation mechanisms and fault rocks in micritic limestones: Examples from Corinth rift normal faults. *J. Struct. Geol.* 77, 191–212
- Caballero, Y., Gironde, C., Le Goff, E., 2012. Ressource en eau thermale de la station d'Amélie-les-Bains. Etat des lieux. Rapport BRGM/RP-60618-FR (French Geological Survey), Orleans, France, 56p
- Cabrera, L., Roca, E., Santanach, P., 1988. Basin formation at the end of a strike-slip fault: the Cerdanya Basin (eastern Pyrenees). *J. Geol. Soc. London.* 145, 261–268. <https://doi.org/10.1144/gsjgs.145.2.0261>
- Caine, J.S., Evans, J.P., Forster, C.B., 1996. Fault zone architecture and permeability structure. *Geology* 24, 1025. [https://doi.org/10.1130/0091-7613\(1996\)024<1025:FZAAPS>2.3.CO;2](https://doi.org/10.1130/0091-7613(1996)024<1025:FZAAPS>2.3.CO;2)
- Caja, M.A., Permanyer, A., 2008. Significance of organic matter in eocene turbidite sediments (SE Pyrenees, Spain). *Naturwissenschaften* 95, 1073–1077. <https://doi.org/10.1007/s00114-008-0416-6>
- Caja, M.A., Permanyer, A., Marfil, R., Al-Aasm, I.S., Martín-Crespo, T., 2006. Fluid flow record from fracture-fill calcite in the Eocene limestones from the South-Pyrenean Basin (NE Spain) and its relationship to oil shows. *J. Geochemical Explor.* 89, 27–32. <https://doi.org/10.1016/j.gexplo.2005.11.009>
- Callot, J.P., Breesch, L., Guilhaumou, N., Roure, F., Swennen, R., Vilasi, N., 2013. Paleo-fluids characterisation and fluid flow modelling along a regional transect in northern United Arab Emirates (UAE). *Front. Earth Sci.* 5, 177–201. https://doi.org/10.1007/978-3-642-30609-9_9
- Cantarero, I., Alías, G., Cruset, D., Carola, E., Lanari, P., Travé, A., 2018. Fluid composition changes in crystalline basement rocks from ductile to brittle regimes. *Glob. Planet. Change* 171, 273–292
- Cantarero, I., Travé, A., Alías, G., Baqués, V., 2014. Polyphasic hydrothermal and meteoric fluid regimes during the growth of a segmented fault involving crystalline and carbonate rocks (Barcelona Plain, NE Spain). *Geofluids* 14, 20–44. <https://doi.org/10.1111/gfl.12021>
- Cantarero, Parcerisa, Plata, Gómez-Gras, Gomez-Rivas, Martín-Martín, Travé, 2020. Fracturing and Near-Surface Diagenesis of a Silicified Miocene Deltaic Sequence: The Montjuïc Hill (Barcelona). *Minerals* 10, 135
- Cardellach, E., Canals, À., Grandia, F., 2003. Recurrent hydrothermal activity induced by successive extensional episodes: the case of the Berta F-(Pb-Zn) vein system (NE Spain). *Ore Geol. Rev.* 22, 133–141
- Carmona, J.M., Bitzer, K., López, E., Bouazza, M., 2000. Isotopic composition and origin of geothermal waters at Caldetes (Maresme-Barcelona). *J. Geochemical Explor.* 69–70, 441–447
- Casas, J.M., Domingo, F., Poblet, J., Soler, A., 1989. On the role of the Hercynian and Alpine thrusts in the Upper Paleozoic rocks of the Central and Eastern Pyrenees. *Geodin. Acta* 3, 135–147
- Casini, G., Gillespie, P.A., Vergés, J., Romaine, I., Fernández, N., Casciello, E., Saura, E., Mehl, C., Homke, S., Embry, J.-C., Aghajari, L., Hunt, D.W., 2011. Sub-seismic fractures in foreland fold and thrust belts: insight from the Lurestan Province, Zagros Mountains, Iran. *Pet. Geosci.* 17, 263–282
- Casini, G., Romaine, I., Casciello, E., Saura, E., Vergés, J., Fernández, N., Hunt, D.W., 2018. Fracture characterization in sigmoidal folds: Insights from the Siah Kuh anticline, Zagros, Iran. *Am. Assoc. Pet. Geol. Bull.* 102, 369–399. <https://doi.org/10.1306/0503171615817076>

- Cello, G., Invernizzi, C., Mazzoli, S., Tondi, E., 2001. Fault properties and fluid flow patterns from Quaternary faults in the Apennines, Italy. *Tectonophysics* 336, 63–78. [https://doi.org/10.1016/S0040-1951\(01\)00094-4](https://doi.org/10.1016/S0040-1951(01)00094-4)
- Cerling, T.E., 1984. The stable isotopic composition of modern soil carbonate and its relationship to climate. *Earth Planet. Sci. Lett.* 71, 229–240. [https://doi.org/10.1016/0012-821X\(84\)90089-X](https://doi.org/10.1016/0012-821X(84)90089-X)
- Chester, J.S., 2003. Mechanical stratigraphy and fault–fold interaction, Absaroka thrust sheet, Salt River Range, Wyoming. *J. Struct. Geol.* 25, 1171–1192. [https://doi.org/10.1016/S0191-8141\(02\)00151-7](https://doi.org/10.1016/S0191-8141(02)00151-7)
- Choukroune, P., 1989. The Ecore Pyrenean deep seismic profile reflection data and the overall structure of an orogenic belt. *Tectonics* 8, 23–39. <https://doi.org/10.1029/TC008i001p00023>
- Cochelin, B., Lemirre, B., Denèle, Y., de Saint Blanquat, M., Lahfid, A., Duchêne, S., 2018. Structural inheritance in the Central Pyrenees: the Variscan to Alpine tectonometamorphic evolution of the Axial Zone. *J. Geol. Soc. London.* 175, 336–351. <https://doi.org/10.1144/jgs2017-066>
- Conti, S., Fontana, D., Mecozzi, S., Panieri, G., Pini, G.A., 2010. Late Miocene seep-carbonates and fluid migration on top of the Montepetra intrabasinal high (Northern Apennines, Italy): Relations with synsedimentary folding. *Sediment. Geol.* 231, 41–54. <https://doi.org/10.1016/j.sedgeo.2010.08.001>
- Cooper, M., 2007. Structural style and hydrocarbon prospectivity in fold and thrust belts: a global review. *Geol. Soc. London, Spec. Publ.* 272, 447–472. <https://doi.org/10.1144/GSL.SP.2007.272.01.23>
- Cosgrove, J.W., 2015. The association of folds and fractures and the link between folding, fracturing and fluid flow during the evolution of a fold–thrust belt: a brief review. *Geol. Soc. London, Spec. Publ.* 421, 41–68
- Cox, S.F.J., Knackstedt, M.A., Braun, J.W., 2001. Principles of Structural Control on Permeability and Fluid Flow in Hydrothermal Systems, in: *Structural Controls on Ore Genesis*. Society of Economic Geologists, pp. 1–24. <https://doi.org/10.5382/Rev.14.01>
- Crognier, N., Hoareau, G., Aubourg, C., Dubois, M., Lacroix, B., Branellec, M., Callot, J.P., Vennemann, T., 2018. Syn-orogenic fluid flow in the Jaca basin (south Pyrenean fold and thrust belt) from fracture and vein analyses. *Basin Res.* 30, 187–216. <https://doi.org/10.1111/bre.12249>
- Cruset, D., 2019. Sequential fluid migration along a fold and thrust belt: SE Pyrenees from Late Cretaceous to Oligocene. PhD Thesis, Univ. Barcelona 350p.
- Cruset, D., Cantarero, I., Benedicto, A., John, C.M., Vergés, J., Albert, R., Gerdes, A., Travé, A., 2020a. From hydroplastic to brittle deformation: Controls on fluid flow in fold and thrust belts. Insights from the Lower Pedraforca thrust sheet (SE Pyrenees). *Mar. Pet. Geol.* 120, 104517
- Cruset, D., Cantarero, I., Travé, A., Vergés, J., John, C.M., 2016. Crestal graben fluid evolution during growth of the Puig-reig anticline (South Pyrenean fold and thrust belt). *J. Geodyn.* 101, 30–50
- Cruset, D., Cantarero, I., Vergés, J., John, C.M., Muñoz-López, D., Travé, A., 2018. Changes in fluid regime in syn-orogenic sediments during the growth of the south Pyrenean fold and thrust belt. *Glob. Planet. Change* 171, 207–224. <https://doi.org/10.1016/j.gloplacha.2017.11.001>
- Cruset, D., Vergés, J., Albert, R., Gerdes, A., Benedicto, A., Cantarero, I., Travé, A., 2020b. Quantifying deformation processes in the SE Pyrenees using U–Pb dating of fracture-filling calcites. *J. Geol. Soc. London.* 177, 1186–1196. <https://doi.org/10.1144/jgs2020-014>
- Deming, D., 1994. Fluid flow and heat transport in the upper continental crust. *Geol. Soc. London, Spec. Publ.* 78, 27–42. <https://doi.org/10.1144/GSL.SP.1994.078.01.04>
- Dennis, K.J., Affek, H.P., Passey, B.H., Schrag, D.P., Eiler, J.M., 2011. Defining an absolute reference frame for ‘clumped’ isotope studies of CO₂. *Geochim. Cosmochim. Acta* 75, 7117–7131

- Deweever, B., Berwouts, I., Swennen, R., Breesch, L., Ellam, R.M., 2010. Fluid flow reconstruction in karstified Panormide platform limestones (north-central Sicily): Implications for hydrocarbon prospectivity in the Sicilian fold and thrust belt. *Mar. Pet. Geol.* 27, 939–958. <https://doi.org/10.1016/j.marpetgeo.2009.10.018>
- Deweever, B., Swennen, R., Breesch, L., 2013. Fluid flow compartmentalization in the Sicilian fold and thrust belt: Implications for the regional aqueous fluid flow and oil migration history. *Tectonophysics* 591, 194–209
- Dimmen, V., Rotevatn, A., Nixon, C.W., 2020. The Relationship between Fluid Flow, Structures, and Depositional Architecture in Sedimentary Rocks: An Example-Based Overview. *Geofluids* 2020, 1–19. <https://doi.org/10.1155/2020/3506743>
- Duddy, I.R., Green, P.F., Bray, R.J., Hegarty, K.A., 1994. Recognition of the thermal effects of fluid flow in sedimentary basins. *Geol. Soc. London, Spec. Publ.* 78, 325–345
- Enlow, R.L., Koons, P.O., 1998. Critical wedges in three dimensions: Analytical expressions from Mohr-Coulomb constrained perturbation analysis. *J. Geophys. Res. Solid Earth.* <https://doi.org/10.1029/97jb03209>
- Evans, M.A., Bebout, G.E., Brown, C.H., 2012. Changing fluid conditions during folding: An example from the central Appalachians. *Tectonophysics* 576–577, 99–115. <https://doi.org/10.1016/j.tecto.2012.03.002>
- Evans, M.A., Fischer, M.P., 2012. On the distribution of fluids in folds: A review of controlling factors and processes. *J. Struct. Geol.* 44, 2–24. <https://doi.org/10.1016/j.jsg.2012.08.003>
- Faulds, J., Coolbaugh, M., Bouchot, V., Moeck, I., Oğuz, K., Cedex, O., 2010. Characterizing Structural Controls of Geothermal Reservoirs in the Great Basin , USA , and Western Turkey : Developing Successful Exploration Strategies in Extended Terranes. *World C.* 25–29.
- Faulkner, D.R., Jackson, C.A.L., Lunn, R.J., Schlische, R.W., Shipton, Z.K., Wibberley, C.A.J., Withjack, M.O., 2010. A review of recent developments concerning the structure, mechanics and fluid flow properties of fault zones. *J. Struct. Geol.* 32, 1557–1575. <https://doi.org/10.1016/j.jsg.2010.06.009>
- Ferket, H., Swennen, R., Ortuño Arzate, S., Roure, F., 2006. Fluid flow evolution in petroleum reservoirs with a complex diagenetic history: An example from Veracruz, Mexico. *J. Geochemical Explor.* 89, 108–111
- Ferket, H., Swennen, R., Ortuño, S., Roure, F., 2003. Reconstruction of the fluid flow history during Laramide foreland fold and thrust belt development in eastern Mexico: cathodoluminescence and O - C isotope trends of calcite-cemented fractures. *J. Geochemical Explor.* 78–79, 163–167. <https://doi.org/10.1016/S0375-6742>
- Fernández, M., Banda, E., 1990. Geothermal anomalies in the Valles-Penedes Graben Master Fault: Convection through the Horst as a possible mechanism. *J. Geophys. Res.* 95, 4887
- Ferry, J.M., Dipple, G.M., 1991. Fluid flow, mineral reactions, and metasomatism. *Geology* 19, 211. [https://doi.org/10.1130/0091-7613\(1991\)019<0211:FFMRAM>2.3.CO;2](https://doi.org/10.1130/0091-7613(1991)019<0211:FFMRAM>2.3.CO;2)
- Fischer, M.P., Higuera-Díaz, I.C., Evans, M.A., Perry, E.C., Leticariu, L., 2009. Fracture-controlled paleohydrology in a map-scale detachment fold: Insights from the analysis of fluid inclusions in calcite and quartz veins. *J. Struct. Geol.* 31, 1490–1510. <https://doi.org/10.1016/j.jsg.2009.09.004>
- Fischer, M.P., Wilkerson, M.S., 2000. Predicting the orientation of joints from fold shape: Results of pseudo-three-dimensional modeling and curvature analysis. *Geology* 28, 15–18

- Fitz-Diaz, E., Hudleston, P., Siebenaller, L., Kirschner, D., Camprubí, A., Tolson, G., Puig, T.P., 2011. Insights into fluid flow and water-rock interaction during deformation of carbonate sequences in the Mexican fold-thrust belt. *J. Struct. Geol.* 33, 1237–1253. <https://doi.org/10.1016/j.jsg.2011.05.009>
- Gallemí, J., Martínez Ribas, R., Pons, J., 1982. Unidades del Cretácico superior en los alrededores de San Corneli (Provincia de Lleida). *J. Iber. Geol. - An Int. Publ. Earth Sci.* 8, 935–948
- Garcés, M., López-Blanco, M., Valero, L., Beamud, E., Muñoz, J.A., Oliva-Urcia, B., Vinyoles, A., Arbués, P., Cabello, P., Cabrera, L., 2020. Paleogeographic and sedimentary evolution of the South Pyrenean foreland basin. *Mar. Pet. Geol.* 113, 104105. <https://doi.org/10.1016/j.marpetgeo.2019.104105>
- García-Sansegundo, J., Poblet, J., Alonso, J.L., Clariana, P., 2011. Hinterland-foreland zonation of the Variscan orogen in the Central Pyrenees: comparison with the northern part of the Iberian Variscan Massif. *Geol. Soc. London, Spec. Publ.* 349, 169–184. <https://doi.org/10.1144/SP349.9>
- García-Senz, J.M., 2002. Cuencas Extensivas del Cretácico Inferior en los Pirineos Centrales, formación y subsecuente inversión. PhD Thesis Univ. Barcelona 310p.
- Garrido-Megías, A., Ríos, J.M., 1972. Síntesis geológica del Secundario y Terciario entre los ríos Cinca y Segre (Pirineo central de la vertiente surpirenaica, provincias de Huesca y Lérida). *Boletín Geológico y Min. España* 83, 1–47.
- Garven, G., 1989. A hydrogeologic model for the formation of the giant oil sands deposits of the Western Canada sedimentary basin. *Am. J. Sci.* 289, 105–166. <https://doi.org/10.2475/ajs.289.2.105>
- Goula, X., Olivera, C., Fleta, J., Grellet, B., Lindo, R., Rivera, L., Cisternas, A., Carbon, D., 1999. Present and recent stress regime in the eastern part of the Pyrenees. *Tectonophysics* 308, 487–502
- Grant, N.T., Banks, D.A., McCaig, A.M., Yardley, B.W.D., 1990. Chemistry, Source and Behaviour of Fluids Involved in Alpine Thrusting of the Central Pyrenees. *J. Geophys. Res.* 95, 9123–9131.
- Grasby, S.E., Hutcheon, I., 2001. Controls on the distribution of thermal springs in the southern Canadian Cordillera. *Can. J. Earth Sci.* 38, 427–440. <https://doi.org/10.1139/cjes-38-3-427>
- Grool, A.R., Ford, M., Vergés, J., Huisman, R.S., Christophoul, F., Dielforder, A., 2018. Insights Into the Crustal-Scale Dynamics of a Doubly Vergent Orogen From a Quantitative Analysis of Its Forelands: A Case Study of the Eastern Pyrenees. *Tectonics* 37, 450–476. <https://doi.org/10.1002/2017TC004731>
- Gudmundsson, A., 2001. Fluid overpressure and flow in fault zones: field measurements and models. *Tectonophysics* 336, 183–197. [https://doi.org/10.1016/S0040-1951\(01\)00101-9](https://doi.org/10.1016/S0040-1951(01)00101-9)
- Gudmundsson, A., 1999. Fluid overpressure and stress drop in fault zones. *Geophys. Res. Lett.* 26, 115–118
- Guillaume, B., Dhont, D., Brusset, S., 2008. Three-dimensional geologic imaging and tectonic control on stratigraphic architecture: Upper Cretaceous of the Tremp Basin (south-central Pyrenees, Spain). *AAPG Bulletin*, v. 92, no. 2, pp. 249–269
- Gudmundsson, A., Berg, S.S., Lyslo, K.B., Skurtveit, E., 2001. Fracture networks and fluid transport in active fault zones. *J. Struct. Geol.* 23, 343–353. [https://doi.org/10.1016/S0191-8141\(00\)00100-0](https://doi.org/10.1016/S0191-8141(00)00100-0)
- Guo, W., Mosenfelder, J.L., Goddard, W.A., Eiler, J.M., 2009. Isotopic fractionations associated with phosphoric acid digestion of carbonate minerals: Insights from first-principles theoretical modeling and clumped isotope measurements. *Geochim. Cosmochim. Acta* 73, 7203–7225
- Gutmanis, J., Ardèvol i Oró, L., Díez-Canseco, D., Chebbihi, L., Awdal, A., Cook, A., 2018. Fracture analysis of outcrop analogues to support modelling of the subseismic domain in carbonate reservoirs, south-central Pyrenees. *Geol. Soc. London, Spec. Publ.* 459, 139–156. <https://doi.org/10.1144/SP459.2>

- Haines, S.H., 2008. Transformations in clay-rich fault-rocks: constraining fault zone processes and the kinematic evolution of regions. PhD Thesis, Univ. Michigan 295p.
- Hartevelt, J.J.A., 1970. Geology of the Upper Segre and Valira Valleys, Central Pyrenees, Andorra, Spain. Geological Institute, Leiden University, Leiden, 45, 167-236.
- Hausegger, S., Kurz, W., Rabitsch, R., Kiechl, E., Brosch, F.J., 2010. Analysis of the internal structure of a carbonate damage zone: Implications for the mechanisms of fault breccia formation and fluid flow. *J. Struct. Geol.* 32, 1349–1362. <https://doi.org/10.1016/j.jsg.2009.04.014>
- Henderson, I.H.C., McCaig, A.M., 1996. Fluid pressure and salinity variations in shear zone-related veins, central Pyrenees, France: Implications for the fault-valve model. *Tectonophysics* 262, 321–348
- Henry, C., Burkhard, M., Goffé, B., 1996. Evolution of synmetamorphic veins and their wallrocks through a Western Alps transect: no evidence for large-scale fluid flow. Stable isotope, major- and trace-element systematics. *Chem. Geol.* 127, 81–109. [https://doi.org/10.1016/0009-2541\(95\)00106-9](https://doi.org/10.1016/0009-2541(95)00106-9)
- Hilgers, C., Kirschner, D.L., Breton, J.-P., Urai, J.L., 2006. Fracture sealing and fluid overpressures in limestones of the Jabal Akhdar dome, Oman mountains. *Geofluids* 6, 168–184
- Hilgers, C., Sindern, S., 2005. Textural and isotopic evidence on the fluid source and transport mechanism of antitaxial fibrous microstructures from the Alps and the Appalachians. *Geofluids* 5, 239–250
- Humphrey, E., Gomez-Rivas, E., Koehn, D., Bons, P.D., Neilson, J., Martín-Martín, J.D., Schoenherr, J., 2019. Stylolite-controlled diagenesis of a mudstone carbonate reservoir: A case study from the Zechstein_2_Carbonate (Central European Basin, NW Germany). *Mar. Pet. Geol.* 109, 88–107
- Huntington, K.W., Eiler, J.M., Affek, H.P., Guo, W., Bonifacie, M., Yeung, L.Y., Thiagarajan, N., Passey, B., Tripathi, A., Daëron, M., Came, R., 2009. Methods and limitations of “clumped” CO₂ isotope ($\Delta 47$) analysis by gas-source isotope ratiomass spectrometry. *J. Mass Spectrom.* 44, 1318–1329. <https://doi.org/10.1002/jms.1614>
- Hurai, V., Huraiová, M., Slobodník, M., Thomas, R., 2015. Stable Isotope Geochemistry of Geofluids, in: *Geofluids*. Elsevier, pp. 293–344. <https://doi.org/10.1016/B978-0-12-803241-1.00009-5>
- Incerpi, N., Martire, L., Manatschal, G., Bernasconi, S.M., 2017. Evidence of hydrothermal fluid flow in a hyperextended rifted margin: the case study of the Err nappe (SE Switzerland). *Swiss J. Geosci.* 110, 439–456
- John, C.M., Bowen, D., 2016. Community software for challenging isotope analysis: First applications of ‘Easotope’ to clumped isotopes. *Rapid Commun. Mass Spectrom.* 30, 2285–2300
- Jolley, S.J., Barr, D., Walsh, J.J., Knipe, R.J., 2007. Structurally complex reservoirs: an introduction. *Geol. Soc. London, Spec. Publ.* 292, 1–24. <https://doi.org/10.1144/SP292.1>
- Kim, S.-T., O’Neil, J.R., 1997. Equilibrium and nonequilibrium oxygen isotope effects in synthetic carbonates. *Geochim. Cosmochim. Acta* 61, 3461–3475. [https://doi.org/10.1016/S0016-7037\(97\)00169-5](https://doi.org/10.1016/S0016-7037(97)00169-5)
- Kim, Y.-S., Peacock, D.C.P., Sanderson, D.J., 2004. Fault damage zones. *J. Struct. Geol.* 26, 503–517
- Kluge, T., John, C.M., Jourdan, A.-L., Davis, S., Crawshaw, J., 2015. Laboratory calibration of the calcium carbonate clumped isotope thermometer in the 25–250 °C temperature range. *Geochim. Cosmochim. Acta* 157, 213–227. <https://doi.org/10.1016/j.gca.2015.02.028>
- Krimissa, M., Chery, L., Fouillac, C., Michelot, J.L., 1994. Origin and Recharge Altitude of the Thermo-Mineral Waters of the Eastern Pyrenees. *Isot. Environ. Heal. Stud.* 30, 317–331

REFERENCES

- Labaume, P., Carrio-Schaffhauser, E., Gamond, J.-F., Renard, F., 2004. Deformation mechanisms and fluid-driven mass transfers in the recent fault zones of the Corinth Rift (Greece). *Comptes Rendus Geosci.* 336, 375–383. <https://doi.org/10.1016/j.crte.2003.11.010>
- Labaume, P., Sheppard, S., Moretti, I., 2000. Structure and hydraulic behaviour of cataclastic thrust fault zones in sandstones, Sub-Andean Zone, Bolivia. *J. Geochemical Explor.* 69–70, 487–492
- Lacroix, B., Baumgartner, L.P., Bouvier, A.-S., Kempton, P.D., Vennemann, T., 2018. Multi fluid-flow record during episodic mode I opening: A microstructural and SIMS study (Cotiella Thrust Fault, Pyrenees). *Earth Planet. Sci. Lett.* 503, 37–46
- Lacroix, B., Buatier, M., Labaume, P., Travé, A., Dubois, M., Charpentier, D., Ventalon, S., Convert-Gaubier, D., 2011. Microtectonic and geochemical characterization of thrusting in a foreland basin: Example of the South-Pyrenean orogenic wedge (Spain). *J. Struct. Geol.* 33, 1359–1377
- Lacroix, B., Leclère, H., Buatier, M., Fabbri, O., 2013. Weakening processes in thrust faults: insights from the Monte Perdido thrust fault (southern Pyrenees, Spain). *Geofluids* 13, 56–65. <https://doi.org/10.1111/gfl.12010>
- Lacroix, B., Travé, A., Buatier, M., Labaume, P., Vennemann, T., Dubois, M., 2014. Syntectonic fluid-flow along thrust faults: Example of the South-Pyrenean fold-and-thrust belt. *Mar. Pet. Geol.* 49, 84–98
- Lago, M., Arranz, E., Pocoví, A., Galé, C., Gil-Imaz, A., 2004. Permian magmatism and basin dynamics in the southern Pyrenees: a record of the transition from late Variscan transtension to early Alpine extension. *Geol. Soc. London, Spec. Publ.* 223, 439–464. <https://doi.org/10.1144/GSL.SP.2004.223.01.19>
- Lanaja, J.M., 1987. Contribucion de la Exploracion Petrolifera al Conocimiento de la Geologia de España. IGME 465p.
- Laubach, S.E., Olson, J.E., Gross, M.R., 2009. Mechanical and fracture stratigraphy. *Am. Assoc. Pet. Geol. Bull.* 93, 1413–1426. <https://doi.org/10.1306/07270909094>
- Leticariu, L., Perry, E.C., Fischer, M.P., Banner, J.L., 2005. Evolution of fluid compartmentalization in a detachment fold complex. *Geology* 33, 69. <https://doi.org/10.1130/G20592.1>
- Li, K., Cai, C., He, H., Jiang, L., Cai, L., Xiang, L., Huang, S., Zhang, C., 2010. Origin of palaeo-waters in the Ordovician carbonates in Tahe oilfield, Tarim Basin: constraints from fluid inclusions and Sr, C and O isotopes. *Geofluids* 11, 71–86. <https://doi.org/10.1111/j.1468-8123.2010.00312.x>
- Liotta, D., Ruggieri, G., Brogi, A., Fulignati, P., Dini, A., Nardini, I., 2010. Migration of geothermal fluids in extensional terrains: the ore deposits of the Boccheggiano-Montieri area (southern Tuscany, Italy). *Int. J. Earth Sci.* 99, 623–644. <https://doi.org/10.1007/s00531-008-0411-3>
- Lisa M. Pratt, Eric R. Force, B., 1991. Coupled Manganese and Carbon-isotopic Events in Marine Carbonates at the Cenomanian-turonian Boundary. *SEPM J. Sediment. Res.* Vol. 61
- Mangenot, X., Bonifacie, M., Gasparrini, M., Götz, A., Chaduteau, C., Ader, M., Rouchon, V., 2017. Coupling Δ_{47} and fluid inclusion thermometry on carbonate cements to precisely reconstruct the temperature, salinity and $\delta^{18}\text{O}$ of paleo-groundwater in sedimentary basins. *Chem. Geol.* 472, 44–57
- Mangenot, X., Gasparrini, M., Rouchon, V., Bonifacie, M., 2018. Basin-scale thermal and fluid flow histories revealed by carbonate clumped isotopes (Δ_{47}) - Middle Jurassic carbonates of the Paris Basin depocentre. *Sedimentology* 65, 123–150. <https://doi.org/10.1111/sed.12427>
- Marshall, J.D., 1992. Climatic and oceanographic isotopic signals from the carbonate rock record and their preservation. *Geol. Mag.* 129, 143–160. <https://doi.org/10.1017/S0016756800008244>
- Martí, J., 1996. Genesis of crystal-rich volcanoclastic facies in the Permian red beds of the Central Pyrenees (NE Spain). *Sediment. Geol.* 106, 1–19. [https://doi.org/10.1016/0037-0738\(95\)00143-3](https://doi.org/10.1016/0037-0738(95)00143-3)

- Martí, J., 1991. Caldera-like structures related to Permo-Carboniferous volcanism of the Catalan Pyrenees (NE Spain). *J. Volcanol. Geotherm. Res.* 45, 173–186. [https://doi.org/10.1016/0377-0273\(91\)90057-7](https://doi.org/10.1016/0377-0273(91)90057-7)
- McArthur, J.M., Howarth, R.J., Shields, G.A., 2012. Strontium Isotope Stratigraphy, in: *The Geologic Time Scale*. Elsevier, pp. 127–144. <https://doi.org/10.1016/B978-0-444-59425-9.00007-X>
- McCaig, A.M., Wayne, D.M., Marshall, J.D., Banks, D., Henderson, I., 1995a. Isotopic and fluid inclusion studies of fluid movement along the Gavarnie Thrust, central Pyrenees: reaction fronts in carbonate mylonites. *Am. J. Sci.* 295, 309–343.
- McCaig, A.M., Wayne, D.M., Marshall, J.D., Banks, D., Henderson, I., 1995b. Isotopic and fluid inclusion studies of fluid movement along the Gavarnie Thrust, central Pyrenees; reaction fronts in carbonate mylonites. *Am. J. Sci.* 295, 309–343. <https://doi.org/10.2475/ajs.295.3.309>
- McCaig, A.M., Wayne, D.M., Rosenbaum, J.M., 2000. Fluid expulsion and dilatancy pumping during thrusting in the Pyrenees: Pb and Sr isotope evidence. *Geol. Soc. Am. Bull.* 112, 1199–1208
- McCrea, J.M., 1950. On the Isotopic Chemistry of Carbonates and a Paleotemperature Scale. *J. Chem. Phys.* 18, 849–857. <https://doi.org/10.1063/1.1747785>
- Mencos, J., 2010. Metodologies de reconstrucció i modelització 3D d'estructures geològiques: anticlinal de Sant Corneli-Bóixols (Pirineus centrals). PhD Thesis Univ. Barcelona 403p.
- Mencos, J., Carrera, N., Muñoz, J.A., 2015. Influence of rift basin geometry on the subsequent postrift sedimentation and basin inversion: The Organyà Basin and the Bóixols thrust sheet (south central Pyrenees). *Tectonics* 34, 1452–1474. <https://doi.org/10.1002/2014TC003692>
- Mencos, J., Muñoz, J.A., Hardy, S., 2011. Three-dimensional Geometry and Forward Numerical Modeling of the Sant Corneli Anticline (Southern Pyrenees, Spain). *AAPG Mem.* 94, 283–300
- Mey, P.H.W., 1967. The geology of the upper Ribagorzana and Baliera Valleys, Central Pyrenees, Spain. *Leidse Geol. Meded.* 41, 153–220.
- Mey, P.H.W., Nagtegaal, P.J.C., Roberti, K.J., Hartevelt, J.J.A., 1968. Lithostratigraphic subdivision of Post-Hercynian deposits in the South-Central Pyrenees, Spain. *Leidse Geol. Meded.* 41, 221–228.
- Mitiku, A.B., Bauer, S., 2013. Optimal use of a dome-shaped anticline structure for CO₂ storage: a case study in the North German sedimentary basin. *Environ. Earth Sci.* 70, 3661–3673
- Mitra, S., 1990. Fault-Propagation Folds: Geometry, Kinematic Evolution, and Hydrocarbon Traps. *Am. Assoc. Pet. Geol. Bull.* 74, 617–620. <https://doi.org/10.1306/0C9B23CB-1710-11D7-8645000102C1865D>
- Morad, S., Al-Ramadan, K., Ketzer, J.M., De Ros, L.F., 2010. The impact of diagenesis on the heterogeneity of sandstone reservoirs: A review of the role of depositional facies and sequence stratigraphy. *Am. Assoc. Pet. Geol. Bull.* 94, 1267–1309. <https://doi.org/10.1306/04211009178>
- Moretti, I., 1998. The role of faults in hydrocarbon migration. *Pet. Geosci.* 4, 81–94
- Moretti, I., Labaume, P., Sheppard, S., Boulegue, J., 2000. Compartmentalisation of fluid flow by thrust faults, Sub-Andean Zone, Bolivia. *J. Geochemical Explor.* 69–70, 493–497.
- Moretti, I., Labaume, P., Sheppard, S.M.F., Boulègue, J., 2002. Compartmentalisation of fluid migration pathways in the sub-Andean Zone, Bolivia. *Tectonophysics* 348, 5–24
- Morley, C.K., Warren, J., Tingay, M., Boonyasaknanon, P., Julapour, A., 2014. Comparison of modern fluid distribution, pressure and flow in sediments associated with anticlines growing in deepwater (Brunei) and continental environments (Iran). *Mar. Pet. Geol.* 51, 210–229. <https://doi.org/10.1016/j.marpetgeo.2013.11.011>

- Mozafari, M., Swennen, R., Balsamo, F., El Desouky, H., Storti, F., Taberner, C., 2019. Fault-controlled dolomitization in the Montagna dei Fiori Anticline (Central Apennines, Italy): record of a dominantly pre-orogenic fluid migration. *Solid Earth* 10, 1355–1383. <https://doi.org/10.5194/se-10-1355-2019>
- Mozafari, M., Swennen, R., Muchez, P., Vassilieva, E., Balsamo, F., Storti, F., Pironon, J., Taberner, C., 2017. Origin of the saline paleofluids in fault-damage zones of the Jabal Qusaybah Anticline (Adam Foothills, Oman): Constraints from fluid inclusions geochemistry. *Mar. Pet. Geol.* 86, 537–546
- Muchez, P., Sintubin, M., 1998. Contrasting origin of palaeofluids in a strike-slip fault system. *Chem. Geol.* 145, 105–114. [https://doi.org/10.1016/S0009-2541\(97\)00164-2](https://doi.org/10.1016/S0009-2541(97)00164-2)
- Muñoz-López, D., Cruset, D., Cantarero, I., Benedicto, A., John, C.M., Travé, A., 2020. Fluid Dynamics in a Thrust Fault Inferred from Petrology and Geochemistry of Calcite Veins: An Example from the Southern Pyrenees. *Geofluids* 2020, 1–25. <https://doi.org/10.1155/2020/8815729>
- Muñoz-López, D., Alías, G., Cruset, D., Cantarero, I., John, C.M., Travé, A., 2020. Influence of basement rocks on fluid evolution during multiphase deformation: the example of the Estamariu thrust in the Pyrenean Axial Zone. *Solid Earth* 11, 2257–2281. <https://doi.org/10.5194/se-11-2257-2020>
- Muñoz, J.A., 1992. Evolution of a continental collision belt: ECORS-Pyrenees crustal balanced cross-section, in: *Thrust Tectonics*. Springer Netherlands, Dordrecht, pp. 235–246
- Muñoz, J.A., Martinez, A., Verges, J., 1986. Thrust sequences in the eastern Spanish Pyrenees. *J. Struct. Geol.* 8, 399–405.
- Nardini, N., Muñoz-López, D., Cruset, D., Cantarero, I., Martín-Martín, J., Benedicto, A., Gomez-Rivas, E., John, C., Travé, A., 2019. From Early Contraction to Post-Folding Fluid Evolution in the Frontal Part of the Bóixols Thrust Sheet (Southern Pyrenees) as Revealed by the Texture and Geochemistry of Calcite Cements. *Minerals* 9, 117. <https://doi.org/10.3390/min9020117>
- Nelson, S.T., Mayo, A.L., Gilfillan, S., Dutson, S.J., Harris, R.A., Shipton, Z.K., Tingey, D.G., 2006. Enhanced fracture permeability and accompanying fluid flow in the footwall of a normal fault: The Hurricane fault at Pah Tempe hot springs, Washington County, Utah. *Geol. Soc. Am. Bull.* preprint, 1
- Nuriel, P., Wotzlaw, J.-F., Ovtcharova, M., Vaks, A., Stremtan, C., Šála, M., Roberts, N.M.W., Kylander-Clark, A.R.C., 2021. The use of ASH-15 flowstone as a matrix-matched reference material for laser-ablation U – Pb geochronology of calcite. *Geochronology* 3, 35–47. <https://doi.org/10.5194/gchron-3-35-2021>
- Ogata, K., Senger, K., Braathen, A., Tveranger, J., 2014. Fracture corridors as seal-bypass systems in siliciclastic reservoir-cap rock successions: Field-based insights from the Jurassic Entrada Formation (SE Utah, USA). *J. Struct. Geol.* 66, 162–187. <https://doi.org/10.1016/j.jsg.2014.05.005>
- Oliver, J., 1986. Fluids expelled tectonically from orogenic belts: Their role in hydrocarbon migration and other geologic phenomena. *Geology* 14, 99.
- Oliver, N.H.S., Bons, P.D., 2001. Mechanisms of fluid flow and fluid-rock interaction in fossil metamorphic hydrothermal systems inferred from vein-wall rock patterns, geometry and microstructure. *Geofluids* 1, 137–162. <https://doi.org/10.1046/j.1468-8123.2001.00013.x>
- Pagel, M., Bonifacie, M., Schneider, D.A., Gautheron, C., Brigaud, B., Calmels, D., Cros, A., Saint-Bezar, B., Landrein, P., Sutcliffe, C., Davis, D., Chaduteau, C., 2018. Improving paleohydrological and diagenetic reconstructions in calcite veins and breccia of a sedimentary basin by combining $\Delta 47$ temperature, $\delta 18\text{O}_{\text{water}}$ and U-Pb age. *Chem. Geol.* 481, 1–17. <https://doi.org/10.1016/j.chemgeo.2017.12.026>
- Petracchini, L., Antonellini, M., Billi, A., Scrocca, D., 2012. Fault development through fractured pelagic carbonates of the Cingoli anticline, Italy: Possible analog for subsurface fluid-conductive fractures. *J. Struct. Geol.* 45, 21–37. <https://doi.org/10.1016/j.jsg.2012.05.007>

- Pfeifer, H.-R., Oberhänsli, H., Epprecht, W., 1988. Geochemical evidence for a synsedimentary hydrothermal origin of Jurassic iron-manganese deposits at Gonzen (Sargans, Helvetic Alps, Switzerland). *Mar. Geol.* 84, 257–272. [https://doi.org/10.1016/0025-3227\(88\)90105-3](https://doi.org/10.1016/0025-3227(88)90105-3)
- Pizzati, M., Balsamo, F., Storti, F., Mozafari, M., Iacumin, P., Tinterri, R., Swennen, R., 2018. From axial parallel to orthogonal groundwater flow during fold amplification: insights from carbonate concretion development during the growth of the Quattro Castella Anticline, Northern Apennines, Italy. *J. Geol. Soc. London.* 175, 806–819. <https://doi.org/10.1144/jgs2018-031>
- Plaziat, J.-C., 1981. Late cretaceous to late eocene palaeogeographic evolution of southwest Europe. *Palaeogeogr. Palaeoclimatol. Palaeoecol.* 36, 263–320. [https://doi.org/10.1016/0031-0182\(81\)90110-3](https://doi.org/10.1016/0031-0182(81)90110-3)
- Poblet, J., 1991. Estructura herciniana i alpina del vessant sud de la zona axial del Pirineu central. PhD Thesis, Univ. Barcelona 604p.
- Pomerol, B., 1983. Geochemistry of the late Cenomanian-early Turonian chalks of the Paris Basin: Manganese and carbon isotopes in carbonates as paleoceanographic indicators. *Cretac. Res.* 4, 85–93
- Popp, B.N., Podosek, F.A., Brannon, J.C., Anderson, T.F., Pier, J., 1986. $^{87}\text{Sr}/^{86}\text{Sr}$ ratios in Permo-Carboniferous sea water from the analyses of well-preserved brachiopod shells. *Geochim. Cosmochim. Acta* 50, 1321–1328. [https://doi.org/10.1016/0016-7037\(86\)90308-X](https://doi.org/10.1016/0016-7037(86)90308-X)
- Puigdefàbregas, C., Souquet, P., 1986. Tecto-sedimentary cycles and depositional sequences of the Mesozoic and Tertiary from the Pyrenees. *Tectonophysics* 129, 173–203. [https://doi.org/10.1016/0040-1951\(86\)90251-9](https://doi.org/10.1016/0040-1951(86)90251-9)
- Pujalte, V., Baceta, J.I., Schmitz, B., Orue-Etxebarria, X., Payros, A., Bernaola, G., Apellaniz, E., Caballero, F., Robador, A., Serra-Kiel, J., Tosquella, J., 2009. Redefinition of the Ilerdian Stage (early Eocene). *Geol. Acta* 7, 177–194. <https://doi.org/10.1344/105.000000268>
- Putnis, A., 2002. Mineral replacement reactions: from macroscopic observations to microscopic mechanisms. *Mineral. Mag.* 66, 689–708. <https://doi.org/10.1180/0026461026650056>
- Reches, Z., Lockner, D.A., 1994. Nucleation and growth of faults in brittle rocks. *J. Geophys. Res. Solid Earth* 99, 18159–18173. <https://doi.org/10.1029/94JB00115>
- Ring, U., Gerdes, A., 2016. Kinematics of the Alpenrhein-Bodensee graben system in the Central Alps: Oligocene/Miocene transtension due to formation of the Western Alps arc. *Tectonics* 35, 1367–1391
- Robert, R., Robion, P., Souloumiac, P., David, C., Sallet, E., 2018. Deformation bands, early markers of tectonic activity in front of a fold-and-thrust belt: Example from the Tremp-Graus basin, southern Pyrenees, Spain. *J. Struct. Geol.* 110, 65–85. <https://doi.org/10.1016/j.jsg.2018.02.012>
- Roca, E., 1996. The Neogene Cerdanya and Seu d'Urgell intramontane basins (Eastern Pyrenees), in: Friend, P.F., Dabrio, C.J. (Eds.), *Tertiary Basins of Spain*. Cambridge University Press, Cambridge, pp. 114–119
- Roca, E., Guimerà, J., 1992. The Neogene structure of the eastern Iberian margin: Structural constraints on the crustal evolution of the Valencia trough (western Mediterranean). *Tectonophysics* 203, 203–218
- Roure, F., Andriessen, P., Callot, J.P., Faure, J.L., Ferket, H., Gonzales, E., Guilhaumou, N., Lacombe, O., Malandain, J., Sassi, W., Schneider, F., Swennen, R., Vilasi, N., 2010. The use of palaeo-thermobarometers and coupled thermal, fluid flow and pore-fluid pressure modelling for hydrocarbon and reservoir prediction in fold and thrust belts. *Geol. Soc. Spec. Publ.* 348, 87–114. <https://doi.org/10.1144/SP348.6>
- Roure, F., Choukroune, P., Berastegui, X., Munoz, J. a., Villien, A., Matheron, P., Bareyt, M., Seguret, M., Camara, P., Deramond, J., 1989. Ecore deep seismic data and balanced cross sections: Geometric constraints on the evolution of the Pyrenees. *Tectonics* 8, 41–50. <https://doi.org/10.1029/TC008i001p00041>

- Roure, F., Swennen, R., Schneider, F., Faure, J.L., Ferket, H., Guilhaumou, N., Osadetz, K., Robion, P., Vandeginste, V., 2005. Incidence and Importance of Tectonics and Natural Fluid Migration on Reservoir Evolution in Foreland Fold-And-Thrust Belts. *Oil Gas Sci. Technol.* 60, 67–106
- Rye, D.M., Bradbury, H.J., 1988. Fluid flow in the crust; an example from a Pyrenean thrust ramp. *Am. J. Sci.* 288, 197–235. <https://doi.org/10.2475/ajs.288.3.197>
- Salomon, E., Rotevatn, A., Kristensen, T.B., Grundvåg, S.-A., Henstra, G.A., Meckler, A.N., Albert, R., Gerdes, A., 2020. Fault-controlled fluid circulation and diagenesis along basin-bounding fault systems in rifts – insights from the East Greenland rift system. *Solid Earth* 11, 1987–2013. <https://doi.org/10.5194/se-11-1987-2020>
- Saura, E., 2004. Anàlisi estructural de la Zona de les Nogueres (Pirineus Centrals). PhD Thesis Univ. Barcelona 398p.
- Saura, E., Teixell, A., 2006. Inversion of small basins: effects on structural variations at the leading edge of the Axial Zone antiformal stack (Southern Pyrenees, Spain). *J. Struct. Geol.* 28, 1909–1920
- Scholz, C.H., Dawers, N.H., Yu, J.-Z., Anders, M.H., Cowie, P.A., 1993. Fault growth and fault scaling laws: Preliminary results. *J. Geophys. Res. Solid Earth* 98, 21951–21961. <https://doi.org/10.1029/93JB01008>
- Séguret, M., Daignières, M., 1986. Crustal scale balanced cross-sections of the Pyrenees; discussion. *Tectonophysics* 129, 303–318. [https://doi.org/10.1016/0040-1951\(86\)90258-1](https://doi.org/10.1016/0040-1951(86)90258-1)
- Shackleton, J.R., Cooke, M.L., Sussman, A.J., 2005. Evidence for temporally changing mechanical stratigraphy and effects on joint-network architecture. *Geology* 33, 101–104. <https://doi.org/10.1130/G20930.1>
- Shackleton, J.R., Cooke, M.L., Vergés, J., Simó, T., 2011. Temporal constraints on fracturing associated with fault-related folding at Sant Corneli anticline, Spanish Pyrenees. *J. Struct. Geol.* 33, 5–19
- Sibson, R., Scott, J., 1998. Stress/fault controls on the containment and release of overpressured fluids: Examples from gold-quartz vein systems in Juneau, Alaska; Victoria, Australia and Otago, New Zealand. *Ore Geol. Rev.* 13, 293–306. [https://doi.org/10.1016/S0169-1368\(97\)00023-1](https://doi.org/10.1016/S0169-1368(97)00023-1)
- Sibson, R., 2004. Frictional Mechanics of Seismogenic Thrust Systems in the Upper Continental Crust—Implications for Fluid Overpressures and Redistribution. *Thrust tectonics Hydrocarb. Syst. AAPG Mem.* 82 1–17.
- Sibson, R.H., 2019. Arterial faults and their role in mineralizing systems. *Geosci. Front.* 1–9
- Sibson, R.H., 2017. Tensile overpressure compartments on low-angle thrust faults. *Earth, Planets Sp.* 69, 113
- Sibson, R.H., 2003. Brittle-failure controls on maximum sustainable overpressure in different tectonic regimes. *Am. Assoc. Pet. Geol. Bull.* 87, 901–908. <https://doi.org/10.1306/01290300181>
- Sibson, R.H., 1996. Structural permeability of fluid-driven fault-fracture meshes. *J. Struct. Geol.* 18, 1031–1042. [https://doi.org/10.1016/0191-8141\(96\)00032-6](https://doi.org/10.1016/0191-8141(96)00032-6)
- Sibson, R.H., 1995. Selective fault reactivation during basin inversion: potential for fluid redistribution through fault-valve action. *Geol. Soc. London, Spec. Publ.* 88, 3–19. <https://doi.org/10.1144/GSL.SP.1995.088.01.02>
- Sibson, R.H., 1977. Fault rocks and fault mechanisms. *J. Geol. Soc. London.* 133, 191–213
- Simó, A., 1986. Carbonate platform depositional sequences, Upper Cretaceous, south-central Pyrenees (Spain). *Tectonophysics* 129, 205–231. [https://doi.org/10.1016/0040-1951\(86\)90252-0](https://doi.org/10.1016/0040-1951(86)90252-0)

- Srivastava, S.P., Schouten, H., Roest, W.R., Klitgord, K.D., Kovacs, L.C., Verhoef, J., Macnab, R., 1990. Iberian plate kinematics: a jumping plate boundary between Eurasia and Africa. *Nature* 344, 756–759
- Stewart, I.S., Hancock, P.L., 2007. Normal fault zone evolution and fault scarp degradation in the Aegean region. *Basin Res.* 1, 139–153. <https://doi.org/10.1111/j.1365-2117.1988.tb00011.x>
- Stewart, I.S., Hancock, P.L., 1990. Brecciation and fracturing within neotectonic normal fault zones in the Aegean region. *Geol. Soc. London, Spec. Publ.* 54, 105–110. <https://doi.org/10.1144/GSL.SP.1990.054.01.11>
- Sun, X., 2021. Carbon capture and storage in compressional basins: global to reservoir-scale assessments and integrated case study of the Puig-reig anticline (SE Pyrenees). PhD thesis, Universitat de Barcelona.
- Sun, X., Alcalde, J., Gomez-Rivas, E., Struth, L., Johnson, G., Travé, A., 2020. Appraisal of CO₂ storage potential in compressional hydrocarbon-bearing basins: Global assessment and case study in the Sichuan Basin (China). *Geosci. Front.* 11, 2309–2321. <https://doi.org/10.1016/j.gsf.2020.02.008>
- Swennen, R., Muskha, K., Roure, F., 2000. Fluid circulation in the Ionian fold and thrust belt (Albania): implications for hydrocarbon prospectivity. *J. Geochemical Explor.* 69–70, 629–634
- Taillefer, A., Guillou-Frottier, L., Soliva, R., Magri, F., Lopez, S., Courrioux, G., Millot, R., Ladouche, B., Le Goff, E., 2018. Topographic and Faults Control of Hydrothermal Circulation Along Dormant Faults in an Orogen. *Geochemistry, Geophys. Geosystems* 19, 4972–4995. <https://doi.org/10.1029/2018GC007965>
- Taillefer, A., Soliva, R., Guillou-Frottier, L., Le Goff, E., Martin, G., Seranne, M., 2017. Fault-Related Controls on Upward Hydrothermal Flow: An Integrated Geological Study of the Têt Fault System, Eastern Pyrénées (France). *Geofluids* 2017, 1–19. <https://doi.org/10.1155/2017/8190109>
- Tavani, S., Granado, P., Arbués, P., Corradetti, A., Muñoz, J.A., 2017. Syn-thrusting, near-surface flexural-slipping and stress deflection along folded sedimentary layers of the Sant Corneli-Bóixols anticline (Pyrenees, Spain). *Solid Earth* 8, 405–419. <https://doi.org/10.5194/se-8-405-2017>
- Tavani, S., Mencos, J., Bausà, J., Muñoz, J.A., 2011. The fracture pattern of the Sant Corneli Bóixols oblique inversion anticline (Spanish Pyrenees). *J. Struct. Geol.* 33, 1662–1680
- Taylor, B.D., 1987. Stable isotope geochemistry of ore-forming fluids. *Short Course Handbook. Mineral. Assoc. Canada* 13, 337–445.
- Toussaint, R., Aharonov, E., Koehn, D., Gratier, J.P., Ebner, M., Baud, P., Rolland, A., Renard, F., 2018. Stylolites: A review. *J. Struct. Geol.* 114, 163–195. <https://doi.org/10.1016/j.jsg.2018.05.003>
- Travé, A., Calvet, F., 2001. Syn-rift geofluids in fractures related to the early-middle Miocene evolution of the Vallès-Penedès half-graben (NE Spain). *Tectonophysics* 336, 101–120
- Travé, A., Calvet, F., Sans, M., Vergés, J., Thirlwall, M., 2000. Fluid history related to the Alpine compression at the margin of the south-Pyrenean Foreland basin: the El Guix anticline. *Tectonophysics* 321, 73–102
- Travé, A., Calvet, F., Soler, A., Labaume, P., 1998. Fracturing and fluid migration during Palaeogene compression and Neogene extension in the Catalan Coastal Ranges, Spain. *Sedimentology* 45, 1063–1082
- Travé, A., Labaume, P., Calvet, F., Soler, A., 1997. Sediment dewatering and pore fluid migration along thrust faults in a foreland basin inferred from isotopic and elemental geochemical analyses (Eocene southern Pyrenees, Spain). *Tectonophysics* 282, 375–398. [https://doi.org/10.1016/S0040-1951\(97\)00225-4](https://doi.org/10.1016/S0040-1951(97)00225-4)
- Travé, Anna, Labaume, P., Calvet, F., Soler, A., Tritlla, J., Buatier, M., Potdevin, J.-L., Séguret, M., Raynaud, S., Briquieu, L., 1998. Fluid migration during Eocene thrust emplacement in the south Pyrenean

- foreland basin (Spain): an integrated structural, mineralogical and geochemical approach. *Geol. Soc. London, Spec. Publ.* 134, 163–188. <https://doi.org/10.1144/GSL.SP.1998.134.01.08>
- Travé, A., Labaume, P., Vergés, J., 2007. Fluid Systems in Foreland Fold-and-Thrust Belts: An Overview from the Southern Pyrenees, in: Lacombe, O., Roure, F., Lavé, J., Vergés, Jaume (Eds.), *Thrust Belts and Foreland Basins, Frontiers in Earth Sciences*. Springer Berlin Heidelberg, Berlin, Heidelberg, pp. 93–115
- Trincal, V., Buatier, M., Charpentier, D., Lacroix, B., Lanari, P., Labaume, P., Lahfid, A., Vennemann, T., 2017. Fluid–rock interactions related to metamorphic reducing fluid flow in meta-sediments: example of the Pic-de-Port-Vieux thrust (Pyrenees, Spain). *Contrib. to Mineral. Petrol.* 172, 78
- Upton, P., Begbie, M., Craw, D., 2008. Numerical modelling of mechanical controls on coeval steep and shallow dipping auriferous quartz vein formation in a thrust zone, Macraes mine, New Zealand. *Miner. Depos.* 43, 23–35. <https://doi.org/10.1007/s00126-007-0148-0>
- Van Geet, M., Swennen, R., Durmishi, C., Roure, F., Muchez, P.H., 2002. Paragenesis of Cretaceous to Eocene carbonate reservoirs in the Ionian fold and thrust belt (Albania): Relation between tectonism and fluid flow. *Sedimentology* 49, 697–718. <https://doi.org/10.1046/j.1365-3091.2002.00476.x>
- Vandeginste, V., Swennen, R., Allaey, M., Ellam, R.M., Osadetz, K., Roure, F., 2012. Challenges of structural diagenesis in foreland fold-and-thrust belts: A case study on paleofluid flow in the Canadian Rocky Mountains West of Calgary. *Mar. Pet. Geol.* 35, 235–251. <https://doi.org/10.1016/j.marpetgeo.2012.02.014>
- Veizer, J., 1992. Depositional and diagenetic history of limestones: Stable and radiogenic isotopes, in: *Isotopic Signatures and Sedimentary Records*. Springer-Verlag, Berlin/Heidelberg, pp. 13–48
- Veizer, J., Ala, D., Azmy, K., Bruckschen, P., Buhl, D., Bruhn, F., Carden, G.A.F., Diener, A., Ebner, S., Godderis, Y., Jasper, T., Korte, C., Pawellek, F., Podlaha, O.G., Strauss, H., 1999. $^{87}\text{Sr}/^{86}\text{Sr}$, $\delta^{13}\text{C}$ and $\delta^{18}\text{O}$ evolution of Phanerozoic seawater. *Chem. Geol.* 161, 59–88. [https://doi.org/10.1016/S0009-2541\(99\)00081-9](https://doi.org/10.1016/S0009-2541(99)00081-9)
- Vergés, J., 1993. *Estudi geològic del vessant Sud del Pirineu Oriental i Central: Evolució cinemàtica en 3D*. PhD Thesis. Universitat Barcelona 203p.
- Vergés, J., Fernández, M., 2012. Tethys–Atlantic interaction along the Iberia–Africa plate boundary: The Betic–Rif orogenic system. *Tectonophysics* 579, 144–172. <https://doi.org/10.1016/j.tecto.2012.08.032>
- Vergés, J., Fernández, M., Martínez, A., 2002. The Pyrenean orogen: pre-, syn-, and post-collisional evolution. *J. Virtual Explor.* 08, 55–74. <https://doi.org/10.3809/jvirtex.2002.00058>
- Vergés, J., Muñoz, J.A., 1990. Thrust sequence in the southern central Pyrenees. *Bull. la Société Géologique Fr.* VI, 265–271. <https://doi.org/10.2113/gssgfbull.VI.2.265>
- Vermilye, J.M., Scholz, C.H., 1998. The process zone: A microstructural view of fault growth. *J. Geophys. Res. Solid Earth* 103, 12223–12237. <https://doi.org/10.1029/98JB00957>
- Vidal-Royo, O., Muñoz, J.A., Hardy, S., Koyi, H., Cardozo, N., 2013. Structural evolution of Pico del Águila anticline (External sierras, southern Pyrenees) derived from sandbox, numerical and 3D structural modelling techniques. *Geol. Acta* 11, 1–26. <https://doi.org/10.1344/105.000001780>
- Vilasi, N., 2011. Study of reservoir analogues in foreland fold-and-thrust belts: sedimentology, diagenesis, deformation and fracturing of the upper cretaceous-eocene carbonate systems of the ionian zone (Southern Albania). PhD Thesis. Ecole des Mines de Paris, Paris. 190 p.
- Vilasi, N., Malandain, J., Barrier, L., Callot, J.-P., Amrouch, K., Guilhaumou, N., Lacombe, O., Muska, K., Roure, F., Swennen, R., 2009. From outcrop and petrographic studies to basin-scale fluid flow modelling: The use of the Albanian natural laboratory for carbonate reservoir characterisation. *Tectonophysics* 474, 367–392

- Vilasi, N., Swennen, R., Roure, F., 2006. Diagenesis and fracturing of Paleocene-Eocene carbonate turbidite systems in the Ionian Basin: The example of the Kelçyra area (Albania). *J. Geochemical Explor.* 89, 409–413
- Watkins, H., Butler, R.W.H., Bond, C.E., Healy, D., 2015. Influence of structural position on fracture networks in the Torridon Group, Achnashellach fold and thrust belt, NW Scotland. *J. Struct. Geol.* 74, 64–80
- Watkins, H., Healy, D., Bond, C.E., Butler, R.W.H., 2018. Implications of heterogeneous fracture distribution on reservoir quality; an analogue from the Torridon Group sandstone, Moine Thrust Belt, NW Scotland. *J. Struct. Geol.* 108, 180–197. <https://doi.org/10.1016/j.jsg.2017.06.002>
- Wayne, D.M., McCaig, A.M., 1998. Dating fluid flow in shear zones: Rb-Sr and U-Pb studies of syntectonic veins in the Néouvielle Massif, Pyrenees. *Geol. Soc. London, Spec. Publ.* 144, 129–135
- Wilkinson, J.J., Johnston, J.D., 1996. Pressure fluctuations, phase separation, and gold precipitation during seismic fracture propagation. *Geology* 24, 395–398
- Williams, R.T., Goodwin, L.B., Mozley, P.S., 2017. Diagenetic controls on the evolution of fault-zone architecture and permeability structure: Implications for episodicity of fault-zone fluid transport in extensional basins. *Geol. Soc. Am. Bull.* 129, 464–478. <https://doi.org/10.1130/B31443.1>
- Williams, R.T., Goodwin, L.B., Mozley, P.S., Beard, B.L., Johnson, C.M., 2015. Tectonic controls on fault zone flow pathways in the rio grande rift, New Mexico, USA. *Geology* 43, 723–726. <https://doi.org/10.1130/G36799.1>
- Wiltshko, D. V., Lambert, G.R., Lamb, W., 2009. Conditions during syntectonic vein formation in the footwall of the Absaroka Thrust Fault, Idaho–Wyoming–Utah fold and thrust belt. *J. Struct. Geol.* 31, 1039–1057
- Woodcock, N.H., Mort, K., 2008. Classification of fault breccias and related fault rocks. *Geol. Mag.* 145, 435–440. <https://doi.org/10.1017/S0016756808004883>
- Ziegler, P.A., 1988. Evolution of the Arctic-North Atlantic and the Western Tethys, in: AAPG Memoir Volume 43: Evolution of the Arctic-North Atlantic and the Western Tethys. <https://doi.org/10.1306/M43478>
- Zwart, H.J., 1986. The variscan geology of the Pyrenees. *Tectonophysics* 129, 9–27

Annex

Article 1

Muñoz-López, D., Alías, G., Cruset, D., Cantarero, I., Jonh, C. M., and Travé, A., 2020: Influence of basement rocks on fluid evolution during multiphase deformation: the example of the Estamariu thrust in the Pyrenean Axial Zone, *Solid Earth*, 11, 2257–2281. <https://doi.org/10.5194/se-11-2257-2020>. Impact factor: 2.921. Position: Q1 (41/235) in *Geology* (2020).



Influence of basement rocks on fluid evolution during multiphase deformation: the example of the Estamariu thrust in the Pyrenean Axial Zone

Daniel Muñoz-López¹, Gemma Alías¹, David Cruset², Irene Cantarero¹, Cédric M. John³, and Anna Travé¹

¹Department de Mineralogia, Petrologia i Geologia Aplicada, Facultat de Ciències de la Terra, Universitat de Barcelona (UB), C/ Martí i Franquès s/n, 08028 Barcelona, Spain

²Group of Dynamics of the Lithosphere (GDL), Geosciences Barcelona, GEO3BCN-CSIC, Lluís Solé i Sabarís s/n, 08028 Barcelona, Spain

³Department of Earth Science and Engineering, Imperial College London, London SW7 2BP, UK

Correspondence: Daniel Muñoz-López (munoz-lopez@ub.edu)

Received: 21 April 2020 – Discussion started: 5 May 2020

Revised: 7 October 2020 – Accepted: 14 October 2020 – Published: 25 November 2020

Abstract. Calcite veins precipitated in the Estamariu thrust during two tectonic events are studied in order to (i) decipher the temporal and spatial relationships between deformation and fluid migration in a long-lived thrust and (ii) determine the influence of basement rocks on the fluid chemistry during deformation. Structural and petrological observations constrain the relative timing of fluid migration and vein formation, whilst geochemical analyses ($\delta^{13}\text{C}$, $\delta^{18}\text{O}$, $^{87}\text{Sr}/^{86}\text{Sr}$, clumped isotope thermometry, and elemental composition) applied to the related calcite cements and host rocks indicate the fluid origin, pathways, and extent of fluid–rock interaction. The first tectonic event, recorded by calcite cements Cc1a and Cc2, is attributed to the Alpine reactivation of the Estamariu thrust. Analytical data indicate that these cements precipitated from heated meteoric fluids (temperatures in the range of 50 to 100 °C) that had interacted with basement rocks ($^{87}\text{Sr}/^{86}\text{Sr} > 0.71$) before upflowing through the thrust zone. The second tectonic event, attributed to the Neogene extension, is characterized by the reactivation of the Estamariu thrust and the formation of normal faults and shear fractures sealed by calcite cements Cc3, Cc4, and Cc5. Analytical data indicate that cements Cc3 and Cc4 precipitated from hydrothermal fluids (temperatures between 130 and 210 °C and between 100 and 170 °C, respectively) that had interacted with basement rocks ($^{87}\text{Sr}/^{86}\text{Sr} > 0.71$) and been expelled through fault zones during deformation. In contrast, cement Cc5 probably precipitated from meteoric

waters that likely percolated from the surface through small shear fractures.

The comparison between our results and already published data in other structures from the southern Pyrenees suggests that regardless of the origin of the fluids and the tectonic context, basement rocks have a significant influence on the fluid chemistry, particularly on the $^{87}\text{Sr}/^{86}\text{Sr}$ ratio. Accordingly, the cements precipitated from fluids that have interacted with basement rocks have significantly higher $^{87}\text{Sr}/^{86}\text{Sr}$ ratios (> 0.710) with respect to those precipitated from fluids that have interacted with the sedimentary cover (< 0.710), which involves younger and less radiogenic rocks.

1 Introduction

Deformation associated with crustal shortening is mainly accommodated by thrust faulting and related fault zone structures (Mouthereau et al., 2014; Muñoz, 1992; Sibson, 1994). Successive faulting may occur, and favorably oriented structures may undergo reactivation during different tectonic events in a long-lived orogenic belt (Cochelin et al., 2018; Sibson, 1995). The reactivation of faults may produce changes in the hydraulic behavior of fault zones as well as in the origin and regime of fluids circulating through them (Arndt et al., 2014; Barker and Cox, 2011; Cantarero et al., 2018; Cruset et al., 2018; Lacroix et al., 2018; Travé et al.,

2007). Consequently, constraining the timing of deformation and fluid migration is essential to better understand the main factors leading to the current configuration of a mountain belt, its evolution through time, and the mobilization of different fluids during successive deformation events (Baqués et al., 2012; Crespo-Blanc et al., 1995; Faÿ-Gomord et al., 2018; Fitz-Diaz et al., 2011; Lacroix et al., 2014). Understanding basin-scale fluid flow is of primary importance to reconstruct the diagenetic history of a sedimentary basin, as fluids take part in a wide range of geological processes including precipitation of new mineral phases, dolomitization, and petroleum migration, among others (Barker et al., 2009; Foden, 2001; Fontana et al., 2014; Gomez-Rivas et al., 2014; Martín-Martín et al., 2015; Mozafari et al., 2019; Piessens et al., 2002). Due to economic interest in these processes, in particular related to oil and ore deposit exploration, CO₂ sequestration, seismic activity, and water management, many researchers have addressed the relationship between deformation and fluid migration (Beaudoin et al., 2014; Breesch et al., 2009; Cox, 2007; Dewever et al., 2013; Gasparrini et al., 2013; Muñoz-López et al., 2020; Suchy et al., 2000; Travé et al., 2009; Voicu et al., 2000; Warren et al., 2014).

In the Pyrenees, the basement rocks from the Axial Zone are affected by numerous fault systems related to the Variscan orogeny (late Paleozoic) but reactivated during the Pyrenean compression (Late Cretaceous to Oligocene) (Cochelin et al., 2018; Poblet, 1991). However, no real consensus exists about the influence of the Alpine deformation on the basement rocks, and the age of basement-involved structures is still debated (Cochelin et al., 2018; García-Sanseguno et al., 2011). As a consequence, the relationships between deformation and fluid flow have widely focused on structures from the Mesozoic and Cenozoic cover (Beaudoin et al., 2015; Crognier et al., 2018; Cruset et al., 2016, 2018, 2020a; Lacroix et al., 2011, 2014; Martínez Casas et al., 2019; Muñoz-López et al., 2020; Nardini et al., 2019; Travé et al., 1997, 1998, 2000), where the timing of deformation and thrust emplacement is well-constrained (Cruset et al., 2020b; Vergés, 1993; Vergés and Muñoz, 1990). In contrast, few studies, only concentrated along the Gavarnie thrust system, have examined the relationship between deformation and fluid migration in the Paleozoic basement (Banks et al., 1991; Grant et al., 1990; Henderson and McCaig, 1996; McCaig et al., 1995, 2000a; Rye and Bradbury, 1988; Trincal et al., 2017). Another important aspect of studying the fault–fluid system is related to the heat flow and the influence of faults on the development of geothermal systems (Faulds et al., 2010; Grasby and Hutcheon, 2001; Liotta et al., 2010; Rowland and Sibson, 2004). Particularly, in the NE part of the Iberian Peninsula (including the Pyrenees and the Catalan Coastal Range), high-permeability Neogene extensional faults, acting as conduits for upward migration, provide efficient pathways for hydrothermal fluids to flow from deeper to shallower crustal levels (Carmona et al., 2000; Fernández and Banda, 1990; Taillefer et al., 2017, 2018). In this sense,

understanding the fault–fluid system evolution and the relative timing of hydrothermal fluid migration is of great importance to characterize the potential geothermal resources of this area.

In this contribution, we report the temporal and spatial relationships between deformation and fluid migration in a long-lived Variscan thrust deforming basement rocks in the Pyrenean Axial Zone. For this purpose, we combine structural, petrological, and geochemical analyses of calcite veins precipitated in the Estamariu thrust during two reactivation episodes related to the Alpine compression (Late Cretaceous to Oligocene) and the Neogene extension. Structural and petrological observations allow us to unravel the relative timing of fluid migration and vein formation in relation to the involved tectonic events. The geochemistry of the vein cements and related host rocks provides information on the fluid origin, pathways, and extent of fluid–rock interaction during deformation. Therefore, the main objectives of this paper are the following: (i) to constrain the relative timing of vein formation and fluid migration; (ii) to determine the fluid origin and pathways during successive compressional and extensional deformation phases; (iii) to assess the influence of basement rocks on the chemistry of fluids circulating during deformation; and (iv) to provide insights into the fluid flow at regional scale in the NE part of the Iberian Peninsula, where the presence of hydrothermal fluids has been reported from Neogene times to present.

2 Geological setting

The Pyrenees constitute an asymmetric and doubly verging orogenic belt that resulted from the Alpine (Late Cretaceous to Oligocene) convergence between the Iberian and European plates (Choukroune, 1989; Muñoz, 1992; Roure et al., 1989; Sibuet et al., 2004; Srivastava et al., 1990; Vergés and Fernández, 2012). The Pyrenean structure consists of a central antiformal stack of basement-involved rocks from the Axial Zone, flanked by two oppositely verging fold-and-thrust belts and their associated foreland basins (Muñoz, 1992; Muñoz et al., 1986) (Fig. 1A). The Pyrenean Axial Zone has been deformed by successive Variscan, Alpine, and Neogene phases (Saura and Teixell, 2006). In the eastern Axial Pyrenees, an E–W to ENE–WSW fault system developed during the Neogene extension (Roca, 1996; Roca and Guimerà, 1992; Vergés et al., 2002). The main fault, La Tet fault, has associated a set of E–W extensional basins such as La Cerdanya, Conflent, La Seu d’Urgell, and Cerc (Cabrera et al., 1988; Roca, 1996). The Cerc basin consists of a Stephano-Permian accumulation of volcanic rocks discordantly overlying Cambro-Ordovician materials. This basin is thrust in its eastern limit by the Estamariu thrust, whereas the northern and southern boundaries correspond to two Neogene extensional faults, La Seu d’Urgell fault and the Ortadó fault, respectively (Hartvelt, 1970; Roca, 1996; Saura,

2004) (Fig. 1B, C). In the NW part of the basin, the limit between the Stephano-Permian unit and the upper Ordovician sequence corresponds to a Stephano-Permian extensional fault formed coevally with the deposition of the volcanic sequence (Saura, 2004). This fault was reactivated during the latest stages of the Neogene extension (Saura, 2004) and is referred to here as the Sant Antoni fault (Fig. 1C).

The Estamariu thrust is a basement-involved reverse fault originated during the Variscan orogeny with a minimum displacement of 27 km (Poblet, 1991). However, in its southwestern termination, it juxtaposes the Devonian Rueda Formation against the Stephano-Permian Erill Castell Formation. The Erill Castell Formation developed during the late to post-orogenic collapse of the Variscan belt (Lago et al., 2004; Martí, 1991, 1996; Ziegler, 1988), evidencing the reactivation of the Estamariu thrust during the Alpine orogeny (Poblet, 1991; Saura, 2004). Rocks cropping out around the Estamariu thrust and the Cerc basin range from upper Ordovician to Miocene (Fig. 1C). However, due to the complex structural setting, the stratigraphic record is discontinuous and only upper Ordovician, Devonian, Stephano-Permian, and Neogene rocks are present in the study area. The basement lithologies consist of upper Ordovician and Devonian metasedimentary rocks affected by multiscale folds and related pervasive axial plane regional foliation (Bons, 1988; Casas et al., 1989; Cochelin et al., 2018; Zwart, 1986). This deformation is linked to low-grade metamorphic conditions developed during the Variscan orogeny (Hartevelt, 1970; Poblet, 1991; Saura, 2004). The upper Ordovician succession includes an alternation of shales, sandstones, conglomerates, quartzites, and phyllites, and the Devonian sequence consists of an alternation of limestones and black slates (Rueda Formation) (Mey, 1967). The Stephano-Permian sequence developed during the late to post-orogenic extensional collapse of the Variscan belt and in the study area is represented by a volcanic and volcanoclastic unit (the Erill Castell Formation) (Martí, 1991; Mey et al., 1968) involving tuffs and ignimbrites at the base and andesites in the upper part (Martí, 1996; Saura and Teixell, 2006). Finally, the Neogene sequence is constituted by detrital and poorly lithified sediments, mainly shales, sandstones, and conglomerates deposited during the Neogene extension associated with the opening of the NW Mediterranean Sea (Roca, 1996).

3 Methods

This study integrates a field compilation of structural data as well as petrological and geochemical analyses of calcite cements and related host rocks. The structural data include the orientation of bedding, foliations, and fractures in addition to crosscutting relationships and kinematics. Such data were plotted in equal-area lower-hemisphere projections, and different fracture sets were established according to their type, strike, mineral infillings, and relative age deduced from

crosscutting relationships. All these data were integrated in a schematic map and a cross section of the Estamariu thrust and the Cerc basin (Figs. 2a, b and 3). Samples considered representative of the involved host rocks and all calcite vein generations observed in the different fracture sets and fault-related structures were selected for petrological and geochemical analyses. Thin sections of these samples were prepared and studied under a Zeiss Axiophot optical microscope and a cold cathodoluminescence (CL) microscope model 8200 Mk5-1 operating between 16–19 kV and 350 μ A gun current.

The geochemical analyses have been performed in calcite cements and related host rocks in order to determine the origin, composition, and temperature of the vein-forming fluids in addition to the extent of fluid–rock interaction. These analyses include (i) stable isotope analyses in 37 calcite cements and the carbonate portion of the Devonian rocks, (ii) the elemental composition of 12 samples analyzed using high-resolution inductively coupled plasma mass spectrometry (HR-ICP-MS), (iii) the $^{87}\text{Sr}/^{86}\text{Sr}$ and $^{143}\text{Nd}/^{144}\text{Nd}$ ratios of eight representative samples, and (iv) clumped isotope thermometry of calcite cements (three samples), the results of which were converted to temperatures by applying the calibration method of Kluge et al. (2015). Calculated $\delta^{18}\text{O}_{\text{fluid}}$ values are expressed in per mill (‰) with respect to the Vienna Standard Mean Ocean Water (VSMOW). Details on methods and procedures can be found in the Supplement.

4 Results

4.1 Structure and associated calcite cements

The Estamariu thrust strikes N–S to NW–SE and dips between 40 and 70° towards the NE. It has a displacement of a few hundred meters and juxtaposes a Devonian alternation of limestones and shales in the hanging wall against Stephano-Permian andesites in the footwall (Poblet, 1991) (Figs. 2–4). The main slip plane is undulose and generates a 2–3 m thick thrust zone affecting both the hanging wall and footwall, but it is thicker in the hanging wall, up to 2.5 m thick. In the footwall the thrust zone is less than 1 m thick and has associated minor restricted thrust zones developed as subsidiary accommodation structures related to the main thrust fault (Fig. 2a, b). All kinematic indicators, including S–C structures and slickenlines, indicate reverse displacement towards the west.

The mesostructures and microstructures observed in the study area are described below according to their structural position in relation to the Estamariu thrust, that is, hanging wall, thrust zone, and footwall (Figs. 3, 4). The relative timing of the different mesostructures and microstructures has been determined by means of crosscutting relationships and microstructural analysis.

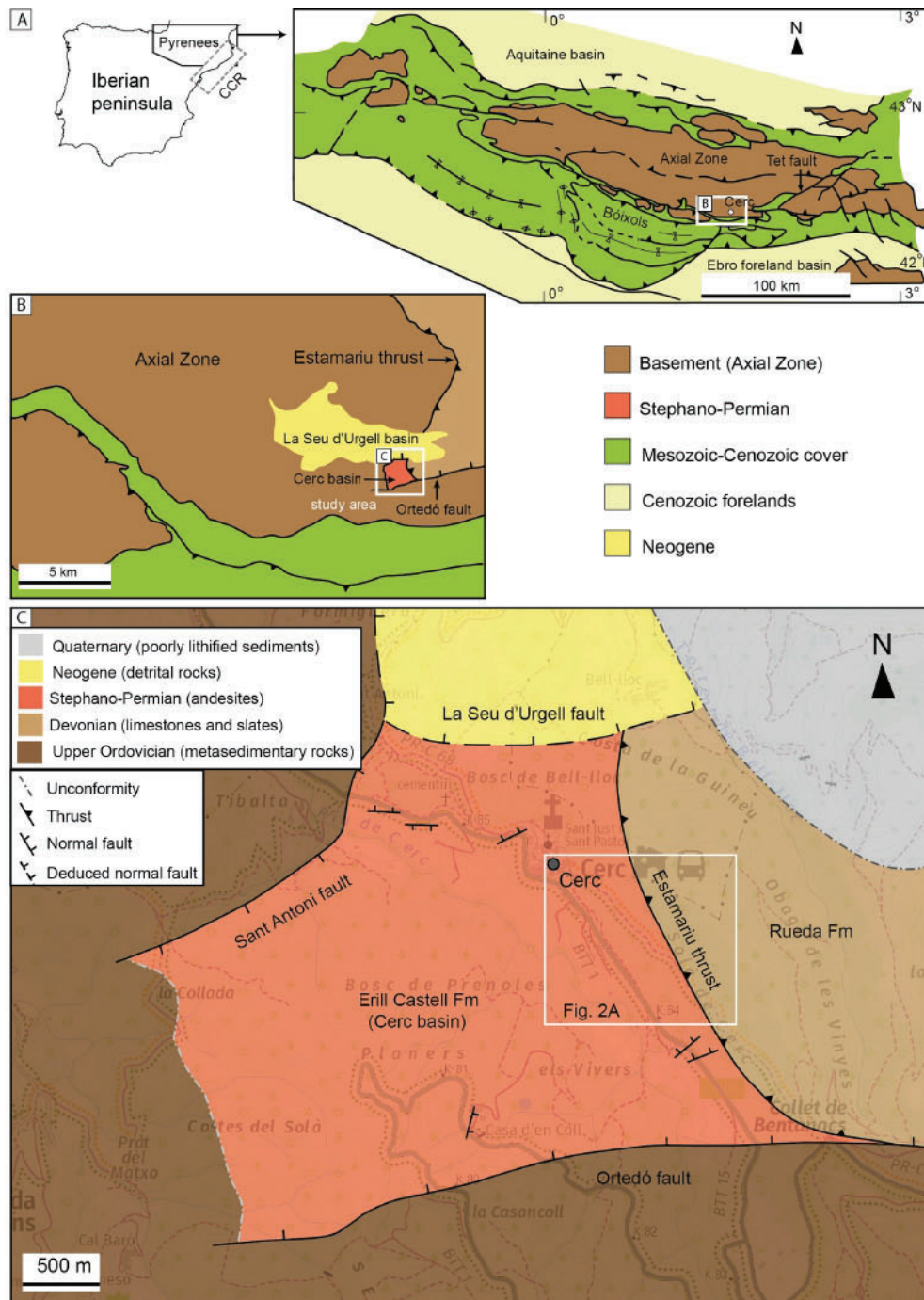


Figure 1. (A) Simplified geological map of the Pyrenees modified from Muñoz (2017) and its location in the Iberian Peninsula (location of the Catalan Coastal Range, CCR, is also shown). (B) Detail of the study area located within the Pyrenean Axial Zone. (C) Geological map of the Cerc basin (using data from Saura, 2004, and our own data) with the Estamariu thrust located in its eastern termination and the Neogene extensional faults in the northern and southern limits. The white square indicates the location of the main outcrop (Fig. 2a).

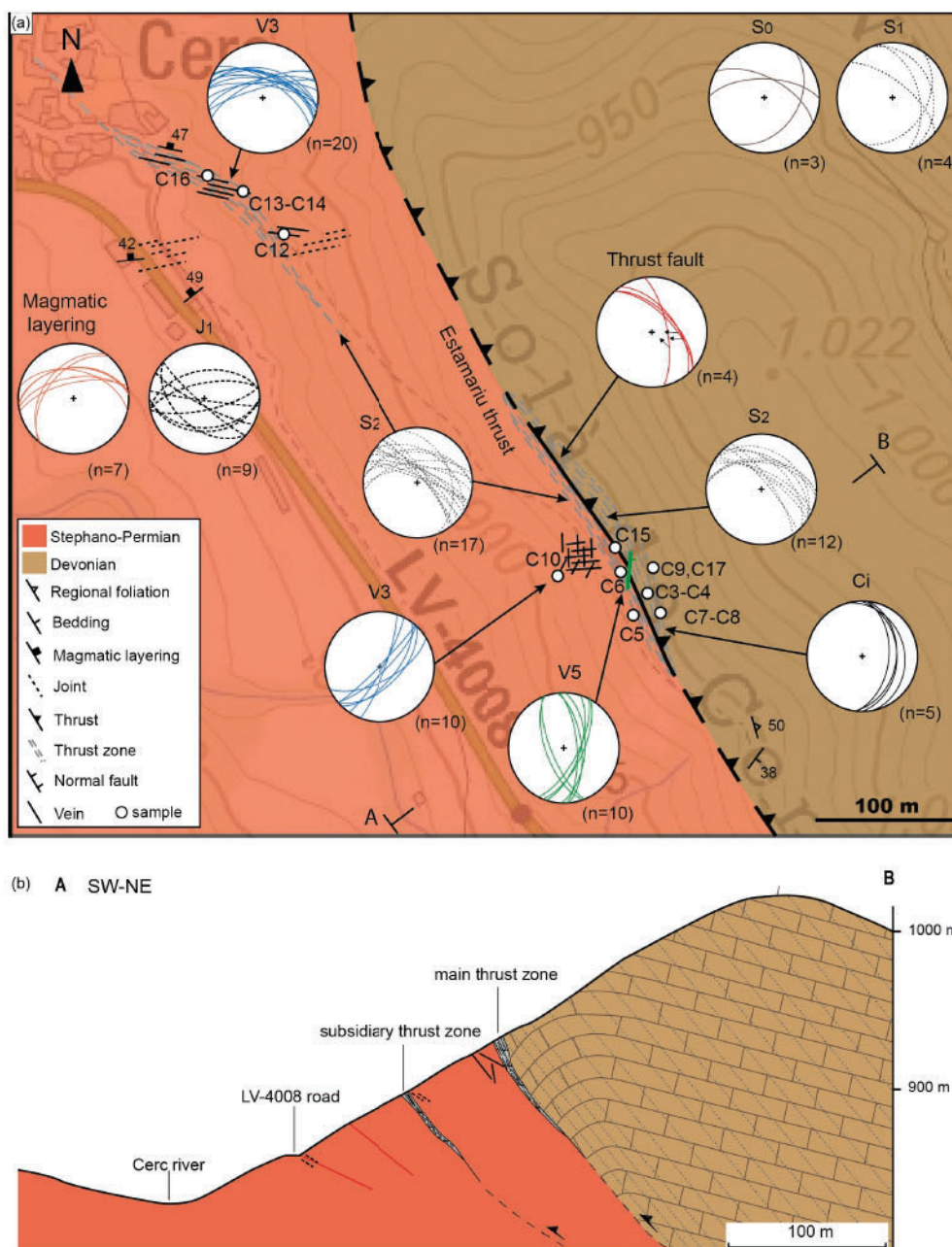


Figure 2. (a) Geological map and (b) cross section of the Estamariu thrust, which juxtaposes a Devonian unit against a Stephano-Permian sequence ($H = V$, no vertical exaggeration). Lower-hemisphere equal-area stereoplots of the Devonian bedding (S_0), regional foliation (S_1), and thrust zone foliation affecting the hanging wall and footwall (S_2); magmatic layering and the different faults and veins observed in the study area are also included. Location in Fig. 1B.

4.1.1 Hanging wall

In the studied outcrops, the Devonian Rueda Formation is characterized by a well-bedded alternation of dark to light grey limestones with subordinate dark grey shales (S_0) (Fig. 5a). Limestones are made up of encrinites, which consist of a bioclastic packstone formed essentially of crinoid stems (Fig. 5b). Under cathodoluminescence, en-

crinites show dark to bright orange colors (Fig. 5c). Devonian rocks form a decametric anticline oriented NW–SE with a well-developed axial plane foliation (S_1) concentrated in the pelitic intervals. S_1 , which is oriented NNW–SSE, is a pervasive regional foliation dipping 30 to 55° towards the E and NE and is generally between 2 and 5 cm spaced. In the hinge of the anticline, bedding (S_0) dips towards the SE and forms a high angle with S_1 (Figs. 2b and 5a), whereas in its eastern

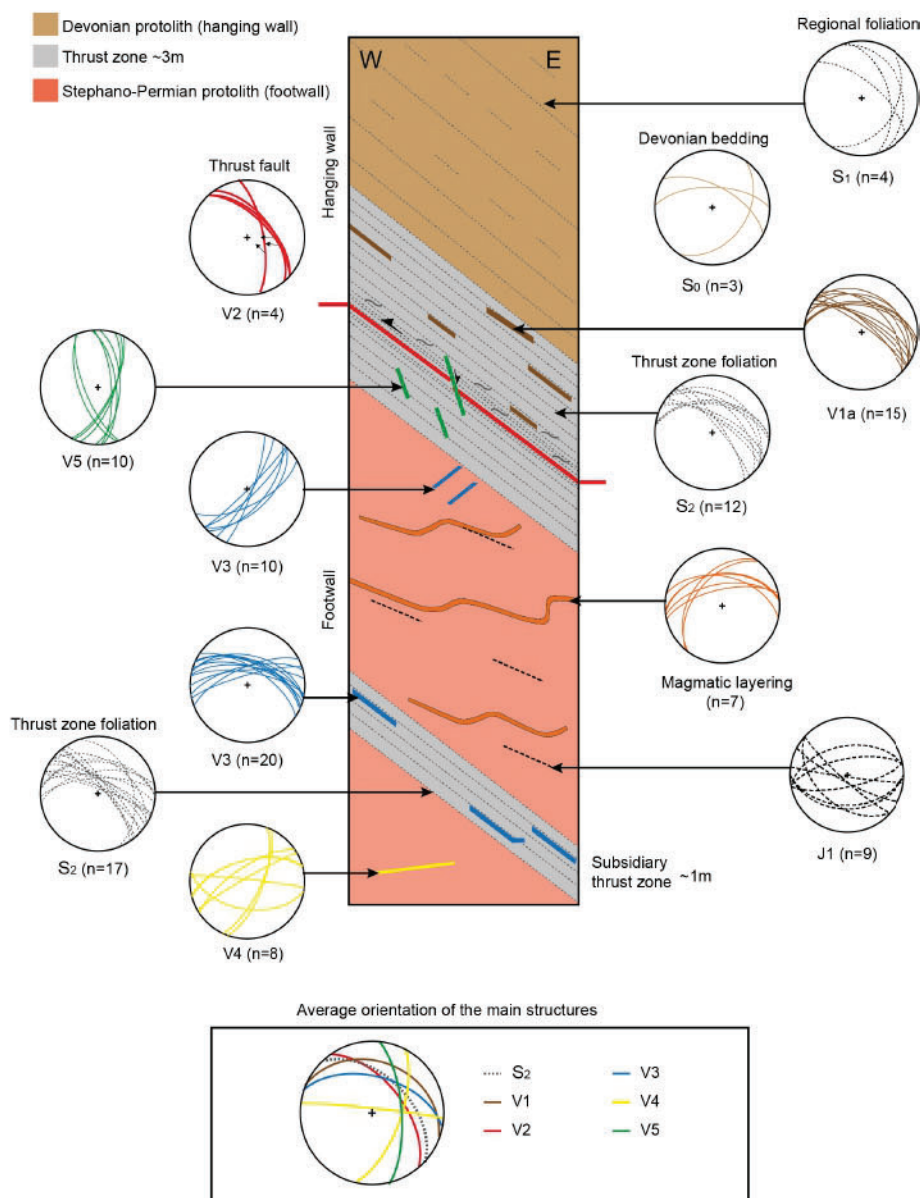


Figure 3. Sketch showing the spatial distribution of mesoscale structures within the main outcrop and lower-hemisphere equal-area stereoplots of the different mesostructures. The average orientation of the main structures is also provided.

limb, the regional foliation (S_1) dips steeper than S_0 . These geometric relationships between bedding and foliation have been used to determine the fold type at large scale (i.e., as shown in Fig. 2b).

4.1.2 Thrust zone

The thrust zone consists of a deformation zone affecting both the hanging wall and the footwall. Within the hanging wall, the Devonian host rocks are still recognizable, but the intensity of deformation progressively increases towards the main thrust plane. This deformation consists of a penetrative thrust zone foliation (S_2), two generations of stylolites (e_1 , e_2),

and three generations of calcite veins (V_0 , V_{1a} , and V_{1b}) (Figs. 3, 6). These structures are described below in chronological order.

The foliation within the thrust zone affecting the Devonian hanging wall (S_2) strikes NW–SE and dips 40 – 50° NE, similar to the regional foliation (S_1), but it is more closely spaced, generally between 0.2 and 1 cm (Fig. 6a, b). This observation points to a progressive transposition of the regional foliation within the thrust zone during thrusting. At mesoscale, S_2 has related shear surfaces (C_i) defining centimetric S–C-type structures, again indicating reverse kinematics (Fig. 6a).

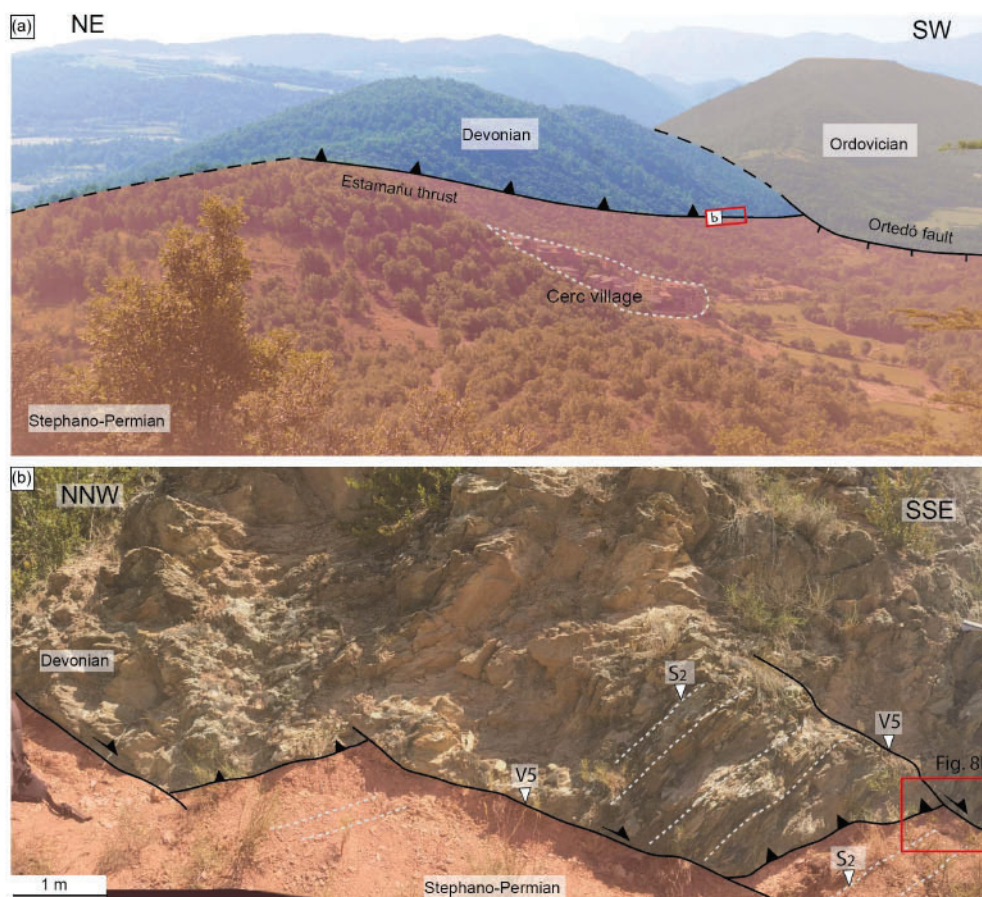


Figure 4. Main outcrop of the Estamariu thrust. (a) Panoramic view from the Sant Antoni hill showing the extensional Ortedó fault postdating the Estamariu thrust. (b) Main outcrop showing the Estamariu thrust and the related thrust zone foliation developed in the Devonian hanging wall and in the Stephano-Permian footwall (S_2). The thrust is displaced by later shear fractures locally mineralized with calcite (V5).

Stylolites e1 have a wave-like shape and trend subparallel to the thrust zone foliation (S_2) (Fig. 6b, c). When present, these stylolites are very systematic, exhibiting a spacing of 1–2 mm (Fig. 6c).

The first calcite vein generation (V0), only observed at microscopic scale (Fig. 6b, c), corresponds to up to 1 cm long and less than 1 mm thick veins cemented by blocky to elongated blocky calcite crystals featuring a dark brown luminescence (cement Cc0). Veins V0 and stylolites e1 are perpendicular between them and show ambiguous crosscutting relationships. These microstructures are concentrated into discontinuous fragments of the Devonian host rocks within the thrust zone. Calcite veins V1a crosscut the previous vein generation (V0) as well as the stylolites e1 and are developed within S_2 surfaces (Figs. 3, 6d). These veins are the most abundant, exhibit a white to brownish color in hand samples, and are up to 10 cm long and 1 cm thick. The vein cement (Cc1a) is formed of anhedral crystals up to 3–4 mm in size displaying a blocky texture and a dark brown luminescence (Fig. 6e).

Stylolites e2, more abundant than stylolites e1, are up to 10 cm long and show spacing between 0.5 and 2 cm (Fig. 6d, f). These stylolites mainly correspond to sutured areas developed between the host rock and the calcite veins V1a and between foliation surfaces S_2 .

Calcite veins V1b, up to 1 cm long and less than 1 mm thick, were also identified at microscopic scale (Fig. 6d, f). The vein cement (Cc1b) consists of up to 0.1 mm calcite crystals with a blocky texture and a bright yellow luminescence. These veins postdate the previous V0 and V1a generations and trend perpendicular to stylolites e2.

Towards the fault plane, the thrust zone foliation S_2 is progressively more closely spaced, and stylolites e2 become more abundant (showing millimeter spacing) and exhibit ambiguous crosscutting relationships with veins V1b (Fig. 6f). The main slip surface corresponds to a discrete plane that contains calcite slickensides (veins V2). The vein cement (Cc2) is milky white in hand samples and consists of up to 3 mm blocky to elongated blocky crystals (Fig. 6g) with a dull to bright orange luminescence (Fig. 6h).

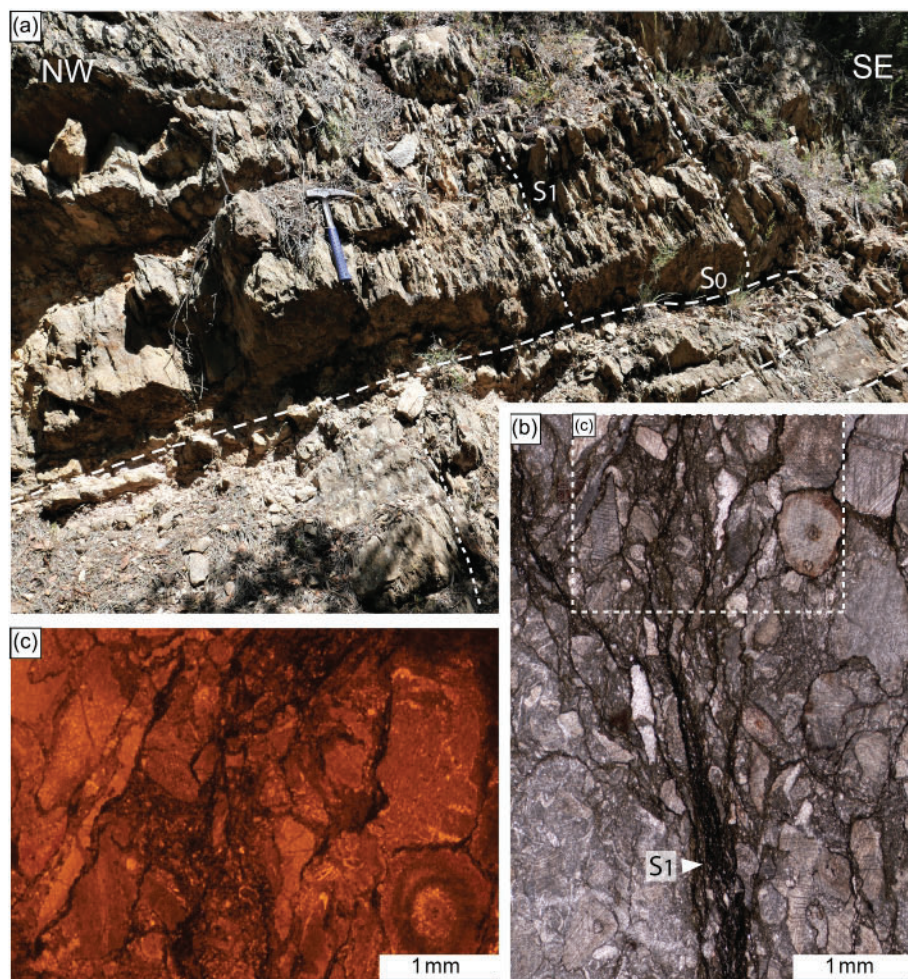


Figure 5. Devonian protolith. (a) Field image showing the relationship between bedding (S_0) and regional foliation (S_1). (b) Plane-polarized light and (c) cathodoluminescence microphotographs of the encrinites alternating with pelitic-rich bands, where the S_1 is concentrated.

Deformation in the footwall is concentrated within the main thrust zone and subsidiary thrust zones and corresponds to the thrust zone foliation (S_2) and calcite veins V3 (Fig. 3). This foliation (S_2) strikes NW–SE, dips towards the NE, and is millimeter to centimeter spaced (Fig. 7a). Calcite veins V3 are generally 1–2 cm thick and strike NW–SE. They are parallel or locally branch off, cutting the S_2 planes in the subsidiary thrust zone (Fig. 7a, b). Outside the thrust zone, veins V3 are locally present but have a NE–SW strike. These veins are mostly less than 1 m long and are spaced between a few centimeters and 50 cm. The vein cement (Cc3) is made up of a milky white calcite characterized by up to 3 mm long fibrous crystals oriented perpendicular to the vein walls (Fig. 7c). Locally, anhedral blocky crystals ranging in size from 0.1 to 1 mm are also present. This cement displays a bright yellow to bright orange luminescence (Fig. 7d).

4.1.3 Footwall

In the footwall, the Stephano-Permian Erill Castell Formation comprises massive, dark greenish andesitic levels showing a rhythmic magmatic layering (Fig. 7e), which corresponds to a fluidal structure of the host rock. The local presence of pyroclastic and brecciated volcanoclastic levels is also ubiquitous, mainly in the lower part of this sequence. Andesites are characterized by a porphyritic texture defined by a dark fine-grained spherulitic matrix partially devitrified, large zoned crystals of plagioclase (Fig. 7f) up to 2–3 cm long, and less abundant biotite and hornblende. These mafic phenocrysts are systematically pseudomorphosed by clay minerals and frequently show evidence of oxidation and chloritization. Andesites are affected by E–W-striking open joints (J1) dipping indistinctively towards the north and south (Fig. 7e). These joints locally trend parallel to the magmatic layering (Fig. 3).

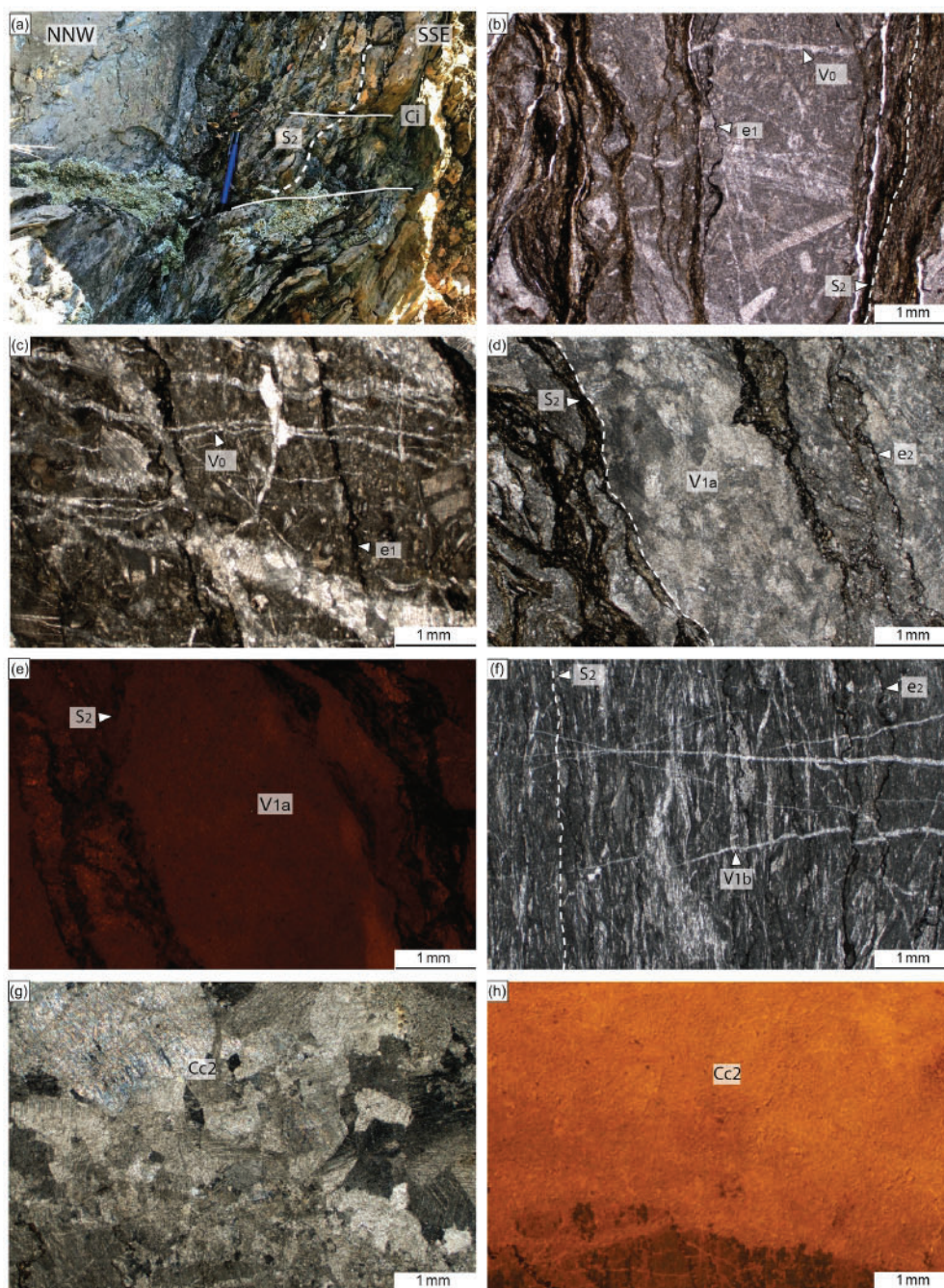


Figure 6. Mesostructures and microstructures found within the thrust zone affecting the hanging wall. (a) Outcrop image of the thrust zone foliation (S_2) and related C planes indicating reverse kinematics (C_1). Microphotographs of (b) thrust zone foliation (S_2), (c) stylolites e_1 and veins V_0 affecting the Devonian encrinites, and (d) cross-polarized light and (e) cathodoluminescence microphotographs of veins V_1a concentrated between foliation surfaces. (f) Thrust zone foliation (S_2) near the fault plane and ambiguous and perpendicular relationships between V_1b and e_2 . (g) Cross-polarized light and (h) cathodoluminescence microphotographs of calcite cement Cc_2 located on the main thrust plane (V_2).

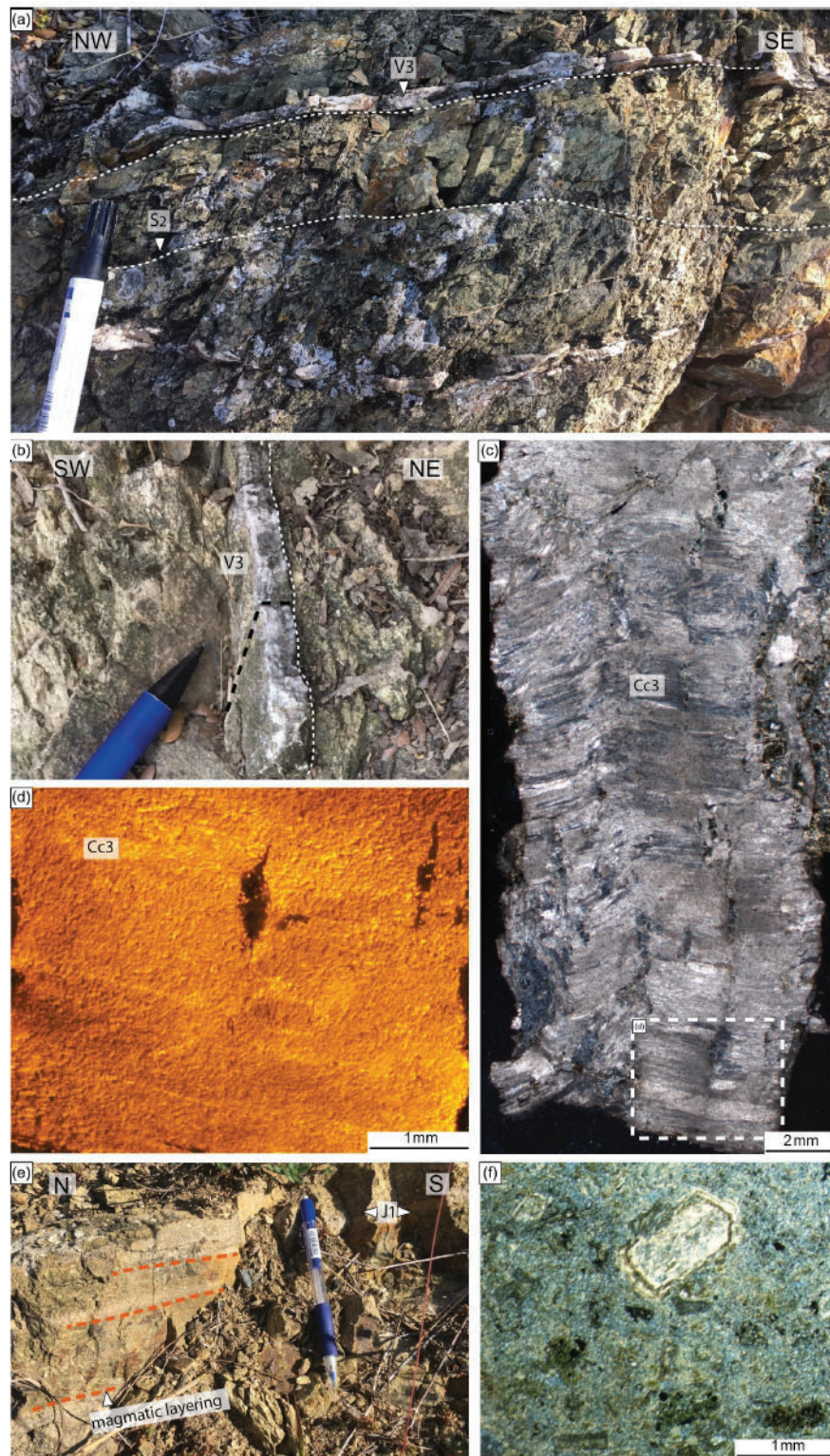


Figure 7. Mesoscale and microscale structures present in the Stephano-Permian volcanic footwall. (a) Field image of the subsidiary thrust zone in the footwall showing the thrust zone foliation (S_2) and the veins V3. (b) Detail of veins V3, also in the subsidiary thrust zone. The black dashed line indicates the original position of the thin section observed in panel (c). (c) Cross-polarized light and (d) cathodoluminescence microphotographs of veins V3, characterized by calcite fibers growing perpendicular to the vein walls (Cc3). (e) Field image of the footwall andesites showing the magmatic layering and joints J1. (f) Plane-polarized light microphotograph of the volcanic andesites exhibiting a porphyritic texture with a large plagioclase crystal.

Finally, as described above, the northern and southern limits of both the Cerc basin and the Estamariu thrust correspond to two Neogene extensional faults, La Seu d'Urgell and the Ortedó fault systems (Fig. 1C). These faults are subvertical or steeply dip towards the north. In the northern part, the slip plane of the La Seu d'Urgell fault has not been observed, and the limit between the Stephano-Permian rocks and the Neogene deposits is not well-constrained due to the poor quality of the Neogene outcrops and the presence of Quaternary deposits. In the southern part, the Ortedó fault generates a dark greyish to brown fault zone that is several meters thick and characterized by the presence of clay-rich incohesive fault rocks developed at the contact between Stephano-Permian and upper Ordovician rocks. Related to these main fault systems, mesoscale normal faults commonly affect the andesites within the Cerc basin. These faults are mainly E–W and locally NE–SW, are subvertical, and dip indistinctly towards the N and S. Fault planes are locally mineralized with calcite cement (veins V4) and exhibit two striae set generations indicating dip-slip and strike-slip movements (Fig. 8a). The calcite cement (Cc4) consists of up to 2 mm blocky to elongated blocky crystals (Fig. 8b) with a homogeneous dark orange luminescence (Fig. 8c). On the other hand, the main Estamariu thrust zone is locally displaced by shear fractures (Fig. 8d) and a later set of shear bands (Cn) (Fig. 8e), both having an overall NNW–SSE to NNE–SSW strike (Fig. 3) that indicates a minor normal displacement. Shear fractures are locally mineralized with calcite (veins V5). The vein cement consists of a greyish microsparite calcite cement (Cc5) (Fig. 8f, g).

4.2 Geochemistry of calcite cements and host rocks

The geochemistry ($\delta^{18}\text{O}$, $\delta^{13}\text{C}$, $\delta^{18}\text{O}_{\text{fluid}}$, $^{87}\text{Sr}/^{86}\text{Sr}$, $^{143}\text{Nd}/^{144}\text{Nd}$, and elemental composition) and the calculated temperature of precipitation of the different calcite cements Cc1a to Cc5 are described below. Veins V0 and V1b were only observed at microscopic scale and their calcite cement Cc0 and Cc1b could not be sampled to perform these geochemical analyses.

The $\delta^{18}\text{O}$ and $\delta^{13}\text{C}$ isotopic composition of the carbonate fraction of the Devonian hanging wall and the different calcite cements (Cc1a to Cc5) are summarized in Table 1 and represented in Fig. 9. The micritic matrix of the Devonian packstone ranges in $\delta^{18}\text{O}$ values between -10.5‰ VPDB and -8.4‰ VPDB and in $\delta^{13}\text{C}$ values between $+1.5\text{‰}$ VPDB and $+2.8\text{‰}$ VPDB, whereas the calcite cements have a broader range of values depending on the cement generation (Fig. 9).

Calcite cement Cc1a has $\delta^{18}\text{O}$ values between -11.3‰ VPDB and -10.3‰ VPDB and $\delta^{13}\text{C}$ values between $+0.8\text{‰}$ VPDB and $+2.1\text{‰}$ VPDB. Cc2 is characterized by $\delta^{18}\text{O}$ values between -14.9‰ VPDB and -12.9‰ VPDB and $\delta^{13}\text{C}$ values between -1.2‰ VPDB and $+1.5\text{‰}$ VPDB. Cc3 has $\delta^{18}\text{O}$ values between

-14.3‰ VPDB and -13.4‰ VPDB and $\delta^{13}\text{C}$ values between -9.3‰ VPDB and -6.9‰ VPDB. Cc4 exhibits $\delta^{18}\text{O}$ values between -13.8‰ VPDB and -13.4‰ VPDB and $\delta^{13}\text{C}$ values between -7.4‰ VPDB and -7.2‰ VPDB. Cc5 ranges in $\delta^{18}\text{O}$ between -8.1‰ VPDB and -5.7‰ VPDB and in $\delta^{13}\text{C}$ between -8.2‰ VPDB and -3.8‰ VPDB. The calcite cement Cc1a, precipitated in the fault zone affecting the Devonian hanging wall, has enriched $\delta^{13}\text{C}$ values, whilst the calcite cement within the fault plane (Cc2) exhibits either negative or positive $\delta^{13}\text{C}$ values, and the calcite cements hosted in the Stephano-Permian andesites (Cc3 to Cc5) have more depleted $\delta^{13}\text{C}$ values (Fig. 9). In addition, calcite cements show a progressive depletion in $\delta^{18}\text{O}$ from Cc1a to Cc4, whereas Cc5 displays more enriched $\delta^{18}\text{O}$ values.

The obtained Δ_{47} values from clumped isotope thermometry were converted into temperatures and $\delta^{18}\text{O}_{\text{fluid}}$ (Table 1 and Fig. 10) using the equations of Kluge et al. (2015) and Friedman and O'Neil (1977), respectively. The calculated T and $\delta^{18}\text{O}_{\text{fluid}}$ for calcite cement Cc2 range between 50 and 100 °C and between -6.4‰ VSMOW and -0.3‰ VSMOW, respectively. Cement Cc3 shows T and $\delta^{18}\text{O}_{\text{fluid}}$ in the range of 130 to 210 °C and $+4.3\text{‰}$ VSMOW to $+12.1\text{‰}$ VSMOW, respectively. Cc4 exhibits T and $\delta^{18}\text{O}_{\text{fluid}}$ in the range of 100 to 170 °C and $+0.9\text{‰}$ VSMOW to $+8.1\text{‰}$ VSMOW, respectively.

The $^{87}\text{Sr}/^{86}\text{Sr}$ ratios of calcite cements Cc1a to Cc5 and host rocks are reported in Table 1 and Fig. 11. Devonian limestones from the hanging wall have a $^{87}\text{Sr}/^{86}\text{Sr}$ ratio of 0.710663, whilst the Stephano-Permian andesites in the footwall exhibit a more radiogenic $^{87}\text{Sr}/^{86}\text{Sr}$ ratio of 0.743983. The calcite cements have more radiogenic $^{87}\text{Sr}/^{86}\text{Sr}$ ratios than the Devonian limestones but lower radiogenic values than the Stephano-Permian andesites. This ratio is 0.713018 to 0.714092 in Cc1a, 0.718294 for Cc2, 0.714619 for Cc3, 0.717706 for Cc4, and 0.716923 for Cc5. These results are compared with already published data from synkinematic veins and deformed rocks in other Pyrenean structures developed in the basement and in the sedimentary cover during the Pyrenean compression (Fig. 11). This comparison shows that values obtained in this study are (1) significantly more radiogenic than the values of marine carbonates and synkinematic veins precipitated in the sedimentary cover (i.e., in the south Pyrenean fault and thrust belt) and (2) within the same range of values of synkinematic veins and deformed rocks in the Pyrenean basement (Axial Zone).

The analyzed samples for $^{143}\text{Nd}/^{144}\text{Nd}$ ratios in calcite cements and host rocks are reported in Table 1. However, due to the general low Nd concentrations in most of the analyzed calcite cements and the limited number of powdered samples that were available, only calcite cement Cc5 and the andesite host rock (footwall) could be measured. Cc5 has a $^{143}\text{Nd}/^{144}\text{Nd}$ ratio of 0.512178, which is similar that of its footwall host rocks: 0.512196.

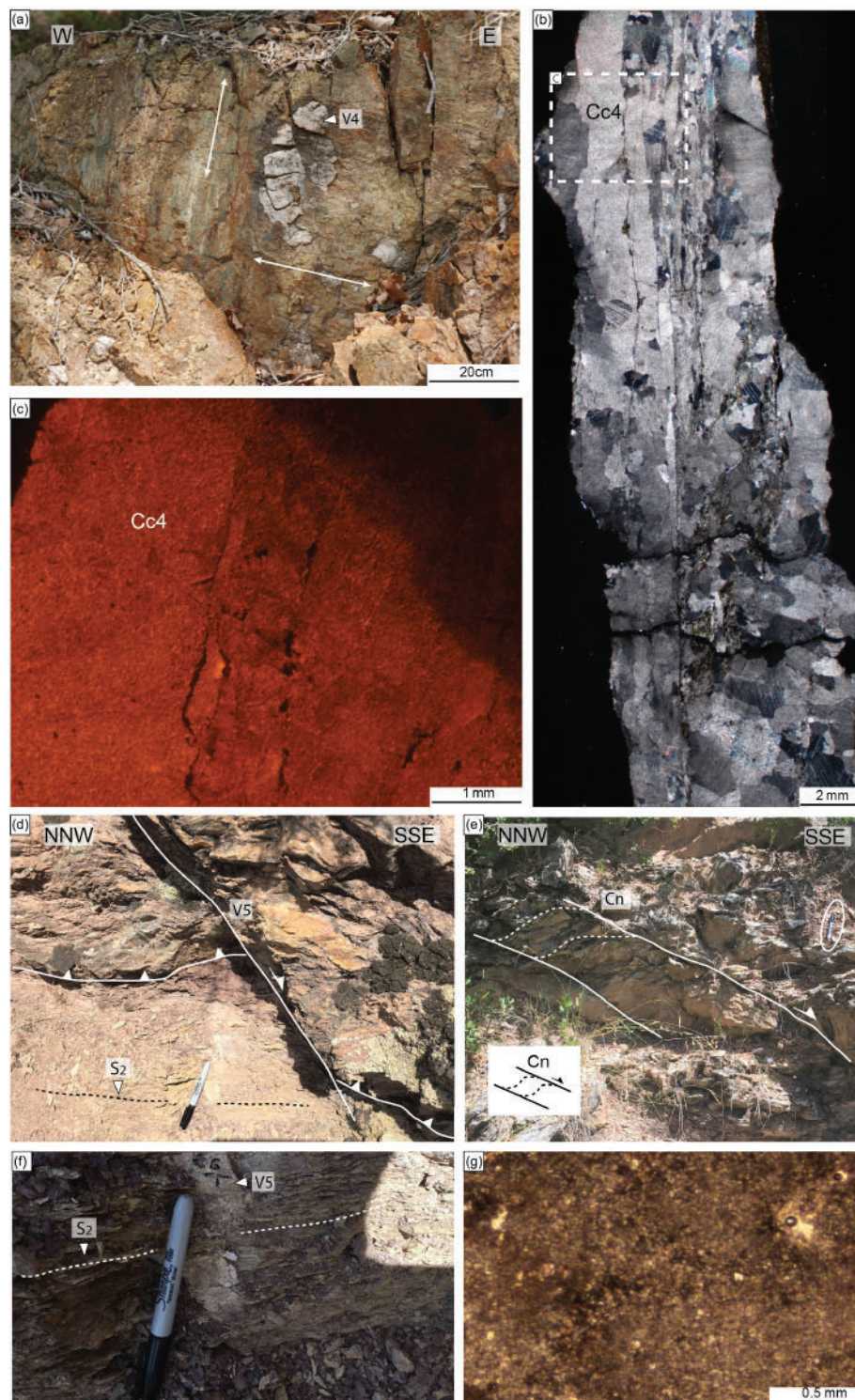


Figure 8. (a) Field image of a subvertical and E–W fault plane mineralized with calcite (veins V4) and showing two striae set generations (white arrows) indicating dip-slip and strike-slip kinematics. (b) Cross-polarized light and (c) cathodoluminescence microphotographs of the vein-related calcite cement (Cc4). (d) Shear fracture postdating the thrust zone foliation, locally mineralized with calcite veins V5. (e) Shear bands (Cn) with normal kinematics located in the main thrust zone, indicating a later reactivation of the Estamariu thrust. (f) Field image of a calcite vein V5 and (g) plane-polarized light of the vein-related cement (Cc5).

Table 1. $\delta^{18}\text{O}$, $\delta^{13}\text{C}$, $^{87}\text{Sr}/^{86}\text{Sr}$, and $^{143}\text{Nd}/^{144}\text{Nd}$ ratios of the calcite cements and related host rocks. The calculated precipitation temperature and the $\delta^{18}\text{O}_{\text{fluid}}$ of the parent fluids are also indicated. NR indicates analyzed samples for which no result was obtained.

Sample	Vein	Cement	$\delta^{18}\text{O}$ ‰ VPDB	$\delta^{13}\text{C}$ ‰ VPDB	$^{87}\text{Sr}/^{86}\text{Sr}$	$^{143}\text{Nd}/^{144}\text{Nd}$	Δ_{47}	T °C	$\delta^{18}\text{O}_{\text{fluid}}$ ‰ SMOW
C9	V1a	Cc1a	-11.2	+0.91					
C8B	V1a	Cc1a	-10.7	+2					
C8A.I	V1a	Cc1a	-10.4	+2					
C8A.II	V1a	Cc1a	-10.96	+1.3	0.713018	NR			
C8A.III	V1a	Cc1a	-10.9	+1.2					
C7.I	V1a	Cc1a	-10.9	+2.1					
C7.II	V1a	Cc1a	-10.8	+0.8					
C7.III	V1a	Cc1a	-10.4	+1.96					
C4B	V1a	Cc1a	-10.3	+1.9	0.714092	NR			
C3A.I	V1a	Cc1a	-11.2	+1.9					
C3A.II	V1a	Cc1a	-11.3	+1.7					
C3A.III	V1a	Cc1a	-10.5	+1.98					
C15.I	V2	Cc2	-14.9	-1.2	0.718294	NR	0.567	50 to 100	-0.3 to -6.4
C15.II	V2	Cc2	-13.3	+0.5					
C15.III	V2	Cc2	-12.91	+1.54					
C13	V3	Cc3	-13.8	-7.1	0.714619	NR	0.445	130 to 210	+4.3 to +12.1
C12.II	V3	Cc3	-14.3	-7.3					
C10	V3	Cc3	-14.2	-9.3					
C11A	V3	Cc3	-14.2	-8.7					
C13.II	V3	Cc3	-13.6	-7.2					
C14.I	V3	Cc3	-13.4	-6.9					
C14.II	V3	Cc3	-13.7	-7.4					
C16A	V3	Cc3	-13.8	-7.2					
C16B	V3	Cc3	-14	-7					
C16C	V3	Cc3	-14.1	-6.9					
C18.I	V4	Cc4	-13.4	-7.2	0.717706	NR	0.48	100 to 170	+0.9 to +8.1
C18.II	V4	Cc4	-13.8	-7.4					
C12.I	V5	Cc5	-8.1	-7.8	0.716923	0.512178			
C6.I	V5	Cc5	-6.7	-8.2					
C6.II	V5	Cc5	-7.4	-7.4					
C11B	V5	Cc5	-5.7	-3.8					
C3A.HR	Devonian		-9.5	+2.4	0.710663	NR			
C17.HR	carbonates		-10.5	+1.5					
C4.HR			-8.4	+2.7					
C11.HR	Andesites			-	-	0.743983	0.512196		

The obtained elemental composition broadly varies among the different calcite cements and related host rocks (Table 2 and Fig. 12). In the thrust zone affecting the hanging wall, calcite cement Cc1a shows a similar trend to that of the Devonian limestones, both having high Sr, intermediate to high Mg and Fe, and low Mn contents (Fig. 12). In the main thrust plane, calcite cement Cc2 has low Mg and Fe and intermediate Mn and Sr contents with respect to the other cements. In the footwall, Cc3 and Cc4 have similar elemental composition, characterized by high Mn, intermediate to high Sr, intermediate to low Fe, and low Mg contents. Finally, calcite cement Cc5 follows a similar trend to that of the Stephano-

Permian andesites, both having the highest Fe and Mg and the lowest Sr and Mn contents with respect to the other cements and host rocks.

5 Discussion

5.1 Chronology of the observed structures

The Estamariu thrust, affecting basement rocks in the Axial Pyrenees, resulted from a long-lived tectonic history that

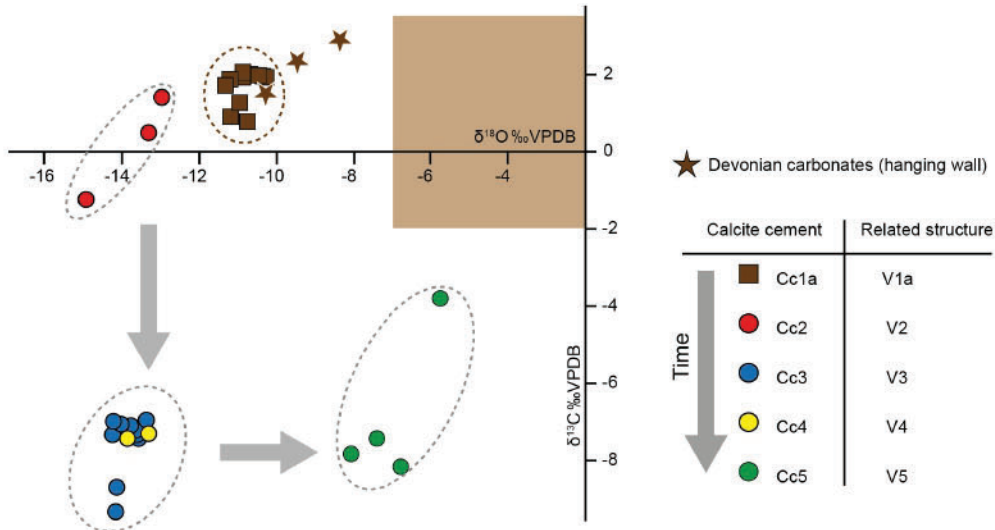


Figure 9. $\delta^{18}\text{O}$ and $\delta^{13}\text{C}$ values of calcite cements Cc1a to Cc5 and the Devonian carbonates from the hanging wall. Arrows indicate evolution over time according to the inferred relative timing of cements. The brown box refers to typical values of Devonian marine carbonates (Veizer et al., 1999).

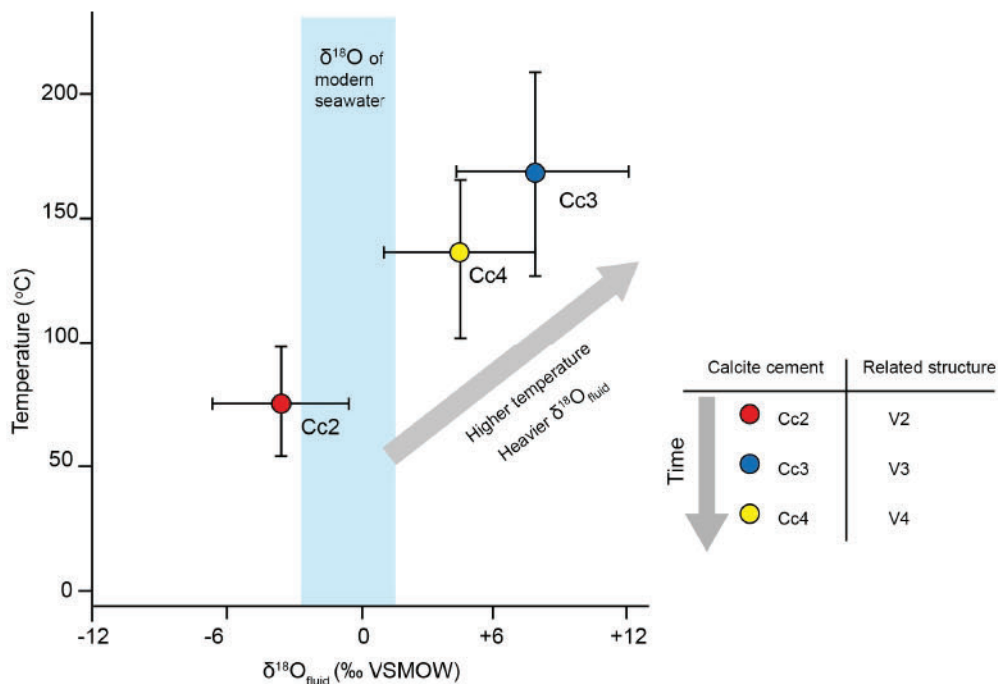


Figure 10. Temperatures ($^{\circ}\text{C}$) vs. $\delta^{18}\text{O}_{\text{fluid}}$ calculated for cements Cc2 to Cc4. The typical $\delta^{18}\text{O}$ values for modern seawater (blue band) are from Veizer et al. (1999).

lasted from late Paleozoic (Variscan orogeny) to Neogene times.

The Paleozoic metasedimentary rocks from the Pyrenean basement are broadly affected by multiscale folds and axial plane regional foliation developed during the main Variscan deformation phase (Bons, 1988; Cochelin et al., 2018; Zwart, 1986). Similar structures, a decametric-scale anticline, and

pervasive axial plane foliation (S_1) are found in the Devonian sequence located in the thrust hanging wall (Fig. 2b). We therefore consider them to have developed during the Variscan compression, contemporaneous with the main activity of the Estamariu thrust. Veins V0 are perpendicular to stylolites e1 and show ambiguous crosscutting relationships between them. Thus, they are interpreted as originat-

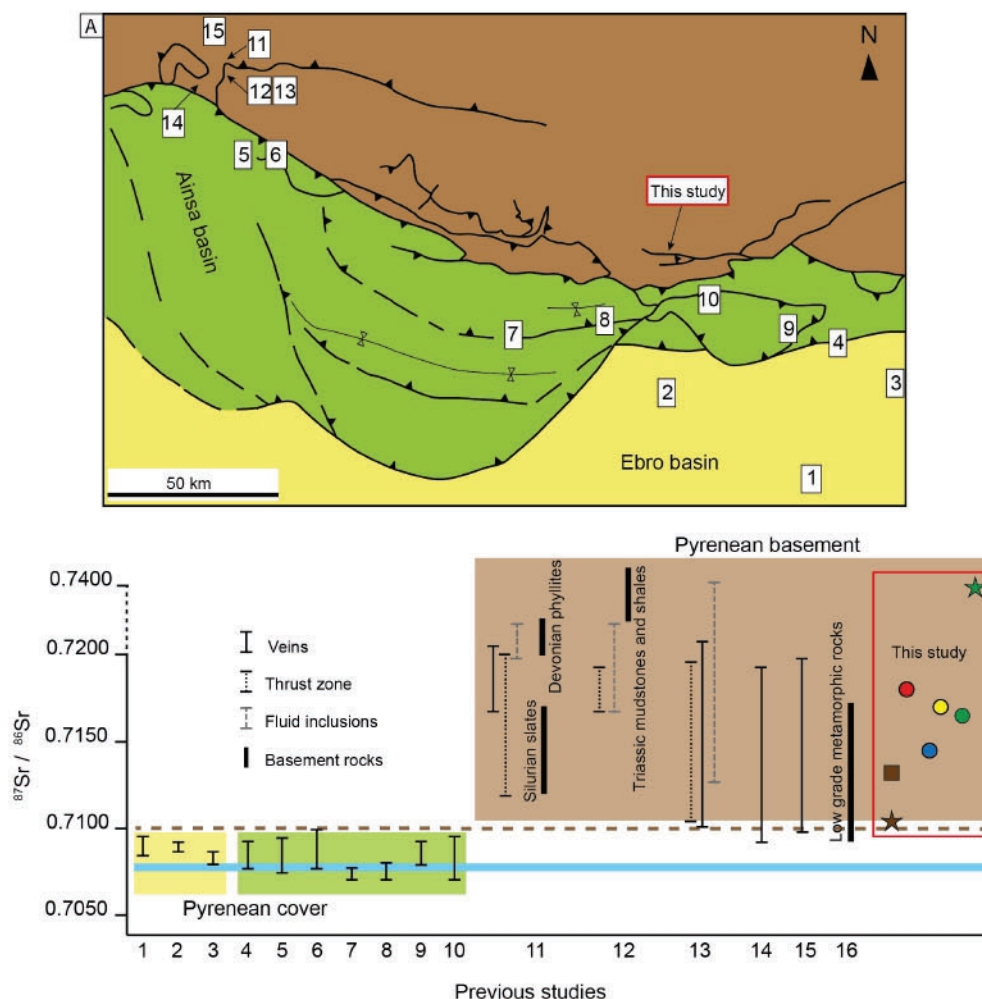


Figure 11. Simplified geological map of the south-central Pyrenees showing the location of structures where $^{87}\text{Sr}/^{86}\text{Sr}$ analyses have been carried out. Below are $^{87}\text{Sr}/^{86}\text{Sr}$ ratios from this study compared to results from other structures involving either cover units (1–10) or basement rocks (11–16). The thick blue line refers to the $^{87}\text{Sr}/^{86}\text{Sr}$ range of Phanerozoic seawater, and the dashed brown line represents the $^{87}\text{Sr}/^{86}\text{Sr}$ limit value between basement and cover structures. (1) El Guix anticline (Travé et al., 2000), (2) Puig Reig anticline (Cruset et al., 2016), (3) L’Escala thrust (Cruset et al., 2018), (4) Vallfogona thrust (Cruset et al., 2018), (5) Ainsa basin (Travé et al., 1997), (6) Ainsa–Bielsa area (McCaig et al., 1995), (7) Minor Bóixols thrust (Muñoz-López et al., 2020), (8) Bóixols anticline (Nardini et al., 2019), (9) lower Pedraforca thrust (Cruset et al., 2020a), (10) upper Pedraforca thrust (Cruset, 2019), (11) Gavarnie thrust (McCaig et al., 1995), (12) Pic de Port Vieux thrust (Banks et al., 1991), (13) Pic de Port Vieux thrust (McCaig et al., 2000b), (14) Plan de Larri thrust (McCaig et al., 1995), (15) La Glere shear zone (Wayne and McCaig, 1998), (16) Trois Seigneurs Massif (not on the map) (Bickle et al., 1988).

ing coevally. Both microstructures are concentrated into discontinuous fragments of the Devonian host rocks and are therefore considered inherited microstructures likely developed in Variscan times. However, as pointed out above, in the study area the Estamariu thrust affects late to post-Variscan Stephano-Permian andesites, thus confirming its reactivation during the Alpine orogeny. Accordingly, the structures that are strictly attributed to the Alpine reactivation of the thrust are those structures indicating reverse kinematics or associated with a compressional stress, which are found within the thrust zone deformation at the contact between Devonian and Stephano-Permian units. Contrarily, the magmatic lay-

ering and joints J1 are broadly present in the andesitic foot-wall, outside the thrust zone, and in other Stephano-Permian basins; they are therefore considered inherited fluidal and cooling structures, respectively. For this reason, the calcite veins V1a and V2 (and related cements Cc1a and Cc2), exclusively occurring within the thrust zone, have been associated with the reactivation of the Estamariu thrust. During this period, and associated with ongoing deformation and progressive shortening, stylolites e2 developed as sutured areas between host rock and veins V1a and between foliation surfaces, coevally with the development of veins V1b, as denoted by their crosscutting relationships and orientations.

Table 2. Elemental composition (Ca, Mg, Fe, Mn, Sr) of the calcite cements Cc1a to Cc5 and host rocks from the hanging wall (HW) and footwall (FW). The qualitative scale in green indicates different contents (for each element, the darkest green points to the highest concentration and vice versa).

Sample	Ca ppm	Mg ppm	Fe ppm	Mn ppm	Sr ppm
Cc1a	391618	1335.9	5603.5	1243.7	543.7
Cc1a	349063	1548.6	4121.3	781.6	460.2
Cc1a	351134	1231.8	5205.4	810.3	545.5
Cc1a	337588	1126.6	3914.9	680.7	704.0
Cc2	328169	501.2	1061.4	3629.3	248.5
Cc3	364995	331.9	1647.8	8277.9	122.3
Cc3	333123	909.5	5545.9	7695.5	424.9
Cc4	333563	624.4	3814.9	4034.6	72.2
Cc5	233784	2260.0	8656.6	161.4	72.1
Cc5	281741	1626.2	4078.0	138.8	25.3
HW	320038	2752.6	6289.0	621.1	449.4
FW	4234	12830.5	43107.1	466.6	18.6

Higher content Lower content

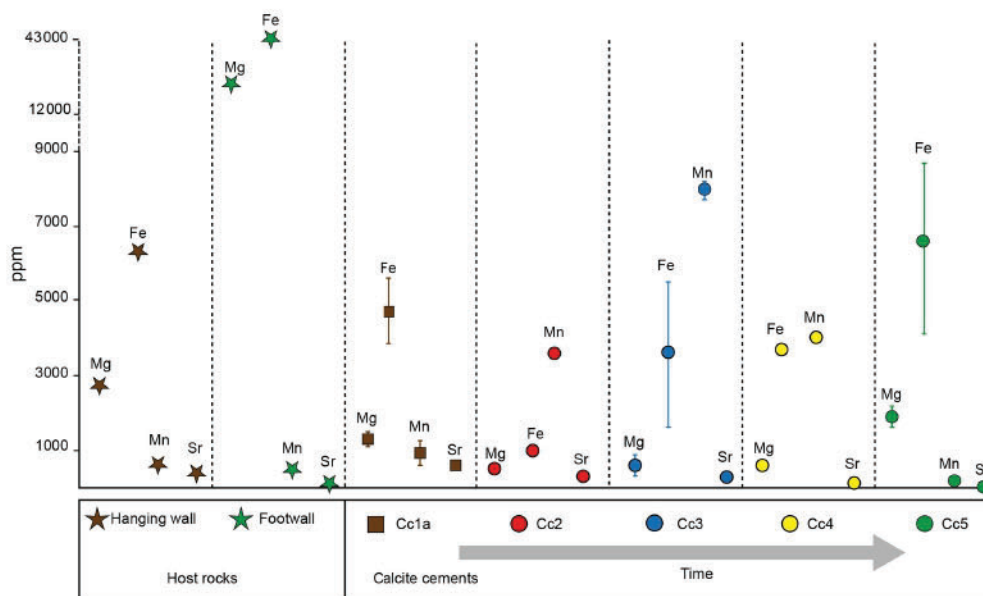


Figure 12. Elemental composition (including Mg, Fe, Mn, and Sr) in parts per million of the different calcite cements and host rocks. Bars indicate maximum, minimum, and average composition.

Other structures present in the study area, such as veins V3 to V5 and related cements Cc3 to Cc5, are attributed to the Neogene extension. Veins V3 precipitated in the subsidiary thrust zone developed in the footwall of the Estamariu thrust. These veins strike parallel to the thrust zone foliation (S_2) (Fig. 7a, b) but are characterized by calcite fibers growing perpendicular to the vein walls and to the foliation surfaces (Fig. 7c), thus evidencing their extensional character. The presence of extensional calcite veins opened

along previously formed foliation surfaces in a thrust zone has been reported in other structures in the Pyrenees and has been considered to postdate the thrust activity (Lacroix et al., 2011, 2014). Veins V4 precipitated in subvertical and E–W mesoscale faults affecting the Stephano-Permian andesites (Fig. 8) outside the thrust zone (Fig. 3). The fault orientation and dip as well as the two striae set generations observed on the fault planes are compatible with the Neogene extensional faults that bound the Cerc basin and postdate the Esta-

mariu thrust (Cabrera et al., 1988; Roca, 1996; Saura, 2004). Calcite cements Cc3 and Cc4, occluding veins V3 and V4, have a similar geochemical composition (Figs. 9–12), supporting the idea that their precipitation occurred during the same tectonic event associated with a similar fluid regime (i.e., although these cements precipitated in different structures, they are likely contemporaneous). Finally, veins V5 (and related cement Cc5) precipitated locally in shear fractures crosscutting and postdating the thrust-related deformation (Figs. 3, 4, and 8d). These veins strike parallel to the shear bands (Cn) located in the main thrust zone (Fig. 8e), exhibiting normal slip kinematics, postdating the reverse structures, and therefore indicating reactivation of the Estamariu thrust during the Neogene extension.

5.2 Fluid system during the Alpine reactivation of the Estamariu thrust

As veins V1a and V2 are consistent with the Alpine reactivation of the Estamariu thrust, the geochemistry of their related calcite cements Cc1a and Cc2 is interpreted to record the fluid system during this tectonic event.

Cements Cc1a and Cc2 are characterized by high $^{87}\text{Sr}/^{86}\text{Sr}$ ratios (from 0.713 to 0.714 for Cc1a and 0.718 for Cc2), significantly higher radiogenic than ratios of Phanerozoic seawater (between 0.7070 and 0.7090) (McArthur et al., 2012). This may reflect the incorporation of radiogenic Sr from a fluid that derived from or interacted with Rb-rich and/or Sr-rich basement rocks such as those underlying the Estamariu thrust. In addition, Cc1a has a narrow range of $\delta^{13}\text{C}$, between +0.91‰ VPDB and +2‰ VPDB, consistent with values of the Devonian marine limestones from the hanging wall (between +1.54‰ VPDB and +2.75‰ VPDB) and within the range of Devonian marine carbonate values (Veizer et al., 1999). Likewise, the elemental composition of Cc1a follows a similar trend to that of its Devonian host, both having high Mg and Sr and low Mn contents with respect to the other calcite cements (Fig. 12). These geochemical similarities indicate significant fluid–rock interaction and buffering of the carbon and elemental composition of the precipitating fluid by the Devonian carbonates (Marshall, 1992). Calcite cement Cc2 has slightly lower $\delta^{13}\text{C}$, lower Mg and Sr, and higher Mn contents with respect to both Cc1a and the Devonian host. On the other hand, the temperature and the $\delta^{18}\text{O}$ composition of the vein-forming fluids, calculated from clumped isotope thermometry of Cc2, range between 50 and 100 °C and between –6.4‰ SMOW and –0.3‰ SMOW, respectively. These values are interpreted as the involvement of meteoric fluids that were probably heated at depth and enriched in radiogenic Sr during their flow and interaction with basement rocks. These fluids flowed preferentially along the thrust zone (Fig. 13a), as evidenced by the exclusive presence of calcite in this area, likely due to the enhanced permeability associated with the thrust discontinuity (McCaig et al.,

1995; Trincal et al., 2017). As Cc1a and Cc2 precipitated in the thrust zone during the same tectonic event, they likely precipitated from the same fluids, which progressively increased the extent of fluid–rock interaction from the thrust plane (Cc2) towards the hanging wall (Cc1a), as indicated by the host-rock-buffered composition of the latter. Previous studies already reported syntectonic migration of fluids that had interacted at depth with basement rocks before upflowing along thrust zones in other structures from the Pyrenean basement, such as the Gavarnie thrust and the related Pic de Port Vieux thrust (McCaig et al., 1995).

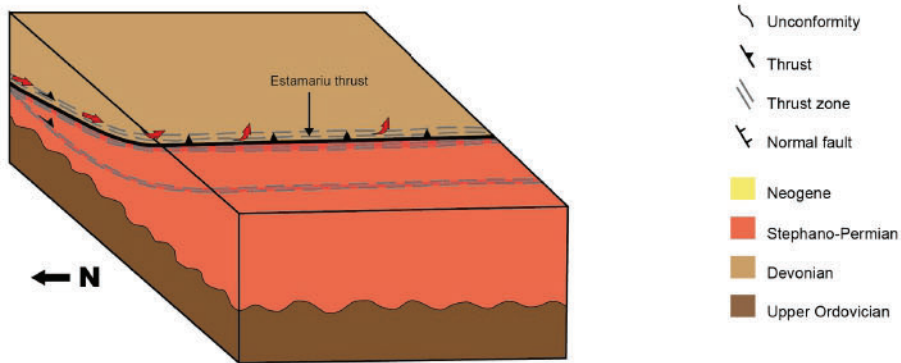
5.3 Fluid system during the Neogene extension

Calcite veins V3 to V5 are attributed to the Neogene extension, and the geochemistry of their related calcite cements Cc3 to Cc5 characterizes the fluid system during this period.

Cc3 and Cc4 have considerably high $^{87}\text{Sr}/^{86}\text{Sr}$ ratios (0.714619 and 0.717706, respectively), similar to the ones reported for Cc1a and Cc2 (Fig. 11), indicating interaction with basement rocks. The $\delta^{18}\text{O}_{\text{fluid}}$ calculated from clumped isotopes, between +4.3‰ SMOW and +12.1‰ SMOW for Cc3 and between +0.9‰ SMOW and +8.1‰ SMOW for Cc4, falls within the range of metamorphic and/or formation brines (Taylor, 1987). The $\delta^{18}\text{O}$ -depleted values of these cements (around –14‰ VPDB) are due to the high temperatures of the fluids (between 130 and 210 °C for Cc3 and between 100 and 170 °C for Cc4). Assuming a normal geothermal gradient of 30 °C, these temperatures would have been reached at a minimum depth of 3–5 km. However, these veins have never reached such a burial depth, since during the Neogene extension the studied structure acquired its current configuration (Saura, 2004) and was only buried under the Devonian sequence (hanging wall), which has a maximum thickness of several hundred meters (Mey, 1967). This assumption evidences the hydrothermal character of the circulating fluids, which probably migrated rapidly enough through normal faults to maintain their high temperatures and to be in thermal disequilibrium with the surrounding rocks. Similarly, the high Mn content of Cc3 and Cc4 (around 7700–8300 and 4000 ppm, respectively), responsible of their bright luminescence (Figs. 7d, 8c), is consistent with hydrothermal waters (Pfeifer et al., 1988; Pomerol, 1983; Pratt et al., 1991). On the other hand, the $\delta^{13}\text{C}$ -depleted values of these cements are indicative of the influence of organic-derived carbon (Cerling, 1984; Vilasi et al., 2006). The most probable source for these low $\delta^{13}\text{C}$ values is the Silurian black shales that do not crop out in the study area but acted as the main detachment level during the Variscan compression and locally during the Alpine compression in the Pyrenean Axial Zone (Mey, 1967). These black shales have significant organic carbon contents (TOC around 2.3 %), and around the Gavarnie thrust, they exhibit syntectonic carbonate veins yielding $\delta^{13}\text{C}$ values between –2‰ VPDB and –8‰ VPDB (McCaig et al., 1995). Thus, cements Cc3 and Cc4 precipitated from hy-

(a) **Alpine compression**

Reactivation of the Estamariu thrust. Calcite cements Cc1a and Cc2



Regional tectonism	(a) Alpine compression		(b) Neogene extension		
Calcite cement	Cc1a	Cc2	Cc3	Cc4	Cc5
Related structure	V1a	V2	V3	V4	V5
Geochemistry	$\delta^{13}\text{C}_{\text{calcite}}$ +	■	●	●	●
	$\delta^{18}\text{O}_{\text{calcite}}$ +	■	●	●	●
	$^{87}\text{Sr}/^{86}\text{Sr}$ +	■	●	●	●
	Mg +	■	●	●	●
	Fe +	■	●	●	●
	Mn +	■	●	●	●
	Sr +	■	●	●	●
	$\delta^{18}\text{O}_{\text{fluid}}$ +		●	●	●
Temperature +		●	●	●	
Fluid source	Upward meteoric fluid		Upward hydrothermal fluid		Downward meteoric fluid
Implications	Change in the fluid regime. Increasing extent of fluid-rock interaction			Main change in the fluid regime	

(b) **Neogene extension**

Reactivation of the Estamariu thrust and development of normal faults
Calcite cement Cc3, Cc4 and Cc5

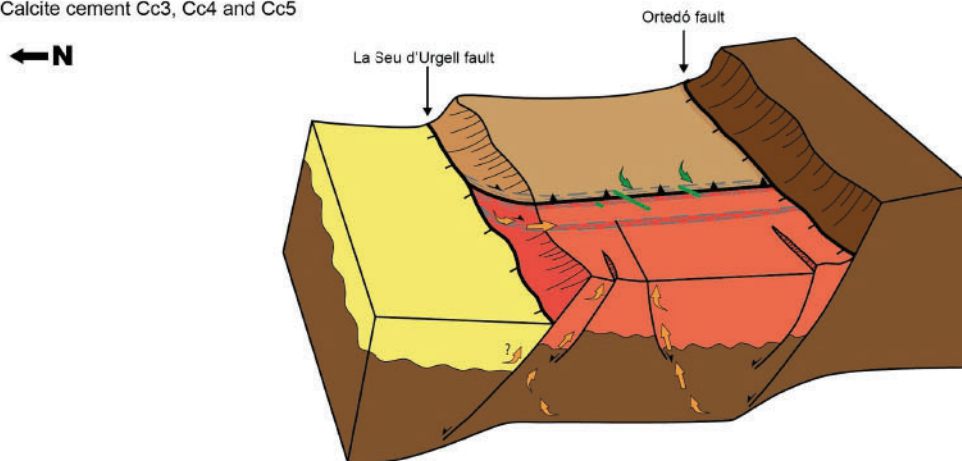


Figure 13. Tectonic and geochemical evolution of the study area (not to scale) and relationships with the evolution of the fluid system. (a) During the Alpine reactivation of the Estamariu thrust, a meteoric fluid (red arrows) interacted at depth with basement rocks and then migrated along the fault plane towards the hanging wall, precipitating cements Cc1a and Cc2. (b) During the Neogene extension, basement-derived hydrothermal fluids (orange arrows) flowed upwards through newly formed and reactivated fault zones. This fluid precipitated calcite cements Cc3 and Cc4. Finally, during ongoing deformation, meteoric fluids (green arrows) percolated in the system and precipitated Cc5, revealing a main change in the fluid regime.

drothermal fluids derived from and/or equilibrated with basement rocks expelled through newly formed and reactivated fault zones during deformation (Fig. 13b). The hydrothermal character of the fluids involved in this deformation event, and their relatively high temperatures (up to 210 °C), could have altered the clumped isotope composition of the previous calcite cement generations (Cc1a and Cc2). Clumped isotopes may be reset by recrystallization and by solid-state isotopic exchange reactions and diffusion within the mineral lattice (Shenton et al., 2015; Stolper and Eiler, 2015). However, in the studied vein samples there is no evidence of calcite recrystallization (for instance, grain coarsening linked to grain boundary migration). Therefore, we conclude that although it is possible, there is little evidence for clumped isotopes of cements Cc1a and Cc2 to have been reset during precipitation of Cc3 and Cc4.

Finally, the isotopic signature of Cc5, ranging between -8.1‰ VPDB and -5.7‰ VPDB for $\delta^{18}\text{O}$ and between -8.2‰ VPDB and -3.8‰ VPDB for $\delta^{13}\text{C}$, falls within the range of meteoric carbonates (Travé et al., 2007; Veizer, 1992). The similar tendency in the elemental composition of this cement and the Stephano-Permian volcanic rocks, both having the highest Mg and Fe and the lowest Mn and Sr contents with respect to the other cements and host rocks, reveals significant fluid–rock interaction with the footwall rocks. The significant water–rock interaction is also demonstrated by the Nd isotopic composition of Cc5 (0.512178), yielding values similar to the volcanic host (0.512196). This fact indicates that this cement precipitated from percolation of meteoric fluids, the geochemistry of which was controlled by the volcanic host rock. Studies focused on infiltration of meteoric fluids and subsequent upflowing along the La Tet fault during the Neogene extension have shown that meteoric waters in the area infiltrate at high altitudes of around 2000 m and low temperatures of around 5 °C (Krimissa et al., 1994; Taillefer et al., 2018). Therefore, we suggest that Cc5 probably precipitated during the latest stages of extension after the fluid regime changed from upward fluid migration to percolation of cold meteoric waters, as also occurred in the Barcelona Plain (Catalan Coastal Range) (Cantarero et al., 2014).

In conclusion, the high $^{87}\text{Sr}/^{86}\text{Sr}$ ratios of the different calcite cements (Cc1a to Cc5) evidence the interaction between the vein-forming fluids and Paleozoic basement rocks with a more radiogenic signature. The geochemical evolution of these cement generations also highlights the progressive change in the fluid regime and composition during successive compressional and extensional tectonic events (Fig. 13). The continuous increase in precipitation temperatures and enrichment in $\delta^{18}\text{O}_{\text{fluid}}$ from calcite cements Cc1a and Cc2 (Alpine) to cements Cc3 and Cc4 (Neogene) is probably linked to a higher extent of fluid–rock interaction with basement rocks. By contrast, during the latest stages of extension, the infiltration of meteoric fluids likely indicates a more significant change in the fluid regime from upward to downward fluid migration (Fig. 13).

5.4 Influence of Paleozoic basement rocks on the $^{87}\text{Sr}/^{86}\text{Sr}$ ratios of the fluids circulating during deformation

In this section, we assess the influence of basement rocks on the chemistry of fluids circulating during deformation in the Pyrenees. The comparison between previous studies and the new data provided in this contribution evidences that fluids migrating through basement or cover units have a different geochemical signature, which is recorded in the $^{87}\text{Sr}/^{86}\text{Sr}$ ratios of the vein cements. The high $^{87}\text{Sr}/^{86}\text{Sr}$ ratios (0.713 to 0.718) of the analyzed cements, originated during successive compressional and extensional tectonic events, indicate that regardless of the origin of the fluids and the tectonic context, basement rocks have a significant influence on the fluid chemistry. Accordingly, cements precipitated from fluids that have circulated through basement rocks have significantly high $^{87}\text{Sr}/^{86}\text{Sr}$ ratios (> 0.710) (Fig. 11), reflecting the interaction between the vein-forming fluids and rocks with a more radiogenic signature. Similar radiogenic $^{87}\text{Sr}/^{86}\text{Sr}$ ratios have also been attributed to basement-derived fluids in the Glarus nappe (Swiss Alps) (Burkhard et al., 1992). By contrast, vein cements precipitated from fluids that have circulated through the Mesozoic–Cenozoic sedimentary cover in the Pyrenees (i.e., through younger rocks with a different radiogenic signature) have significantly lower $^{87}\text{Sr}/^{86}\text{Sr}$ ratios (< 0.710). Such lower values may be similar to Phanerozoic seawater values, evidencing interaction between the vein-forming fluids and marine carbonate units, or they may be higher, evidencing interaction with siliciclastic rocks (Cruset et al., 2018; Travé et al., 2007). A previous study, focused on fluid flow along the Gavarnie thrust in the central-western Axial Pyrenees, used this limit value ($^{87}\text{Sr}/^{86}\text{Sr} = 0.710$) to differentiate between the unaltered limestone protolith and the Cretaceous thrust-related carbonate mylonite affected by fluids carrying radiogenic Sr (McCaig et al., 1995). In addition, Williams et al. (2015) also attributed $^{87}\text{Sr}/^{86}\text{Sr}$ ratios > 0.710 to the input of basement-derived fluids in the Rio Grande rift, USA.

5.5 Fluid flow at regional scale: the NE part of the Iberian Peninsula during the Neogene extension

As pointed out above, the structural and geochemical data indicate that calcite cements Cc3 and Cc4 (veins V3 and V4, respectively) precipitated from hydrothermal fluids (up to 210 °C) that interacted at depth with basement rocks before ascending through newly formed and reactivated structures during the Neogene extension. These interpretations are consistent with the presence of several hydrothermal springs (temperatures of 29 to 73 °C) currently upwelling aligned along the La Tet fault and related Neogene deformation in the Pyrenean Axial Zone (Krimissa et al., 1994; Taillefer et al., 2017, 2018). Several studies indicate the origin of these hot-water springs as meteoric fluids infiltrated at high-elevated

reliefs above 2000 m, warmed at great depths by normal geothermal gradients, and migrated upwards along permeability anisotropies related to fault zones (Taillefer et al., 2017, 2018). The $^{87}\text{Sr}/^{86}\text{Sr}$ ratios of these springs, ranging between 0.715 and 0.730 (Caballero et al., 2012), are within the range of values obtained in this study and also account for interaction between circulating fluids and basement lithologies. Studies based on numerical models suggest that the La Tet fault and the involved basement rocks are still permeable down to 3 km of depth (Taillefer et al., 2017, 2018), although the fault has been dormant since the Mio-Pliocene (Goula et al., 1999). It has also been suggested that the footwall topography, which induces high hydraulic gradients and produces fluid advection, is the major factor controlling the infiltration of meteoric fluids, the circulation depth, and the maximum temperature reached by the migrating fluids (Taillefer et al., 2017).

A similar geological context and fluid regime evolution to those explained above are found in the Barcelona Plain and the Vallès Basin, located in the northeast part of the Catalan Coastal Range (CCR) (Fig. 1A). Consequently, the comparison between the two geological contexts allows us to give insights into the fluid circulation in extensional basins at regional scale (in the NE part of Iberia). In these locations of the CCR, the main fault system associated with the Neogene extension acted as a conduit for hydrothermal fluid circulation at temperatures between 130 and 150 °C during synkinematic periods (Cantarero et al., 2014; Cardellach et al., 2003) and is also responsible for the present-day circulation of hot-water springs up to 70 °C (Carmona et al., 2000; Fernández and Banda, 1990). In both cases, fluids would have been topographically driven from elevated areas to great depths (Cantarero et al., 2014), where they circulated through basement rocks, acquiring high $^{87}\text{Sr}/^{86}\text{Sr}$ ratios (> 0.712) and high temperatures (Cardellach et al., 2003) before ascending through fault discontinuities. However, in the Penedès basin, which corresponds to the southwestern termination of the Neogene structure in the CCR, basement lithologies do not crop out and the extensional faults only involve Neogene deposits filling the basin and a Mesozoic sedimentary substrate. In this location, the main fault system acted as a conduit for several episodes of meteoric fluids percolation during the Neogene extension, and evidence of hydrothermal fluid circulation has not been reported in the area (Travé and Calvet, 2001; Travé et al., 1998; Baqués et al., 2010, 2012). This fact agrees with previous studies that highlight the fact that hydrothermal activity, in particular the occurrence of hot-water springs in the Pyrenees and in the CCR, is preferably concentrated in basement rocks, which constitute the elevated footwall of the main extensional fault systems (Taillefer et al., 2017; Carmona et al., 2000).

All these observations indicate an open fluid system in the NE part of the Iberian Peninsula associated with the Neogene extensional deformation. This extensional fault system acted as a conduit for the circulation of hot fluids in Neogene times

and does so in the present. This fault-controlled fluid flow could have been continuous through time or could be related to intermittent pulses. Fault control on upflowing of hot fluids along fault systems is a common process in different geological settings and has been reported in the Great Basin, USA (Faulds et al., 2010; Nelson et al., 2009), in western Turkey (Faulds et al., 2010), in the southern Canadian Cordillera (Grasby and Hutcheon, 2001), and in southern Tuscany, Italy (Liotta et al., 2010).

6 Conclusions

This study assesses the influence of basement rocks on the fluid chemistry during deformation in the Pyrenees and provides insights into the fluid regime in the NE part of the Iberian Peninsula. Our data indicate that regardless of the fluid origin and the tectonic context, the fluids that have interacted with basement rocks have a higher $^{87}\text{Sr}/^{86}\text{Sr}$ ratio (> 0.710) than those that have circulated through the sedimentary cover (< 0.710). On the other hand, extensional deformation structures in both the eastern Pyrenees and the northeastern part of the Catalan Coastal Range acted as conduits for hydrothermal fluid migration in Neogene times and do so in the present. These fluids likely interacted with basement rocks before ascending through fault zones and related structures.

The studied thrust resulted from a multistage late Paleozoic (Variscan) to Neogene tectonic evolution. In the study area, it places a Devonian pre-Variscan unit against a Stephano-Permian late to post-Variscan sequence, and therefore the structures present within the thrust zone, affecting both sequences, are attributed to the Alpine compression (Late Cretaceous to Oligocene) and subsequent Neogene extension. During the Alpine compression, the reactivation of the thrust resulted in the transposition of the Variscan regional foliation within the thrust zone and in the formation of a subsidiary thrust zone affecting the andesites in the footwall. Geochemical analyses indicate that meteoric fluids circulated through the thrust during this period at temperatures between 50 and 100 °C. These fluids progressively increased the extent of fluid–rock interaction from the thrust plane towards the hanging wall, as suggested by the host-rock-buffered composition of the calcite in the hanging wall deformation structures. During the Neogene extension, the Estamariu thrust was likely reactivated, and normal faults and shear fractures were formed. Geochemical data reveal that basement-derived fluids circulated through these structures at temperatures up to 210 °C. Finally, during the latest to post-stages of extension and uplift of the structure, the fluid regime changed to percolation of meteoric fluids that were buffered by the volcanic host rocks.

Data availability. All data are available in Tables 1 and 2 and in the Supplement.

Supplement. The supplement related to this article is available online at: <https://doi.org/10.5194/se-11-2257-2020-supplement>.

Author contributions. DML, GA, DC, IC, and AT were responsible for conceptualization. DML handled data curation. DML, GA, DC, IC, CMJ, and AT conducted the formal analysis, carried out the investigation, contributed to the methodology, and participated in review and editing. AT was responsible for funding acquisition. DML was responsible for writing and original draft preparation.

Competing interests. The authors declare that they have no conflict of interest.

Special issue statement. This article is part of the special issue “Faults, fractures, and fluid flow in the shallow crust”. It is not associated with a conference.

Acknowledgements. We acknowledge the constructive comments from Owen Callahan and Brice Lacroix, who helped to improve the quality of the paper, as well as the editorial guidance of Randolph Williams. We also thank Josep Maria Casas from the Universitat de Barcelona for showing us the location of the studied outcrops. Carbon and oxygen isotopic analyses were carried out at the Centre Científics i Tecnològics of the Universitat de Barcelona. Strontium and neodymium analyses were performed at the CAI de Geocronología y Geoquímica Isotópica of the Universidad Complutense de Madrid. The elemental composition was analyzed at the geochemistry facility labGEOTOP of Geosciences Barcelona (GEO3BCN-CSIC). Clumped isotope thermometry was carried out at the Imperial College London. This research was carried out within the framework of the DGICYT Spanish project PGC2018-093903-B-C22 (Ministerio de Ciencia, Innovación y Universidades/Agencia Estatal de Investigación/Fondo Europeo de Desarrollo Regional, Unión Europea) and the Grup Consolidat de Recerca “Geologia Sedimentària” (2017-SGR-824). The PhD research of DML is supported by the FPI2016 (BES-2016-077214) Spanish program from MINECO.

Financial support. This research was carried out within the framework of the DGICYT Spanish project PGC2018-093903-B-C22 (Ministerio de Ciencia, Innovación y Universidades/Agencia Estatal de Investigación/Fondo Europeo de Desarrollo Regional, Unión Europea) and the Grup Consolidat de Recerca “Geologia Sedimentària” (2017-SGR-824). The PhD research of DML is supported by the FPI2016 (BES-2016-077214) Spanish program from MINECO.

Review statement. This paper was edited by Randolph Williams and reviewed by Brice Lacroix and Owen Callahan.

References

- Arndt, M., Virgo, S., Cox, S. F., and Urai, J. L.: Changes in fluid pathways in a calcite vein mesh (Natih Formation, Oman Mountains): insights from stable isotopes, *Geofluids*, 14, 391–418, <https://doi.org/10.1111/gfl.12083>, 2014.
- Banks, D., Da Vies, G., Yardley, B. W., McCaig, A., and Grant, N.: The chemistry of brines from an Alpine thrust system in the Central Pyrenees: An application of fluid inclusion analysis to the study of fluid behaviour in orogenesis, *Geochim. Cosmochim. Ac.*, 55, 1021–1030, [https://doi.org/10.1016/0016-7037\(91\)90160-7](https://doi.org/10.1016/0016-7037(91)90160-7), 1991.
- Baqués, V., Travé, A., Benedicto, A., Labaume, P., and Cantarero, I.: Relationships between carbonate fault rocks and fluid flow regime during propagation of the Neogene extensional faults of the Penedès basin (Catalan Coastal Ranges, NE Spain), *J. Geochemical Explor.*, 106, 24–33, <https://doi.org/10.1016/j.gexplo.2009.11.010>, 2010.
- Baqués, V., Travé, A., Roca, E., Marin, M., and Cantarero, I.: Geofluid behaviour in successive extensional and compressional events: a case study from the southwestern end of the Valles-Penedes Fault (Catalan Coastal Ranges, NE Spain), *Pet. Geosci.*, 18, 17–31, <https://doi.org/10.1144/1354-079311-017>, 2012.
- Barker, S. L. L. and Cox, S. F.: Evolution of fluid chemistry and fluid-flow pathways during folding and faulting: an example from Taemas, NSW, Australia, *J. Geol. Soc. London, Spec. Publ.*, 359, 203–227, <https://doi.org/10.1144/SP359.12>, 2011.
- Barker, S. L. L., Bennett, V. C., Cox, S. F., Norman, M. D., and Gagan, M. K.: Sm-Nd, Sr, C and O isotope systematics in hydrothermal calcite-fluorite veins: Implications for fluid-rock reaction and geochronology, *Chem. Geol.*, 268, 58–66, <https://doi.org/10.1016/j.chemgeo.2009.07.009>, 2009.
- Beaudoin, N., Bellahsen, N., Lacombe, O., Emmanuel, L., and Pironon, J.: Crustal-scale fluid flow during the tectonic evolution of the Bighorn Basin (Wyoming, USA), *Basin Res.*, 26, 403–435, <https://doi.org/10.1111/bre.12032>, 2014.
- Beaudoin, N., Huyghe, D., Bellahsen, N., Lacombe, O., Emmanuel, L., Mouthereau, F., and Ouanhnon, L.: Fluid systems and fracture development during syn-depositional fold growth: An example from the Pico del Aguila anticline, Sierras Exteriores, southern Pyrenees, Spain, *J. Struct. Geol.*, 70, 23–38, <https://doi.org/10.1016/j.jsg.2014.11.003>, 2015.
- Bickle, M. J., Wickham, S. M., Chapman, H. J., and Taylor, H. P.: A strontium, neodymium and oxygen isotope study of hydrothermal metamorphism and crustal anatexis in the Trois Seigneurs Massif, Pyrenees, France, *Contrib. Mineral. Petr.*, 100, 399–417, <https://doi.org/10.1007/BF00371371>, 1988.
- Bons, A.: Intracrystalline deformation and slaty cleavage development in very low-grade slates from the Central Pyrenees, *Geol. Ultraiectina*, 56, 173 pp., ISBN 90715770909789071577093, 1988.
- Breesch, L., Swennen, R., and Vincent, B.: Fluid flow reconstruction in hanging and footwall carbonates: Compartmentalization by Cenozoic reverse faulting in the Northern Oman Mountains (UAE), *Mar. Petrol. Geol.*, 26, 113–128, <https://doi.org/10.1016/j.marpetgeo.2007.10.004>, 2009.
- Burkhard, M., Kerrich, R., Maas, R., and Fyfe, W. S.: Stable and Sr-isotope evidence for fluid advection during thrusting of the glarus nappe (swiss alps), *Contrib. Mineral. Petr.*, 112, 293–311, <https://doi.org/10.1007/BF00310462>, 1992.

- Caballero, Y., Gironde, C., and Le Goff, E.: Ressource en eau thermale de la station d'Ameilie-les-Bains, Etat des lieux, Rapport BRGM/RP-60618-FR, BRGM (French Geological Survey), Orleans, France, 56 pp., 2012.
- Cabrera, L., Roca, E., and Santanach, P.: Basin formation at the end of a strike-slip fault: the Cerdanya Basin (eastern Pyrenees), *J. Geol. Soc. London*, 145, 261–268, <https://doi.org/10.1144/gsjgs.145.2.0261>, 1988.
- Cantarero, I., Travé, A., Alías, G., and Baqués, V.: Polyphasic hydrothermal and meteoric fluid regimes during the growth of a segmented fault involving crystalline and carbonate rocks (Barcelona Plain, NE Spain), *Geofluids*, 14, 20–44, <https://doi.org/10.1111/gfl.12021>, 2014.
- Cantarero, I., Alías, G., Cruset, D., Carola, E., Lanari, P., and Travé, A.: Fluid composition changes in crystalline basement rocks from ductile to brittle regimes, *Global Planet. Change*, 171, 273–292, <https://doi.org/10.1016/j.gloplacha.2018.03.002>, 2018.
- Cardellach, E., Canals, À., and Grandia, F.: Recurrent hydrothermal activity induced by successive extensional episodes: the case of the Berta F-(Pb-Zn) vein system (NE Spain), *Ore Geol. Rev.*, 22, 133–141, [https://doi.org/10.1016/S0169-1368\(02\)00112-9](https://doi.org/10.1016/S0169-1368(02)00112-9), 2003.
- Carmona, J. M., Bitzer, K., López, E., and Bouazza, M.: Isotopic composition and origin of geothermal waters at Caldetes (Maresme-Barcelona), *J. Geochem. Explor.*, 69–70, 441–447, [https://doi.org/10.1016/S0375-6742\(00\)00127-8](https://doi.org/10.1016/S0375-6742(00)00127-8), 2000.
- Casas, J. M., Domingo, F., Poblet, J., and Soler, A.: On the role of the Hercynian and Alpine thrusts in the Upper Paleozoic rocks of the Central and Eastern Pyrenees, *Geodin. Acta*, 3, 135–147, <https://doi.org/10.1080/09853111.1989.11105181>, 1989.
- Cerling, T. E.: The stable isotopic composition of modern soil carbonate and its relationship to climate, *Earth Planet. Sci. Lett.*, 71, 229–240, [https://doi.org/10.1016/0012-821X\(84\)90089-X](https://doi.org/10.1016/0012-821X(84)90089-X), 1984.
- Choukroune, P.: The Ecore Pyrenean deep seismic profile reflection data and the overall structure of an orogenic belt, *Tectonics*, 8, 23–39, <https://doi.org/10.1029/TC008i001p00023>, 1989.
- Cochelin, B., Lemirre, B., Denèle, Y., de Saint Blanquat, M., Lahfid, A., and Duchêne, S.: Structural inheritance in the Central Pyrenees: the Variscan to Alpine tectonometamorphic evolution of the Axial Zone, *J. Geol. Soc. London*, 175, 336–351, <https://doi.org/10.1144/jgs2017-066>, 2018.
- Cox, S. F.: Structural and isotopic constraints on fluid flow regimes and fluid pathways during upper crustal deformation: An example from the Taemas area of the Lachlan Orogen, SE Australia, *J. Geophys. Res.*, 112, B08208, <https://doi.org/10.1029/2006JB004734>, 2007.
- Crespo-Blanc, A., Masson, H., Sharp, Z., Cosca, M., and Hunziker, J.: A stable and $^{40}\text{Ar}/^{39}\text{Ar}$ isotope study of a major thrust in the Helvetic nappes (Swiss Alps): Evidence for fluid flow and constraints on nappe kinematics, *Geol. Soc. Am. Bull.*, 107, 1129–1144, [https://doi.org/10.1130/0016-7606\(1995\)107<1129:ASAAAI>2.3.CO;2](https://doi.org/10.1130/0016-7606(1995)107<1129:ASAAAI>2.3.CO;2), 1995.
- Crognier, N., Hoareau, G., Aubourg, C., Dubois, M., Lacroix, B., Branellec, M., Callot, J. P., and Vennemann, T.: Syn-orogenic fluid flow in the Jaca basin (south Pyrenean fold and thrust belt) from fracture and vein analyses, *Basin Res.*, 30, 187–216, <https://doi.org/10.1111/bre.12249>, 2018.
- Cruset, D.: Sequential fluid migration along a fold and thrust belt SE pyrenees from late Cretaceous to Oligocene, PhD thesis, Universitat de Barcelona, 352 pp., 2019.
- Cruset, D., Cantarero, I., Travé, A., Vergés, J., and John, C. M.: Crestal graben fluid evolution during growth of the Puig-reig anticline (South Pyrenean fold and thrust belt), *J. Geodyn.*, 101, 30–50, <https://doi.org/10.1016/j.jog.2016.05.004>, 2016.
- Cruset, D., Cantarero, I., Vergés, J., John, C. M., Muñoz-López, D., and Travé, A.: Changes in fluid regime in syn-orogenic sediments during the growth of the south Pyrenean fold and thrust belt, *Global Planet. Change*, 171, 207–224, <https://doi.org/10.1016/j.gloplacha.2017.11.001>, 2018.
- Cruset, D., Cantarero, I., Benedicto, A., John, C. M., Vergés, J., Albert, R., Gerdes, A., and Travé, A.: From hydroplastic to brittle deformation: Controls on fluid flow in fold and thrust belts. Insights from the Lower Pedraforca thrust sheet (SE Pyrenees), *Mar. Petrol. Geol.*, 120, 104517, <https://doi.org/10.1016/j.marpetgeo.2020.104517>, 2020a.
- Cruset, D., Vergés, J., Albert, R., Gerdes, A., Benedicto, A., Cantarero, I., and Travé, A.: Quantifying deformation processes in the SE Pyrenees using U-Pb dating of fracture-filling calcites, *J. Geol. Soc. London*, 177, 1186–1196, <https://doi.org/10.1144/jgs2020-014>, 2020b.
- Deweever, B., Swennen, R., and Breesch, L.: Fluid flow compartmentalization in the Sicilian fold and thrust belt: Implications for the regional aqueous fluid flow and oil migration history, *Tectonophysics*, 591, 194–209, <https://doi.org/10.1016/j.tecto.2011.08.009>, 2013.
- Faulds, J., Coolbaugh, M., Bouchot, V., Moeck, I., Oğuz, K., and Cedex, O.: Characterizing Structural Controls of Geothermal Reservoirs in the Great Basin, USA, and Western Turkey: Developing Successful Exploration Strategies in Extended Terranes, *World Geothermal Congress 2010*, 25–29, 2010.
- Faj-Gomord, O., Allanic, C., Verbiest, M., Honlet, R., Champenois, F., Bonifacie, M., Chaduteau, C., Wouters, S., Muchez, P., Lasseur, E., and Swennen, R.: Understanding Fluid Flow during Tectonic Reactivation: An Example from the Flamborough Head Chalk Outcrop (UK), *Geofluids*, vol. 2018, 1–17, <https://doi.org/10.1155/2018/9352143>, 2018.
- Fernández, M. and Banda, E.: Geothermal anomalies in the Valles-Penedes Graben Master Fault: Convection through the Horst as a possible mechanism, *J. Geophys. Res.*, 95, 4887, <https://doi.org/10.1029/JB095iB04p04887>, 1990.
- Fitz-Diaz, E., Hudleston, P., Siebenaller, L., Kirschner, D., Campubí, A., Tolson, G., and Puig, T. P.: Insights into fluid flow and water-rock interaction during deformation of carbonate sequences in the Mexican fold-thrust belt, *J. Struct. Geol.*, 33, 1237–1253, <https://doi.org/10.1016/j.jsg.2011.05.009>, 2011.
- Foden, J.: Sr-isotopic evidence for Late Neoproterozoic rifting in the Adelaide Geosyncline at 586Ma: implications for a Cu ore forming fluid flux, *Precambrian Res.*, 106, 291–308, [https://doi.org/10.1016/S0301-9268\(00\)00132-7](https://doi.org/10.1016/S0301-9268(00)00132-7), 2001.
- Fontana, S., Nader, F. H., Morad, S., Ceriani, A., Al-Aasm, I. S., Daniel, J. M., and Mengus, J. M.: Fluid-rock interactions associated with regional tectonics and basin evolution, *Sedimentology*, 61, 660–690, <https://doi.org/10.1111/sed.12073>, 2014.
- Friedman, I. and O'Neil, J. R.: Compilation of stable isotope fractionation factors of geochemical interest, *Data of Geo-*

- chemistry, U. S. Gov. Print. Off, Washington D. C., p. 11, <https://doi.org/10.3133/pp440KK>, 1977.
- García-Sansegundo, J., Poblet, J., Alonso, J. L., and Clariana, P.: Hinterland-foreland zonation of the Variscan orogen in the Central Pyrenees: comparison with the northern part of the Iberian Variscan Massif, *Geol. Soc. London, Spec. Publ.*, 349, 169–184, <https://doi.org/10.1144/SP349.9>, 2011.
- Gasparrini, M., Ruggieri, G., and Brogi, A.: Diagenesis versus hydrothermalism and fluid-rock interaction within the Tuscan Nappe of the Monte Amiata CO₂-rich geothermal area (Italy), *Geofluids*, 13, 159–179, <https://doi.org/10.1111/gfl.12025>, 2013.
- Gomez-Rivas, E., Bons, P. D., Koehn, D., Urai, J. L., Arndt, M., Virgo, S., Laurich, B., Zeeb, C., Stark, L., and Blum, P.: The Jabal Akhdar dome in the Oman Mountains: Evolution of a dynamic fracture system, *Am. J. Sci.*, 314, 1104–1139, <https://doi.org/10.2475/07.2014.02.2014>, 2014.
- Goula, X., Olivera, C., Fleta, J., Grellet, B., Lindo, R., Rivera, L. A., Cisternas, A., and Carbon, D.: Present and recent stress regime in the eastern part of the Pyrenees, *Tectonophysics*, 308, 487–502, [https://doi.org/10.1016/S0040-1951\(99\)00120-1](https://doi.org/10.1016/S0040-1951(99)00120-1), 1999.
- Grant, N. T., Banks, D. A., McCaig, A. M., and Yardley, B. W. D.: Chemistry, source, and behavior of fluids involved in alpine thrusting of the Central Pyrenees, *J. Geophys. Res.*, 95, 9123, <https://doi.org/10.1029/JB095iB06p09123>, 1990.
- Grasby, S. E. and Hutcheon, I.: Controls on the distribution of thermal springs in the southern Canadian Cordillera, *Can. J. Earth Sci.*, 38, 427–440, <https://doi.org/10.1139/cjes-38-3-427>, 2001.
- Hartevelt, J. J. A.: Geology of the Upper Segre and Valira Valleys, Central Pyrenees, Andorra, Spain, Geological Institute, Leiden University, Leiden, 45, 167–236, 1970.
- Henderson, I. H. C. and McCaig, A. M.: Fluid pressure and salinity variations in shear zone-related veins, central Pyrenees, France: Implications for the fault-valve model, *Tectonophysics*, 262, 321–348, [https://doi.org/10.1016/0040-1951\(96\)00018-2](https://doi.org/10.1016/0040-1951(96)00018-2), 1996.
- Kluge, T., John, C. M., Jourdan, A.-L., Davis, S., and Crawshaw, J.: Laboratory calibration of the calcium carbonate clumped isotope thermometer in the 25–250 °C temperature range, *Geochim. Cosmochim. Ac.*, 157, 213–227, <https://doi.org/10.1016/j.gca.2015.02.028>, 2015.
- Krimissa, M., Chery, L., Fouillac, C., and Michelot, J. L.: Origin and Recharge Altitude of the Thermo-Mineral Waters of the Eastern Pyrenees, *Isot Environ. Healt. S.*, 30, 317–331, <https://doi.org/10.1080/00211919408046747>, 1994.
- Lacroix, B., Buatier, M., Labaume, P., Travé, A., Dubois, M., Charpentier, D., Ventalon, S., and Convert-Gaubier, D.: Microtectonic and geochemical characterization of thrusting in a foreland basin: Example of the South-Pyrenean orogenic wedge (Spain), *J. Struct. Geol.*, 33, 1359–1377, <https://doi.org/10.1016/j.jsg.2011.06.006>, 2011.
- Lacroix, B., Travé, A., Buatier, M., Labaume, P., Vennemann, T., and Dubois, M.: Syntectonic fluid-flow along thrust faults: Example of the South-Pyrenean fold-and-thrust belt, *Mar. Petrol. Geol.*, 49, 84–98, <https://doi.org/10.1016/j.marpetgeo.2013.09.005>, 2014.
- Lacroix, B., Baumgartner, L. P., Bouvier, A.-S., Kempton, P. D., and Vennemann, T.: Multi fluid-flow record during episodic mode I opening: A microstructural and SIMS study (Cotiella Thrust Fault, Pyrenees), *Earth Planet. Sc. Lett.*, 503, 37–46, <https://doi.org/10.1016/j.epsl.2018.09.016>, 2018.
- Lago, M., Arranz, E., Pocoví, A., Galé, C., and Gil-Imaz, A.: Permian magmatism and basin dynamics in the southern Pyrenees: a record of the transition from late Variscan transtension to early Alpine extension, *Geol. Soc. London, Spec. Publ.*, 223, 439–464, <https://doi.org/10.1144/GSL.SP.2004.223.01.19>, 2004.
- Liotta, D., Ruggieri, G., Brogi, A., Fulignati, P., Dini, A., and Nardini, I.: Migration of geothermal fluids in extensional terranes: the ore deposits of the Boccheggiano-Montieri area (southern Tuscany, Italy), *Int. J. Earth Sci.*, 99, 623–644, <https://doi.org/10.1007/s00531-008-0411-3>, 2010.
- Marshall, J. D.: Climatic and oceanographic isotopic signals from the carbonate rock record and their preservation, *Geol. Mag.*, 129, 143–160, <https://doi.org/10.1017/S0016756800008244>, 1992.
- Martí, J.: Caldera-like structures related to Permo-Carboniferous volcanism of the Catalan Pyrenees (NE Spain), *J. Volcanol. Geoth. Res.*, 45, 173–186, [https://doi.org/10.1016/0377-0273\(91\)90057-7](https://doi.org/10.1016/0377-0273(91)90057-7), 1991.
- Martí, J.: Genesis of crystal-rich volcanoclastic facies in the Permian red beds of the Central Pyrenees (NE Spain), *Sediment. Geol.*, 106, 1–19, [https://doi.org/10.1016/0037-0738\(95\)00143-3](https://doi.org/10.1016/0037-0738(95)00143-3), 1996.
- Martín-Martín, J. D., Travé, A., Gomez-Rivas, E., Salas, R., Sizun, J. P., Vergés, J., Corbella, M., Stafford, S. L., and Alfonso, P.: Fault-controlled and stratabound dolostones in the Late Aptian-earliest Albian Benassal Formation (Maestrat Basin, E Spain): Petrology and geochemistry constrains, *Mar. Petrol. Geol.*, 65, 83–102, <https://doi.org/10.1016/j.marpetgeo.2015.03.019>, 2015.
- Martinez Casas, L. F., Travé, A., Cruset, D., and Muñoz-López, D.: The Montagut Fault System: Geometry and Fluid Flow Analysis (Southern Pyrenees, Spain), in: *Petrogenesis and Exploration of the Earth's Interior, Proceedings of the 1st Springer Conference of the Arab. J. Geosci. (CAJG-1), Tunisia 2018*, 211–214., 2019.
- McArthur, J. M., Howarth, R. J., and Shields, G. A.: Strontium Isotope Stratigraphy, in: *The Geologic Time Scale*, vol. 1–2, Elsevier, 127–144, ISBN 9780444594259, 2012.
- McCaig, A. M., Wayne, D. M., Marshall, J. D., Banks, D., and Henderson, I.: Isotopic and fluid inclusion studies of fluid movement along the Gavarnie Thrust, central Pyrenees; reaction fronts in carbonate mylonites, *Am. J. Sci.*, 295, 309–343, <https://doi.org/10.2475/ajs.295.3.309>, 1995.
- McCaig, A. M., Tritlla, J., and Banks, D.: Fluid mixing and recycling during Pyrenean thrusting: evidence from fluid inclusion halogen ratios, *Geochim. Cosmochim. Ac.*, 64, 3395–3412, [https://doi.org/10.1016/S0016-7037\(00\)00437-3](https://doi.org/10.1016/S0016-7037(00)00437-3), 2000a.
- McCaig, A. M., Wayne, D. M., and Rosenbaum, J. M.: Fluid expulsion and dilatancy pumping during thrusting in the Pyrenees: Pb and Sr isotope evidence, *Geol. Soc. Am. Bull.*, 112, 1199–1208, [https://doi.org/10.1130/0016-7606\(2000\)112<1199:FEADPD>2.0.CO;2](https://doi.org/10.1130/0016-7606(2000)112<1199:FEADPD>2.0.CO;2), 2000b.
- Mey, P. H. W.: The geology of the upper Ribagorzana and Baliera Valleys, Central Pyrenees, Spain, *Leidse Geol. Meded.*, 41, 153–220, 1967.
- Mey, P. H. W., Nagtegaal, P. J. C., Roberti, K. J., and Hartevelt, J. J. A.: Lithostratigraphic subdivision of Post-Hercynian deposits in the South-Central Pyrenees, Spain, *Leidse Geol. Meded.*, 41, 221–228, 1968.
- Mouthereau, F., Filleaudeau, P. Y., Vacherat, A., Pik, R., Lacombe, O., Fellin, M. G., Castellort, S., Christophoul, F.,

- and Masini, E.: Placing limits to shortening evolution in the Pyrenees: Role of margin architecture and implications for the Iberia/Europe convergence, *Tectonics*, 33, 2283–2314, <https://doi.org/10.1002/2014TC003663>, 2014.
- Mozafari, M., Swennen, R., Balsamo, F., El Desouky, H., Storti, F., and Taberner, C.: Fault-controlled dolomitization in the Montagna dei Fiori Anticline (Central Apennines, Italy): record of a dominantly pre-orogenic fluid migration, *Solid Earth*, 10, 1355–1383, <https://doi.org/10.5194/se-10-1355-2019>, 2019.
- Muñoz, J. A.: Evolution of a continental collision belt: ECORS-Pyrenees crustal balanced cross-section, in: *Thrust Tectonics*, Springer Netherlands, Dordrecht, 235–246, ISBN 978-0-412-43900-1, 1992.
- Muñoz, J. A.: Fault-related folds in the southern Pyrenees, *Am. Assoc. Petr. Geol. B.*, 101, 579–587, <https://doi.org/10.1306/011817D1G17037>, 2017.
- Muñoz, J. A., Martínez, A. and Verges, J.: Thrust sequences in the eastern Spanish Pyrenees, *J. Struct. Geol.*, 8, 399–405, 1986.
- Muñoz-López, D., Cruset, D., Cantarero, I., Benedicto, A., John, C. M., and Travé, A.: Fluid Dynamics in a Thrust Fault Inferred from Petrology and Geochemistry of Calcite Veins: An Example from the Southern Pyrenees, *Geofluids*, 2020, 8815729, <https://doi.org/10.1155/2020/8815729>, 2020.
- Nardini, N., Muñoz-López, D., Cruset, D., Cantarero, I., Martín-Martín, J., Benedicto, A., Gomez-Rivas, E., John, C., and Travé, A.: From Early Contraction to Post-Folding Fluid Evolution in the Frontal Part of the Bóixols Thrust Sheet (Southern Pyrenees) as Revealed by the Texture and Geochemistry of Calcite Cements, *Minerals*, 9, 117, 1–29, <https://doi.org/10.3390/min9020117>, 2019.
- Nelson, S. T., Mayo, A. L., Gilfillan, S., Dutson, S. J., Harris, R. A., Shipton, Z. K., and Tingey, D. G.: Enhanced fracture permeability and accompanying fluid flow in the footwall of a normal fault: The Hurricane fault at Pah Tempe hot springs, Washington County, Utah, *Geol. Soc. Am. Bull.*, 121, 236–246, <https://doi.org/10.1130/B26285.1>, 2009.
- Pfeifer, H.-R., Oberhänsli, H., and Epprecht, W.: Geochemical evidence for a synsedimentary hydrothermal origin of Jurassic iron-manganese deposits at Gonzen (Sargans, Helvetic Alps, Switzerland), *Mar. Geol.*, 84, 257–272, [https://doi.org/10.1016/0025-3227\(88\)90105-3](https://doi.org/10.1016/0025-3227(88)90105-3), 1988.
- Piessens, K., Muechez, P., Dewaele, S., Boyce, A., De Vos, W., Sintubin, M., Debacker, T. N., Burke, E. A. J., and Viaene, W.: Fluid flow, alteration and polysulphide mineralisation associated with a low-angle reverse shear zone in the Lower Palaeozoic of the Anglo-Brabant fold belt, Belgium, *Tectonophysics*, 348, 73–92, [https://doi.org/10.1016/S0040-1951\(01\)00250-5](https://doi.org/10.1016/S0040-1951(01)00250-5), 2002.
- Poblet, J.: Estructura herciniana i alpina del vessant sud de la zona axial del Pirineu centra, Universitat de Barcelona, 604 pp., 1991.
- Pomerol, B.: Geochemistry of the late Cenomanian-early Turonian chalks of the Paris Basin: Manganese and carbon isotopes in carbonates as paleoceanographic indicators, *Cretaceous Res.*, 4, 85–93, [https://doi.org/10.1016/0195-6671\(83\)90025-3](https://doi.org/10.1016/0195-6671(83)90025-3), 1983.
- Pratt, L. M., Force, E. R., and Pomerol, B.: Coupled manganese and carbon-isotopic events in marine carbonates at the Cenomanian-Turonian boundary, *J. Sediment. Petrol.*, 61, 370–383, <https://doi.org/10.1306/D4267717-2B26-11D7-8648000102C1865D>, 1991.
- Roca, E.: The Neogene Cerdanya and Seu d'Urgell intramontane basins (Eastern Pyrenees), in: *Tertiary basins of Spain*, edited by: Friend, P. F. and Dabrio, C. J., Cambridge University Press, Cambridge, 114–119, 1996.
- Roca, E. and Guimerà, J.: The Neogene structure of the eastern Iberian margin: Structural constraints on the crustal evolution of the Valencia trough (western Mediterranean), *Tectonophysics*, 203, 203–218, [https://doi.org/10.1016/0040-1951\(92\)90224-T](https://doi.org/10.1016/0040-1951(92)90224-T), 1992.
- Roure, F., Choukroune, P., Berastegui, X., Muñoz, J. A., Villien, A., Matheron, P., Bareyt, M., Seguret, M., Camara, P., and Deramond, J.: Ecors deep seismic data and balanced cross sections: Geometric constraints on the evolution of the Pyrenees, *Tectonics*, 8, 41–50, <https://doi.org/10.1029/TC008i001p00041>, 1989.
- Rowland, J. V. and Sibson, R. H.: Structural controls on hydrothermal flow in a segmented rift system, Taupo Volcanic Zone, New Zealand, *Geofluids*, 4, 259–283, <https://doi.org/10.1111/j.1468-8123.2004.00091.x>, 2004.
- Rye, D. M. and Bradbury, H. J.: Fluid flow in the crust; an example from a Pyrenean thrust ramp, *Am. J. Sci.*, 288, 197–235, <https://doi.org/10.2475/ajs.288.3.197>, 1988.
- Saura, E.: Anàlisi estructural de la Zona de les Nogues (Pirineus Centrals), PhD thesis, Universitat de Barcelona, 398 pp., 2004.
- Saura, E. and Teixell, A.: Inversion of small basins: effects on structural variations at the leading edge of the Axial Zone antiformal stack (Southern Pyrenees, Spain), *J. Struct. Geol.*, 28, 1909–1920, <https://doi.org/10.1016/j.jsg.2006.06.005>, 2006.
- Shenton, B. J., Grossman, E. L., Passey, B. H., Henkes, G. A., Becker, T. P., Laya, J. C., Perez-Huerta, A., Becker, S. P., and Lawson, M.: Clumped isotope thermometry in deeply buried sedimentary carbonates: The effects of bond reordering and recrystallization, *Geol. Soc. Am. Bull.*, 127, B31169.1, <https://doi.org/10.1130/B31169.1>, 2015.
- Sibson, R. H.: Crustal stress, faulting and fluid flow, *Geol. Soc. London, Spec. Publ.*, 78, 69–84, <https://doi.org/10.1144/GSL.SP.1994.078.01.07>, 1994.
- Sibson, R. H.: Selective fault reactivation during basin inversion: potential for fluid redistribution through fault-valve action, *Geol. Soc. London, Spec. Publ.*, 88, 3–19, <https://doi.org/10.1144/GSL.SP.1995.088.01.02>, 1995.
- Sibuet, J.-C., Srivastava, S. P. and Spakman, W.: Pyrenean orogeny and plate kinematics, *J. Geophys. Res.*, 109, 1–18, <https://doi.org/10.1029/2003JB002514>, 2004.
- Srivastava, S. P., Schouten, H., Roest, W. R., Klitgord, K. D., Kovacs, L. C., Verhoeft, J., and Macnab, R.: Iberian plate kinematics: A jumping plate boundary between Eurasia and Africa, *Nature*, 344, 756–759, <https://doi.org/10.1038/344756a0>, 1990.
- Stolper, D. A. and Eiler, J. M.: The kinetics of solid-state isotope-exchange reactions for clumped isotopes: A study of inorganic calcites and apatites from natural and experimental samples, *Am. J. Sci.*, 315, 363–411, <https://doi.org/10.2475/05.2015.01>, 2015.
- Suchy, V., Heijnen, W., Sykorova, I., Muechez, P., Dobes, P., Hladikova, J., Jackova, I., Safanda, J., and Zeman, A.: Geochemical study of calcite veins in the Silurian and Devonian of the Barrandian Basin (Czech Republic): evidence for widespread post-Variscan fluid flow in the central part of the Bohemian Massif, *Sediment. Geol.*, 131, 201–219, [https://doi.org/10.1016/S0037-0738\(99\)00136-0](https://doi.org/10.1016/S0037-0738(99)00136-0), 2000.

- Taillefer, A., Soliva, R., Guillou-Frottier, L., Le Goff, E., Martin, G., and Seranne, M.: Fault-Related Controls on Upward Hydrothermal Flow: An Integrated Geological Study of the Têt Fault System, Eastern Pyrénées (France), *Geofluids*, vol. 2017, 1–19, <https://doi.org/10.1155/2017/8190109>, 2017.
- Taillefer, A., Guillou-Frottier, L., Soliva, R., Magri, F., Lopez, S., Courrioux, G., Millot, R., Ladouche, B., and Le Goff, E.: Topographic and Faults Control of Hydrothermal Circulation Along Dormant Faults in an Orogen, *Geochem. Geophys. Geosy.*, 19, 4972–4995, <https://doi.org/10.1029/2018GC007965>, 2018.
- Taylor, B. D.: Stable isotope geochemistry of the ore forming fluids, edited by: Kyser, T. K.: *Mineralogical Association of Canada*, 13, 337–445, 1987.
- Travé, A., Labaume, P., Calvet, F., and Soler, A.: Sediment dewatering and pore fluid migration along thrust faults in a foreland basin inferred from isotopic and elemental geochemical analyses (Eocene southern Pyrenees, Spain), *Tectonophysics*, 282, 375–398, [https://doi.org/10.1016/S0040-1951\(97\)00225-4](https://doi.org/10.1016/S0040-1951(97)00225-4), 1997.
- Travé, A., Labaume, P., Calvet, F., Soler, A., Tritilla, J., Buatier, M., Potdevin, J.-L., Séguret, M., Raynaud, S., and Briquieu, L.: Fluid migration during Eocene thrust emplacement in the south Pyrenean foreland basin (Spain): an integrated structural, mineralogical and geochemical approach, *Geol. Soc. London, Spec. Publ.*, 134, 163–188, <https://doi.org/10.1144/GSL.SP.1998.134.01.08>, 1998.
- Travé, A., Calvet, F., Sans, M., Vergés, J., and Thirlwall, M.: Fluid history related to the Alpine compression at the margin of the south-Pyrenean Foreland basin: the El Guix anticline, *Tectonophysics*, 321, 73–102, [https://doi.org/10.1016/S0040-1951\(00\)00090-1](https://doi.org/10.1016/S0040-1951(00)00090-1), 2000.
- Travé, A., Labaume, P., and Vergés, J.: Fluid Systems in Foreland Fold-and-Thrust Belts: An Overview from the Southern Pyrenees, in: *Thrust Belts and Foreland Basins*, edited by: Lacombe, O., Roure, F., Lavé, J., and Vergés, J., Springer Berlin Heidelberg, Berlin, Heidelberg, 93–115, ISBN 978-3-540-69426-7, 2007.
- Travé, A., Roca, E., Playà, E., Parcerisa, D., Gómez-Gras, D., and Martín-Martín, J. D.: Migration of Mn-rich fluids through normal faults and fine-grained terrigenous sediments during early development of the Neogene Vallès-Penedès half-graben (NE Spain), *Geofluids*, 9, 303–320, <https://doi.org/10.1111/j.1468-8123.2009.00258.x>, 2009.
- Trincal, V., Buatier, M., Charpentier, D., Lacroix, B., Lanari, P., Labaume, P., Lahfid, A., and Vennemann, T.: Fluid–rock interactions related to metamorphic reducing fluid flow in meta-sediments: example of the Pic-de-Port-Vieux thrust (Pyrenees, Spain), *Contrib. Mineral. Petr.*, 172, 78, <https://doi.org/10.1007/s00410-017-1394-5>, 2017.
- Veizer, J.: Depositional and diagenetic history of limestones: Stable and radiogenic isotopes, in: *Isotopic Signatures and Sedimentary Records*, edited by: Clauer, N. and Chaudhuri, S., Springer-Verlag, Berlin, Heidelberg, 43, 13–48, ISBN 978-3-540-47294-0, 1992.
- Veizer, J., Ala, D., Azmy, K., Bruckschen, P., Buhl, D., Bruhn, F., Carden, G. A. F., Diener, A., Ebner, S., Godderis, Y., Jasper, T., Korte, C., Pawellek, F., Podlaha, O. G., and Strauss, H.: $^{87}\text{Sr}/^{86}\text{Sr}$, $\delta^{13}\text{C}$ and $\delta^{18}\text{O}$ evolution of Phanerozoic seawater, *Chem. Geol.*, 161, 59–88, [https://doi.org/10.1016/S0009-2541\(99\)00081-9](https://doi.org/10.1016/S0009-2541(99)00081-9), 1999.
- Vergés, J.: *Estudi geològic del vessant Sud del Pirineu Oriental i Central: Evolució cinemàtica en 3D*, PhD thesis, University of Barcelona, Barcelona, 203 pp., 1993.
- Vergés, J. and Fernández, M.: Tethys–Atlantic interaction along the Iberia–Africa plate boundary: The Betic–Rif orogenic system, *Tectonophysics*, 579, 144–172, <https://doi.org/10.1016/j.tecto.2012.08.032>, 2012.
- Vergés, J. and Muñoz, J. A.: Thrust sequences in the southern central Pyrenees, *Bull. French Geol. Soc.*, 2, 265–271, 1990.
- Vergés, J., Fernández, M., and Martínez, A.: The Pyrenean orogen: pre-, syn-, and post-collisional evolution, *J. Virtual Explor.*, 8, p. 4, <https://doi.org/10.3809/jvirtex.2002.00058>, 2002.
- Vilasi, N., Swennen, R., and Roure, F.: Diagenesis and fracturing of Paleocene-Eocene carbonate turbidite systems in the Ionian Basin: The example of the Kelçyra area (Albania), *J. Geochem. Explor., Spec. Iss.*, 89, 409–413, <https://doi.org/10.1016/j.gexplo.2005.11.018>, 2006.
- Voicu, G., Bardoux, M., Stevenson, R., and Jébrak, M.: Nd and Sr isotope study of hydrothermal scheelite and host rocks at Omai, Guiana Shield: implications for ore fluid source and flow path during the formation of orogenic gold deposits, *Miner. Deposita*, 35, 302–314, <https://doi.org/10.1007/s001260050243>, 2000.
- Warren, J., Morley, C. K., Charoentitirat, T., Cartwright, I., Ampaiwan, P., Khositichaisri, P., Mirzaloo, M., and Yingyuen, J.: Structural and fluid evolution of Saraburi Group sedimentary carbonates, central Thailand: A tectonically driven fluid system, *Mar. Petrol. Geol.*, 55, 100–121, <https://doi.org/10.1016/j.marpetgeo.2013.12.019>, 2014.
- Wayne, D. M. and McCaig, A. M.: Dating fluid flow in shear zones: Rb–Sr and U–Pb studies of syntectonic veins in the Néouvielle Massif, Pyrenees, *Geol. Soc. London, Spec. Publ.*, 144, 129–135, <https://doi.org/10.1144/GSL.SP.1998.144.01.09>, 1998.
- Williams, R. T., Goodwin, L. B., Mozley, P. S., Beard, B. L., and Johnson, C. M.: Tectonic controls on fault zone flow pathways in the rio grande rift, New Mexico, USA, *Geology*, 43, 723–726, <https://doi.org/10.1130/G36799.1>, 2015.
- Ziegler, P. A.: Evolution of the Arctic–North Atlantic and the Western Tethys, *Am. Assoc. Petr. Geol. B.*, 43, 200 pp., ISBN 9781629811338, 1988.
- Zwart, H. J.: The variscan geology of the Pyrenees, *Tectonophysics*, 129, 9–27, [https://doi.org/10.1016/0040-1951\(86\)90243-X](https://doi.org/10.1016/0040-1951(86)90243-X), 1986.

Article 2

Muñoz-López, D., Cruset, D., Cantarero, I., Benedicto, A., John, C. M., and Travé, A., 2020: Fluid dynamics in a thrust fault inferred from petrology and geochemistry of calcite veins: An example from the Southern Pyrenees, *Geofluids* 2020, 1-25. <https://doi.org/10.1155/2020/8815729>. Impact factor: 1.534. Position: Q2 (77/187) in General Earth and Planetary Sciences (2020).

Research Article

Fluid Dynamics in a Thrust Fault Inferred from Petrology and Geochemistry of Calcite Veins: An Example from the Southern Pyrenees

Daniel Muñoz-López ¹, David Cruset,² Irene Cantarero ¹, Antonio Benedicto,³ Cédric M. John,⁴ and Anna Travé¹

¹Departament de Mineralogia, Petrologia i Geologia Aplicada, Facultat de Ciències de la Terra, Universitat de Barcelona (UB), Martí i Franquès s/n, 08028 Barcelona, Spain

²Group of Dynamics of the Lithosphere (GDL), Geosciences Barcelona, GEO3BCN-CSIC, Lluís Solé i Sabarís s/n, 08028 Barcelona, Spain

³UMR CNR GEOPS, Université Paris-Saclay, 91405 Orsay, France

⁴Department of Earth Science and Engineering, Imperial College London, London SW7 2BP, UK

Correspondence should be addressed to Daniel Muñoz-López; munoz-lopez@ub.edu

Received 8 April 2020; Revised 10 August 2020; Accepted 2 September 2020; Published 25 September 2020

Academic Editor: Paul D. Bons

Copyright © 2020 Daniel Muñoz-López et al. This is an open access article distributed under the Creative Commons Attribution License, which permits unrestricted use, distribution, and reproduction in any medium, provided the original work is properly cited.

Petrographic and geochemical analyses ($\delta^{18}\text{O}$, $\delta^{13}\text{C}$, $^{87}\text{Sr}/^{86}\text{Sr}$, clumped isotopes, and elemental composition) coupled with field structural data of synkinematic calcite veins, fault rocks, and host rocks are used to reconstruct the episodic evolution of an outstanding exposed thrust zone in the Southern Pyrenees and to evaluate the fault behavior as a conduit or barrier to fluid migration. The selected thrust displaces the steeply dipping southern limb of the Sant Corneli-Bóixols anticline, juxtaposing a Cenomanian-Turonian carbonate unit against a Coniacian carbonate sequence. Successive deformation events are recorded by distinct fracture systems and related calcite veins, highlighting (i) an episodic evolution of the thrust zone, resulting from an upward migration of the fault tip (process zone development) before growth of the fault (thrust slip plane propagation), and (ii) compartmentalization of the thrust fault zone, leading to different structural and fluid flow histories in the footwall and hanging wall. Fractures within the footwall comprise three systematically oriented fracture sets (F1, F2, and F3), each sealed by a separate generation calcite cement, and a randomly oriented fracture system (mosaic to chaotic breccia), cemented by the same cements as fracture sets F1 and F2. The formation of fractures F1 and F2 and the mosaic to chaotic breccia is consistent with dilatant fracturing within the process zone (around the fault tip) during initial fault growth, whereas the formation of the latest fracture system points to hybrid shear-dilatational failure during propagation of the fault. The continuous formation of different fracture systems and related calcite cementation phases evidences that the structural permeability in the footwall was transient and that the fluid pathways and regime evolved due to successive events of fracture opening and calcite cementation. Clumped isotopes evidence a progressive increase in precipitation temperatures from around 50°C to 117°C approximately, interpreted as burial increase linked to thrust sheet emplacement. During this period, the source of fluid changed from meteoric fluids to evolved meteoric fluids due to the water-rock interaction at increasing depths and temperatures. Contrary to the footwall, within the hanging wall, only randomly oriented fractures are recognized and the resulting crackle proto-breccia is sealed by a later and different calcite cement, which is also observed in the main fault plane and in the fault core. This cement precipitated from formation fluids, at around 95°C, that circulated along the fault core and in the hanging wall block, again supporting the interpretation of compartmentalization of the thrust structure. The integration of these data reveals that the studied thrust fault acted as a transverse barrier, dividing the thrust zone into two separate fluid compartments, and a longitudinal drain for migration of fluids. This study also highlights the similarity in deformation processes and mechanisms linked to the evolution of fault zones in compressional and extensional regimes involving carbonate rocks.

1. Introduction

The study of outcrop analogues in fractured carbonate reservoirs is important to better understand the characteristics and evolution of synkinematic fracture systems and their control on fluid migration during crustal deformation [1–4]. In areas undergoing compressional regimes, the largest fluid fluxes, mass transfer, and heat transport commonly occur along the main thrust faults and related fracture networks because of the loading induced by thrust sheet emplacement [5–7]. By contrast, fluid flow rates in adjacent rock-matrix and poorly connected synkinematic fractures are commonly very low and fluid composition are often rock-buffered [6, 8]. In some cases, the development of thrust systems may also inhibit vertical fluid transport inducing fluid overpressure [9–11] leading to hydraulic fracturing [12–14]. Whether a fault zone will constitute either a conduit or barrier to fluid migration depends, among other factors, on the architecture of the fault zone and the permeability associated with the developed structures [15, 16]. Since the fault zone consists of a fault core, which is usually formed of low-permeability fault rocks, and a damage zone, which mainly includes extensional fractures and faults, overall permeability of the fault is conditioned by the amount, the spatial distribution, and the internal composition of these two fault zone elements [15, 17]. Besides, such structural permeability is dynamic and may vary spatially and temporally across the fault zone due to successive episodes of fracture opening and cementation [18, 19].

Although numerous studies based primarily on structural and numerical data have provided conceptual and analytical models on the architecture, mechanical properties, and fluid flow along fault zones [7, 15, 20], there exist only a few studies coupling field data and geochemistry of synkinematic minerals filling fractures that characterize the fluid migration through a thrust zone [21–25] and its spatial behavior as a conduit or barrier system [26, 27]. An outstanding exposed thrust in the Southern Pyrenees was chosen as a case study to evaluate qualitatively the fault-related permeability and its control on the fluid flow within and around the fault zone. Here, we combine structural, petrological, and geochemical data of calcite veins and host rocks present in the studied thrust zone. Therefore, the main objectives of this paper are (i) to determine the origin, composition, and temperature of the vein-forming fluids and the timing of fluid migration in relation to the fracturing events and (ii) to discern the fluid pathways, the extent of fluid-rock interaction, and the transfer of fluids across a fault zone during thrusting. The field and lab results are then compared with other studies reporting fluid flow within fault zones in other geological settings to generalize our conclusions to fault zones in carbonate settings.

2. Geological Setting

The Pyrenees constitute an asymmetrical and doubly verging orogenic belt that resulted from the Alpine convergence between the Iberian and European plates from Late Cretaceous to Oligocene, causing the inversion of previous Mesozoic rift basins and their incorporation into the thrust

system [28–32]. The Pyrenean structure consists of a central antiformal stack of basement-involved thrust sheets from the axial zone [30], flanked by two oppositely vergent fold-and-thrust belts and their related Cenozoic Aquitaine and Ebro foreland basins [30, 33] (Figure 1(a)).

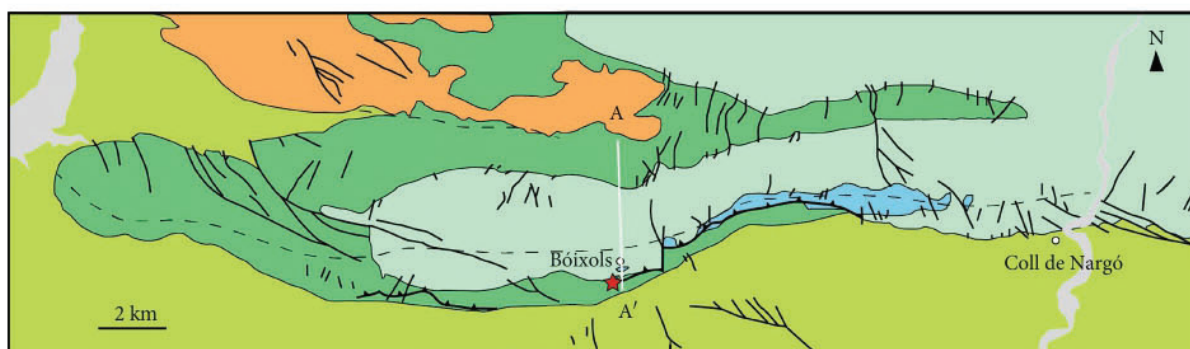
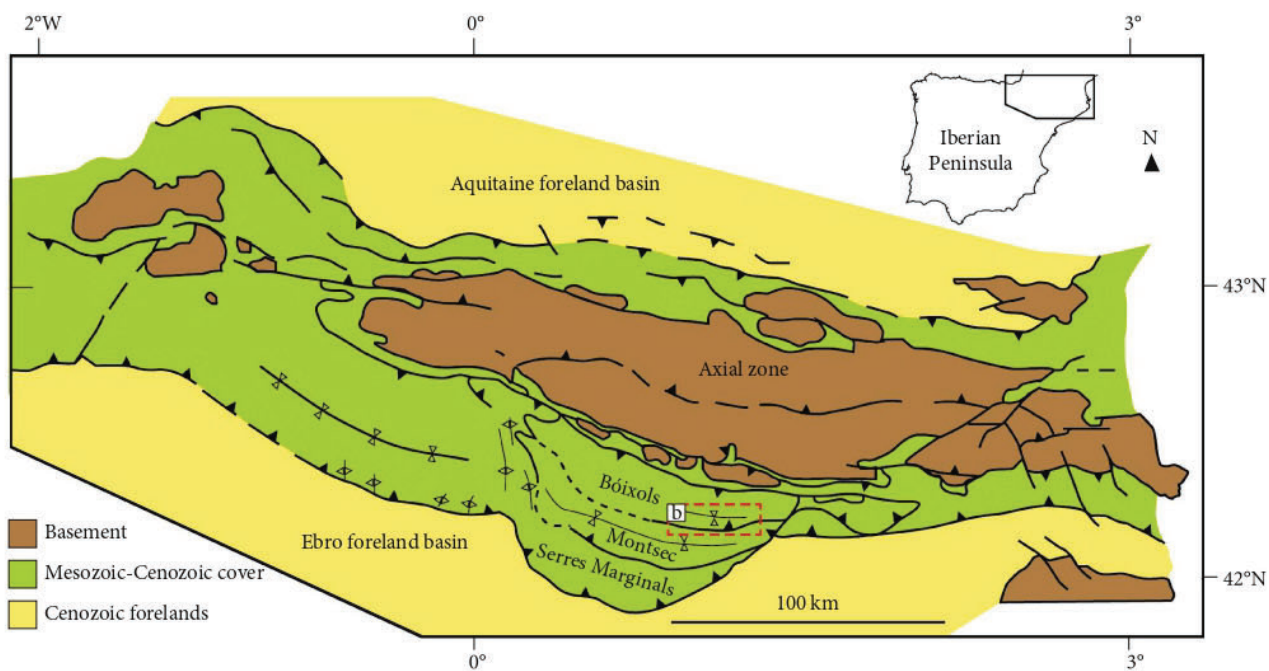
The South Pyrenean fold-and-thrust belt comprises a piggy-back imbrication of south verging and east-west striking thrust sheets involving Mesozoic and Tertiary cover rocks detached above Late Triassic evaporites [34] and transported southwards over the Ebro foreland basin. From north to south, they are the Bóixols thrust sheet, emplaced during the Late Cretaceous to Paleocene, the Montsec thrust sheet, originated during the Paleocene to late Ypresian, and the Serres Marginals thrust sheet, formed during the Lutetian-Oligocene [35, 36] (Figure 1(a)). In the frontal part of the Bóixols thrust sheet, a south verging and east-west trending fault-related anticline developed in relation to the propagation of the Bóixols thrust (the Sant Corneli-Bóixols anticline; Figures 1(b) and 1(c)). It is characterized by a gently dipping northern backlimb and a vertical to overturned southern forelimb [37].

Rocks cropping out along the Bóixols anticline comprise a large stratigraphic record ranging in age from Jurassic to Oligocene and deposited during the main tectonic events that affected the study area [38] (Figures 1(b) and 2). The stratigraphic sequence includes prerift Jurassic limestones and dolostones, synrift Lower Cretaceous limestones, marls and clays, preorogenic (postrift) Late Cenomanian to Santonian limestones, sandy limestones and marls and synorogenic Late Santonian to Oligocene marls and clays, sandstones, sandy limestones, and conglomerates ([38] and references therein).

In the central part of this anticline, the southern tilted forelimb is offset by minor low-dipping south-directed thrusts developed after the main folding phase, as evidenced by the displacement of already folded beds [38–40]. Therefore, they have been interpreted as postfolding accommodation structures or as hanging wall splays of the main Bóixols thrust [39, 40, 42]. One of these minor thrust faults is well exposed 2 km southeast of the Bóixols village (15 km of the L511 road), in the southern-central Pyrenees (Figure 3), exhibiting a complex calcite-filled fracture network developed in the fault core and damage zone of both the footwall and hanging wall of this reverse fault. This outcrop represents an exceptional field analogue to observe in a 300 m long outcrop the variation in deformation mechanisms developed across a fault zone and its contribution as seal or conduit for fluids. In this area, the studied thrust juxtaposes the Upper Cretaceous Santa Fe Formation against the Collada Gassó Formation (Figures 2 and 3). The Collada Gassó Formation [43] is formed of Coniacian grainstones with the variable presence of quartz, marly limestones, and limestones with abundant fossil content and has a general thickness of 150 to 250 m [38]. The Santa Fe Formation [44] is basically constituted of Cenomanian-Turonian limestones with a general thickness of 20 m [38].

3. Methodology

This study combines field structural data, including bedding and fracture orientation and dips, fracture type identification,



- Village
 - ★ Outcrop
 - Fold trace
 - Paleocene-Oligocene syn-orogenic sequence
 - Santonian-Eocene syn-orogenic sequence
 - Cenomanian-Santonian pre-orogenic (post-rift) sequence
 - Lower Cretaceous syn-rift sequence
 - Jurassic pre-rift sequence
- (b)

FIGURE 1: Continued.

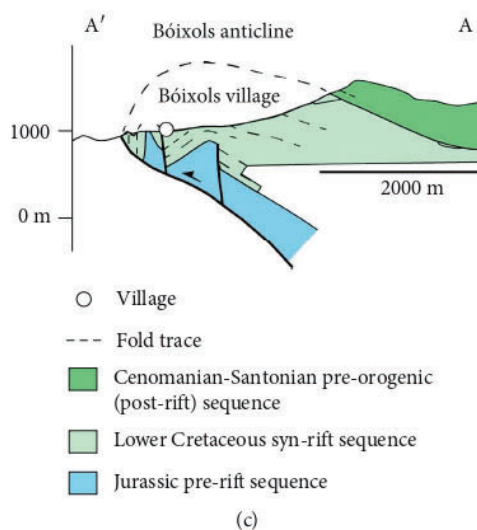


FIGURE 1: (a) Simplified geological map of the Pyrenees (modified from [32]). (b) Geological map of the Sant Corneli-Bóixols anticline showing the studied outcrop (modified from [38, 39]). (c) N-S cross section of the Sant Corneli-Bóixols anticline (modified from [40]). Location is shown in (b).

kinematics, and crosscutting relationships, with petrological and geochemical analyses. Structural data were plotted in equal-area lower-hemisphere projections, and different fracture sets were established according to their type, strike, orientation respect to bedding, mineral infillings, and relative age deduced from crosscutting relationships. Representative samples of each fracture generation and related host rocks were sampled in order to perform petrological and geochemical analyses. Thin sections were prepared and studied under optical and cathodoluminescence microscopes at the Facultat de Ciències de la Terra of the Universitat de Barcelona, using a Zeiss Axiophot optical microscope and a Technosyn Cold Cathodoluminescence microscope, model 8200 Mk5-1 operating between 16–19 kV and 350 μ A gun current.

Thirty-one samples of calcite cements and host rocks were sampled for carbon and oxygen isotopic analysis using a 500 μ m-diameter dental drill. Around 50–100 μ g of each sample was reacted with 100% phosphoric acid for two minutes at 70°C. The resultant CO_2 was analyzed with an automated Kiel Carbonate Device attached to a Thermal Ionization Mass Spectrometer Thermo Electron MAT-252 (Thermo Fisher Scientific) following the method of [45]. The International Standard NBS-18 and the internal standard RC-1, traceable to the International Standard NBS-19, were used for calibration. The standard deviation is $\pm 0.03\%$ for $\delta^{13}\text{C}$ and $\pm 0.05\%$ for $\delta^{18}\text{O}$ expressed with respect to the VPDB standard (Vienna Pee Dee Belemnite). Analyses were carried out at “Centre Científics i Tecnològics” of the Universitat de Barcelona (CCiTUB).

The elemental composition of the calcite cements and related host rocks (12 samples in total) was analyzed with a high-resolution inductively coupled plasma-mass spectrometer (HR-ICP-MS, model Element XR, Thermo Fisher Scientific). Around 100 mg of each sample was extracted with a 400/500 μ m-diameter dental drill, and then, powdered samples were dried at 40°C for 24 h. Then, 100 mg of sample

was acid digested in closed polytetrafluoroethylene (PTFE) vessels with a combination of $\text{HNO}_3 + \text{HF} + \text{HClO}_4$ (2.5 mL : 5 mL : 2.5 mL v/v/v). The samples were evaporated, and 1 mL of HNO_3 was added to make a double evaporation. Finally, the samples were redissolved and diluted with Milli-Q water ($18.2 \text{ M}\Omega \text{ cm}^{-1}$) and 1 mL of HNO_3 in a 100 mL volume flask. In order to improve the sensitivity of the ICP-MS, a tuning solution containing 1 g L^{-1} Li, B, Na, K, Sc, Fe, Co, Cu, Ga, Y, Rh, In, Ba, Tl, and U was used, and as internal standard, 20 mg L^{-1} of a mono-elemental solution of ^{115}In was used. Reference materials are the BCS-CRM no. 393 (ECRM 752-1) limestone, JA-2 andesite, and JB-3 basalt. The precision of the results was expressed in terms of two standard deviations of a set of eight reference material measurements (reference material JA-2), whereas accuracy (%) was calculated using the absolute value of the difference between the measured values obtained during the analysis and the certified values of a set of eight reference material analysis (reference material BCS-CRM no. 393 for major oxides and JA-2 for trace elements). The detection limit (DL) was calculated as three times the standard deviation of the average of ten blanks. Analyses were performed at the Geochemistry Facility of labGEOTOP of Geoscience Barcelona (GEO3BCN-CSIC).

The $^{87}\text{Sr}/^{86}\text{Sr}$ isotope ratios were analyzed in calcite cements and host rocks (9 samples). Powdered samples were fully dissolved in 5 mL of 10% acetic acid. After centrifugation, the supernatant was dried and dissolved in 1 mL of 1 M HNO_3 . The resulted solid residue, generated after evaporation, was diluted in 3 mL of 3 M HNO_3 and loaded into chromatographic columns to separate the Rb-free Sr fraction, by using SrResin™ (crown-ether (4,4'(5')-di-t-butylcyclohexano-18-crown-6)) and 0.05 M HNO_3 as eluent. After evaporation, samples were loaded onto a Re filament along with 1 μ L of 1 M phosphoric acid and 2 μ L of Ta_2O_5 . Isotopic ratio analyses were carried out in a TIMS-Phoenix mass

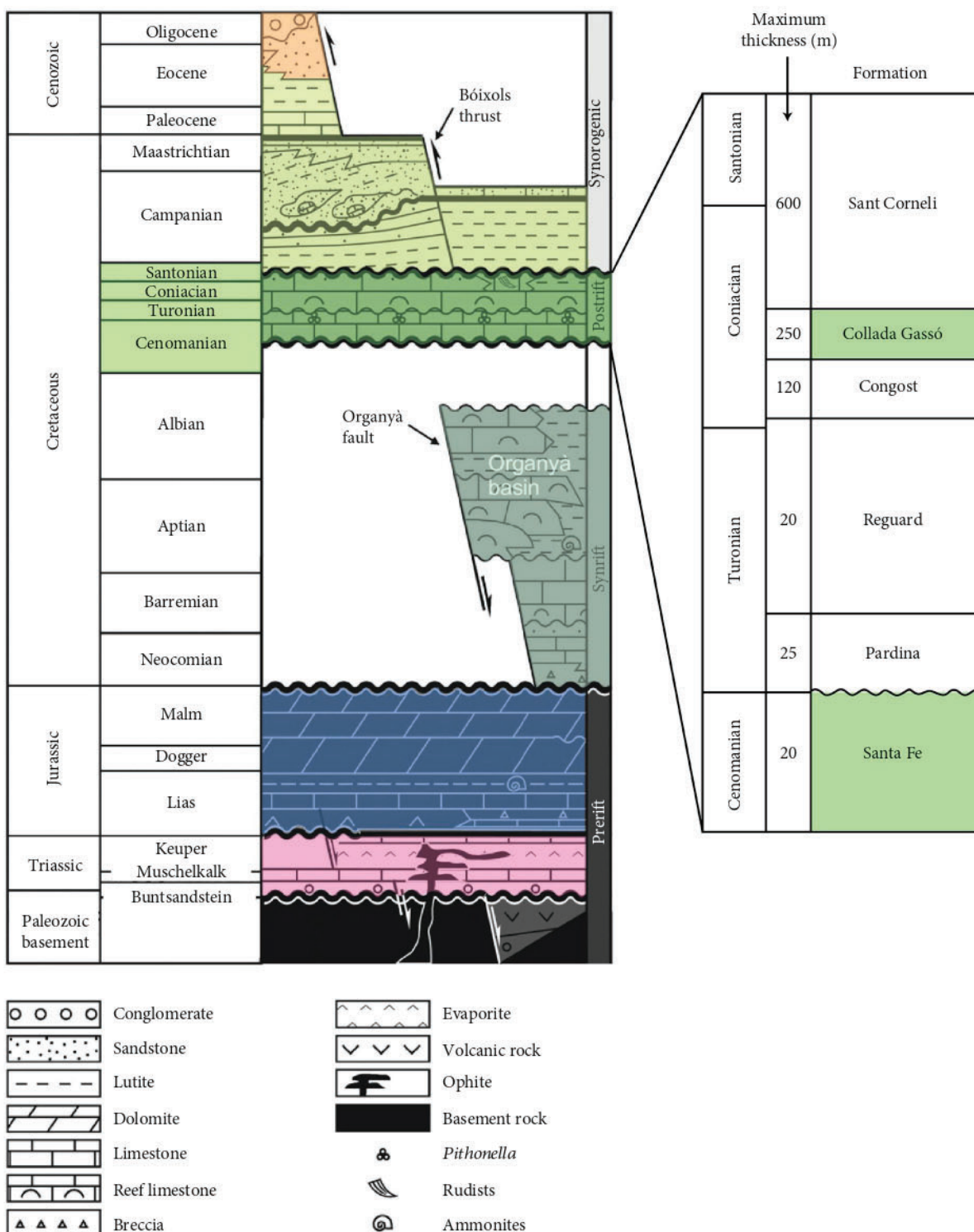


FIGURE 2: Chronostratigraphic diagram showing the main stratigraphic sequences and their related tectonic event [41]. The preorogenic (postrift) sequence, where the thrust was emplaced, is colored in green. The right panel shows a detail of the formations forming this sequence. Thickness and age of these formations are based on [38].

spectrometer (Isotopx) following a dynamic multicollection method, during 10 blocks of 16 cycles each one, maintaining a ⁸⁸Sr beam intensity of 3-V. Isotopic ratios were corrected for ⁸⁷Rb interferences and normalized using the reference

value of ⁸⁸Sr/⁸⁶Sr = 0.1194, in order to correct for the possible mass fractionation during loading and analysis of the sample. During sample analysis, the isotopic standard NBS-987 was analyzed six times, yielding an average value of 0.710243 ±

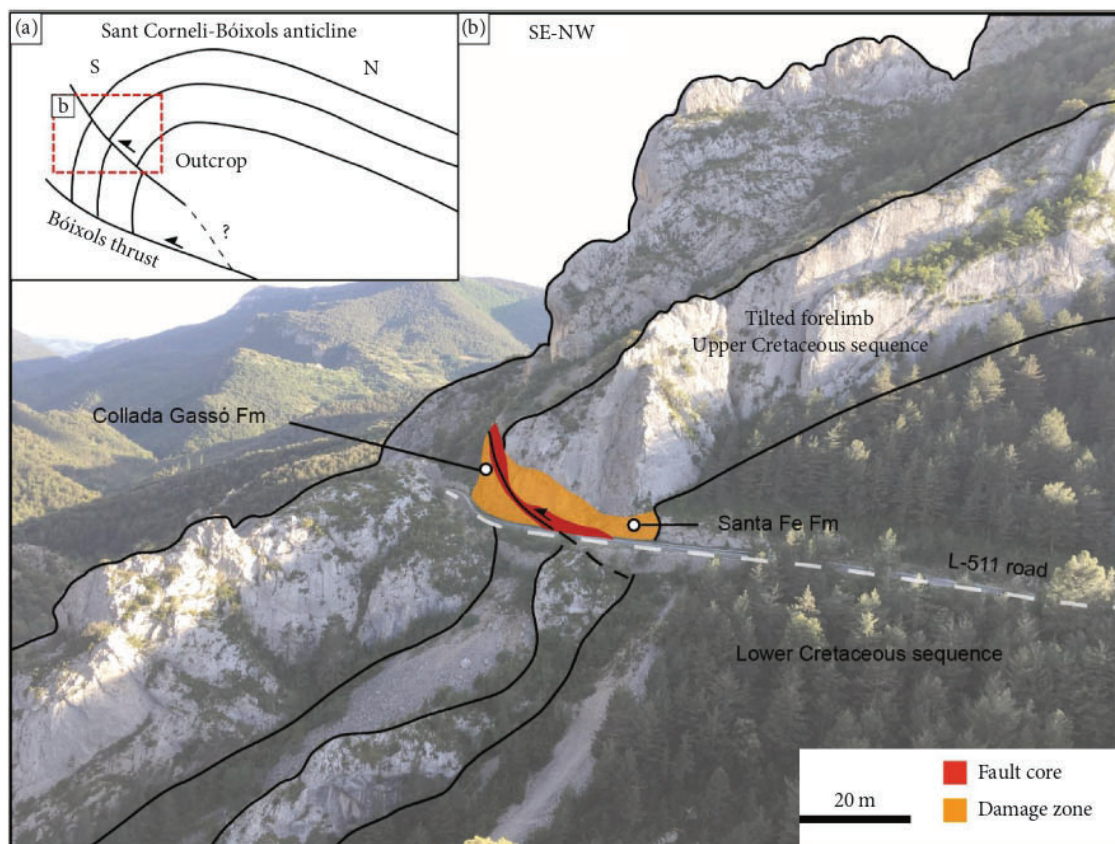


FIGURE 3: (a) Sketch and (b) panoramic view of the studied thrust offsetting the southern limb of the Sant Corneli-Bóixols anticline.

0.000009 (standard deviation, 2σ). NBS 987 data have been used to correct the sample ratios for standard drift from the certified value. The analytical error in the $^{87}\text{Sr}/^{86}\text{Sr}$ ratio, referred to two standard deviations, was 0.01%, whilst the internal precision is 0.000003. Sr procedural blanks were always below 0.5 ng. Analyses were carried out at the “CAI de Geocronología y Geoquímica Isotópica” of the Universidad Complutense de Madrid.

The $^{143}\text{Nd}/^{144}\text{Nd}$ isotope ratios were also analyzed in calcite cements and host rocks (9 samples in total). Samples were weighed in Teflon® vessels, with enriched spike solution (^{149}Sm - ^{150}Nd , Oak Ridge) and dissolved in 5 mL of ultrapure HF and 3 mL of ultrapure HNO_3 (Merck-Suprapur™). The PFA vessels were placed for 65 hours into an oven at 120°C . Then, cold vials were evaporated on a heat plate at 120°C . 4 mL of distilled 6N HCl was added to the dried samples and placed in an oven overnight at 120°C . The resulted solid residue, generated after evaporation, was dissolved in 3 mL of distilled and titrated 2.5N HCl. In order to separate the dissolved fraction from the residue, if any, samples were centrifuged for 10 minutes at 4000 rpm. Chromatographic separation of the total group of REE was performed using cation exchange resin DOWEX 50W-X8 200-400 mesh (previously calibrated). Then, recovered REE fractions were completely dried and again dissolved in $200\ \mu\text{L}$ 0.18N HCl. These solutions were passed in a new chromatographic step (Ln-resin) in order to obtain a complete separation between the Nd and the Sm fractions (using 0.3N HCl and 0.4N

HCl as eluent, respectively). Dried Sm and Nd samples dissolved with $2\ \mu\text{L}$ of 0.05 M phosphoric acid were loaded onto a side rhenium (Re) filament of a triple Re filament arrangement. Nd ratios were analyzed in a mass spectrometer TIMS-Phoenix®, following a dynamic multicollection method, through 160 cycles at a stable intensity of 1 V for the ^{144}Nd mass. In turn, Sm ratios were analyzed in the same spectrometer, following a single static method through 112 cycles maintaining 1 V intensity for the ^{149}Sm mass. Nd measurements were corrected for possible ^{142}Ce and ^{144}Sm interferences and they were normalized to a constant ratio of $^{146}\text{Nd}/^{144}\text{Nd} = 0.7219$ to correct the possible mass fractionation during the processes of loading and analyzing at the TIMS. Nd isotopic standard JNdi-1 was checked along with the samples to correct the sample ratios for standard drift from the certified value. The analytical error (2STD) in the $^{147}\text{Sm}/^{144}\text{Nd}$ ratio was 0.1% and in the $^{143}\text{Nd}/^{144}\text{Nd}$ ratio was 0.006%. Procedural blanks were always below 0.1 ng. Analyses were performed at the “CAI de Geocronología y Geoquímica Isotópica” of the Universidad Complutense de Madrid.

Clumped isotope thermometry was applied to four representative samples of the calcite cements Cc1 to Cc4 in order to determine the temperature and $\delta^{18}\text{O}_{\text{fluid}}$ in ‰VSMOW of the vein-forming fluids. Around 2–3 mg aliquots of powdered calcite cements was measured with an automated line developed at Imperial College London (the Imperial Batch Extraction system, IBEX). Samples were dropped in 105%

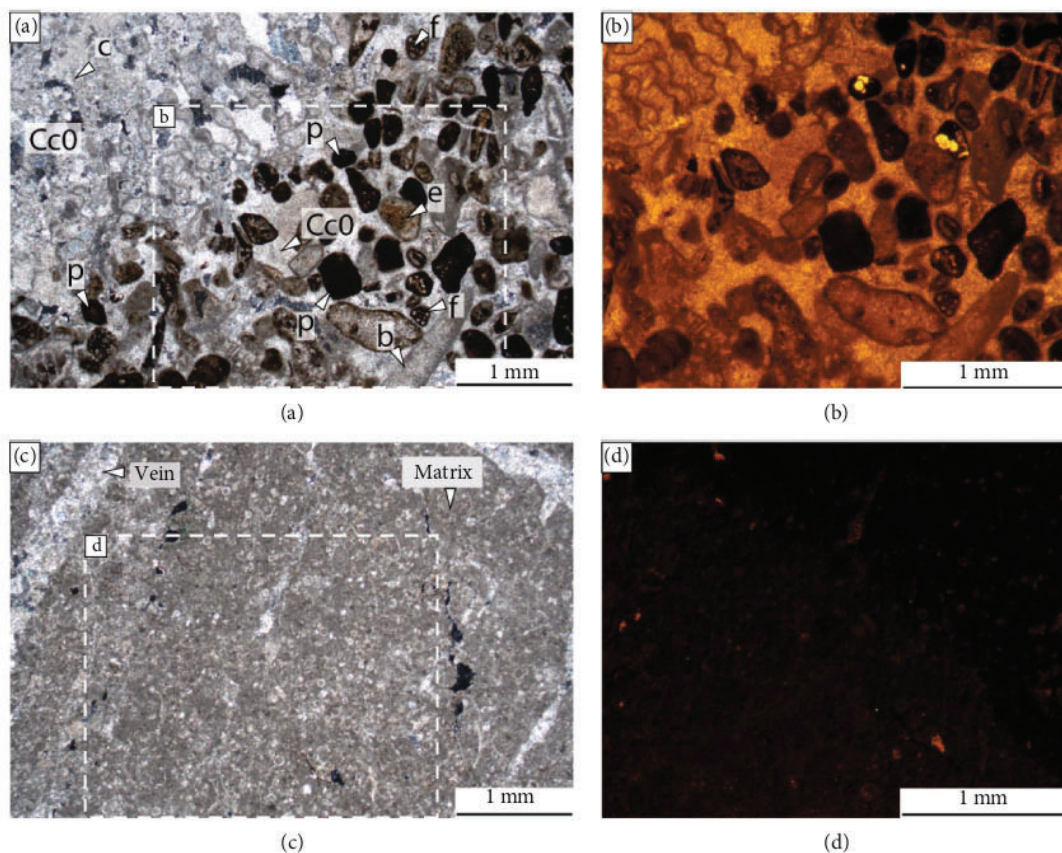


FIGURE 4: (a, b) Plane-polarized light and cathodoluminescence microphotographs of the footwall host rocks consisting of a grainstone made up of corals (c), foraminifers (f), bivalves (b), echinoids (e), and peloids (p), cemented by calcite (Cc0). (c, d) Plane-polarized light and cathodoluminescence microphotographs of the hanging wall host rocks composed of a wackestone of calcispheres and planktonic foraminifera.

phosphoric acid at 90°C and reacted for 30 minutes. The reactant CO₂ was separated with a Poropak Q column and transferred into the bellows of a Thermo Scientific MAT 253 mass spectrometer. The characterization of a single replicate consisted of 8 acquisitions in dual inlet mode with 7 cycles per acquisition. The total time of analysis per replicate is ~2 hours, and each sample was replicated at least 3 times. The postacquisition processing was completed with software for clumped isotope analyses (Easotope) [46]. During phosphoric acid digestion, Δ_{47} values were corrected for isotope fractionation with a phosphoric acid correction of 0.069‰ at 90°C for calcite [47]. The data were also corrected for non-linearity applying the heated gas method [48] and projected into the reference frame of [49]. Carbonate $\delta^{18}\text{O}$ values were calculated with the acid fractionation factors of [50]. Results were converted to temperatures applying the calibration method of [51]. Calculated $\delta^{18}\text{O}_{\text{fluid}}$ values are expressed in ‰ with respect to the Vienna Standard Mean Ocean Water (VSMOW).

4. Results

4.1. Nature of Host Rocks. In the study area, two Upper Cretaceous sequences are present [38, 42]: the Collada Gassó Formation, located in the footwall, and the Santa Fe Formation, located in the hanging wall.

The Collada Gassó Formation consists of massive to well-bedded dark grey to brown limestones with an E-W orientation and dipping 80° towards the north. The limestones consist of grainstones made up of bivalves, gastropods, echinoids, bryozoans, corals, miliolids, partially to totally micritized components (i.e., peloids), and locally quartz grains. The inter- and intraparticle porosity is cemented by calcite cement (Cc0) (Figure 4(a)). Under cathodoluminescence, the skeletal components show a dull to bright brown color, whereas the inter- and intraparticle calcite cement (Cc0) displays a bright yellow color (Figure 4(b)). This formation is characterized by the widespread presence of bedding-parallel compaction stylolites, developed during progressive burial prior to deformation.

The Santa Fe Formation consists of a massive succession of grey limestones with an E-W orientation and dipping 80–85° towards the north. The limestones are made up of wackestones, locally packstones, with a notably presence of calcispheres and planktonic foraminifera (Figure 4(c)). Under cathodoluminescence, it exhibits a very dark orange color (Figure 4(d)).

4.2. Fault Zone Structure. The studied fault zone exhibits a classical fault organization with a main slip plane, a fault core, and two surrounding damage zones within the footwall and hanging wall, respectively (Figures 5 and 6). The slip plane

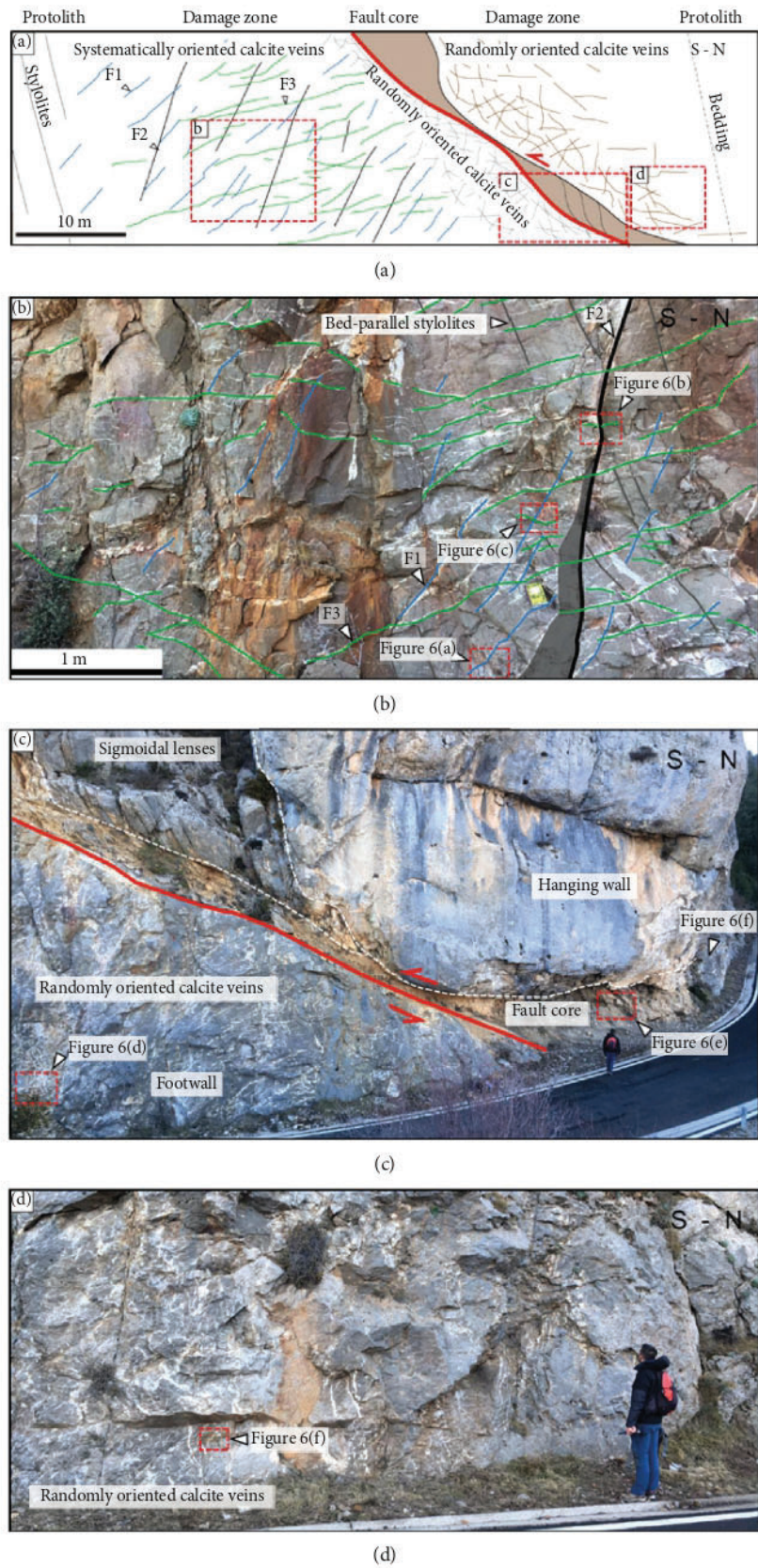


FIGURE 5: (a) Sketch of the spatial distribution of veins within the outcrop. In the footwall, three systematically oriented vein systems (F1 to F3) (b) evolve to randomly oriented veins located next to the fault core (c). In the hanging wall, only randomly oriented veins are observed (d).

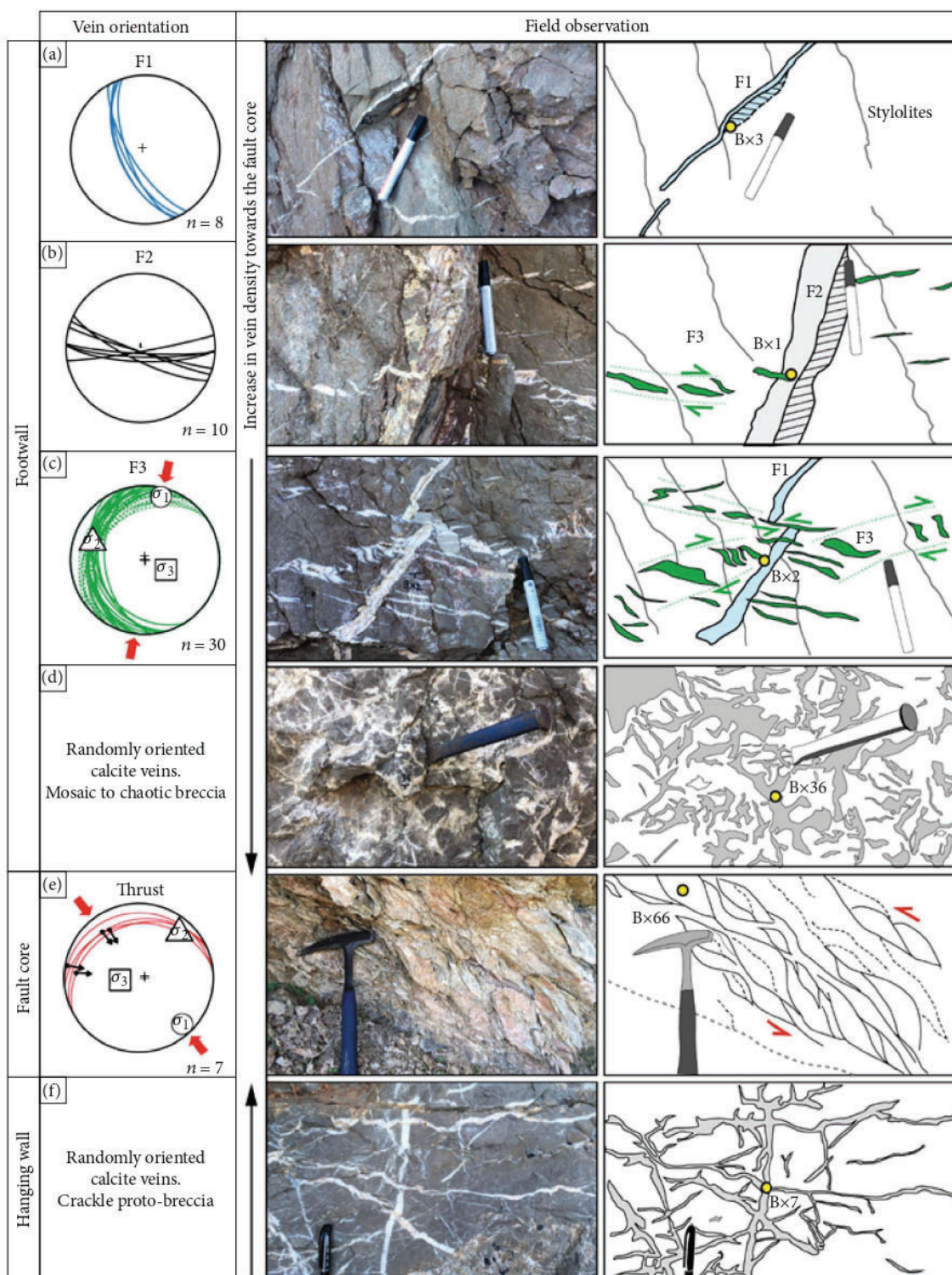


FIGURE 6: Spatial distribution and crosscutting relationships between veins developed within the studied thrust zone. Vein density increases towards the fault plane. In the footwall, three vein systems (F1, F2, and F3) (a, b, and c, respectively) evolve to randomly oriented veins (d) on approaching the fault core (e). In the hanging wall, only randomly oriented veins are observed, being more chaotic towards the fault plane (f). The yellow circle refers to sample location.

locates immediately below the fault core (Figure 5(a)), strikes E-W, dips between 15 and 30°N, and has a displacement of several hundred meters juxtaposing the Cenomanian-

Turonian sequence of the hanging wall against the Coniacian succession of the footwall [38, 42] (Figures 3 and 5). The fault core overlying the slip plane consists of a 2 to 7 m thick, light

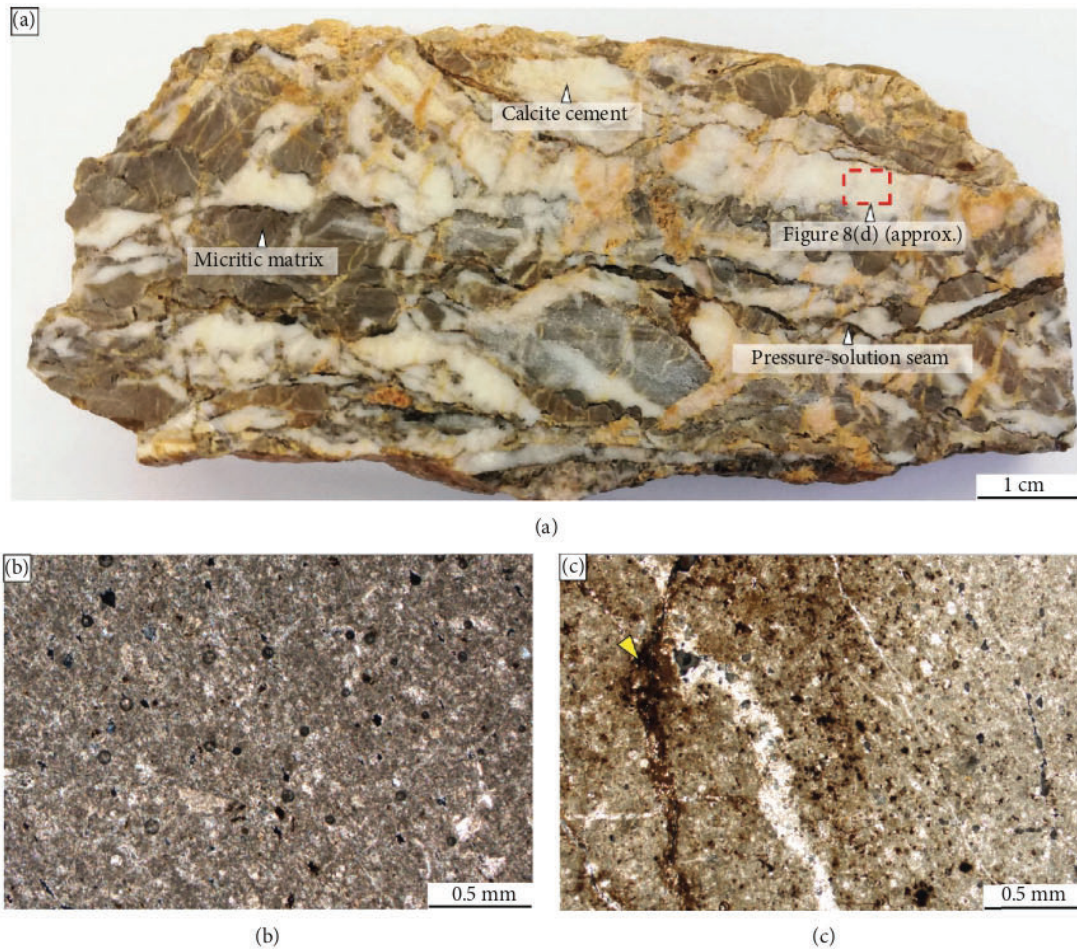


FIGURE 7: Fault core images. (a) Hand sample photograph of the foliated cataclasite showing S-C shear lenses (lithons) of grey host rock micritic limestone and calcite, bounded by dissolution seams or stylolites. Detail of the calcite cement can be found in Figure 8(d). (b, c) Optical microphotographs of the foliated cataclasite matrix with the presence of reddish clay minerals concentrated along pressure solution surfaces (yellow arrow).

grey to yellowish foliated cataclasite (Figure 7). This foliated cataclasite is characterized by well-developed S-C shears forming sigmoidal lenses (imbricated lithons), a combination of host rock carbonate and calcite lenses within a fine-grained micritic matrix (Figure 7(b)) with abundant calcite cement (Figures 6(e) and 7). Imbricated lithons are bounded by well-developed pressure-dissolution seams or stylolites (Figure 7(a)). S-C shears and stylolites strike ENE-WSW, compatible with the NNW-SSE shortening direction. Orange to reddish clay minerals concentrate along pressure-dissolution surfaces and are locally scattered within the micritic matrix (Figure 7(c)).

The transition from the fault core to the hanging wall damage zone is marked by discrete S-C sigmoidal shears without the development of foliated cataclasite, or by a discrete, discontinuous slip plane mineralized with calcite (Figure 5(c)).

Both the footwall and hanging wall damage zones comprise multiple sets of systematically and randomly oriented calcite-cemented fractures (i.e., veins) developed at both sides of the fault core (Figures 5 and 6). Although in both cases, there is a progressive increase in deforma-

tion and vein intensity from the protolith towards the fault core (Figure 5(a)), the geometry of veins differs from one to another damage zone.

In the footwall damage zone, there are two areas showing different vein characteristics (Figure 5(a)). The first area is around 30 m wide from the protolith and is characterized by three systematically oriented vein systems (F1 to F3) with clear crosscutting relationships between them (Figures 5(a)–5(c)). F1 consists of NNW-SSE extensional veins dipping between 50 and 70° to the SW. They are up to 1–2 m long and less than 2 cm thick (Figures 5(a), 5(b), and 6(a)). F2 is characterized by E-W extensional veins steeply dipping to the S-SW. These veins are several meters long and up to 5 cm thick (Figures 5(a), 5(b), and 6(b)). F3 consists of N-S and NE-SW *en échelon* conjugate sets of tension gashes (i.e., hybrid extensional-shear calcite veins) gently dipping towards the NW (Figure 6(c)). These veins are centimetric-sized and have sigmoidal shapes. The second area observed in the footwall covers around 15–20 m between the first area and the fault core and is dominated by randomly oriented calcite veins defining a dilational mosaic to chaotic breccia [52] (Figure 6(d)).

By contrast, in the hanging wall, the damage zone is narrower, only concentrated in the 15–20 meters near the fault core (Figure 6(e)), and it is defined by randomly oriented calcite veins defining an incipient crackle breccia (proto-breccia) [52] (Figure 6(f)). Fracture density is lower than within the footwall damage zone.

4.3. Calcite Cements of Veins and Breccias. The damage zones in the footwall and hanging wall not only differ in the type and distribution of fracture systems, as previously described, but also they also show different fracture-filling calcite cements, characterized by distinct petrological and geochemical features.

In the footwall, three calcite cement generations (Cc1 to Cc3) have been observed filling the fracture systems F1 to F3 and two of those calcite cements (Cc1 and Cc2) are also present in the mosaic to chaotic breccia (randomly oriented fractures).

Calcite cement Cc1 exhibits a milky to slightly brownish color in hand sample and consists of up to 1 mm-sized anhedral crystals showing mechanical twinning and featuring a blocky to elongated blocky texture, in which crystals grow syntaxially. This cement shows a dark to light orange cathodoluminescence (Figure 8(a)). Calcite Cc1 precipitated in fractures F1 and in the mosaic to chaotic breccia of the footwall.

Cc2 displays a white to translucent aspect in hand sample. It is formed of anhedral to subhedral calcite crystals, ranging in size from approximately 0.2 to 5 mm, with a blocky to elongated blocky texture. The elongated blocky Cc2 cement grows syntaxially from the fracture walls (Figures 8(a) and 8(b)). Crystals present abundant twin planes and show a nonluminescent to bright orange concentric zonation under cathodoluminescence in which the zoning pattern generally coincides with the crystal growth (Figure 8(b)). Calcite Cc2 precipitated in fractures F2 as well as in fractures F1 and in the mosaic to chaotic breccia of the footwall after Cc1.

Cc3 exhibits a milky appearance in hand sample and is constituted of up to 0.5 mm anhedral blocky, locally elongated crystals. It has mechanical twinning and presents a dull orange luminescence (Figure 8(c)). Cc3 precipitated in fractures F3.

On the other hand, in the hanging wall and in the fault core, only one calcite cement (Cc4) is observed. Cc4 precipitated in the main fault plane and in randomly oriented fractures. This cement has a milky aspect in hand sample and is characterized by up to 1 mm anhedral crystals with a nonluminescent to dark brown luminescence (Figure 8(d)).

4.4. Oxygen and Carbon Isotopes. The $\delta^{18}\text{O}$ and $\delta^{13}\text{C}$ isotopic composition of the calcite cements Cc1 to Cc4, adjacent host rocks, and fault rocks is summarized in Table 1 and presented in Figure 9. The calcite cement Cc0 in the interparticle porosity of the grainstone from the Collada Gassó Formation (footwall) has $\delta^{18}\text{O}$ values between -7.2 and -6.7‰ VPDB and $\delta^{13}\text{C}$ values between -0.5 and $+0.7\text{‰}$ VPDB. The micrite matrix of the wackestone from the Santa Fe Formation (hanging wall) shows $\delta^{18}\text{O}$ values between -6.2 and -5.8‰

VPDB and $\delta^{13}\text{C}$ values between $+2.1$ and $+2.2\text{‰}$ VPDB. The carbonate micritic matrix from the cataclasite yields $\delta^{18}\text{O}$ values between -7.1 and -6‰ VPDB and $\delta^{13}\text{C}$ values between $+2.3$ and $+3\text{‰}$ VPDB.

The calcite cements Cc1 to Cc4 exhibit a wider range of values (Figure 9). Cc1 has $\delta^{18}\text{O}$ values ranging between -8.2 and -6.5‰ VPDB and $\delta^{13}\text{C}$ values between -2 and -1.5‰ VPDB. Cc2 is characterized by $\delta^{18}\text{O}$ values between -8.2 and -5.4‰ VPDB and $\delta^{13}\text{C}$ values between -6.3 and -3.3‰ VPDB. Cc3 shows $\delta^{18}\text{O}$ values between -13 and -11.7‰ VPDB and $\delta^{13}\text{C}$ values between -3.2 and -1.9‰ VPDB and Cc4 has $\delta^{18}\text{O}$ values between -13.1 and -11.9‰ VPDB and $\delta^{13}\text{C}$ values between -0.6 and $+2.4\text{‰}$ VPDB. Calcite cements precipitated in the footwall (Cc1, Cc2, and Cc3) exhibit negative $\delta^{13}\text{C}$ isotopic values, whilst the calcite cement precipitated within the fault plane and hanging wall (Cc4) displays heavier $\delta^{13}\text{C}$ values (Figure 9(a)). In addition, the $\delta^{18}\text{O}$ values also exhibit two different trends within the four calcite cements: Cc1 and Cc2 show $\delta^{18}\text{O}$ values similar to those of Cc0 and host rocks (Figures 9(a) and 9(b)), whereas Cc3 and Cc4 have lighter $\delta^{18}\text{O}$ values with respect to the host carbonate values (Figures 9(a) and 9(b)).

4.5. Clumped Isotopes. Temperatures in $^{\circ}\text{C}$ and $\delta^{18}\text{O}_{\text{fluid}}$ in ‰ VSMOW of the vein-forming fluids are calculated from the measured Δ_{47} using the formula of [54, 55], respectively (Table 1 and Figure 10). The Δ_{47} value for Cc1 ranges between 0.619 and 0.642, which translates into temperatures of 42 – 51°C and $\delta^{18}\text{O}_{\text{fluid}}$ of -1.8 to -0.1‰ VSMOW. For Cc2, Δ_{47} is between 0.562 and 0.589, implying temperatures between 64 and 78°C and $\delta^{18}\text{O}_{\text{fluid}}$ between $+3.7$ and $+5.9\text{‰}$ VSMOW. For Cc3, Δ_{47} varies between 0.498 and 0.515, which translates to temperatures between 105 and 117°C and $\delta^{18}\text{O}_{\text{fluid}}$ between $+3.2$ and $+5.5\text{‰}$ VSMOW. Finally, Δ_{47} values of Cc4, between 0.53 and 0.535, imply temperatures of 93 to 96°C and $\delta^{18}\text{O}_{\text{fluid}}$ between $+0.7$ and $+1.9\text{‰}$ VSMOW. In the footwall, the calculated temperatures progressively increase from Cc1 to Cc3 and the $\delta^{18}\text{O}_{\text{fluid}}$ is lighter in Cc1, whilst Cc2 and Cc3 have a similar value.

4.6. Strontium Isotopes. A selected number of samples from each calcite cement generation (Cc0 to Cc4) and related host rocks were analyzed for Sr isotopic composition (Table 1 and Figure 11). Cc0 (in the footwall host rocks) has a $^{87}\text{Sr}/^{86}\text{Sr}$ ratio of 0.707606, whereas host rocks from the hanging wall have a $^{87}\text{Sr}/^{86}\text{Sr}$ ratio of 0.707718. These values fall within the range of values expected for Upper Cretaceous marine carbonates [56] (Figure 11(b)).

The calcite cements in the footwall exhibit higher $^{87}\text{Sr}/^{86}\text{Sr}$ ratios with respect to the calcite cement (Cc0) cementing their adjacent host rock (Figure 11(a)). This ratio is 0.707707 for Cc1, ranges from 0.707695 to 0.707699 for Cc2, and is 0.707698 for Cc3. By contrast, the calcite cement Cc4 has a $^{87}\text{Sr}/^{86}\text{Sr}$ ratio similar to its adjacent host carbonate in the case of the crackle proto-breccia veins located in the hanging wall (0.707715) and more radiogenic than the host rock in the case of the fault plane (0.707771) (Figure 11(a)).

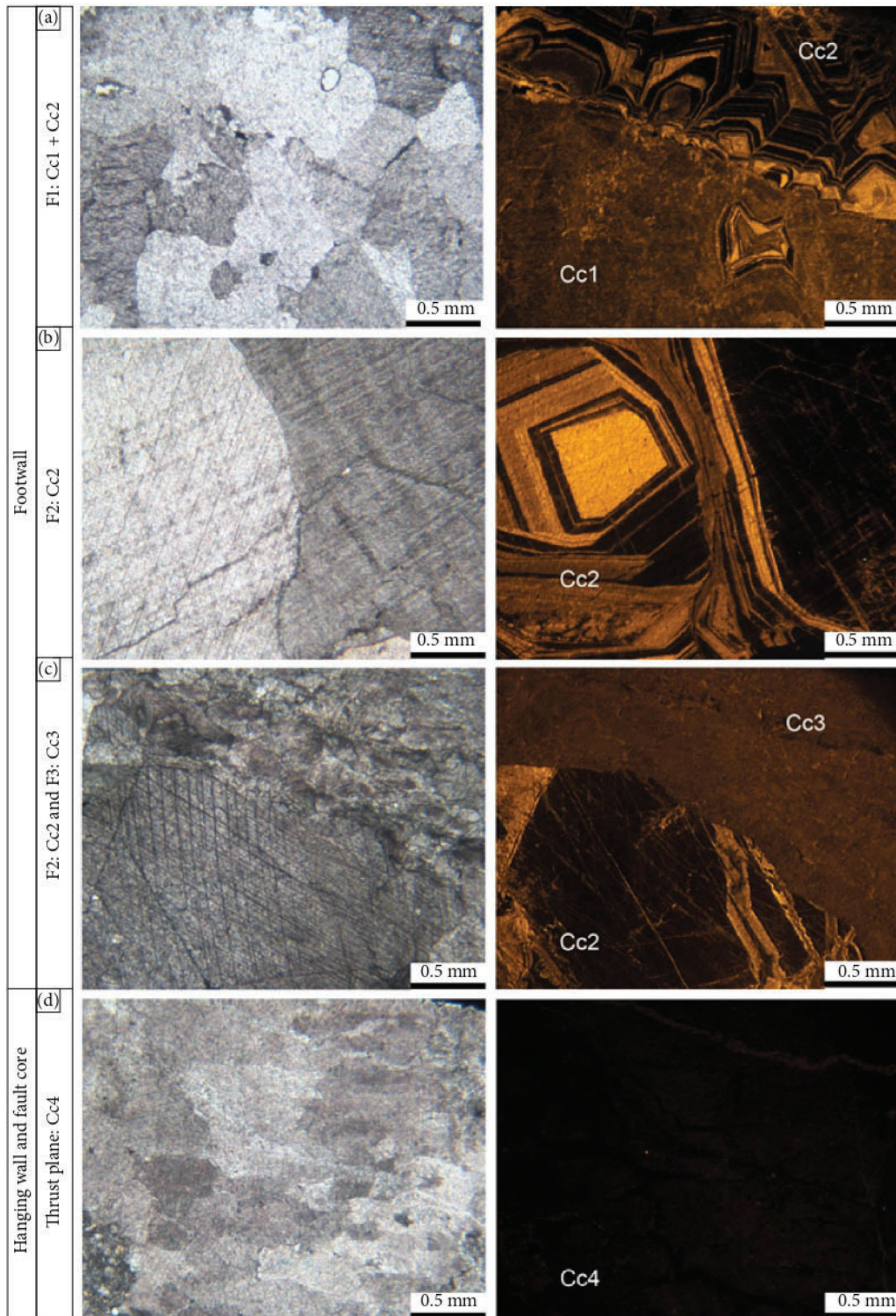


FIGURE 8: Paired optical and CL microphotographs from calcite cements precipitated within the fault core and fault damage zone of the studied thrust. (a) Fracture F1 cemented by calcite cements Cc1 and Cc2. (b) Calcite cement Cc2, with its characteristic CL zonation, filling a fracture F2. (c) Cc3 filling a F3 fracture, postdating a fracture F2 filled with Cc2. (d) Cc4 in the main fault plane.

4.7. Elemental Composition. The elemental composition (Ca, Mg, Fe, Mn, and Sr), including rare earth elements (REE) and yttrium (Y), was measured for each calcite cement generation

and their host carbonates and the results are presented in Tables 2 and 3 and in Figure 12. In general, the trace element compositions widely vary depending on the calcite cement,

TABLE 1: $\delta^{18}\text{O}$, $\delta^{13}\text{C}$, and $^{87}\text{Sr}/^{86}\text{Sr}$ isotopic signature of the calcite cements, fault rocks, and host rocks. The Δ_{47} , $\delta_{18}\text{O}_{\text{fluid}}$, and precipitation temperatures obtained from clumped isotopes are also included. Fw means footwall and Hw means hanging wall.

Sample	Fracture	Cement	$\delta^{18}\text{O}$ ‰VPDB	$\delta^{13}\text{C}$ ‰VPDB	$^{87}\text{Sr}/^{86}\text{Sr}$	Δ_{47}	$\delta_{18}\text{O}_{\text{fluid}}$ ‰VSMOW	T (°C)
Bx1B	F2	Cc1	-8.2	-1.7	0.707707	0.619/0.642	-1.8 to -0.1	42 to 51
Bx 3	F1	Cc1	-7.3	-1.8				
Bx36.I	Breccia (Fw)	Cc1	-7.6	-2				
Bx36.IV	Breccia (Fw)	Cc1	-7.4	-1.6				
Bx36.V	Breccia (Fw)	Cc1	-6.5	-1.5				
Bx3.III	F1	Cc2	-8.2	-3.7				
Bx1A.I	F2	Cc2	-7	-4.6	0.707699	0.562/0.589	+3.7 to +5.9	64 to 78
Bx1B.II	F2	Cc2	-6.3	-4.6				
Bx3.II	F1	Cc2	-7	-3.3				
Bx36.II	Breccia (Fw)	Cc2	-7.8	-5.6	0.707695			
Bx36.III	Breccia (Fw)	Cc2	-7.2	-6.3				
Bx35	F2	Cc2	-5.4	-4	0.707765			
Bx1A.II	F3	Cc3	-13	-1.9				
Bx2A	F3	Cc3	-12.1	-2.9	0.707698	0.498/0.515	+3.2 to +5.5	105 to 117
Bx2B	F3	Cc3	-11.9	-2.8				
Bx4	F3	Cc3	-11.7	-3.2				
Bx5	Thrust plane	Cc4	-12.9	+0.4	0.707771	0.53/0.535	+0.7 to +1.9	93 to 96
Bx6	Breccia (Hw)	Cc4	-12.3	+2.4				
Bx7.I	Breccia (Hw)	Cc4	-13.1	+0.4	0.707715			
Bx7.II	Breccia (Hw)	Cc4	-11.9	+0.9				
Bx 8	Breccia (Hw)	Cc4	-12.3	-0.6				
Bx66.C	Slip plane	Cc4	-12	+1.6				
Bx1.HR	Host rock (Fw)	Cc0	-7.2	-0.5				
Bx2A.HR	Host rock (Fw)	Cc0	-6.7	+0.7	0.707606			
Bx3.HR	Host rock (Fw)	Cc0	-7	+0.1				
Bx7	Host rock (Hw)		-5.8	+2.2				
Bx8	Host rock (Hw)		-6.2	+2.1	0.707718			
Bx6.I	Fault rock (matrix)		-6.9	+2.9				
Bx6.II	Fault rock (matrix)		-7.1	+3				
Bx66	Fault rock (matrix)		-6.6	+2.6				
Bx67	Fault rock (matrix)		-6	+2.3				

whilst the REY (REE and Y) pattern in the four cements follows a trend comparable to that of the adjacent host rock (Figure 12(c)).

In the footwall, the calcite cements Cc1 and Cc2 are characterized by low Mg and Sr contents, intermediate Mn, and variable Fe concentrations, whereas Cc3 has high Mn and Fe contents, intermediate Mg values, and variable-high Sr concentrations (Figure 12(a)). The REY concentration of these cements (Cc1 to Cc3) is lower compared to that of the cement within the host rock (Cc0), but follows a similar flat trend, with a slight negative Ce anomaly (Figures 12(b) and 12(c)) and a slight positive Y anomaly (except for Cc2 that may exhibit either a positive or negative Ce anomaly) (Figure 12(c)).

In the fault core and hanging wall, Cc4 exhibits high Mg and Sr concentrations, intermediate Fe values, and low Mn contents. The REY pattern of Cc4 is also flat with a better defined negative Ce anomaly and a positive Y anomaly,

which are also present in the hanging wall host rock. The REY concentrations are lower in cement Cc4 than in its adjacent host rocks, except for the calcite in the fault plane that exhibits higher concentrations (Figure 12(c)).

Mg/Ca and Sr/Ca molar ratios of the parent fluids that precipitated the calcite cements were calculated using the formula of [57] for low temperature (25–40°C) and for higher temperature (90–100°C) of precipitation using distribution coefficients ($K_{\text{Mg}} = 0.012$ at 25°C [58], $K_{\text{Mg}} = 0.1163$ at 90°C [59], $K_{\text{Sr}} = 0.054$ at 25°C [60], and $K_{\text{Sr}} = 0.08$ at 100°C [61]). The obtained molar ratios are presented in Table 2.

4.8. Neodymium Isotopes. Nine representative samples from calcite cements and related host rocks were also analyzed for Nd isotopic composition. However, although the Nd concentration is above the detection limit for all the analyzed samples (Table 3), the $^{143}\text{Nd}/^{144}\text{Nd}$ ratio could not be measured. This is attributed to both the low Nd concentration

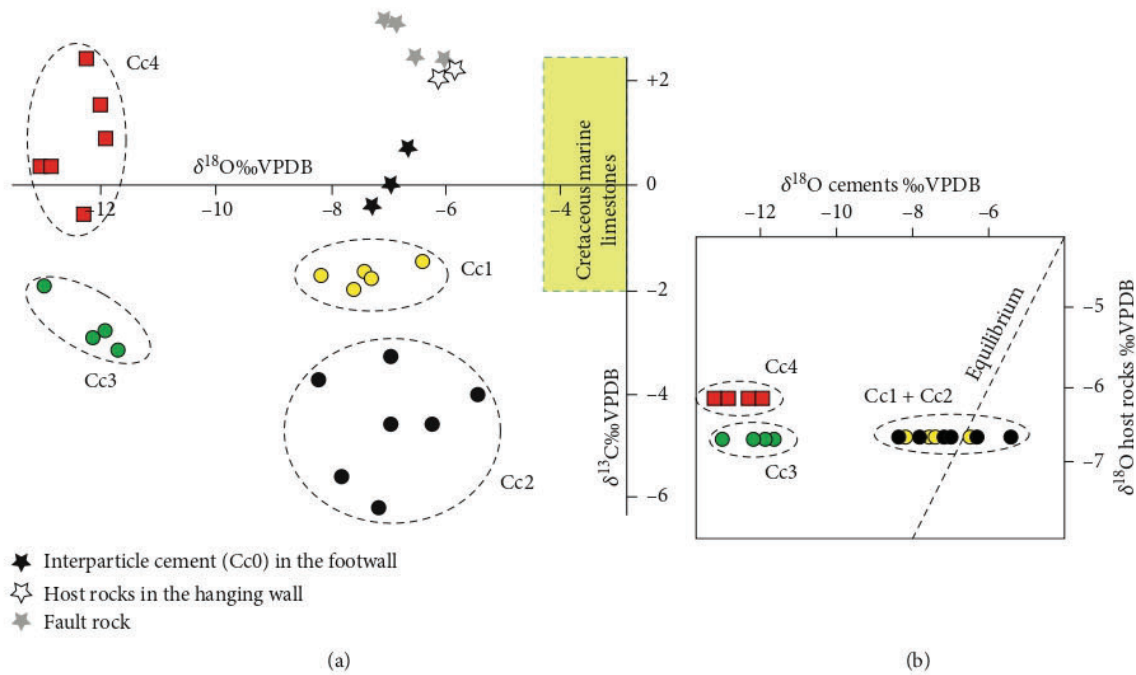


FIGURE 9: (a) Crossplot showing the $\delta^{18}\text{O}$ and $\delta^{13}\text{C}$ compositions of the calcite cements, host rocks, and fault rocks (carbonate matrix from the cataclastite). Cretaceous marine limestone values (green box) are from [53]. (b) $\delta^{18}\text{O}$ values of the calcite cements versus $\delta^{18}\text{O}$ values of the related host rocks.

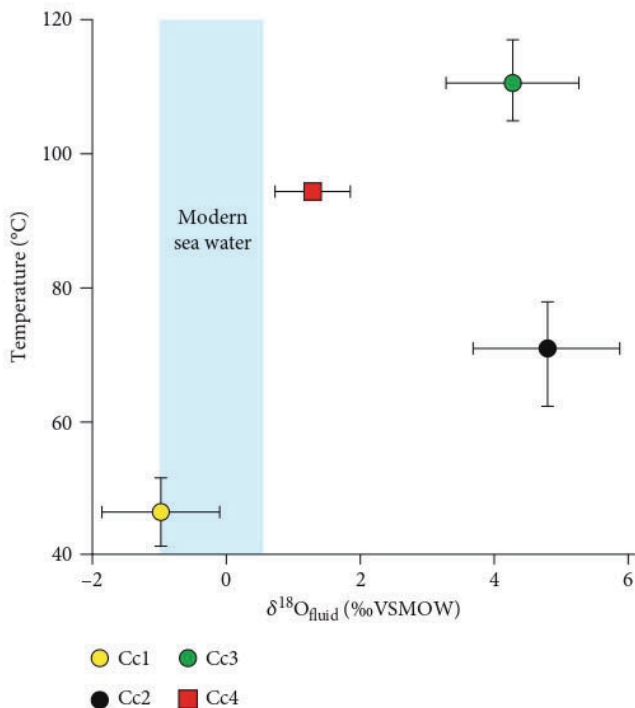


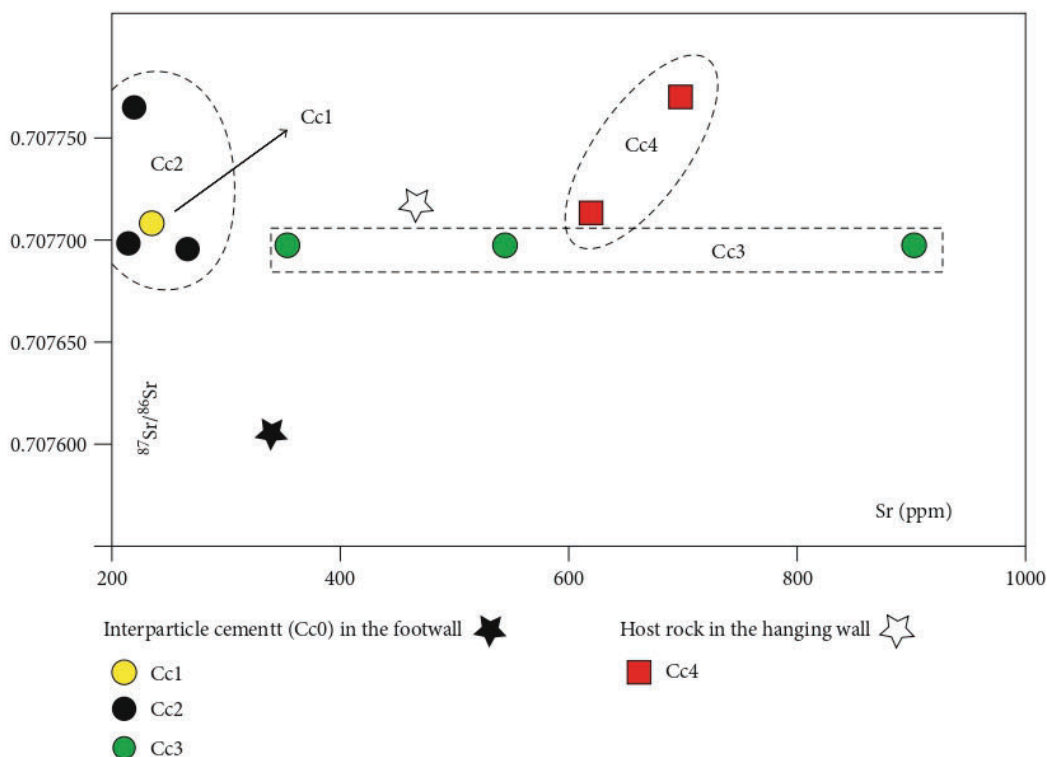
FIGURE 10: Temperatures (°C) vs. $\delta^{18}\text{O}_{\text{fluid}}$ (‰VSMOW) calculated from clumped isotope thermometry for calcite cements Cc1 to Cc4.

in the samples, ranging between 0.5 and around 10 ppm (Table 3), and the scarce quantity of sample that was possible to collect, generally around 30 mg, which was not enough for a dynamic multicollection method through 160 cycles at a stable intensity of 1 V.

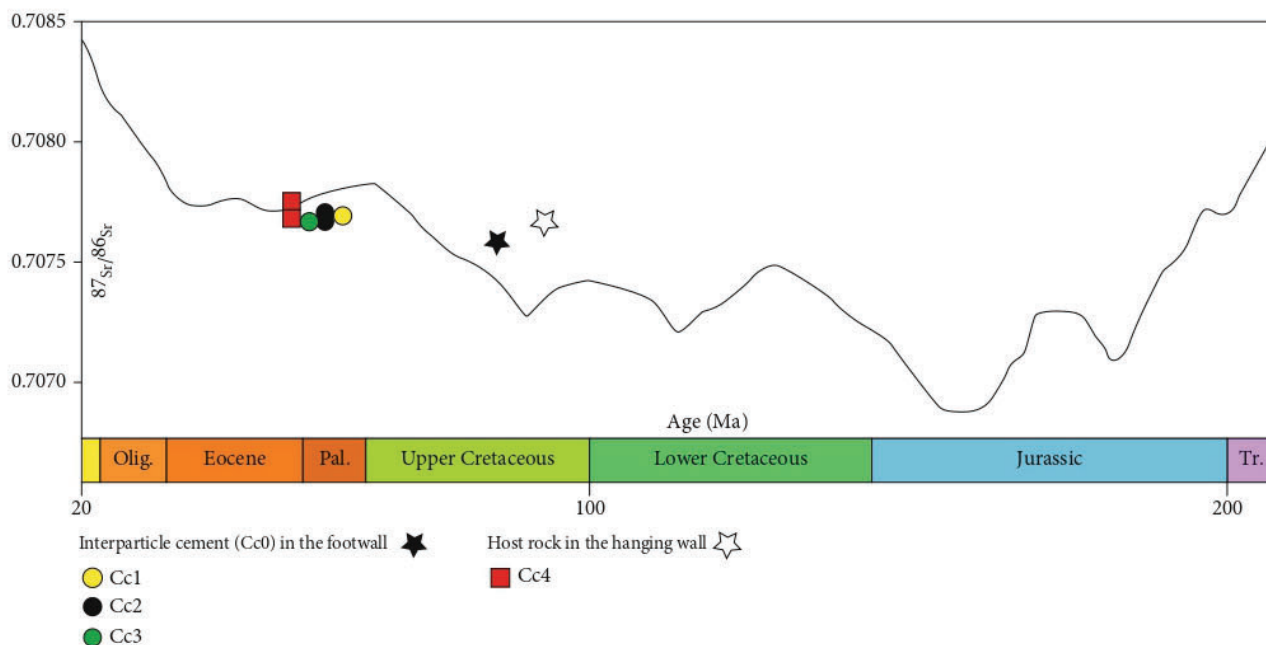
5. Discussion

5.1. Dissolution versus Precipitation Zones. The studied fault zone has different brittle structures accommodating deformation both in the fault core and in the damage zone. Within the fault core, the presence of tectonic stylolites and S-C structures evidences processes of pressure solution and/or frictional sliding [54, 55]. Such processes are associated with contractional stress concentration and slip accommodation imposed by the advancing thrust [64, 65]. By contrast, within the damage zone, the widespread presence of veins represents dilational sites where calcite precipitated [66, 67]. The mechanism of calcite precipitation was likely induced by the rapid fluid pressure drop due to fluid trapping in the fractures developed in the footwall and hanging wall [10, 66, 68, 69]. The repartition of such structures, stylolites, S-C foliation, and veins, and therefore of zones of dissolution and zones of precipitation, is the result of a heterogeneous distribution of stress and the variation in deformation intensity across the fault zone [54].

5.2. Structural Context of Fracturing and Veining. The main stress orientations responsible for the development of the studied thrust system have been calculated plotting the main plane orientation and related slickenlines (Figure 6(e)). The estimated stress field shows a SSE transport direction, compatible with the N-S to NNW-SSE shortening direction reported in the Pyrenees [28, 30, 39], and a vertical minimum principal stress ($\sigma_v = \sigma_3$), characteristic of compressional regimes [9, 10]. The studied vein systems are interpreted as developed during the thrust activity under the same compressional regime [8, 42, 70]. The synchronicity between



(a)



(b)

FIGURE 11: (a) $^{87}\text{Sr}/^{86}\text{Sr}$ isotopic ratios of calcite cements and host carbonates plotted against the Sr content. (b) $^{87}\text{Sr}/^{86}\text{Sr}$ ratios compared with the $^{87}\text{Sr}/^{86}\text{Sr}$ isotopic ratios of seawater through time from the LOWESS curve [56].

thrusting and veining is supported by the exclusive presence of veins in the damage zone as well as by the gradual increase in vein density and slight change in strike when approaching the main thrust plane. However, the steeply dipping orientation of F1 and F2 with respect to the subhorizontal σ_1 axis differs with theoretical models that describe the formation

of flat-lying extensional fractures that open in the σ_3 vertical direction (i.e., oriented parallel to the σ_1 axis) [9, 10, 13, 68, 71]. Despite this apparent discrepancy, the presence of the same calcite cements (Cc1 and Cc2) in F1-F2 fractures and in the mosaic to chaotic breccia developed along the fault plane corroborates the synchronicity between thrusting and

TABLE 2: Elemental composition (Ca, Mg, Fe, Mn, and Sr) of the different calcite cements (Cc1 to Cc4), the interparticle cement Cc0 in the footwall host rocks (FW), and the hanging wall rocks (HW). The calculated Mg/Ca and Sr/Ca molar ratios of the parent fluid using the distribution coefficient equation [57] are also shown.

Sample	Ca (ppm)	Mg (ppm)	Fe (ppm)	Mn (ppm)	Sr (ppm)	Mg/Ca low T	Mg/Ca high T	Sr/Ca low T	Sr/Ca high T
Cc1	37236	859.7	2518.8	236.8	239	0.317	0.033	0.0049	0.0037
Cc2	378096	921.1	1249.4	222.3	216.2	0.335	0.035	0.0044	0.0033
Cc2	385024	741.0	1188.8	151.5	219.5	0.264	0.027	0.0043	0.0033
Cc2	393269	865.9	564.1	86.6	270.7	0.303	0.031	0.0052	0.0039
Cc3	387653	1912.4	2967.2	380.5	906.8	0.678	0.070	0.0178	0.0134
Cc3	300362	1997.7	2704.6	409.3	548.1	0.914	0.094	0.0139	0.0104
Cc3	350768	1397.6	2997.7	661.1	356.1	0.548	0.056	0.0077	0.0058
Cc4	322604	3637.8	2345.2	97.3	699.5	1.550	0.160	0.0165	0.0124
Cc4	366243	1908.1	1658.3	80.3	623.6	0.716	0.074	0.0130	0.0097
Cc4	346495	1784.2	1298.2	65.2	625.3	0.708	0.073	0.0138	0.0103
FW	298763	3376.3	3248.8	345.6	340.8	1.553	0.160	0.0087	0.0065
HW	321638	2968.0	980.1	68.8	468.9	1.268	0.131	0.0111	0.0083

TABLE 3: REE and Y contents of the different calcite cements (Cc1 to Cc4), the interparticle cement Cc0 from the footwall (FW), and the host rocks from the hanging wall (HW). Values are given in ppm. *DL: detection limit.

Sample	La	Ce	Pr	Nd	Sm	Eu	Gd	Tb	Dy	Y	Ho	Er	Tm	Yb	Lu
DL*	0.21	0.32	0.04	0.15	0.03	0.01	0.02	0.003	0.02	0.2	0.003	0.01	0.002	0.01	0.01
Cc1	7.13	13.46	1.81	6.01	1.38	0.26	1.35	0.19	1.05	7.04	0.17	0.45	0.08	0.37	0.06
Cc2	3.03	9.96	0.85	3.00	0.75	0.14	0.66	0.08	0.43	3.31	0.07	0.19	0.03	0.16	0.03
Cc2	3.48	4.35	1.07	3.81	0.95	0.20	0.88	0.13	0.71	5.43	0.12	0.35	0.06	0.30	0.05
Cc2	0.81	1.26	0.17	0.59	0.23	0.04	0.17	0.02	0.15	1.29	0.03	0.07	0.01	0.06	<LD
Cc3	6.15	10.73	1.64	5.77	1.36	0.26	1.21	0.17	0.92	6.53	0.15	0.39	0.06	0.31	0.05
Cc3	5.22	9.19	1.22	4.38	0.95	0.19	0.96	0.13	0.72	5.44	0.12	0.32	0.05	0.24	0.04
Cc3	1.31	2.38	0.38	1.45	0.37	0.08	0.33	0.04	0.25	2.37	0.05	0.13	0.02	0.10	0.02
Cc4	2.73	6.03	0.86	2.89	0.69	0.13	0.58	0.08	0.43	3.35	0.07	0.19	0.03	0.15	0.02
Cc4	0.78	1.05	0.17	0.58	0.24	0.04	0.14	0.02	0.14	1.87	0.03	0.09	0.02	0.08	<LD
Cc4	2.08	1.84	0.53	1.82	0.44	0.08	0.36	0.05	0.25	2.45	0.05	0.14	0.03	0.13	0.02
Cc0	9.83	23.27	3.04	10.56	2.44	0.49	2.16	0.28	1.52	8.70	0.22	0.61	0.11	0.51	0.08
HW	2.39	3.52	0.52	1.75	0.41	0.07	0.36	0.05	0.33	3.23	0.06	0.18	0.03	0.17	0.03

fracturing. In the case of conjugated fracture systems F3, their bisector angle indicates a subhorizontal σ_1 and a subvertical σ_3 , and therefore, their formation is compatible with the prevailing stress field associated with thrusting ($\sigma_v = \sigma_3$).

Two mechanisms, a local variation of the stress axes as well as high fluid pressure conditions, are invoked to explain the formation of the steeply dipping F1 and F2 fractures in relation to the low angle reverse fault [72–74]. In the first case, the remote stress fields could have varied locally within a constant far-field compressional regime to become properly oriented for the development of these fractures [71, 72, 75]. Such a local variation of the magnitude and orientation of the remote stress fields is attributed to the formation of a process zone at the front of the fault tip during thrust (slip plane) propagation [71, 76]. This occurs, firstly, because the fault tip acts as a stress concentrator amplifying the magnitude of the remote stress [76] and, secondly, because the main compressive stress (σ_1) exhibits different angles with

the fault in compressive quadrants with respect to dilational quadrants in propagating faults [71, 76].

Several observations, which are described below, indicate that the formation of the studied fractures occurred under high fluid pressure conditions, and therefore, it is associated with a hydraulic (over)pressure mechanism. Fluid overpressure may explain the high concentration of systematically oriented extensional (F1, F2) and extensional-shear (F3) veins, as well as the absence of any structural orientation of veins in the breccias [77]. Comparable fracture systems (systematic arrays of extensional and extensional-shear fractures) are expected to develop in compressional settings when the tensile overpressure condition is achieved, that is, when the pore fluid pressure exceeds the least compressive stress ($P_f > \sigma_3$) [9, 10, 78]. Such a fluid pressure is common during the propagation of thrust faults in compressional regimes [9, 12, 67, 79] and is attributed to the following: (i) the constraint stress field around the fault tip may generate overpressure of a confined fluid [80, 81], (ii) the low dip of

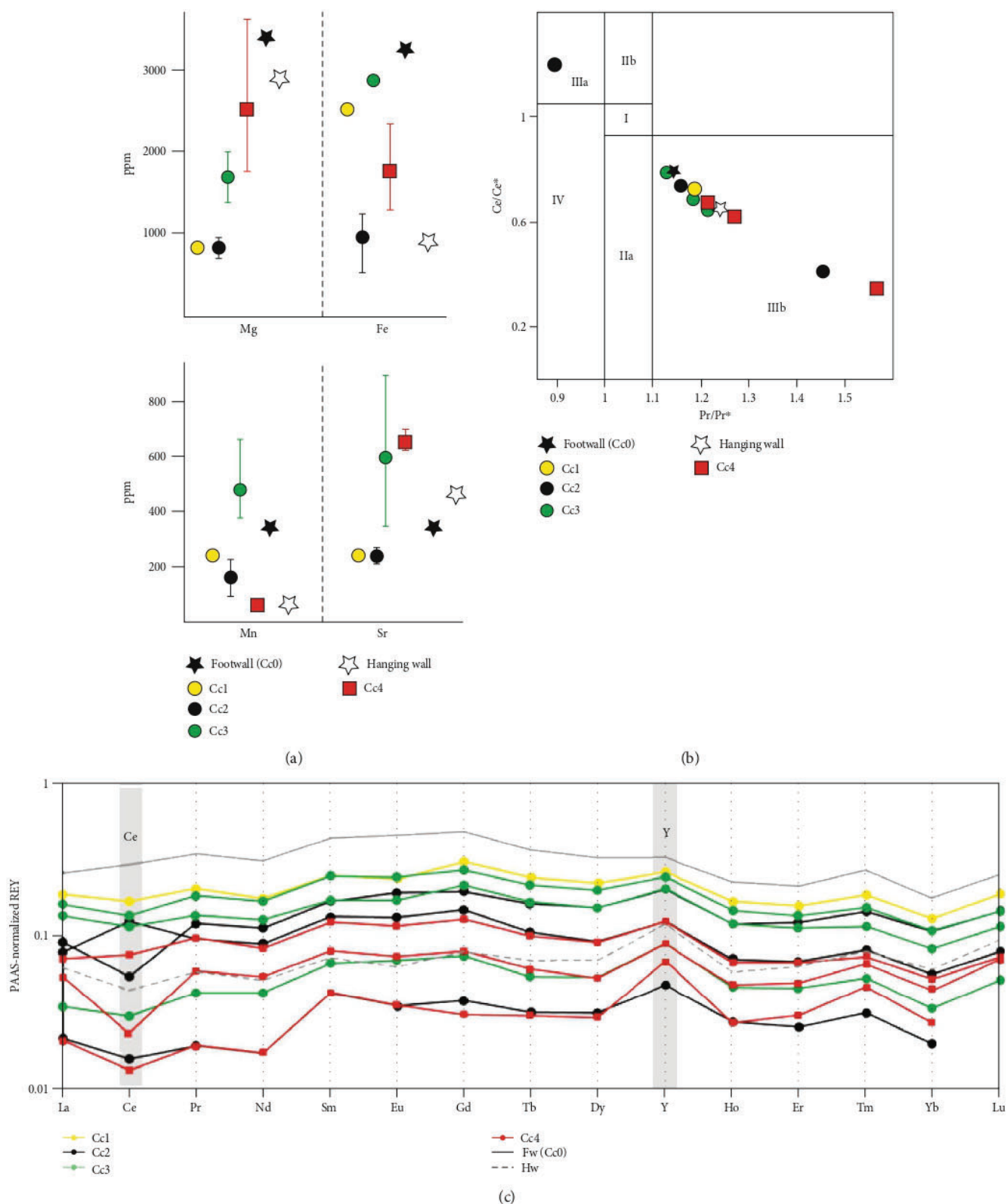


FIGURE 12: (a) Elemental composition (Mg, Fe, Mn, and Sr) in ppm of calcite cements and host rocks. Bars indicate maximum, minimum, and average composition. (b) PAAS-normalized Ce/Ce^* vs. Pr/Pr^* crossplot showing the Ce and Pr anomalies of calcite cements and host rocks using the method of [62] modified by [63]. Field I: no anomaly. Field IIa: positive La anomaly and no Ce anomaly. Field IIb: negative La anomaly and no Ce anomaly. Field IIIa: positive Ce anomaly. Field IIIb: negative Ce anomaly. Field IV: positive Ce and La anomalies. (c) PAAS-normalized rare elements and yttrium (REY) patterns of calcite cements and host rocks.

thrusts prevents vertical flow [14, 68], and (iii) it is because of sediment compaction induced by loading during thrust sheet emplacement [77, 81].

5.3. Fluid History and Pathways. The widespread presence of calcite cements in the different fracture sets indicates that these structures themselves were traps for fluids migrating during thrusting. Field observations based mainly on the macroscopic vein features and crosscutting relationships between them together with the above presented petrological and geochemical data evidence the formation of four calcite cementation phases (Cc1 to Cc4) that record the evolution of the fluid system during the thrust activity. Since the footwall and hanging wall exhibit different fracture systems and different calcite cements, the fluid system was compartmentalized [26, 27, 82, 83].

5.3.1. Fluid System in the Footwall. The evolution of the fluid system in the footwall during thrusting is inferred from the geochemical data of calcite cements Cc1, Cc2, and Cc3.

Calcite cement Cc1 is observed within fractures F1 and within the mosaic to chaotic breccia located in the footwall. This cement has $\delta^{18}\text{O}$ (-8.2 to -6.5‰VPDB) and $\delta^{13}\text{C}$ values (-2 to -1.5‰VPDB) similar or slightly more depleted with respect to those of the interparticle calcite cement (Cc0) in the adjacent host rocks (Figures 9(a) and 9(b)). This fact, together with the observed positive Y anomaly in both Cc1 and Cc0, indicates buffering of the vein-forming fluids by the adjacent host carbonates due to fluid-rock interaction [84]. The fluid-rock interaction is also recorded in the $\delta^{18}\text{O}_{\text{fluid}}$ obtained from clumped isotopes, yielding values between -1.8 and -0.1‰VSMOW. These values may result from interaction between meteoric waters, which have typically negative $\delta^{18}\text{O}$ values, and marine carbonates, with $\delta^{18}\text{O}$ values around 0‰PDB [64]. This fact is supported by the calculated Mg/Ca and Sr/Ca molar ratios, indicating the involvement of meteoric fluids, and the diluted elemental composition in Cc1 with respect to Cc0, showing lower REY concentration and lower Mg, Mn, and Sr contents (Figure 12(a)). Likewise, the $^{87}\text{Sr}/^{86}\text{Sr}$ ratio of Cc1 is slightly more radiogenic than Cc0 but is still between the ranges of Cretaceous marine carbonates (Figure 11). The homogeneous orange luminescence of Cc1 is interpreted as constant precipitation rates during a single precipitation event, and the presence of a negative Ce anomaly suggests precipitation in an oxic environment [84] (Figures 12(b) and 12(c)). Finally, the temperature of Cc1, also obtained from clumped isotope thermometry, ranges between 42 and 51°C. The presence of meteoric fluids and the relatively low temperatures could indicate shallow burial depths, probably less than 1 km if we consider a normal geothermal gradient of 25–30°C/km and a surface temperature of 20°C. Therefore, Cc1 precipitated from meteoric fluids (Figure 13(a)) with a composition strongly buffered by the Cretaceous host carbonates.

Calcite cement Cc2 is found in fractures F1 and F2 and within the mosaic to chaotic breccia from the footwall. This cement has similar $^{87}\text{Sr}/^{86}\text{Sr}$ ratios and $\delta^{18}\text{O}$ values to Cc1 but precipitated at higher temperatures (between 64 and 78°C) and from heavier $\delta^{18}\text{O}_{\text{fluid}}$ (between +3.7 and +5.9‰

VSMOW). These higher temperatures and the $\delta^{18}\text{O}_{\text{fluid}}$ imply hot formation waters. However, the low $\delta^{13}\text{C}$ values (Figure 9), the diluted Mg, Sr, and REY concentrations (Figure 12), and the calculated Mg/Ca and Sr/Ca molar ratios of Cc2 reveal the involvement of meteoric fluids with increasing influence of organic-derived carbon [85–89] (Figure 12(b)). The CL zonation of Cc2, alternating between non- and bright luminescent zones, the presence of positive and negative Ce anomalies (Figures 12(b) and 12(c)), and the oscillations in the Fe and Mn contents (Figure 12(a)) indicate oxidizing-reducing fluctuation, typical of the meteoric environment [6, 90–93]. These facts indicate that Cc2 precipitated from formation fluids that likely evolved from heated meteoric waters during the development of the second fracturing event (F2). The evolution of these fluids probably involved water-rock interactions during progressive increase in burial depths and temperatures linked to thrust sheet emplacement [94–96].

Calcite cement Cc3, occluding fractures F3, shows an $^{87}\text{Sr}/^{86}\text{Sr}$ ratio similar to cements Cc1 and Cc2 (Figure 11), $\delta^{13}\text{C}$ within the same range of values of Cc2 (Figure 9(a)), and a lighter $\delta^{18}\text{O}$ than the previous cement generations and the adjacent host carbonates (Figures 9(a) and 9(b)). Such depletion is related to hotter precipitation conditions (between 105 and 117°C). On the other hand, the $\delta^{18}\text{O}_{\text{fluid}}$ (between +3.2 and +5.2‰VSMOW), the high Sr, Mn, and Fe contents (Figure 12(a)), and the calculated Mg/Ca and Sr/Ca molar ratios for the vein-forming fluids are within the range of formation waters [57, 87, 95]. The homogeneous bright-orange luminescence points to complete precipitation of Cc3 during a single precipitation event [97], and the presence of a negative Ce anomaly indicates oxic precipitation conditions [84] (Figure 12(b)).

In conclusion, the progressive depletion in $\delta^{18}\text{O}$ values from Cc1 to Cc3, as well as the continuous increase in precipitation temperatures and enrichment in $\delta^{18}\text{O}_{\text{fluid}}$ and in the elemental composition, evidences a progressive change in the fluid regime during ongoing deformation. This change may result from a continuous shift in the fluid composition, due to the evolution of the meteoric waters, or from a progressive change in the fluid origin, from percolation of diluted meteoric waters to the upflow of hotter formation fluids. The evolution of the fluid system is also attested by the disequilibrium between Cc3 and its adjacent host rocks (Figure 9(b)) and may be indicative of a continuous opening of the fluid system, which is in turn attributed to the increase in fracture density and superposition of different fracturing events [4, 98–102]. Previous contributions reported the relationships between folding, fracturing, and fluid migration in the eastern part of the Sant Corneli-Bóixols anticline (around the Coll de Nargó area, Figure 1(b)) [37]. During the latest stages of deformation in the frontal part of the anticline, these authors also reported a change in the fluid origin and composition, that is, from percolation of meteoric waters, circulating at approximately 40°C, to migration of hotter formation fluids, at temperatures around 90°C [103]. Consequently, the comparison between both studies suggests a common fluid behavior during the latest-folding to postfolding stages of deformation in the whole anticline.

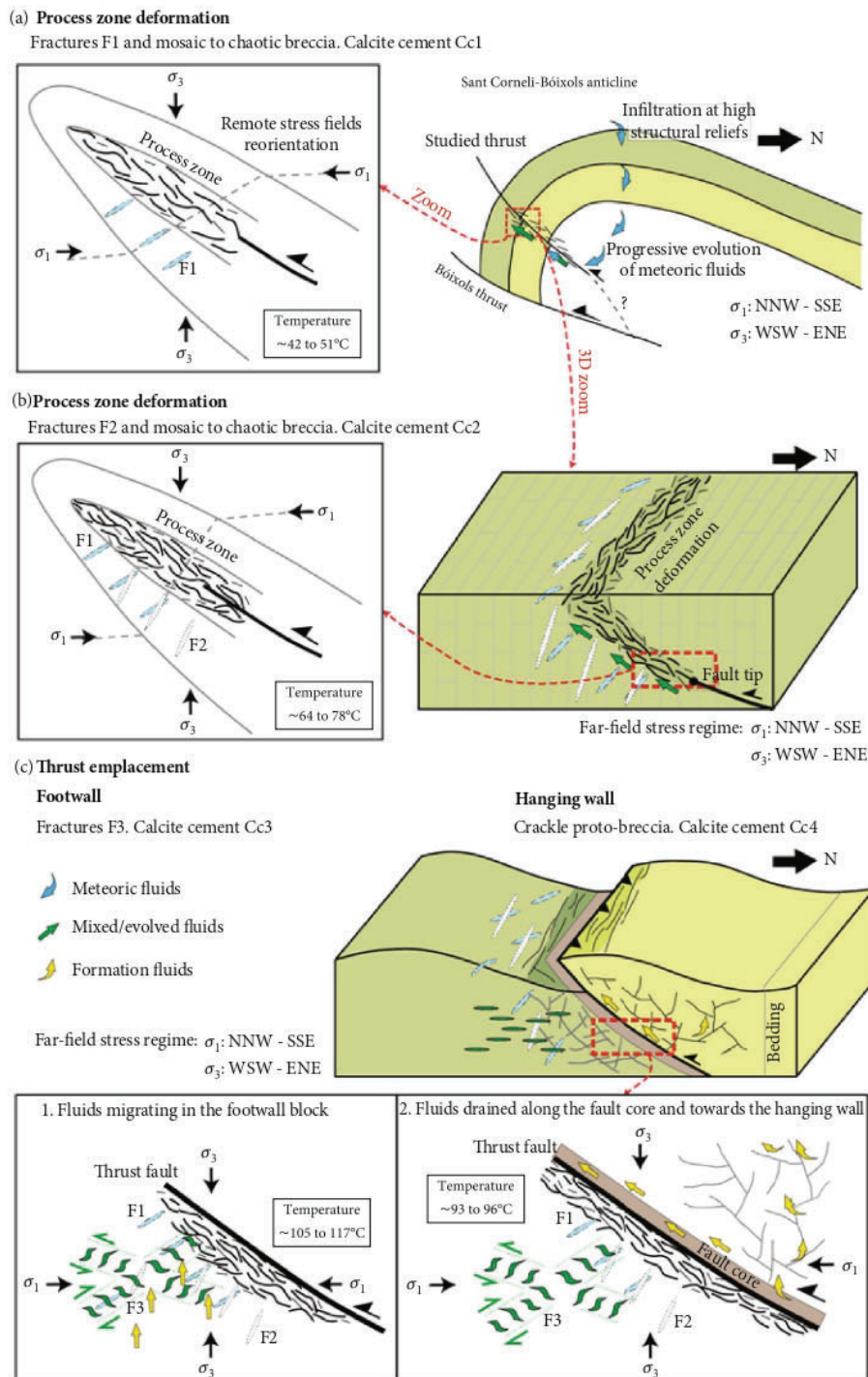


FIGURE 13: Fluid flow model during the evolution of the studied thrust (not to scale) showing the relationships between synkinematic fracture development, the stress state at each deformation phase, and the involved fluid flow event. (a) During initial fault growth, deformation was concentrated in the process zone (around the fault tip) allowing the formation of fractures F1 and randomly oriented fractures (mosaic to chaotic breccia). During this episode, meteoric fluids infiltrated at high structural reliefs, warmed at depth, and then migrated through diffused deformation around the fault tip. (b) During progressive deformation, new fractures develop and meteoric fluids evolved at increasing depths and temperatures. During these two initial fracturing events (F1-F2), the remote stress field varied locally within the process zone to generate steeply dipping fractures. (c) As the thrust developed, fractures F3 were formed in the footwall damage zone. The orientation of these fractures reflects the far-field stress regime unaltered by faulting. The fluid involved in this stage evidences the continuous increase in precipitation temperatures due to burial during thrust emplacement. From this stage, the thrust drained fluids that only infiltrated in the hanging wall. These fluids were likely expelled from underlying Cretaceous carbonates due to rock compaction during thrusting.

5.3.2. Fluid System in the Hanging Wall. Calcite cement Cc4 precipitated within the main fault plane, within the fault core, and within the randomly oriented fractures (crackle protobreccia) located in the hanging wall. The similarity between $\delta^{13}\text{C}$ values in Cc4 and its host carbonates, together with the high Mg contents and the REY pattern showing a well-defined negative Ce anomaly and a positive Y anomaly, similar to that of the host rocks, indicates buffering of the precipitating fluid by the hanging wall carbonates (Figures 9 and 12). This buffered composition of the fluids is also recorded in the $\delta^{18}\text{O}_{\text{fluid}}$ obtained from clumped isotopes and yielding values between +0.7 and +1.9‰VSMOW. However, the depletion in $\delta^{18}\text{O}$ values in Cc4 in relation to the adjacent rocks suggests that the system was opened to advection of the vein-forming fluid (Figures 9(a) and 9(b)). The Mg/Ca and Sr/Ca molar ratios calculated for the fluid that precipitated Cc4 reveal the presence of formation waters, which precipitated at temperatures between 93 and 96°C (according to clumped isotope thermometry). The $^{87}\text{Sr}/^{86}\text{Sr}$ ratio of Cc4, similar to that of the hanging wall host rock (0.707718) in the crackle proto-breccia (0.707715), but more radiogenic in the fault plane (0.707771) (Figure 11), reveals a channelized ascending fluid migrating through the thrust plane towards the hanging wall, where it progressively increased the fluid-rock interaction. Cretaceous evaporated seawater is the most probable source for these formation fluids, if we take into account that (i) Cretaceous carbonates are broadly present around and underlying the studied thrust, (ii) the $^{87}\text{Sr}/^{86}\text{Sr}$ ratios of Cc4 are consistent with Cretaceous seawater and the $\delta^{18}\text{O}_{\text{fluid}}$ is slightly more enriched with respect to marine values (Figure 10), and (iii) during the Late Cretaceous, there was a transition from marine to lagoonal and thus more restricted and evaporative conditions [104]. Upward migration of Cretaceous connate seawater was also reported during the postfolding stages of evolution in the eastern part of the Sant Corneli-Bóixols anticline [37].

5.4. Thrust Zone Evolution. The successive deformation stages, associated with different fracture systems, record an episodic evolution of the studied thrust zone. We interpret this evolution to result from an upward propagation of the fault tip leading to distributed deformation within the process zone before propagation of the fault [71, 89, 105, 106].

During initial fault growth, deformation at the fault tip, i.e., within the process zone, was dominated by concentration of dilatant (extensional) fracturing, giving rise to fractures F1 and the mosaic to chaotic breccia from the footwall (Figure 13(a)). The fluid associated with this initial deformation stage responsible for precipitation of calcite cement Cc1 was a host-rock buffered meteoric fluid. Meteoric fluids probably infiltrated the system on high structural reliefs that were likely elevated during growth of the Sant Corneli-Bóixols anticline (Figure 13(a)). These fluids warmed up to ~50°C at depth by a normal geothermal gradient and then migrated through diffuse deformation developed in the process zone before the growth and propagation of the thrust slip plane (Figure 13(a)) [71, 89, 105]. As deformation continued, new dilatant fractures F2 developed, and F1 fractures reopened and randomly oriented fractures from the breccia con-

tinued forming. This synchronicity is evidenced by the presence of the same calcite cement (Cc2) in the aforementioned fractures. The second fluid flow event, associated with the second deformation stage, was characterized by the progressive evolution of meteoric fluids due to water-rock interactions at increasing depths and temperatures (Figure 13(b)). During these two initial stages of deformation, the remote stress fields varied locally in the process zone, allowing for the formation of steeply dipping fractures (F1 and F2) (Figures 13(a) and 13(b)).

Finally, the thrust slip plane propagated through the process zone. Frictional processes occurred along the thrust surface as well as the progressive weakening of the fault zone, which led to the formation of the foliated cataclasite, characterized by S-C shear fabric, pressure solution seams, calcite mineralization, and carbonate fine-grained matrix. This micritic matrix is petrographically similar to that of the hanging wall protolith (Figures 4(c) and 7(b) and 7(c)) and displays comparable isotopic composition (Figure 9). These observations indicate that the cataclasite matrix derived from the hanging wall carbonates. During this period of thrust sheet emplacement, fractures F3 developed. We interpret that the orientation of these fractures represents the far-field stress regime unaltered by faulting (Figure 13(c)). The calcite cement Cc3, precipitated in fractures F3, reflects the presence of formation fluids and the progressive increase in precipitation temperatures, up to ~117°C, which could indicate progressive burial during fault growth from calcite cement Cc1 to Cc3 [107].

Later, the thrust acted as a preferential pathway for fluids that only infiltrated in the hanging wall block (Figure 13(c)) as indicated by the presence of the same calcite cement (Cc4) along the thrust slip plane, in the fault core and within the crackle proto-breccia from the hanging wall. Thus, this observation corroborates the compartmentalization of the fluid system. As proposed in other settings where faults compartmentalize fluid flow between the footwall and hanging wall, the presence of veins without a preferred structural orientation (i.e., randomly oriented veins) is indicative of overpressured fluid migrating during deformation. Pressured fluids were likely expelled from Cretaceous carbonates due to sediment compaction during thrust sheet emplacement [77] (Figure 13(c)).

The interpreted evolution of the studied fault zone is similar to models already proposed in other extensional settings during upward propagation of normal faults deforming carbonate rocks [71, 80, 89, 105, 108, 109]. Therefore, the comparison between these studies allows us to provide insights into deformation processes and mechanisms related to propagation of faults in different geological settings. Interestingly, all these contributions reported an initial stage of fault nucleation related to the development of a process zone (in the fault tip) before individualization of the fault plane. This period was characterized by the formation of hydraulic extension fracturing and brecciation and the presence of a fluid in chemical equilibrium with the host rocks. Finally, the progressive deformation resulted in the propagation of the fault (slip plane) through the process zone and the circulation of external fluids along the main slip surfaces (i.e.,

longitudinal fluid migration). These studies also reported an evolution of the fracture connectivity, a continuous opening of the fluid regime, and a progressive change in the fluid composition and origin during the evolution of the fault zone [80, 89, 105].

5.5. Structural Permeability: Thrust Sealing Capability and Fluid Pressuring. The petrology and geochemistry of the studied calcite cements indicate that the thrust separates two compartments with different deformation and fluid flow patterns. It is therefore likely that the thrust acted as a transversal barrier for fluids migrating between the footwall and hanging wall. The barrier role of the thrust is attributed (i) to the poor permeability of the foliated cataclasite and its micritic carbonate matrix with concentration of clay minerals associated with pressure-solution surfaces and (ii) to the nonporous character of the hanging wall carbonates (i.e., wackestones). In the latter case, although it has not been measured, the permeability is likely lower in the hanging wall wackestones with respect to the footwall grainstones. Therefore, the thrust acted as a transversal barrier and a longitudinal drain from fluids [15].

Additionally, considering the footwall damage zone as a high fractured compartment, its structural permeability is qualitatively evaluated. In this compartment, systematically oriented fractures (F1 to F3) were cemented by three generations of calcite cement (Cc1 to Cc3) and the randomly oriented fractures were cemented by Cc1 and Cc2. This evidences that the structural permeability was transient and that successive episodes of fracturing added new pathways to fluids that were rapidly occluded by calcite precipitation and sealing [18, 70]. According to theoretical models, the presence of existing fractures appropriately oriented for reactivation prevents the formation of new fracturing events [10]. Therefore, a new fracturing episode developed when the previous fracture system regained cohesive strength by calcite precipitation [10]. The fact that the calcite cements Cc1 to Cc3 vary geochemically through time demonstrate that the fluid pathways, path lengths (associated with different fracture sizes), and the extent of fluid-rock interaction changed during the thrust nucleation (process zone development) and growth (thrust slip plane propagation), which has been corroborated by the different fluid compositions and temperatures obtained from clumped isotopes. In the same location, a previous study [42] documented the distribution of fractures developed in the footwall and discussed the permeability properties of the footwall damage zone in terms of porosity creation and occluding processes based on structural analysis and crosscutting relationships between veins. These authors also concluded that the footwall damage zone had to be considered as a low-quality reservoir analogue because any porosity developed during fracturing was rapidly sealed by cementation processes [42].

The comparison between the above described scenario and the model proposed in the Oman Mountains [26] highlights that fluid behavior during thrusting greatly varies in different geological settings. In particular, the analysis of calcite cements precipitated across the fault zone in both studies reveals that the thrust faults acted as transversal barriers to

fluid migration but were preferential paths for channelized fluids along the thrust planes (longitudinal drains). In the studied outcrop, fluids in the footwall did not reach the hanging wall because of the impermeable fault core rock (foliated cataclasite) and a different fluid migrated upwards along the thrust plane and towards the hanging wall. By contrast, in the outcrop of Oman [26], fluids migrated along the thrust fault and towards the footwall, the only block in which syntectonic fractures developed. Our contribution and that of [26] highlight the importance of a good understanding of the timing of fracturing and the associated fluids in order to characterize the hydraulic behavior of a fault zone.

6. Conclusions

The studied thrust displaces a subvertical Upper Cretaceous carbonate succession located in the southern limb of the Sant Corneli-Bóixols anticline, in the Southern Pyrenees. Structural data together with petrological and geochemical analyses of synkinematic calcite veins developed within the fault zone constrain the evolution of the structural permeability and the thrust sealing capability and provide insights into the paleofluid system at the time of thrusting:

- (i) The heterogeneous distribution of deformation mechanisms across the thrust zone resulted in strong host rock dissolution within the fault core and calcite precipitation in veins within the damage zone
- (ii) The evolution of the thrust zone resulted from the upward propagation of the fault tip, producing distributed deformation in the process zone and subsequent propagation of the fault (slip plane), similar to the models already proposed for normal faults deforming carbonate rocks. During this evolution, the different deformation and fluid flow histories in the footwall and hanging wall indicate that the fault core acted as a transversal barrier due to its low permeability associated with the foliated cataclasite arrangement and matrix cementation. In the footwall, three systematically oriented fracture systems (F1 to F3) and randomly oriented fractures developed during progressive deformation. The structural permeability in the footwall damage zone was transient, and successive episodes of fracturing added new pathways to fluids but were rapidly occluded by calcite precipitation. By contrast, in the hanging wall, only randomly oriented fractures are present
- (iii) Three calcite cements (Cc1 to Cc3) precipitated within the fracture systems developed in the footwall. The petrology and geochemistry of Cc1 to Cc3 reveal a progressive change in the fluid origin and/or composition from percolation of meteoric fluids at temperatures between 42 and 51°C to upward migration of hotter formation waters at temperatures between 105 and 117°C. On the other hand, only one calcite cement (Cc4) precipitated in the hanging wall and in the fault core from hot

formation waters at 95°C. These formation fluids were probably expelled from Cretaceous carbonates and migrated along the thrust plane towards the hanging wall during deformation. The comparison between the present study and previous data reported in the eastern part of the Sant Corneli-Bóixols anticline reveals the same fluid regimen and evolution of the fluid system during the post-folding stages of deformation in the whole anticline

Data Availability

All data used to support the findings of this study are included within the article.

Conflicts of Interest

The authors declare that there is no conflict of interest regarding the publication of this paper.

Acknowledgments

This research was carried out within the framework of the Dirección General de Investigación Científica y Técnica Spanish Project (PGC2018-093903-B-C22) (Ministerio de Ciencia, Innovación y Universidades/Agencia Estatal de Investigación/Fondo Europeo de Desarrollo Regional, Unión Europea) and the Grup Consolidat de Recerca “Geologia Sedimentària” (2017-SGR-824). The PhD research of DM-L is supported by the FPI2016 (BES-2016-077214) Spanish program from MINECO.

References

- [1] H. Watkins, D. Healy, C. E. Bond, and R. W. H. Butler, “Implications of heterogeneous fracture distribution on reservoir quality; an analogue from the Torridon Group sandstone, Moine Thrust Belt, NW Scotland,” *Journal of Structural Geology*, vol. 108, pp. 180–197, 2018.
- [2] J. W. Cosgrove, “The association of folds and fractures and the link between folding, fracturing and fluid flow during the evolution of a fold–thrust belt: a brief review,” *Geological Society, London, Special Publications*, vol. 421, no. 1, pp. 41–68, 2015.
- [3] A. Travé, P. Labaume, and J. Vergés, “Fluid systems in foreland fold-and-thrust belts: an overview from the Southern Pyrenees,” in *Thrust Belts and Foreland Basins*, O. Lacombe, F. Roure, J. Lavé, and J. Vergés, Eds., pp. 93–115, Frontiers in Earth Sciences; Springer Berlin Heidelberg, Berlin, Heidelberg, 2007.
- [4] E. Fitz-Diaz, P. Hudleston, L. Siebenaller et al., “Insights into fluid flow and water-rock interaction during deformation of carbonate sequences in the Mexican fold-thrust belt,” *Journal of Structural Geology*, vol. 33, no. 8, pp. 1237–1253, 2011.
- [5] J. Oliver, “Fluids expelled tectonically from orogenic belts: their role in hydrocarbon migration and other geologic phenomena,” *Geology*, vol. 14, no. 2, p. 99, 1986.
- [6] P. Muchez and M. Sintubin, “Contrasting origin of palaeo-fluids in a strike-slip fault system,” *Chemical Geology*, vol. 145, no. 1–2, pp. 105–114, 1998.
- [7] A. Gudmundsson, “Fluid overpressure and flow in fault zones: field measurements and models,” *Tectonophysics*, vol. 336, no. 1–4, pp. 183–197, 2001.
- [8] A. Gudmundsson, S. S. Berg, K. B. Lyslo, and E. Skurtveit, “Fracture networks and fluid transport in active fault zones,” *Journal of Structural Geology*, vol. 23, no. 2–3, pp. 343–353, 2001.
- [9] R. Sibson, “Frictional mechanics of seismogenic thrust systems in the upper continental crust—implications for fluid overpressures and redistribution,” *Thrust Tectonics and Hydrocarbon Systems*, vol. 82, pp. 1–17, 2004.
- [10] R. H. Sibson, “Tensile overpressure compartments on low-angle thrust faults,” *Earth, Planets and Space*, vol. 69, no. 1, p. 113, 2017.
- [11] R. H. Sibson, “Crustal stress, faulting and fluid flow,” *Geological Society, London, Special Publications*, vol. 78, no. 1, pp. 69–84, 1994.
- [12] C. Hilgers, D. L. Kirschner, J.-P. Breton, and J. L. Urai, “Fracture sealing and fluid overpressures in limestones of the Jabal Akhdar dome, Oman mountains,” *Geofluids*, vol. 6, no. 2, pp. 168–184, 2006.
- [13] R. Sibson and J. Scott, “Stress/fault controls on the containment and release of overpressured fluids: examples from gold-quartz vein systems in Juneau, Alaska; Victoria, Australia and Otago, New Zealand,” *Ore Geology Reviews*, vol. 13, no. 1–5, pp. 293–306, 1998.
- [14] R. H. Sibson, “Arterial faults and their role in mineralizing systems,” *Geoscience Frontiers*, vol. 10, no. 6, pp. 2093–2100, 2019.
- [15] J. S. Caine, J. P. Evans, and C. B. Forster, “Fault zone architecture and permeability structure,” *Geology*, vol. 24, no. 11, p. 1025, 1996.
- [16] S. J. Jolley, D. Barr, J. J. Walsh, and R. J. Knipe, “Structurally complex reservoirs: an introduction,” *Geological Society, London, Special Publications*, vol. 292, no. 1, pp. 1–24, 2007.
- [17] F. Agosta, M. Alessandrini, M. Antonellini, E. Tondi, and M. Giorgioni, “From fractures to flow: a field-based quantitative analysis of an outcropping carbonate reservoir,” *Tectonophysics*, vol. 490, no. 3–4, pp. 197–213, 2010.
- [18] F. Agosta, M. Prasad, and A. Aydin, “Physical properties of carbonate fault rocks, fucino basin (Central Italy): implications for fault seal in platform carbonates,” *Geofluids*, vol. 7, no. 1, pp. 19–32, 2007.
- [19] S. Barker, *Dynamics of fluid flow and fluid chemistry during crustal shortening*, vol. 250, pp. 331–344, 2007.
- [20] A. Taillefer, R. Soliva, L. Guillou-Frottier, E. Le Goff, G. Martin, and M. Seranne, “Fault-related controls on upward hydrothermal flow: an integrated geological study of the Têt fault system, Eastern Pyrénées (France),” *Geofluids*, vol. 2017, 19 pages, 2017.
- [21] A. Travé, P. Labaume, F. Calvet, and A. Soler, “Sediment dewatering and pore fluid migration along thrust faults in a foreland basin inferred from isotopic and elemental geochemical analyses (Eocene southern Pyrenees, Spain),” *Tectonophysics*, vol. 282, no. 1–4, pp. 375–398, 1997.
- [22] B. Lacroix, L. P. Baumgartner, A.-S. Bouvier, P. D. Kempton, and T. Vennemann, “Multi fluid-flow record during episodic mode I opening: a microstructural and SIMS study (Cotiella thrust fault, Pyrenees),” *Earth and Planetary Science Letters*, vol. 503, pp. 37–46, 2018.

- [23] V. Trincal, M. Buatier, D. Charpentier et al., “Fluid–rock interactions related to metamorphic reducing fluid flow in meta-sediments: example of the Pic-de-Port-Vieux thrust (Pyrenees, Spain),” *Contributions to Mineralogy and Petrology*, vol. 172, no. 9, p. 78, 2017.
- [24] A. Travé, P. Labaume, F. Calvet et al., “Fluid migration during Eocene thrust emplacement in the south Pyrenean foreland basin (Spain): an integrated structural, mineralogical and geochemical approach,” *Geological Society, London, Special Publications*, vol. 134, no. 1, pp. 163–188, 1998.
- [25] L. F. Martínez Casas, A. Travé, D. Cruset, and D. Muñoz-López, “The Montagut fault system: geometry and fluid flow analysis (Southern Pyrennes, Spain),” *Petrogenesis and Exploration of the Earth’s Interior*, pp. 211–214, 2019.
- [26] L. Breesch, R. Swennen, and B. Vincent, “Fluid flow reconstruction in hanging and footwall carbonates: compartmentalization by Cenozoic reverse faulting in the Northern Oman Mountains (UAE),” *Marine and Petroleum Geology*, vol. 26, no. 1, pp. 113–128, 2009.
- [27] I. Moretti, P. Labaume, S. M. F. Sheppard, and J. Boulègue, “Compartmentalisation of fluid migration pathways in the sub-Andean Zone, Bolivia,” *Tectonophysics*, vol. 348, no. 1–3, pp. 5–24, 2002.
- [28] P. Choukroune, “The Ecors Pyrenean deep seismic profile reflection data and the overall structure of an orogenic belt,” *Tectonics*, vol. 8, no. 1, pp. 23–39, 1989.
- [29] S. P. Srivastava, H. Schouten, W. R. Roest et al., “Iberian plate kinematics: a jumping plate boundary between Eurasia and Africa,” *Nature*, vol. 344, no. 6268, pp. 756–759, 1990.
- [30] J. A. Muñoz, “Evolution of a continental collision belt: ECORS-Pyrenees crustal balanced cross-section,” in *Thrust Tectonics*, pp. 235–246, Springer Netherlands, Dordrecht, 1992.
- [31] J. Vergés and M. Fernández, “Tethys–Atlantic interaction along the Iberia–Africa plate boundary: the Betic–Rif orogenic system,” *Tectonophysics*, vol. 579, pp. 144–172, 2012.
- [32] J. A. Muñoz, “Fault-related folds in the southern Pyrenees,” *American Association of Petroleum Geologists Bulletin*, vol. 101, no. 4, pp. 579–587, 2017.
- [33] J. A. Muñoz, A. Martínez, and J. Vergés, “Thrust sequences in the eastern Spanish Pyrenees,” *Journal of Structural Geology*, vol. 8, no. 3–4, pp. 399–405, 1986.
- [34] M. Seguret and M. Daignières, “Crustal scale balanced cross-sections of the Pyrenees; discussion,” *Tectonophysics*, vol. 129, no. 1–4, pp. 303–318, 1986.
- [35] F. Roure, P. Choukroune, X. Berastegui et al., “Ecors deep seismic data and balanced cross sections: geometric constraints on the evolution of the Pyrenees,” *Tectonics*, vol. 8, no. 1, pp. 41–50, 1989.
- [36] J. Vergés and J. A. Muñoz, “Thrust sequence in the southern central Pyrenees,” *Bulletin de la Société Géologique de France*, vol. VI, no. 2, pp. 265–271, 1990.
- [37] R. M. G. Bond and K. R. McClay, “Inversion of a Lower Cretaceous extensional basin, south central Pyrenees, Spain,” *Geological Society, London, Special Publications*, vol. 88, no. 1, pp. 415–431, 1995.
- [38] J. Mencos, “Metodologies de reconstrucció i modelització 3D d’estructures geològiques: anticlinal de Sant Corneli-Bóixols (Pirineus centrals),” *Universitat de Barcelona*, 2010, PhD thesis.
- [39] S. Tavani, J. Mencos, J. Bausà, and J. A. Muñoz, “The fracture pattern of the Sant Corneli Bóixols oblique inversion anticline (Spanish Pyrenees),” *Journal of Structural Geology*, vol. 33, no. 11, pp. 1662–1680, 2011.
- [40] J. M. Garcia-Senz, *Cuencas Extensivas del Cretácico Inferior en los Pirineos Centrales, formación y subsecuente inversión*. PhD Thesis, Universitat de Barcelona, Barcelona, 2002.
- [41] J. Mencos, N. Carrera, and J. A. Muñoz, “Influence of rift basin geometry on the subsequent postrift sedimentation and basin inversion: the Organyà Basin and the Bóixols thrust sheet (south central Pyrenees),” *Tectonics*, vol. 34, no. 7, pp. 1452–1474, 2015.
- [42] J. Gutmanis, L. Ardèvol i Oró, D. Díez-Canseco, L. Chebbihi, A. Awdal, and A. Cook, “Fracture analysis of outcrop analogues to support modelling of the subseismic domain in carbonate reservoirs, south-central Pyrenees,” *Geological Society, London, Special Publications*, vol. 459, no. 1, pp. 139–156, 2018.
- [43] J. Gallemí Paulet, R. Martínez Ribas, and J. Pons, *Unidades del Cretácico superior en los alrededores de San Corneli (Provincia de Lleida)*, Cuadernos de Geología Ibérica, Madrid, Spain, 1982.
- [44] P. H. W. Mey, P. J. C. Nagtegaal, K. J. Roberti, and J. J. A. Hartevelt, “Lithostratigraphic subdivision of post-Hercynian deposits in the South-Central Pyrenees,” *Leidse geologische mededelingen*, vol. 41, pp. 221–228, 1968.
- [45] J. M. McCrea, “On the isotopic chemistry of carbonates and a paleotemperature scale,” *The Journal of Chemical Physics*, vol. 18, no. 6, pp. 849–857, 1950.
- [46] C. M. John and D. Bowen, “Community software for challenging isotope analysis: first applications of ‘Easotope’ to clumped isotopes,” *Rapid Communications in Mass Spectrometry*, vol. 30, no. 21, pp. 2285–2300, 2016.
- [47] W. Guo, J. L. Mosenfelder, W. A. Goddard, and J. M. Eiler, “Isotopic fractionations associated with phosphoric acid digestion of carbonate minerals: insights from first-principles theoretical modeling and clumped isotope measurements,” *Geochimica et Cosmochimica Acta*, vol. 73, no. 24, pp. 7203–7225, 2009.
- [48] K. W. Huntington, J. M. Eiler, H. P. Affek et al., “Methods and limitations of “clumped” CO₂ isotope (Δ_{47}) analysis by gas-source isotope ratio mass spectrometry,” *Journal of Mass Spectrometry*, vol. 44, no. 9, pp. 1318–1329, 2009.
- [49] K. J. Dennis, H. P. Affek, B. H. Passey, D. P. Schrag, and J. M. Eiler, “Defining an absolute reference frame for ‘clumped’ isotope studies of CO₂,” *Geochimica et Cosmochimica Acta*, vol. 75, no. 22, pp. 7117–7131, 2011.
- [50] S.-T. Kim and J. R. O’Neil, “Equilibrium and nonequilibrium oxygen isotope effects in synthetic carbonates,” *Geochimica et Cosmochimica Acta*, vol. 61, no. 16, pp. 3461–3475, 1997.
- [51] T. Kluge, C. M. John, A.-L. Jourdan, S. Davis, and J. Crawshaw, “Laboratory calibration of the calcium carbonate clumped isotope thermometer in the 25–250 °C temperature range,” *Geochimica et Cosmochimica Acta*, vol. 157, pp. 213–227, 2015.
- [52] N. H. Woodcock and K. Mort, “Classification of fault breccias and related fault rocks,” *Geological Magazine*, vol. 145, no. 3, pp. 435–440, 2008.
- [53] J. Veizer, D. Ala, K. Azmy et al., “⁸⁷Sr/⁸⁶Sr, δ^{13} C and δ^{18} O evolution of Phanerozoic seawater,” *Chemical Geology*, vol. 161, no. 1–3, pp. 59–88, 1999.

- [54] C. Delle Piane, M. B. Clennell, J. V. A. Keller, A. Giwelli, and V. Luzin, "Carbonate hosted fault rocks: a review of structural and microstructural characteristic with implications for seismicity in the upper crust," *Journal of Structural Geology*, vol. 103, pp. 17–36, 2017.
- [55] G. S. Lister and A. W. Snoke, "S-C mylonites," *Journal of Structural Geology*, vol. 6, no. 6, pp. 617–638, 1984.
- [56] J. M. McArthur and R. J. Howarth, "Shields, G.A. Strontium isotope stratigraphy," in *The Geologic Time Scale*, vol. 1–2, pp. 127–144, Elsevier, 2012.
- [57] W. L. McIntire, "Trace element partition coefficients—a review of theory and applications to geology," *Geochimica et Cosmochimica Acta*, vol. 27, no. 12, pp. 1209–1264, 1963.
- [58] A. Mucci and J. W. Morse, "The incorporation of Mg^{2+} and Sr^{2+} into calcite overgrowths: influences of growth rate and solution composition," *Geochimica et Cosmochimica Acta*, vol. 47, no. 2, pp. 217–233, 1983.
- [59] A. Katz, "The interaction of magnesium with calcite during crystal growth at 25–90°C and one atmosphere," *Geochimica et Cosmochimica Acta*, vol. 37, no. 6, pp. 1563–1586, 1973.
- [60] A. Katz, E. Sass, A. Starinsky, and H. D. Holland, "Strontium behavior in the aragonite-calcite transformation: an experimental study at 40–98°C," *Geochimica et Cosmochimica Acta*, vol. 36, no. 4, pp. 481–496, 1972.
- [61] D. J. J. Kinsman, "Interpretation of Sr^{+2} concentrations in carbonate minerals and rocks," *SEPM Journal of Sedimentary Research*, vol. Vol. 39, 1969.
- [62] M. Bau and P. Dulski, "Distribution of yttrium and rare-earth elements in the Penge and Kuruman iron-formations, Transvaal Supergroup, South Africa," *Precambrian Research*, vol. 79, no. 1–2, pp. 37–55, 1996.
- [63] G. E. Webb and B. S. Kamber, "Rare earth elements in Holocene reefal microbialites: a new shallow seawater proxy," *Geochimica et Cosmochimica Acta*, vol. 64, no. 9, pp. 1557–1565, 2000.
- [64] F. Salvini, A. Billi, and D. U. Wise, "Strike-slip fault-propagation cleavage in carbonate rocks: the Mattinata fault zone, southern Apennines, Italy," *Journal of Structural Geology*, vol. 21, no. 12, pp. 1731–1749, 1999.
- [65] B. Lacroix, A. Travé, M. Buatier, P. Labaume, T. Vennemann, and M. Dubois, "Syntectonic fluid-flow along thrust faults: example of the south-Pyrenean fold-and-thrust belt," *Marine and Petroleum Geology*, vol. 49, pp. 84–98, 2014.
- [66] P. D. Bons, M. A. Elburg, and E. Gomez-Rivas, "A review of the formation of tectonic veins and their microstructures," *Journal of Structural Geology*, vol. 43, pp. 33–62, 2012.
- [67] K. Bitzer, A. Travé, and J. M. Carmona, "Fluid flow processes at basin scale," *Acta Geologica Hispánica*, vol. 36, pp. 1–20, 2001.
- [68] R. H. Sibson, "Brittle-failure controls on maximum sustainable overpressure in different tectonic regimes," *American Association of Petroleum Geologists Bulletin*, vol. 87, no. 6, pp. 901–908, 2003.
- [69] D. M. Saffer and H. J. Tobin, "Hydrogeology and mechanics of subduction zone forearcs: fluid flow and pore pressure," *Annual Review of Earth and Planetary Sciences*, vol. 39, no. 1, pp. 157–186, 2011.
- [70] V. F. Bense, T. Gleeson, S. E. Loveless, O. Bour, and J. Scibek, "Fault zone hydrogeology," *Earth-Science Reviews*, vol. 127, pp. 171–192, 2013.
- [71] J. M. Vermilye and C. H. Scholz, "The process zone: a microstructural view of fault growth," *Journal of Geophysical Research - Solid Earth*, vol. 103, no. B6, pp. 12223–12237, 1998.
- [72] P. Upton, M. Begbie, and D. Craw, "Numerical modelling of mechanical controls on coeval steep and shallow dipping auriferous quartz vein formation in a thrust zone, Macraes mine, New Zealand," *Mineralium Deposita*, vol. 43, no. 1, pp. 23–35, 2008.
- [73] M. J. Begbie and D. Craw, "Geometry and petrography of stockwork vein swarms, macraes mine, Otago schist, New Zealand," *New Zealand Journal of Geology and Geophysics*, vol. 49, no. 1, pp. 63–73, 2006.
- [74] R. L. Enlow and P. O. Koons, "Critical wedges in three dimensions: analytical expressions from Mohr-Coulomb constrained perturbation analysis," *Journal of Geophysical Research - Solid Earth*, vol. 103, no. B3, pp. 4897–4914, 1998.
- [75] J. J. Wilkinson and J. D. Johnston, "Pressure fluctuations, phase separation, and gold precipitation during seismic fracture propagation," *Geology*, vol. 24, no. 5, pp. 395–398, 1996.
- [76] C. H. Scholz, N. H. Dawers, J.-Z. Yu, M. H. Anders, and P. A. Cowie, "Fault growth and fault scaling laws: preliminary results," *Journal of Geophysical Research - Solid Earth*, vol. 98, no. B12, pp. 21951–21961, 1993.
- [77] B. Dewever, R. Swennen, and L. Breesch, "Fluid flow compartmentalization in the Sicilian fold and thrust belt: implications for the regional aqueous fluid flow and oil migration history," *Tectonophysics*, vol. 591, pp. 194–209, 2013.
- [78] Y. Branquet, A. Cheilletz, G. Giuliani, B. Laumonier, and O. Blanco, "Fluidized hydrothermal breccia in dilatant faults during thrusting: the Colombian emerald deposits," *Geological Society, London, Special Publications*, vol. 155, no. 1, pp. 183–195, 1999.
- [79] S. F. J. Cox, M. A. Knackstedt, and J. W. Braun, "Principles of structural control on permeability and fluid flow in hydrothermal systems," *Structural Controls on Ore Genesis; Society of Economic Geologists*, pp. 1–24, 2001.
- [80] M. Bussolotto, A. Benedicto, L. Moen-Maurel, and C. Invernizzi, "Fault deformation mechanisms and fault rocks in micritic limestones: examples from Corinth rift normal faults," *Journal of Structural Geology*, vol. 77, pp. 191–212, 2015.
- [81] R. H. Sibson, "Structural permeability of fluid-driven fault-fracture meshes," *Journal of Structural Geology*, vol. 18, no. 8, pp. 1031–1042, 1996.
- [82] P. Labaume, S. Sheppard, and I. Moretti, "Structure and hydraulic behaviour of cataclastic thrust fault zones in sandstones, Sub-Andean Zone, Bolivia," *Journal of Geochemical Exploration*, vol. 69–70, pp. 487–492, 2000.
- [83] I. Moretti, P. Labaume, S. Sheppard, and J. Boulegue, "Compartmentalisation of fluid flow by thrust faults, Sub-Andean Zone, Bolivia," *Journal of Geochemical Exploration*, vol. 69–70, pp. 493–497, 2000.
- [84] R. Tostevin, G. A. Shields, G. M. Tarbuck, T. He, M. O. Clarkson, and R. A. Wood, "Effective use of cerium anomalies as a redox proxy in carbonate-dominated marine settings," *Chemical Geology*, vol. 438, pp. 146–162, 2016.
- [85] H. Irwin, C. Curtis, and M. Coleman, "Isotopic evidence for source of diagenetic carbonates formed during burial of organic-rich sediments," *Nature*, vol. 269, no. 5625, pp. 209–213, 1977.

- [86] T. E. Cerling, J. Quade, Y. Wang, and J. R. Bowman, "Carbon isotopes in soils and palaeosols as ecology and palaeoecology indicators," *Nature*, vol. 341, no. 6238, pp. 138-139, 1989.
- [87] M. R. Howson, A. D. Pethybridge, and W. A. House, "Synthesis and distribution coefficient of low-magnesium calcites," *Chemical Geology*, vol. 64, no. 1-2, pp. 79-87, 1987.
- [88] I. Cantarero, A. Travé, G. Alías, and V. Baqués, "Pedogenic products sealing normal faults (Barcelona Plain, NE Spain)," *Journal of Geochemical Exploration*, vol. 106, no. 1-3, pp. 44-52, 2010.
- [89] V. Baqués, A. Travé, A. Benedicto, P. Labaume, and I. Cantarero, "Relationships between carbonate fault rocks and fluid flow regime during propagation of the Neogene extensional faults of the Penedès basin (Catalan Coastal Ranges, NE Spain)," *Journal of Geochemical Exploration*, vol. 106, no. 1-3, pp. 24-33, 2010.
- [90] S. Boggs and D. Krinsley, *Application of Cathodoluminescence Imaging to the Study of Sedimentary Rocks*, Cambridge University Press, Cambridge, UK, 2006.
- [91] V. Vandeginste, R. Swennen, M. Allaey, R. M. Ellam, K. Osadetz, and F. Roure, "Challenges of structural diagenesis in foreland fold-and-thrust belts: a case study on paleofluid flow in the Canadian Rocky Mountains West of Calgary," *Marine and Petroleum Geology*, vol. 35, no. 1, pp. 235-251, 2012.
- [92] N. Beaudoin, N. Bellahsen, O. Lacombe, and L. Emmanuel, "Fracture-controlled paleohydrogeology in a basement-cored, fault-related fold: Sheep Mountain Anticline, Wyoming, United States," *Geochemistry, Geophysics, Geosystems*, vol. 12, no. 6, 2011.
- [93] H. G. Machel, "Application of cathodoluminescence to carbonate diagenesis," in *Cathodoluminescence in Geosciences*, pp. 271-301, Springer Berlin Heidelberg, Berlin, Heidelberg, 2000.
- [94] R. Worden, "Quantitative diagenesis: recent developments and applications to reservoir geology," *Marine and Petroleum Geology*, vol. 13, no. 5, pp. 597-598, 1996.
- [95] A. Travé, F. Calvet, M. Sans, J. Vergés, and M. Thirlwall, "Fluid history related to the Alpine compression at the margin of the south-Pyrenean foreland basin: the El Guix anticline," *Tectonophysics*, vol. 321, no. 1, pp. 73-102, 2000.
- [96] I. P. Montañez and L. J. Crossey, "Diagenesis," in *Encyclopedia of Geochemistry*, W. M. White, Ed., Encyclopedia of Earth Sciences Series; Springer International Publishing, Cham, 2017.
- [97] P. Nuriel, G. Rosenbaum, J.-X. Zhao et al., "U-Th dating of striated fault planes," *Geology*, vol. 40, no. 7, pp. 647-650, 2012.
- [98] N. Vilasi, R. Swennen, and F. Roure, "Diagenesis and fracturing of Paleocene-Eocene carbonate turbidite systems in the Ionian Basin: the example of the Kelcyra area (Albania)," *Journal of Geochemical Exploration*, vol. 89, no. 1-3, pp. 409-413, 2006.
- [99] L. Lefticariu, E. C. Perry, M. P. Fischer, and J. L. Banner, "Evolution of fluid compartmentalization in a detachment fold complex," *Geology*, vol. 33, no. 1, p. 69, 2005.
- [100] M. P. Fischer, I. C. Higuera-Díaz, M. A. Evans, E. C. Perry, and L. Lefticariu, "Fracture-controlled paleohydrology in a map-scale detachment fold: insights from the analysis of fluid inclusions in calcite and quartz veins," *Journal of Structural Geology*, vol. 31, no. 12, pp. 1490-1510, 2009.
- [101] M. A. Evans, G. E. Bebout, and C. H. Brown, "Changing fluid conditions during folding: an example from the Central Appalachians," *Tectonophysics*, vol. 576-577, pp. 99-115, 2012.
- [102] D. Cruset, I. Cantarero, J. Vergés, C. M. John, D. Muñoz-López, and A. Travé, "Changes in fluid regime in synorogenic sediments during the growth of the south Pyrenean fold and thrust belt," *Global and Planetary Change*, vol. 171, pp. 207-224, 2018.
- [103] N. Nardini, D. Muñoz-López, D. Cruset et al., "From early contraction to post-folding fluid evolution in the frontal part of the Bóixols thrust sheet (Southern Pyrenees) as revealed by the texture and geochemistry of calcite cements," *Minerals*, vol. 9, no. 2, p. 117, 2019.
- [104] O. Oms, V. Fondevilla, V. Riera et al., "Transitional environments of the lower Maastrichtian South-Pyrenean Basin (Catalonia, Spain): the Fumanya member tidal flat," *Cretaceous Research*, vol. 57, pp. 428-442, 2016.
- [105] P. Labaume, E. Carrio-Schaffhauser, J.-F. Gamond, and F. Renard, "Deformation mechanisms and fluid-driven mass transfers in the recent fault zones of the Corinth Rift (Greece)," *Comptes Rendus Geoscience*, vol. 336, no. 4-5, pp. 375-383, 2004.
- [106] Z. Reches and D. A. Lockner, "Nucleation and growth of faults in brittle rocks," *Journal of Geophysical Research-Solid Earth*, vol. 99, no. B9, pp. 18159-18173, 1994.
- [107] F. X. Passelègue, O. Fabbri, M. Dubois, and S. Ventalon, "Fluid overpressure along an Oligocene out-of-sequence thrust in the Shimanto Belt, SW Japan," *Journal of Asian Earth Sciences*, vol. 86, pp. 12-24, 2014.
- [108] I. S. Stewart and P. L. Hancock, "Brecciation and fracturing within neotectonic normal fault zones in the Aegean region," *Geological Society, London, Special Publications*, vol. 54, no. 1, pp. 105-110, 1990.
- [109] I. S. Stewart and P. L. Hancock, "Normal fault zone evolution and fault scarp degradation in the Aegean region," *Basin Research*, vol. 1, pp. 139-153, 1988.

Article 3

Nardini, N., **Muñoz-López, D.**, Cruset, D., Cantarero, I., Martín-Martín, J., Benedicto, A., Gomez-Rivas, E., John, C. M., and Travé, A., 2019: From early contraction to post-folding fluid evolution in the frontal part of the Bóixols thrust sheet (Southern Pyrenees) as revealed by the texture and geochemistry of calcite cements, *Minerals*, 9(2), 117, doi:10.3390/min9020117. Impact factor: 2.380. Position: Q2 (90/235) in Geology (2020).

Article

From Early Contraction to Post-Folding Fluid Evolution in the Frontal Part of the Bóixols Thrust Sheet (Southern Pyrenees) as Revealed by the Texture and Geochemistry of Calcite Cements

Nicholas Nardini ¹, Daniel Muñoz-López ^{1,*} , David Cruset ¹, Irene Cantarero ¹, Juan Diego Martín-Martín ¹, Antonio Benedicto ², Enrique Gomez-Rivas ^{1,3} , Cédric M. John ⁴  and Anna Travé ¹ 

¹ Departament de Mineralogia, Petrologia i Geologia Aplicada, Facultat de Ciències de la Terra, Universitat de Barcelona (UB), Martí i Franquès s/n, 08028 Barcelona, Spain; nicholasnardini91@gmail.com (N.N.); d.cruset@ub.edu (D.C.); i_cantarero@ub.edu (I.C.); juandiegomartin@ub.edu (J.D.M.-M.); e.gomez-rivas@ub.edu (E.G.-R.); atrave@ub.edu (A.T.)

² UMR Geops, Université Paris Sud, 91405 Orsay, France; antonio.benedicto@u-psud.fr

³ School of Geosciences, King's College, University of Aberdeen, Aberdeen AB24 3UE, UK

⁴ Department of Earth Science and Engineering, Imperial College London, London SW7 2BP, UK; cedric.john@imperial.ac.uk

* Correspondence: munoz-lopez@ub.edu; Tel.: +34-934031165

Received: 28 December 2018; Accepted: 14 February 2019; Published: 16 February 2019



Abstract: Structural, petrological and geochemical ($\delta^{13}\text{C}$, $\delta^{18}\text{O}$, clumped isotopes, $^{87}\text{Sr}/^{86}\text{Sr}$ and ICP-MS) analyses of fracture-related calcite cements and host rocks are used to establish a fluid-flow evolution model for the frontal part of the Bóixols thrust sheet (Southern Pyrenees). Five fracture events associated with the growth of the thrust-related Bóixols anticline and Coll de Nargó syncline during the Alpine orogeny are distinguished. These fractures were cemented with four generations of calcite cements, revealing that such structures allowed the migration of different marine and meteoric fluids through time. During the early contraction stage, Lower Cretaceous seawater circulated and precipitated calcite cement Cc1, whereas during the main folding stage, the system opened to meteoric waters, which mixed with the connate seawater and precipitated calcite cement Cc2. Afterwards, during the post-folding stages, connate evaporated marine fluids circulated through newly formed NW-SE and NE-SW conjugate fractures and later through strike-slip faults and precipitated calcite cements Cc3 and Cc4. The overall paragenetic sequence reveals the progressive dewatering of Cretaceous marine host sediments during progressive burial, deformation and fold tightening and the input of meteoric waters only during the main folding stage. This study illustrates the changes of fracture systems and the associated fluid-flow regimes during the evolution of fault-associated folds during orogenic growth.

Keywords: geochemistry of calcite cements; meteoric and marine fluids; fractures; Bóixols thrust sheet; southern Pyrenees

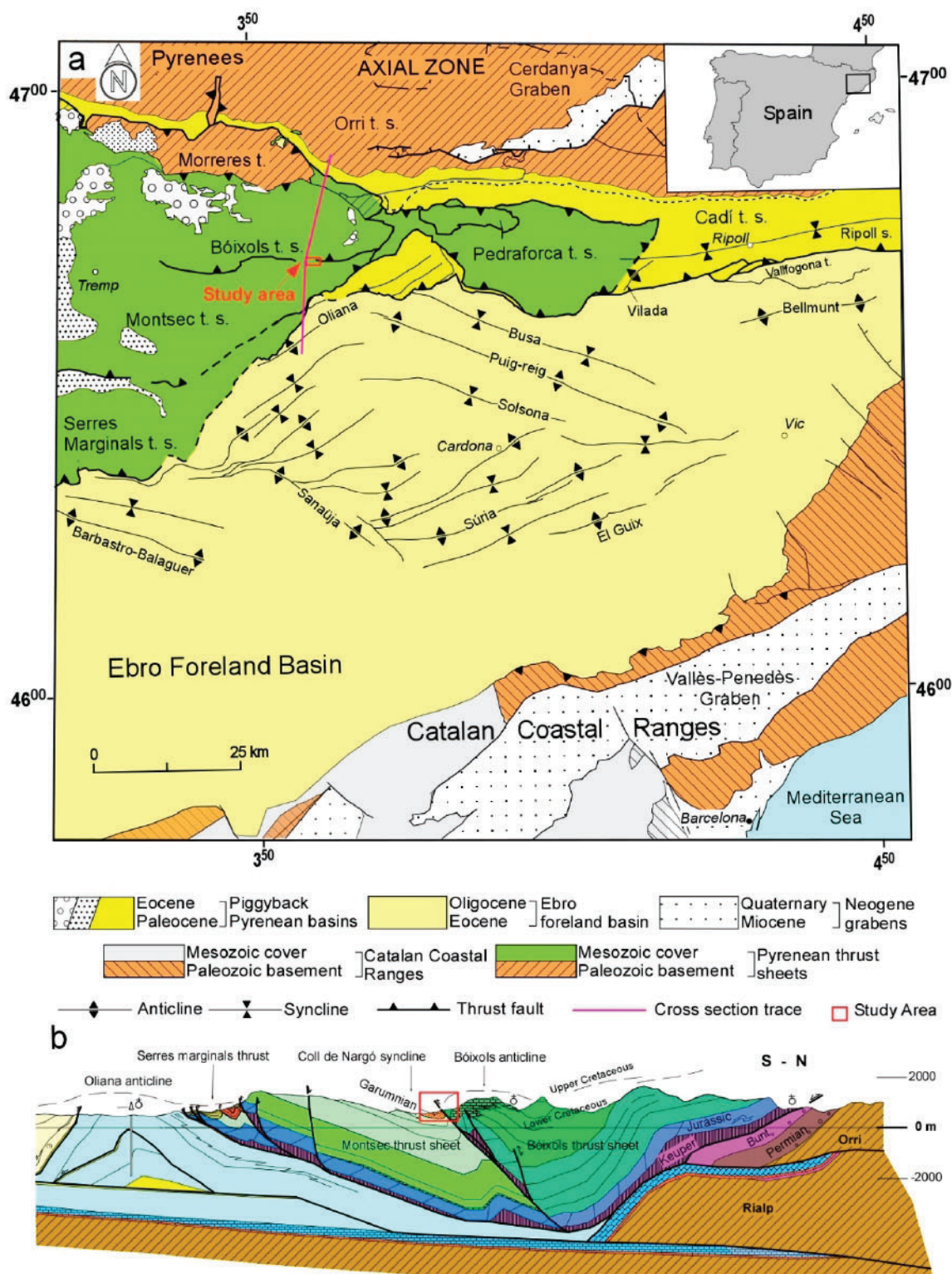
1. Introduction

Fluids play an important role on the Earth's crust as, on one hand, they transport solutes and distribute heat, controlling mineral reactions including precipitation and dissolution [1–8], and on the other hand, they can change the effective stress, favoring the reactivation of existing fractures and the formation of new ones [9–12].

During the geodynamic evolution of fold and thrust belts and related foreland basins, fluid migration controls diagenetic processes and the propagation of fractures and faults. In turn, the fracture geometry and architecture conditions their role as either conduits or seals for fluids, thus controlling fluid distribution [13,14]. In this geodynamic setting, the fluid sources change with time as foreland basins usually evolve from marine to continental conditions [15,16]. Moreover, thrusts may act also as paths for deep-sourced fluids while fold-associated fractures for low-temperature meteoric fluids [17,18].

Structural analysis of fractures, together with petrographical and geochemical studies of vein calcite cements and their host rocks, allow to assess the interplay between rock deformation and diagenetic reactions, the degree of fluid-rock interaction, the fluid-flow regime during deformation and the relative timing of fluid circulation [18–20]. Likewise, the type and origin of fluids can be unraveled [21–23], and thus decipher if the fluids that formed the different veins flowed locally in a closed paleohydrogeological regime [24–26] or in a relatively open system with possible interaction between fluids from different sources [16,27]. Studies integrating the evolution of fracture systems and related cements are needed to constrain the fluid-flow history of an area during orogenic growth and, therefore, understand the nature and origin of fluids that circulate through time, the diagenetic process evolution, changes in reservoir properties such as porosity and permeability and the distribution of minerals and hydrocarbons [28,29].

During recent years, the interest in this topic has significantly increased [30–33], giving rise to many new studies that have tackled this topic in compressional, extensional and strike-slip tectonic settings worldwide. Some recent examples are from the Ionian fold and thrust belt in Albania [22,34,35], the Apennines [36–40], the Alps [41,42], the Zagros Mountains [43], the Sicilian belt [44], the Oman Mountains [45–48], the Catalan Coastal Range [49–53] and the Pyrenees [16,17,19,24,54–57]. The South Pyrenean fold and thrust belt is well known as an outstanding field analogue for the study of fluid migration during orogenic compression due to the excellent preservation of its sedimentary record, the high-quality exposure of structures and the complex relationships between folding and thrusting and syntectonic sediments [19,58]. This contribution presents a detailed case study of the frontal part of the Bóixols thrust sheet to decipher the fluid-flow regime during the earliest stages of the evolution of the South-Central Pyrenean Unit (Figure 1), as it corresponds to the oldest emplaced thrust sheet in the area. The analyzed structures include the southern limb of the fault-related Bóixols anticline and its associated footwall, the Coll de Nargó syncline. We combine structural field data with the petrological and geochemical study of involved host rocks and fracture-filling cements in order to: (1) constrain the fracture network developed during the tectonic evolution of the study area, (2) characterize the type of fluid system and their origin, their flow pathways and the degree of fluid-rock interaction and, (3) propose a conceptual model that explains the fracture-controlled fluid-flow evolution of the frontal part of the Bóixols thrust sheet.



2. Geological Setting

The Pyrenees formed by the continental collision between the Iberian and European plates and consist of an asymmetrical and doubly-verging orogenic system generated from the Late Cretaceous to

the Oligocene [60–63]. This orogen is constituted by an antiformal stack of basement-involved thrusts (i.e., Axial Zone) surrounded by two fold and thrust belts that were transported to the north and south over the Aquitanian and Ebro foreland basins, respectively [61,64,65]. The South-Central Pyrenean Unit consists of three south-verging imbricated thrust sheets detached over Triassic evaporites: Bóixols, Montsec and Serres Marginals [66]. The Bóixols thrust sheet represents the northernmost and oldest emplaced structure and was originated by the inversion of the Organyà extensional basin during the Upper Santonian [59,67–69]. It is bounded to the south by the Bóixols thrust and to the north by the Morreres back-thrust and is characterized by a set of structures roughly striking E-W [66]. The study area is located in the frontal part of the Bóixols thrust sheet and comprises the southern limb of the Bóixols anticline and the northern limb of the Coll de Nargó syncline (Figure 1). Existing stratigraphic data [70,71] reveals that the main stage of development of the Bóixols thrust was from the Campanian (83.6–72.1 Ma) to the late Maastrichtian (72.1–66 Ma) [72]. Additionally, authigenic illite dating of the above-mentioned fault gouge indicates an age of 71.2 ± 6.4 Ma [73]. This result is consistent with the age estimated through stratigraphic data, confirming the onset of the Pyrenean convergence and associated deformation by the Late Cretaceous.

2.1. Lithology and Petrography

The stratigraphic record in the Bóixols thrust sheet has been divided into four main sequences related to the main tectonic events (Figure 2) [67,72,74]: (1) The pre-rift sequence mainly consists of evaporites and clays of the Triassic Keuper facies, which acted as a detachment level of the Bóixols thrust [75], and Jurassic dolostones; (2) The Lower Cretaceous syn-rift sequence is represented by platform carbonates and basinal marls [67,69]; (3) The post-rift sequence, with an age from Upper Cenomanian to Early Santonian, is composed of limestones, sandstones and marls [69]; and, finally, (4) the syn-orogenic sequence is represented by Upper Santonian to Campanian turbiditic deposits [76], Late Campanian to Maastrichtian shallow marine sequences and uppermost Maastrichtian to Paleocene fluvial lacustrine red beds. The succession cropping out in the study area (Figures 3 and 4) is described as follows. The Jurassic pre-rift sequence mainly consists of limestones, marls and dolostones with a thickness ranging from 600 to 1,200 m [72]. However, this unit often appears incomplete in the study area because of erosion [69,72]. These sediments were incorporated into the hanging wall of the Bóixols thrust sheet during the Alpine orogeny. The Lower Cretaceous syn-rift Lluçà Formation (Aptian-Albian in age) consists of a rhythmic alternation of dark grey marls, marly limestones and limestones containing silt to fine quartz grains and sporadic glauconite grains, representing water depth variations. The abundant fossiliferous content (ammonites, sponges, rudists and isolated calcispheres) suggests that these sediments were deposited from a shallow to deeper marine environment below the wave action zone [69]. The Upper Cretaceous post-rift Santa Fe Formation deposited prior to the Alpine compression [58]. It is bounded by two unconformities and consists of a rigid 30-m thick succession of grey homogeneous bioclastic wackestones constituted of miliolida, bivalves, bryozoans, echinoderms, *Textularia* and *Praealveolina*. Bio-erosion evidence on fossil fragments suggests that deposition of this unit took place during low sedimentation rates and/or shallow conditions.

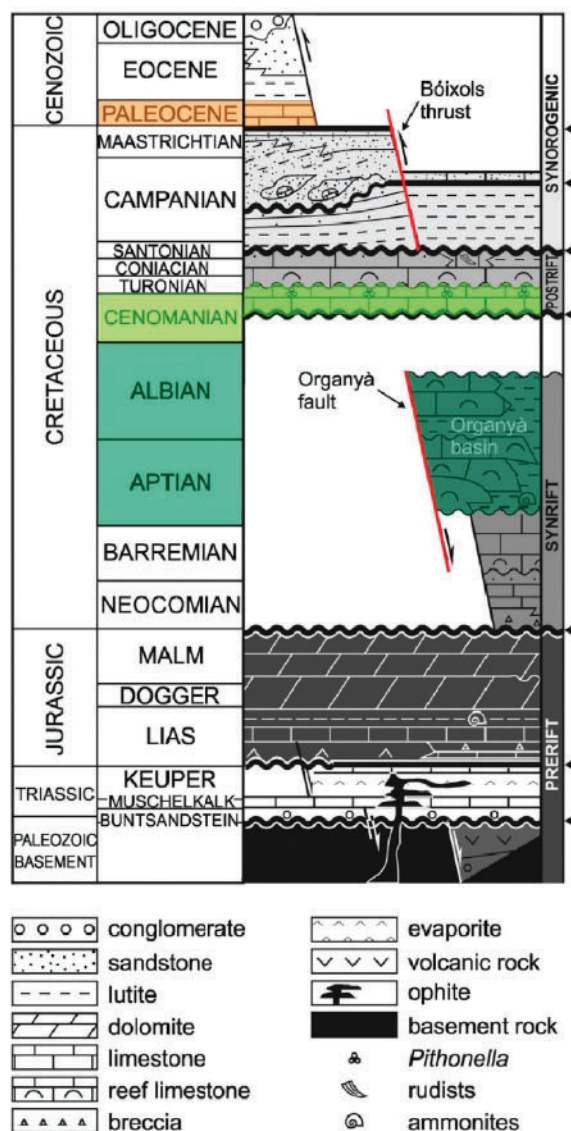


Figure 2. Chronostratigraphic diagram showing the principal stratigraphic units and their related tectonic events [72]. The outcropping units, where all the samples were taken from, are colored in orange (Garumnian facies), light green (Santa Fe Fm.) and dark green (Lluçà Fm.).

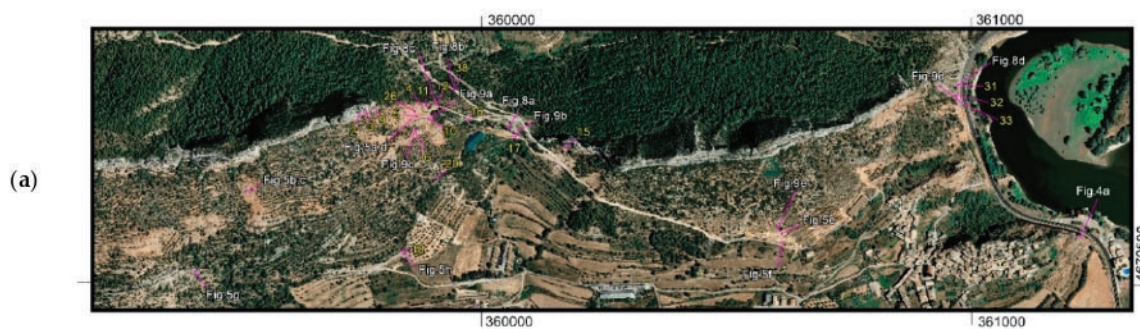


Figure 3. Cont.

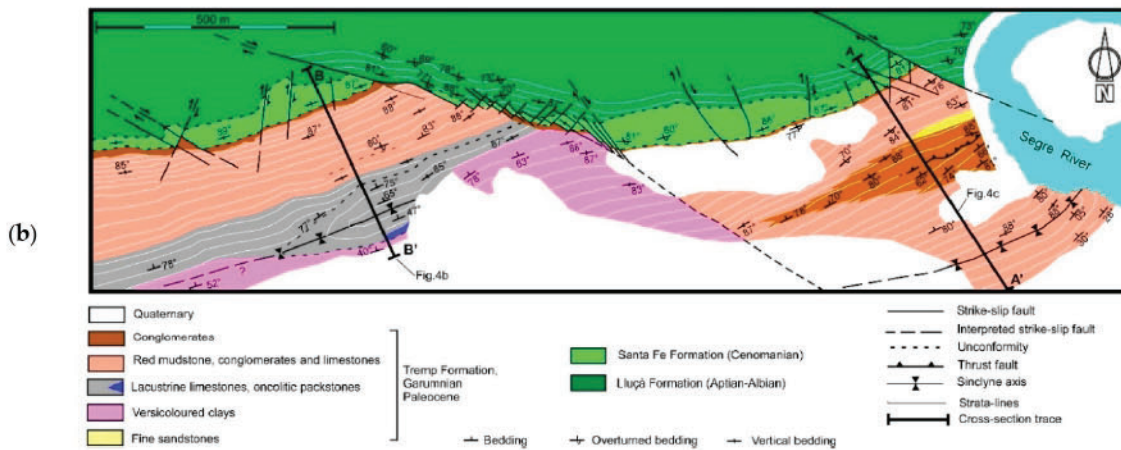


Figure 3. (a) Aerial view with sample location (yellow numbers) and situation of Figures 5, 8 and 9. Figure 7a, representing the Bóixols thrust outcrop, is about 11 km to the west of the Coll de Nargó village. (b) Geological map of the main outcrop. The Paleocene syn-orogenic sequence (Garumnian facies) fossilizes the Bóixols thrust in this area. Location in Figure 1. A-A' and B-B' cross sections in Figure 4.

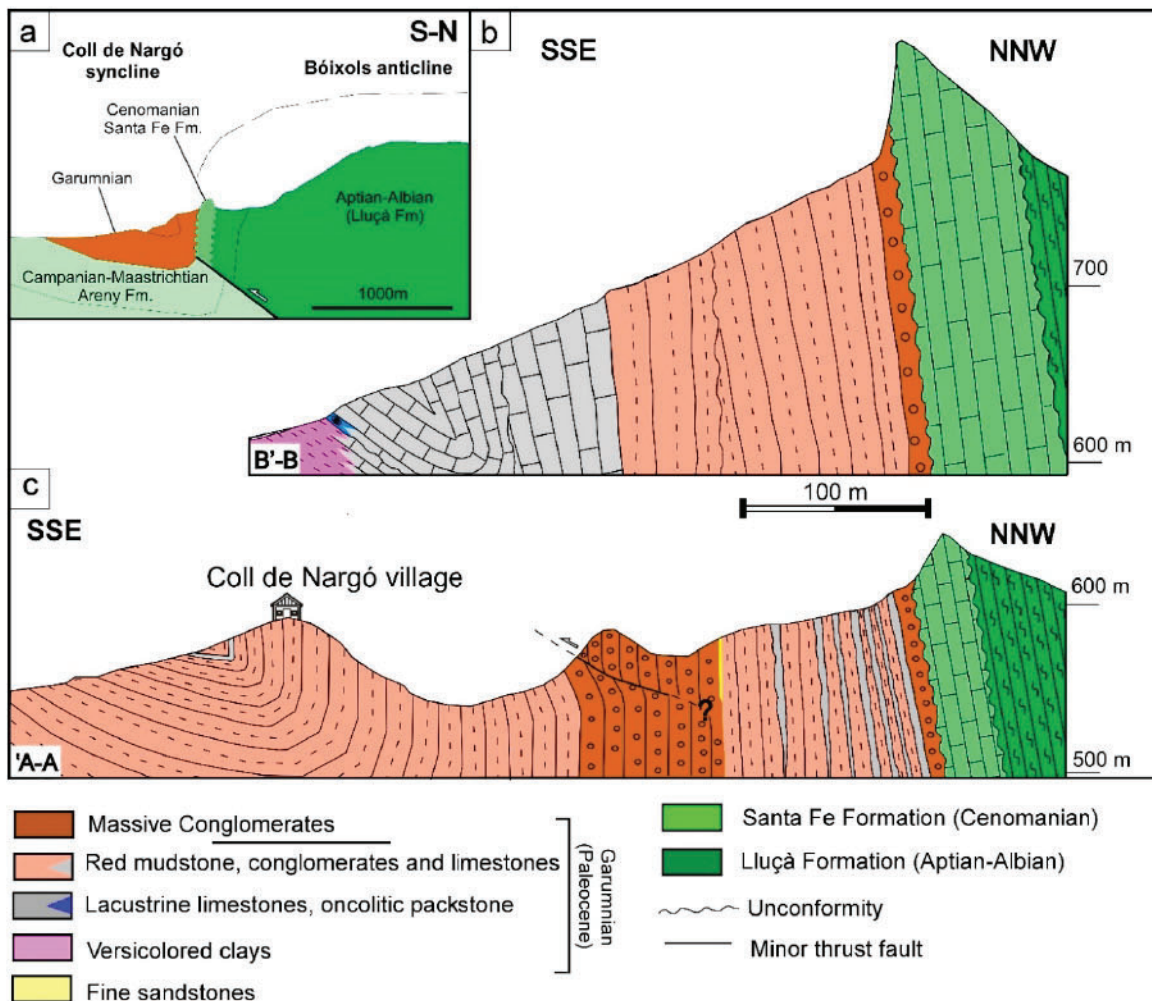


Figure 4. (a) Cross-section of the Coll de Nargó syncline and the Bóixols anticline. The northern limb of the Coll de Nargó syncline belongs to the southern limb of the Bóixols anticline. (b,c) schematic cross sections in the frontal part of the Bóixols thrust sheet in the study area. Location in Figure 3.

The uppermost Cretaceous to Paleocene syn-orogenic Garumnian facies (i.e., Tremp Formation) are composed of fluvial-alluvial and lacustrine facies comprising red mudstones, limestones, sandstones, conglomerates and versicolored clays (Figure 5a–g). Conglomerates are polymictic, clast-supported and formed by 70–80% of Mesozoic extrabasinal calcareous pebbles, characterized by a wide grain size range (1–20 cm) and shape varying from sub-angular to sub-rounded with low to high sphericity. The remaining part is constituted by 10–30% matrix, 10–20% calcite cement and negligible porosity (0–5%). Red-brick floodplain mudstones are characterized by high iron oxide concentration. Lacustrine limestones generally occur interbedded with red and nodular mudstones. Petrographically, they consist of wackestones composed of fragments of bivalves and gastropods, which originally were composed of low-Mg calcite [77]. Locally they change to oncolitic packstones (Figure 5h) displaying a peloidal fabric related to microbial processes. Fine and coarse-grained sandstones are stacked in tabular and channelized bodies. Versicolored clays appear altered by oxide-reduction processes related to paleo-soils. Locally, packstone with *Microcodium* is also observed (Figure 5i).

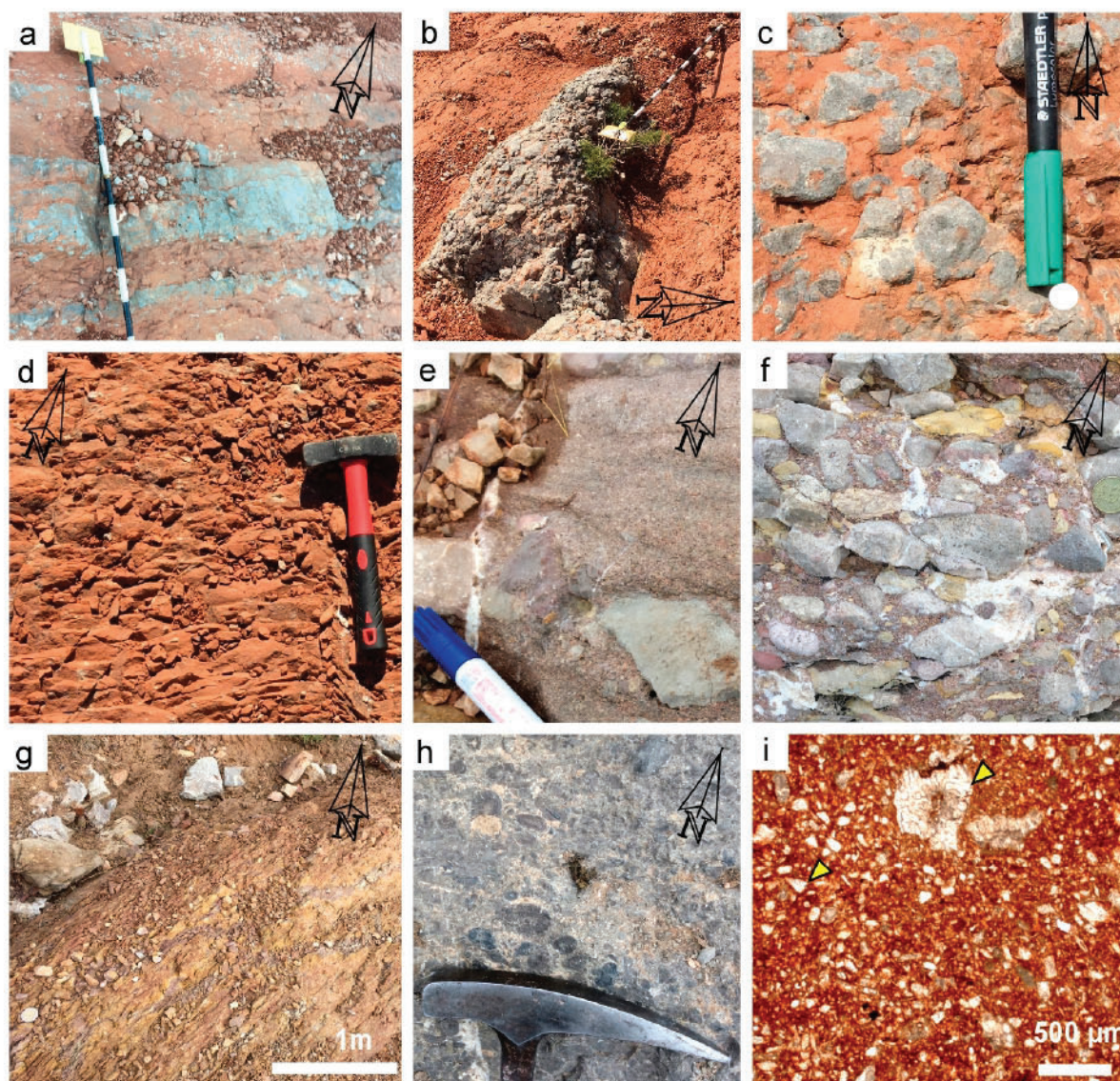


Figure 5. Field and photomicrographs of Paleocene Garumnian facies. (a) Red mudstones alternating with lacustrine limestones. (b,c) nodular lacustrine limestones. (d) Red mudstones. (e) Coarse sandstones with pebbles at the base. (f) Conglomerates. (g) Versicolored clays. (h) Oncolitic packstone. (i) Plane polarized photomicrograph of *Microcodium* packstones. The yellow arrows point to massive *Microcodium* and reworked fragments.

2.2. The Coll de Nargó Syncline

The Coll de Nargó syncline is a narrow, asymmetric and E-W oriented fold formed in response to the Bóixols thrusting and located at the north-eastern boundary of the Montsec thrust sheet (Figures 3 and 4). It includes the Areny Formation (Maastrichtian) and the Garumnian facies (Paleocene), which unconformably overly the Santa Fe Formation (Cenomanian). In the northern limb, bedding ranges from vertical to slightly overturned, while it gently dips (30–40°) towards the north in the southern flank (Figure 4). The syntectonic deposition of the Garumnian facies is highlighted through successive unconformities registered along the sedimentary record.

3. Methods

This study has been carried out by an integrated geological approach. Structural data were collected in the field including fracture and bedding orientation, types, crosscutting relationships between different fracture sets and kinematics when possible. Structural data were plotted and analyzed with the software Win-Tensor (v.5.8.8) [78]. Host rocks and vein calcite cements were systematically sampled for petrographical and geochemical analyses.

3.1. Petrography

In order to distinguish different calcite cement generations, forty polished thin-sections (notated as CN1 to CN40) were prepared and analyzed with a Zeiss Axiophot optical microscope and a Technosyn Cold Cathodoluminescence microscope, model 8200 Mk5-1 operating between 16–18 kV and 250 μ A gun current. The terminology of vein types and vein microstructures is based on the classification of Reference [79].

3.2. Carbon and Oxygen Isotopes

The calcite cements and their related carbonate host rocks were carefully sampled for carbon and oxygen isotopic analysis using a 400/500 μ m-diameter dental drill to extract 50–100 μ g of powder. Calcite powders were reacted with 100% phosphoric acid for two minutes at 70 °C. The resultant CO₂ was analyzed using an automated Kiel Carbonate Device attached to a Thermal Ionization Mass Spectrometer Thermo Electron MAT-252 (Thermo Fisher Scientific, Bremen, Germany) following the method of [80]. The International Standard NBS-18 and the internal standard RC-1, traceable to the International Standard NBS-19, were used for calibration. The standard deviation is $\pm 0.03\%$ for $\delta^{13}\text{C}$ and $\pm 0.05\%$ for $\delta^{18}\text{O}$ expressed with respect to the VPDB standard (Vienna Pee Dee Belemnite). The list of analyzed samples is shown in Table 1.

Table 1. $\delta^{18}\text{O}$ and $\delta^{13}\text{C}$ values of the host rocks and related calcite cements. Sx and dx in Fracture Set F5 indicates the main slip movement (left-lateral and right-lateral, respectively).

Sample	Fracture Set	Cement	$\delta^{18}\text{O}$ (‰ VPDB)	$\delta^{13}\text{C}$ (‰ VPDB)
CN2A	F4	Cc4	−13.73	−6.13
CN3A	F5 sx	Cc4	−14.21	−5.81
CN4A	F5 dx	Cc4	−14.3	−7.38
CN4B	F5 dx	Cc4	−12.93	−7.78
CN5A	F4	Cc4	−14.31	−12.48
CN5B		Garumnian mudstone	−7.67	−13.06
CN6A	F4A	Cc4	−13.02	−10.85
CN9A	F4	Cc4	−13.58	−5.83
CN10A	F5 dx	Cc4	−13.85	−12.51
CN11A	F3 NW-SE	Cc1	−12.77	+1.58
CN12A	F3 NE-SW	Cc2	−7.87	+1.25
CN12B	F3 NW-SE	Cc1	−11.83	+1.34
CN12C		Lluçà Fm	−3.31	+1.76

Table 1. Cont.

Sample	Fracture Set	Cement	$\delta^{18}\text{O}$ (‰ VPDB)	$\delta^{13}\text{C}$ (‰ VPDB)
CN15A-A	F5 sx	Cc4	−10.06	−5.38
CN15A-B	F5 sx	Cc4	−13.66	−4.07
CN15B-A	F5 sx	Cc4	−10.88	−5.76
CN16A	F5 sx	Cc4	−13.06	−5.05
CN16B		Santa Fe Fm	−6.65	−2.14
CN16C	F5 sx	Cc4	−9.86	−5.51
CN17A	F5 dx	Cc4	−10.22	−5.4
CN18A	F4A	Cc3	−7.82	−8.3
CN20A	F4	Cc3	−8.28	−10.43
CN20B		Garumnian limestone	−6.84	−11.01
CN26A	F4	Cc3	−7.79	−10.14
CN26B	F4	Cc4	−13.84	−8.22
CN27A	F1	Cc1	−12.28	+1.13
CN27B		Jurassic limestone	−6.22	+0.72
CN28A	F1	Cc1	−10.43	+1.67
CN28B		Jurassic limestone	−8.66	+1.69
CN31A		Lluçà Fm	−3.62	+2.4
CN31B	F3 NW-SE	Cc2	−9.23	+1.8
CN32A	F3 NW-SE	Cc2	−8.42	+1.03
CN32B	F3 NW-SE	Cc1	−13.22	+0.82
CN32C		Lluçà Fm	−5.06	+1.59
CN32D	F3 NW-SE	Cc2	−8.64	+1.04
CN33A	F3 NE-SW	Cc1	−11.09	+1.19
CN33B	F3 NE-SW	Cc1	−12.71	+0.37
CN38A	F3 NW-SE	Cc2	−6.59	+2.7
CN38B	F3 NE-SW	Cc2	−8.19	+2.41
CN38C		Lluçà Fm	−3	+2.51

3.3. Clumped Isotope Thermometry

Clumped isotope thermometry was carried out in order to calculate temperatures and $\delta^{18}\text{O}$ values of the fluids from which the different generations of calcite cements precipitated. This technique is giving good results in this kind of study [16,17,81] and it is becoming a key method in order to establish temperature and fluid composition in carbonate cements, where usually fluid inclusion microthermometric analyses cannot be performed due to stretching. Samples CN33, CN38, CN20 and CN15 were chosen as representative of each calcite cement generation (Cc1 to Cc4, respectively). For this, 2–3 mg aliquots from cements were measured with the Imperial Batch Extraction system (IBEX), an automated line developed at Imperial College. Each sample was dropped in 105% phosphoric acid at 90 °C and reacted for 30 min. The reactant CO_2 was separated using a poropak-Q column, and transferred into the bellows of a Thermo Scientific MAT 253 mass spectrometer (Thermo Fisher GmbH, Bremen, Germany). The characterization of a replicate consisted of 8 acquisitions in dual inlet mode with 7 cycles per acquisition. The post-acquisition processing was completed with a software for clumped isotope analysis named Easotope [82]. Δ_{47} values were corrected for isotope fractionation during phosphoric acid digestion employing a phosphoric acid correction of 0.069 ‰ at 90 °C for calcite [83], the data were also corrected for non-linearity applying the heated gas method [84] and projected into the reference frame of [85]. Carbonate $\delta^{18}\text{O}$ values were calculated with the acid fractionation factors of [86]. Samples were measured two times, except CN38 with only one replicate, and the average result was converted to temperatures with the calibration method of [87]. Calculated $\delta^{18}\text{O}$ values of the fluid are expressed in ‰ with respect to the VSMOW standard (Vienna Standard Mean Ocean Water).

3.4. Strontium Isotopes

Ten representative samples of calcite cements (samples CN6, CN12, CN15, CN18, CN20, CN27, CN33, CN38) and host rocks (CN12 and CN16) were sampled for $^{87}\text{Sr}/^{86}\text{Sr}$ analyses. Powdered samples were completely dissolved in 5 mL of 10% acetic acid, dried and again dissolved in 1 mL of 65% HNO_3 . After evaporation, the resulted solid residue was diluted in 3 mL of 3M HNO_3 to be charged in the chromatographic columns in order to obtain the Sr. In the chromatographic columns, a SrResinTM (Triskem Internacional) (crown-ether (4,4'(5')-di-t-butylcyclohexano-18-crown-6)) resin was used and Sr was recovered using 0.05M HNO_3 as an eluent. After evaporation, samples were loaded onto a Re filament with 1 μL of 1 M phosphoric acid and 2 μL of Ta_2O_5 . Isotopic ratio measurements were carried out in a TIMS-Phoenix mass spectrometer (Isotopx, Cheshire, UK) with a dynamic multicollection during 10 blocks of 16 cycles each one, with a ^{88}Sr beam intensity of 3 V. Isotopic ratios were corrected from ^{87}Rb interferences and normalized using the measured value of $^{88}\text{Sr}/^{86}\text{Sr} = 0.1194$ to correct for the possible mass fractionation during loading and analysis of the sample. During sample analysis, the isotopic standard NBS-987 was measured six times, obtaining a media of 0.710243 and a standard deviation 2σ of 0.000009. These values have been used for the correction of the analyzed values in the samples. The analytical error in the $^{87}\text{Sr}/^{86}\text{Sr}$ ratio, referred to two standard deviations, is 0.01%. The standard error or internal precision is 0.000003.

3.5. Elemental Composition

Eight samples (CN6, CN12, CN15, CN18, CN20, CN27, CN33, CN38), two from each calcite cement, were analyzed for major, trace and rare earth element geochemistry using HR-ICP-MS in order to obtain a range of compositions for each cement generation. This technique was chosen due to its higher resolution compared to other methods (i.e., electron microprobe) and the possibility to perform a multielemental analysis including rare earth elements (REE), which give important information about fluid origin and redox conditions. Trims were sampled using a 400/500 μm -diameter dental drill to extract 100 mg of powder. Powdered samples were dried at 40 °C during 24 h and later 100 mg of sample were acid digested in closed polytetrafluoroethylene (PTFE) vessels with a combination of $\text{HNO}_3 + \text{HF} + \text{HClO}_4$ (2.5 mL: 5 mL: 2.5 mL v/v). The samples were evaporated and, 1 mL of HNO_3 was added to make a double evaporation. Finally, the sample was re-dissolved and diluted with MilliQ water (18.2 $\text{M}\Omega \text{ cm}^{-1}$) and 1 mL of HNO_3 in a 100 mL volume flask. Analyses were performed using a high resolution inductively coupled plasma-mass spectrometry (HR-ICP-MS, model Element XR, Thermo Fisher Scientific, Bremen, Germany). In order to improve the sensitivity of the ICP-MS, a tuning solution containing 1 g L^{-1} Li, B, Na, K, Sc, Fe, Co, Cu, Ga, Y, Rh, In, Ba, Tl, U was used, and as internal standard, 20 mg L^{-1} of a monoelemental solution of ^{115}In . Reference materials are the BCS-CRM n° 393 (ECRM 752-1) limestone, JA-2 Andesite and JB-3 Basalt. The precision of the results was expressed in terms of two standard deviations of a set of eight reference materials measurements (reference material JA-2), whereas accuracy (%) was calculated using the absolute value of the difference between the measured values obtained during the analysis and the certified values of a set of eight reference material analysis (reference material BCS-CRM n° 393 for major oxides and JA-2 for trace elements). The detection limit (DL) was calculated as three times the standard deviation of the average of ten blanks. Detection limits and two standard deviations of each element are shown in Supplementary Data. Several commercial solutions were used in order to perform the different calibration curves. Calibration standards for Fe, Al, P, Ti, Na, K, Ca, Mg were Monoelemental Solutions (10,000 $\mu\text{g/mL}$) of Inorganic Ventures; for Sr, Ba, Li, Be, V, Cr, Ni, Cu, Ga, As, Se, Rb, Cs, Bi Monoelemental Solutions (1000 $\mu\text{g/mL}$) of Inorganic Ventures; for Ce, Dy, Er, Eu, Gd, Ho, La, Lu, Nd, Pr, Sm, Sc, Tb, Th, U, Y a Multielemental Solution IV-CCS-1 Rare Earths Standard in HNO_3 , 125 mL (100 $\mu\text{g/mL}$) of Inorganic Ventures; for Sb, Ge, Hf, Mo, Nb, Re, Ta, Sn a Multielemental Solution IV-CCS-5 (100 $\mu\text{g/mL}$) Fluoride Soluble ICP-MS Std 1.2% HF(v/v) 7.14% $\text{HNO}_3(\text{v/v})$, 125 mL of Inorganic Ventures; and, finally, for Cd, Cr, Cu Co a Multielemental Solution IV-CCS-6 (100 $\mu\text{g/mL}$) Transition Elements ICP-MS Standard in HNO_3 , 125 mL of Inorganic Ventures.

4. Results

4.1. Fracture Sets and Calcite Cements

Five fracture sets (F1–F5) have been identified in the study area (Figure 6) and correlated with other fractures recognized in the western part of the Sant Corneli-Bóixols anticline in previous structural studies [88,89]. We use the term “fracture set” to include both unfilled and cemented fractures (i.e., veins).

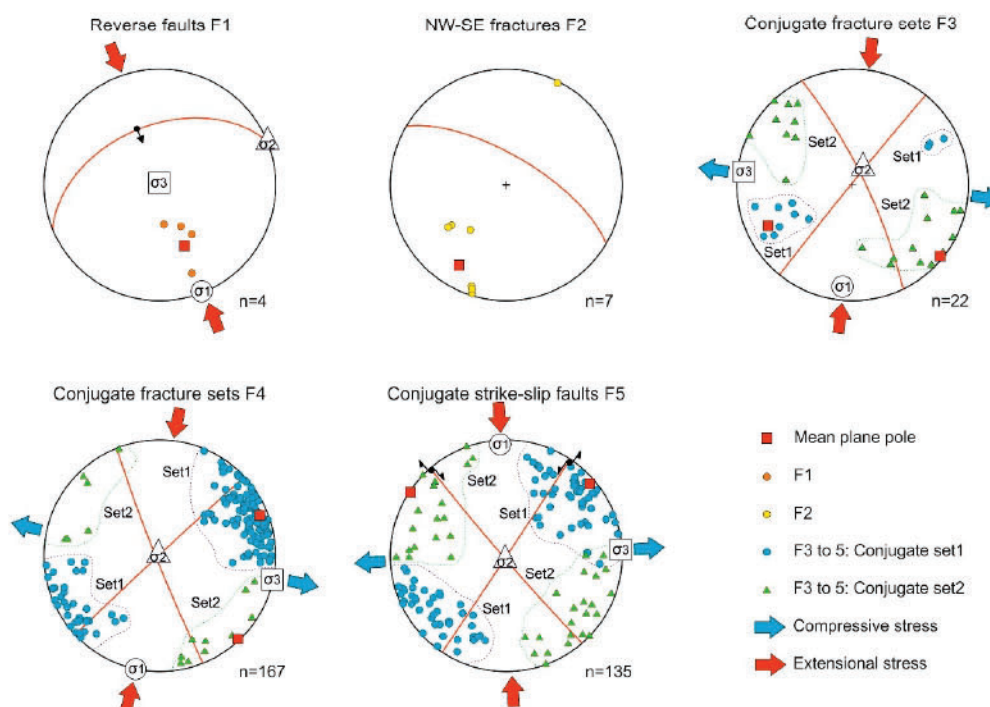


Figure 6. Lower hemisphere, equal area stereoplots of the fracture sets recognized in the frontal part of the Bóixols thrust sheet. Dots represent poles and lines represent the mean principal planes. F2 and F3 have been restored with respect to bedding.

4.1.1. Fracture Set 1 (F1): ENE-WSW Reverse Faults and Related Calcite Cement Cc1

This set is represented by the Bóixols thrust and minor E-W reverse faults dipping to the NNW affecting the Lluçà Formation. The Bóixols thrust is a nearly 40 km long, E-W trending, south-verging reverse fault associated with the growth of the Bóixols anticline and Coll de Nargó syncline. Although most of the Bóixols structure has been sealed by synorogenic sediments, it emerges 3 km east of the village of Bóixols and 12 km west of the Coll de Nargó (Figure 7a). There, Jurassic dolomitic limestones from the hanging wall cut through Santonian limestones interbedded with shales of the footwall. The fault damage zone is nearly 15 m thick with a 0.5 m thick fault core, which contains dark grey-greenish gouge. The outcropping part of the thrust-related veins were sampled in order to compare them with the vein-related cements from the Coll de Nargó area.

The calcite cement Cc1 is identified in reverse faults F1 and precipitated in irregular-shaped and centimetric veins. This cement consists of: (a) elongate blocky crystals with the c-axis perpendicular to the fracture walls, ranging from 0.1 to 0.15 mm wide and from 1 to 1.5 mm long (Figure 7b), and (b) anhedral to subhedral blocky calcite crystals ranging in size from 0.1 to 4 mm with dirty yellowish-brown color and thin mechanical twin planes at the microscopic scale (Figure 7c). Most of the crystals are affected by dissolution along the edges and are crosscut by tectonic stylolites sub-parallel to the thrust trend. Elongate blocky crystals can either completely fill the fractures or partially grow from the vein edges inwards (i.e., syntaxially), where the remaining space is filled by blocky crystals. Cc1 shows a nearly black to dull-orange luminescence (Figure 7d).

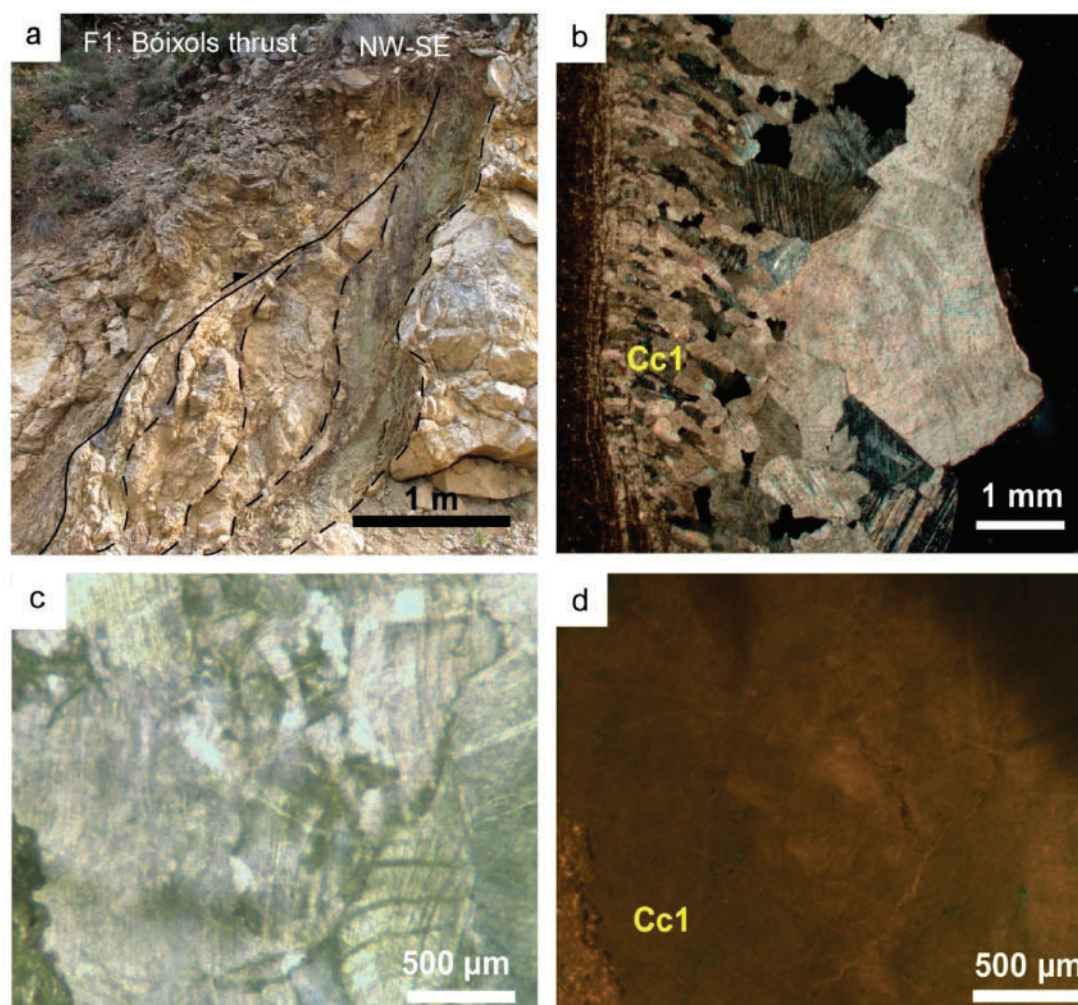


Figure 7. (a) Outcrop of the Bóixols thrust (F1) (b) Cc1 showing both calcite elongate blocky crystals grown in the same fracture (sample CN 33). (c,d) Calcite cement Cc1 seen in polarized optical microscope and cathodoluminescence (CL), respectively (sample CN27).

4.1.2. Fracture Set 2 (F2): NW-SE Fractures

Fracture set 2 (F2) is formed by bed-perpendicular, NW-SE trending fractures dipping from 50 to 90° to the NE, affecting the verticalized Santa Fe Formation (Figure 8a). They are open and locally filled with pedogenic nodules.

4.1.3. Fracture Set 3 (F3): NW-SE and NE-SW Conjugate Fractures and Related Calcite Cements Cc1 and Cc2

Fracture Set 3 consists of NW-SE and NE-SW conjugate fractures, dipping between 40° and 80° and affecting only the Lluçà Formation (Figure 8b,c). Once fracture data is rotated so that bedding is horizontal, all the data from the different outcrops fit well with a strike-slip stress field (Figure 6). These fractures have a regular shape, straight walls and openings ranging from 1 to 15 mm. Their occurrence is concentrated in competent layers of marly limestones. Besides, some of these fractures were reactivated first as strike-slip structures and afterwards with minor dip-slip movement, as highlighted by slickenlines and overprinting striae sets on fracture planes (Figure 8d).

F3 fractures contain two generations of calcite cements: Cc1 (described above) and Cc2, represented by a white-greyish calcite in hand sample, characterized by 0.1–0.7 mm in size elongate crystals and up to 2 mm in size blocky crystals. Evidence of dissolution along crystal edges is common. Cc2 is almost entirely non-luminescent and clearly crosscuts, and therefore postdates, Cc1 (Figure 8e,f).



Figure 8. (a) F2: NW-SE non-mineralized fractures in the Santa Fe Formation. (b,c) F3: NW-SE and NE-SW conjugate fracture set. (d) F3 fracture showing a later reactivation with strike-slip movement (white arrow) and dip-slip movement (grey arrow). (e,f) Crosscutting relationship between calcite cements Cc1 and Cc2 (sample CN12). Cc2 clearly crosscuts and postdates Cc1 in F3 conjugate joints.

4.1.4. Fracture Set 4 (F4): NE-SW and NW-SE Conjugate Fractures and Related Calcite Cements Cc3 and Cc4

Fracture Set 4 affects the entire Garumnian sequence and corresponds to NE-SW and NW-SE conjugate fractures dipping between 60° and 85° , which formed as well under a strike-slip stress field (Figure 6). They are 20–40 cm spaced with increasing density towards fault segments of Fracture Set 5 (F5) (Figure 9a) and have opening widths from 3 to 20 mm. Fracture edges are sharp in competent layers, such as conglomerates and lacustrine limestones, whereas in red-mudstones pressure-solution seams create fuzzy edges. Centimetric-scale vuggy porosity is associated with this type of fractures and developed by partial rock dissolution (Figure 9c).

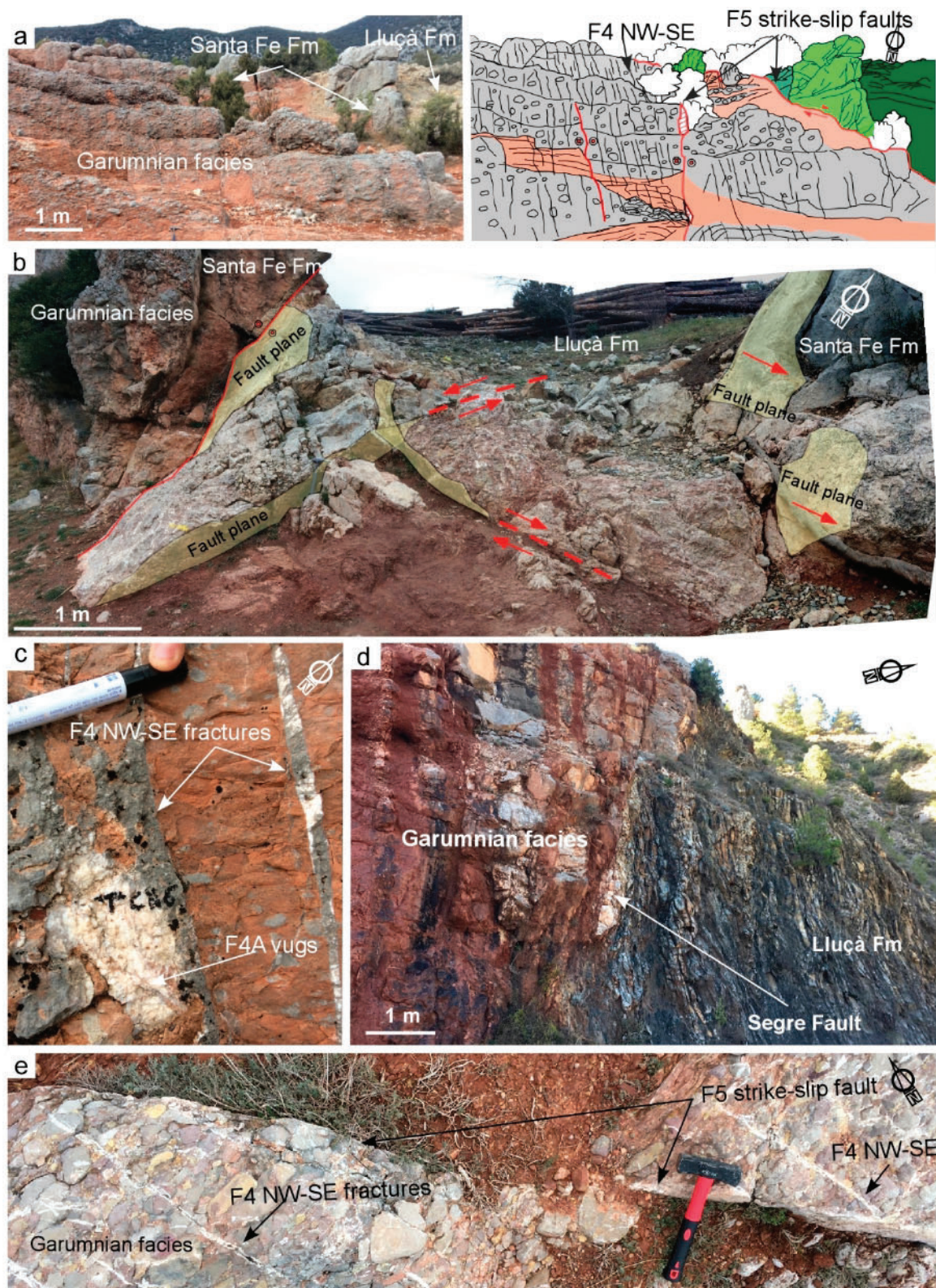


Figure 9. (a) Panoramic view and interpreted sketch of the studied formations. Note that the fracture density of F4 increases towards F5 and also the reactivation of some F4 fractures as F5 strike-slip faults. (b) Interpreted field view of F5 right-lateral and left-lateral strike-slip conjugate faults. (c) F4 fractures and associated vugs. (d) The Segre strike-slip fault juxtaposes the Lluçà Formation against Garumnian facies. (e) Crosscutting relationship between F4 fractures and F5 strike slip faults.

F4 fractures and the associated dissolution vugs are filled with two generations of calcite cements: Cc3 and Cc4. Cc3 consists of both blocky and elongate crystals growing with the c-axis perpendicular to the fracture walls and ranging from 1 to 4 mm long and 0.2 to 0.5 mm wide (Figure 10a–c) and showing an orange to bright yellow luminescence (Figure 10b). Cc4 is characterized by subhedral to anhedral blocky calcite crystals ranging in size from 0.1 to 2 mm (Figure 10c) with a dull to bright orange luminescence. Twin mechanical planes and evidence of dissolution are present in most of the borders, where spotty accumulation of iron oxides occurs. Cc4 was formed during successive deformation events as it appears extremely reworked. Some relicts of host rock fragments are also observed between Cc4 crystals (Figure 10d).

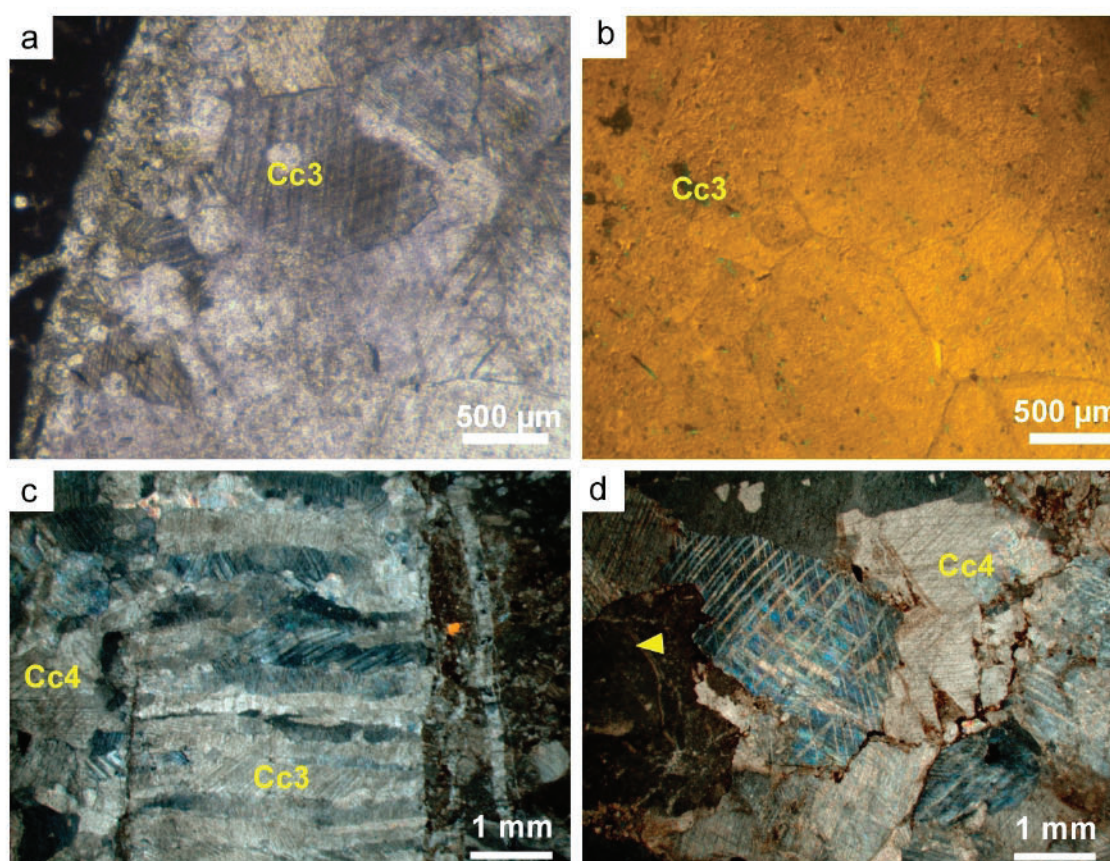


Figure 10. (a,b) Calcite cement Cc3 under polarized optical microscope and CL, respectively (sample CN20). (c) Crosscutting relationship between calcite cements Cc3 and Cc4 (sample CN26). (d) Calcite cement Cc4 with tabular thick twin planes (sample CN3). The yellow arrow points a carbonate clast from the Garumnian conglomerates.

4.1.5. Fracture Set 5 (F5): NW-SE and NE-SW Conjugate Strike-Slip Faults Filled with Calcite Cement Cc4

Both NW-SE right-lateral and NE-SW left-lateral conjugate strike-slip faults affect three of the studied units (Lluçà and Santa Fe Formations, and Garumnian facies), dipping from 50° to 90° both to the south and north. They intersect bedding at high angles and show moderate displacements, from centimeters up to a few meters. A right-lateral strike-slip fault (the Segre Fault) with 100 m of horizontal offset that juxtaposes the Lower Cretaceous Lluçà Formation against the Paleocene Garumnian facies was studied (Figure 9d). In this location, deformation is mainly accommodated along a 2–3 m wide fault core. In other areas, these faults truncate and displace Mesozoic and Paleocene units to their current configuration (Figures 3 and 9e). In competent layers of the Garumnian facies, such as conglomerates and lacustrine limestones, deformation is localized on discrete planar polished slip surfaces with displacements ranging from a few centimeters to a few meters. Sub-horizontal

slickenlines developed on fault planes indicate a pure strike-slip motion. In incompetent red mudstone beds deformation is diffuse through centimetric shear bands with associated drag folds. In major fault segments, deformation is accommodated along a fault core up to 1 m thick, represented by a brittle incohesive fault rock formed by host rock fragments, earlier cements and fractured veins. F5 strike-slip faults are filled by calcite cement Cc4 described above.

4.2. Oxygen and Carbon Isotopes

The oxygen and carbon isotopic composition of host rocks and calcite cements are represented in Figure 11 and summarized in Table 1. Host rocks from the Lluçà Formation have $\delta^{18}\text{O}$ values ranging from -5.1 to -3‰ VPDB, and $\delta^{13}\text{C}$ from $+1.6$ to $+2.5\text{‰}$ VPDB. The Santa Fe Formation host rock displays $\delta^{18}\text{O}$ values of -6.6‰ VPDB and $\delta^{13}\text{C}$ of -2.1‰ VPDB. The Jurassic marine limestones show $\delta^{18}\text{O}$ values from -8.7 to -6.2‰ VPDB and $\delta^{13}\text{C}$ from $+0.7$ and $+1.7\text{‰}$ VPDB. The continental Garumnian facies host rocks have $\delta^{18}\text{O}$ compositions ranging from -7.7 to -6.6‰ VPDB and in $\delta^{13}\text{C}$ from -13.1 to -11‰ VPDB.

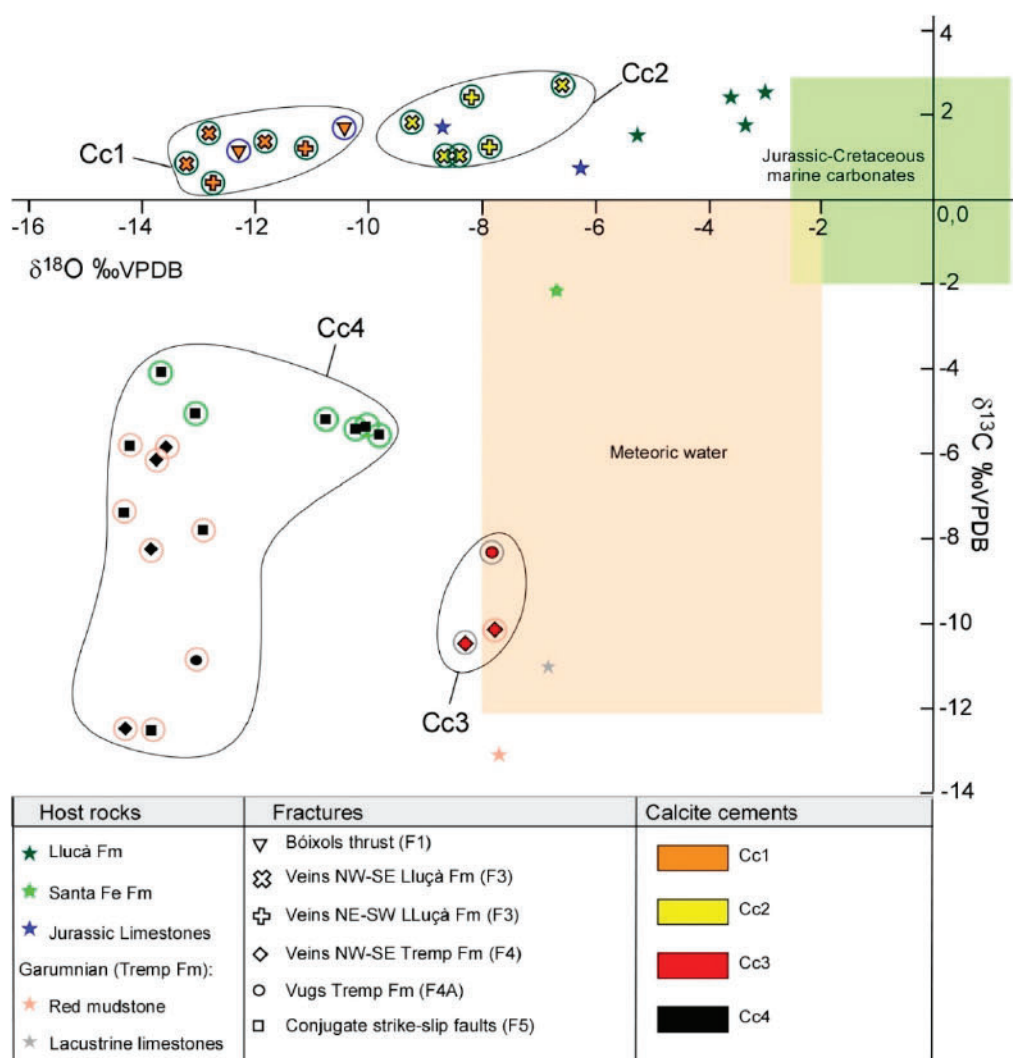


Figure 11. $\delta^{18}\text{O}$ vs $\delta^{13}\text{C}$ cross-plot of carbonate host rocks and calcite cements. Stars represent host rocks, other symbols represent different fracture sets, colors of symbols represent cement generations and the color of the circles englobing fracture symbols represent the associated host rocks. Meteoric water range of values is from Reference [90] and Jurassic-Cretaceous marine carbonate values from Reference [91].

Cc1 ranges in $\delta^{18}\text{O}$ values from -13.2 to -10.4‰ VPDB and $\delta^{13}\text{C}$ from $+0.4$ to $+1.7\text{‰}$ VPDB. Cc2 shows $\delta^{18}\text{O}$ values from -9.2 to -6.6‰ VPDB and $\delta^{13}\text{C}$ from $+1$ to $+2.7\text{‰}$ VPDB. Cc3 shows $\delta^{18}\text{O}$ values from -8.3 to -7.8‰ VPDB and $\delta^{13}\text{C}$ from -10.4 to -8.3‰ VPDB. Finally, Cc4 is characterized by $\delta^{18}\text{O}$ values from -14.3 to -9.9‰ VPDB and $\delta^{13}\text{C}$ from -12.5 to -4.1‰ VPDB.

4.3. Clumped Isotopes

The measured Δ_{47} values from clumped isotope thermometry of the different calcite cement generations were converted into temperatures and $\delta^{18}\text{O}$ values of the precipitating fluid using the equations of [87] and [92], respectively. These values are summarized in Table 2 and Figure 12.

Table 2. $\delta^{18}\text{O}$, $\delta^{13}\text{C}$, Δ_{47} , temperature and $\delta^{18}\text{O}_{\text{fluid}}$ values calculated from clumped isotope thermometry.

Sample	Fracture Set	Cements	n	$\delta^{18}\text{O}$ (‰ VPDB)	$\delta^{13}\text{C}$ (‰ VPDB)	Δ_{47}	T (°C)	$\delta^{18}\text{O}_{\text{fluid}}$ (‰ VSMOW)
CN33	F3 NE-SW	Cc1	2	-12.39	$+0.77$	0.542 ± 0.006	88.4 ± 3.8	$+0.6 \pm 0.8$
CN38	F3 NE-SW	Cc2	1	-6.91	$+2.56$	0.646	40.7 ± 16.1	-1.3 ± 2.9
CN20	F4	Cc3	2	-11.04	-10.3	0.548 ± 0.007	85.3 ± 4	$+1.6 \pm 0.6$
CN15	F5	Cc4	2	-12.18	-4.38	0.544 ± 0.001	87.6 ± 0.6	$+0.7 \pm 0.2$

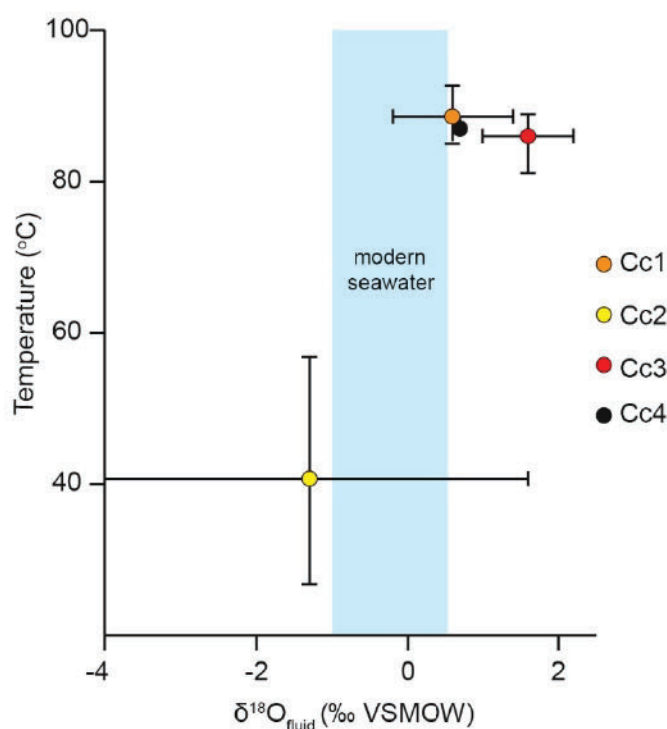


Figure 12. Temperatures (°C) vs $\delta^{18}\text{O}$ (‰ VSMOW) calculated for fluids from which the different generations of calcite cements precipitated using clumped isotope geochemistry. The blue box represents $\delta^{18}\text{O}$ average values for modern seawater [91].

4.4. Strontium Isotopes

The $^{87}\text{Sr}/^{86}\text{Sr}$ ratios of host rocks and calcite cements are represented in Figure 13. Host rocks from the Lluçà Formation have a $^{87}\text{Sr}/^{86}\text{Sr}$ ratio of 0.707317 (CN12) whereas host rocks from the Santa Fe Formation have a $^{87}\text{Sr}/^{86}\text{Sr}$ ratio of 0.708329 (CN16). Cc1 ranges in $^{87}\text{Sr}/^{86}\text{Sr}$ values from 0.707468 to 0.708028 (CN33 and CN27), Cc2 between 0.707298 and 0.707326 (CN38 and CN12), Cc3 between 0.707614 and 0.707706 (CN20 and CN18) and Cc4 between 0.707586 and 0.707612 (CN6 and CN15).

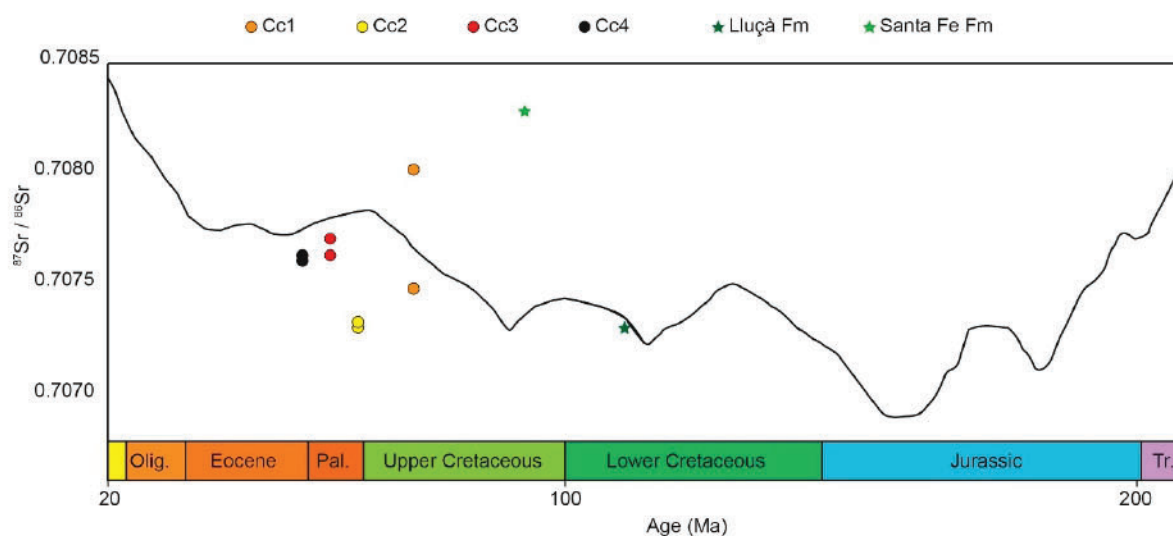


Figure 13. $^{87}\text{Sr}/^{86}\text{Sr}$ composition of calcite cements and carbonate host rocks. The $^{87}\text{Sr}/^{86}\text{Sr}$ variation of seawater through time is represented with the black line [93].

4.5. Elemental Composition

Elemental composition (major and REE + Y) was measured in the four generations of calcite cements. The main analyzed elements used for discussion are summarized in Table 3. The minimum and maximum Mn, Sr, Mg and Fe contents are also represented in Figure 14. For the complete elemental composition of the cements, see Supplementary Data.

Table 3. Elemental composition of the different generations of calcite cements. Values are given in ppm.

Sample	Fracture Set	Cements	Mn	Sr	Mg	Fe	Y	Ce	Pr	Ho
CN27	F1	Cc1	135	409	5280	3943	2.4	3.6	0.5	0.05
CN33	F3 NE-SW	Cc1	320	795	3218	7981	7	3.9	0.7	0.1
CN38	F3 NE-SW	Cc2	47	241	873	2291	0.7	0.4	0.05	0.02
CN12	F3 NE-SW	Cc2	225	501	3613	7840	6.1	4.2	0.6	0.1
CN20	F4	Cc3	501	389	1080	2956	0.7	0.7	0.1	0.01
CN18	F4	Cc3	1380	450	1084	3116	1.1	1.6	0.2	0.02
CN6	F4	Cc4	186	391	2621	3433	5.8	6.8	1.1	0.1
CN15	F5 sx	Cc4	119	520	1956	1986	2.8	2.4	0.4	0.05

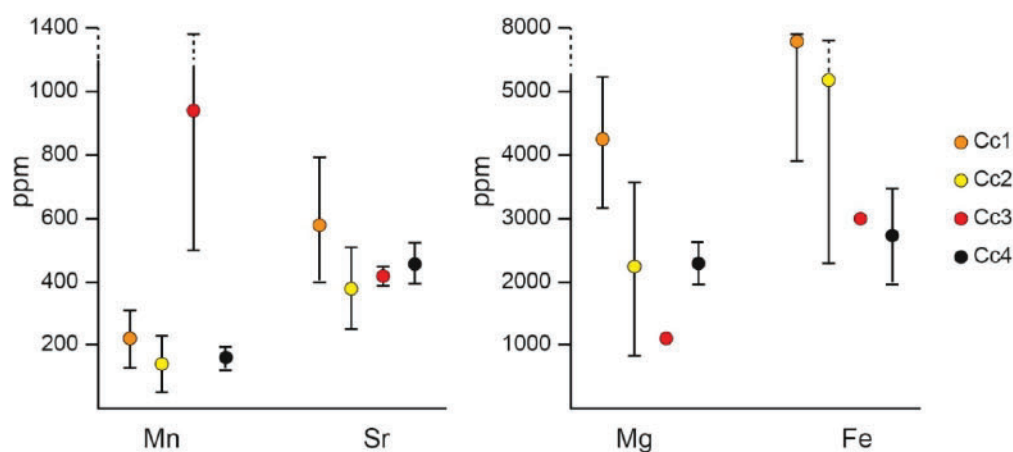


Figure 14. Elemental composition in parts per million (ppm) measured on the four generations of calcite cements. Bars indicate maximum, minimum and average composition of each cement.

In the case of REE and Yttrium, four variables were used in order to better understand and constrain their variation among the different generation of calcite cements [94,95] (Figure 15): Y/Ho, Ce anomalies (Ce/Ce^*), Pr anomalies (Pr/Pr^*) and $\text{Log}(Ce/Ce^*)$. REE + Y have been normalized with respect to post Archean Australian Shale (PAAS) [96]. Ce and Pr anomalies were calculated following the equation of [97] and [98]. The four calcite cement generations show Y/Ho ratios ranging between 46.3 and 53.4 (Figure 15a). Cc1, Cc3 and one sample of Cc2 have positive La anomalies (field IIa), whereas Cc4 and one sample of Cc2 show negative Ce anomalies (field IIIb) (Figure 15b), and $\text{Log}(Ce/Ce^*)$ values higher than -0.10 , in the case of Cc3 and some samples from Cc1 and Cc2, and lower than -0.10 in the case of Cc4 and some samples from Cc1 and Cc2 (Figure 15c).

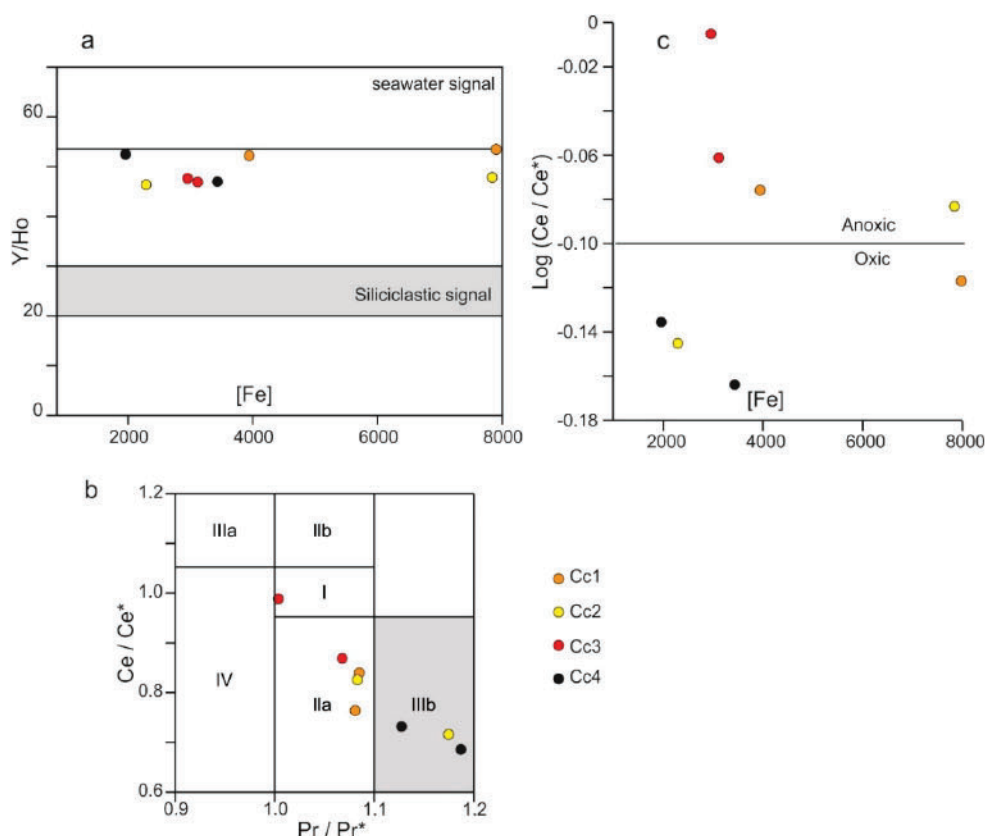


Figure 15. (a) Y/Ho ratios vs Fe content cross-plot for calcite cements Cc1 to Cc4. Y/Ho values for modern seawater and terrigenous sediments are based on [99,100]. (b) PAAS-normalized Ce/Ce^* vs Pr/Pr^* cross-plot showing the Ce and Pr anomalies of calcite cements Cc1 to Cc4. The method of [97] as modified by [101] is used. Field I: no anomaly; Field IIa: positive La anomaly and no Ce anomaly; Field IIb: negative La anomaly and no Ce anomaly; Field IIIa: positive Ce anomaly; Field IIIb: negative Ce anomaly; Field IV: positive Ce and La anomalies. (c) $\text{Log}(Ce/Ce^*)$ vs Fe content cross-plot of calcite cements Cc1 to Cc4. The limit for oxic/anoxic areas is based on Reference [102].

5. Discussion

5.1. Host Rock Diagenesis

This study analyzes fractures and calcite cements hosted in four different rock units. The Jurassic limestones, Lower Cretaceous marls and marly limestones (Lluçà Fm), and Upper Cretaceous limestones (Santa Fe Fm) belong to the hanging wall of the Bóixols thrust sheet, whereas the Paleocene continental series (Garumnian facies) belongs to the footwall. The host rocks from the hanging wall show $\delta^{13}C$ values in good agreement with carbonates precipitated from Jurassic and Cretaceous seawater, but $\delta^{18}O$ values are depleted with respect to marine standard values [91] (Table 1, Figure 11). This depletion in $\delta^{18}O$ is interpreted to result from the increase of temperature and host rock alteration

during progressive burial [103]. Finally, isotopic values from Paleocene continental facies are consistent with deposition in freshwater [104], including paleosoils and lacustrine water carbonates that contain organic matter [105].

5.2. Validity of Clumped Isotope Thermometry

The use of clumped isotopes in order to establish the temperature and $\delta^{18}\text{O}$ of the fluid responsible for calcite precipitation is relatively new, and thus under validation, but it is providing promising results in the research field of diagenesis [106–109]. In this study, clumped isotopes analyses were performed in cements Cc1 to Cc4 obtaining temperatures of about 85–87 °C and $\delta^{18}\text{O}_{\text{fluid}}$ around +1‰ VSMOW in Cc1, Cc3 and Cc4, and temperatures of about 40 °C and $\delta^{18}\text{O}_{\text{fluid}}$ around –1‰ VSMOW in Cc2. Clumped isotopes can potentially be reset by recrystallization and by open-system to closed-system isotope-exchange reactions and diffusion within the mineral lattice [110,111]. In our samples, evidence of calcite recrystallization, such as grain coarsening due to grain boundary migration, is not observed. On the other hand, our vein samples have been buried at a maximum depth of 3 km during the Oligocene to the earliest Miocene, due to the deposition of syntectonic continental conglomerates [112] under a geothermal gradient about 30 °C/km, and probably lower, typical of orogenic systems. Using the parameters of [113] with the aforementioned conditions, burial temperature never exceeded 90 °C and therefore clumped isotopes could not have been modified by intra-crystal diffusion processes, as solid-state reordering requires temperatures above 100–120 °C for a time period of at least 10 million years [114]. Therefore, we can conclude that there is little chance for the clumped isotope to be reset and thus, they registered the circulation of a high-temperature fluid with a similar origin in three different stages (Cc1, Cc3 and Cc4) and a low-temperature fluid (Cc2).

5.3. Fluid-Flow Model: Fracture Development and Related Migrating Fluids

The integration of structural, petrological and geochemical analyses of calcite cements and related host rocks allows us to propose the fluid-flow model for the frontal part of the Bóixols thrust sheet from early contraction to post-folding stage.

5.3.1. Early Contraction Stage (T1)

During the early contraction stage (T1), the emplacement of the Bóixols thrust (F1) occurred together with the development of the two bed-perpendicular fracture sets (F2 and F3), which affect the Santa Fe and Lluçà Formations, respectively (Figure 16). Such a synchronicity is deduced by the orientation of these fractures with respect to the shortening direction, as has also been proposed in other studies carried out in the western sector of the Bóixols anticline [89] and the presence of Cc1 in sets F1 and F3.

Calcite cement Cc1 precipitated within the Bóixols thrust (F1) and related conjugate fracture sets F3. The similarity between $\delta^{13}\text{C}$ values of Cc1 (+0.4 to +1.7‰ VPDB) and host carbonates (+1.6 to +2.5‰ VPDB), indicates high fluid-rock interaction and the buffering of the carbon isotopic composition of the circulating fluid. The $\delta^{18}\text{O}_{\text{fluid}}$ calculated from clumped isotope thermometry for Cc1 (0.6 ± 0.8 ‰ VSMOW) falls within the range of seawater values [91] and the $^{87}\text{Sr}/^{86}\text{Sr}$ ratio (0.707468) is consistent with the values of Lower Cretaceous marine carbonates (0.707167 to 0.707492) [91,93]. In addition, the high Mg and Sr contents (Figure 14) are consistent with the values of original seawater and the high Y/Ho ratio (>36) (Figure 15a) also supports a seawater origin but with a certain siliciclastic influence [95,115]. Moreover, the $\text{Log}(\text{Ce}/\text{Ce}^*)$ values above and below –0.10 (Figure 15c) and the large oscillation in the Fe content may indicate fluctuation between oxic and anoxic conditions in this seawater and also supports a siliciclastic influence [116]. Additionally, the depletion in $\delta^{18}\text{O}$ values of Cc1 (between –13.2 and –11.1‰ VPDB) with respect to the Lower Cretaceous carbonates (–5.1 to –3‰ VPDB) (Figure 11) is explained by the relatively high temperature calculated for this cement with clumped isotope thermometry, between 85 °C and 92 °C (Figure 12). Therefore, although percolation of penecontemporaneous seawater through the strata at the time of

vein formation cannot be discarded, the elevated temperatures obtained from geochemical analyses, together with the low abundance and small dimensions of Cc1 veins, suggest that Cc1 precipitated from connate Cretaceous seawater trapped in the host rock porosity, which was heated during progressive burial and expelled during compaction associated with the emplacement of the Bóixols thrust sheet. Such a dewatering of marine host rocks during thrusting has also been reported in other thrust faults in the Pyrenees [24]. However, one sample from the Bóixols thrust-related deformation (F1) has a considerably higher $^{87}\text{Sr}/^{86}\text{Sr}$ ratio (0.708028). This more radiogenic value could be explained by the interaction of the mineralizing fluid with Triassic sediments which constitute the detachment level of the Bóixols thrust and/or the siliciclastic fraction of marls of the Lluçà Fm and underlying formations.

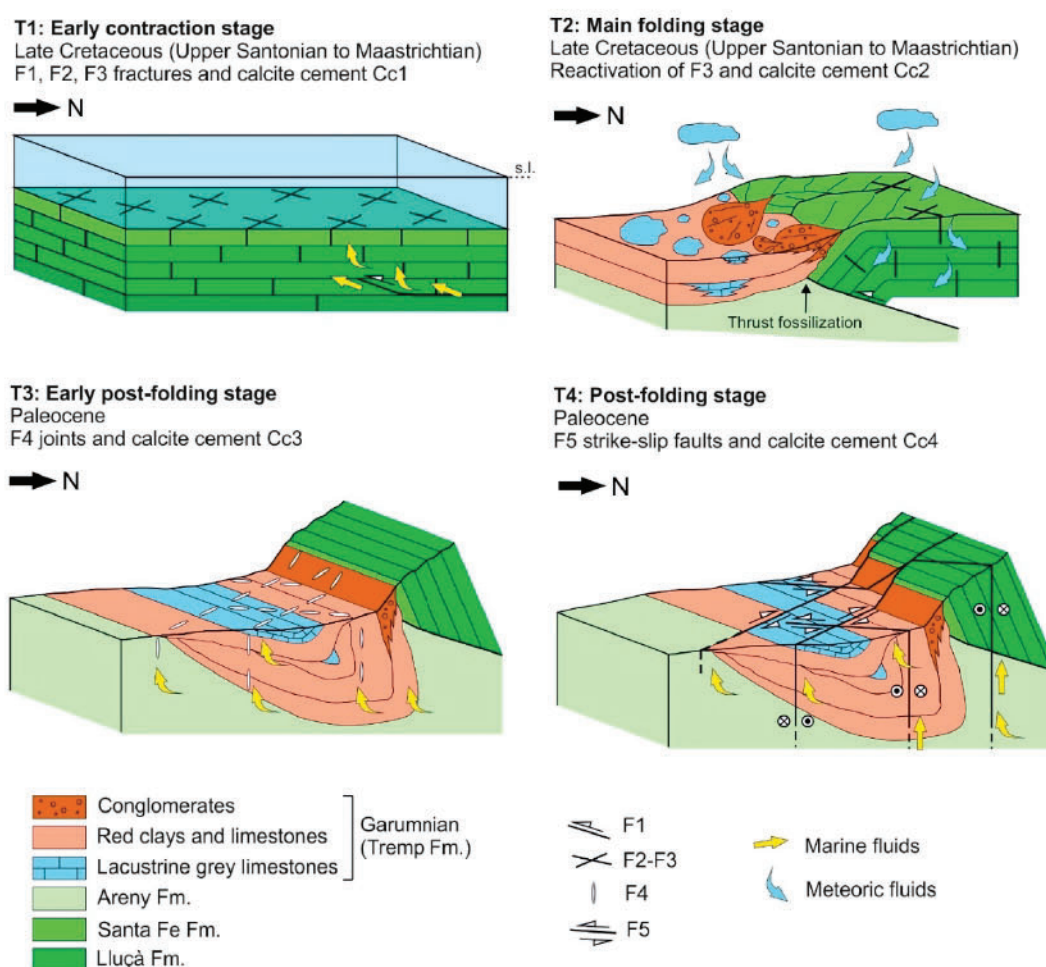


Figure 16. Fluid-flow model for the frontal part of the Bóixols thrust sheet showing the relationship between the structural evolution from early contraction to post-folding stage and the migration of fluids (not to scale).

5.3.2. Main Folding Stage (T2)

During the main folding stage (T2) (Figure 16), the conjugate fracture sets F3 were reactivated allowing the migration of a fluid from which calcite cement Cc2 precipitated. This is evidenced by the presence of two striae sets showing dip-slip and strike-slip kinematics (Figure 8d) and the coexistence of two calcite cements (Cc1 and Cc2) with clear cross-cutting relationships (Figure 8e,f).

The $\delta^{18}\text{O}_{\text{fluid}}$ calculated from clumped isotope thermometry for Cc2 ($-1.3 \pm 2.9\%$ VSMOW) and its temperature (between 27 °C and 57 °C) are interpreted as the infiltration of meteoric fluids during progressive uplift, folding and fossilization of the Bóixols thrust by the continental Paleocene Garumnian facies, which mixed with previous local and connate marine waters (Figure 16). The $^{87}\text{Sr}/^{86}\text{Sr}$ values of Cc2 (between 0.707298 and 0.707326) and $\delta^{13}\text{C}$ (from +1 to +2.7‰ VPDB)

are consistent with the values of Lower Cretaceous marine host carbonates. These meteoric waters lowered the Mg, Sr, Fe, and Mn contents with respect to Cc1, due to its low saturation (Figure 14). Also, the Y/Ho, the Ce and La anomalies between IIa and IIIb fields and the $\log(\text{Ce}/\text{Ce}^*)$ show a major siliciclastic signal and oxidizing-reducing transitional conditions typical of the meteoric environment.

5.3.3. Early Post-Folding Stage (T3)

The NE-SW and NW-SE conjugate Fracture Set F4 and its related calcite cement Cc3 developed during the latest folding stage (T3) (Figure 16). The orientation of F4 remains constant regardless of the different bedding dips, indicating that they developed once the strata had already been folded and turned vertically.

The calcite cement Cc3 shows positive $\delta^{18}\text{O}_{\text{fluid}}$ values, around $+1.6 \pm 0.6\text{‰}$ VSMOW, which can indicate the end of the meteoric water input and again the upflowing of trapped marine waters or fluid interaction with silicate minerals. Late Cretaceous evaporated seawater is the most probable source for this cement, if we take into account that (i) the $^{87}\text{Sr}/^{86}\text{Sr}$ ratios (0.707614–0.707706) are consistent with the values of Late Cretaceous seawater [90,93], and that (ii) during the Late Cretaceous there was a transition between marine to lagoonal-lacustrine environments in the study area [77] and, in consequence, to more restricted and evaporative conditions. The depletion in $\delta^{18}\text{O}$ (from -8.3 to -7.8‰ VPDB) is attributed to the relatively high temperature of the precipitating fluid (between 81 °C and 89 °C). On the other hand, the depletion in $\delta^{13}\text{C}$ values (from -10.4 to -8.3‰ VPDB) with respect to typical marine carbonates [91,104], as well as the relatively low Mg and high Mn contents (Figure 14) are explained by the combined effect of burial diagenesis and the interaction between the original seawater with Paleocene continental host rocks. Therefore, Cc3 precipitated from upflowing evolved evaporated marine fluids heated at depth and expelled from rock porosity by sediment compaction during progressive deformation and fold tightening. The Y/Ho ratio, the presence or absence of La anomaly and the $\log(\text{Ce}/\text{Ce}^*)$ values above -0.10 (Figure 15) indicate a clear influence of siliciclastic sediments, represented by the Garumnian facies, and suboxic to anoxic paleo redox conditions [97,117].

5.3.4. Post-Folding Stage (T4)

During the post-folding stage (T4), two conjugate sets of NW-SE and NE-SW right-lateral and left-lateral strike-slip faults F5 developed (Figure 16), as evidenced by the constant orientation of these faults independently of the dipping of the strata. Previous studies in the Bóixols anticline also attributed these faults to the post-folding stage [89]. Strike-slip faults, observed also in other anticlines worldwide, such as in the Lurestan Province (Zagros Mountains, Iran) are developed when folds reach their maximum amplification and cannot easily accommodate any further orthogonal shortening [118]. These strike-slip faults and conjugate fractures F4 have similar orientations indicating that they formed under the same stress field (Figure 6). As fractures F4 are crosscut by F5 or reactivated as strike-slip faults during T4, they are interpreted as a pre-slip stage of F5. This fracture pattern is similar with the “pump” model of faulting proposed by Reference [119].

The calcite cement Cc4 precipitated in F5 faults and F4 reopened fractures. This cement shows $\delta^{18}\text{O}_{\text{fluid}}$ values ($+0.7 \pm 0.2\text{‰}$ VSMOW), $\delta^{18}\text{O}$ (from -14.3 to -9.9‰ VPDB), a temperature of precipitation (around 88 °C) and $^{87}\text{Sr}/^{86}\text{Sr}$ ratios (between 0.707586 and 0.707612) similar to those obtained for Cc3, indicating that Cc4 also precipitated from heated upflowing evaporated marine fluids expelled during progressive dewatering of Cretaceous marine host carbonates during deformation in the post-folding stage (Figure 16). The negative Ce anomaly (field IIIb) and the lowest $\log(\text{Ce}/\text{Ce}^*)$ values also supports a marine source but more oxygenated compared to earlier cements (Figure 15) [94,95,120]. On the other hand, the Y/Ho ratios point to a variable degree of siliciclastic influence (Figure 15). As faults F5 crosscut all the outcropping sedimentary units, from Lower Cretaceous marine to Paleocene continental host rocks, this variation may have been produced by the interaction of such fluids with marine (higher Y/Ho ratio) or continental (lower Y/Ho ratio) host rocks. Likewise, the $\delta^{13}\text{C}$ (from -12.5 to -4.1‰ VPDB) values of Cc4, depleted with respect to

marine carbonates [90,93], as well as the relative enrichment in Mg and Sr contents respect to Cc3, are also explained by the interaction between the upflowing evolved marine fluids with the different adjacent host rocks (Figure 16).

6. Conclusions

The integration of structural, petrological and geochemical analyses performed in fracture-related calcite cements and host rocks constrains the spatiotemporal paleo-fluid system in the frontal part of the Bóixols thrust sheet, the oldest thrust sheet of the South-Central Pyrenean Unit. Five different fracture sets were recognized affecting marine Jurassic and Cretaceous rocks from the hanging wall and continental Paleocene rocks from the footwall. These fracture sets and related calcite cements reflect the evolution of the thrust/folding system and the relationship between the tectonic evolution and fluid migration: (1) During the early contraction, two bed-perpendicular NW-SE and NE-SW fracture sets developed and were mineralized with calcite cement Cc1, which precipitated from evolved marine-derived fluids expelled from Lower Cretaceous host rocks; (2) During progressive thrusting and the main folding stage, NW-SE and NE-SW conjugate fracture sets were reopened and the Bóixols thrust was fossilized by continental Paleocene facies, allowing the infiltration of meteoric fluids that mixed with marine connate waters and precipitated calcite cement Cc2; (3) During the early post-folding stage, a NW-SE fracture set developed and calcite cement Cc3 precipitated from evolved evaporated marine fluids expelled from rock porosity during progressive deformation and fold tightening; and, (4) During the post-folding stage, previous NW-SE fractures reopened, two conjugate sets of NW-SE and NE-SW strike-slip faults developed and calcite cement Cc4 precipitated again from marine evolved fluids. The comparison between the isotopic and elemental composition measured in the different fracture-related calcite cements and host rocks, reveals the progressive dewatering of Cretaceous marine host sediments during the progressive burial, deformation and fold tightening and the input of meteoric waters only during the main folding stage.

Supplementary Materials: The following are available online at <http://www.mdpi.com/2075-163X/9/2/117/s1>, Table S1: Complete elemental composition of the different generations of calcite cements.

Author Contributions: Conceptualization, A.T.; methodology, all authors; formal analysis, all authors; investigation, N.N., D.M.-L., D.C., I.C. and A.T.; data curation, D.M.-L. and N.N.; Writing—Original Draft preparation, N.N. and D.M.-L.; Writing—Review and Editing, A.T., I.C., J.D.M.-M., A.B. and E.G.-R.; visualization, D.M.-L., N.N. and D.C.; supervision, A.T.; funding acquisition, A.T.

Funding: This research was carried out within the framework of DGICYT Spanish Project CGL2015-66335-C2-1-R and the Grup Consolidat de Recerca “Geologia Sedimentària” (2017-SGR- 824).

Acknowledgments: We thank three anonymous referees for their constructive reviews, which helped to improve the quality of the manuscript, together with the editorial guidance of Hairuo Qing. Carbon and oxygen isotopic analyses were performed at “Centre Científics i Tecnològics” of the Universitat de Barcelona. Strontium analyses were carried out at the “CAI de Geocronologia y Geoquímica Isotópica (UCM-CEI)” of the Universidad Complutense de Madrid. The clumped isotope analyses were done in the Qatar Stable isotope Laboratory of Imperial College of London. Elemental and REE composition analyses were performed at the Geochemistry Facility of labGEOTOP of the Institute of Earth Sciences Jaume Almera (ICTJA-CSIC), a cofounded structure by FEDER-UE (Ref. CSIC08-4E-001). EGR acknowledges the support of the Beatriu de Pinós programme of the Government of Catalonia’s Secretariat for Universities and Research of the Department of Economy and Knowledge (2016 BP 00208).

Conflicts of Interest: The authors declare no conflict of interest.

References

1. Fyfe, W.S.; Price, N.J.; Thompson, A.B. *Fluids in the Earth’s Crust: Their Significance in Metamorphic, Tectonic, and Chemical Transport Processes*; Elsevier Scientific Pub. Co.: Amsterdam, The Netherlands, 1978; ISBN 9780444601483.
2. Ferry, J.M.; Dipple, G.M. Fluid flow, mineral reactions, and metasomatism. *Geology* **1991**, *19*, 211. [[CrossRef](#)]
3. Deming, D. Fluid flow and heat transport in the upper continental crust. *Geol. Soc. Lond. Spec. Publ.* **1994**, *78*, 27–42. [[CrossRef](#)]

4. Garven, G. A hydrogeologic model for the formation of the giant oil sands deposits of the Western Canada sedimentary basin. *Am. J. Sci.* **1989**, *289*, 105–166. [[CrossRef](#)]
5. Duddy, I.R.; Green, P.F.; Bray, R.J.; Hegarty, K.A. Recognition of the thermal effects of fluid flow in sedimentary basins. *Geol. Soc. Lond. Spec. Publ.* **1994**, *78*, 325–345. [[CrossRef](#)]
6. Putnis, A. Mineral replacement reactions: From macroscopic observations to microscopic mechanisms. *Mineral. Mag.* **2002**, *66*, 689–708. [[CrossRef](#)]
7. Trincal, V.; Lanari, P.; Buatier, M.; Lacroix, B.; Charpentier, D.; Labaume, P.; Muñoz, M. Temperature micro-mapping in oscillatory-zoned chlorite: Application to study of a green-schist facies fault zone in the Pyrenean Axial Zone (Spain). *Am. Mineral.* **2015**, *100*, 2468–2483. [[CrossRef](#)]
8. Gasparrini, M.; Ruggieri, G.; Brogi, A. Diagenesis versus hydrothermalism and fluid-rock interaction within the Tuscan Nappe of the Monte Amiata CO₂-rich geothermal area (Italy). *Geofluids* **2013**, *13*, 159–179. [[CrossRef](#)]
9. Sibson, R.H. Fault rocks and fault mechanisms. *J. Geol. Soc. Lond.* **1977**, *133*, 191–213. [[CrossRef](#)]
10. Sibson, R.; Scott, J. Stress/fault controls on the containment and release of overpressured fluids: Examples from gold-quartz vein systems in Juneau, Alaska; Victoria, Australia and Otago, New Zealand. *Ore Geol. Rev.* **1998**, *13*, 293–306. [[CrossRef](#)]
11. Aydin, A. Fractures, faults, and hydrocarbon entrapment, migration and flow. *Mar. Pet. Geol.* **2000**, *17*, 797–814. [[CrossRef](#)]
12. Van Noten, K.; Muchez, P.; Sintubin, M. Stress-state evolution of the brittle upper crust during compressional tectonic inversion as defined by successive quartz vein types (High-Ardenne slate belt, Germany). *J. Geol. Soc. Lond.* **2011**, *168*, 407–422. [[CrossRef](#)]
13. Knipe, R.J.; McCaig, A.M. Microstructural and microchemical consequences of fluid flow in deforming rocks. *Geol. Soc. Lond. Spec. Publ.* **1994**. [[CrossRef](#)]
14. Ogata, K.; Senger, K.; Braathen, A.; Tveranger, J. Fracture corridors as seal-bypass systems in siliciclastic reservoir-cap rock successions: Field-based insights from the Jurassic Entrada Formation (SE Utah, USA). *J. Struct. Geol.* **2014**, *66*, 162–187. [[CrossRef](#)]
15. Travé, A.; Labaume, P.; Vergés, J. Fluid Systems in Foreland Fold-and-Thrust Belts: An Overview from the Southern Pyrenees. In *Thrust Belts and Foreland Basins*; Springer: Berlin/Heidelberg, Germany, 2007; pp. 93–115.
16. Crusset, D.; Cantarero, I.; Vergés, J.; John, C.M.; Muñoz-López, D.; Travé, A. Changes in fluid regime in syn-orogenic sediments during the growth of the south Pyrenean fold and thrust belt. *Glob. Planet. Chang.* **2018**, *171*, 207–224. [[CrossRef](#)]
17. Crusset, D.; Cantarero, I.; Travé, A.; Vergés, J.; John, C.M. Crestal graben fluid evolution during growth of the Puig-reig anticline (South Pyrenean fold and thrust belt). *J. Geodyn.* **2016**, *101*, 30–50. [[CrossRef](#)]
18. Fischer, M.P.; Higuera-Díaz, I.C.; Evans, M.A.; Perry, E.C.; Leticariu, L. Fracture-controlled paleohydrology in a map-scale detachment fold: Insights from the analysis of fluid inclusions in calcite and quartz veins. *J. Struct. Geol.* **2009**, *31*, 1490–1510. [[CrossRef](#)]
19. Travé, A.; Labaume, P.; Vergés, J. *Thrust Belts and Foreland Basins*; Lacombe, O., Roure, F., Lavé, J., Vergés, J., Eds.; Frontiers in Earth Sciences; Springer: Berlin/Heidelberg, Germany, 2007; ISBN 978-3-540-69425-0.
20. Vinet, L.; Zhedanov, A. A ‘missing’ family of classical orthogonal polynomials. *J. Phys. A Math. Theor.* **2011**, *44*, 085201. [[CrossRef](#)]
21. Roure, F.; Swennen, R.; Schneider, F.; Faure, J.L.; Ferket, H.; Guilhaumou, N.; Osadetz, K.; Robion, P.; Vandeginste, V. Incidence and importance of tectonics and natural fluid migration on reservoir evolution in foreland fold-and-thrust belts. *Oil Gas Sci. Technol.* **2005**, *60*, 67–106. [[CrossRef](#)]
22. Van Geet, M.; Swennen, R.; Durmishi, C.; Roure, F.; Muchez, P.H. Paragenesis of Cretaceous to Eocene carbonate reservoirs in the Ionian fold and thrust belt (Albania): Relation between tectonism and fluid flow. *Sedimentology* **2002**, *49*, 697–718. [[CrossRef](#)]
23. Travé, A.; Calvet, F.; Sans, M.; Vergés, J.; Thirlwall, M. Fluid history related to the Alpine compression at the margin of the south-Pyrenean Foreland basin: The El Guix anticline. *Tectonophysics* **2000**, *321*, 73–102. [[CrossRef](#)]
24. Travé, A.; Labaume, P.; Calvet, F.; Soler, A. Sediment dewatering and pore fluid migration along thrust faults in a foreland basin inferred from isotopic and elemental geochemical analyses (Eocene southern Pyrenees, Spain). *Tectonophysics* **1997**, *282*, 375–398. [[CrossRef](#)]

25. Lefticariu, L.; Perry, E.C.; Fischer, M.P.; Banner, J.L. Evolution of fluid compartmentalization in a detachment fold complex. *Geology* **2005**, *33*, 69. [[CrossRef](#)]
26. Evans, M.A.; Bebout, G.E.; Brown, C.H. Changing fluid conditions during folding: An example from the central Appalachians. *Tectonophysics* **2012**, *576–577*, 99–115. [[CrossRef](#)]
27. Lynch, E.A.; van der Pluijm, B. Meteoric fluid infiltration in the Argentine Precordillera fold-and-thrust belt: Evidence from H isotopic studies of neofomed clay minerals. *Lithosphere* **2017**, *9*, 134–145. [[CrossRef](#)]
28. Vandeginste, V.; Swennen, R.; Allaey, M.; Ellam, R.M.; Osadetz, K.; Roure, F. Challenges of structural diagenesis in foreland fold-and-thrust belts: A case study on paleofluid flow in the Canadian Rocky Mountains West of Calgary. *Mar. Pet. Geol.* **2012**. [[CrossRef](#)]
29. Laubach, S.E.; Eichhubl, P.; Hilgers, C.; Lander, R.H. Structural diagenesis. *J. Struct. Geol.* **2010**, *32*, 1866–1872. [[CrossRef](#)]
30. Evans, M.A.; Fischer, M.P. On the distribution of fluids in folds: A review of controlling factors and processes. *J. Struct. Geol.* **2012**, *44*, 2–24. [[CrossRef](#)]
31. Sturrock, C.P.; Catlos, E.J.; Miller, N.R.; Akgun, A.; Fall, A.; Gabitov, R.I.; Yilmaz, I.O.; Larson, T.; Black, K.N. Fluids along the North Anatolian Fault, Nislar basin, north central Turkey: Insight from stable isotopic and geochemical analysis of calcite veins. *J. Struct. Geol.* **2017**, *101*, 58–79. [[CrossRef](#)]
32. Bussolotto, M.; Benedicto, A.; Moen-Maurel, L.; Invernizzi, C. Fault deformation mechanisms and fault rocks in micritic limestones: Examples from Corinth rift normal faults. *J. Struct. Geol.* **2015**, *77*, 191–212. [[CrossRef](#)]
33. Fay-Gomord, O.; Allanic, C.; Verbiest, M.; Honlet, R.; Champenois, F.; Bonifacie, M.; Chaduteau, C.; Wouters, S.; Muchez, P.; Lasseur, E.; et al. Understanding Fluid Flow during Tectonic Reactivation: An Example from the Flamborough Head Chalk Outcrop (UK). *Geofluids* **2018**, *2018*, 1–17. [[CrossRef](#)]
34. Swennen, R.; Muskha, K.; Roure, F. Fluid circulation in the Ionian fold and thrust belt (Albania): Implications for hydrocarbon prospectivity. *J. Geochem. Explor.* **2000**, *69–70*, 629–634. [[CrossRef](#)]
35. Vilasi, N. Study of Reservoir Analogues in Foreland Fold-and-Thrust Belts: Sedimentology, Diagenesis, Deformation and Fracturing of the Upper Cretaceous-Eocene Carbonate Systems of the Ionian Zone (Southern Albania). Ph.D. Thesis, Ecole des Mines de Paris, Paris, France, 2011.
36. Cello, G.; Invernizzi, C.; Mazzoli, S.; Tondi, E. Fault properties and fluid flow patterns from Quaternary faults in the Apennines, Italy. *Tectonophysics* **2001**, *336*, 63–78. [[CrossRef](#)]
37. Conti, S.; Fontana, D.; Mecozzi, S.; Panieri, G.; Pini, G.A. Late Miocene seep-carbonates and fluid migration on top of the Montepetra intrabasinal high (Northern Apennines, Italy): Relations with synsedimentary folding. *Sediment. Geol.* **2010**, *231*, 41–54. [[CrossRef](#)]
38. Petracchini, L.; Antonellini, M.; Billi, A.; Scrocca, D. Fault development through fractured pelagic carbonates of the Cingoli anticline, Italy: Possible analog for subsurface fluid-conductive fractures. *J. Struct. Geol.* **2012**, *45*, 21–37. [[CrossRef](#)]
39. Pizzati, M.; Balsamo, F.; Storti, F.; Mozafari, M.; Iacumin, P.; Tinterri, R.; Swennen, R. From axial parallel to orthogonal groundwater flow during fold amplification: Insights from carbonate concretion development during the growth of the Quattro Castella Anticline, Northern Apennines, Italy. *J. Geol. Soc. Lond.* **2018**, *175*, 806–819. [[CrossRef](#)]
40. Mozafari, M.; Swennen, R.; Balsamo, F.; El Desouky, H.; Storti, F.; Taberner, C. Fault-controlled dolomitization in the Montagna dei Fiori Anticline (Central Apennines, Italy): Record of a dominantly pre-orogenic fluid migration. *Solid Earth Discuss.* **2019**, 1–57. [[CrossRef](#)]
41. Incerpi, N.; Martire, L.; Manatschal, G.; Bernasconi, S.M. Evidence of hydrothermal fluid flow in a hyperextended rifted margin: The case study of the Err nappe (SE Switzerland). *Swiss J. Geosci.* **2017**, *110*, 439–456. [[CrossRef](#)]
42. Hausegger, S.; Kurz, W.; Rabitsch, R.; Kiechl, E.; Brosch, F.J. Analysis of the internal structure of a carbonate damage zone: Implications for the mechanisms of fault breccia formation and fluid flow. *J. Struct. Geol.* **2010**, *32*, 1349–1362. [[CrossRef](#)]
43. Morley, C.K.; Warren, J.; Tingay, M.; Boonyasaknanon, P.; Julapour, A. Reprint of: Comparison of modern fluid distribution, pressure and flow in sediments associated with anticlines growing in deepwater (Brunei) and continental environments (Iran). *Mar. Pet. Geol.* **2014**, *55*, 230–249. [[CrossRef](#)]
44. Dewever, B.; Swennen, R.; Breesch, L. Fluid flow compartmentalization in the Sicilian fold and thrust belt: Implications for the regional aqueous fluid flow and oil migration history. *Tectonophysics* **2013**, *591*, 194–209. [[CrossRef](#)]

45. Gomez-Rivas, E.; Bons, P.D.; Koehn, D.; Urai, J.L.; Arndt, M.; Virgo, S.; Laurich, B.; Zeeb, C.; Stark, L.; Blum, P. The Jabal Akhdar dome in the Oman Mountains: Evolution of a dynamic fracture system. *Am. J. Sci.* **2014**, *314*, 1104–1139. [[CrossRef](#)]
46. Breesch, L.; Swennen, R.; Vincent, B. Fluid flow reconstruction in hanging and footwall carbonates: Compartmentalization by Cenozoic reverse faulting in the Northern Oman Mountains (UAE). *Mar. Pet. Geol.* **2009**, *26*, 113–128. [[CrossRef](#)]
47. Mozafari, M.; Swennen, R.; Muchez, P.; Vassilieva, E.; Balsamo, F.; Storti, F.; Pironon, J.; Taberner, C. Origin of the saline paleofluids in fault-damage zones of the Jabal Qusaybah Anticline (Adam Foothills, Oman): Constraints from fluid inclusions geochemistry. *Mar. Pet. Geol.* **2017**, *86*, 537–546. [[CrossRef](#)]
48. Balsamo, F.; Clemenzi, L.; Storti, F.; Mozafari, M.; Solum, J.; Swennen, R.; Taberner, C.; Tueckmantel, C. Anatomy and paleofluid evolution of laterally restricted extensional fault zones in the Jabal Qusaybah anticline, Salakh arch, Oman. *Geol. Soc. Am. Bull.* **2016**, *128*, 957–972. [[CrossRef](#)]
49. Travé, A.; Calvet, F.; Soler, A.; Labaume, P. Fracturing and fluid migration during palaeogene compression and neogene extension in the Catalan Coastal Ranges, Spain. *Sedimentology* **1998**, *45*, 1063–1082. [[CrossRef](#)]
50. Cantarero, I.; Travé, A.; Alías, G.; Baqués, V. Polyphasic hydrothermal and meteoric fluid regimes during the growth of a segmented fault involving crystalline and carbonate rocks (Barcelona Plain, NE Spain). *Geofluids* **2014**, *14*, 20–44. [[CrossRef](#)]
51. Baqués, V.; Travé, A.; Benedicto, A.; Labaume, P.; Cantarero, I. Relationships between carbonate fault rocks and fluid flow regime during propagation of the Neogene extensional faults of the Penedès basin (Catalan Coastal Ranges, NE Spain). *J. Geochem. Explor.* **2010**, *106*, 24–33. [[CrossRef](#)]
52. Baques, V.; Trave, A.; Roca, E.; Marin, M.; Cantarero, I. Geofluid behaviour in successive extensional and compressional events: A case study from the southwestern end of the Valles-Penedes Fault (Catalan Coastal Ranges, NE Spain). *Pet. Geosci.* **2012**, *18*, 17–31. [[CrossRef](#)]
53. Cantarero, I.; Alías, G.; Cruset, D.; Carola, E.; Lanari, P.; Travé, A. Fluid composition changes in crystalline basement rocks from ductile to brittle regimes. *Glob. Planet. Chang.* **2018**, *171*, 273–292. [[CrossRef](#)]
54. Lacroix, B.; Travé, A.; Buatier, M.; Labaume, P.; Vennemann, T.; Dubois, M. Syntectonic fluid-flow along thrust faults: Example of the South-Pyrenean fold-and-thrust belt. *Mar. Pet. Geol.* **2014**, *49*, 84–98. [[CrossRef](#)]
55. Beaudoin, N.; Huyghe, D.; Bellahsen, N.; Lacombe, O.; Emmanuel, L.; Mouthereau, F.; Ouanhnon, L. Fluid systems and fracture development during syn-depositional fold growth: An example from the Pico del Aguila anticline, Sierras Exteriores, southern Pyrenees, Spain. *J. Struct. Geol.* **2015**, *70*, 23–38. [[CrossRef](#)]
56. Crognier, N.; Hoareau, G.; Aubourg, C.; Dubois, M.; Lacroix, B.; Branellec, M.; Callot, J.P.; Vennemann, T. Syn-orogenic fluid flow in the Jaca basin (south Pyrenean fold and thrust belt) from fracture and vein analyses. *Basin Res.* **2018**, *30*, 187–216. [[CrossRef](#)]
57. Lacroix, B.; Baumgartner, L.P.; Bouvier, A.-S.; Kempton, P.D.; Vennemann, T. Multi fluid-flow record during episodic mode I opening: A microstructural and SIMS study (Cotiella Thrust Fault, Pyrenees). *Earth Planet. Sci. Lett.* **2018**, *503*, 37–46. [[CrossRef](#)]
58. Vergés, J.; Marzo, M.; Muñoz, J. Growth strata in foreland settings. *Sediment. Geol.* **2002**, *146*, 1–9. [[CrossRef](#)]
59. Vergés, J. Estudi Geològic del Vessant Sud del Pirineu Oriental i Central: Evolució Cinemàtica en 3D. Ph.D. Thesis, University of Barcelona, Barcelona, Spain, 1993.
60. Choukroune, P. The Ecors Pyrenean deep seismic profile reflection data and the overall structure of an orogenic belt. *Tectonics* **1989**. [[CrossRef](#)]
61. Munoz, J.A. Evolution of a continental collision belt: ECORS-Pyrenees crustal balanced cross-section. *Thrust Tectonics* **1992**, 235–246. [[CrossRef](#)]
62. Vergés, J.; Fernández, M.; Martínez, A. The Pyrenean orogen: Pre-, syn-, and post-collisional evolution. *J. Virtual Explor.* **2002**, *8*. [[CrossRef](#)]
63. Vergés, J.; Fernández, M. Tethys-Atlantic interaction along the Iberia-Africa plate boundary: The Betic-Rif orogenic system. *Tectonophysics* **2012**, *579*, 144–172. [[CrossRef](#)]
64. ECORS Pyrenees team The ECORS deep reflection seismic survey across the Pyrenees. *Nature* **1988**, *331*, 508. [[CrossRef](#)]
65. Roure, F.; Choukroune, P.; Berastegui, X.; Munoz, J.A.; Villien, A.; Matheron, P.; Bareyt, M.; Seguret, M.; Camara, P.; Deramond, J. Ecors deep seismic data and balanced cross sections: Geometric constraints on the evolution of the Pyrenees. *Tectonics* **1989**. [[CrossRef](#)]

66. Vergés, J.; Muñoz, J.A. Thrust sequence in the southern central Pyrenees. *Bulletin de la Société Géologique de France* **1990**, *VI*, 265–271. [[CrossRef](#)]
67. Berastegui, X.; Garcia-Senz, J.M.; Losantos, M. Tecto-sedimentary evolution of the Organya extensional basin (central south Pyrenean unit, Spain) during the Lower Cretaceous. *Bulletin de la Société Géologique de France* **1990**, *VI*, 251–264. [[CrossRef](#)]
68. Tugend, J.; Manatschal, G.; Kuszniir, N.J. Spatial and temporal evolution of hyperextended rift systems: Implication for the nature, kinematics, and timing of the Iberian-European plate boundary. *Geology* **2015**, *43*, 15–18. [[CrossRef](#)]
69. Garcia-Senz, J.M. Cuencas Extensivas del Cretácico Inferior en los Pirineos Centrales, Formación y Subsecuente Inversión. Ph.D. Thesis, Universitat de Barcelona, Barcelona, Spain, 2002.
70. Ardévol, L.; Klimowitz, J.; Malagón, J.; Nagtegaal, P.J.C. Depositional sequence response to foreland deformation in the upper Cretaceous of the Southern Pyrenees, Spain. *Am. Assoc. Pet. Geol. Bull.* **2000**. [[CrossRef](#)]
71. Guillaume, B.; Dhont, D.; Brusset, S. Three-dimensional geologic imaging and tectonic control on stratigraphic architecture: Upper Cretaceous of the Tremp Basin (south-central Pyrenees, Spain). *Am. Assoc. Pet. Geol. Bull.* **2008**, *92*, 249–269. [[CrossRef](#)]
72. Mencos, J.; Carrera, N.; Muñoz, J.A. Influence of rift basin geometry on the subsequent postrift sedimentation and basin inversion: The Organya Basin and the Bóixols thrust sheet (south central Pyrenees). *Tectonics* **2015**, *34*, 1452–1474. [[CrossRef](#)]
73. Haines, S.H. Transformations in Cly-Rich Fault-Rocks: Constraining Fault Zone Processes and the Kinematic Evolution of Regions. Ph.D. Thesis, University of Michigan, Ann Arbor, MI, USA, 2008.
74. Simó, A. Carbonate platform depositional sequences, Upper Cretaceous, south-central Pyrenees (Spain). *Tectonophysics* **1986**. [[CrossRef](#)]
75. Vergés, J.; Muñoz, J.A.; Martínez, A. South Pyrenean fold and thrust belt: The role of foreland evaporitic levels in thrust geometry. *Thrust Tectonics* **1992**, 255–264. [[CrossRef](#)]
76. Mey, P.H.W.; Nagtegaal, P.J.C.; Roberti, K.J.; Hartevelt, J.J.A. Lithostratigraphic subdivision of Post-Hercynian deposits in the South-Central Pyrenees, Spain. *Leidse Geol. Meded.* **1968**, *41*, 221–228.
77. Oms, O.; Fondevilla, V.; Riera, V.; Marmi, J.; Vicens, E.; Estrada, R.; Anadón, P.; Vila, B.; Galobart, À. Transitional environments of the lower Maastrichtian South-Pyrenean Basin (Catalonia, Spain): The Fumanya Member tidal flat. *Cretac. Res.* **2016**, *57*, 428–442. [[CrossRef](#)]
78. Delvaux, D.; Sperner, B. New aspects of tectonic stress inversion with reference to the TENSOR program. *Geol. Soc. Lond. Spec. Publ.* **2003**, *212*, 75–100. [[CrossRef](#)]
79. Bons, P.D.; Elburg, M.A.; Gomez-Rivas, E. A review of the formation of tectonic veins and their microstructures. *J. Struct. Geol.* **2012**, *43*, 33–62. [[CrossRef](#)]
80. McCrea, J.M. On the isotopic chemistry of carbonates and a paleotemperature scale. *J. Chem. Phys.* **1950**. [[CrossRef](#)]
81. Mangenot, X.; Gasparrini, M.; Gerdes, A.; Bonifacie, M.; Rouchon, V. An emerging thermochronometer for carbonate-bearing rocks: $\Delta 47/(U-Pb)$. *Geology* **2018**, *46*, 1067–1070. [[CrossRef](#)]
82. John, C.M.; Bowen, D. Community software for challenging isotope analysis: First applications of ‘Easotope’ to clumped isotopes. *Rapid Commun. Mass Spectrom.* **2016**, *30*, 2285–2300. [[CrossRef](#)] [[PubMed](#)]
83. Guo, W.; Mosenfelder, J.L.; Goddard, W.A.; Eiler, J.M. Isotopic fractionations associated with phosphoric acid digestion of carbonate minerals: Insights from first-principles theoretical modeling and clumped isotope measurements. *Geochim. Cosmochim. Acta* **2009**, *73*, 7203–7225. [[CrossRef](#)]
84. Huntington, K.W.; Eiler, J.M.; Affek, H.P.; Guo, W.; Bonifacie, M.; Yeung, L.Y.; Thiagarajan, N.; Passey, B.; Tripathi, A.; Daëron, M.; et al. Methods and limitations of “clumped” CO₂ isotope ($\Delta 47$) analysis by gas-source isotope ratiomass spectrometry. *J. Mass Spectrom.* **2009**, *44*, 1318–1329. [[CrossRef](#)]
85. Dennis, K.J.; Affek, H.P.; Passey, B.H.; Schrag, D.P.; Eiler, J.M. Defining an absolute reference frame for ‘clumped’ isotope studies of CO₂. *Geochim. Cosmochim. Acta* **2011**, *75*, 7117–7131. [[CrossRef](#)]
86. Kim, S.-T.; O’Neil, J.R. Equilibrium and nonequilibrium oxygen isotope effects in synthetic carbonates. *Geochim. Cosmochim. Acta* **1997**, *61*, 3461–3475. [[CrossRef](#)]
87. Kluge, T.; John, C.M.; Jourdan, A.-L.; Davis, S.; Crawshaw, J. Laboratory calibration of the calcium carbonate clumped isotope thermometer in the 25–250 °C temperature range. *Geochim. Cosmochim. Acta* **2015**, *157*, 213–227. [[CrossRef](#)]

88. Shackleton, J.R.; Cooke, M.L.; Vergés, J.; Simó, T. Temporal constraints on fracturing associated with fault-related folding at Sant Corneli anticline, Spanish Pyrenees. *J. Struct. Geol.* **2011**, *33*, 5–19. [[CrossRef](#)]
89. Tavani, S.; Mencos, J.; Bausà, J.; Muñoz, J.A. The fracture pattern of the Sant Corneli Bóixols oblique inversion anticline (Spanish Pyrenees). *J. Struct. Geol.* **2011**, *33*, 1662–1680. [[CrossRef](#)]
90. Veizer, J.; Hoefs, J. The nature of O18/O16 and C13/C12 secular trends in sedimentary carbonate rocks. *Geochim. Cosmochim. Acta* **1976**. [[CrossRef](#)]
91. Veizer, J.; Ala, D.; Azmy, K.; Bruckschen, P.; Buhl, D.; Bruhn, F.; Carden, G.A.F.; Diener, A.; Ebner, S.; Godderis, Y.; et al. 87Sr/86Sr, $\delta^{13}\text{C}$ and $\delta^{18}\text{O}$ evolution of Phanerozoic seawater. *Chem. Geol.* **1999**, *161*, 59–88. [[CrossRef](#)]
92. Friedman, I.; O'Neil, J.R. *Compilation of Stable Isotope Fractionation Factors of Geochemical Interest*; Professional Papers; USGS: Reston, VA, USA, 1977; ISBN 9788578110796.
93. McArthur, J.M.; Howarth, R.J.; Bailey, T.R. Strontium Isotope Stratigraphy: LOWESS Version 3: Best Fit to the Marine Sr-Isotope Curve for 0–509 Ma and Accompanying Look-up Table for Deriving Numerical Age. *J. Geol.* **2001**, *109*, 155–170. [[CrossRef](#)]
94. Kocsis, L.; Gheerbrant, E.; Mouflih, M.; Cappetta, H.; Ulianov, A.; Chiaradia, M.; Bardet, N. Gradual changes in upwelled seawater conditions (redox, pH) from the late Cretaceous through early Paleogene at the northwest coast of Africa: Negative Ce anomaly trend recorded in fossil bio-apatite. *Chem. Geol.* **2016**, *421*, 44–54. [[CrossRef](#)]
95. Tostevin, R.; Shields, G.A.; Tarbuck, G.M.; He, T.; Clarkson, M.O.; Wood, R.A. Effective use of cerium anomalies as a redox proxy in carbonate-dominated marine settings. *Chem. Geol.* **2016**, *438*, 146–162. [[CrossRef](#)]
96. McLennan, S.M. Rare earth elements in sedimentary rocks; influence of provenance and sedimentary processes. *Rev. Mineral. Geochem.* **1989**, *21*, 169–200.
97. Bau, M.; Dulski, P. Distribution of yttrium and rare-earth elements in the Penge and Kuruman iron-formations, Transvaal Supergroup, South Africa. *Precambrian Res.* **1996**, *79*, 37–55. [[CrossRef](#)]
98. Lawrence, M.G.; Greig, A.; Collerson, K.D.; Kamber, B.S. Rare Earth Element and Yttrium Variability in South East Queensland Waterways. *Aquat. Geochem.* **2006**, *12*, 39–72. [[CrossRef](#)]
99. Bau, M.; Dulski, P. Evolution of the Yttrium-Holmium Systematics of Seawater Through Time. *Mineral. Mag.* **1994**, *58A*, 61–62. [[CrossRef](#)]
100. Zhao, L.; Chen, Z.-Q.; Algeo, T.J.; Chen, J.; Chen, Y.; Tong, J.; Gao, S.; Zhou, L.; Hu, Z.; Liu, Y. Rare-earth element patterns in conodont albid crowns: Evidence for massive inputs of volcanic ash during the latest Permian biocrisis? *Glob. Planet. Chang.* **2013**, *105*, 135–151. [[CrossRef](#)]
101. Webb, G.E.; Kamber, B.S. Rare earth elements in Holocene reefal microbialites: A new shallow seawater proxy. *Geochim. Cosmochim. Acta* **2000**, *64*, 1557–1565. [[CrossRef](#)]
102. Wright, J.; Schrader, H.; Holser, W.T. Paleoredox variations in ancient oceans recorded by rare earth elements in fossil apatite. *Geochim. Cosmochim. Acta* **1987**, *51*, 631–644. [[CrossRef](#)]
103. Emery, D. Trace-element source and mobility during limestone burial diagenesis—An example from the Middle Jurassic of eastern England. *Geol. Soc. Lond. Spec. Publ.* **1987**. [[CrossRef](#)]
104. Veizer, J.; Prokoph, A. Temperatures and oxygen isotopic composition of Phanerozoic oceans. *Earth-Sci. Rev.* **2015**, *146*, 92–104. [[CrossRef](#)]
105. Pujalte, V.; Schmitz, B.; Baceta, J.I.; Orue-Etxebarria, X.; Bernaola, G.; Dinarès-Turell, J.; Payros, A.; Apellaniz, E.; Caballero, F. Correlation of the Thanetian-Ilerdian turnover of larger foraminifera and the Paleocene-Eocene thermal maximum: Confirming evidence from the Campo area (Pyrenees, Spain). *Geol. Acta* **2009**. [[CrossRef](#)]
106. Loyd, S.J.; Corsetti, F.A.; Eiler, J.M.; Tripathi, A.K. Determining the Diagenetic Conditions of Concretion Formation: Assessing Temperatures and Pore Waters Using Clumped Isotopes. *J. Sediment. Res.* **2012**, *82*, 1006–1016. [[CrossRef](#)]
107. Bergman, S.C.; Huntington, K.W.; Crider, J.G. Tracing paleofluid sources using clumped isotope thermometry of diagenetic cements along the Moab Fault, Utah. *Am. J. Sci.* **2013**, *313*, 490–515. [[CrossRef](#)]
108. Manguot, X.; Gasparrini, M.; Rouchon, V.; Bonifacie, M. Basin-scale thermal and fluid flow histories revealed by carbonate clumped isotopes ($\Delta 47$)—Middle Jurassic carbonates of the Paris Basin depocentre. *Sedimentology* **2018**, *65*, 123–150. [[CrossRef](#)]
109. Honlet, R.; Gasparrini, M.; Muchez, P.; Swennen, R.; John, C.M. A new approach to geobarometry by combining fluid inclusion and clumped isotope thermometry in hydrothermal carbonates. *Terra Nov.* **2018**, *30*, 199–206. [[CrossRef](#)]

110. Stolper, D.A.; Eiler, J.M. The kinetics of solid-state isotope-exchange reactions for clumped isotopes: A study of inorganic calcites and apatites from natural and experimental samples. *Am. J. Sci.* **2015**, *315*, 363–411. [[CrossRef](#)]
111. Shenton, B.J.; Grossman, E.L.; Passey, B.H.; Henkes, G.A.; Becker, T.P.; Laya, J.C.; Perez-Huerta, A.; Becker, S.P.; Lawson, M. Clumped isotope thermometry in deeply buried sedimentary carbonates: The effects of bond reordering and recrystallization. *Geol. Soc. Am. Bull.* **2015**, *127*, B31169.1. [[CrossRef](#)]
112. Coney, P.J.; Muñoz, J.A.; McClay, K.R.; Evenchick, C.A. Syntectonic burial and post-tectonic exhumation of the southern Pyrenees foreland fold–thrust belt. *J. Geol. Soc. Lond.* **1996**, *153*, 9–16. [[CrossRef](#)]
113. Passey, B.H.; Henkes, G.A. Carbonate clumped isotope bond reordering and geospeedometry. *Earth Planet. Sci. Lett.* **2012**, *351–352*, 223–236. [[CrossRef](#)]
114. Henkes, G.A.; Passey, B.H.; Grossman, E.L.; Shenton, B.J.; Pérez-Huerta, A.; Yancey, T.E. Temperature limits for preservation of primary calcite clumped isotope paleotemperatures. *Geochim. Cosmochim. Acta* **2014**, *139*, 362–382. [[CrossRef](#)]
115. Wood, R.A.; Poulton, S.W.; Prave, A.R.; Hoffmann, K.-H.; Clarkson, M.O.; Guilbaud, R.; Lyne, J.W.; Tostevin, R.; Bowyer, F.; Penny, A.M.; et al. Dynamic redox conditions control late Ediacaran metazoan ecosystems in the Nama Group, Namibia. *Precambrian Res.* **2015**, *261*, 252–271. [[CrossRef](#)]
116. Haley, B.A.; Klinkhammer, G.P.; McManus, J. Rare earth elements in pore waters of marine sediments. *Geochim. Cosmochim. Acta* **2004**. [[CrossRef](#)]
117. German, C.R.; Elderfield, H. Application of the Ce anomaly as a paleoredox indicator: The ground rules. *Paleoceanography* **1990**. [[CrossRef](#)]
118. Casini, G.; Gillespie, P.A.; Vergés, J.; Romaine, I.; Fernández, N.; Casciello, E.; Saura, E.; Mehl, C.; Homke, S.; Embry, J.-C.; et al. Sub-seismic fractures in foreland fold and thrust belts: Insight from the Lurestan Province, Zagros Mountains, Iran. *Pet. Geosci.* **2011**, *17*, 263–282. [[CrossRef](#)]
119. Sibson, R.H. Fluid Flow Accompanying Faulting: Field Evidence and Models. *Earthq. Predict.* **1981**, *4*, 593–603.
120. Piper, D.Z.; Bau, M. Normalized Rare Earth Elements in Water, Sediments, and Wine: Identifying Sources and Environmental Redox Conditions. *Am. J. Anal. Chem.* **2013**, *4*, 69–83. [[CrossRef](#)]



© 2019 by the authors. Licensee MDPI, Basel, Switzerland. This article is an open access article distributed under the terms and conditions of the Creative Commons Attribution (CC BY) license (<http://creativecommons.org/licenses/by/4.0/>).

Article 4

Muñoz-López, D., Cruset, D., Vergés, J., Cantarero, I., Benedicto, A., Albert, R., Gerdes, A., Beranoaguirre, A., and Travé, A. (Submitted). Spatio-temporal variation of fluid flow behavior along a fold: the Sant Corneli-Bóixols anticline (Southern Pyrenees) from U-Pb dating and structural, petrographic and geochemical constraints. Submitted to *Marine and Petroleum Geology*. Impact factor: 3.790. Position: Q1 (22/235) in *Geology* (2020); Q1 (3/39) in *Economic Geology* (2020).

Marine and Petroleum Geology

Spatio-temporal variation of fluid flow behavior along a fold: the Sant Corneli-Bóixols anticline (Southern Pyrenees) from U-Pb dating and structural, petrographic and geochemical constraints

--Manuscript Draft--

Manuscript Number:	JMPG-D-21-00577
Article Type:	Full Length Article
Keywords:	Fluid flow; fractures; calcite veins; U-Pb dating; Sant Corneli-Bóixols anticline; Bóixols trust sheet; Southern Pyrenees
Corresponding Author:	Daniel Muñoz-Lopez Universitat de Barcelona Barcelona, SPAIN
First Author:	Daniel Muñoz-Lopez
Order of Authors:	Daniel Muñoz-Lopez David Cruset Jaume Vergés Irene Cantarero Antonio Benedicto Richard Albert Axel Gerdes Aratz Beranoaguirre Anna Travé
Abstract:	<p>This study defines the fracture-fluid interactions across a large-scale fold in order to date and to investigate the relationships between fluid flow and fold evolution. We integrate field data with U-Pb dating and petrographic and geochemical ($\delta^{18}\text{O}$, $\delta^{13}\text{C}$, $^{87}\text{Sr}/^{86}\text{Sr}$, and elemental composition) analyses of calcite veins cutting the Sant Corneli-Bóixols anticline in the Southern Pyrenees. This E-W trending anticline grew from the Late Cretaceous to Paleocene along the front of the Bóixols thrust sheet. The folded units involve Jurassic-mid Upper Cretaceous pre-compression and latest Cretaceous-Paleocene syn-orogenic sedimentary successions detached on Upper Triassic evaporites. U-Pb dating reveals Late Cretaceous to late Miocene age variations. This age variations are coeval with growth strata deposition and Bóixols thrust sheet emplacement (dates from 71.2 ± 6.4 Ma to 56.9 ± 1.4 Ma), tectonic transport of the Bóixols thrust sheet above the southern Pyrenean basal thrust (dates from 55.5 ± 1.2 Ma to 27.4 ± 0.9 Ma) and post-orogenic exhumation of the Sant Corneli-Bóixols anticline (dates younger than 20.8 ± 1.2 Ma). During this deformation history, the geochemistry of calcite veins reveals that the fluid origin and the extent of fluid-rock interaction varied across the different structural positions of the Sant Corneli-Bóixols anticline, evidencing a compartmentalized fluid system. In the core of the anticline and in the lowest part of the syn-orogenic sequence from the footwall of the Bóixols thrust, the fluid system was dominantly closed and derived from the adjacent Lower Cretaceous and Upper Cretaceous carbonates, respectively. Contrarily, along large faults such as the Bóixols thrust, affecting the entire anticline, and in the fold limbs, the paleohydrological system was open. Large faults acted as conduits for the upward migration of formation waters from deeper regions of the Sant Corneli-Bóixols anticline, whereas fold limbs recorded the infiltration of meteoric fluids. The paleohydrological system in the Sant Corneli-Bóixols anticline was restricted to the Bóixols thrust sheet. The evaporitic detachment likely acted as a lower fluid barrier, preventing the input of fluids from deeper parts of the belt.</p>
Suggested Reviewers:	Randy Williams rtwilliams@wisc.edu

1 **Spatio-temporal variation of fluid flow behavior along a fold: the Sant Corneli-**
2 **Bóixols anticline (Southern Pyrenees) from U-Pb dating and structural,**
3 **petrographic and geochemical constraints**

4 **Daniel Muñoz-López¹, David Cruset², Jaume Vergés², Irene Cantarero¹, Antonio**
5 **Benedicto³, Richard Albert⁴, Axel Gerdes⁴, Aratz Beranoaguirre⁴, Anna Travé¹**

6 ¹Departament de Mineralogia, Petrologia i Geologia Aplicada, Facultat de Ciències de la Terra,
7 Universitat de Barcelona, Martí i Franquès s/n, Barcelona, 08028, Spain.

8 ²Group of Dynamics of the Lithosphere (GDL), Geosciences Barcelona, GEO3BCN-CSIC, Lluís Solé i
9 Sabarís s/n, 08028 Barcelona, Spain.

10 ³UMR CNR GEOPS, Université Paris-Saclay, 91405 Orsay, France

11 ⁴Department of Geosciences, Frankfurt Isotope and Element Research Center (FIERCE), Goethe-
12 University Frankfurt, 60438, Frankfurt am Main, Germany.

13 **Abstract**

14 This study defines the fracture-fluid interactions across a large-scale fold in order to date
15 and to investigate the relationships between fluid flow and fold evolution. We integrate
16 field data with U-Pb dating and petrographic and geochemical ($\delta^{18}\text{O}$, $\delta^{13}\text{C}$, $^{87}\text{Sr}/^{86}\text{Sr}$, and
17 elemental composition) analyses of calcite veins cutting the Sant Corneli-Bóixols
18 anticline in the Southern Pyrenees. This E-W trending anticline grew from the Late
19 Cretaceous to Paleocene along the front of the Bóixols thrust sheet. The folded units
20 involve Jurassic-mid Upper Cretaceous pre-compression and latest Cretaceous-Paleocene
21 syn-orogenic sedimentary successions detached on Upper Triassic evaporites. U-Pb
22 dating reveals Late Cretaceous to late Miocene age variations. This age variations are
23 coeval with growth strata deposition and Bóixols thrust sheet emplacement (dates from
24 71.2 ± 6.4 Ma to 56.9 ± 1.4 Ma), tectonic transport of the Bóixols thrust sheet above the
25 southern Pyrenean basal thrust (dates from 55.5 ± 1.2 Ma to 27.4 ± 0.9 Ma) and post-
26 orogenic exhumation of the Sant Corneli-Bóixols anticline (dates younger than 20.8 ± 1.2
27 Ma). During this deformation history, the geochemistry of calcite veins reveals that the
28 fluid origin and the extent of fluid-rock interaction varied across the different structural
29 positions of the Sant Corneli-Bóixols anticline, evidencing a compartmentalized fluid
30 system. In the core of the anticline and in the lowest part of the syn-orogenic sequence
31 from the footwall of the Bóixols thrust, the fluid system was dominantly closed and
32 derived from the adjacent Lower Cretaceous and Upper Cretaceous carbonates,
33 respectively. Contrarily, along large faults such as the Bóixols thrust, affecting the entire
34 anticline, and in the fold limbs, the paleohydrological system was open. Large faults acted
35 as conduits for the upward migration of formation waters from deeper regions of the Sant
36 Corneli-Bóixols anticline, whereas fold limbs recorded the infiltration of meteoric fluids.
37 The paleohydrological system in the Sant Corneli-Bóixols anticline was restricted to the
38 Bóixols thrust sheet. The evaporitic detachment likely acted as a lower fluid barrier,
39 preventing the input of fluids from deeper parts of the belt.

40 **Keywords:** Fluid flow, fractures, calcite veins, U-Pb dating, Sant Corneli-Bóixols
41 anticline, Bóixols trust sheet, Southern Pyrenees.

42 **1. Introduction**

43 Folds are an important deformation feature that occur in worldwide compressional belts
44 (Brandes and Tanner, 2014; Mitra, 1990; Vergés, 1993). Such structures have largely
45 been a target for oil and gas exploration (Mitra, 1990), and in depleted oil fields, they
46 depict important analogues for the assessment of CO₂ storage potential (Mitiku and Bauer,
47 2013). Geological storage of CO₂ (GSC) requires an appropriate reservoir placed at a
48 suitable depth to guarantee efficiency (Alcalde et al., 2014; Bachu, 2000; Sun et al.,
49 2020). However, the presence of subseismic fold-related fractures, which have a critical
50 impact on the distribution of the reservoir quality, is not always easy to characterize at
51 depth, as they are usually below the resolution of standard geophysical techniques
52 (Brandes and Tanner, 2014; Casini et al., 2011; Gutmanis et al., 2018) . Therefore, the
53 orientation and extent of such fractures in the subsurface can only be predicted by using
54 geological models and analogues (Brandes and Tanner, 2014; Tavani et al., 2015).

55 On the other hand, the formation of fold-related fractures strongly controls the origin,
56 evolution and distribution of fluids that migrate during folding (Cosgrove, 2015; Evans
57 and Fischer, 2012; Lefticariu et al., 2005). Therefore, the appraisal of the fold-fracture
58 relationships in natural field analogues is crucial: (i) to predict the orientation of fractures
59 (fluid pathways) in areas where outcrops are absent (Bergbauer and Pollard, 2004); and,
60 (ii) to identify the main factors controlling fluid-rock interactions in orogenic systems
61 (Callot et al., 2013; Ferket et al., 2006; Roure et al., 2005; Swennen et al., 2000; Travé et
62 al., 2007). Additionally, understanding when fluid migration occurs has direct
63 implications in applied fields such as hydrocarbon exploration and recovery, mining,
64 hydrology and CO₂ storage (Benedicto et al., 2021; Cooper, 2007; Macgregor, 1996; Sun
65 et al., 2020).

66 Due to the economic importance of understanding the folding, fracturing and fluid flow
67 relationships, several studies have reported the fluid system associated with the evolution
68 of anticlines in the Pyrenees (Beaudoin et al., 2015; Cruset et al., 2016; Nardini et al.,
69 2019; Travé et al., 2007) and in other worldwide compressional settings (Barbier et al.,
70 2012; Beaudoin et al., 2011; Evans et al., 2012; Fischer et al., 2009; Lefticariu et al.,
71 2005). However, these studies have mainly focused on the fracture-controlled
72 paleohydrological evolution through time or in fluid flow associated with specific
73 domains of the fold (Cruset et al., 2016). Thereby, the spatial variation in the fluid flow
74 behavior and the extent of fluid-rock interaction at the different structural position of a
75 fold have been much less documented (Evans and Fischer, 2012).

76 In this contribution, we report the spatio-temporal variation of the fold-fluid system and
77 the main factors controlling the fluid origin and regime at different structural positions of
78 a large-scale fold, using the Sant Corneli-Bóixols anticline in the Southern Pyrenees as
79 an example. This anticline displays excellent exposures of pre- and syn-orogenic strata
80 involving carbonate and clastic sedimentary units (Mencos, 2010; Muñoz, 2017; Simó,

81 1986). This fact, together with the presence of well data and seismic reflection profiling
82 have allowed to characterize the fold structure and the fold-related fracture systems
83 (Mencos, 2010; Mencos et al., 2011; Muñoz, 2017; Nardini et al., 2019; Shackleton et al.,
84 2011; Tavani et al., 2011; Vergés, 1993). The brittle deformation structures in the Sant
85 Corneli-Bóixols anticline are controlled by inherited extensional faults, resulting in
86 asymmetrical fracture networks that are neither parallel nor perpendicular to the fold axial
87 trend (Tavani et al., 2011).

88 The Sant Corneli-Bóixols anticline, along the front of the Bóixols thrust sheet, evolved
89 from Late Cretaceous to Paleocene and was subsequently transported to the south on top
90 of the South-Central Unit during the emplacement of the Montsec and Serres Marginals
91 thrust sheets (Vergés and Muñoz, 1990). Therefore, this anticline, which registered a long
92 deformation history during the evolution of the South Pyrenean fold-and-thrust belt,
93 represents a natural field analogue to study the fluid history in a complex structural
94 setting. Previous studies have analyzed fluid flow in specific structures of the Sant
95 Corneli-Bóixols anticline (Labraña de Miguel, 2004; Muñoz-López et al., 2020b; Nardini
96 et al., 2019) but the results were not enough integrated at the fold scale. Therefore, the
97 main objectives of this contribution are: 1) to report the absolute timing of fracturing and
98 fluid flow in the Sant Corneli-Bóixols anticline by providing 23 U-Pb ages measured in
99 fracture-filling calcite veins; 2) to qualitatively evaluate the fracture-related permeability
100 and the main factors controlling the scale of fluid migration and the extent of fluid-rock
101 interaction; and 3) to unravel the origin, distribution and variation of fluids across the
102 Sant Corneli-Bóixols anticline and to compare our results with those reported in similar
103 compressional settings worldwide.

104 In order to address these objectives in such a challenging structural and tectonic setting,
105 we provide field structural data (around 1500 fracture dip and orientation measurements),
106 together with petrographic, geochemical ($\delta^{18}\text{O}$, $\delta^{13}\text{C}$, $^{87}\text{Sr}/^{86}\text{Sr}$ and elemental
107 composition) and geochronological (23 U-Pb ages) analyses of vein cements. This robust
108 dataset has been completed with already published data in the area including absolute
109 ages of fracture-filling cements (Cruset et al., 2020b; Haines, 2008) and clumped isotope
110 thermometry data (Muñoz-López et al., 2020b; Nardini et al., 2019).

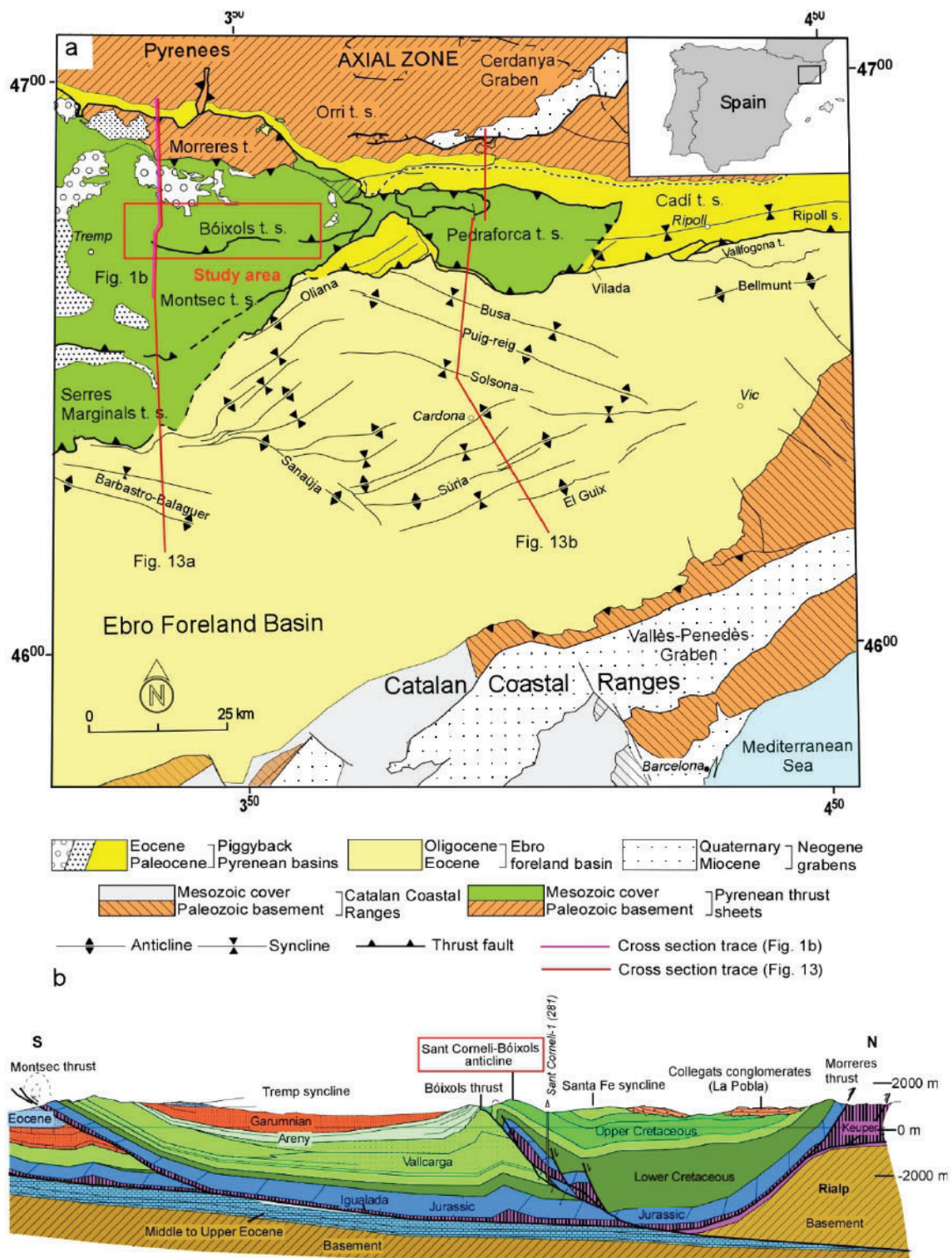
111 **2. Geological setting**

112 The Pyrenees consist of an asymmetrical and doubly verging orogenic wedge that resulted
113 from the Alpine collision between the Iberian and European plates from Late Cretaceous
114 to Miocene, causing the inversion of previous Mesozoic rift basins and subsequent growth
115 of the orogenic belt (Choukroune, 1989; Groot et al., 2018; Muñoz, 1992; Tugend et al.,
116 2014; Vergés et al., 2002; among many others). The Pyrenean structure comprises an
117 antiformal stack of basement-involved thrust sheets from the Axial Zone flanked by two
118 oppositely verging fold-and-thrust belts and their related foreland basins (Figs 1a, b)
119 (Muñoz, 1992; Séguret and Daignières, 1986). The southern fold-and-thrust belt includes
120 a piggy-back imbrication of Mesozoic-Cenozoic cover thrust sheets that have been
121 detached from the Paleozoic basement along Upper Triassic evaporites, and transported
122 southwards over the Ebro foreland basin (Roure et al., 1989; Séguret and Daignières,

123 1986). In the South-Central Pyrenees, these cover thrust sheets are, from north and older
124 to south and younger, the Bóixols thrust sheet, active from the Late Cretaceous to
125 Paleocene, the Montsec thrust sheet emplaced during the Paleocene to late Ypresian, and
126 the Serres Marginals thrust sheet emplaced from Lutetian to Oligocene times (Roure et
127 al., 1989; Vergés and Muñoz, 1990). The Bóixols thrust sheet represents the tectonic
128 inversion of the Lower Cretaceous Organyà extensional basin (Berástegui et al., 1990;
129 Bond and McClay, 1995; Garcia-Senz, 2002; Vergés, 1993). The basal thrust of the
130 Bóixols thrust sheet has been interpreted as a footwall shortcut of the pre-existing Lower
131 Cretaceous extensional fault (Mencos et al., 2011) (Fig. 1b).

132 The complete stratigraphic record involved in the Sant Corneli-Bóixols anticline includes
133 Upper Triassic to Upper Cretaceous pre-orogenic rocks and Upper Cretaceous to
134 Paleocene syn-orogenic units (Berástegui et al., 1990; Mencos et al., 2015; Simó, 1986)
135 (Fig. 2). The pre-orogenic sequence includes up to 5 km of pre-rift, syn-rift and post-rift
136 (pre-orogenic) rocks located in the hanging wall of the Bóixols thrust. The Pre-rift
137 sequence crops out discontinuously in the study area (only present next to the trace of the
138 Bóixols thrust) and includes Upper Triassic shales and evaporites, which constitutes the
139 main detachment level in the Pyrenees, and Jurassic dolomitic limestones and dolostones.
140 The thickness of the pre-rift sequence is up to a few thousands of meters (Lanaja, 1987;
141 Mencos et al., 2011). The syn-rift Lower Cretaceous sequence extensively crops out in
142 the core of the anticline (Fig. 3) exhibiting syn-faulting deformation structures and syn-
143 tectonic slump intervals (Tavani et al., 2011). This sequence ranges from a few meters
144 and up to 4000 m thick, and includes an intercalation of basinal marls, marly limestones
145 and limestones (i.e., the Lluçà Formation), whose lower part abruptly evolves to platform
146 limestones (the Setcomelles Member) (Berástegui et al., 1990; Garcia-Senz, 2002).

147 The upper Cenomanian to lower Santonian post-rift (pre-orogenic) sequence is around
148 800 m thick and mainly consists of carbonate rocks divided in five sedimentary
149 formations, which in the study area are known as the Santa Fe, the Reguard, the Congost,
150 the Collada Gassó and the Sant Corneli Formations (Gallemí et al., 1982; Mencos, 2010;
151 Simó, 1986).

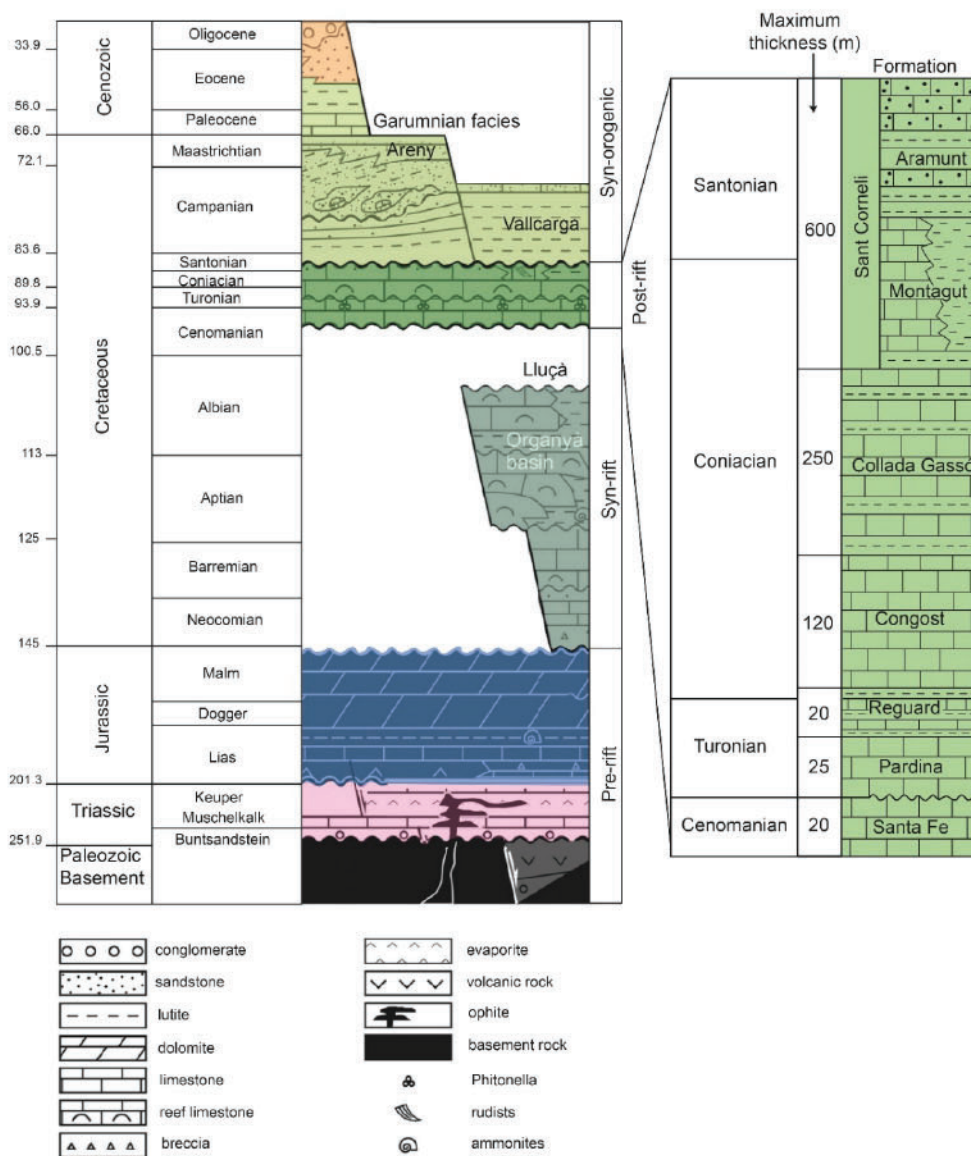


152

153 **Fig. 1.** (a) Simplified geological map and (b) cross-section of the main structural units from the south
 154 Pyrenean fold-and-thrust belt (Vergés, 1993). The red square indicates the location of the Sant Corneli-
 155 Bóixols anticline along the front of the Bóixols thrust sheet.

156 The Upper Cretaceous to Paleocene syn-orogenic succession comprises three shallowing
 157 upward sequences grading from turbidites and marls into shallow marine, fluvial and
 158 continental deposits (Mencos, 2010; Mey et al., 1968). These sequences are located in the
 159 footwall of the Bóixols thrust and belong to the Vallcarga Formation and to the Areny

160 and the Tremp Groups. The Vallcarga Formation (upper Santonian to middle Campanian)
 161 mainly consists of hemipelagic marls. The middle part of this formation consists of a
 162 slope-toe chaotic unit (i.e., the Puimanyons Member) developed due to the destabilization
 163 of the carbonate platform and characterized by growth faulting and olistostrome resulting
 164 from basin margin collapse during the growth of the Sant Corneli-Bóixols anticline (Bond
 165 and McClay, 1995; Simó, 1986). The Areny Group (late Campanian to Maastrichtian)
 166 deposited coevally with the Bóixols thrust and its related Sant Corneli-Bóixols anticline
 167 evolution (Bond and McClay, 1995; Mencos et al., 2011; Robert et al., 2018). This
 168 sequence mainly consists of shallow marine to coastal deposits. Finally, the Maastrichtian
 169 to Paleocene Tremp Group (i.e., Garumnian facies) includes alluvial, fluvial, lacustrine
 170 and carbonate deposits.



171

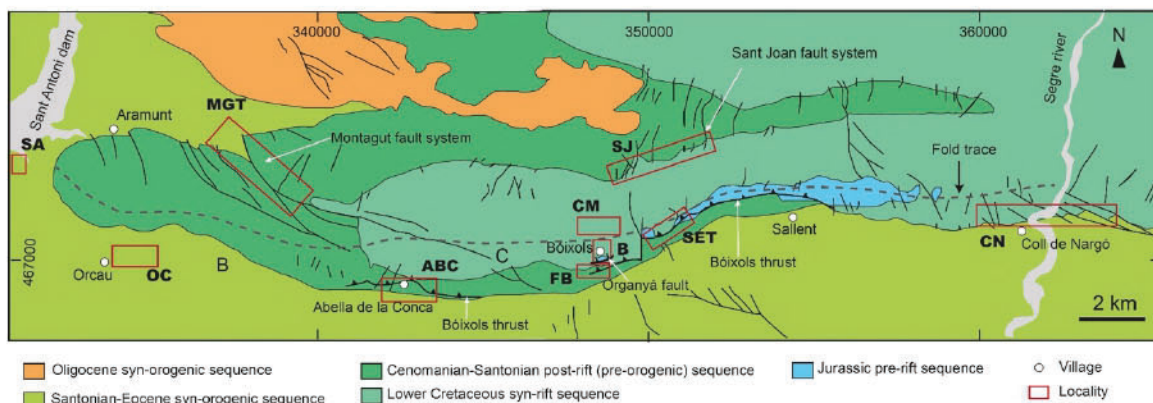
172 **Fig. 2.** Chronostratigraphic diagram displaying the main stratigraphic sequences found around the Sant
 173 Corneli-Bóixols anticline and their associated tectonic event (Mencos et al., 2015).

174 The structure of the Bóixols thrust sheet is composite, formed by the large Santa Fe
 175 syncline and the two linked and south-verging anticlines of Sant Corneli and Bóixols (the

176 Sant Corneli-Bóixols anticline) (Fig. 3). The surficial expression of the Sant Corneli-
177 Bóixols anticline crops out along more than 40 km showing a well-defined geometry in
178 its central-western segment. This geometry is characterized by a gently dipping (around
179 40°) northern backlimb and a subvertical to overturned southern forelimb.

180 During the inversion and growth of the Sant Corneli-Bóixols anticline, shortening
181 direction has been determined as NNW-SSE, and thus slightly oblique to assumed E-W
182 trending inverted normal fault (Tavani et al., 2011) conditioning the fracture orientation
183 developed during the evolution of this frontal anticline (Shackleton et al., 2011; Tavani
184 et al., 2011).

185 The Bóixols thrust along the forelimb of the Sant Corneli-Bóixols anticline is well
186 preserved, near the village of Bóixols and in Abella de la Conca village (Fig. 3).
187 Contrarily, around the Coll de Nargó locality, the Bóixols thrust is blind and sealed by
188 syn-orogenic deposits and the southern limb of the Bóixols anticline is cut by decametric
189 to kilometeric subvertical strike-slip faults (e.g., Nardini et al., 2019) (Fig. 3). The northern
190 limb of the Sant Corneli-Bóixols anticline is cut by well-preserved large normal faults
191 beautifully exposed when displacing Upper Cretaceous carbonate sequences in Montagut
192 and Sant Joan localities. These different scale fractures record a significant part of the
193 structural-fluid flow history of the Bóixols thrust sheet preserving both pre-shortening
194 fractures and folding and fracturing during compression.



195

196 **Fig. 3.** (a) Simplified geological map (Mencos, 2010; Tavani et al., 2011) of the Sant Corneli-Bóixols
197 anticline showing the studied localities. Location in Fig. 1a.

198 3. Methodology

199 This study integrates field data and petrographic, geochemical and geochronological
200 analyses of vein cements and related host rocks from 10 representative localities (Fig 4-
201 5). The field data comprise bedding and fractures dips and dip directions and their
202 crosscutting relationships and kinematics. Such data are plotted in equal-area lower-
203 hemisphere stereoplots to stablish different fracture systems according to their type,
204 orientation, vein cement and relative/absolute age obtained from crosscutting
205 relationships and U-Pb geochronology, respectively. Restoration of the fracture systems
206 with respect to the adjacent bedding and determination of the associated stress
207 orientations have been carried out using Win-Tensor software (Delvaux and Sperner,

208 2003). Up to 185 samples of the involved host rocks and all vein cement generations
209 occluding the recognized fractures systems have been selected for petrographic,
210 geochemical and geochronological analyses. Around 135 polished thin sections of these
211 samples have been analyzed for petrographic descriptions with a Zeiss Axiophot
212 microscope and a cold cathodoluminescence (CL) microscope operating at 15 – 18 kV
213 and 350 μ A current.

214 The U-Pb geochronology has been previously described in (Burisch et al., 2017; Ring and
215 Gerdes, 2016). U-Pb ages were obtained with a laser ablation-inductively coupled plasma
216 mass spectrometry (LA-ICPMS) at FIERCE (Frankfurt Isotope and Element Research
217 Center, Goethe University), following a modified method of (Gerdes and Zeh, 2009,
218 2006). A Thermo Scientific Element XR sector field ICPMS was coupled to a
219 RESolution 193nm ArF excimer laser (COMpexPro 102) equipped with a two-volume
220 ablation cell (Laurin Technic S155). Samples were firstly ablated in a helium atmosphere
221 (300 mL/min) and then mixed in the ablation funnel with 1100 mL/min argon and 5
222 mL/min nitrogen. Signal strength at the ICP-MS was tuned for maximum sensitivity but
223 keeping the oxide formation (monitored as $^{248}\text{ThO}/^{232}\text{Th}$) below 0.2% and low
224 fractionation of the Th/U ratio. Static ablation used a spot size of 193 μm and a fluency
225 of about 2 J/cm² at 12 Hz.

226 Data were obtained in fully automated mode overnight in two sequences of 598 analyses
227 each one. Each analysis comprised 18 s of background acquisition, 18 s of sample
228 ablation, and 25 s of washout. During 36 s of data acquisition, the signal of ^{206}Pb , ^{207}Pb ,
229 ^{208}Pb , ^{232}Th , and ^{238}U was detected by peak jumping in pulse-counting and analogue mode
230 with a total integration time of \sim 0.1s, resulting in 360 mass scans. Each spot was pre-
231 ablated with 8 laser pulses to remove surface contamination before analysis. Soda-lime
232 glass NIST SRM-612 was used as primary reference material (spot size of 50 μm , 8 Hz)
233 together with four carbonate reference materials, which were bracketed in between the
234 analysis of samples.

235 Raw data were corrected offline with an in-house VBA spreadsheet program (Gerdes and
236 Zeh, 2009, 2006). Following background correction, outliers ($\pm 2\sigma$) were rejected based
237 on the time-resolved $^{207}\text{Pb}/^{206}\text{Pb}$, $^{208}\text{Pb}/^{206}\text{Pb}$, $^{206}\text{Pb}/^{238}\text{U}$, and $^{232}\text{Th}/^{238}\text{U}$ ratios. Such ratios
238 were corrected for mass biases and drift over time, using NIST SRM-612. Because of the
239 carbonate matrix, it was applied an additional correction (sequence 1: 21.5%, sequence
240 2: 19.6%) that was determined using WC-1 carbonate reference material (Roberts et al.,
241 2017). The $^{206}\text{Pb}/^{238}\text{U}$ downhole-fractionation during 20s depth profiling was estimated
242 to be 3%, based on the common Pb corrected WC-1 analyses, and was applied as an
243 external correction to all carbonate analyses. Uncertainties for each isotopic ratio are the
244 quadratic addition of the within run precision, counting statistic uncertainties of each
245 isotope, excess of scatter (calculated from NIST SRM-612) and the excess of variance
246 (calculated from WC-1) after drift correction (Horstwood et al., 2016). To account for the
247 long-term reproducibility of the method we added by quadratic addition an expanded
248 uncertainty of 1.5% to the final age of all analysed carbonates. This was deducted from
249 repeated analyses ($n = 7$) of ASH-15D between 2017 and 2019.

250 Carbonate reference materials were measured for quality control. Reference material B6
251 (41.86 ± 0.53 Ma and 42.12 ± 0.88 Ma) (Pagel et al., 2018) was measured in sequences 1
252 and 2, whereas reference material ASH-15D (2.907 ± 0.210 Ma) (Nuriel et al., 2021) was
253 measured in sequence 1. Results on the secondary reference materials indicate an
254 accuracy and repeatability of the method of about 1.5 to 2%. Data were displayed in Tera-
255 Wasserburg plots, and ages were calculated as lower concordia-curve intercepts using the
256 same algorithms as Isoplot 4.14 (Ludwig, 2012). The ages discussed in this paper are the
257 Tera-Wasserburg intercept ages. All uncertainties are reported at the 2σ level. Analytical
258 results, Concordia graphs and a summary of the U-Pb dating procedure are reported in
259 the supplement.

260 The performed geochemical analyses consist of stable and radiogenic isotopes as well as
261 the elemental composition of vein cements and host rocks. 150 samples were prepared
262 for carbon and oxygen isotopes. Between 50 and 100 μm of each powdered sample was
263 reacted with 100% phosphoric acid at 70 $^{\circ}\text{C}$ for 2 minutes. The resultant CO_2 was
264 analyzed following the method of (McCrea, 1950) and using an automated Kiel
265 Carbonate Device attached to a Thermal Ionization Mass Spectrometer Thermo Electron
266 MAT-252 (Thermo Fisher Scientific). For calibration, the internal standard RC-1,
267 traceable to the International Standard NBS-19, and the International Standard NBS-18
268 have been employed. Results are expressed in ‰ with respect to the Vienna Pee Dee
269 Belemnite (VPDB). Standard deviation is ± 0.05 ‰ for $\delta^{18}\text{O}$ and ± 0.03 ‰ for $\delta^{13}\text{C}$.

270 For $^{87}\text{Sr}/^{86}\text{Sr}$ ratios, 43 samples of powdered calcite cements and host rock have been
271 analyzed. These samples have been dissolved in 5 mL of 10% acetic acid and then
272 centrifuged. The supernatant was dried and dissolved in 1 mL of 1M HNO_3 . The solid
273 residue, resulted after evaporation, was diluted in 3 mL of 3M HNO_3 and then loaded into
274 chromatographic columns to separate the Rb-free Sr fraction, using SrResinTM (crown-
275 ether (4,4'(5')-di-t-butylcyclohexano-18-crown-6)) and 0.05M HNO_3 as eluent. After
276 evaporation, samples were loaded onto a Re filament with 2 μL of Ta_2O_5 and 1 μL of 1
277 M phosphoric acid. Analyses of isotopic ratios have been performed in a TIMS-Phoenix
278 mass spectrometer (Isotopx) according to a dynamic multicollection method, during 10
279 blocks of 16 cycles each one, maintaining a ^{88}Sr beam intensity of 3-V. Obtained ratios
280 have been corrected for ^{87}Rb interferences and normalized with a $^{88}\text{Sr}/^{86}\text{Sr} = 0.1194$
281 reference value, aiming at correcting possible mass fractionation during sample loading
282 and analysis. The isotopic standard NBS-987 has been analyzed 6 times, yielding an
283 average value of 0.710243 ± 0.000009 (standard deviation, 2σ). NBS 987 data have been
284 used to correct the sample ratios for standard drift from the certified value. The analytical
285 error in the $^{87}\text{Sr}/^{86}\text{Sr}$ ratio was 0.01% (referred to two standard deviations). The internal
286 precision is 0.000003. Sr procedural blanks were below 0.5 ng.

287 To determine the elemental composition of calcite cements and host rocks, 69 samples
288 were analyzed employing a magnetic sector field Element XR (HR-ICP-MS, high
289 resolution inductively coupled plasma-mass spectrometer, Thermo Fisher Scientific). In
290 this case, the LR (low resolution) and the MR (medium resolution) have only been used.
291 100 mg of each powdered sample was firstly dried at 40 $^{\circ}\text{C}$ during 24h and then acid

292 digested in closed polytetrafluoroethylene (PTFE) vessels with a combination of
293 HNO₃+HF+HClO₄ (2.5mL: 5mL: 2.5mL v/v). Samples have been evaporated and, to
294 make a double evaporation, 1 mL of HNO₃ was added. Then, samples have been re-
295 dissolved and diluted with MilliQ water (18.2 MΩ cm⁻¹) and 1 mL of HNO₃ in a 100 mL
296 volume flask. A tuning solution of 1 μg L⁻¹ Li, B, Na, K, Sc, Fe, Co, Cu, Ga, Y, Rh, In,
297 Ba, Tl, U was employed to improve the sensitivity of the ICP-MS and 20 mg L⁻¹ of a
298 monoelemental solution of ¹¹⁵In were used as internal standard. Reference materials are
299 the BCS-CRM n° 393 (ECRM 752-1) limestone, JA-2 andesite and JB-3 basalt. Precision
300 of results is expressed in terms of two standard deviations of a set of eight reference
301 materials measurements (reference material JA-2). Accuracy (%) has been calculated
302 employing the absolute value of the difference between the measured values obtained
303 during the analysis and the certified values of a set of eight reference material analysis
304 (reference material BCS-CRM n° 393 for major oxides and JA-2 for trace elements). The
305 DL (detection limit) has been calculated as three times the standard deviation of the
306 average of ten blanks.

307 **4. Fractures-fluid flow interaction results**

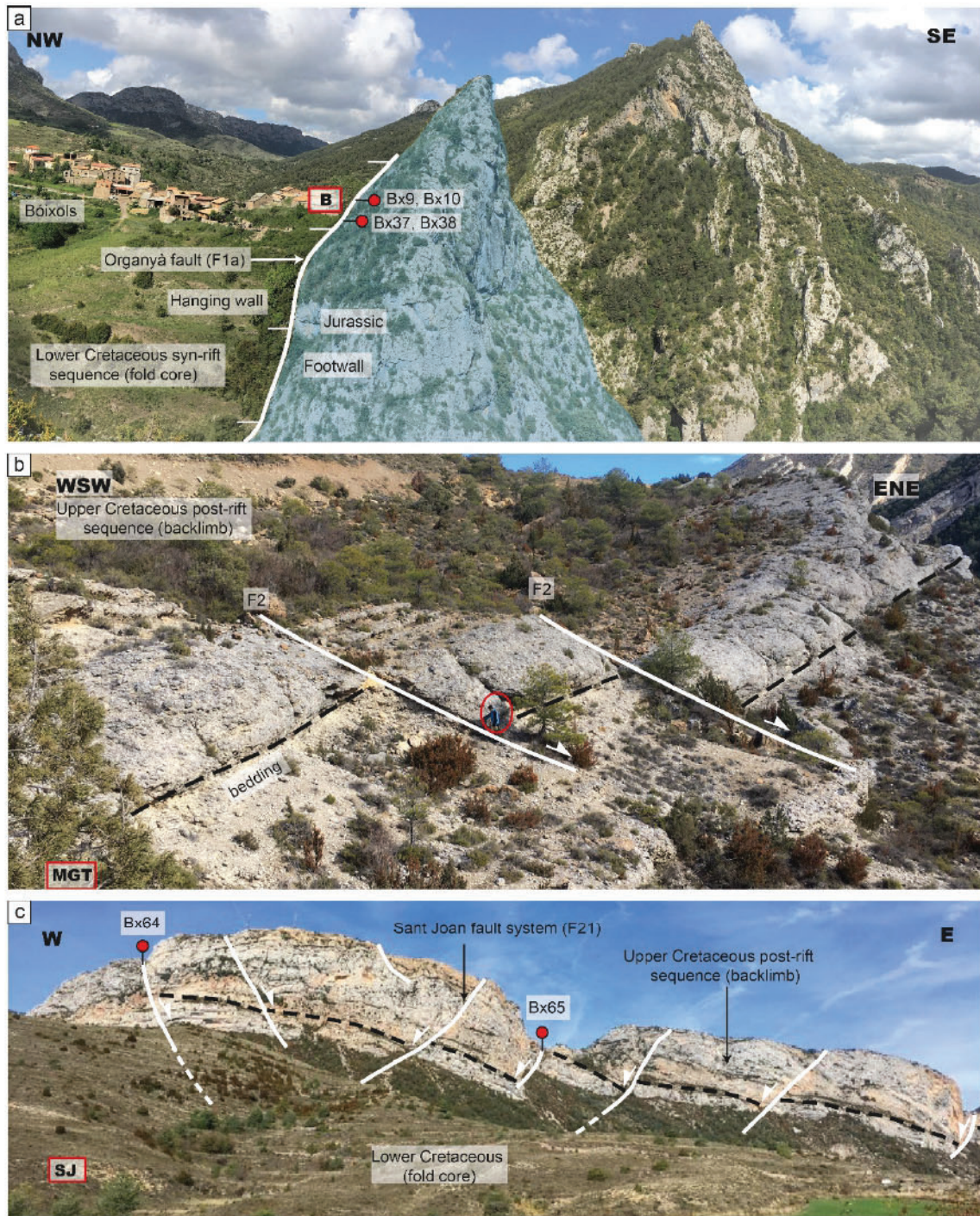
308 **4.1 Studied localities**

309 The studied localities attempt to summarize the entire fractures-fluid flow interactions in
310 the Sant Corneli-Bóixols anticline (Figs 4 & 5). Therefore, ten sampling localities were
311 selected as representative of the different fracture networks as well as the involved host
312 rocks already described in the geological setting. The main characteristics of these
313 localities are described below.

314 The Bóixols locality (B) is located closed to the Bóixols village, next to the axial surface
315 of the anticline (Fig. 4a). In this locality, the upper part of the main E-W Early Cretaceous
316 extensional fault has been preserved affecting Lower Cretaceous limestones and marls
317 (the syn-rift sequence) in the hanging wall and Jurassic dolomitic limestones (the pre-rift
318 succession) from the footwall (Berástegui et al., 1990; Garcia-Senz, 2002).

319 The Cal Mestre locality (CM) is located 0.5 km to the northeast of the Bóixols village, in
320 the core of the Bóixols anticline. In this area, the Lower Cretaceous limestones and marls
321 from the syn-rift sequence are broadly exposed exhibiting a minimum thickness of 2500
322 m according to well data (Lanaja, 1987).

323 The Montagut (MGT) and the Sant Joan (SJ) localities are located in the northern limb of
324 the anticline, affecting Upper Cretaceous limestones from the post-rift (pre-orogenic)
325 sequence. The structure of the Montagut locality consists of a relatively well exposed
326 system of normal and strike-slip faults with a lateral continuity of several kilometers (Fig.
327 4b) (i.e., the Montagut fault system). The structure of the Sant Joan locality consists of
328 two conjugate sets of strike-slip faults and a set of normal faults (Fig. 4c).



329

330 **Fig. 4.** Field images showing the main features of Bóixols, Montagut and Sant Joan localities. (a) Bóixols
 331 locality showing the main E-W extensional fault (the Organyà fault, F1a), which juxtaposes the Jurassic
 332 sequence (in the footwall) and the Lower Cretaceous unit (in the hanging wall). (b) Montagut locality
 333 showing NNW-SSE extensional faults (F2) affecting the Upper Cretaceous sequence in the backlimb of the
 334 Sant Corneli-Bóixols anticline. (c) Sant Joan locality showing the main NNE-SSW extensional faults (F21)
 335 also affecting the Upper Cretaceous sequence in the backlimb. Red circles indicate sample location.

336 The remaining localities are located along the frontal region of the Bóixols thrust sheet,
 337 and include fractures that cut pre-orogenic depositional units from the southern limb of
 338 the Sant Corneli-Bóixols anticline and syn-orogenic units deposited in the footwall of the
 339 Bóixols thrust sheet. The Bóixols thrust has been studied in Abella de la Conca (ABC),

340 Forat de Bóixols (FB) and Setcomelles (SET) localities (Figs 5a-c). In Abella de la Conca
341 and Forat de Bóixols localities, the E-W trending and north-dipping Bóixols thrust offsets
342 subvertical post-rift Upper Cretaceous limestones along the southern limb of the Sant
343 Corneli-Bóixols anticline. The Abella de la Conca locality also includes a reduced Upper
344 Cretaceous syn-orogenic sequence. The Forat de Bóixols locality, located 2 km southwest
345 of the Bóixols village, preserves a good exposure that allows to study the evolution of
346 fractures across the Bóixols thrust zone (Fig. 5b) (Muñoz-López et al., 2020b). In the
347 Setcomelles locality, between Bóixols and Sallent villages, the Bóixols thrust is
348 interpreted as a footwall shortcut of the previous Lower Cretaceous Organyà fault. In this
349 area, Jurassic dolomitized limestones juxtapose against Upper Cretaceous limestones
350 (García-Senz, 2002) (Fig. 5c).

351 The Sant Antoni (SA), Orcau (OC) and Coll de Nargó (CN) localities are aligned along
352 the footwall of the Bóixols thrust, involving Upper Cretaceous to Paleocene syn-orogenic
353 sequences showing growth strata patterns (Bond and McClay, 1995; Garrido-Megías and
354 Ríos, 1972; Mencos et al., 2011; Tavani et al., 2017; Vergés and Muñoz, 1990). The Sant
355 Antoni locality, next to the Sant Antoni dam, comprises the lowest part of the syn-
356 orogenic sequence integrated in the Vallcarga Fm. (Fig. 5d). The Orcau locality, next to
357 the Orcau village, constitutes the middle part of the syn-orogenic unit integrated in the
358 Areny Group. Finally, the Coll de Nargó locality, near the Coll de Nargó village, involves
359 the upper part of the syn-orogenic sequence integrated within the Garumnian facies from
360 the Tremp Group. In this area, the Bóixols thrust is buried and the syn-orogenic deposits
361 are deposited in angular discordance on the front of the anticline.



362

363 **Fig. 5.** Field images showing the main features of Abella de la Conca, Forat de Bóixols, Setcomelles and
 364 Sant Antoni localities. (a) The Bóixols thrust in the Abella de la Conca locality offsetting the steeply dipping
 365 Upper Cretaceous sequence located in the forelimb of the Sant Corneli-Bóixols anticline. (b) The Bóixols
 366 thrust in the Forat de Bóixols locality showing a well exposed thrust zone that also displaces the southern
 367 limb of the anticline. (c) The Bóixols thrust in the Setcomelles locality juxtaposing Jurassic dolomitized
 368 limestones in its hanging wall with Upper Cretaceous limestones in its footwall. (d) Main structural features
 369 of Sant Antoni locality showing normal faults (F5b), bed-parallel slip surfaces (F8) and strike-slip faults
 370 (F17) affecting the base of the syn-orogenic sequence located in the footwall of the Bóixols thrust sheet.
 371 Red circles indicate sample location.

372

4.2 Petrographic description of host rocks

373

374

375

376

377

378

379

380

381

382

383

384

In this section, we summarize the main petrographic features of the studied host rocks. The syn-rift Lower Cretaceous Lluçà Formation, made up of mudstones with isolated sponge spicules and agglutinated foraminifera (Fig. 6a), features a dark brown to non-luminescence (Fig. 6b). The lower part of the Lluçà Fm (the Setcomelles Member) is formed of wackestones, locally packstones, made up of corals, red algae (*Agardhiellopsis cretacea*), echinoderms, bryozoans and foraminifera. The moldic porosity is filled with micrite sediment with a geopetal distribution, which indicates vadose environment, and the remanent intraparticle porosity is filled by calcite cement (Fig. 6c). The micrite matrix exhibits a brown to dark orange luminescence, whereas the intraparticle micrite sediment shows an orange luminescence and the cement has a non- to bright yellow zonation (Fig. 6d).

385

386

387

388

389

390

391

392

393

394

395

396

397

398

399

400

401

402

403

404

405

The Upper Cretaceous post-rift (pre-orogenic) sequence includes five sedimentary formations, which are known as the Santa Fe, the Reguard, the Congost, the Collada Gassó and the Sant Corneli Formations. The Santa Fe Fm. includes wackestones, locally packstones with calcispheres and planktonic foraminifera. Under cathodoluminescence, it exhibits a very dark orange color. The Reguard Fm. consists of mudstones, locally wackestones, made up of foraminifera (mainly miliolids) and showing a dark brown luminescence. The Congost Fm. is made up of packstones, locally grainstones formed of bivalves, foraminifera, echinoderms, corals, bryozoans and partially to totally micritized components (i.e., peloids) (Fig. 6e). The micritic matrix as well as the inter- and intraparticle calcite cement is dark brown to non-luminescent (Fig. 6f). The Collada Gassó Fm. is formed of grainstones made up of gastropods, bivalves, echinoids, corals, bryozoans, miliolids, peloids, and locally quartz grains. The inter- and intraparticle porosity is cemented by calcite cement, which exhibits a bright yellow luminescence, whereas the skeletal components display a dull to bright brown luminescence. The Sant Corneli Fm. is divided in two members (the Montagut Mb and the Aramunt Vell Mb). The Montagut Mb. consists of peloidal wackestones to packstones with abundant presence of rudists, miliolids, corals, equinoderms and local quartz detrital components. Under cathodoluminescence, these packstones exhibit a dark to bright brown color. The Aramunt Vell Mb. consists of bioclastic grainstones with variable quartz content and abundant presence of miliolids, bryozoans, equinoderms and bivalves. The interparticle calcite cement displays a dark orange luminescence.

406

407

408

409

410

411

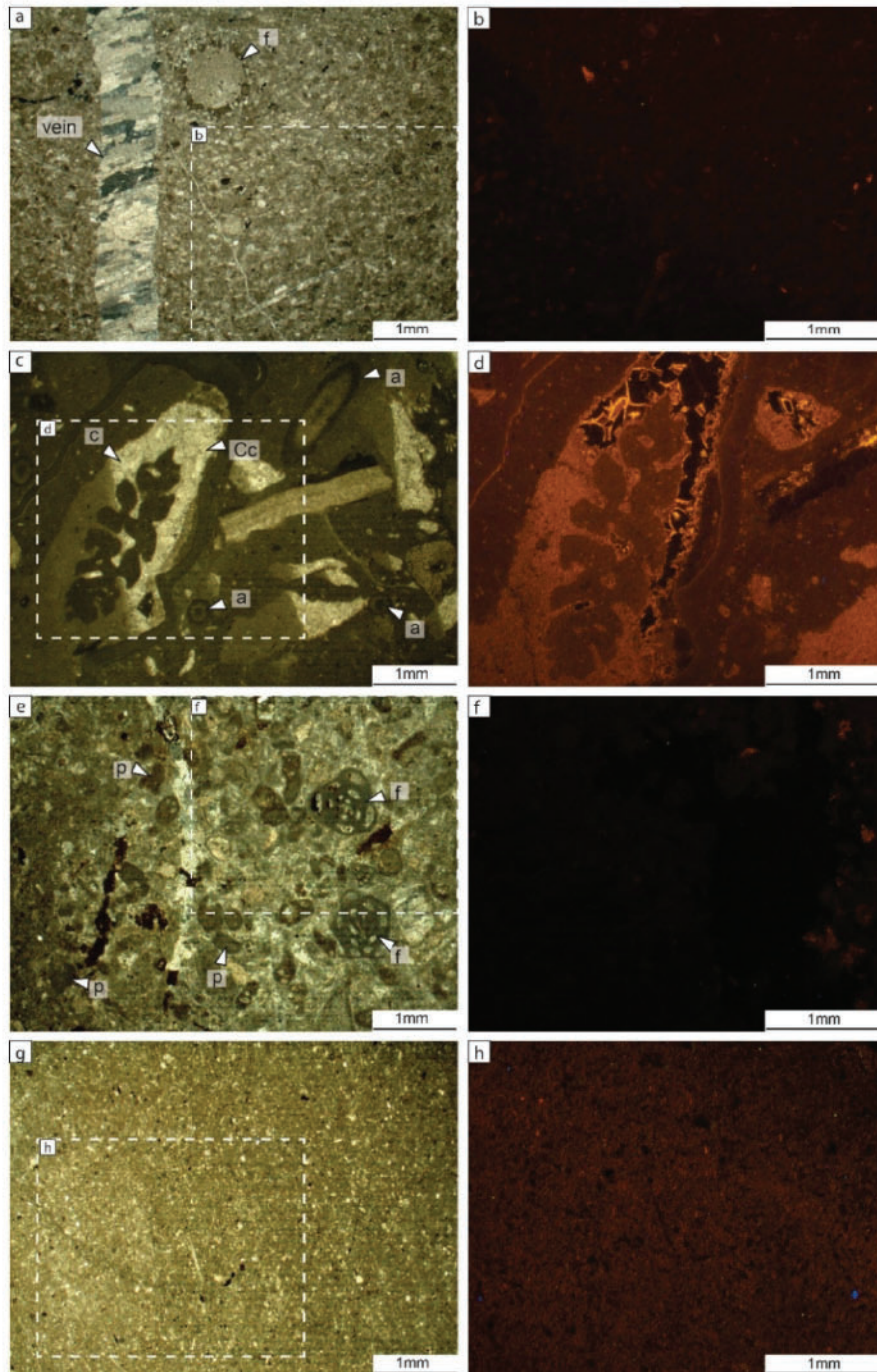
412

413

414

415

The Upper Cretaceous to Paleocene syn-orogenic successions include the Vallcarga Formation, the Areny Group and the Tremp Group (Garumnian facies). The Vallcarga Formation consist of mudstones that are brown to non-luminescent (Figs 6g-h). The Areny Group, in the study localities, is composed of grainstones made up of peloids, local bryozoans and miliolids, and upward increasing detrital quartz content. The interparticle calcite cement is bright yellow luminescent. The Tremp Group (i.e., Garumnian facies) is constituted of fluvial-alluvial and lacustrine detrital and carbonate rocks. Detrital units include versicolored clays with abundant *Microcodium*, fine-grained sandstones and polymictic conglomerates. Carbonate units include red nodular mudstones, grey wackestones with charophytes and oncolytic packstones.



416

417 **Fig. 6.** Paired optical and CL microphotographs showing the main petrographic characteristics of the
 418 studied host rocks. (a) and (b) Mudstones from the Lower Cretaceous Lluçà Fm. with an isolated
 419 agglutinated foraminifera [f] and featuring a dark brown luminescence. (c) and (d) Wackestones to
 420 packstones from the Lower Cretaceous Setcomelles Mb made up of corals [c], red algae [a], presence of
 421 micritic sediment filling moldic porosity with a geopetal distribution and calcite cement [Cc] filling the rest
 422 of the intraparticle porosity. The micritic matrix has a brown to dark orange luminescence, the intraparticle
 423 micrite sediment has an orange luminescent and the intraparticle cement is zoned, varying from a non-
 424 luminescence to bright yellow. (e) and (f). Packstones to grainstones from the Upper Cretaceous Congost
 425 Fm. with abundant presence of foraminifera [f] and peloids [p] and displaying a non-luminescence. (g) and
 426 (h) Mudstones from the Vallcarga Fm. featuring a brown luminescence.

427

4.3 Fracture analysis

428
429 The folded sequence within the Sant Corneli-Bóixols anticline is affected by up to 23
430 fracture sets (F1 to F23) that include the main fault systems affecting the anticline (the
431 Organyà fault, the Bóixols thrust, the Montagut fault system and the Sant Joan fault
432 system) and the background deformation (centimetric to metric fractures). These fracture
433 sets have been grouped according to fracture type, orientation, kinematics, crosscutting
434 relationships and U-Pb geochronology of fracture-filling calcite cements. We use the term
435 “fracture set” to include extensional (mode I) fractures and shear fractures (faults) (Bons
436 et al., 2012). These sets are summarized in Fig. 7 and are described below in chronological
437 order.

438 Fracture set F1 corresponds to E-W to WNW-ESE normal faults that have been attributed
439 to the Early Cretaceous extension (Garcia-Senz, 2002). This fracture set includes the main
440 extensional fault, the Organyà fault (F1a), preserved next to the axial surface of the
441 anticline in the Bóixols locality. In this locality, the Organyà fault is subvertical or steeply
442 dips towards the north and juxtaposes the Jurassic pre-rift sequence in its footwall with
443 the Lower Cretaceous syn-rift sequence in its the hanging wall. Meter-scale normal faults
444 (F1b), which dip 40° to 70° towards the NE and SW and only affect the Lower Cretaceous
445 (syn-rift) Lluçà Formation in Cal Mestre locality, are also included in fracture set F1.

446 Fracture set F2 corresponds to a backlimb normal fault around the Montagut fault system.
447 This metric fault strikes NNW-SSE and cuts the Upper Cretaceous pre-orogenic sequence
448 in the backlimb of the anticline (Montagut locality). These faults exhibit subvertical striae
449 sets and dip between 40° and 80° predominantly towards the SW.

450 F3 represents the main Bóixols thrust, which consists of an E-W trending and south
451 verging reverse fault associated with the growth of the Sant Corneli-Bóixols anticline.
452 Although most of the fault trace has been buried by syn-orogenic deposits, its frontal
453 ramp crops out between Bóixols and Sallent villages (in Setcomelles locality) juxtaposing
454 Jurassic rocks in its hanging wall with Upper Cretaceous carbonates in its footwall. The
455 Bóixols thrust zone is around 15-meter-thick and contains a 2-meter-thick fault core
456 characterized by a dark grey to greenish fine-grained foliated gouge featuring well-
457 developed S-C structures. Kinematic indicators indicate reverse kinematics towards the
458 S-SE.

459 F4 consists of two NW-SE and NE-SW conjugated and centimetric vein systems dipping
460 between 50° and 80°. These veins have regular shapes and show extensional (mode I)
461 openings ranging from 1 to 15 mm. F4 occurs in the Lower Cretaceous syn-rift sequence
462 in Coll de Nargó locality. The orientation of the conjugated F4 sets is compatible with the
463 shortening direction reported for the Bóixols thrust (F3) (Nardini et al., 2019; Tavani et
464 al., 2011).

465 F5 is constituted of meter-scale WNW-ESE extensional faults dipping between 40 and
466 80° towards the NE and SW. These faults, which exhibit subvertical striae sets indicating
467 pure dip-slip kinematics, affect the syn-orogenic succession in the Sant Antoni locality
468 (F5b).

469 F6 consists of meter-scale and steeply dipping vein systems found in several localities of
470 the Sant Corneli-Bóixols anticline. F6a is mostly NE-SW and occurs in the backlimb of
471 the anticline affecting the pre-orogenic sequence (Sant Joan locality). F6b includes two
472 NW-SE and NE-SW conjugate vein sets, which consist of a reactivation of previous F4
473 fractures (Coll de Nargó locality), revealed by the presence of two calcite cements
474 showing clear crosscutting relationships. F6c consists of two WNW-ESE and NNW-SSE
475 vein sets affecting the syn-orogenic unit (Orcau locality).

476 F7 consists of a NNW-SSE vein set dipping between 70° and 85° towards the SW and
477 NE. These veins are up to 1 meter long and show up to 1-centimeter extensional openings.
478 F7 veins crosscut (postdate) the F6c fractures in the Orcau locality.

479 F8 consists of bed-parallel slip surfaces developed between well-bedded layers of marls
480 and marly limestones in the syn-rift sequence (Cal Mestre locality) and the base of the
481 syn-orogenic sequence (Sant Antoni and Abella de la Conca localities). These surfaces
482 correspond to centimeter-thick and striated discrete planes cemented by calcite.

483 F9 consists of WNW-ESE right-lateral strike slip faults affecting pre-orogenic units in
484 Montagut locality (decametric F9a faults) and Cal Mestre locality (metric F9b faults). In
485 the Cal Mestre locality, these faults developed during the strike-slip reactivation of earlier
486 F1b extensional faults due to their favorable orientation with respect to N-S to NNW-SSE
487 shortening direction. This is evidenced by the presence of slicken lines and striae sets
488 showing crosscutting relationships. F9b includes subordinate NNE-SSW left-lateral
489 faults.

490 F10 consists of E-W to WSW-ENE centimetric and steeply dipping veins affecting the
491 syn-orogenic sequence in Abella de la Conca locality. These veins are bed-perpendicular,
492 up to 1 or 2 cm thick and show extensional (mode I) openings.

493 F11 to F13 consist of three vein sets differentiated by their orientation and crosscutting
494 relationships between them. These vein sets exclusively occurring in the damage zone of
495 the Bóixols thrust in Forat de Bóixols locality (F14a). F11 consists of NNW-SSE
496 extensional calcite veins dipping 50 to 70° towards the SW. They are up to 1 – 2 meter
497 long and have opening widths around 1-2 centimeters. F12 consists of E-W extensional
498 veins steeply dipping towards the S-SW. These veins have lengths of several meters and
499 have openings up to 5 centimeters. F13 is constituted of centimetric N-S and NE-SW
500 striking en-échelon calcite veins, showing sigmoidal shapes and gently dipping towards
501 the NW.

502 F14 consists of the E-W trending and south-verging Bóixols thrust dipping 15° to 30°
503 towards the north in the Forat the Bóixols and in Abella de la Conca localities (F14a and
504 F14b, respectively). In both localities, the Bóixols thrust displaces the vertical to
505 overturned southern forelimb of the Sant Corneli-Bóixols anticline generating up to 7 m
506 thick fault cores. These fault cores consist of light grey-yellowish fine-grained foliated
507 gouges characterized by well-developed S-C structures. Striation surfaces present on the
508 main slip planes and S-C structures indicate reverse kinematics towards the S-SE. The

509 evolution of Bóixols thrust in the Forat the Bóixols and its relation to fractures F11 to F13
510 has been studied in Muñoz-López et al., 2020b.

511 F15 are E-W to WSW- ENE calcite veins oriented sub-perpendicular to the bedding
512 strikes. These veins are up to 1 meter long and less than 1 centimeter thick and are present
513 in the pre-orogenic unit (Cal Mestre locality) and in the syn-orogenic sequence (Orcau
514 locality).

515 F16 corresponds to metric N-S to NW-SE and subordinated NE-SW conjugate calcite
516 veins dipping between 60° and 85°. The occurrence of these veins (fracture intensity)
517 increases towards F17 faults. F16 veins affect the syn-rift unit (Cal Mestre locality) and
518 the lower and upper part of the syn-orogenic sequence (Abella de la Conca and Coll de
519 Nargó localities, respectively).

520 F17 consists of N-S to NW-SE and less abundant NE-SW conjugate strike slip faults.
521 This set includes decametric (F17a, F17b, F17d) and metric (F17c, F17e) faults that are
522 mainly subvertical, regardless of the bedding dips, and that show displacements from a
523 few centimeters up to several meters. Deformation associated with F17 faults is either
524 localized on discrete polished slip surfaces or accommodated along an up to 1 m thick
525 fault core formed of brittle incohesive fault rocks. Sub-horizontal slickenlines present on
526 the slip planes indicate pure strike-slip kinematics. F17 faults affect most of the studied
527 units and are observed in all the structural positions of the anticline, that is, in the
528 backlimb (Montagut and Sant Joan localities), in the fold core (Cal Mestre locality) and
529 in the syn-orogenic sequence (Sant Antoni and Coll de Nargó localities).

530 F18 includes metric to decametric NNW-SSE extensional faults dipping 50° to 80° either
531 towards the SW or NE and affecting the pre-orogenic sequence around the Montagut fault
532 system (Montagut locality). Deformation associated with these faults is mainly localized
533 in discrete slip planes exhibiting subvertical striae sets or in centimetric fault cores
534 constituted of grey to reddish calcite-cemented breccias. F18 faults exhibit centimetric to
535 metric displacements.

536 F19 consists of metric and steeply dipping NE-SW and NW-SE extensional faults
537 deforming the syn-orogenic sequence in Abella de la Conca locality. Deformation
538 associated with these faults is localized in discrete polished slip planes showing
539 centimetric displacements.

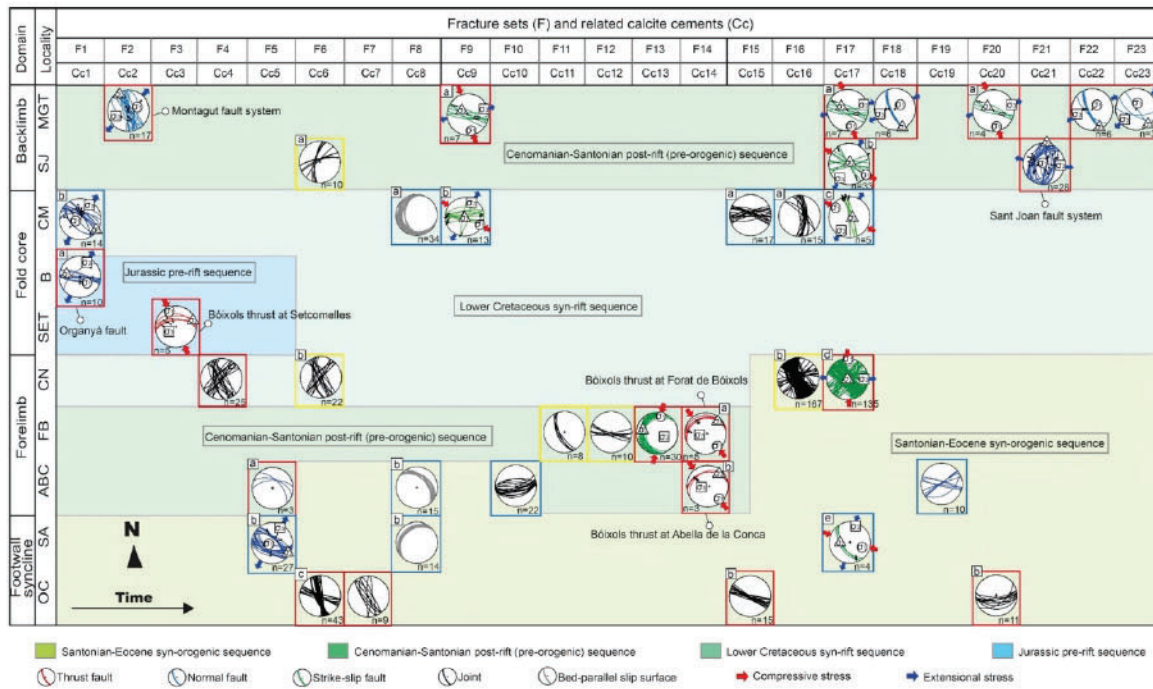
540 F20a is constituted of WNW-ESE right-lateral strike slip reactivations of earlier
541 developed faults (F9a) in the Montagut fault system (Montagut locality) as evidenced by
542 the presence two different calcite cements. F20b corresponds to WSW-ENE calcite veins
543 dipping between 60 and 80° towards the south. They are less than 1 meter long and occur
544 in the syn-orogenic sequence (Orcau locality).

545 F21 corresponds to the Sant Joan fault system, which consists of metric to decametric
546 NNE-SSW to NE-SW extensional faults dipping around 60° towards the NW and SE in
547 Sant Joan locality. These faults present striae sets indicating dip-slip kinematics and are
548 widely present offsetting the pre-orogenic Upper Cretaceous sequence in the backlimb of

549 the anticline. Deformation associated with F21 faults is accommodated in discrete slip
 550 planes or in up to two-meter-thick fault cores that are constituted of calcite-cemented
 551 breccias.

552 F22 and F23 correspond to NNW-SSE to WNW-ESE normal faults and strike-slip faults
 553 developed as subsidiary metric slip planes around the Montagut fault system (Montagut
 554 locality).

555



556

557 **Fig. 7.** Spatial and temporal distribution of fractures (F1 to F23) and related calcite cements (Cc1 to Cc23)
 558 within the Sant Corneli-Bóixols anticline. The lower-hemisphere equal-area projections are arranged
 559 according to the structural position of the anticline, the studied localities and the involved host rocks. Plots
 560 are also grouped in three geochemical groups (blue, red and yellow squares) that will be explained in Fig.
 561 9-11.

562 **4.4 Petrographic description of vein cements**

563 The integrated use of crosscutting relationships as well as petrographic, geochemical and
 564 geochronological analyses applied to vein cements have allowed us to characterize the
 565 whole paragenetic sequence in the Sant Corneli-Bóixols anticline. The petrographic
 566 description using conventional and cathodoluminescence (CL) microscopes of the
 567 successive vein cements from fractures is summarized in Table 1 and Fig. 8.

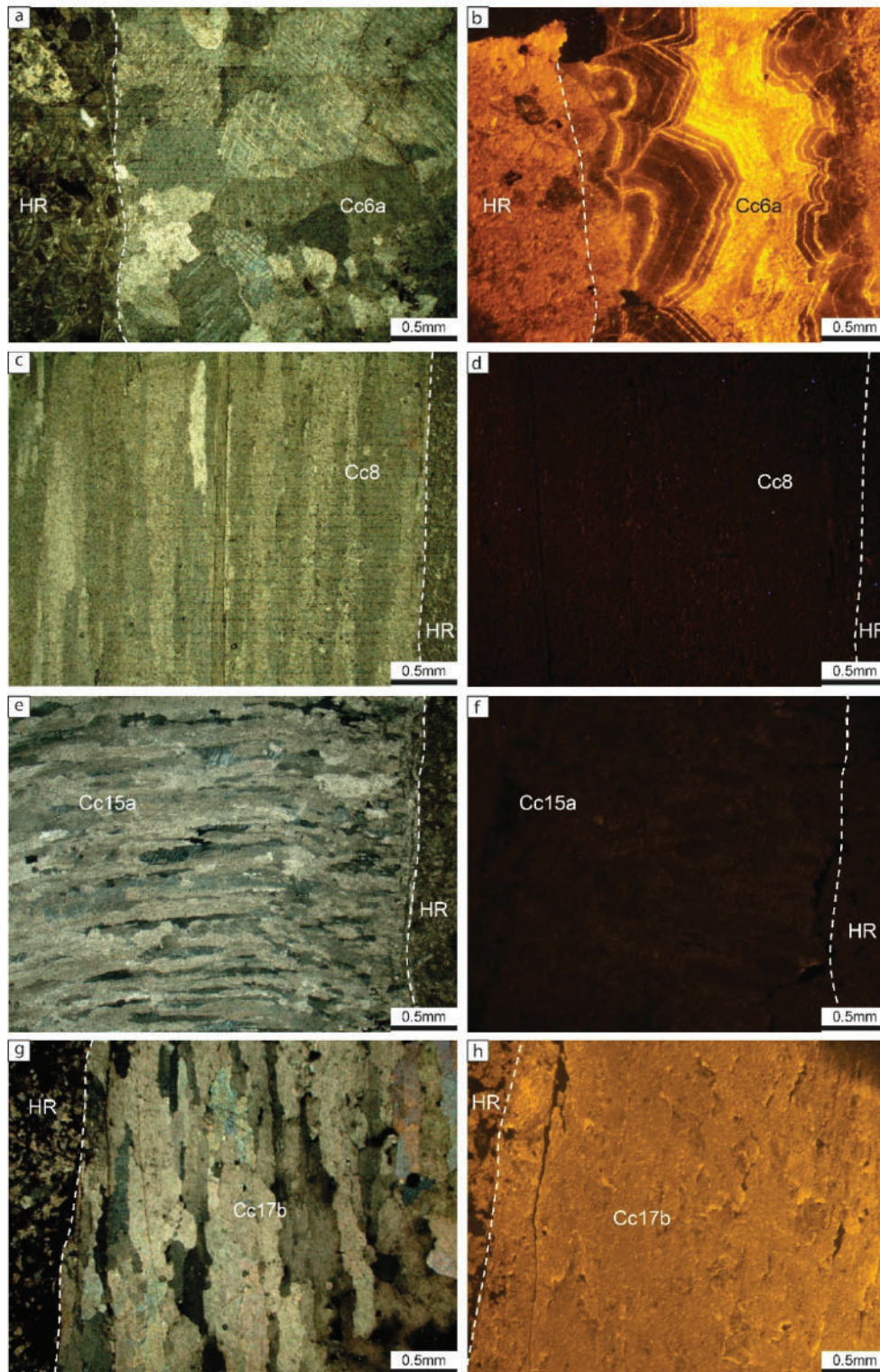
568

569

570

571 **Table 1.** Main petrographic characteristics of the calcite cements (Cc1 to Cc23) from fractures.

Cc	F	Locality	CL	Main textural and petrographic features
Cc1a	F1a	B	Dull brown to dark orange	Up to 3 – 4 mm elongate to fibrous crystals.
Cc1b	F1b	CM	Dark brown to non-luminescent	Up to 7 mm elongated to fibrous, locally blocky crystals.
Cc2	F2	MGT	Brown to dark yellow	0.4 to 1 mm-sized blocky crystals, local presence of thin twin planes.
Cc3	F3	SET	Brown	Up to 3-4 mm-sized elongated to fibrous crystals.
Cc4	F4	CN	Dull orange to non-luminescent	Up to 1.5 mm-sized elongated blocky crystals, growing perpendicular to the fracture walls, locally up to 4 mm anhedral to subhedral blocky crystals.
Cc5a	F5a	ABC	Dark brown to dark orange	Up to 2 mm-sized anhedral blocky crystals.
Cc5b	F5b	SA	Dark brown to non-luminescent	Up to 7 mm elongate to fibrous crystals.
Cc6a	F6a	SJ	Zoned bright orange to non-luminescent	0.5 to 5 mm long blocky to elongate blocky crystals (Figs 8a-b).
Cc6b	F6b	CN	Non-luminescent	Up to 4 mm elongated to fibrous crystals, locally up to 2 mm in blocky crystals.
Cc6c	F6c	OC	Dark to bright brown	Up to 5 mm blocky and up to 7 mm elongate crystals growing perpendicular to the fracture walls.
Cc7	F7	OC	Brown to dark orange	Up to 5–6 mm long blocky crystals.
Cc8	F8	CM SA ABC	Dark brown to non-luminescent	Up to 5 mm elongated to fibrous crystals arranged parallel to the fracture walls and parallel to bedding surfaces (Figs 8c-d).
Cc9a	F9a	MGT	Dark orange	Up to 5 mm-sized blocky crystals.
Cc9b	F9b	CM	Dark brown	Up to 4 -5 mm-sized elongated to fibrous crystals.
Cc10	F10	ABC	Dark brown to non-luminescent	Up to 1 mm-sized blocky crystals with local thin twin planes and up to 5 mm-sized elongated crystals growing syntaxially.
Cc11	F11	FB	Dark- to bright orange	Up to 1 mm-sized blocky crystals locally displaying mechanical twinning and growing syntaxially.
Cc12	F12	FB	Non-luminescent to bright orange concentric zonation	0.2 to 5 mm-sized blocky to elongated blocky crystals growing syntaxially.
Cc13	F13	FB	Dull orange	Up to 0.5 mm-sized anhedral blocky to elongated blocky crystals.
Cc14a	F14a	FB	Dark brown	Up to 1 mm anhedral crystals.
Cc14b	F14b	ABC	Dark brown	Up to 2 mm anhedral to subhedral blocky crystals.
Cc15a	F15a	CM	Dark brown to non-luminescent	Up to 5 mm elongated to fibrous crystals, growing perpendicular to the fracture walls, and local up to 2 mm long anhedral blocky crystals (Figs 8e-f).
Cc15b	F15b	OC	Dark orange	Up to 3–4 mm blocky crystals.
Cc16a	F16a	CM	Non-luminescent	Up to 1 mm blocky crystals.
Cc16b	F16b	CN	Orange to bright yellow	Blocky and elongate blocky crystals ranging in size from 1 to 4 mm.
Cc17a	F17a	MGT	Brown to dark orange	Up to 1.5 mm long elongated blocky crystals.
Cc17b	F17b	SJ	Dull to bright yellow	Up to 6 mm elongated to fibrous crystals (Figs 8g-h).
Cc17c	F17c	CM	Dark to bright brown	Up to 3 mm elongated to fibrous crystals and up to 1 mm long blocky crystals.
Cc17d	F17d	CN	Dull to bright orange	Anhedral to subhedral blocky crystal ranging in size from 0.1 to 2 mm.
Cc17e	F17e	SA	Dark brown	Elongated to fibrous crystals ranging in size from 0.1 to 2 mm.
Cc18	F18	MGT	Dark brown	0.1 to 4 mm-sized elongated blocky crystals.
Cc19	F19	ABC	Dull brown	0.2 to 4 mm-sized crystals with a blocky texture.
Cc20a	F20a	MGT	Dark orange	Up to 4 mm-sized blocky to elongated blocky crystals.
Cc20b	F20b	OC	Dark to light brown	Up to 1 mm in size blocky crystals.
Cc21	F21	SJ	Bright brown to dark orange	0.1 to 1 mm-sized (locally up to 4 mm) blocky and inequigranular crystals.
Cc22	F22	MGT	Dark brown	Up to 2 mm-sized blocky crystals showing local twin planes.
Cc23	F23	MGT	Dark orange	Up to 8 mm-sized anhedral to subhedral crystals with a blocky texture.



572

573 **Fig. 8.** Paired optical and CL microphotographs showing the main textural features of the studied calcite
 574 cements. (a) and (b) Cement Cc6a with a blocky texture and exhibiting a concentric zoned luminescence.
 575 (c) and (d) Cement Cc8 exhibiting elongated to fibrous crystals arranged parallel to the vein walls an
 576 featuring a dark brown to non-luminescence. (e) and (f) Cements Cc15a characterized by elongated to
 577 fibrous crystals arranged perpendicular to the vein walls and displaying a dark to non-luminescence. (g)
 578 and (h) Cement Cc17b with and elongated blocky texture and a dull yellow luminescence.

579

580 **4.5 Geochemistry of calcite cements and host rocks**

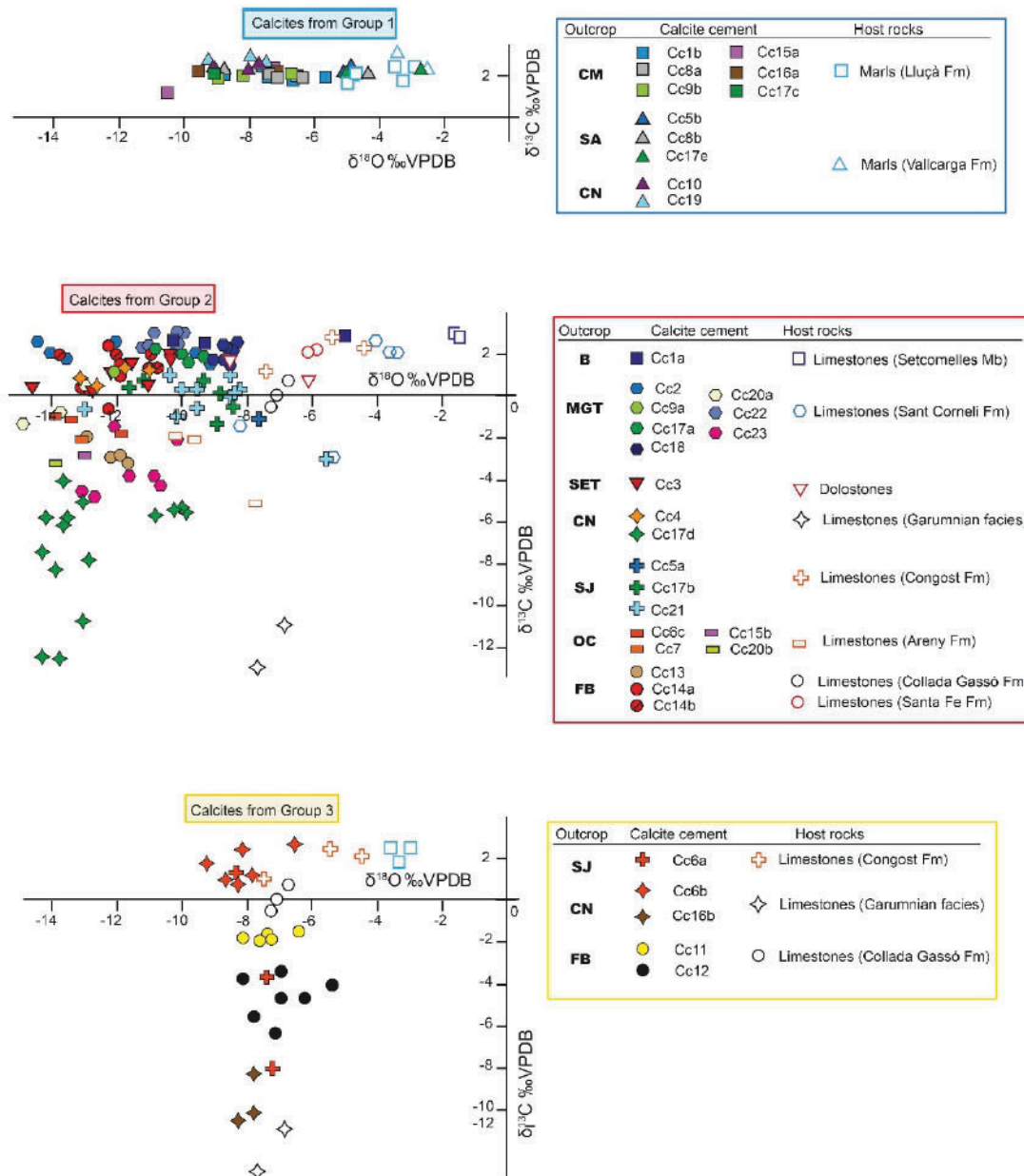
581 Stable isotopes ($\delta^{18}\text{O}$ and $\delta^{13}\text{C}$), $^{87}\text{Sr}/^{86}\text{Sr}$ and elemental composition of the successive
 582 calcite vein generations and related host rocks are summarized in Table 2 and Figs 9-11.
 583 In order to discuss all the complexity of the geochemical values, the studied calcite
 584 cements have been assembled in three groups (Figs 9-11), according to similarities of the
 585 main geochemical features:

586 **Table 2.** $\delta^{18}\text{O}$, $\delta^{13}\text{C}$, $^{87}\text{Sr}/^{86}\text{Sr}$ of calcite veins and host rocks. The elemental composition, including Sr and
 587 Mn contents as well as the Y/Ho ratios, is also given. Cc refers to calcite cement generation, F refers to the
 588 associated fracture set and n corresponds to the number of analyses.

Cc (F) – Locality	Group	$\delta^{18}\text{O}(\text{‰VPDB})$		$\delta^{13}\text{C}(\text{‰VPDB})$		$^{87}\text{Sr}/^{86}\text{Sr}$		Sr (ppm)			Mn (ppm)		Y/Ho			
		n	min	max	min	max	n	min	max	n	min	max	min	max	min	max
Cc1a (F1a) - B	2	3	-10.3	-5.1	+2.4	+2.7	1	0.707627		3	304	708.2	89.5	150	69.2	78
Cc1b (F1b) - CM	1	5	-8.7	-5.6	+1.9	+2.1	1	0.707333		1	1213		95		81.7	
Cc2 (F2) - MGT	2	7	-14.5	-9.1	+1.7	+2.5	1	0.707542		1	749		166.5		52.9	
Cc3 (F3) - SET	2	7	-14.7	-10.4	+0.3	+1.9	2	0.707857	0.708028	2	408.7	711.5	43	82.8	52.2	60.3
Cc4 (F4) - CN	2	4	-13.2	-11.1	+0.4	+1.2	1	0.707468		1	794.7		319.5		53.4	
Cc5a (F5a) - ABC	2	1	-7.8		-1.4		1			1	581.6		66.3		56.2	
Cc5b (F5b) - SA	1	2	-5.2	-5	+2.1	+2.2	1	0.707669		2	3240	3719	175.5	178	78.5	102.7
Cc6a (F6a) - SJ	3	3	-8.5	-7.3	-8.2	+1.3	1	0.707762		2	164.5	441	116.5	318.4	52.3	57
Cc6b (F6b) - CN	3	6	-9.2	-6.6	+1	+2.7	2	0.707298	0.707326	2	240.6	501.2	46.6	225.3	46.3	47.8
Cc6c (F6c) - OC	2	3	-13.9	-11.9	-1.8	-1	1	0.707835		1	1421		477.2		62.7	
Cc7 (F7) - OC	2	1	-13.1		-2.1		1	0.707894		1	1161		512		61.5	
Cc8a (F8a) - CM	1	4	-7.4	-6.5	+2	+2.1	1	0.707389		2	636.7	2618	79.7	84	71.5	86
Cc8b (F8b) - SA	1	2	-4.4		+2.2		2	0.707512	0.707699	2	2070	3916	83.5	164.2	80.8	90.5
Cc9a (F9a) - MGT	2	1	-12.1		+1.2		1	0.707615		1	503		51.4		55.2	
Cc9b (F9b) - CM	1	3	-9	-6.7	+2	+2.2	1	0.707285		2	2119	4689	59	72.2	71.4	90.2
Cc10 (F10) - ABC	1	3	-9.3	-7.9	+2.5	+2.8				2	1131.8	1381	38.1	52.5	57.5	64
Cc11 (F11) - FB	3	5	-8.2	-6.5	-2	-1.5	1	0.707707		1	239		236.7		42.2	
Cc12 (F12) - FB	3	7	-8.2	-5.4	-6.3	-3.3	3	0.707695	0.707765	3	216.2	270.7	86.6	222.3	45.3	47.6
Cc13 (F13) - FB	2	4	-13	-11.7	-3.2	-1.9	1	0.707698		3	356.2	906.7	380.5	661	44.7	51.6
Cc14a (F14a) - FB	2	6	-13.1	-11.9	-0.5	+2.4	2	0.707715	0.707771	3	626.6	670	65.2	97.3	49.9	69.6
Cc14b (F14b) - ABC	2	5	-13.8	-10.8	+1.4	+2										
Cc15a (F15a) - CM	1	3	-10.7	-5.8	+1.4	+2.4	1	0.707355		1	2835		78.9		74.7	
Cc15b (F15b) - OC	2	2	-12.9	-9.3	-2.8	-2.7	1	0.707920		2	530.2	805	431	467.4	54.6	60.1
Cc16a (F16a) - CM	1	2	-9.6	-7.3	+2.2	+2.4				1	4630		82.8		74.9	
Cc16b (F16b) - CN	3	3	-8.3	-7.8	-10.4	-8.3	2	0.707614	0.707706	2	389.4	449.8	501	1380	46.9	47.6
Cc17a (F17a) - MGT	2	5	-10.8	-8.8	+1.4	+2.2				1	1813.4		174.3		45	
Cc17b (F17b) - SJ	2	6	-11.7	-8.5	-1.3	+0.9	1	0.707807		2	413	446	90.1	466.4	76.6	77.8
Cc17c (F17c) - CM	1	1	-9.3		+2.2		1	0.707346		1	4746		43		84.1	
Cc17d (F17d) - CN	2	15	-14.3	-9.9	-12.5	-5	2	0.707586	0.707612	2	391	519.7	119.3	186	47	52
Cc17e (F17e) - SA	1	2	-5.1	-2.8	+2.1	+2.3	1	0.707667		1	3904		164.2		74.7	
Cc18 (F18) - MGT	2	7	-9	-8.4	+1.8	+2.6										
Cc19 (F19) - ABC	1	4	-9.3	-7.5	+2.3	+2.7				1	1463		56.5		75.5	
Cc20a (F20a) - MGT	2	3	-13.1		+0.2											
Cc20b (F20b) - OC	2	1	-13.8		-3.7		1	0.708018		1	707		320		56.4	
Cc21 (F21) - SJ	2	11	-13	-5.6	-2.5	+0.9	1	0.707683		2	314.6	362.5	93.2	636.2	48.2	65.2
Cc22 (F22) - MGT	2	6	-11.2	-10	+2	+2.6										
Cc23 (F23) - MGT	2	7	-13	-10.2	-4.1	-1.2	1	0.707700		2	338.7	1348	74.5	196.5	50.8	54.2
Jurassic	- SET	2	-8.7	-6.2	+0.7	+1.7				1	995.5		60.1		69.6	
Setcomelles Mb.	- B	1	-1.6		+2.97		1	0.707530		1	722.7		104		54.4	
Lluçà Fm.	- CM	1	-4.9		+2.1		1	0.707329		1	3352		80.5		60.6	
Lluçà Fm.	- CN	4	-5	-3	+1.7	+2.5	1	0.707317		1	1813		76.4		70.3	
Santa Fe Fm.	- FB	2	-6.1	-5.8	+2.1	+2.2	1	0.707718		1	468.9		68.8		55.7	
Congost Fm.	- SJ	3	-5.5	-4.5	+1	+2.4				1	682		110		46.9	
Collada Gassó Fm.	- FB	3	-7	-6.6	-0.5	+0.7	1	0.707606		1	340.8		345.6		38.8	
Sant Corneli Fm.	- MGT	4	-5.6	-3.6	+2.2	+2.6										
Vallcarga Fm.	- SA ABC	2	-3.5	-2.6	+2.4	+2.8	1	0.707695		2	2643	2909	48.3	135.9	48.6	50.3
Areny Group	- OC	3	-10.2	-7.8	-5	-1.9				1	1382.4		325		70.1	
Garumnian	- CN	2	-7.7	-6.8	-13.1	-11				2	771.7	1362	58.5	329	50.4	54

589

590



591

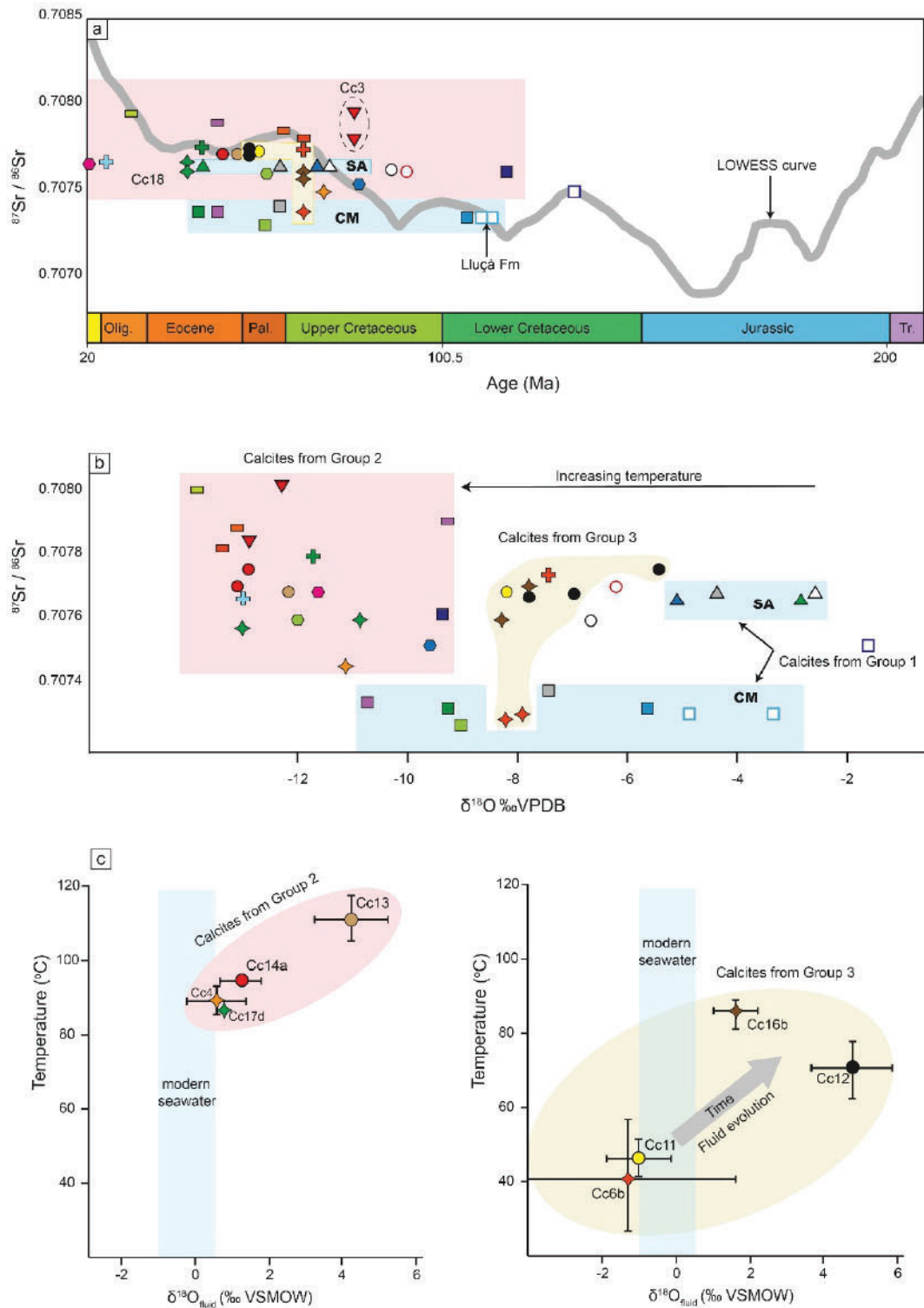
592 **Fig. 9.** Stable isotopic composition ($\delta^{18}\text{O}$ vs $\delta^{13}\text{C}$) of the three groups of calcite cements and related host
 593 rocks. Solid symbols refer to calcite cements and open symbols refer to their associated host rocks.

594 Group 1 includes dark to non-luminescent calcite cements, similar to their adjacent
 595 marine host rocks, either the Lower Cretaceous marls of the Lluçà Formation or the Upper
 596 Cretaceous marls of the Vallcarga Formation. These cements also show $\delta^{13}\text{C}$ values and
 597 $^{87}\text{Sr}/^{86}\text{Sr}$ ratios similar to their adjacent host rocks, which are typical of marine carbonates
 598 (Figs 9 & 10) (Veizer et al., 1999). They are also characterized by Sr contents higher than
 599 1100 ppm, Mn contents lower than 200 ppm, and Y/Ho ratios higher than 50 (Fig. 11).
 600 The $\delta^{18}\text{O}$ values of these cements are similar to or up to 5 ‰VPDB lighter than those
 601 values of their correspondent host rocks (Figs 9 & 10b). These calcite cements are present
 602 in Cal Mestre locality (Cc1b, Cc8, Cc9b, Cc15a, Cc16a and Cc17c), Sant Antoni locality
 603 (Cc5b, Cc8 and Cc17e) and locally in Abella de la Conca locality (Cc10 and Cc19). The

604 geochemistry of all these cements reflect in general the composition of their host
605 carbonates.

606 Group 2 includes calcite cements with the lightest $\delta^{18}\text{O}$ values, from -14 ‰VPDB to -8
607 ‰VPDB, which are up to 10 ‰VPDB lighter than their correspondent host rocks (Figs
608 9 & 10b). These cements have $^{87}\text{Sr}/^{86}\text{Sr}$ ratios between 0.7074 and 0.7080 (Figs 10a-b),
609 and $\delta^{13}\text{C}$ between -12 ‰VPDB and +2 ‰VPDB, which may either be similar or lighter
610 than those values of their adjacent host rocks (Figs. 9). Additionally, comparing all
611 cements, calcites from group 2 exhibit low to intermediate Sr contents (between 390 and
612 2000 ppm), intermediate Mn contents (less than 700 ppm), and intermediate Y/Ho ratios
613 (between 40 and 80) (Figs 11a-c). All these calcite cements precipitated in large-scale
614 faults and related fractures (Cc1a, Cc2, Cc3, Cc4, Cc5a, Cc6c, Cc7, Cc9a, Cc13, Cc14a,
615 Cc14b, Cc15b, Cc17a, Cc17b, Cc17d, Cc18, Cc20a, Cc20b, Cc21, Cc22 and Cc23).
616 Previous studies applied clumped isotopes to Cc4, Cc13, Cc14a and Cc17d calcite
617 cements (Fig. 10c) (Muñoz-López et al., 2020b; Nardini et al., 2019). In these studies, the
618 reported temperatures and $\delta^{18}\text{O}_{\text{fluid}}$ for Cc4 range between 85 and 92 °C and between -0.2
619 and +1.4 ‰SMOW, respectively. For Cc13 range between 105 to 117 °C and between
620 +3.2 to +5.5 ‰SMOW, respectively. For Cc14a range between 93 and 96 °C and between
621 +0.7 and +1.9 ‰SMOW, respectively. And Cc17 displays a T around 88 °C and a $\delta^{18}\text{O}_{\text{fluid}}$
622 around +0.7 ‰SMOW.

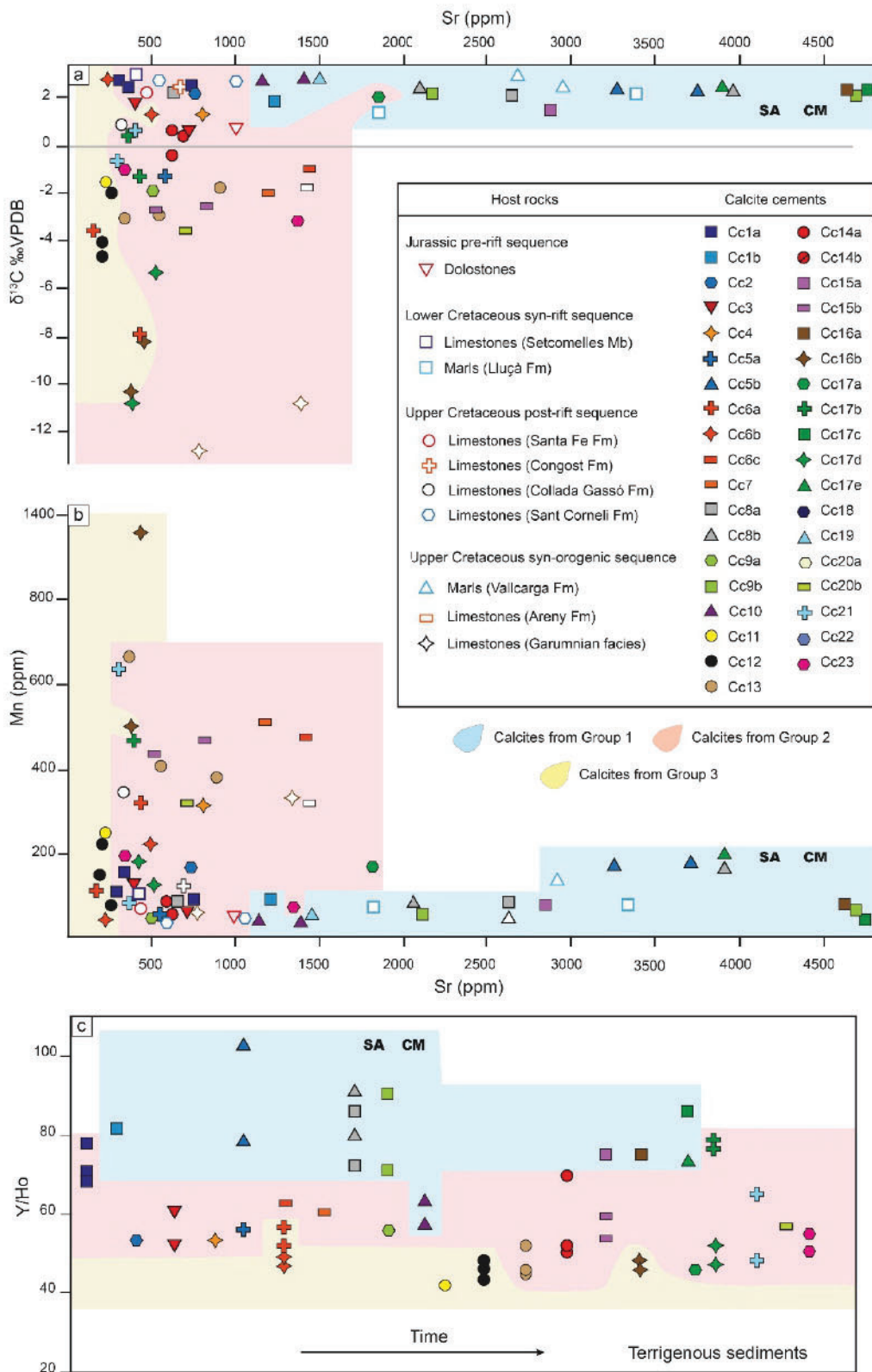
623 Group 3 of calcites (Figs 9-11) includes cements characterized by a narrow range of the
624 $\delta^{18}\text{O}$ values, between -8 and -6 ‰ VPDB (Figs 9 & 10b), and $\delta^{13}\text{C}$ -depleted values,
625 between -10 and +2 ‰ VPDB, which are up to 10 ‰ VPDB lighter than their surrounding
626 host rocks (Fig. 9). The $^{87}\text{Sr}/^{86}\text{Sr}$ ratios of these calcites, between 0.7073 and 0.7077, are
627 lower than values of their correspondent host rocks but within the range of Cretaceous
628 carbonates, which range between 0.7072 and 0.7079, approximately (McArthur et al.,
629 2012) (Figs 10a-b). Finally, these cements display the lowest Sr contents (less than 500
630 ppm) and Y/Ho ratios (less than 60) (Fig. 11). Cements from group 3 precipitated in
631 centimetric to metric-scale fractures in the backlimb (Cc6a in Sant Joan locality) and
632 forelimb (Cc6b/Cc16b in Coll de Nargó locality and Cc11-Cc12 in Forat de Bóixols
633 locality) of the Sant Corneli-Bóixols anticline. The previous contributions of Muñoz-
634 López et al., 2020b; Nardini et al., 2019 also reported the temperature of precipitation and
635 composition of the parent fluids for cements Cc6b, Cc11, Cc12, Cc16b from group 3. The
636 measured temperature and $\delta^{18}\text{O}_{\text{fluid}}$ for Cc6b range between 25 and 57 °C and between -
637 4.2 and +1.6 ‰SMOW, respectively. The calculated T and $\delta^{18}\text{O}_{\text{fluid}}$ for Cc11 range from
638 42 to 51 °C and -1.8 to -0.1 ‰SMOW, respectively. Cc12 exhibits T and $\delta^{18}\text{O}_{\text{fluid}}$ between
639 64 and 78 °C and between +3.7 and +5.9 ‰SMOW, respectively. Cc16b displays T and
640 a $\delta^{18}\text{O}_{\text{fluid}}$ in the range of 80 to 90 °C and from +1 to +2 ‰SMOW.



641

642 **Fig. 10.** (a) $^{87}\text{Sr}/^{86}\text{Sr}$ ratios of the three groups of calcites compared with the $^{87}\text{Sr}/^{86}\text{Sr}$ ratios of seawater
 643 trough time from the LOWESS curve (thick gray line) (McArthur et al., 2012). (b) $^{87}\text{Sr}/^{86}\text{Sr}$ ratio plotted
 644 against the $\delta^{18}\text{O}$ values. (c) The temperature (T) of precipitation and the $\delta^{18}\text{O}_{\text{fluid}}$ reported for cements Cc4,
 645 Cc6b, Cc16b (from Nardini et al., 2019) and cements Cc11, Cc12, Cc13, Cc14a (from Muñoz-López et al.,
 646 2020b).

647



648

649 **Fig. 11.** Elemental composition of the three groups of calcites and their associated host rocks. (a) Sr content
 650 vs $\delta^{13}\text{C}$ values. (b) Mn content vs Sr content. (c) Y/Ho ratio.

651

5. U-Pb geochronology of fracture-filling calcite cements

652

653 Twenty-three ages were obtained for different fracture-filling calcite cements (Table 3),
654 varying from Late Cretaceous (79.8 ± 1.2 Ma) to late Miocene (9.0 ± 4.6 Ma). Most of
655 these U-Pb ages were acquired for calcite cements from group 2 (18 out of 23), which
656 precipitated along the Bóixols thrust, the Montagut fault system and other large faults and
657 related fractures affecting the entire anticline. The other ages were measured in cements
658 from group 1 (3 out of 23) and cements from group 3 (2 out of 23). These results together
659 with eight previously published dates (Cruset et al., 2020b; Haines, 2008) provide a well
660 constrained absolute timing of deformation in the frontal anticline of the Bóixols thrust
661 sheet.

662 The Bóixols thrust has been studied in Setcomelles, Forat de Bóixols and Abella de la
663 Conca localities (F3, F14a and F14b, respectively). At Setcomelles, a previously reported
664 date for the Bóixols thrust yielded a Late Cretaceous age (71.2 ± 6.4 Ma) (Haines, 2008),
665 whereas the reported age at Forat de Bóixols was 55.5 ± 1.2 Ma (Cruset et al., 2020b).
666 Both dates are older than the new U-Pb age reported in this study for the Bóixols thrust
667 at Abella de la Conca (36.6 ± 7.9 Ma).

668 In the several faults that constitute the Montagut fault system we obtained 13 U-Pb dates.
669 These present important age variations from the oldest one during the Late Cretaceous at
670 79.8 ± 1.2 Ma (for Cc2) to the youngest one during the late Miocene at 9 ± 4.6 Ma (for
671 Cc23). This dataset has been completed with two previously published dates in the area,
672 which also yielded early and middle Miocene ages at 18.5 ± 0.5 Ma and 12.7 ± 2.9 Ma
673 (Cruset et al., 2020b). These results point to successive episodes of fault development
674 and/or reactivation affecting the Upper Cretaceous Sant Corneli Formation at the
675 Montagut locality. In this locality, we report the formation and/or reactivation of normal
676 faults during precipitation of calcite cements Cc2 (at 79.8 ± 1.2 Ma), Cc18 (at 48.8 ± 8.6
677 Ma to 43.9 ± 0.7 Ma), Cc22 (at 20.8 ± 1.2 Ma to 16.8 ± 0.2 Ma) and Cc23 (9 ± 4.6 Ma),
678 which precipitated in fractures F2, F18, F22 and F23, respectively. Therefore, the calcite
679 cement Cc2 yielded a Late Cretaceous date, which is: (i) the oldest obtained age in this
680 contribution and, (ii) older than the first age documented for the Bóixols thrust ($71.2 \pm$
681 6.4 Ma, Haines, 2008). Ages for the Organyà fault and other pre-shortening fractures were
682 not obtained in this study.

683 In the same way, at the Montagut locality, we document the formation and/or reactivation
684 of strike-slip faults during precipitation of calcite cements Cc9a (at 58.7 ± 1.1 Ma), Cc17a
685 (at 45.5 ± 0.8 Ma to 37.8 ± 3.5 Ma) and Cc20a (at 27.6 ± 2.3 Ma), which precipitated in
686 fractures F9a, F17a and F20a, respectively. The precipitation of calcite cement Cc17a in
687 strike-slip faults during the Lutetian, coincides with the formation of similar strike-slip
688 faults in other localities, according to the age of their related cements Cc17b at 43.4 ± 3
689 Ma (Sant Joan locality) and cement Cc17e at 45.7 ± 9.7 (Sant Antoni locality).

690 At the Sant Joan locality, we did not obtain ages for the Sant Joan fault system (F21).
691 However, we measured two dates for calcite cement Cc6a (67.1 ± 2.2 Ma and 65.4 ± 1.3
692 Ma), which precipitated in metric fractures (F6) in this locality. The former age has a

693 mean squared weighted deviate (MSWD) of 10.6 (Table 3). As this values is higher than
 694 2, it could indicate a mixing of ages, an open system or an incomplete initial equilibration
 695 of the Pb isotopes (Rasbury and Cole, 2009).

696 Other obtained ages in the Sant Corneli Bóixols anticline account for the background
 697 deformation represented by fracture systems at different scales and studied at distinct
 698 localities. In this line, we document the formation of layer-parallel slip surfaces at $61 \pm$
 699 21.8 Ma, according to its associated calcite cement Cc8 at Cal Mestre Locality. Similarly,
 700 we also report the formation and/or reactivation of meter-scale fractures during the Late
 701 Cretaceous to Oligocene, according to precipitation of calcite cements Cc6b (at $67.9 \pm$
 702 3.9 Ma), Cc10 (at 56.9 ± 1.4 Ma), Cc15a-Cc15b (at 44.7 ± 4 Ma to 43.9 ± 1 Ma) and
 703 Cc20b (at 27.4 ± 0.9 Ma). These cements precipitated in fractures F6b, F10, F15 and
 704 F20b, respectively.

705 **Table 3.** U-Pb ages obtained for the different calcite vein generations. Data for Cc3 comes from Haines,
 706 2008; the age for Cc5b has been estimated by Guillaume et al., 2008, and the data for Cc6b, Cc14a, Cc15a,
 707 Cc17e, Cc22 and Cc23 has been reported in Cruset et al., 2020b.

Cc	Sample	F	Locality	Age (Ma)	$\pm 2\sigma$	MSWD	Upper intercept	Number of spots
Cc2	Mgt21a	F2	MGT	79.8	1.2	1.3	0.7982 ± 0.1746	20
Cc3	-	F3	SET	71.2	6.4	-	-	-
Cc5a	Abc34	F5a	ABC	67	0.7	1.3	0.8227 ± 0.0041	12
Cc5b	-	F5b	SA	69	-	-	-	-
Cc6a	Bx47a	F6a	SJ	67.1	2.2	10.6	0.8118 ± 0.0160	20
Cc6a	Bx47	F6a	SJ	65.4	1.3	1.3	0.8157 ± 0.0070	20
Cc6b	Cn38	F6b	CN	67.9	3.9	1	0.8364 ± 0.0110	27
Cc8	Abc24	F8a	CM	61.2	21.8	1.5	0.8415 ± 0.038	25
Cc9a	Mgt35a	F9a	MGT	58.7	1.1	1	0.8213 ± 0.0157	20
Cc10	Abc22	F10	ABC	56.9	1.4	1.3	0.8261 ± 0.0239	20
Cc14a	Bx5	F14a	FB	55.5	1.2	1.3	0.8210 ± 0.0065	24
Cc14b	Abc3	F14b	ABC	36.6	7.9	0.78	0.8055 ± 0.0145	21
Cc15a	Bx16	F15a	CM	44.7	4	0.5	0.8483 ± 0.0091	23
Cc15b	Bx26	F15b	OC	43.9	1	1.5	0.8446 ± 0.0050	21
Cc17a	Mgt15	F17a	MGT	45.5	0.8	1.4	0.8341 ± 0.0072	21
Cc17a	Mgt15a	F17a	MGT	42.1	2.6	1.4	0.8521 ± 0.0102	20
Cc17a	Mgt20	F17a	MGT	37.8	3.5	1.2	0.8288 ± 0.0043	19
Cc17b	Bx46	F17b	SJ	43.4	3	1	0.8232 ± 0.0064	20
Cc17e	Bx33	F17e	SA	45.7	9.7	0.7	0.8417 ± 0.0081	20
Cc18	Mgt24	F18	MGT	48.8	8.6	0.9	0.8449 ± 0.0253	24
Cc18	Mgt21b	F18	MGT	45.3	2.5	0.4	0.8074 ± 0.0568	20
Cc18	Mgt3	F18	MGT	43.9	0.7	1.2	0.7629 ± 0.0598	20
Cc19	Abc32	F19	ABC	33.2	0.8	0.9	0.8219 ± 0.0098	20
Cc20a	Mgt35b	F20a	MGT	27.6	2.3	0.5	0.8061 ± 0.0438	21
Cc20b	Bx28	F20b	OC	27.4	0.9	1.3	0.8389 ± 0.0074	20
Cc22	Mgt3	F22	MGT	20.8	1.2	1.2	0.8143 ± 0.0059	18
Cc22	Mgt2	F22	MGT	18.1	0.5	1.3	0.8392 ± 0.0087	9
Cc22	Mgt1	F22	MGT	16.8	0.2	1.6	0.8115 ± 0.0815	15
Cc22	Mgt9	F22	MGT	18.5	0.5	1.4	0.8232 ± 0.0092	27
Cc23	Mgt9	F23	MGT	12.7	2.9	0.9	0.8234 ± 0.0039	23
Cc23	Mgt33	F23	MGT	9	4.6	0.4	0.8134 ± 0.0025	21

708

709 **6. Discussion**

710 **6.1 Timing of deformation: fracture development and related tectonic** 711 **setting**

712 Field data coupled with U-Pb geochronology of the calcite cements allow to constrain the
713 absolute timing of fracturing and to characterize the evolution of deformation in the Sant
714 Corneli-Bóixols anticline as summarized below.

715 The oldest obtained date (79.8 ± 1.2 Ma), in a backlimb small normal fault from the
716 Montagut locality (F2), is younger than the base of the syntectonic strata along the
717 southern limb of the Sant Corneli-Bóixols anticline. Ages for the Organyà fault (F1a) and
718 other pre-shortening fractures (F1b) were not obtained in this study. However, this pre-
719 shortening deformation consists of WNW-ESE normal faults that are consistent with the
720 NNE-SSW extensional regime that predates the Pyrenean compression (Berástegui et al.,
721 1990). On the other hand, the Organyà fault juxtaposes the Jurassic pre-rift sequence in
722 its footwall with the Lower Cretaceous syn-rift sequence in its hanging wall and thereby,
723 this fault has previously been associated with the Early Cretaceous rifting (Berástegui et
724 al., 1990; Garcia-Senz, 2002). Faults F1b only affect the Lower Cretaceous syn-rift Lluçà
725 Formation, which exhibits syn-faulting sedimentary geometries. Therefore, normal faults
726 F1b have been considered syn-sedimentary faults and also attributed to the Early
727 Cretaceous extension (Tavani et al., 2011).

728 Dates ranging from 71.2 ± 6.4 to 56.9 ± 1.4 Ma (calcite cements Cc3 to Cc10) are coeval
729 with growth strata deposition along the southern limb of the Sant Corneli-Bóixols
730 anticline. Therefore, these ages, which have been obtained for fracture sets F3 to F10, are
731 interpreted to record the emplacement of the Bóixols thrust sheet and growth of the Sant
732 Corneli-Bóixols anticline along its front during the Late Cretaceous to Paleocene. This is
733 consistent with previous estimates placing the emplacement of the Bóixols thrust sheet and
734 its eastern equivalent structure, the Upper Pedraforca thrust sheet, from 70.6 ± 0.9 to 55.3
735 ± 0.5 Ma (Cruset et al., 2020b). Similarly, authigenic illite dating of the Bóixols thrust-
736 related deformation in the Setcomelles locality (F3) yielded an age of 71.2 ± 6.4 Ma
737 (Haines, 2008), which agrees with growth strata that set the onset of shortening at ca. 72
738 Ma (Bond and McClay, 1995; Puigdefàbregas and Souquet, 1986). Besides, we did not
739 obtain age for the two conjugated fracture sets (F4). However, the orientation of these
740 fractures are compatible with the shortening direction of the Bóixols thrust (F3), and the
741 similar petrographic and geochemical features of calcite cements Cc3 and Cc4, which
742 precipitated in F3 and F4, accounts for a synchronous development. Fracture set F6
743 postdates fractures F4, as evidenced by crosscutting relationships and by the younger U-
744 Pb age of F6, which yielded 67.9 ± 3.9 to 65.4 ± 1.3 Ma. Similarly, fracture set F7
745 postdates fractures F6 but are characterized by a similar orientation, thus indicating that
746 they developed under the same stress field. The orientation of both F6 and F7 coincides
747 with the NNW-SSE to NNE-SSW orientation of fractures that have previously been
748 interpreted as developed during the main folding stage in the western termination of the
749 Sant Corneli-Bóixols anticline (Shackleton et al., 2011). Fractures F8 represents bed-
750 parallel slip surfaces. Although the obtained age for the cement Cc8 has a large error (61.2

751 ± 21.8 Ma), the formation of these surfaces is compatible with flexural-slip folding, which
752 in turn is attributed to growth of the of the Sant Corneli-Bóixols anticline during the
753 Bóixols thrust sheet emplacement (Tavani et al., 2017, 2011). Fracture set F9 is
754 characterized by the strike-slip reactivation of inherited extensional faults developed
755 during the pre-shortening deformation in the Cal Mestre and Montagut localities (F1b and
756 F2, respectively). This reactivation is supported by the presence of overprinting striae sets
757 and slickenlines exhibiting dip-slip and strike-slip kinematics and by the coexistence of
758 two calcite cements in the same fractures (Cc9a postdating Cc1b and Cc9b postdating
759 Cc2). Finally, fracture set F10 yielded a U-Pb age of 56.9 ± 1.4 Ma that postdates the
760 previous deformation. The E-W orientation of set F10 is parallel to the fold axis.
761 Therefore, these fractures have been associated with local extension due to strata bending,
762 as interpreted by Beaudoin et al., 2015 in the Pico del Aguila anticline in the Sierras
763 Exteriores in the Central-Western Pyrenees.

764 Dates ranging from 55.5 ± 1.2 to 27.4 ± 0.9 Ma, obtained for fractures F14 to F20, are
765 Post-Paleocene and postdate the syn-tectonic strata that fossilizes the Bóixols structure.
766 Therefore, these ages are interpreted to record the tightening of the entire Bóixols thrust
767 sheet including its frontal Sant Corneli-Bóixols anticline during Eocene and Oligocene
768 times. The major structural elements of this post-emplacement deformation are
769 represented by fractures with a constant orientation independently of the bedding dips,
770 and by strike-slip faults (F17) and frontal thrusts (F14) offsetting the steeply dipping
771 limbs of the Sant Corneli-Bóixols anticline. Therefore, all these fracture sets developed
772 once the strata had already been folded, coeval with the tectonic transport of the Bóixols
773 thrust sheet to the south over the basal thrust of the South-Central Pyrenean Unit during
774 a period that is characterized by maximum shortening rates (Cruset et al., 2020b; Groot
775 et al., 2018; Vergés et al., 2002). In this line, the obtained U-Pb age for the Bóixols thrust
776 in the Forat de Bóixols locality (F14a) yielded an age of 55.5 ± 1.2 Ma. Fractures F11 to
777 F13 exclusively occur in the fault zone of this Bóixols thrust and they are considered to
778 have developed during the same process of thrusting (Muñoz-López et al., 2020b). In
779 addition, the obtained U-Pb age for the Bóixols thrust in the Forat de Bóixols locality
780 (F14a), differs by almost 20 million years from that obtained for this thrust in the Abella
781 de la Conca locality (F14b, 36.6 ± 8.0 Ma). However, in both places, the Bóixols thrust
782 has the same orientation and exhibit the same relation with respect to bedding dips (i.e.,
783 it displaces the steeply dipping southern limb of the Sant Corneli-Bóixols anticline).
784 Therefore, the obtained time span could be explained by a long-lasting faulting history or
785 by a later movement of the main thrust fault during the post-emplacement deformation.
786 Fractures F15 have a similar orientation to WSW-ENE fractures F10 and are also
787 subperpendicular to the bedding strike. However, the obtained U-Pb ages for cements
788 Cc15a and Cc15b (44.7 ± 4.0 to 43.9 ± 1.0 Ma), postdating the age of cement Cc10,
789 allowed us to discern distinct fracture systems and to attribute them to different
790 deformation stages. Fractures F16 predate strike-slip faults F17, although they have a
791 similar orientation. Fractures F16 are interpreted as a pre-slip stage of F17, as already
792 discussed in (Nardini et al., 2019). On the other hand, the obtained ages for Cc17a, Cc17b
793 and Cc17e, ranging between 45.7 ± 9.7 and 37.8 ± 3.5 Ma, are consistent with the

794 formation of strike-slip faults F17 in the Lutetian, during the post-emplacment
795 deformation. Faults F18 and F19 are extensional and their formation indicates a local
796 extension perpendicular to the main Pyrenean shortening direction. Finally, the obtained
797 U-Pb ages for fracture set F20, ranging from 27.6 ± 2.3 to 27.4 ± 1.0 Ma, mark the end
798 of the post-emplacment deformation during the Oligocene.

799 Finally, ages ranging from 20.8 ± 1.2 to 9.0 ± 4.6 Ma, obtained for sets F21 to F23, are
800 post-Oligocene. Sets F21 to F23 are represented by normal faults that displace already
801 folded beds in the northern backlimb of the anticline (the Sant Joan fault system) and by
802 subsidiary faults developed around the Montagut fault system (Montagut locality). As
803 compressional deformation in the SE Pyrenees is estimated to have finished in the
804 Oligocene (Vergés et al., 2020; Grool et al., 2018), such faults likely developed during
805 the post-orogenic exhumation of the Bóixols thrust sheet and the Sant Corneli-Bóixols
806 anticline along its front during the Miocene. This post-orogenic deformation has also been
807 reported in the eastern equivalent of the Bóixols thrust, which corresponds to the Upper
808 Pedraforca thrust sheet (Cruset et al., 2020b).

809 To sum up, we interpret the evolution of deformation in the study area as a record of the
810 pre-shortening fractures, developed previously to 79.8 ± 1.2 Ma, and the syn-compression
811 folding and fracturing linked to the emplacement of the Bóixols thrust sheet and growth
812 of the Sant Corneli-Bóixols anticline along its front between 71.2 ± 6.4 and 56.9 ± 1.4 Ma.
813 Our data also reveal the post-emplacment deformation during tectonic transport of the
814 Bóixols thrust sheet to the south over the basal thrust of the South-Central Pyrenean Unit,
815 from 55.5 ± 1.2 to 27.4 ± 0.9 Ma, and the post-orogenic exhumation of the Bóixols
816 structure, from 20.8 ± 1.2 to 9 ± 4.6 Ma. In addition, the pre-shortening deformation is
817 consistent with a NNE-SSW extensional regimen. By contrast, during the emplacement
818 and post-emplacment evolution of the Bóixols thrust sheet, deformation is consistent
819 with a N-S to NNW-SSE compressional deformation, which is in agreement with the
820 mean tectonic transport direction in the Pyrenees (Macchiavelli et al., 2017).

821 **6.2 Open vs closed fluid behavior: implications for fluid** 822 **compartmentalization and fracture-related permeability**

823 The presence of different calcite vein generations developed during the structural
824 evolution of the study area, as well as the wide range of isotopic and elemental
825 composition of the vein cements (Figs 9-11), evidence a complex evolution of the fluid
826 system throughout the entire deformation history.

827 In two localities, Cal Mestre and Sant Antoni localities, present in the core of the Sant
828 Corneli-Bóixols anticline and in the base of the syntectonic deposits in the footwall of the
829 Bóixols thrust sheet, respectively, the calcite cements associated with successive episodes
830 of fracturing and vein formation (i.e., group 1 of calcites) do not record significant
831 changes in the fluid composition through time (Figs 9-11). Accordingly, all cements from
832 this group have similar $\delta^{13}\text{C}$ values to their associated carbonate host rocks (Lluçà and
833 Vallcarga Formations, respectively), which in turn yield typical marine values (Fig. 9)
834 (Veizer et al., 1999). The $^{87}\text{Sr}/^{86}\text{Sr}$ ratios of the vein cements are similar to those ratios of
835 local host rocks, which also reflect the composition of contemporaneous seawater

836 (LOWESS curve in Fig. 10a). Indeed, the low Mn content of calcites group 1 and
837 correspondent host rocks, responsible for their dark to non-luminescence, together with
838 their high Sr content (Fig. 11a-b) and high Y/Ho ratios (Fig. 11c) approaches the
839 elemental composition of marine carbonates derived from well-oxygenated seawater
840 (Popp et al., 1986). Therefore, the similar petrographic and geochemical features of all
841 calcite cements and host rocks from Cal Mestre and Sant Antoni localities indicate very
842 low water-rock ratios (i.e., diffusive flow) and precipitation of successive calcite cements
843 in a closed/rock-buffered system during different fracturing events (Boutoux et al., 2014;
844 Hurai et al., 2015; Vandeginste et al., 2012). A plausible source for this host rock-buffered
845 fluid was the interstitial seawater trapped in the Lower Cretaceous and Upper Cretaceous
846 marine carbonates present in Cal Mestre and Sant Antoni localities, respectively.
847 Alternatively, the local host carbonates could have been the source for the successive
848 calcite cements by means of pressure-solution and/or diffusion processes (Bons et al.,
849 2012; Oliver and Bons, 2001; Salomon et al., 2020; Toussaint et al., 2018; Vandeginste
850 et al., 2012). In this scenario, the slight depletion in $\delta^{18}\text{O}$ values of calcites group 1 (Fig.
851 10a), with respect to host rocks and typical marine values, likely indicate variation in fluid
852 temperatures during different events of calcite cement precipitation. These varying
853 conditions are expected during progressive deformation linked to the emplacement of the
854 Bóixols thrust and growth of the Sant Corneli-Bóixols anticline.

855 The geochemical data of calcite cements from group 2, precipitated in decametric to
856 kilometric faults (the Bóixols thrust, the Montagut fault system, the Sant Joan fault
857 system) and related fractures, evidence a very different scenario. These calcites display
858 the most depleted $\delta^{18}\text{O}$ values, with respect to other cements, and exhibit up to 10
859 ‰VPDB lighter values than their adjacent host rocks (Fig. 9). This $\delta^{18}\text{O}$ -depletion, which
860 indicates that the parent fluids were external, is linked to a relative high temperature of
861 precipitation ($>80\text{ }^{\circ}\text{C}$ and up to $120\text{ }^{\circ}\text{C}$), as has been reported in previous studies using
862 clumped isotope temperatures applied to calcites from group 2 (Fig. 10c) (Muñoz-López
863 et al., 200b; Nardini et al., 2019). Indeed, the $\delta^{18}\text{O}_{\text{fluid}}$, between +0.6 and +5.5
864 ‰VSMOW, obtained from clumped isotopes, indicates formation waters circulating
865 through fault zones and related fractures during faulting. On the other hand, the scattered
866 $\delta^{13}\text{C}$ values and $^{87}\text{Sr}/^{86}\text{Sr}$ ratios of these cements (Figs 9 & 10), as well as their variable
867 enrichment in Mn content (Fig. 11b), and their differing luminescence characteristics
868 could indicate that the formation fluids evolved from distinct fluid origins (marine,
869 connate and/or meteoric) and that they interacted with different sedimentary units (Travé
870 et al., 2007; Vandeginste et al., 2012). Similarly, the Y/Ho ratios of group 2 of cements
871 indicate a variable degree of siliciclastic and marine influence (Fig. 11c). As large-scale
872 faults affect all stratigraphic sequences involved in the anticline, from Jurassic marine to
873 Paleocene continental host rocks, such variation may result from the interaction between
874 the vein-forming fluids and marine (high Y/Ho ratio) or continental (low Y/Ho ratio)
875 rocks (Bau and Dulski, 1994; Nardini et al., 2019). Accordingly, the geochemical
876 composition of calcites from group 2 indicate that these cements precipitated from fluids
877 in geochemical and probably thermal disequilibrium with respect to their adjacent host
878 rocks. Therefore, the Bóixols thrust, the Montagut fault system, the Sant Joan fault system

879 and other large faults and related fractures acted as efficient conduits for fluid migration
880 during their formation at different stages of the deformation history.

881 Cements from group 3 precipitated in centimetric to metric scale fractures in the limbs of
882 the Sant Corneli-Bóixols anticline. The isotopic signature of these cements, ranging
883 between -8 and -6 ‰VPDB for $\delta^{18}\text{O}$ and between -10 and +2 ‰VPDB for $\delta^{13}\text{C}$, fall
884 within the range of meteoric carbonates (Pujalte et al., 2009; Travé et al., 2007; Veizer,
885 1992), although with occasional marine influence evidenced by the positive $\delta^{13}\text{C}$ values
886 of cements Cc6a and Cc6b (Fig. 9). The meteoric origin of cements from group 3 is
887 supported by their $^{87}\text{Sr}/^{86}\text{Sr}$ ratios, which are lower than those values of their adjacent
888 host rocks (Fig. 10a), and by the elemental composition of these cements, yielding the
889 lowest Sr contents with respect to other cements and host rocks. The low Y/Ho ratios,
890 which indicates the influence of terrigenous sediments (Bau and Dulski, 1994), and the
891 CL zonation of Cc6a and Cc12 (Fig. 8b), which points to oxidizing-reducing fluctuations,
892 are again characteristic features of the meteoric environment. At outcrop scale, clumped
893 isotopes reveal a progressive increase in precipitation temperatures, from 40 °C to 80 °C
894 (Forat de Bóixols locality) and from 25 °C to 85 °C approximately (Coll de Nargó
895 locality), as well as an enrichment in $\delta^{18}\text{O}_{\text{fluid}}$, from -1.8 to +5.9 ‰VSMOW and from -
896 4.2 to +2 ‰VSMOW, respectively (Fig. 10c). This fact indicates a continuous shift in the
897 fluid composition, from meteoric fluids to evolved meteoric fluids due to water-rock
898 interactions at increasing temperatures during deformation. Therefore, these geochemical
899 features indicate that the fluid system associated with fractures F6a, F6b, F11, F12 and
900 F16b was open to the input of meteoric fluids, which geochemistry was influenced by the
901 surrounding host carbonates.

902 **6.3 Spatio-temporal variation of fluids across the Sant Corneli-Bóixols** 903 **anticline**

904 In this section, we discuss the distribution and variations of fluids in the distinct structural
905 positions of the Sant Corneli-Bóixols anticline.

906 The host-rock buffered fluids from which calcites group 1 precipitated characterizes the
907 paleohydrological system in the core of the Sant Corneli-Bóixols anticline and in the base
908 of the syntectonic deposits along the southern flank of the fold, where Cal Mestre and
909 Sant Antoni localities are located, respectively (Fig. 12).

910 In the core of the anticline (Cal Mestre locality), the Lower Cretaceous mudstones and
911 marls from the Lluçà Formation have a minimum thickness of 2500 m (Lanaja, 1987).
912 Due to the expected non-permeable character of this unit and its considerable thickness,
913 the small-scale fractures (up to several meters long) occurring in this locality, likely
914 represented poorly efficient conduits to connect different hydro-stratigraphic reservoirs,
915 thus preventing the input of external fluids. A similar rock-buffered fluid behavior has
916 been observed in the core of the el Guix anticline in the Ebro foreland basin (Travé et al.,
917 2000). The results presented by these authors show that the $\delta^{13}\text{C}$ and $\delta^{18}\text{O}$ values of
918 fracture-filling calcites are in geochemical equilibrium with their adjacent host
919 carbonates. Contrarily, in the crestal domain of anticlines, the fluid system is often the
920 opposite. Examples of this are the Puig-reig anticline, also in the Ebro foreland basin, and

921 the Pico del Águila anticline in the Sierras Exteriores (Beaudoin et al., 2015; Cruset et
922 al., 2016). These authors concluded that large faults and well-connected vein networks in
923 shallow positions of these anticlines facilitated opening of the fluid system and the
924 percolation of meteoric fluids in disequilibrium with their adjacent host rocks. These
925 observations, together with that of this study, reveal the compartmentalization of fold
926 structures during deformation.

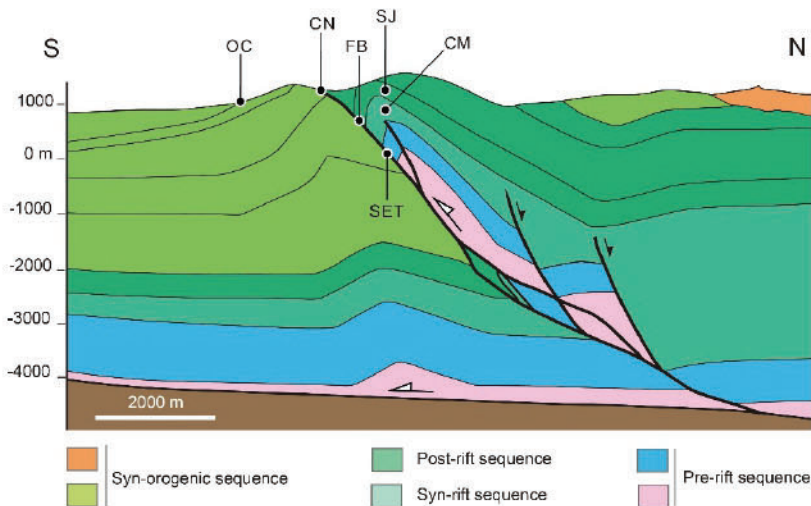
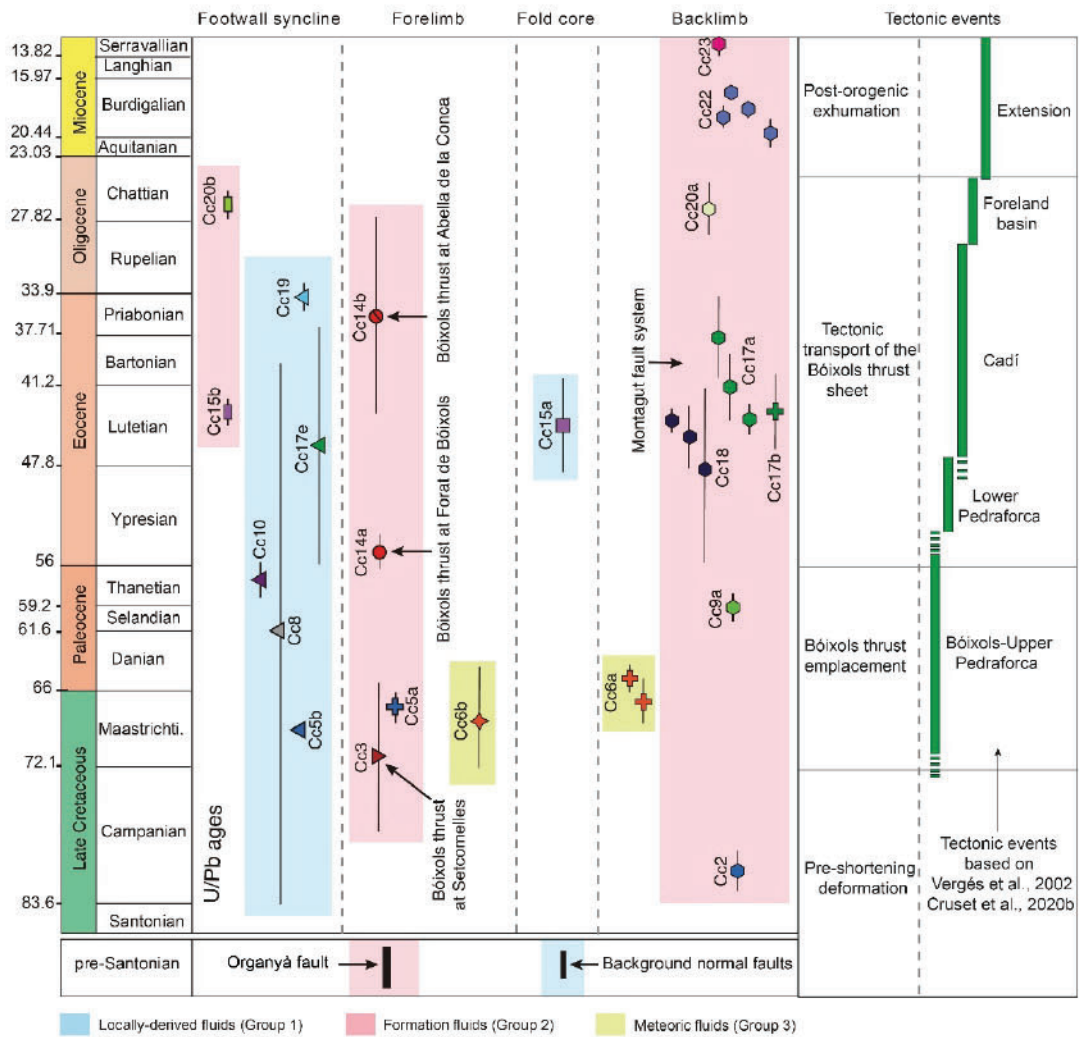
927 In the base of the syntectonic deposits (Sant Antoni locality), the Upper Cretaceous
928 marine mudstones from the Vallcarga Formation were deposited during the early
929 contraction and initial growth of the Sant Corneli-Bóixols anticline (Ardèvol et al., 2000).
930 Therefore, the local origin of the fluids in this domain is consistent with the marine setting
931 of deformation that likely affected recently deposited and poorly lithified sediments
932 (Travé et al., 2007).

933 Formation waters from which calcites group 2 precipitated characterizes the fluid system
934 associated with large-scale faults and related fractures, which affect the different
935 structural and stratigraphic positions of the Sant Corneli-Bóixols anticline and developed
936 throughout its whole deformation history (Fig. 12). The development of these larger
937 fracture systems facilitated the transference of fluids between different hydro-
938 stratigraphic units decreasing the extent of interaction between fluids and host rocks, as
939 has already been documented in the frontal domain in the anticline. In this line, according
940 to Nardini et al. (2019), strike-slip faults F17 from Coll de Nargó locality acted as transfer
941 zones for the migration of deeper Late Cretaceous connate waters to shallower non-
942 marine sediments of the Garumnian facies. Likewise, the Bóixols thrust in Forat de
943 Bóixols locality (F14a) acted as an efficient conduits for the migration of deep formation
944 waters (Muñoz-López et al., 2020b). In both examples, fluids were in chemical, and
945 probably in thermal disequilibrium with their adjacent host rocks and were likely expelled
946 due to vertical compaction linked to thrust sheet emplacement and/or tectonic horizontal
947 shortening (squeeze-type fluid flow) during continuous compression (Oliver, 1986;
948 Roure et al., 2010; Vandeginste et al., 2012).

949 Finally, meteoric waters from which calcites group 3 precipitated characterizes the fluid
950 system in the limbs of the Sant Corneli-Bóixols anticline, where Forat the Bóixols, Coll
951 de Nargó and Sant Joan localities are located (Fig. 12). Meteoric waters generally
952 infiltrate at high structural reliefs such as the crestal domain of anticlines (Beaudoin et
953 al., 2015; Cruset et al., 2016). However, in the Sant Corneli-Bóixols anticline meteoric
954 fluid percolation was recorded in the fold limbs because most of the crestal domain was
955 eroded synchronously with folding (Tavani et al., 2011). This interpretation is in line with
956 the exclusive presence of calcites from group 3 in the forelimb (Coll de Nargó and Forat
957 de Bóixols localities) and backlimb (Sant Joan locality) of the anticline. On the other
958 hand, the geochemical and geochronological data of calcite cements Cc6a and Cc6b (both
959 from group 3) set the initial infiltration of meteoric fluids at the Maastrichtian, during
960 formation of fractures F6 at ca. 67 – 65 Ma (Fig. 7). This fluid flow event coincides with
961 the transition from marine to continental conditions, during the progressive uplift of the
962 structure, coevally with sedimentation of the non-marine continental Garumnian facies

963 (Trempe Group) from Late Maastrichtian to Paleocene (Garcés et al., 2020; Plaziat et al.,
964 1981). This scenario of meteoric fluid infiltration during the main folding stage and
965 during the change from marine to continental conditions have also been reported in other
966 studies focused on the evolution of the fold-fluid system (Beaudoin et al., 2015; Evans
967 and Fischer, 2012; Nardini et al., 2019; Travé et al., 2007).

968 In conclusion, our data reveal that the fluid flow history varied at the several structural
969 positions of the Sant Corneli-Bóixols anticline and according to the age and nature of
970 their stratigraphy and the involved fracture networks. This indicates a
971 compartmentalization of the fluid system (Fig. 12). Thus, in the core of the fold, at least
972 around Cal Mestre locality, and in the base of the syn-tectonic deposits (Sant Joan locality),
973 the fluid system was essentially stratified and locally derived from the Lower Cretaceous
974 and Upper Cretaceous marine carbonates, revealing high extent of fluid-rock interaction.
975 Contrarily, along large faults, affecting different parts of the anticline, and in the fold
976 limbs, the paleohydrological system was open to the input of external fluids in
977 geochemical and probably thermal disequilibrium with their adjacent host rocks. Large
978 faults acted as conduits for the upward migration of formation waters from deeper regions
979 of the Sant Corneli-Bóixols anticline, whereas the fold limbs registered the infiltration of
980 meteoric waters (Fig. 12). Therefore, in the studied anticline, the scale, connectivity and
981 distribution of the main fracture networks together with the involved stratigraphy were
982 the main controls on the source and distribution of fluids, the degree of fluid-rock
983 interactions and the scale of fluid migration during deformation.



984

985 **Fig. 12.** Cross-section of the Sant Corneli-Bóixols anticline along the front of the Bóixols thrust sheet
 986 showing the spatial variation of fluids in the several structural positions of this fold. The U-Pb ages of the
 987 different calcite vein generations and related tectonic events are also included. Cross-section modified from
 988 Vergés, 1993.

989

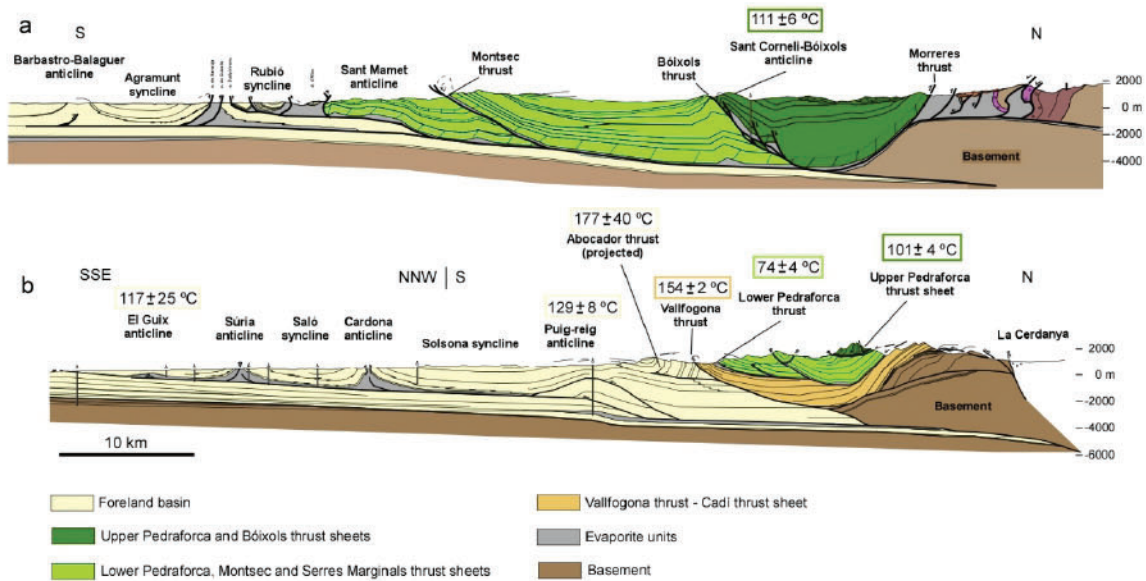
6.4 Scale of fluid flow and comparison with other compressional settings

990
991 In this section, we evaluate the scale of fluid flow in rocks forming the Bóixols thrust
992 sheet and compare our results with other Pyrenean structures and other worldwide
993 compressional belts. The Bóixols thrust sheet corresponds to the uppermost and oldest
994 emplaced structure of the southern-central Pyrenean cover thrust units. Therefore, the
995 structural position of this thrust sheet, detached in Upper Triassic evaporites and above
996 Lower Triassic detrital sediments of the Buntsandstein and the Paleozoic basement,
997 allows us to assess the possible input of external fluids derived from these three potential
998 reservoirs. In a previous section, we concluded that advective fluid flow was linked to the
999 presence of major fault zones (including the Bóixols thrust) and associated fractures,
1000 which acted as preferential fluid flow pathways. Therefore, the geochemical signature of
1001 calcite cements precipitated in these fractures (group 2 calcites) provide evidence on the
1002 relative scale of fluid flow and the fluid circulation depth. Thus, during precipitation of
1003 group 2 calcites, a maximum temperature of around 120 °C was obtained from clumped
1004 isotopes in calcites precipitated in fractures associated with the Bóixols thrust in Forat de
1005 Bóixols locality (Fig. 10c) (Muñoz-López et al., 2020b). Assuming a normal geothermal
1006 gradient of 30°C/km (Travé et al., 2007), these temperatures would have been reached at
1007 3-4 km depth. Considering the thickness of the Bóixols thrust sheet (around 5 km thick),
1008 such temperatures imply circulation of fluids along fault zones that were originated in the
1009 deeper regions of the sedimentary cover. Indeed, the $\delta^{18}\text{O}_{\text{fluid}}$ of this group of cements,
1010 yielding maximum values of +5.5 ‰VSMOW, indicate the presence of formation waters,
1011 as has been explained before, and discard the input of basement-related fluids such water
1012 derived from and/or equilibrated with metamorphic rocks (Taylor, 1987). In the same
1013 way, the $^{87}\text{Sr}/^{86}\text{Sr}$ ratios of the vein cements documented in this study are (1) within the
1014 range of marine carbonates (LOWESS curve in Fig. 10a), (2) within the range of
1015 synkinematic veins precipitated in the sedimentary cover (i.e., $^{87}\text{Sr}/^{86}\text{Sr} < 0.710$) (Muñoz-
1016 López et al., 2020a), and (3) significantly lower than values of cements precipitated from
1017 fluids that have interacted with Triassic evaporites or with Paleozoic basement rocks
1018 (Muñoz-López et al., 2020a). All these observations indicate that the fluid system in the
1019 study area was restricted to the scale of the Bóixols thrust sheet and rule out the input of
1020 external fluids derived from the underlying Triassic detachment, from deeper cover units
1021 such as the Buntsandstein or from the Paleozoic basement. An exception arises for the
1022 cement precipitated in the Bóixols thrust-related deformation at the Setcomelles locality
1023 (Cc3), which exhibits the most radiogenic $^{87}\text{Sr}/^{86}\text{Sr}$ ratio in this study, similar to Upper
1024 Triassic values (Fig. 10a). Therefore, fluids derived from Upper Triassic evaporites acting
1025 as a main detachment of the Bóixols thrust sheet could have locally infiltrated the
1026 paleohydrological system, as has also been reported in other salt-detached Pyrenean
1027 structures (Crognier et al., 2018; Cruset et al., 2020a; Lacroix et al., 2011; Travé et al.,
1028 2007).

1029 The results presented in this study also reveal that the frontal anticline (the Sant Corneli-
1030 Bóixols anticline) of the Bóixols thrust sheet shares a common fluid flow behavior with
1031 other worldwide compressional structures above evaporitic detachments. In these
1032 structures, the paleohydrological system only involves fluids sourced above the

1033 detachment levels, which may act as a lower boundary for the fluid system, preventing
1034 the input of fluids from deeper parts of the compressional belt. This fluid flow scenario
1035 in the Bóixols thrust sheet is similar to that of: 1) worldwide detachment folds (Beaudoin
1036 et al., 2014); 2) other south Pyrenean structures detached in Triassic and Eocene
1037 evaporitic units such as the Pico del Águila and El Guix anticlines (Beaudoin et al., 2015;
1038 Travé et al., 2000), the Monte Perdido and Abocador thrusts (Cruset et al., 2018; Lacroix
1039 et al., 2011), and the Upper and Lower Pedraforca thrust sheets (Cruset; 2019; Cruset et
1040 al., 2020a); 3) other worldwide detached structures such as the Sierra Madre Oriental
1041 (Fischer et al., 2009; Lefticariu et al., 2005) and the Central Appalachians (Evans et al.,
1042 2012).

1043 Besides, in order to examine the scale of fluid in the Southern Pyrenees, we compare
1044 different paleohydrological studies performed along central-eastern part of the south
1045 Pyrenean wedge (Cruset et al., 2020a, 2018; Muñoz-López et al., 2020b; Nardini et al.,
1046 2019) (Fig. 13). Our comparison reveals that the fluids migrating through upper thrust
1047 sheets, emplaced from Late Cretaceous to middle Eocene, reached maximum
1048 temperatures of 120 °C during the emplacement of the Bóixols thrust (Muñoz-López et
1049 al., 2020b) (Fig. 13). Similarly, in the Upper Pedraforca thrust sheet, which constitutes
1050 the eastern equivalent of the Bóixols structure, a maximum temperature of 100 °C has
1051 been reported (Cruset, 2019). In contrast, the fluids migrating through the Vallfogona
1052 thrust, which represents the frontal thrust fault of the Southeastern Pyrenees, reached
1053 maximum temperatures of around 150 °C (Cruset et al., 2018; Fig. 13). Similar high
1054 temperatures have also been reported for the fluids circulating through the thrust faults
1055 affecting the sediments of the Ebro foreland basin. These high temperatures, which are
1056 ~180 °C for the Abocador thrust and ~130 °C for the Puig-reig anticline, could not have
1057 been reached by burial (Cruset et al., 2018). Therefore, the major thrust faults likely acted
1058 as preferential pathways for the upward migration of hot fluids circulating during
1059 compression. In the sections of the south Pyrenean cover thrust sheets that are only
1060 affected by background deformation, the geochemical composition of these hot fluids was
1061 modified as they interacted with surrounding host rocks and when moving away from the
1062 major thrust zones (Muñoz-López et al., 2020b, 2020a). Therefore, this background
1063 deformation was characterized by the migration of formation waters with high interaction
1064 with their surrounding host rocks.



1065

1066 **Fig. 13.** Cross-sections along the central (a) and eastern (b) Southern Pyrenees (Vergés, 1993) showing the
 1067 maximum temperatures obtained from clumped isotopes applied to syn-kinematic calcite veins precipitated
 1068 in the main structural units. Location of cross-sections in Fig. 1a. Temperatures are from (Cruset et al.,
 1069 2020a, 2018; Muñoz-López et al., 2020b; Nardini et al., 2019).

1070

7. Conclusions

1071

1072 Our field and analytical data allowed to date and to analyze the relationships between
 1073 fluid flow and fold evolution across different structural domains of the Sant Corneli-
 1074 Bóixols anticline as summarized below.

1074

- 1075 1. We measured 23 U-Pb dates in different sets of fracture-filling calcite cements
 1076 developed in the Sant Corneli-Bóixols anticline presenting important age
 1077 variations from the oldest Late Cretaceous at 79.8 ± 1.2 Ma to the youngest late
 1078 Miocene at 9 ± 4.6 Ma.
- 1079 2. The oldest date (79.8 ± 1.2 Ma), in a backlimb small normal fault, is younger than
 1080 the base of the syntectonic deposits along the southern flank of the Sant Corneli-
 1081 Bóixols anticline. Ten ages ranging from 71.2 ± 6.4 to 56.9 ± 1.4 Ma (calcite
 1082 cements Cc3 to Cc10) are coeval with growth strata deposition and Bóixols thrust
 1083 sheet emplacement.
- 1084 3. Ages from 55.5 ± 1.2 to 27.4 ± 0.9 Ma (calcite cements Cc14a to Cc27b)
 1085 precipitated in the frontal Bóixols thrust zone, at Forat de Bóixols and Abella de
 1086 la Conca localities, in hundred-meters scale fractures with a constant orientation
 1087 with respect to bedding regardless of dip, and in strike slip faults (F17) that offset
 1088 the tilted limbs of the anticline. These dates are consistent with the tectonic
 1089 transport of the Bóixols thrust sheet above the basal thrust of the South Pyrenean
 1090 Unit.
- 1091 4. The youngest Miocene dates from 20.8 ± 1.2 to 9 ± 4.6 Ma (calcite cements Cc21
 1092 to Cc23) are partially coeval with the post-orogenic exhumation of the Sant
 1093 Corneli-Bóixols anticline.

- 1093 5. Twenty-three fracture-filling calcite cements were identified by both crosscutting
1094 relationships between fractures and petrographic analysis from which three
1095 groups were distinguished. Group 1 includes calcites with similar petrographic
1096 and geochemical features with respect to their host carbonates (i.e., non-
1097 luminescent calcite cements with $\delta^{13}\text{C}$ values and $^{87}\text{Sr}/^{86}\text{Sr}$ ratios typical of marine
1098 carbonates); group 2 comprises calcites with the lightest $\delta^{18}\text{O}$ values, down to -14
1099 ‰VPDB, and the highest temperature of precipitation (up to 120 °C); and group
1100 3 includes calcites with $\delta^{18}\text{O}$ from -8 to -6 ‰VPDB, $\delta^{13}\text{C}$ down to -10 ‰VPDB
1101 and the lowest Sr contents.
- 1102 6. In the core of the anticline and in the lowest part of the syn-orogenic sequence
1103 from the footwall of the Bóixols thrust, group 1 cements indicate an essentially
1104 closed fluid system. Along large faults such as the Bóixols thrust, the Montagut
1105 fault system and the Sant Joan fault system, group 2 cements indicate an open
1106 fluid system evidencing that these large faults acted as conduits for the upward
1107 migration of formation fluids. In the limbs of the Sant Corneli-Bóixols anticline,
1108 group 3 cements indicate the presence of meteoric waters that likely infiltrated at
1109 high structural reliefs that were elevated during growth of the Sant Corneli-
1110 Bóixols anticline.
- 1111 7. The major faults acted as preferential pathways for the upwards migration of
1112 fluids during compression, whereas background fracturing registered the presence
1113 of formation fluids that highly interacted with their adjacent host rocks. The
1114 paleohydrological system in the Sant Corneli-Bóixols anticline was restricted to
1115 the Bóixols thrust sheet above the Upper Triassic evaporites along its basal
1116 detachment thrust as interpreted in other detached thrust systems as the Central
1117 Appalachians and Sierra Madre Oriental.

1118 **Acknowledgements**

1119 This research was carried out within the framework of the DGICYT Spanish project
1120 PGC2018-093903-B-C22 (Ministerio de Ciencia, Innovación y Universidades/Agencia
1121 Estatal de Investigación/Fondo Europeo de Desarrollo Regional, Unión Europea) and the
1122 Grup Consolidat de Recerca “Geologia Sedimentària” (2017-SGR-824). This work was
1123 partially funded by ALORBE project (PIE-CSIC-202030E310). The PhD research of
1124 DML is supported by the FPI2016 (BES-2016-077214) Spanish program from MINECO.
1125 We thank Luis Fernando Martínez for helping in the fieldwork during his master degree
1126 at the Universitat de Barcelona. Carbon and oxygen isotopic analyses were carried out at
1127 the Centre Científics i Tecnològics of the Universitat de Barcelona. Strontium analyses
1128 were performed at the CAI de Geocronología y Geoquímica Isotópica of the Universidad
1129 Complutense de Madrid. The elemental composition was analyzed at the geochemistry
1130 facility labGEOTOP of Geosciences Barcelona (GEO3BCN-CSIC). U-Pb analyses were
1131 performed at the Frankfurt Isotope and Element Research Center (FIERCE) from the
1132 Goethe-University Frankfurt (Germany).

- 1134 Alcalde, J., Marzán, I., Saura, E., Martí, D., Ayarza, P., Juhlin, C., Pérez-Estaún, A., Carbonell, R., 2014.
1135 3D geological characterization of the Hontomín CO₂ storage site, Spain: Multidisciplinary
1136 approach from seismic, well-log and regional data. *Tectonophysics* 627, 6–25.
1137 <https://doi.org/10.1016/j.tecto.2014.04.025>
- 1138 Ardèvol, L., Klimowitz, J., Malagón, J., Nagtegaal, P.T.C., 2000. Depositional Sequence Response to
1139 Foreland Deformation in the Upper Cretaceous of the Southern Pyrenees, Spain. *Am. Assoc. Pet.*
1140 *Geol. Bull.* 84, 427–53. <https://doi.org/10.1306/C9EBCE55-1735-11D7-8645000102C1865D>
- 1141 Bachu, S., 2000. Sequestration of CO₂ in geological media: criteria and approach for site selection in
1142 response to climate change. *Energy Convers. Manag.* 41, 953–970. [https://doi.org/10.1016/S0196-8904\(99\)00149-1](https://doi.org/10.1016/S0196-8904(99)00149-1)
- 1144 Barbier, M., Leprêtre, R., Callot, J.-P., Gasparrini, M., Daniel, J.-M., Hamon, Y., Lacombe, O., Floquet,
1145 M., 2012. Impact of fracture stratigraphy on the paleo-hydrogeology of the Madison Limestone in
1146 two basement-involved folds in the Bighorn basin, (Wyoming, USA). *Tectonophysics* 576–577,
1147 116–132. <https://doi.org/10.1016/j.tecto.2012.06.048>
- 1148 Bau, M., Dulski, P., 1994. Evolution of the Yttrium-Holmium Systematics of Seawater Through Time.
1149 *Mineral. Mag.* 58A, 61–62. <https://doi.org/10.1180/minmag.1994.58A.1.35>
- 1150 Beaudoin, N., Bellahsen, N., Lacombe, O., Emmanuel, L., 2011. Fracture-controlled paleohydrogeology
1151 in a basement-cored, fault-related fold: Sheep Mountain Anticline, Wyoming, United States.
1152 *Geochemistry, Geophys. Geosystems* 12, 1–15. <https://doi.org/10.1029/2010GC003494>
- 1153 Beaudoin, N., Bellahsen, N., Lacombe, O., Emmanuel, L., Pironon, J., 2014. Crustal-scale fluid flow
1154 during the tectonic evolution of the Bighorn Basin (Wyoming, USA). *Basin Res.* 26, 403–435.
1155 <https://doi.org/10.1111/bre.12032>
- 1156 Beaudoin, N., Huyghe, D., Bellahsen, N., Lacombe, O., Emmanuel, L., Mouthereau, F., Ouahnon, L.,
1157 2015. Fluid systems and fracture development during syn-depositional fold growth: An example
1158 from the Pico del Aguila anticline, Sierras Exteriores, southern Pyrenees, Spain. *J. Struct. Geol.* 70,
1159 23–38. <https://doi.org/10.1016/j.jsg.2014.11.003>
- 1160 Benedicto, A., Abdelrazek, M., Ledru, P., Mackay, C., Kinar, D., 2021. Structural Controls of Uranium
1161 Mineralization in the Basement of the Athabasca Basin, Saskatchewan, Canada. *Geofluids* 2021.
1162 <https://doi.org/10.1155/2021/3853468>
- 1163 Berástegui, X., Garcia-Senz, J.M., Losantos, M., 1990. Tecto-sedimentary evolution of the Organya
1164 extensional basin (central south Pyrenean unit, Spain) during the Lower Cretaceous. *Bull. la Soc.*
1165 *Geol. Fr.* VI, 251–264. <https://doi.org/10.2113/gssgfbull.VI.2.251>
- 1166 Bergbauer, S., Pollard, D.D., 2004. A new conceptual fold-fracture model including prefolding joints,
1167 based on the Emigrant Gap anticline, Wyoming. *Bull. Geol. Soc. Am.* 116, 294–307.
1168 <https://doi.org/10.1130/B25225.1>
- 1169 Bond, R.M.G., McClay, K.R., 1995. Inversion of a Lower Cretaceous extensional basin, south central
1170 Pyrenees, Spain. *Geol. Soc. London, Spec. Publ.* 88, 415–431.
1171 <https://doi.org/10.1144/GSL.SP.1995.088.01.22>
- 1172 Bons, P.D., Elburg, M.A., Gomez-Rivas, E., 2012. A review of the formation of tectonic veins and their
1173 microstructures. *J. Struct. Geol.* 43, 33–62. <https://doi.org/10.1016/j.jsg.2012.07.005>
- 1174 Boutoux, A., Verlaguet, A., Bellahsen, N., Lacombe, O., Villemant, B., Caron, B., Martin, E., Assayag,
1175 N., Cartigny, P., 2014. Fluid systems above basement shear zones during inversion of pre-orogenic
1176 sedimentary basins (External Crystalline Massifs, Western Alps). *Lithos* 206–207, 435–453.
1177 <https://doi.org/10.1016/j.lithos.2014.07.005>
- 1178 Brandes, C., Tanner, D.C., 2014. Fault-related folding: A review of kinematic models and their
1179 application. *Earth-Science Rev.* 138, 352–370. <https://doi.org/10.1016/j.earscirev.2014.06.008>
- 1180 Burisch, M., Gerdes, A., Walter, B.F., Neumann, U., Fettel, M., Markl, G., 2017. Methane and the origin

- 1181 of five-element veins: Mineralogy, age, fluid inclusion chemistry and ore forming processes in the
 1182 Odenwald, SW Germany. *Ore Geol. Rev.* 81, 42–61.
 1183 <https://doi.org/10.1016/j.oregeorev.2016.10.033>
- 1184 Callot, J.P., Breesch, L., Guilhaumou, N., Roure, F., Swennen, R., Vilasi, N., 2013. Paleo-fluids
 1185 characterisation and fluid flow modelling along a regional transect in northern United Arab
 1186 Emirates (UAE). *Front. Earth Sci.* 5, 177–201. https://doi.org/10.1007/978-3-642-30609-9_9
- 1187 Casini, G., Gillespie, P.A., Vergés, J., Romaine, I., Fernández, N., Casciello, E., Saura, E., Mehl, C.,
 1188 Homke, S., Embry, J.-C., Aghajari, L., Hunt, D.W., 2011. Sub-seismic fractures in foreland fold
 1189 and thrust belts: insight from the Lurestan Province, Zagros Mountains, Iran. *Pet. Geosci.* 17, 263–
 1190 282. <https://doi.org/10.1144/1354-079310-043>
- 1191 Choukroune, P., 1989. The Ecore Pyrenean deep seismic profile reflection data and the overall structure
 1192 of an orogenic belt. *Tectonics* 8, 23–39. <https://doi.org/10.1029/TC008i001p00023>
- 1193 Cooper, M., 2007. Structural style and hydrocarbon prospectivity in fold and thrust belts: a global review.
 1194 *Geol. Soc. London, Spec. Publ.* 272, 447–472. <https://doi.org/10.1144/GSL.SP.2007.272.01.23>
- 1195 Cosgrove, J.W., 2015. The association of folds and fractures and the link between folding, fracturing and
 1196 fluid flow during the evolution of a fold–thrust belt: a brief review. *Geol. Soc. London, Spec. Publ.*
 1197 421, 41–68. <https://doi.org/10.1144/SP421.11>
- 1198 Crognier, N., Hoareau, G., Aubourg, C., Dubois, M., Lacroix, B., Branellec, M., Callot, J.P., Vennemann,
 1199 T., 2018. Syn-orogenic fluid flow in the Jaca basin (south Pyrenean fold and thrust belt) from
 1200 fracture and vein analyses. *Basin Res.* 30, 187–216. <https://doi.org/10.1111/bre.12249>
- 1201 Cruset, D., 2019. Sequential fluid migration along a fold and thrust belt: SE Pyrenees from Late
 1202 Cretaceous to Oligocene. PhD Thesis, Univ. Barcelona 350p.
- 1203 Cruset, D., Cantarero, I., Benedicto, A., John, C.M., Vergés, J., Albert, R., Gerdes, A., Travé, A., 2020a.
 1204 From hydroplastic to brittle deformation: Controls on fluid flow in fold and thrust belts. Insights
 1205 from the Lower Pedraforca thrust sheet (SE Pyrenees). *Mar. Pet. Geol.* 120, 104517.
 1206 <https://doi.org/10.1016/j.marpetgeo.2020.104517>
- 1207 Cruset, D., Cantarero, I., Travé, A., Vergés, J., John, C.M., 2016. Crestal graben fluid evolution during
 1208 growth of the Puig-reig anticline (South Pyrenean fold and thrust belt). *J. Geodyn.* 101, 30–50.
 1209 <https://doi.org/10.1016/j.jog.2016.05.004>
- 1210 Cruset, D., Cantarero, I., Vergés, J., John, C.M., Muñoz-López, D., Travé, A., 2018. Changes in fluid
 1211 regime in syn-orogenic sediments during the growth of the south Pyrenean fold and thrust belt.
 1212 *Glob. Planet. Change* 171, 207–224. <https://doi.org/10.1016/j.gloplacha.2017.11.001>
- 1213 Cruset, D., Vergés, J., Albert, R., Gerdes, A., Benedicto, A., Cantarero, I., Travé, A., 2020b. Quantifying
 1214 deformation processes in the SE Pyrenees using U–Pb dating of fracture–filling calcites. *J. Geol.*
 1215 *Soc. London.* 177, 1186–1196. <https://doi.org/10.1144/jgs2020-014>
- 1216 Delvaux, D., Sperner, B., 2003. New aspects of tectonic stress inversion with reference to the TENSOR
 1217 program. *Geol. Soc. London, Spec. Publ.* 212, 75–100.
 1218 <https://doi.org/10.1144/GSL.SP.2003.212.01.06>
- 1219 Evans, M.A., Bebout, G.E., Brown, C.H., 2012. Changing fluid conditions during folding: An example
 1220 from the central Appalachians. *Tectonophysics* 576–577, 99–115.
 1221 <https://doi.org/10.1016/j.tecto.2012.03.002>
- 1222 Evans, M.A., Fischer, M.P., 2012. On the distribution of fluids in folds: A review of controlling factors
 1223 and processes. *J. Struct. Geol.* 44, 2–24. <https://doi.org/10.1016/j.jsg.2012.08.003>
- 1224 Ferket, H., Swennen, R., Ortuño Arzate, S., Roure, F., 2006. Fluid flow evolution in petroleum reservoirs
 1225 with a complex diagenetic history: An example from Veracruz, Mexico. *J. Geochemical Explor.* 89,
 1226 108–111. <https://doi.org/10.1016/j.gexplo.2005.11.040>
- 1227 Fischer, M.P., Higuera-Díaz, I.C., Evans, M.A., Perry, E.C., Lefticariu, L., 2009. Fracture-controlled
 1228 paleohydrology in a map-scale detachment fold: Insights from the analysis of fluid inclusions in
 1229 calcite and quartz veins. *J. Struct. Geol.* 31, 1490–1510. <https://doi.org/10.1016/j.jsg.2009.09.004>

- 1230 Gallemí, J., Martínez Ribas, R., Pons, J., 1982. Unidades del Cretácico superior en los alrededores de San
1231 Corneli (Provincia de Lleida). *J. Iber. Geol. - An Int. Publ. Earth Sci.* 8, 935–948.
1232 https://doi.org/10.5209/rev_CGIB.1982.v8.2794
- 1233 Garcia-Senz, J.M., 2002. Cuencas Extensivas del Cretácico Inferior en los Pirineos Centrales, formación
1234 y subsecuente inversión. PhD Thesis Univ. Barcelona 310p.
- 1235 Garrido-Megías, A., Ríos, J.M., 1972. Síntesis geológica del Secundario y Terciario entre los ríos Cinca y
1236 Segre (Pirineo central de la vertiente surpirenaica, provincias de Huesca y Lérida). *Boletín*
1237 *Geológico y Min. España* 83, 1–47.
- 1238 Gerdes, A., Zeh, A., 2009. Zircon formation versus zircon alteration — New insights from combined U–
1239 Pb and Lu–Hf in-situ LA-ICP-MS analyses, and consequences for the interpretation of Archean
1240 zircon from the Central Zone of the Limpopo Belt. *Chem. Geol.* 261, 230–243.
1241 <https://doi.org/10.1016/j.chemgeo.2008.03.005>
- 1242 Gerdes, A., Zeh, A., 2006. Combined U–Pb and Hf isotope LA-(MC-)ICP-MS analyses of detrital
1243 zircons: Comparison with SHRIMP and new constraints for the provenance and age of an
1244 Armorican metasediment in Central Germany. *Earth Planet. Sci. Lett.* 249, 47–61.
1245 <https://doi.org/10.1016/j.epsl.2006.06.039>
- 1246 Grool, A.R., Ford, M., Vergés, J., Huisman, R.S., Christophoul, F., Dielforder, A., 2018. Insights Into
1247 the Crustal-Scale Dynamics of a Doubly Vergent Orogen From a Quantitative Analysis of Its
1248 Forelands: A Case Study of the Eastern Pyrenees. *Tectonics* 37, 450–476.
1249 <https://doi.org/10.1002/2017TC004731>
- 1250 Gutmanis, J., Ardèvol i Oró, L., Díez-Canseco, D., Chebbihi, L., Awdal, A., Cook, A., 2018. Fracture
1251 analysis of outcrop analogues to support modelling of the subseismic domain in carbonate
1252 reservoirs, south-central Pyrenees. *Geol. Soc. London, Spec. Publ.* 459, 139–156.
1253 <https://doi.org/10.1144/SP459.2>
- 1254 Haines, S.H., 2008. Transformations in cly-rich fault-rocks: constraining fault zone processes and the
1255 kinematic evolution of regions. PhD Thesis, Univ. Michigan 295p.
- 1256 Horstwood, M.S.A., Košler, J., Gehrels, G., Jackson, S.E., McLean, N.M., Paton, C., Pearson, N.J.,
1257 Sircombe, K., Sylvester, P., Vermeesch, P., Bowring, J.F., Condon, D.J., Schoene, B., 2016.
1258 Community-Derived Standards for LA-ICP-MS U-(Th-)Pb Geochronology - Uncertainty
1259 Propagation, Age Interpretation and Data Reporting. *Geostand. Geoanalytical Res.* 40, 311–332.
1260 <https://doi.org/10.1111/j.1751-908X.2016.00379.x>
- 1261 Hurai, V., Huraiová, M., Slobodník, M., Thomas, R., 2015. Stable Isotope Geochemistry of Geofluids, in:
1262 *Geofluids*. Elsevier, pp. 293–344. <https://doi.org/10.1016/B978-0-12-803241-1.00009-5>
- 1263 Labraña de Miguel, G., 2004. Evolució de fluids en un anticlinal: estudi pilot en l'anticlinal de Sant
1264 Corneli, Pallars Jussà, Llieda. MsC thesis, Universitat de Barcelona, 114 p.
- 1265 Lacroix, B., Buatier, M., Labaume, P., Travé, A., Dubois, M., Charpentier, D., Ventalon, S., Convert-
1266 Gaubier, D., 2011. Microtectonic and geochemical characterization of thrusting in a foreland basin:
1267 Example of the South-Pyrenean orogenic wedge (Spain). *J. Struct. Geol.* 33, 1359–1377.
1268 <https://doi.org/10.1016/j.jsg.2011.06.006>
- 1269 Lanaja, J.M., 1987. Contribucion de la Exploracion Petrolifera al Conocimiento de la Geologia de
1270 España. IGME 465p.
- 1271 Lefticariu, L., Perry, E.C., Fischer, M.P., Banner, J.L., 2005. Evolution of fluid compartmentalization in a
1272 detachment fold complex. *Geology* 33, 69. <https://doi.org/10.1130/G20592.1>
- 1273 Ludwig, K.R., 2012. Use's manual for Isoplot 3.75: A Geochronological Toolkit for Microsoft Excel.
1274 Berkeley Geochronol. Center, Spec. Publ. 5.
- 1275 Macchiavelli, C., Vergés, J., Schettino, A., Fernández, M., Turco, E., Casciello, E., Torne, M., Pierantoni,
1276 P.P., Tunini, L., 2017. A New Southern North Atlantic Isochron Map: Insights Into the Drift of the
1277 Iberian Plate Since the Late Cretaceous. *J. Geophys. Res. Solid Earth* 122, 9603–9626.
1278 <https://doi.org/10.1002/2017JB014769>

- 1279 Macgregor, D.S., 1996. Factors controlling the destruction or preservation of giant light oilfields. *Pet.*
1280 *Geosci.* 2, 197–217. <https://doi.org/10.1144/petgeo.2.3.197>
- 1281 McArthur, J.M., Howarth, R.J., Shields, G.A., 2012. Strontium Isotope Stratigraphy, in: *The Geologic*
1282 *Time Scale*. Elsevier, pp. 127–144. <https://doi.org/10.1016/B978-0-444-59425-9.00007-X>
- 1283 McCrea, J.M., 1950. On the Isotopic Chemistry of Carbonates and a Paleotemperature Scale. *J. Chem.*
1284 *Phys.* 18, 849–857. <https://doi.org/10.1063/1.1747785>
- 1285 Mencos, J., 2010. Metodologies de reconstrucció i modelització 3D d'estructures geològiques: anticlinal
1286 de Sant Corneli-Bóixols (Pirineus centrals). PhD Thesis Univ. Barcelona 403p.
- 1287 Mencos, J., Carrera, N., Muñoz, J.A., 2015. Influence of rift basin geometry on the subsequent postrift
1288 sedimentation and basin inversion: The Organyà Basin and the Bóixols thrust sheet (south central
1289 Pyrenees). *Tectonics* 34, 1452–1474. <https://doi.org/10.1002/2014TC003692>
- 1290 Mencos, J., Muñoz, J.A., Hardy, S., 2011. Three-dimensional Geometry and Forward Numerical
1291 Modeling of the Sant Corneli Anticline (Southern Pyrenees, Spain). *AAPG Mem.* 94, 283–300.
1292 <https://doi.org/10.1306/13251342M943434>
- 1293 Mey, P.H.W., Nagtegaal, P.J.C., Roberti, K.J., Hartevelt, J.J.A., 1968. Lithostratigraphic subdivision of
1294 Post-Hercynian deposits in the South-Central Pyrenees, Spain. *Leidse Geol. Meded.* 41, 221–228.
- 1295 Mitiku, A.B., Bauer, S., 2013. Optimal use of a dome-shaped anticline structure for CO₂ storage: a case
1296 study in the North German sedimentary basin. *Environ. Earth Sci.* 70, 3661–3673.
1297 <https://doi.org/10.1007/s12665-013-2580-z>
- 1298 Mitra, S., 1990. Fault-Propagation Folds: Geometry, Kinematic Evolution, and Hydrocarbon Traps. *Am.*
1299 *Assoc. Pet. Geol. Bull.* 74, 617–620. <https://doi.org/10.1306/0C9B23CB-1710-11D7-8645000102C1865D>
- 1301 Muñoz-López, D., Alías, G., Cruset, D., Cantarero, I., John, C.M., Travé, A., 2020a. Influence of
1302 basement rocks on fluid evolution during multiphase deformation: the example of the Estamariu
1303 thrust in the Pyrenean Axial Zone. *Solid Earth* 11, 2257–2281. [https://doi.org/10.5194/se-11-2257-](https://doi.org/10.5194/se-11-2257-2020)
1304 [2020](https://doi.org/10.5194/se-11-2257-2020)
- 1305 Muñoz-López, D., Cruset, D., Cantarero, I., Benedicto, A., John, C.M., Travé, A., 2020b. Fluid Dynamics
1306 in a Thrust Fault Inferred from Petrology and Geochemistry of Calcite Veins: An Example from the
1307 Southern Pyrenees. *Geofluids* 2020, 1–25. <https://doi.org/10.1155/2020/8815729>
- 1308 Muñoz, J.A., 2017. Fault-related folds in the southern Pyrenees. *Am. Assoc. Pet. Geol. Bull.* 101, 579–
1309 587. <https://doi.org/10.1306/011817DIG17037>
- 1310 Muñoz, J.A., 1992. Evolution of a continental collision belt: ECORS-Pyrenees crustal balanced cross-
1311 section, in: *Thrust Tectonics*. Springer Netherlands, Dordrecht, pp. 235–246.
1312 https://doi.org/10.1007/978-94-011-3066-0_21
- 1313 Nardini, N., Muñoz-López, D., Cruset, D., Cantarero, I., Martín-Martín, J., Benedicto, A., Gomez-Rivas,
1314 E., John, C., Travé, A., 2019. From Early Contraction to Post-Folding Fluid Evolution in the
1315 Frontal Part of the Bóixols Thrust Sheet (Southern Pyrenees) as Revealed by the Texture and
1316 Geochemistry of Calcite Cements. *Minerals* 9, 117. <https://doi.org/10.3390/min9020117>
- 1317 Nuriel, P., Wotzlaw, J.-F., Ovtcharova, M., Vaks, A., Stremtan, C., Šála, M., Roberts, N.M.W., Kylander-
1318 Clark, A.R.C., 2021. The use of ASH-15 flowstone as a matrix-matched reference material for
1319 laser-ablation U–Pb geochronology of calcite. *Geochronology* 3, 35–47.
1320 <https://doi.org/10.5194/gchron-3-35-2021>
- 1321 Oliver, J., 1986. Fluids expelled tectonically from orogenic belts: Their role in hydrocarbon migration and
1322 other geologic phenomena. *Geology* 14, 99. [https://doi.org/10.1130/0091-](https://doi.org/10.1130/0091-7613(1986)14<99:FETFOB>2.0.CO;2)
1323 [7613\(1986\)14<99:FETFOB>2.0.CO;2](https://doi.org/10.1130/0091-7613(1986)14<99:FETFOB>2.0.CO;2)
- 1324 Oliver, N.H.S., Bons, P.D., 2001. Mechanisms of fluid flow and fluid-rock interaction in fossil
1325 metamorphic hydrothermal systems inferred from vein-wall rock patterns, geometry and
1326 microstructure. *Geofluids* 1, 137–162. <https://doi.org/10.1046/j.1468-8123.2001.00013.x>
- 1327 Pagel, M., Bonifacie, M., Schneider, D.A., Gautheron, C., Brigaud, B., Calmels, D., Cros, A., Saint-

- 1328 Bezar, B., Landrein, P., Sutcliffe, C., Davis, D., Chaduteau, C., 2018. Improving paleohydrological
1329 and diagenetic reconstructions in calcite veins and breccia of a sedimentary basin by combining
1330 $\Delta 47$ temperature, $\delta 18\text{O}$ water and U-Pb age. *Chem. Geol.* 481, 1–17.
1331 <https://doi.org/10.1016/j.chemgeo.2017.12.026>
- 1332 Popp, B.N., Podosek, F.A., Brannon, J.C., Anderson, T.F., Pier, J., 1986. $87\text{Sr}/86\text{Sr}$ ratios in Permo-
1333 Carboniferous sea water from the analyses of well-preserved brachiopod shells. *Geochim.*
1334 *Cosmochim. Acta* 50, 1321–1328. [https://doi.org/10.1016/0016-7037\(86\)90308-X](https://doi.org/10.1016/0016-7037(86)90308-X)
- 1335 Puigdefàbregas, C., Souquet, P., 1986. Tecto-sedimentary cycles and depositional sequences of the
1336 Mesozoic and Tertiary from the Pyrenees. *Tectonophysics* 129, 173–203.
1337 [https://doi.org/10.1016/0040-1951\(86\)90251-9](https://doi.org/10.1016/0040-1951(86)90251-9)
- 1338 Pujalte, V., Baceta, J.I., Schmitz, B., Orue-Etxebarria, X., Payros, A., Bernaola, G., Apellaniz, E.,
1339 Caballero, F., Robador, A., Serra-Kiel, J., Tosquella, J., 2009. Redefinition of the Ilerdian Stage
1340 (early Eocene). *Geol. Acta* 7, 177–194. <https://doi.org/10.1344/105.000000268>
- 1341 Rasbury, E.T., Cole, J.M., 2009. Directly dating geologic events: U-Pb dating of carbonates. *Rev.*
1342 *Geophys.* 47, RG3001. <https://doi.org/10.1029/2007RG000246>
- 1343 Ring, U., Gerdes, A., 2016. Kinematics of the Alpenrhein-Bodensee graben system in the Central Alps:
1344 Oligocene/Miocene transtension due to formation of the Western Alps arc. *Tectonics* 35, 1367–
1345 1391. <https://doi.org/10.1002/2015TC004085>
- 1346 Robert, R., Robion, P., Souloumiac, P., David, C., Sallet, E., 2018. Deformation bands, early markers of
1347 tectonic activity in front of a fold-and-thrust belt: Example from the Tremp-Graus basin, southern
1348 Pyrenees, Spain. *J. Struct. Geol.* 110, 65–85. <https://doi.org/10.1016/j.jsg.2018.02.012>
- 1349 Roberts, N.M.W., Rasbury, E.T., Parrish, R.R., Smith, C.J., Horstwood, M.S.A., Condon, D.J., 2017. A
1350 calcite reference material for LA-ICP-MS U-Pb geochronology. *Geochemistry, Geophys.*
1351 *Geosystems* 18, 2807–2814. <https://doi.org/10.1002/2016GC006784>
- 1352 Roure, F., Andriessen, P., Callot, J.P., Faure, J.L., Ferket, H., Gonzales, E., Guilhaumou, N., Lacombe,
1353 O., Malandain, J., Sassi, W., Schneider, F., Swennen, R., Vilasi, N., 2010. The use of palaeo-
1354 thermo-barometers and coupled thermal, fluid flow and pore-fluid pressure modelling for
1355 hydrocarbon and reservoir prediction in fold and thrust belts. *Geol. Soc. Spec. Publ.* 348, 87–114.
1356 <https://doi.org/10.1144/SP348.6>
- 1357 Roure, F., Choukroune, P., Berastegui, X., Munoz, J. a., Villien, A., Matheron, P., Bareyt, M., Seguret,
1358 M., Camara, P., Deramond, J., 1989. Ecore deep seismic data and balanced cross sections:
1359 Geometric constraints on the evolution of the Pyrenees. *Tectonics* 8, 41–50.
1360 <https://doi.org/10.1029/TC008i001p00041>
- 1361 Roure, F., Swennen, R., Schneider, F., Faure, J.L., Ferket, H., Guilhaumou, N., Osadetz, K., Robion, P.,
1362 Vandeginste, V., 2005. Incidence and importance of tectonics and natural fluid migration on
1363 reservoir evolution in foreland fold-and-thrust belts. *Oil Gas Sci. Technol.*
1364 <https://doi.org/10.2516/ogst:2005006>
- 1365 Salomon, E., Rotevatn, A., Kristensen, T.B., Grundvåg, S.-A., Henstra, G.A., Meckler, A.N., Albert, R.,
1366 Gerdes, A., 2020. Fault-controlled fluid circulation and diagenesis along basin-bounding fault
1367 systems in rifts – insights from the East Greenland rift system. *Solid Earth* 11, 1987–2013.
1368 <https://doi.org/10.5194/se-11-1987-2020>
- 1369 Séguret, M., Daignières, M., 1986. Crustal scale balanced cross-sections of the Pyrenees; discussion.
1370 *Tectonophysics* 129, 303–318. [https://doi.org/10.1016/0040-1951\(86\)90258-1](https://doi.org/10.1016/0040-1951(86)90258-1)
- 1371 Shackleton, J.R., Cooke, M.L., Vergés, J., Simó, T., 2011. Temporal constraints on fracturing associated
1372 with fault-related folding at Sant Corneli anticline, Spanish Pyrenees. *J. Struct. Geol.* 33, 5–19.
1373 <https://doi.org/10.1016/j.jsg.2010.11.003>
- 1374 Simó, A., 1986. Carbonate platform depositional sequences, Upper Cretaceous, south-central Pyrenees
1375 (Spain). *Tectonophysics* 129, 205–231. [https://doi.org/10.1016/0040-1951\(86\)90252-0](https://doi.org/10.1016/0040-1951(86)90252-0)
- 1376 Sun, X., Alcalde, J., Gomez-Rivas, E., Struth, L., Johnson, G., Travé, A., 2020. Appraisal of CO₂ storage
1377 potential in compressional hydrocarbon-bearing basins: Global assessment and case study in the

- 1378 Sichuan Basin (China). *Geosci. Front.* 11, 2309–2321. <https://doi.org/10.1016/j.gsf.2020.02.008>
- 1379 Swennen, R., Muskhah, K., Roure, F., 2000. Fluid circulation in the Ionian fold and thrust belt (Albania):
1380 implications for hydrocarbon prospectivity. *J. Geochemical Explor.* 69–70, 629–634.
1381 [https://doi.org/10.1016/S0375-6742\(00\)00043-1](https://doi.org/10.1016/S0375-6742(00)00043-1)
- 1382 Tavani, S., Granado, P., Arbués, P., Corradetti, A., Muñoz, J.A., 2017. Syn-thrusting, near-surface
1383 flexural-slipping and stress deflection along folded sedimentary layers of the Sant Corneli-Bóixols
1384 anticline (Pyrenees, Spain). *Solid Earth* 8, 405–419. <https://doi.org/10.5194/se-8-405-2017>
- 1385 Tavani, S., Mencos, J., Bausà, J., Muñoz, J.A., 2011. The fracture pattern of the Sant Corneli Bóixols
1386 oblique inversion anticline (Spanish Pyrenees). *J. Struct. Geol.* 33, 1662–1680.
1387 <https://doi.org/10.1016/j.jsg.2011.08.007>
- 1388 Tavani, S., Storti, F., Lacombe, O., Corradetti, A., Muñoz, J.A., Mazzoli, S., 2015. A review of
1389 deformation pattern templates in foreland basin systems and fold-and-thrust belts: Implications for
1390 the state of stress in the frontal regions of thrust wedges. *Earth-Science Rev.* 141, 82–104.
1391 <https://doi.org/10.1016/j.earscirev.2014.11.013>
- 1392 Taylor, B.D., 1987. Stable isotope geochemistry of ore-forming fluids. *Short Course Handbook. Mineral.*
1393 *Assoc. Canada* 13, 337–445.
- 1394 Toussaint, R., Aharonov, E., Koehn, D., Gratier, J.P., Ebner, M., Baud, P., Rolland, A., Renard, F., 2018.
1395 *Stylolites: A review. J. Struct. Geol.* 114, 163–195. <https://doi.org/10.1016/j.jsg.2018.05.003>
- 1396 Travé, A., Calvet, F., Sans, M., Vergés, J., Thirlwall, M., 2000. Fluid history related to the Alpine
1397 compression at the margin of the south-Pyrenean Foreland basin: the El Guix anticline.
1398 *Tectonophysics* 321, 73–102. [https://doi.org/10.1016/S0040-1951\(00\)00090-1](https://doi.org/10.1016/S0040-1951(00)00090-1)
- 1399 Travé, A., Labaume, P., Vergés, J., 2007. Fluid Systems in Foreland Fold-and-Thrust Belts: An Overview
1400 from the Southern Pyrenees, in: Lacombe, O., Roure, F., Lavé, J., Vergés, Jaume (Eds.), *Thrust*
1401 *Belts and Foreland Basins, Frontiers in Earth Sciences.* Springer Berlin Heidelberg, Berlin,
1402 Heidelberg, pp. 93–115. https://doi.org/10.1007/978-3-540-69426-7_5
- 1403 Tugend, J., Manatschal, G., Kuszniir, N.J., Masini, E., Mohn, G., Thion, I., 2014. Formation and
1404 deformation of hyperextended rift systems: Insights from rift domain mapping in the Bay of Biscay-
1405 Pyrenees. *Tectonics* 33, 1239–1276. <https://doi.org/10.1002/2014TC003529>
- 1406 Vandeginste, V., Swennen, R., Allaey, M., Ellam, R.M., Osadetz, K., Roure, F., 2012. Challenges of
1407 structural diagenesis in foreland fold-and-thrust belts: A case study on paleofluid flow in the
1408 Canadian Rocky Mountains West of Calgary. *Mar. Pet. Geol.* 35, 235–251.
1409 <https://doi.org/10.1016/j.marpetgeo.2012.02.014>
- 1410 Veizer, J., 1992. Depositional and diagenetic history of limestones: Stable and radiogenic isotopes, in:
1411 *Isotopic Signatures and Sedimentary Records.* Springer-Verlag, Berlin/Heidelberg, pp. 13–48.
1412 <https://doi.org/10.1007/BFb0009860>
- 1413 Veizer, J., Ala, D., Azmy, K., Bruckschen, P., Buhl, D., Bruhn, F., Carden, G.A.F., Diener, A., Ebner, S.,
1414 Godderis, Y., Jasper, T., Korte, C., Pawellek, F., Podlaha, O.G., Strauss, H., 1999. $^{87}\text{Sr}/^{86}\text{Sr}$,
1415 $\delta^{13}\text{C}$ and $\delta^{18}\text{O}$ evolution of Phanerozoic seawater. *Chem. Geol.* 161, 59–88.
1416 [https://doi.org/10.1016/S0009-2541\(99\)00081-9](https://doi.org/10.1016/S0009-2541(99)00081-9)
- 1417 Vergés, J., 1993. *Estudi geològic del vessant Sud del Pirineu Oriental i Central: Evolució cinemàtica en*
1418 *3D.* PhD Thesis .Universitat Barcelona 203p.
- 1419 Vergés, J., Fernández, M., Martínez, A., 2002. The Pyrenean orogen: pre-, syn-, and post-collisional
1420 evolution. *J. Virtual Explor.* 08, 55–74. <https://doi.org/10.3809/jvirtex.2002.00058>
- 1421 Vergés, J., Muñoz, J.A., 1990. Thrust sequence in the southern central Pyrenees. *Bull. la Société*
1422 *Géologique Fr.* VI, 265–271. <https://doi.org/10.2113/gssgfbull.VI.2.265>
- 1423

Supplementary data

Analytical results, Concordia graphs and summary of the U-Pb procedures

Table S1. Geochemical data in the Estamariu thrust

Sample	Cement	$\delta^{18}\text{O}$ ‰VP DB	$\delta^{13}\text{C}$ ‰VP DB	$^{87}\text{Sr}/^{86}\text{Sr}$	$^{143}\text{Nd}/^{144}\text{Nd}$	Y/Ho	Sr	Mn	REE	Δ_{47}	T (°C)	$\delta^{18}\text{O}_{\text{fluid}}$ ‰SMOW
C9	Cc1a	-11.2	+0.91			42.4	704.0	680.7	131.7			
C8B	Cc1a	-10.7	+2			55.3	460.2	781.6	152.2			
C8A.I	Cc1a	-10.4	+2									
C8A.II	Cc1a	-10.96	+1.3	0.713018	NR	54.8	545.5	810.3	79.6			
C8A.III	Cc1a	-10.9	+1.2									
C7.I	Cc1a	-10.9	+2.1									
C7.II	Cc1a	-10.8	+0.8									
C7.III	Cc1a	-10.4	+1.96									
C4B	Cc1a	-10.3	+1.9	0.714092	NR	40.1	543.7	1243.7	292.9			
C3A.I	Cc1a	-11.2	+1.9									
C3A.II	Cc1a	-11.3	+1.7									
C3A.III	Cc1a	-10.5	+1.98									
C15.I	Ce2	-14.9	-1.2	0.718294	NR	48.7	248.5	3629.3	106.5	0.567	50 to 100	-0.3 to -6.4
C15.II	Ce2	-13.3	+0.5									
C15.III	Ce2	-12.91	+1.54									
C13	Ce3	-13.8	-7.1	0.714619	NR	50.8	424.9	7695.5	719.7	0.445	130 to 210	+4.3 to +12.1
C12.II	Ce3	-14.3	-7.3									
C10	Ce3	-14.2	-9.3			43.7	122.3	8277.9	893.4			
C11A	Ce3	-14.2	-8.7									
C13.II	Ce3	-13.6	-7.2									
C14.I	Ce3	-13.4	-6.9									
C14.II	Ce3	-13.7	-7.4									
C16A	Ce3	-13.8	-7.2									
C16B	Ce3	-14	-7									
C16C	Ce3	-14.1	-6.9									
C18.I	Ce4	-13.4	-7.2	0.717706	NR	52.0	72.2	4034.6	279.9	0.48	100 to 170	+0.9 to +8.1
C18.II	Ce4	-13.8	-7.4									
C12.I	Ce5	-8.1	-7.8	0.716923	0.512178	60.0	25.3	138.8	108.3			
C6.I	Ce5	-6.7	-8.2			47.5	72.1	161.4	73.0			
C6.II	Ce5	-7.4	-7.4									
C11B	Ce5	-5.7	-3.8									
C3A.HR	Devonian	-9.5	+2.4	0.710663	NR	37.5	449.4	621.1	205.1			
C17.HR	carbonates	-10.5	+1.5									
C4.HR		-8.4	+2.7									
C11.HR	Andesites			0.743983	0.512196	35.8	18.6	466.6	95.1			

Table S2. Geochemical data in the Sant Corneli-Bóixols anticline

sample	Cement	$\delta^{18}\text{O}\text{‰VPDB}$	$\delta^{13}\text{C}\text{‰VPDB}$	87Sr/86Sr	Y/Ho	Sr	Mn	REE	D47	$\delta^{18}\text{O}_{\text{fluid}}\text{‰SMOW}$	T (°C)
Bx 9		-5.05	2.69		78.0	304.0	110.4	13.8			
Bx 10	Cc1a	-9.32	2.41	0.707627	70.4	708.5	89.5	2.9			
Bx37		-10.32	2.43		69.2	365.5	150.0	4.5			
Bx 14A		-7.36	1.90								
Bx 15.1		-8.69	1.93								
Bx 15.II	Cc1b	-6.55	1.79								
Bx 15.III		-7.51	2.09								
Bx 12A		-5.62	1.84	0.707333	81.7	1213.1	95.0	19.0			
MGT 4.I		-9.55	2.10	0.707542	52.9	749.0	166.5	47.8			
MGT 4.II		-9.10	1.66								
MGT-2		-10.11	2.20								
MGT-21a	Cc2	-14.43	2.47								
MGT-19a		-14.05	2.19								
MGT-13		-12.04	2.44								
MGT-8a		-13.49	1.84								
CN27A		-12.28	1.13	0.708028	52.2	408.7	135.0	12.1			
CN28A		-10.43	1.67								
Bx68	Cc3	-10.49	1.93								
Bx69		-11.69	1.49								
CN40		-11.16	0.47								
CN41.I		-14.71	0.41	0.707857	60.3	711.5	73.8	54.1			
CN41.II		-12.85	0.28								
CN12B		-11.83	1.34								
CN32B	Cc4	-13.22	0.82								
CN33A		-11.09	1.19	0.707468	53.4	794.7	319.5	19.9	0.536/0.548	-0.2 to +1.4	85 to 92
CN33B		-12.71	0.37								
ABC 34	Cc5a	-7.78	-1.38	/	56.2	581.6	66.3	10.8			
Bx 32	Cc5b	-5.22	2.12		78.5	3718.6	178.0	10.0			
Bx 34		-5.04	2.18	0.707669	102.7	3240.9	175.5	2.0			
Bx47.I		-7.40	-3.63		52.3	441.0	318.4	33.8			
Bx47.II	Cc6a	-8.46	1.34	0.707762	57.0	164.6	116.5	24.6			
Bx47.III		-7.25	-8.18								
CN12A		-7.87	1.25	0.707326	47.8	501.2	225.3	19.1			
CN31B		-9.23	1.8								
CN32A	Cc6b	-8.42	1.03								
CN32D		-8.64	1.04								
CN38A		-6.59	2.7	0.707298	46.3	240.6	46.6	1.9	0.6	-1.3 to +2.9	40.7 to 16.1
CN38B		-8.19	2.41								
Bx 23		-11.86	-1.75								
Bx 24	Cc6c	-13.90	-1.01								
Bx 25.I		-13.37	-1.06	0.707835	62.7	1420.9	477.2	74.5			
Bx 25.II	Cc7	-13.06	-2.07	0.707894	61.5	1160.5	512.0	34.8			
Bx 18		-7.41	2.09	0.707389	86.0	637.0	79.7	10.5			
Bx39.I	Cc8a	-6.47	2.14		71.5	2617.9	84.0	22.0			
Bx39.II		-7.18	2.03								
Bx39.III		-6.60	2.13								
Bx35B.II	Cc8b	-4.39	2.18	0.707699	80.8	3916.3	164.2	4.6			
ABC 24		-8.79	2.30	0.707512	90.5	2070.0	83.5	16.2			
MGT35A	Cc9a	-12.05	1.22	0.707615	55.2	503.1	51.4	18.1			

Bx 11B		-6.69	2.18		90.2	2118.9	59.0	5.1			
Bx 13.I	Cc9b	-9.02	2.04	0.707285	71.4	4688.7	72.2	2.0			
Bx 11A		-8.22	2.17								
ABC 21B		-8.16	2.67		57.5	1131.8	52.5	22.3			
ABC 22	Cc10	-7.90	2.76		64.0	1380.7	38.1	16.4			
ABC 21A		-9.28	2.53								
Bx 1B		-8.18	-1.70	0.707707	42.2	239.0	236.8	40.8	0.619/0.642	-1.8 to -0.1	42 to 51
Bx 3	Cc11	-7.32	-1.79								
Bx36.I		-7.62	-1.97								
Bx36.IV		-7.37	-1.64								
Bx36.V		-6.45	-1.45								
Bx3.III		-8.23	-3.72								
Bx 1A.I		-6.98	-4.63	0.707699	46.9	216.2	222.3	22.7	0.562/0.589	+3.7 to +5.9	64 to 78
Bx1B.II		-6.27	-4.60								
Bx3.II	Cc12	-6.98	-3.28								
Bx36.II		-7.82	-5.62	0.707695	47.6	270.7	86.6	4.9			
Bx36.III		-7.16	-6.27								
Bx35A.II		-5.41	-4.07	0.707765	45.3	219.5	151.5	21.9			
Bx 1A.II		-13.00	-1.88		44.7	906.8	380.5	35.7			
Bx 2A	Cc13	-12.13	-2.94	0.707698	45.4	548.1	409.3	29.2	0.498/0.515	+3.2 to +5.5	105 to 117
Bx2B		-11.93	-2.82								
Bx 4		-11.71	-3.19		51.6	356.2	661.1	9.3			
Bx66Cc		-12	1.6								
Bx 5		-12.90	0.39	0.707771	49.9	699.5	97.3	18.2	0.53/0.535	+0.7 to +1.9	93 to 96
Bx 6	Cc14a	-12.30	2.41								
Bx 7.I		-13.10	0.44								
Bx 7.II		-11.94	0.95	0.707715	69.6	623.6	80.3	5.2			
Bx 8		-12.28	-0.55		51.5	625.3	65.2	10.3			
ABC 1		-12.02	2.01								
ABC 2A		-10.79	1.43								
ABC 35	Cc14b	-10.97	1.91								
ABC 2B		-11.03	1.39								
ABC3		-13.83	1.73								
Bx 17A		-5.83	2.35								
Bx 17B	Cc15a	-7.27	2.39					11.0			
Bx 16		-10.69	1.39	0.707355	74.7	2835.4	78.9	10.5			
Bx 26	Cc15b	-12.98	-2.71		54.6	805.0	467.4	16.5			
Bx 27		-9.26	-2.75	0.707920	60.1	530.2	431.0	48.0			
Bx 17B	Cc16a	-7.27	2.39	/	74.8	4629.9	82.8				
Bx17		-9.60	2.20								
CN18A		-7.82	-8.3	0.707706	47.6	389.4	501.2	5.3			
CN20A	Cc16b	-8.28	-10.43	0.707614	46.9	449.8	1379.8	2.5	0.541/0.555	+1 to +2	80 to 90
CN26A		-7.79	-10.14								
MGT 15A.I		-9.35	1.91								
MGT 15A.II		-9.99	1.95		45.1	1813.4	174.3	105.3			
MGT 15A.III	Cc17a	-9.82	1.54								
MGT-20		-10.81	2.21								
MGT 15A.IV		-8.76	1.44								
Bx 19		-11.67	0.48	0.707807	77.8	412.9	466.4	16.4			
Bx 20.I		-11.19	0.87								
Bx 20.II	Cc17b	-8.88	0.23								
Bx21.I		-9.31	0.82								
Bx21.II		-8.48	-0.43								

Bx46		-8.96	-1.31		76.6	446.0	90.1	30.3			
Bx40	Cc17c	-9.30	2.23	0.707346	84.1	4746.3	43.0	0.8			
CN2A		-13.73	-6.13								
CN3A		-14.21	-5.81								
CN4A		-14.3	-7.38								
CN4B		-12.93	-7.78								
CN5A		-14.31	-12.48								
CN6A	Cc17d	-13.02	-10.85	0.707586	47.0	390.8	185.7	25.5			
CN9A		-13.58	-5.83								
CN10A		-13.85	-12.51								
CN15A-A		-10.06	-5.38	0.707612	52.4	519.7	119.3	10.3	0.543/0.545	0.5 to 0.9	87 to 88
CN15A-B		-13.66	-4.07								
CN15B-A		-10.88	-5.76								
CN16A		-13.06	-5.05								
CN16C		-9.86	-5.51								
CN17A		-10.22	-5.4								
CN26B		-13.84	-8.22								
Bx 33.I	Cc17e	-2.79	2.28	0.707667	74.7	3904.7	197.4	13.6			
Bx 33.II		-5.11	2.13								
MGT-21b		-8.36	2.59								
MGT-3		-8.78	2.48								
MGT 24A	Cc18	-8.51	2.32								
MGT 24B		-9.03	2.04								
MGT 3B		-8.88	2.52								
MGT-16a		-8.62	1.83								
MGT-19b		-8.74	1.90								
ABC 31		-7.47	2.59								
ABC 32	Cc19	-9.30	2.70		75.5	1462.6	56.5	13.3			
ABC 33.I		-9.07	2.30								
ABC 33.II		-7.92	2.66								
MGT 35B	Cc20a	-13.09	0.24								
MGT-31a		-15.61	-1.99								
Bx 28	Cc20b	-13.82	-3.65	0.708018	56.4	706.9	319.9	45.5			
Bx49.I		-8.34	0.02		48.2	314.6	636.1	39.2			
Bx49.II		-10.17	-0.84								
Bx50		-8.28	0.19								
Bx51		-10.06	0.37		65.2	362.5	93.2	10.6			
Bx52.I	Cc21	-8.52	0.86								
Bx52.II		-9.58	0.11								
Bx61		-8.54	0.08								
Bx62		-9.48	-0.47								
Bx65		-10.33	0.84								
Bx64.I		-12.99	-0.58	0.707683							
Bx64.II		-5.64	-2.51								
MGT 3A		-10.08	2.61								
MGT-8b		-9.98	2.58								
MGT-9b(a)	Cc22	-11.16	2.02								
MGT-10(b)		-10.98	2.09								
MGT-11a		-10.87	2.57								
MGT-2		-10.11	2.20								
MGT-9b(b)		-11.55	-3.28		50.8	1348.4	74.5	39.2			
MGT-9b(c)	Cc23	-12.15	-1.15	0.707700	54.3	338.7	196.5	39.8			
MGT-10(a)		-12.65	-4.14								

MGT-11b		-13.03	-3.93				
MGT-33a		-10.90	-3.30				
MGT-33b		-10.22	-1.82				
MGT-36		-10.80	-3.55				
CN27B	Jurassic SET	-6.22	0.72		69.6	995.5	60.1
CN28B		-8.66	1.69				
Bx38	Setcomelles Mb. B	-1.64	2.97	0.707530			
					54.4	422.8	104.0
Bx 12A.HR	Lluçà Fm CM	-4.86	2.08	0.707329	60.6	3352.4	80.5
CN12C		-3.31	1.76	0.707317	70.3	1812.9	76.4
CN31A	Lluçà Fm CN	-3.62	2.4				
CN32C		-5.06	1.59				
CN38C		-3	2.51				
Bx8 HR	Santa Fé Fm FB	-6.15	2.09	0.707718	55.7	468.9	68.8
Bx7.HR		-5.80	2.20				
Bx53 HR		-4.52	2.16		46.9	681.7	109.9
Bx45.I	Congost Fm SJ	-5.52	2.38				
Bx45.II		-7.51	0.98				
Bx2A HR		-6.67	0.74	0.707606	38.8	340.8	345.6
	Collada Gassó Fm FB						
Bx3 HR		-6.99	0.05				
Bx1.HR		-7.20	-0.50				
MGT 38.I (HR)		-5.67	2.26				
MGT 38.II (HR)	Sant Corneli Fm MGT	-4.19	2.64				
MGT-13HR		-3.67	2.36				
MGT-14HR		-3.53	2.32				
Bx42 HR	Vallcarga Fm SA ABC	-2.59	2.39	0.707695			
					50.3	2909.2	135.9
ABC 21B.HR		-3.55	2.82		48.6	2643.3	48.3
Bx 24HR		-10.22	-1.91		70.1	1382.4	325.0
Bx25 HR	Areny Fm OC	-9.64	-2.04				
Bx28 HR		-7.84	-5.01				
CN5B	Garumnian CN	-7.67	-13.06		50.4	771.7	58.5
CN20B		-6.84	-11.01		54.1	1362.1	329.0

Table S3. U-Pb procedure and results. Sequence of analysis 1

grain	name / sample	$^{207}\text{Pb}^a$ (cps)	U^b (ppm)	Pb^b (ppm)	$\frac{\text{Th}^b}{\text{U}}$	$\frac{^{238}\text{U}^d}{^{206}\text{Pb}}$	$\pm 2\sigma$ (%)	$\frac{^{207}\text{Pb}^d}{^{206}\text{Pb}}$	$\pm 2\sigma$ (%)
U285	MGT-3 boundary	74	0.079	0.001	0.017	133.7	6.4	0.1038	16
U286		281	0.081	0.001	0.060	94.81	6.4	0.2924	8.7
U287		102	0.12	0.001	0.00061	136.4	6.2	0.1058	16
U288		34	0.062	0.001	0.0026	142.3	8.2	0.06538	26
U289		183	0.28	0.002	0.0074	139.6	4.9	0.07905	10
U290		263	0.23	0.002	0.021	126.2	4.7	0.1251	7.7
U291		307	0.14	0.002	0.0016	113.4	5.2	0.2201	8.3
U292		193	0.15	0.001	0.063	127.4	7.2	0.1467	17
U293		291	0.42	0.003	0.048	140.5	4.1	0.08679	7.8
U294		156	0.20	0.002	0.020	134.4	4.9	0.09306	11
U295		237	0.17	0.002	0.024	126.4	5.2	0.1540	9.9
U296		235	0.27	0.002	0.021	139.7	4.5	0.1067	12
U297		168	0.32	0.002	0.022	136.5	4.2	0.06351	12
U298		381	0.098	0.002	0.0018	87.95	7.8	0.3080	12
U299		581	0.30	0.004	0.0088	117.6	4.1	0.1999	7.3
U300		166	0.24	0.002	0.054	145.9	4.4	0.08719	11
U301		318	0.14	0.002	0.022	109.2	5.5	0.2207	12
U302		227	0.024	0.001	0.00050	59.18	9.5	0.4650	11
U303		54	0.096	0.001	0.0016	136.9	5.5	0.06394	15
U304		55	0.11	0.001	0.0069	139.9	5.4	0.06381	19
U305	MGT-3	739	0.068	0.003	0.037	65.13	10	0.6689	7.3
U306		919	0.092	0.004	0.24	71.91	8.6	0.6264	7.0
U307		275	0.080	0.001	0.088	151.1	8.4	0.4545	12
U308		43006	0.089	0.16	1.35	1.948	4.3	0.8059	1.2
U309		34151	0.089	0.13	1.17	2.420	8.2	0.8223	1.3
U317		13871	0.096	0.052	0.92	6.129	13	0.7860	1.9
U318		243	0.076	0.001	0.064	151.3	9.1	0.4145	12
U320		1864	0.082	0.007	0.28	36.48	11	0.7317	6.3
U321		682	0.046	0.002	0.26	86.55	6.8	0.6276	7.8
U322		5037	0.015	0.000	0.022	130.4	14	0.4595	16
U323		5710	0.090	0.020	0.60	16.22	7.7	0.7743	2.8
U324		388	0.023	0.001	0.15	63.67	19	0.6748	11
U325		266	0.11	0.001	0.15	176.9	8.3	0.3891	10
U326		1779	0.11	0.005	0.071	77.31	17	0.6426	8.2
U327		751	0.090	0.003	0.37	84.07	5.4	0.5913	5.9
U328		125	0.13	0.001	0.030	248.3	11	0.1802	19
U330		9737	0.10	0.037	0.54	9.129	8.4	0.7793	2.1
U331		2788	0.10	0.008	0.13	70.33	14	0.6635	6.4
U332	MGT-1	220	1.2	0.003	0.039	389.5	3.8	0.06302	8.7
U335		165	0.83	0.002	0.014	384.0	4.8	0.07147	14
U336		256	0.94	0.003	0.026	358.4	4.2	0.09023	12
U338		201	0.88	0.002	0.0013	359.5	4.9	0.07637	9.7
U339		163	0.77	0.002	0.0057	365.7	4.5	0.07226	12
U340		218	0.88	0.003	0.0017	354.6	5.2	0.08085	12
U341		226	1.5	0.004	0.030	364.9	3.8	0.05154	9.7
U343		342	2.0	0.005	0.056	370.3	3.8	0.05864	7.5
U344		364	2.1	0.005	0.024	384.7	3.6	0.06115	7.8
U345		762	6.0	0.014	0.014	391.2	3.3	0.04634	5.3

U346		1367	9.4	0.023	0.012	387.6	3.5	0.05122	4.1
U347		307	1.7	0.005	0.054	369.0	3.8	0.06124	9.2
U348		356	0.32	0.002	0.0076	263.7	6.1	0.2715	7.8
U349		333	0.19	0.002	0.010	225.3	6.2	0.3795	8.6
U350		313	1.8	0.005	0.0072	381.8	4.1	0.06114	7.6
U351	MGT-21 messy	854	0.17	0.005	0.012	58.81	6.8	0.2369	15
U352		179	0.16	0.002	0.00059	77.04	4.6	0.07903	12
U353		269	0.21	0.003	0.0019	77.88	4.2	0.09565	8.9
U354		228	0.17	0.002	0.0019	76.15	4.5	0.09130	9.5
U355		204	0.28	0.003	0.0027	80.07	3.8	0.05444	8.5
U356		159	0.13	0.002	0.00052	76.22	4.8	0.08225	10
U357		151	0.14	0.002	0.00014	78.96	4.9	0.08053	12
U358		130	0.14	0.002	0.00045	76.54	4.4	0.06528	11
U359		165	0.11	0.002	0.00043	76.79	4.7	0.1040	9.4
U360		111	0.074	0.001	0.00015	77.24	6.0	0.1066	14
U361		323	0.17	0.003	0.00022	72.04	4.5	0.1259	7.2
U362		98	0.11	0.001	0.0025	76.22	4.6	0.06095	12
U363		1369	0.77	0.012	0.021	69.69	5.3	0.1134	16
U364		227	0.24	0.003	0.0058	81.87	4.2	0.07015	8.5
U365		583	0.61	0.008	0.015	76.82	3.6	0.06730	5.9
U366		500	0.43	0.006	0.011	76.43	3.8	0.08218	6.6
U367		386	0.30	0.004	0.0025	75.53	3.9	0.08891	7.7
U368		359	0.42	0.005	0.0035	79.54	3.6	0.06332	7.1
U369		316	0.32	0.004	0.015	76.78	4.1	0.06915	7.5
U377		296	0.30	0.004	0.0024	76.05	3.9	0.07057	8.5
U378	MGT-21 white	804	0.19	0.004	0.64	87.76	4.7	0.3368	5.0
U379		1147	0.22	0.006	0.29	80.02	4.4	0.3746	4.1
U380		644	0.11	0.003	0.44	73.49	4.5	0.3908	5.5
U381		1357	0.24	0.007	0.12	76.12	3.9	0.4040	4.1
U382		1438	0.25	0.007	0.13	76.13	4.0	0.4148	5.5
U383		425	0.076	0.002	0.45	76.66	6.1	0.3957	7.2
U384		619	0.13	0.003	0.24	79.01	5.3	0.3676	6.8
U385		274	0.094	0.002	0.45	100.8	5.3	0.2633	9.2
U386		352	0.12	0.002	0.49	99.46	5.2	0.2721	9.0
U387		1047	0.20	0.005	0.060	78.52	4.5	0.3784	4.6
U388		159	0.078	0.001	0.54	112.1	6.1	0.2060	12
U389		470	0.089	0.002	0.60	78.30	5.4	0.3955	6.6
U390		1065	0.18	0.005	0.15	74.38	4.6	0.4109	4.3
U391		820	0.094	0.004	0.037	61.36	4.8	0.4864	6.4
U392		262	0.074	0.001	0.039	92.36	5.9	0.3199	10
U393		349	0.10	0.002	0.29	95.00	5.2	0.3027	7.9
U394		628	0.17	0.004	0.62	90.15	4.3	0.3291	7.2
U395		335	0.083	0.002	0.12	87.13	5.6	0.3310	7.8
U396		283	0.082	0.002	0.43	95.27	5.5	0.3141	10
U397		813	0.16	0.004	0.065	78.39	4.5	0.3882	5.3
U468	ABC-3	688	0.016	0.003	0.0020	16.36	6.0	0.7036	5.3
U469		4127	0.025	0.017	0.84	5.167	7.6	0.8000	2.5
U470		5233	0.019	0.022	0.88	2.924	9.1	0.7892	3.2
U472		841	0.016	0.003	0.022	15.45	6.6	0.7714	5.5
U473		486	0.011	0.002	0.0048	16.52	7.2	0.7431	7.3
U474		486	0.011	0.002	0.00067	15.92	7.4	0.7214	8.0
U475		6370	0.017	0.021	1.76	3.975	7.4	0.7766	3.1
U476		747	0.021	0.007	0.0055	20.17	5.5	0.7127	6.6

U477	775	0.020	0.003	0.0020	19.15	5.4	0.7396	6.2
U478	771	0.018	0.003	0.0023	16.51	5.4	0.7326	6.2
U479	472	0.023	0.002	0.0023	32.00	6.8	0.6828	8.4
U480	648	0.013	0.003	0.11	14.63	8.0	0.7284	6.7
U481	557	0.012	0.003	0.0065	15.03	6.2	0.7077	7.2
U482	653	0.025	0.003	0.0038	27.10	6.5	0.7157	6.4
U483	647	0.032	0.003	0.053	31.98	5.7	0.6584	6.7
U484	783	0.017	0.003	0.0090	15.71	5.9	0.7455	6.0
U485	761	0.024	0.003	0.0023	21.54	6.8	0.6953	7.5
U486	739	0.011	0.003	0.0033	11.18	5.9	0.7564	6.1
U487	1810	0.015	0.008	0.27	6.617	12	0.7766	4.4
U488	564	0.009	0.003	0.054	11.72	6.1	0.7437	6.9
U489	458	0.011	0.002	0.0067	17.41	6.7	0.7263	8.8
RM ₀ (n=24) ^g	525885	37	37	1.01	3.483	1.1	0.9073	0.29
RM ₁ (n=24) ^g	14174	3.0	0.14	0.00025	23.42	5.1	0.09715	26
RM ₂ (n=24) ^g	11166	2.8	0.053	0.0016	99.31	71	0.3246	111
RM ₃ (n=12) ^g	2241	1.1	0.008	0.00003	517.6	95	0.6865	27

Spot sizes = 193 μm (50 for Nist612); crater depth $\sim 15\mu\text{m}$.

^a Within run background-corrected mean ^{207}Pb signal in cps (counts per second).

^b U and Pb concentrations and Th/U ratio were calculated relative to the primary reference material.

^d Corrected for background, within-run Pb/U fractionation (in case of $^{206}\text{Pb}/^{238}\text{U}$) and subsequently normalised to the primary reference material (ID-TIMS value/measured value).

^g RM_i: Reference material i.

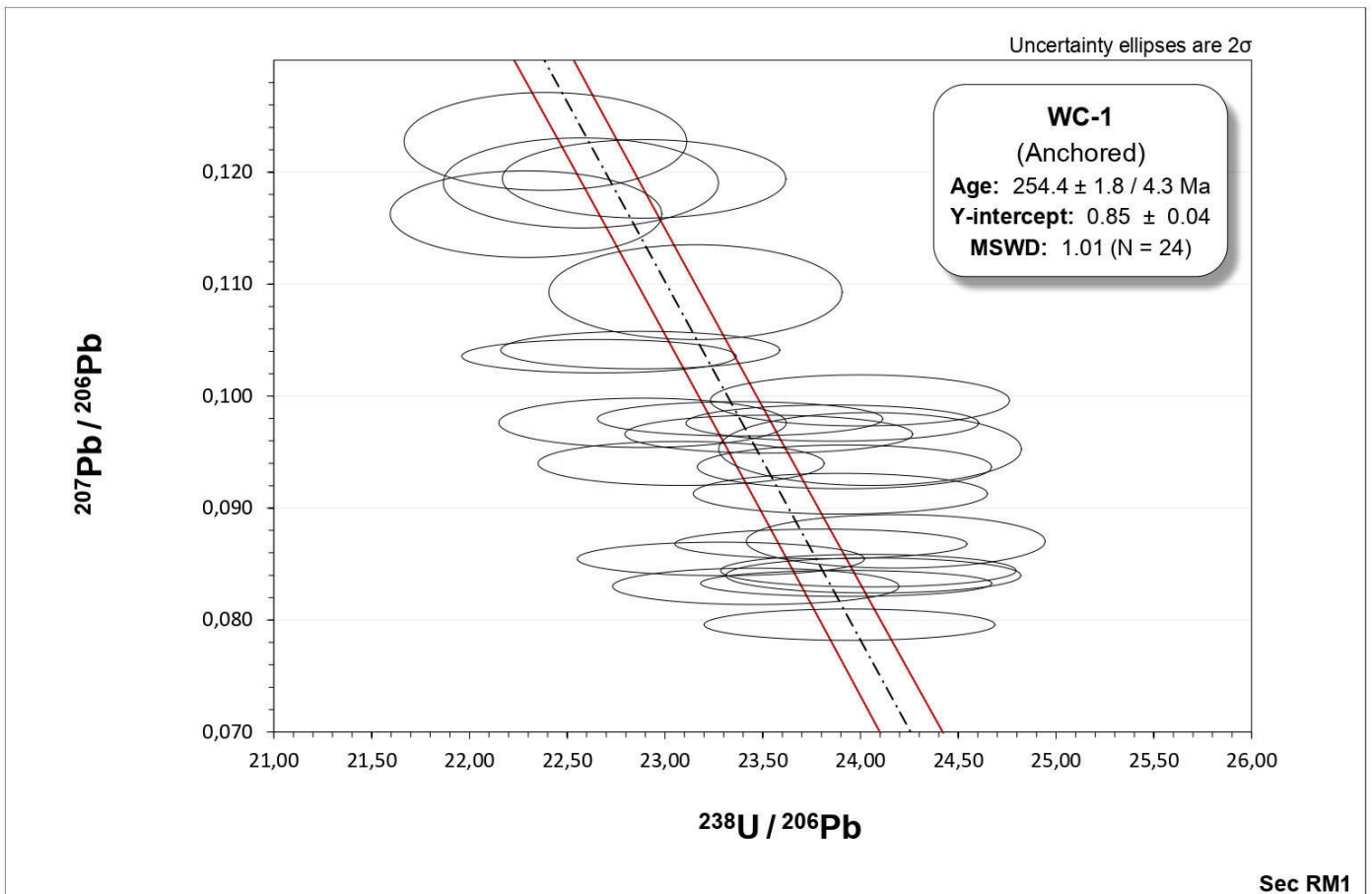
Accuracy and reproducibility was checked by repeated analyses of secondary reference materials; data given as mean with 2 standard deviation uncertainties.

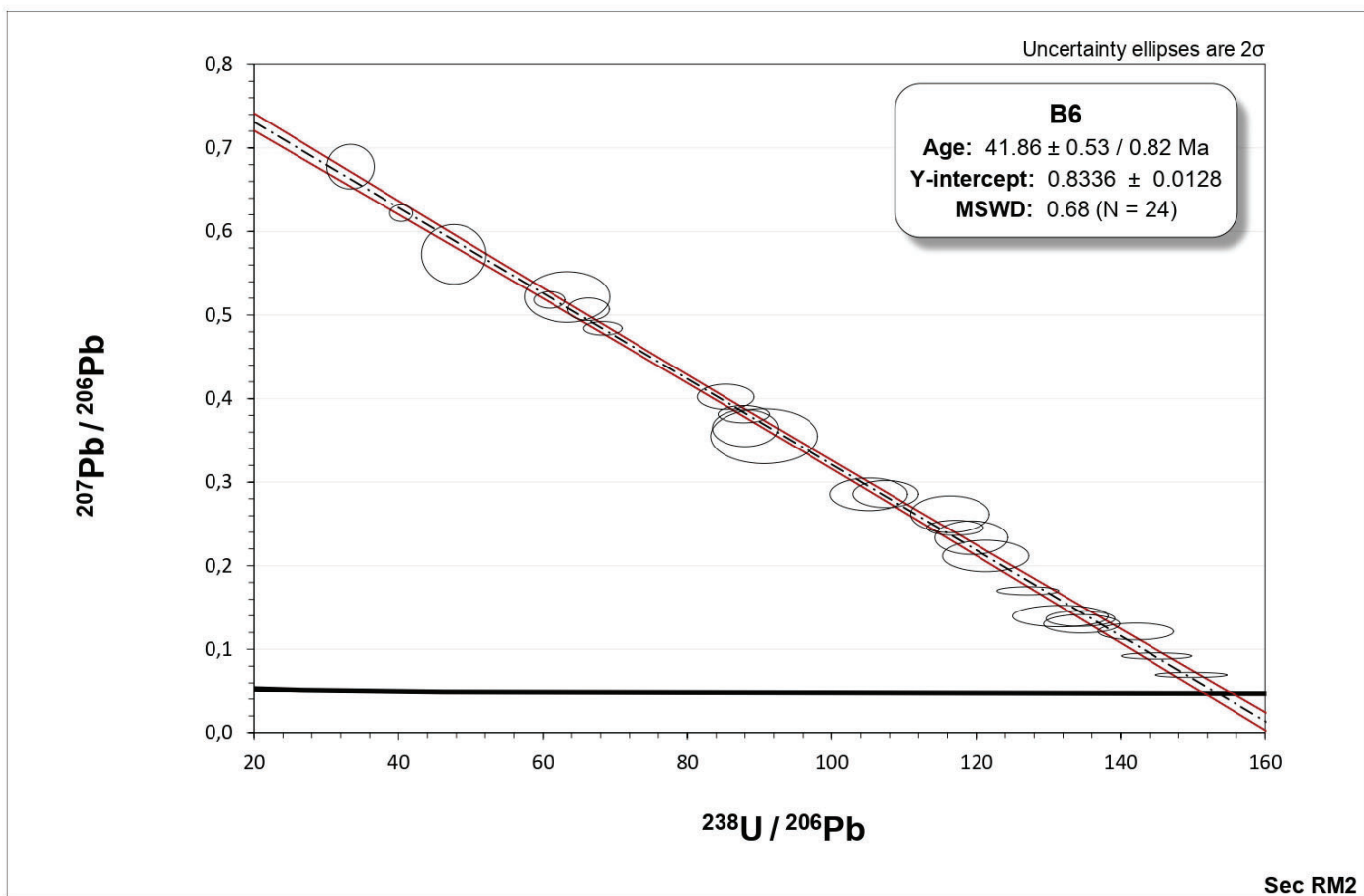
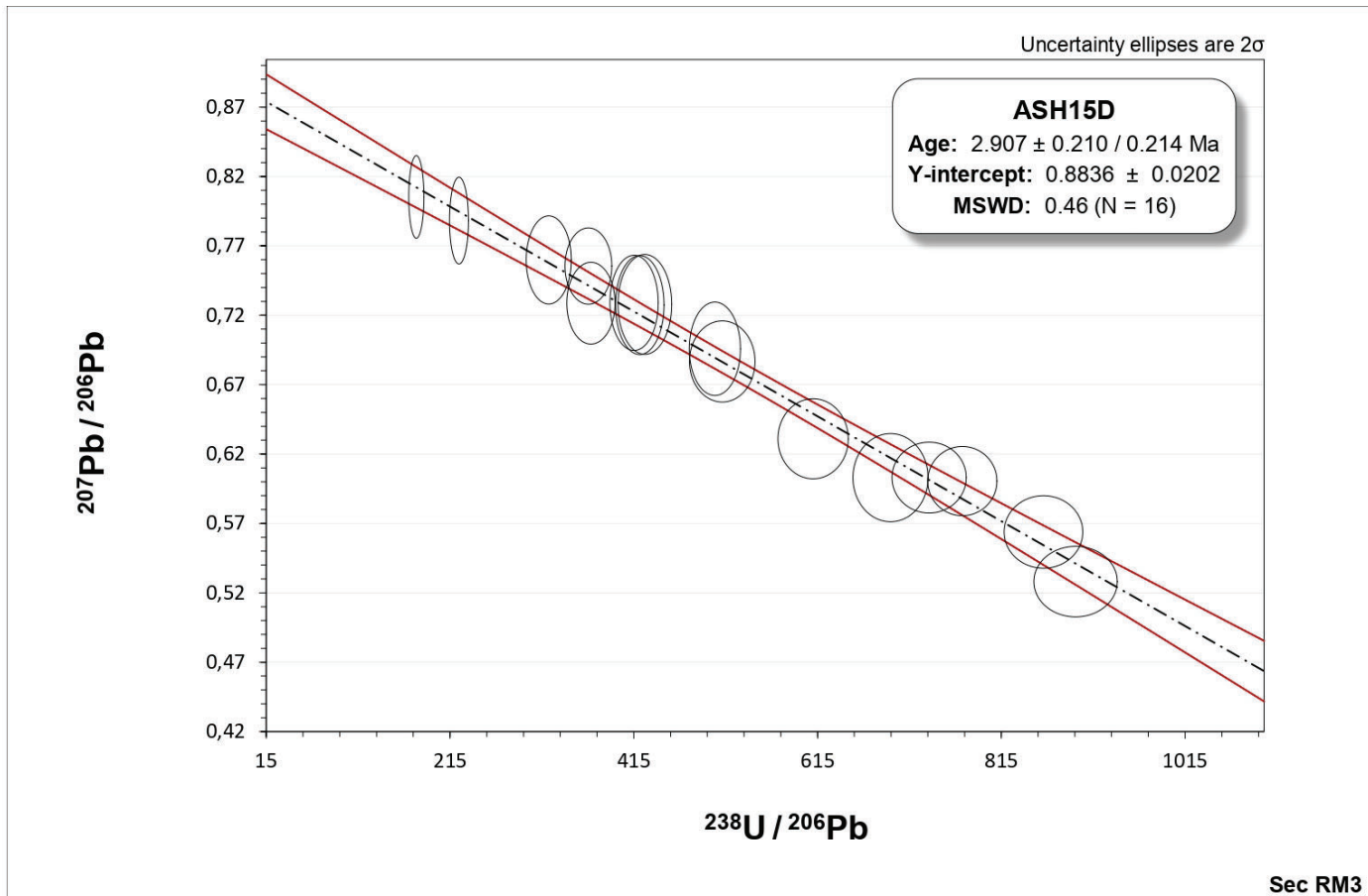
RM₀									
A001	Nist612	618474	37	37	1.01	3.477	0.24	0.9072	0.19
A002	Nist612	634072	38	38	1.01	3.483	0.23	0.9080	0.24
A040	Nist612	614615	38	37	1.01	3.492	0.20	0.9064	0.20
A041	Nist612	611480	37	37	1.01	3.488	0.19	0.9070	0.20
A080	Nist612	601372	38	37	1.01	3.485	0.19	0.9082	0.21
A081	Nist612	604707	38	37	1.01	3.479	0.25	0.9071	0.18
A130	Nist612	578246	37	37	1.01	3.481	0.20	0.9076	0.24
A131	Nist612	578534	37	37	1.01	3.477	0.25	0.9071	0.18
A190	Nist612	552228	37	37	1.01	3.478	0.26	0.9088	0.22
A191	Nist612	565512	38	37	1.01	3.480	0.20	0.9066	0.19
A250	Nist612	539230	37	37	1.01	3.501	0.29	0.9083	0.26
A251	Nist612	543085	37	37	1.01	3.478	0.19	0.9035	0.20
A310	Nist612	508945	37	37	1.01	3.505	0.28	0.9075	0.20
A311	Nist612	525528	38	38	1.01	3.469	0.22	0.9082	0.23
A370	Nist612	496722	38	37	1.01	3.503	0.33	0.9067	0.21
A371	Nist612	505511	38	38	1.01	3.458	0.28	0.9082	0.15
A430	Nist612	466234	37	37	1.02	3.505	0.25	0.9089	0.21
A431	Nist612	485207	38	38	1.01	3.449	0.20	0.9094	0.22
A490	Nist612	443155	37	37	1.01	3.513	0.26	0.9047	0.18
A491	Nist612	460412	38	38	1.01	3.461	0.34	0.9062	0.30
A540	Nist612	424019	37	37	1.01	3.512	0.27	0.9064	0.24
A541	Nist612	438303	38	38	1.01	3.459	0.31	0.9074	0.22
A592	Nist612	406211	37	37	1.01	3.511	0.26	0.9085	0.26

A593	Nist612	419444	38	38	1.01	3.454	0.28	0.9073	0.25
		525885	37	37	1.01	3.483	1.1	0.9073	0.29
RM₁									
B003	WC-1	14859	2.7	0.12	0.00012	24.00	3.2	0.09962	2.3
B004	WC-1	16917	3.2	0.14	0.00052	24.05	3.2	0.09527	3.4
B042	WC-1	14702	2.9	0.13	0.00014	23.92	3.1	0.09368	2.1
B043	WC-1	18571	3.9	0.17	0.00034	24.18	3.2	0.08703	2.7
B082	WC-1	14132	2.3	0.11	0.00010	23.16	3.2	0.1093	3.9
B083	WC-1	12274	2.7	0.12	0.00021	23.93	3.1	0.08327	1.4
B132	WC-1	13027	2.6	0.11	0.00009	23.86	3.1	0.09759	1.7
B133	WC-1	13762	2.7	0.12	0.00033	23.53	3.1	0.09660	1.8
B192	WC-1	15626	3.4	0.15	0.00025	23.90	3.1	0.09128	2.0
B193	WC-1	12502	2.3	0.11	0.00013	22.87	3.1	0.1041	1.6
B252	WC-1	14898	2.8	0.13	0.00015	22.66	3.1	0.1036	1.4
B253	WC-1	18325	2.9	0.15	0.00089	22.39	3.2	0.1227	3.6
B312	WC-1	13812	3.0	0.13	0.00016	23.38	3.1	0.09797	1.6
B313	WC-1	20438	3.4	0.17	0.00050	22.57	3.1	0.1190	3.4
B372	WC-1	11453	3.0	0.13	0.00016	24.04	3.1	0.08441	1.7
B373	WC-1	14734	2.6	0.13	0.00019	22.89	3.2	0.1194	2.9
B432	WC-1	11536	3.4	0.14	0.00024	23.94	3.1	0.07959	1.8
B433	WC-1	13077	3.1	0.14	0.00018	23.08	3.2	0.09399	2.1
B492	WC-1	19853	3.9	0.20	0.00050	22.29	3.1	0.1163	3.3
B493	WC-1	13664	3.3	0.15	0.00019	22.89	3.2	0.09761	2.3
B542	WC-1	11550	3.6	0.15	0.00023	24.07	3.1	0.08398	1.9
B543	WC-1	9693	2.9	0.13	0.00017	23.29	3.2	0.08546	1.7
B594	WC-1	10325	3.2	0.14	0.00005	23.80	3.1	0.08680	1.5
B595	WC-1	10441	3.3	0.14	0.00013	23.47	3.1	0.08301	2.0
		14174	3.0	0.14	0.00025	23.42	5.1	0.09715	26
RM₂									
C005	B6	7230	3.0	0.035	0.00006	121.3	4.9	0.2117	8.9
C006	B6	62852	2.9	0.20	0.014	40.40	4.0	0.6219	1.6
C044	B6	658	0.051	0.002	0.00000	63.37	9.3	0.5217	5.8
C045	B6	3732	1.4	0.018	0.00009	119.3	4.2	0.2336	8.6
C084	B6	26452	2.4	0.094	0.0048	60.94	3.6	0.5181	1.9
C085	B6	6267	1.1	0.025	0.00005	87.81	4.0	0.3814	2.7
C134	B6	4117	0.28	0.015	0.00051	47.66	9.4	0.5727	6.2
C135	B6	1548	0.53	0.007	0.00003	116.4	4.7	0.2616	8.4
C194	B6	8876	3.5	0.046	0.0025	117.1	3.3	0.2454	3.6
C195	B6	1040	0.88	0.008	0.00023	134.6	3.9	0.1304	8.4
C254	B6	2848	2.9	0.023	0.00005	142.1	3.7	0.1213	8.2
C255	B6	5801	0.25	0.021	0.00006	33.37	9.9	0.6776	3.9
C314	B6	32081	6.7	0.15	0.0081	88.01	5.2	0.3648	6.1
C315	B6	12283	1.4	0.050	0.00027	66.32	4.3	0.5070	2.6
C374	B6	16353	3.8	0.081	0.00056	90.64	8.2	0.3550	9.3
C375	B6	3372	3.0	0.028	0.00002	134.4	3.6	0.1366	6.8
C434	B6	4743	7.1	0.053	0.00013	145.0	3.3	0.09213	4.0
C435	B6	8879	1.8	0.045	0.00005	85.32	4.6	0.4022	3.7
C494	B6	10210	3.8	0.061	0.00040	107.5	4.2	0.2857	5.6
C495	B6	33816	4.8	0.16	0.0042	68.30	3.9	0.4841	1.7
C544	B6	2969	6.8	0.045	0.0011	149.8	3.3	0.06960	4.2
C545	B6	7344	5.8	0.059	0.00016	127.1	3.4	0.1699	2.8
C596	B6	1149	1.3	0.012	0.00068	131.7	5.0	0.1396	9.2
C597	B6	3376	1.4	0.022	0.00005	105.1	5.1	0.2854	6.8
		11166	2.8	0.053	0.0016	99.31	71	0.3246	111

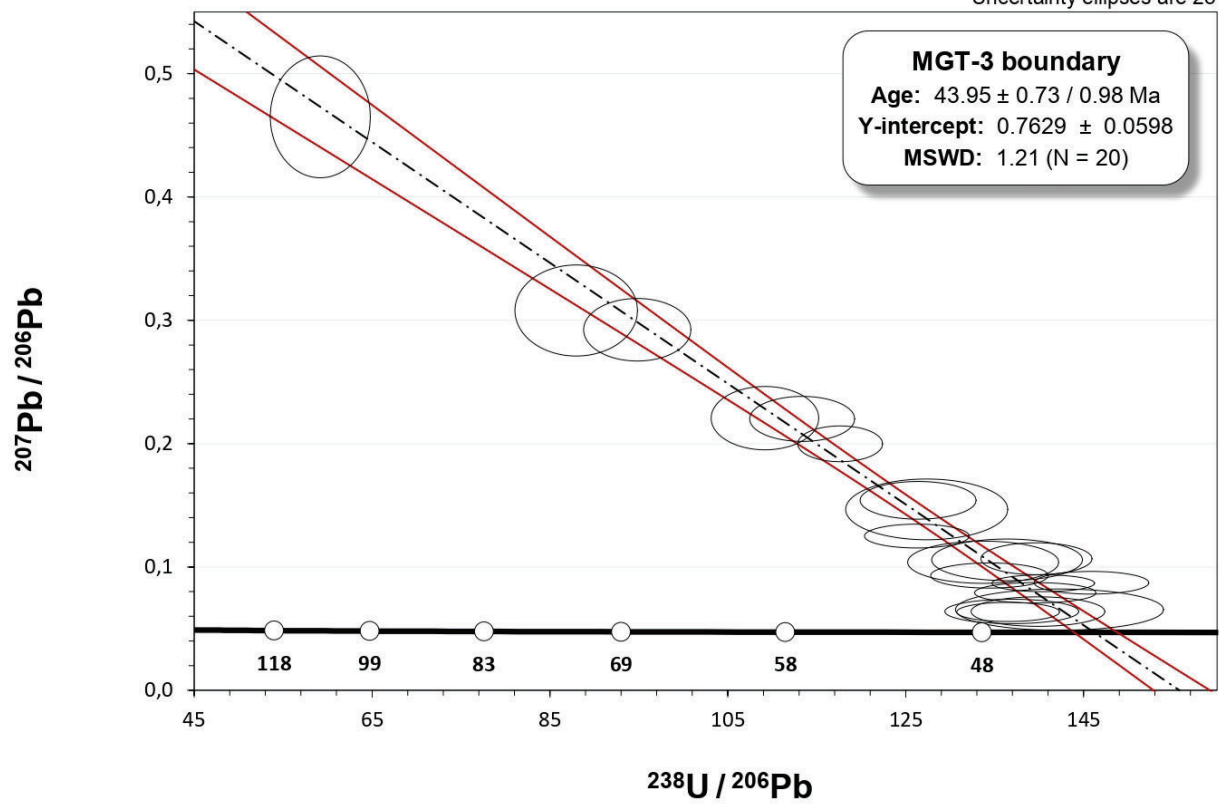
RM ₃										
D007	ASH15D	1677	0.85	0.005	0.00000	503.2	5.5	0.6999	4.8	
D046	ASH15D	2410	0.83	0.007	0.00000	365.5	7.0	0.7595	3.6	
D086	ASH15D	2189	2.1	0.007	0.00000	772.5	4.9	0.6046	4.1	
D136	ASH15D	950	0.81	0.003	0.00000	694.3	5.9	0.6071	5.2	
D196	ASH15D	1077	1.2	0.004	0.00000	860.8	5.0	0.5679	4.6	
D256	ASH15D	3870	1.7	0.014	0.00018	368.3	7.1	0.7328	4.0	
D316	ASH15D	5269	1.3	0.019	0.00011	224.7	4.6	0.7923	3.9	
D376	ASH15D	649	0.89	0.003	0.00000	895.8	5.1	0.5322	4.8	
D436	ASH15D	2850	0.74	0.015	0.00002	322.4	7.6	0.7639	4.2	
D496	ASH15D	3068	0.67	0.013	0.00001	178.3	4.6	0.8093	3.7	
D546	ASH15D	1817	1.1	0.008	0.00000	415.3	6.3	0.7330	4.7	
D598	ASH15D	1073	0.69	0.003	0.00001	610.1	6.3	0.6351	4.5	
		2241	1.1	0.008	0.00003	517.6	95	0.6865	27	

Concordia graphs 1

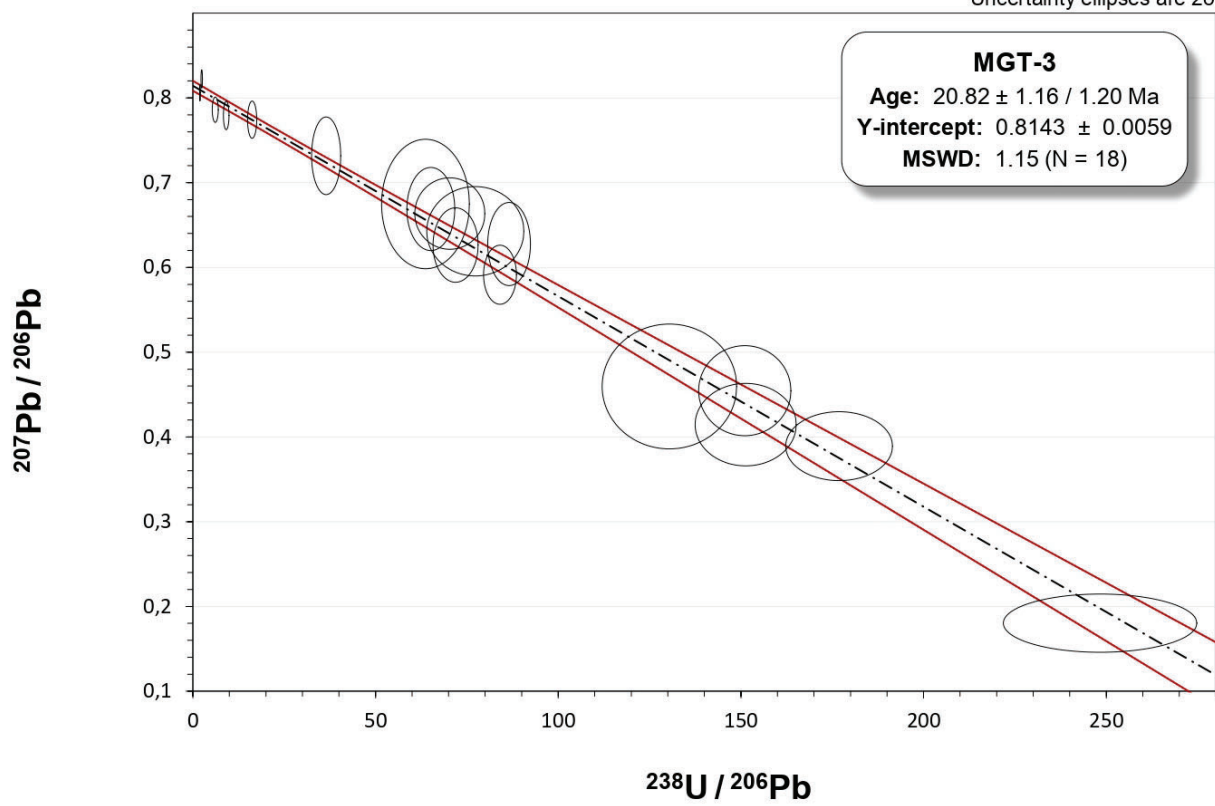


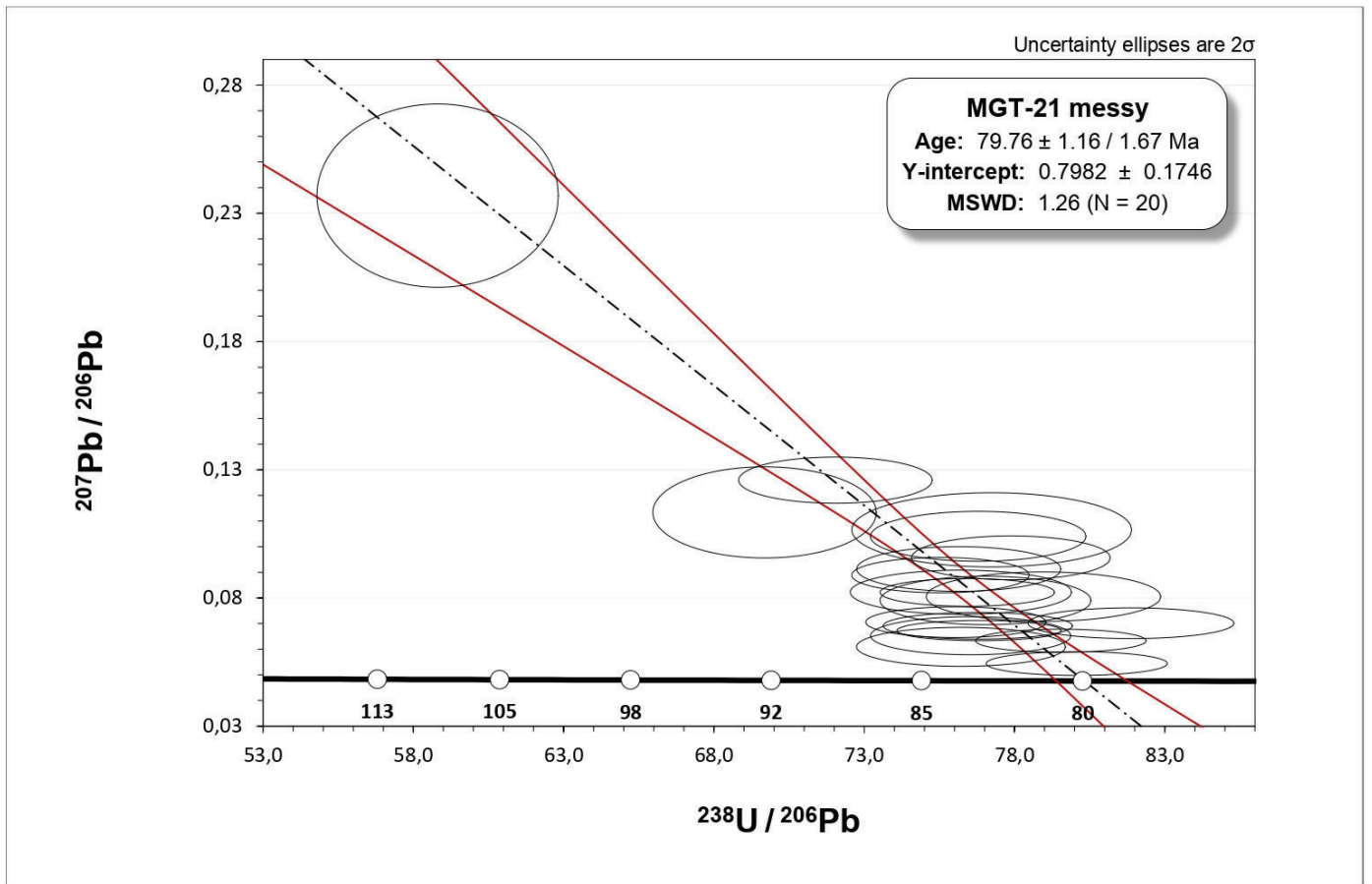
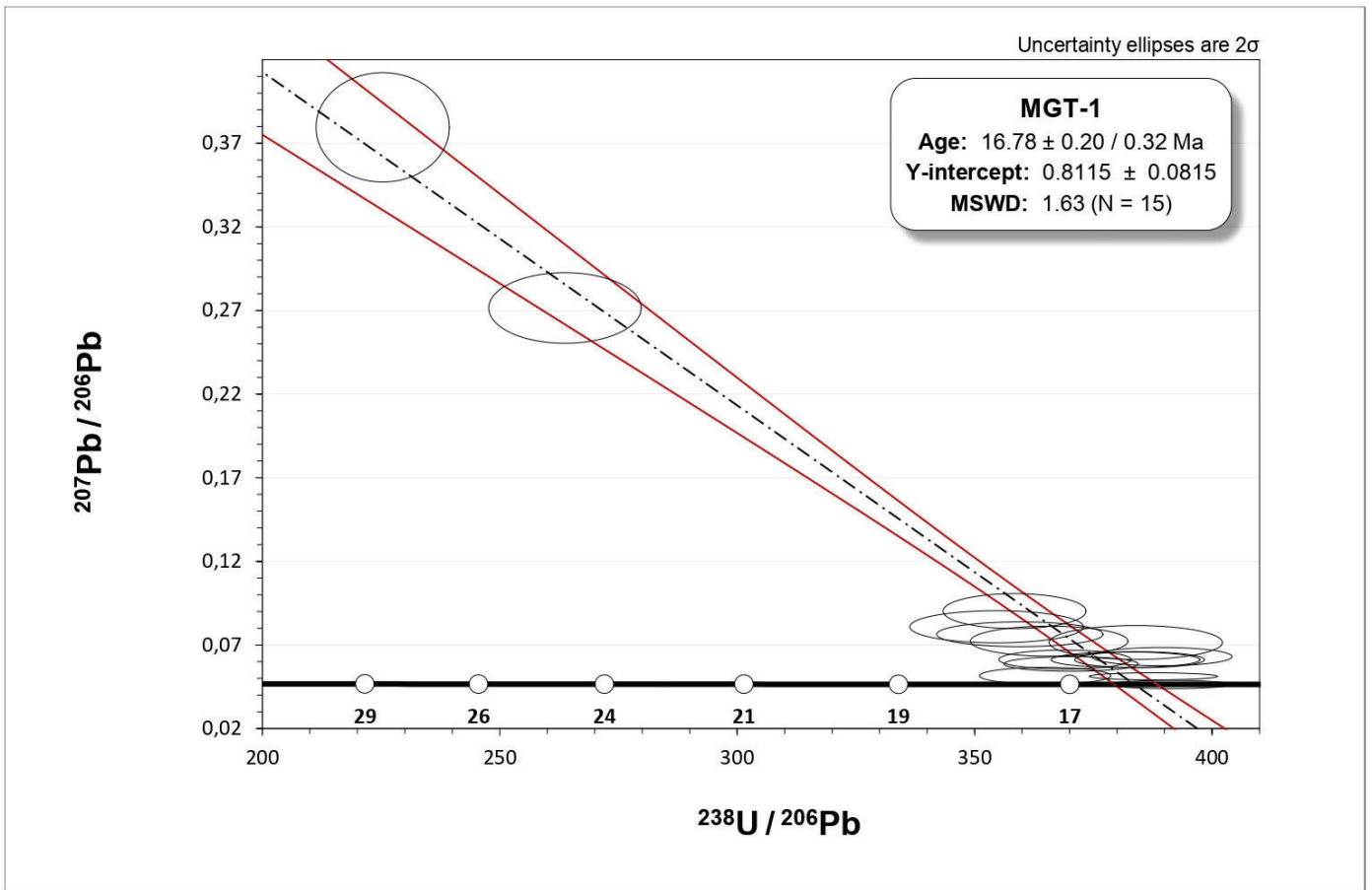


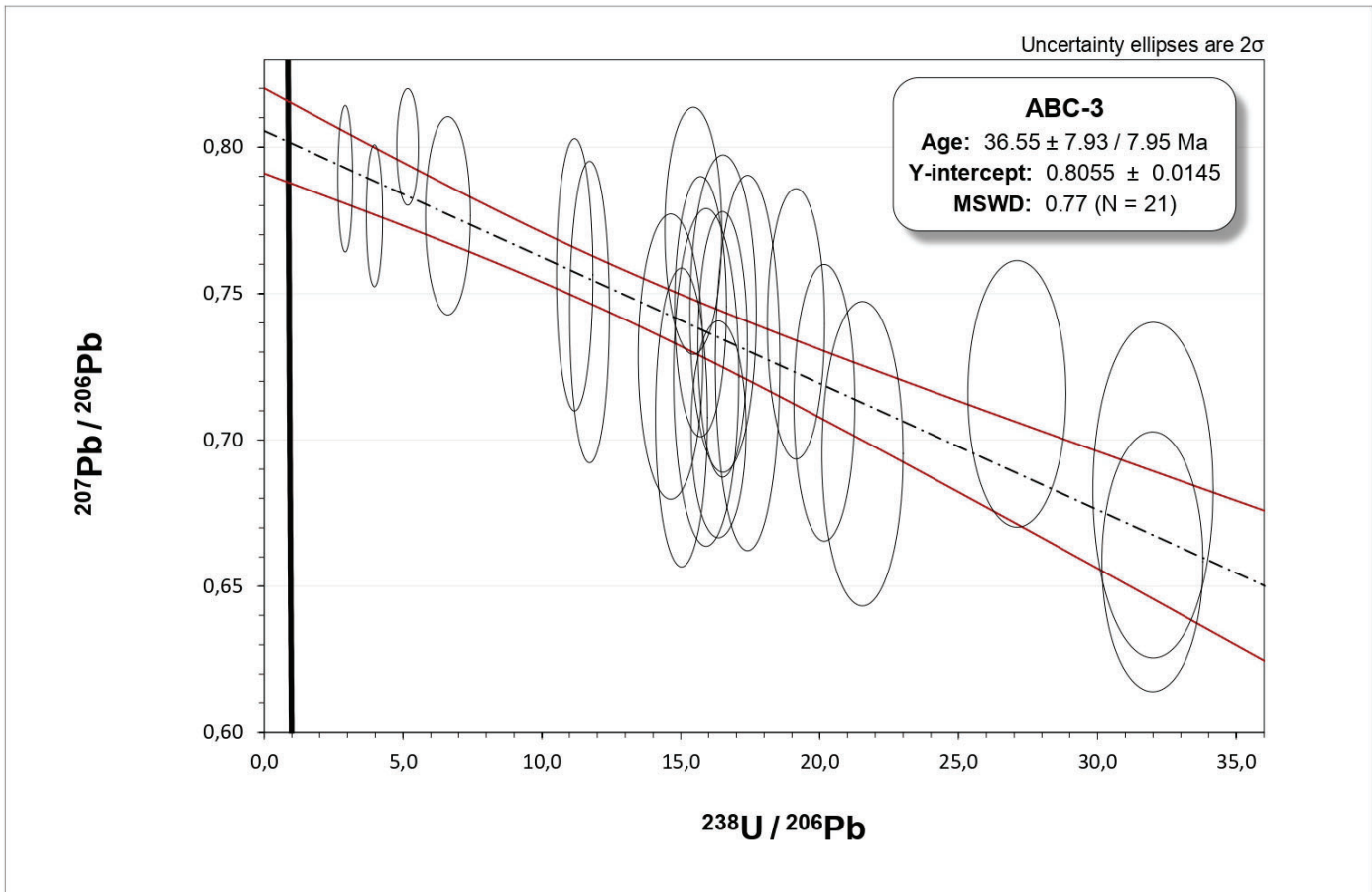
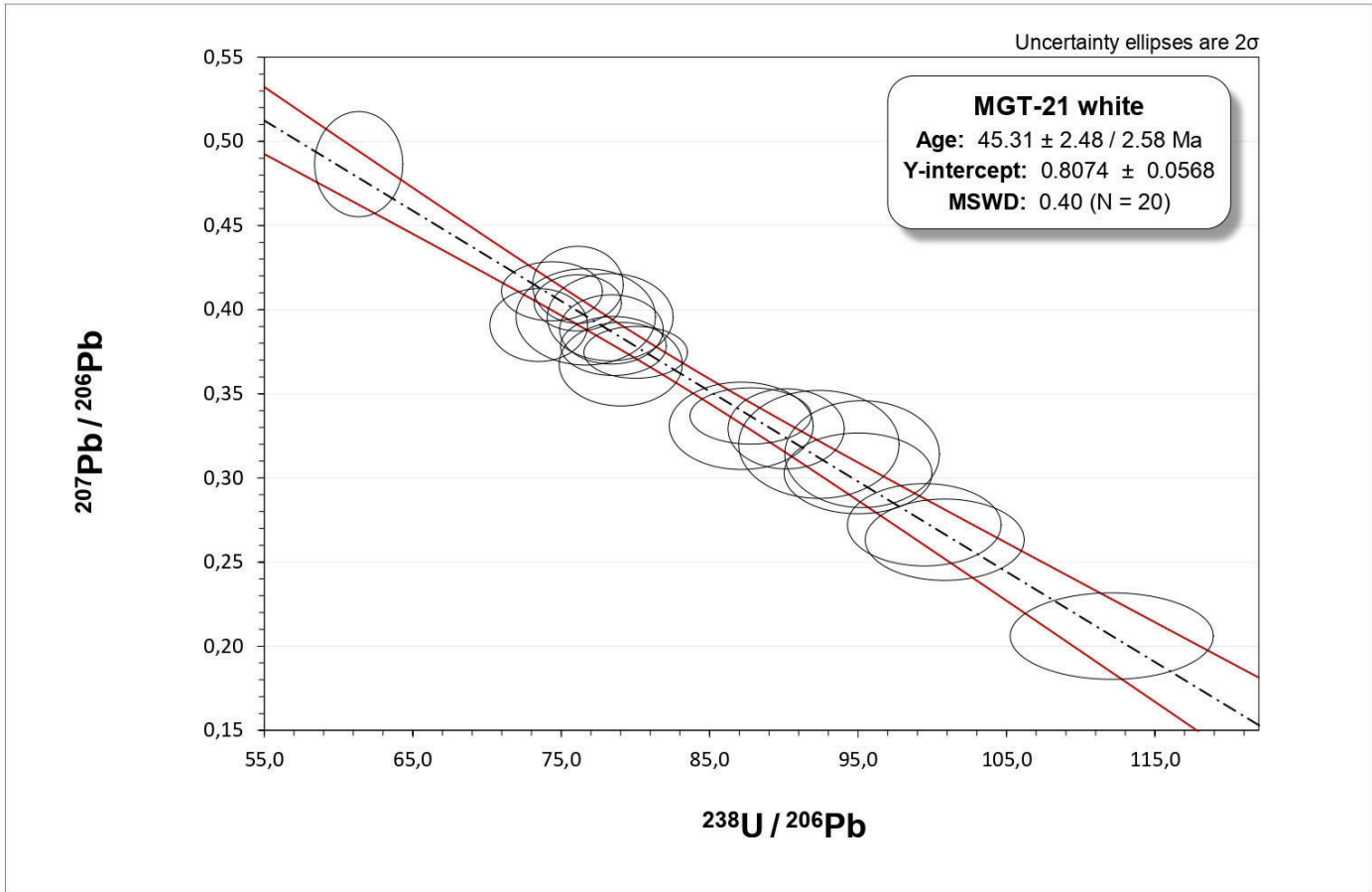
Uncertainty ellipses are 2σ



Uncertainty ellipses are 2σ







LA-ICP-MS U-Th-Pb data report

Laboratory & Sample Preparation	
Laboratory name	FIERCE, Frankfurt Isotope & Element Research Center Goethe Univesität, Frankfurt am Main
Sample type/mineral	Carbonate
Sample preparation	25 mm polished resin mounts
Imaging	Petrographic microscope & 2400 dpi digital scan
Laser ablation system	
Make, Model & type	RESolution ArF excimer laser (COMPex Pro 102)
Ablation cell	Two-volume ablation cell (Laurin Technic S155)
Laser wavelength	193 nm
Pulse width	20 ns
Fluence	2 J/cm ²
Repetition rate	12 Hz (8 Hz for primary standard)
Pre-ablation	4 pulses (same parameters as main ablation)
Ablation duration	18 s
Ablation rate	~ 0.6 µm/s
Spot shape & size	Circle, 193 µm (diameter), 50 µm for primary standard.
Sampling mode	Static spot ablation
Gasses	Sample cell: He. Funnel: He + Ar. Tubbing: He + Ar + N
Gas flows	He (300 ml/min), Ar (1100 ml/min), N (5 ml/min).
ICP-MS Instrument	
Make, Model & type	ThermoScientific ElementXr sector field ICP-MS
Sample introduction	Ablation aerosol
RF power	1300 W
Detection system	Secondary electron multiplier (with conversion dynode at -8kV). Simultaneous analogue and counting (pulse) modes of detection (conversion factors calculated per mass and applied offline). Magnetic field fixed. Detection by peak jumping with electrostatic analyzer.
Masses measured	206, 207, 208, 232, 238
Dwell times	206: 6.4 ms, 207: 7.5 ms, 208: 3.0 ms, 232: 2.0 ms, 238: 4.6 ms
Samples per peak/integration type	4 for all masses/average
Total time per run	99 ms
Number of runs/total time	370 / 36.6 s
Acquisition mode	Trigger from laser (20 s after pre-ablation), background: 18 s, ablation: 18 s
Dead time	29 ns
Data Processing	
Gas blank	20 s on-peak zero subtracted.
Calibration strategy	NIST SRM-612 as primary RM, WC-1 as offset RM, ASH15D and B6 as validation RM.
Reference Material (RM) information	Soda-lime glass NIST SRM-612, WC-1 (Roberts et al., 2017), ASH15D (Vaks et al., 2003), B6 (Pagel et al., 2018).
Data processing / LIEF correction	In-house VBA spreadsheet program (Gerdes and Zeh, 2006, 2009). Intercept method for LIEF correction, assumes cPb corrected WC-1 and samples behave identically.
Mass discrimination	²⁰⁷ Pb/ ²⁰⁶ Pb (0.5%) and ²⁰⁶ Pb/ ²³⁸ U (8%) normalised to primary standard
Common-Pb correction	No common-Pb correction applied to the data.
Uncertainty level & propagation	Uncertainties are quoted at 2σ absolute and are propagated by quadratic addition of the within run precision, counting statistics, the excess of scatter derived from the primary RM and the excess of variance (see below).
Other information	An excess of variance of 1.45 % (1σ), calculated from WC-1, was added quadratically to the ²⁰⁶ Pb/ ²³⁸ U ratios of the secondary RM and unknowns. Long term reproducibility was determined to be 1.5% (2σ) and was added as an expanded uncertainty.

Table S4. Sequence of analysis 2

grain	name / sample	²⁰⁷ Pb ^a (cps)	U ^b (ppm)	Pb ^b (ppm)	Th ^b U	²³⁸ U ^d ²⁰⁶ Pb	±2σ (%)	²⁰⁷ Pb ^d ²⁰⁶ Pb	±2σ (%)	Seq
U008	ABC24	422	0,006	0,001	0,0091	14,64	13	0,7258	16	2
U009		463	0,007	0,002	0,049	16,06	7,4	0,7324	11	2
U010		617	0,005	0,002	0,0022	8,532	8,3	0,8232	7,9	2
U011		467	0,005	0,002	0,0099	9,521	6,6	0,7231	9,2	2
U012		647	0,005	0,002	0,012	9,110	11	0,8140	7,1	2
U013		533	0,004	0,002	0,014	8,049	7,8	0,7737	9,1	2
U014		468	0,007	0,003	0,16	12,50	12	0,6585	9,9	2
U015		456	0,004	0,001	0,010	9,537	8,8	0,8248	10	2
U016		681	0,008	0,002	0,063	11,64	8,7	0,7699	7,4	2
U017		858	0,011	0,003	0,55	13,04	12	0,7547	8,1	2
U018		857	0,004	0,002	0,0037	6,414	11	0,8461	8,3	2
U019		436	0,005	0,001	0,0084	11,02	7,8	0,7572	9,9	2
U020		621	0,005	0,002	0,0040	9,217	8,6	0,7941	8,4	2
U021		782	0,009	0,002	0,0067	11,71	7,5	0,7645	8,1	2
U022		400	0,005	0,001	0,0074	11,28	9,2	0,6752	9,9	2
U023		581	0,005	0,002	0,083	8,543	8,8	0,7399	8,9	2
U024		420	0,004	0,001	0,072	10,35	9,6	0,7852	10	2
U025		456	0,012	0,001	0,080	24,36	8,5	0,6809	11	2
U026		474	0,008	0,001	0,0047	16,42	9,5	0,6913	9,1	2
U027		824	0,008	0,003	0,022	9,742	5,6	0,7986	7,0	2
U028		531	0,005	0,002	0,00049	9,974	11	0,7454	9,4	2
U029		479	0,009	0,001	0,0084	18,67	6,6	0,7319	8,8	2
U030	300	0,008	0,001	0,021	23,82	9,3	0,6357	12	2	
U031	578	0,006	0,002	0,089	11,36	6,9	0,7734	9,2	2	
U032	616	0,003	0,002	0,0015	5,264	10	0,7420	8,3	2	
U033	ABC32	412	0,10	0,002	0,072	123,6	8,0	0,3440	19	2
U034		3142	0,063	0,009	0,18	24,06	12	0,7298	4,8	2
U035		177	0,023	0,002	0,051	83,82	9,6	0,5059	14	2
U036		197	0,12	0,001	0,061	155,8	7,5	0,1950	13	2
U037		218	0,15	0,001	0,041	160,1	6,5	0,1736	14	2
U038		180	0,10	0,001	0,072	157,8	7,1	0,2135	15	2
U039		32877	0,13	0,092	0,33	5,365	3,9	0,7986	1,2	2
U047		483	0,051	0,002	0,11	77,82	7,3	0,5403	8,2	2
U048		451	0,052	0,002	0,15	81,80	9,1	0,5365	8,1	2
U049		164	0,086	0,001	0,21	158,9	6,4	0,2309	11	2
U050		202	0,096	0,001	0,20	141,2	11	0,2206	20	2
U051		152	0,072	0,001	0,20	143,7	7,2	0,2268	15	2
U052		209	0,093	0,001	0,20	145,1	9,3	0,2405	12	2
U053		116	0,017	0,000	0,27	90,41	14	0,4681	19	2
U054	112	0,070	0,001	0,30	151,2	6,8	0,1715	15	2	
U055	290	0,13	0,001	0,15	142,4	7,6	0,2304	12	2	
U056	170	0,031	0,001	0,14	94,25	10	0,4140	14	2	
U057	247	0,093	0,001	0,012	138,4	6,8	0,2697	11	2	
U058	189	0,078	0,001	0,0072	146,8	9,7	0,2449	20	2	
U059	179	0,037	0,001	0,035	116,0	8,8	0,3936	16	2	
U060	MGT15 - yellow	2650	0,016	0,009	0,23	5,487	5,2	0,8187	5,1	2
U061		2026	0,017	0,006	0,0075	9,065	5,9	0,8250	4,3	2
U062		2814	0,017	0,009	0,21	6,648	4,9	0,8414	3,8	2

U063		11515	0,025	0,035	0,10	2,327	7,0	0,8277	1,8	2
U064		6895	0,028	0,021	0,46	4,391	3,5	0,8359	2,6	2
U065		990	0,009	0,003	0,00057	9,622	7,4	0,8023	6,1	2
U066		6247	0,027	0,019	0,33	4,737	9,8	0,8343	2,8	2
U067		1102	0,019	0,004	0,47	15,83	7,2	0,7407	6,4	2
U068		975	0,034	0,003	0,011	30,81	5,3	0,6853	6,5	2
U069		1294	0,064	0,004	0,011	41,07	5,4	0,6503	5,8	2
U070		801	0,048	0,003	0,0014	45,40	4,3	0,5943	5,9	2
U071		1005	0,066	0,003	0,00094	49,84	5,0	0,5550	5,0	2
U072		1108	0,056	0,004	0,0046	43,35	4,4	0,6428	5,4	2
U073		1041	0,057	0,003	0,0013	44,41	5,4	0,6408	6,2	2
U074		1736	0,059	0,006	0,012	29,71	6,2	0,6872	5,7	2
U075		1026	0,044	0,004	0,059	35,02	4,9	0,6468	5,9	2
U076		1135	0,071	0,004	0,064	49,50	5,0	0,6267	5,6	2
U077		1043	0,072	0,003	0,0033	50,82	5,3	0,5857	6,4	2
U078		2021	0,069	0,007	0,0011	30,43	4,5	0,7090	4,2	2
U079		1582	0,051	0,005	0,00092	27,95	3,8	0,6881	4,7	2
U087	MGT15 - white	1656	0,028	0,006	0,087	15,96	4,1	0,7715	4,9	2
U088		4025	0,25	0,014	0,020	45,91	3,7	0,5756	2,9	2
U089		2157	0,014	0,007	0,075	6,150	4,3	0,7772	3,9	2
U090		1166	0,73	0,008	0,010	121,1	3,2	0,1515	5,0	2
U091		707	0,20	0,003	0,092	103,3	4,1	0,2838	5,7	2
U092		7070	0,11	0,024	1,64	14,43	3,3	0,7531	2,7	2
U093		2107	0,18	0,008	0,10	55,76	4,0	0,5345	4,1	2
U094		13873	0,18	0,047	2,03	11,79	5,2	0,7568	1,7	2
U095		422	0,18	0,002	0,11	107,6	4,5	0,2024	7,7	2
U096		373	0,30	0,003	0,021	127,0	3,9	0,1225	10,0	2
U097		865	0,21	0,006	0,020	98,21	4,0	0,3199	5,6	2
U098		307	0,019	0,001	0,064	44,28	9,1	0,6020	11	2
U099		146	0,047	0,001	0,28	102,8	7,4	0,2621	16	2
U100		425	0,062	0,003	0,032	73,61	7,8	0,4076	9,4	2
U101		238	0,003	0,001	0,024	13,86	13	0,7960	16	2
U102		1865	0,18	0,007	0,022	59,08	3,6	0,4946	4,0	2
U103		16920	0,052	0,055	9,84	3,217	3,0	0,8255	1,7	2
U104		11231	0,046	0,036	3,83	4,200	3,4	0,8129	1,7	2
U105		473	0,032	0,002	0,0071	49,41	6,5	0,5541	11	2
U106		956	0,050	0,003	0,034	39,48	5,2	0,6011	6,9	2
U107		1028	0,15	0,004	0,024	77,56	4,7	0,4146	6,0	2
U108	ABC22	119	0,042	0,001	0,040	89,63	8,0	0,1865	19	2
U109		355	0,11	0,002	0,041	91,51	5,3	0,2209	10	2
U110		2751	0,045	0,009	0,043	15,14	10	0,6989	3,9	2
U111		154	0,042	0,001	0,0079	87,40	7,1	0,2511	16	2
U112		761	0,14	0,003	0,058	72,95	5,1	0,3120	7,2	2
U113		2000	0,10	0,007	0,085	38,65	5,5	0,5845	4,8	2
U114		2206	0,082	0,007	0,065	31,63	7,8	0,6449	5,6	2
U115		1328	0,064	0,004	0,041	38,03	9,6	0,5520	6,0	2
U116		355	0,036	0,002	0,0016	55,50	7,2	0,4219	13	2
U117		71	0,072	0,001	0,046	103,6	5,9	0,07669	18	2
U118		128	0,020	0,001	0,0011	68,93	12	0,3367	19	2
U119		196	0,019	0,001	0,00006	58,58	10	0,3796	15	2
U120		383	0,039	0,002	0,055	52,48	7,0	0,4291	11	2
U121		116	0,049	0,001	0,57	95,67	7,2	0,1905	20	2
U122		49	0,030	0,000	0,13	103,3	8,1	0,1156	25	2

U123		158	0,044	0,001	0,028	81,66	7,6	0,2328	15	2
U124		413	0,060	0,002	0,019	69,48	6,2	0,3800	8,6	2
U125		78	0,073	0,001	0,0031	105,9	7,6	0,09368	20	2
U126		176	0,064	0,005	0,086	92,11	6,7	0,2030	14	2
U127		167	0,099	0,001	0,056	100,5	5,9	0,1335	13	2
U128	BX26	8006	0,11	0,026	0,34	13,77	3,3	0,7663	2,4	2
U129		34676	0,10	0,11	0,57	3,035	2,9	0,8280	1,3	2
U137		2088	0,031	0,007	0,38	13,81	4,4	0,7444	4,2	2
U138		3872	0,046	0,013	0,89	11,46	3,5	0,7803	3,3	2
U139		84738	0,22	0,28	0,20	2,633	2,8	0,8322	0,83	2
U140		2414	0,090	0,009	1,05	30,45	3,7	0,6540	4,1	2
U141		7499	0,26	0,026	0,37	29,31	4,0	0,6829	2,4	2
U142		502	0,25	0,003	0,079	115,3	4,7	0,1884	7,7	2
U143		960	0,22	0,005	0,34	93,05	3,7	0,3329	5,5	2
U144		1268	0,050	0,004	0,23	34,22	4,9	0,6772	6,0	2
U145		1083	0,11	0,004	0,29	63,93	5,4	0,5019	5,0	2
U146		4173	0,13	0,014	0,33	26,70	3,9	0,6977	3,4	2
U147		601	0,20	0,003	0,15	106,4	3,9	0,2655	6,4	2
U148		5675	0,26	0,020	0,066	36,68	3,4	0,6522	2,6	2
U149		5616	0,022	0,018	1,26	3,973	3,6	0,8126	2,7	2
U150		5044	0,20	0,022	0,14	32,84	3,2	0,6696	3,0	2
U151		335	0,021	0,001	0,12	47,87	8,3	0,6137	9,9	2
U152		1811	0,13	0,007	0,41	49,29	3,9	0,5787	4,8	2
U153		2926	0,065	0,010	0,56	19,72	4,1	0,7091	3,6	2
U154		2702	0,19	0,010	0,21	52,18	4,0	0,6057	4,1	2
U155		2612	0,27	0,010	0,16	63,56	3,6	0,5052	4,6	2
U156	BX28	4165	0,066	0,014	0,15	15,34	3,8	0,8011	3,6	2
U157		345	0,090	0,001	0,11	126,5	6,0	0,4037	9,7	2
U158		3671	0,068	0,012	0,34	17,49	6,1	0,7528	3,8	2
U159		4167	0,11	0,014	0,24	23,85	4,4	0,7392	3,2	2
U160		1433	0,040	0,005	0,29	27,41	5,0	0,7770	5,5	2
U161		3668	0,12	0,013	0,059	30,54	3,7	0,7479	3,7	2
U162		7026	0,086	0,023	0,15	12,50	3,8	0,7999	2,6	2
U163		181	0,080	0,001	0,13	159,6	7,4	0,2923	13	2
U164		325	0,057	0,001	0,14	106,4	7,6	0,4963	11	2
U165		205	0,090	0,001	0,053	186,1	8,4	0,2521	22	2
U166		419	0,062	0,001	0,17	95,61	6,1	0,5241	9,0	2
U167		423	0,073	0,002	0,092	110,1	6,5	0,5124	8,3	2
U168		262	0,16	0,001	0,072	179,1	5,3	0,2391	11	2
U169		5143	0,099	0,017	0,34	18,25	5,7	0,7637	3,0	2
U170		4090	0,13	0,014	0,26	29,25	3,2	0,7348	3,5	2
U171		6094	0,10	0,020	0,025	16,00	3,0	0,7902	2,3	2
U172		1020	0,23	0,004	0,23	118,5	4,3	0,4212	5,2	2
U173		3683	0,14	0,012	0,64	34,62	4,1	0,7423	3,1	2
U174		21961	0,058	0,073	0,044	2,695	3,1	0,8289	1,4	2
U175		212	0,062	0,001	0,13	131,7	8,0	0,3613	11	2
U278	MGT24	873	0,021	0,003	0,0050	19,92	6,4	0,7368	7,7	2
U279		621	0,014	0,002	0,047	18,76	7,7	0,7312	9,3	2
U280		896	0,015	0,003	0,44	14,20	6,6	0,7679	6,4	2
U281		699	0,011	0,002	0,15	14,81	5,9	0,7976	8,7	2
U282		896	0,019	0,003	1,35	18,61	5,3	0,7494	6,4	2
U283		749	0,021	0,003	0,0031	23,76	5,1	0,7327	6,8	2
U284		700	0,014	0,003	0,45	17,52	6,9	0,7430	8,3	2

U285		670	0,009	0,002	0,075	11,34	6,1	0,7587	7,6	2
U286		848	0,011	0,003	0,34	12,70	6,9	0,8045	7,2	2
U287		878	0,017	0,003	0,33	17,77	6,7	0,7829	7,7	2
U288		1945	0,014	0,007	1,77	6,565	4,7	0,7956	4,4	2
U289		648	0,011	0,002	0,0018	15,58	7,6	0,7635	7,3	2
U290		794	0,016	0,003	0,023	17,61	5,5	0,7470	5,7	2
U291		1102	0,014	0,004	0,13	11,67	6,3	0,7966	6,8	2
U292		644	0,024	0,002	0,13	30,16	7,1	0,6638	9,2	2
U293		390	0,016	0,002	0,24	29,67	6,7	0,6421	10	2
U294		946	0,017	0,004	0,16	14,22	5,5	0,7247	5,6	2
U295		750	0,014	0,003	0,040	14,65	5,0	0,7101	6,1	2
U296		642	0,017	0,002	0,0022	22,38	6,1	0,7175	8,5	2
U297		686	0,031	0,003	0,070	31,46	5,5	0,6222	6,8	2
U298		358	0,026	0,001	0,52	47,23	7,5	0,5731	9,8	2
U299		843	0,017	0,003	0,63	17,24	6,1	0,7434	7,1	2
U300		657	0,025	0,003	1,29	29,45	6,0	0,6577	7,9	2
U301		1289	0,027	0,005	0,29	17,31	5,8	0,7371	5,9	2
U317	MGT-2	12484	2,8	0,050	0,00001	137,3	2,9	0,5398	1,9	2
U318		10078	1,1	0,038	0,00001	80,88	3,2	0,6587	1,8	2
U319		12563	1,4	0,048	0,00000	85,23	2,8	0,6557	1,7	2
U320		23498	4,2	0,094	0,00024	115,9	2,9	0,5760	1,5	2
U321		10194	1,4	0,039	-0,00001	97,01	3,0	0,6255	2,1	2
U322		10100	2,5	0,042	0,00002	146,3	3,2	0,5159	1,7	2
U323		3812	3,0	0,020	0,00011	249,5	2,7	0,2796	2,9	2
U325		10052	1,0	0,039	0,00000	74,24	3,1	0,6572	2,0	2
U326		44016	1,1	0,15	0,00000	26,03	4,5	0,7826	1,2	2
U327	MGT20	25210	0,23	0,092	0,0023	8,141	2,7	0,7808	1,4	2
U328		22568	0,27	0,084	0,00011	10,36	3,6	0,7855	1,6	2
U329		5512	0,34	0,022	0,00072	43,90	3,7	0,6294	2,7	2
U330		18796	0,17	0,069	0,021	7,965	2,8	0,7837	1,4	2
U331		26464	0,36	0,098	0,00013	11,93	2,9	0,7666	1,9	2
U332		26895	0,29	0,100	0,00039	9,537	3,1	0,7819	1,3	2
U333		38753	0,44	0,14	0,00011	9,967	2,9	0,7841	1,2	2
U334		28162	0,18	0,10	0,00051	5,606	2,7	0,7944	1,4	2
U335		24524	0,14	0,089	0,29	5,131	15	0,8021	1,6	2
U336		25973	0,053	0,096	0,0031	1,875	3,1	0,8208	1,4	2
U337		23757	0,044	0,087	0,00010	1,692	3,1	0,8198	1,5	2
U338		14949	0,15	0,055	0,0021	9,047	2,8	0,7858	1,9	2
U339		21817	0,13	0,079	0,012	5,443	3,4	0,8046	1,4	2
U340		28474	0,058	0,10	0,018	1,870	3,5	0,8204	1,6	2
U341		26420	0,19	0,097	0,0034	6,334	3,1	0,8094	1,3	2
U342		28312	0,19	0,10	0,0040	6,100	2,7	0,8080	1,4	2
U343		17131	0,10	0,063	0,0014	5,376	3,3	0,8161	1,9	2
U344		16197	0,18	0,059	0,0018	9,627	3,0	0,7970	1,9	2
U345		21491	0,072	0,079	0,014	3,042	3,2	0,8164	1,5	2
U429	BX47a	860	0,074	0,004	0,30	44,03	5,5	0,4806	7,0	2
U437		7997	0,19	0,032	0,15	17,88	3,4	0,6885	2,3	2
U438		7532	0,092	0,030	0,12	9,642	3,5	0,7318	2,1	2
U439		500	0,22	0,003	0,18	85,18	4,5	0,1756	6,8	2
U440		850	0,13	0,005	0,59	57,60	4,8	0,3529	4,8	2
U441		4682	0,13	0,020	0,23	18,98	4,6	0,6521	3,0	2
U442		6449	0,15	0,026	0,47	16,83	3,1	0,6718	2,5	2
U443		8557	0,32	0,036	0,26	24,15	3,8	0,6155	2,3	2

U444		3979	0,065	0,016	0,20	12,69	4,3	0,7232	3,1	2
U445		3537	0,10	0,014	0,10	20,63	4,1	0,6635	3,3	2
U446		13879	0,095	0,053	0,39	5,769	3,1	0,7858	1,7	2
U447		2095	0,11	0,009	0,30	31,01	4,2	0,5748	4,5	2
U448		6674	0,21	0,028	0,27	21,21	4,0	0,6454	2,5	2
U449		8744	0,18	0,035	0,076	15,14	3,4	0,6921	1,8	2
U450		5479	0,28	0,023	0,15	31,88	3,4	0,5771	2,9	2
U451		339	0,13	0,002	0,23	78,27	4,2	0,1956	6,8	2
U452		1031	0,29	0,006	0,18	72,48	3,6	0,2440	4,0	2
U453		950	0,27	0,006	0,19	72,98	4,2	0,2458	5,4	2
U454		236	0,12	0,002	0,22	85,68	4,9	0,1495	9,2	2
U455		745	0,077	0,003	0,20	48,76	5,7	0,4311	7,7	2
U456	BX47 b (or also a)_	63904	0,24	0,25	0,030	3,093	13	0,8018	0,96	2
U457		13815	7,7	0,11	0,0030	85,27	2,6	0,1428	1,1	2
U458		24980	8,9	0,16	0,0063	76,94	2,6	0,2048	1,4	2
U459		4904	0,066	0,020	0,097	10,26	4,8	0,7187	2,6	2
U460		6367	1,0	0,033	0,011	58,66	2,8	0,3356	2,5	2
U461		18124	0,22	0,072	0,095	9,339	3,7	0,7263	1,5	2
U462		11909	0,92	0,052	0,035	41,03	3,2	0,4979	1,9	2
U463		14784	0,27	0,059	0,20	13,66	4,1	0,7001	1,8	2
U464		13435	7,8	0,11	0,0034	85,12	2,6	0,1382	1,7	2
U465		27951	8,4	0,17	0,015	74,00	2,6	0,2333	1,9	2
U466		6086	3,4	0,049	0,0057	83,49	2,7	0,1418	2,0	2
U467		9960	2,5	0,057	0,0049	67,93	3,3	0,2605	2,6	2
U468		9812	0,028	0,039	0,36	2,240	8,2	0,8102	2,1	2
U469		30756	4,3	0,15	0,012	56,84	2,7	0,3818	1,3	2
U470		12024	1,2	0,055	0,019	45,83	3,5	0,4347	3,0	2
U471		38799	6,0	0,20	0,0051	54,30	2,9	0,3279	2,1	2
U472		114622	3,1	0,47	0,025	18,87	4,5	0,6514	1,2	2
U473		24638	0,006	0,10	0,21	0,1997	5,7	0,8321	1,4	2
U474		29299	1,3	0,13	0,056	25,79	2,8	0,5767	1,0	2
U475		31352	8,0	0,18	0,0088	72,85	2,7	0,2715	1,4	2
U476	MGT-35a	444	0,12	0,003	0,060	79,23	5,4	0,2794	8,1	2
U477		280	0,12	0,002	0,016	87,14	4,4	0,1900	12	2
U478		439	0,12	0,003	0,065	74,55	5,4	0,2611	6,8	2
U479		678	0,20	0,004	0,045	81,11	3,8	0,2631	6,4	2
U480		801	0,095	0,004	0,068	55,63	5,2	0,4476	6,6	2
U481		312	0,16	0,002	0,0062	91,77	4,5	0,1710	7,5	2
U482		268	0,11	0,002	0,0071	83,94	4,8	0,1975	8,5	2
U483		708	0,11	0,004	0,0075	60,74	4,3	0,3750	7,0	2
U484		626	0,097	0,003	0,017	63,00	4,8	0,3839	7,5	2
U485		513	0,11	0,003	0,0085	71,89	4,4	0,3201	7,0	2
U486		370	0,095	0,002	0,059	77,17	4,9	0,2812	8,7	2
U487		561	0,14	0,010	0,034	74,31	3,9	0,2919	6,7	2
U488		416	0,13	0,002	0,032	81,41	5,9	0,2571	9,6	2
U489		2132	0,10	0,009	0,042	30,73	4,0	0,5879	4,1	2
U497		2654	0,10	0,011	0,028	25,62	4,0	0,6419	3,5	2
U498		8625	0,10	0,033	0,036	10,03	5,1	0,7465	2,5	2
U499		1420	0,068	0,006	0,019	31,49	4,3	0,6191	4,6	2
U500		313	0,088	0,002	0,010	80,03	5,8	0,2750	8,9	2
U501		943	0,17	0,005	0,022	66,19	3,7	0,3516	4,0	2
U502		483	0,100	0,003	0,030	71,61	4,5	0,3265	7,1	2
U503	MGT-35b	282	0,066	0,002	0,00058	108,2	6,3	0,4312	10	2

U504		816	0,064	0,003	0,00041	52,73	5,7	0,6493	6,7	2
U505		370	0,081	0,002	0,00047	99,93	5,9	0,4542	10	2
U506		312	0,025	0,001	0,0012	53,67	7,8	0,6141	9,7	2
U507		380	0,099	0,002	0,00020	119,1	6,7	0,4258	9,7	2
U508		257	0,039	0,001	0,00084	87,17	9,6	0,5327	12	2
U509		401	0,075	0,002	0,00047	93,32	7,4	0,4753	13	2
U510		451	0,071	0,002	0,00057	88,16	7,0	0,5210	10	2
U511		468	0,059	0,002	0,00018	74,96	6,1	0,5780	11	2
U512		303	0,028	0,001	0,00093	58,00	8,5	0,6195	10	2
U513		460	0,062	0,002	0,00089	79,88	8,6	0,5584	9,5	2
U514		367	0,043	0,002	0,00033	73,54	6,5	0,5888	9,0	2
U515		201	0,070	0,001	0,00048	127,8	7,7	0,3576	11	2
U516		310	0,057	0,001	0,0062	94,87	6,9	0,5066	13	2
U517		410	0,064	0,002	0,00004	89,04	6,8	0,5360	11	2
U518		317	0,091	0,001	0,00050	126,9	6,4	0,4208	11	2
U519		357	0,054	0,002	0,00058	83,92	7,0	0,5291	8,8	2
U520		293	0,098	0,001	0,022	134,7	6,6	0,3853	12	2
U521		465	0,16	0,002	0,0010	135,4	5,8	0,3781	8,8	2
U522		818	0,15	0,004	0,00011	94,52	4,8	0,4973	6,0	2
U523		426	0,061	0,002	0,00089	76,52	6,6	0,5313	7,3	2
U524	MGT33	52776	0,13	0,21	0,36	2,073	2,8	0,8095	1,1	2
U525		49097	0,38	0,20	0,0047	6,409	4,7	0,8036	1,1	2
U526		175698	0,058	0,69	0,77	0,2789	2,8	0,8144	0,73	2
U527		62828	0,24	0,25	0,053	3,214	2,8	0,8102	1,2	2
U528		46166	0,26	0,18	0,035	4,762	2,9	0,8097	1,1	2
U529		11339	0,19	0,045	0,14	13,83	3,0	0,7986	1,7	2
U530		42593	0,20	0,17	0,10	4,044	2,9	0,8114	1,2	2
U531		40335	0,24	0,16	0,099	5,062	2,8	0,8099	1,2	2
U532		34970	0,28	0,14	0,030	6,525	2,9	0,8058	1,2	2
U533		75637	0,12	0,30	0,094	1,321	2,7	0,8115	0,92	2
U534		91930	0,17	0,36	0,086	1,568	3,1	0,8170	0,77	2
U535		54866	0,25	0,22	0,033	3,745	3,0	0,8067	1,1	2
U536		134769	0,72	0,54	0,016	4,441	3,6	0,8085	0,73	2
U537		193107	0,31	0,76	0,049	1,346	2,9	0,8095	0,61	2
U538		58400	0,48	0,23	0,030	6,860	2,9	0,8061	0,98	2
U539		98997	0,32	0,40	0,12	2,695	2,7	0,8094	0,73	2
U547		88758	0,15	0,35	0,21	1,366	3,4	0,8091	0,83	2
U548		13398	0,27	0,053	0,095	16,72	2,9	0,7949	1,6	2
U549		43621	0,26	0,17	0,050	4,921	3,4	0,8116	1,3	2
U550		78744	0,17	0,31	0,097	1,797	2,8	0,8133	0,98	2
U551		13445	0,16	0,054	0,19	9,622	3,4	0,8044	1,6	2
U553	ABC34	664	0,69	0,008	0,00000	90,32	3,1	0,08493	5,3	2
U554		1707	0,52	0,011	0,0026	73,67	3,1	0,2382	4,2	2
U555		1909	2,1	0,024	0,00001	91,06	2,8	0,08062	3,3	2
U556		3970	0,31	0,018	0,019	40,35	3,3	0,4962	2,8	2
U557		15241	2,5	0,078	0,0014	59,38	2,8	0,3464	1,5	2
U558		5585	1,2	0,031	0,0022	64,77	3,0	0,3031	3,3	2
U559		2974	3,6	0,039	0,00008	90,43	2,7	0,07390	2,5	2
U560		86189	0,17	0,34	0,33	1,706	3,4	0,8106	0,89	2
U561		164005	0,021	0,66	0,0083	0,1041	5,4	0,8190	0,67	2
U563		1795	0,27	0,009	0,016	58,08	3,4	0,3758	3,8	2
U564		28983	0,88	0,12	0,072	21,97	3,4	0,6485	1,3	2
U565		3275	2,9	0,035	0,00057	88,35	2,7	0,09821	3,0	2

U571	DX46	14365	0,068	0,058	0,0023	3,838	2,9	0,7998	1,5	2
U572		7728	0,090	0,031	0,0037	9,302	3,4	0,7667	2,7	2
U573		12470	0,071	0,051	0,0011	4,646	3,1	0,7980	2,2	2
U574		4975	0,057	0,020	0,016	9,102	3,6	0,7848	3,1	2
U575		3525	0,046	0,011	0,015	23,36	5,6	0,6898	4,7	2
U576		7485	0,044	0,030	0,00044	4,927	3,4	0,8130	2,6	2
U577		7291	0,047	0,029	0,00032	5,255	3,3	0,8001	2,3	2
U578		1075	0,045	0,005	0,00082	28,38	5,8	0,6725	6,0	2
U579		1436	0,14	0,007	0,00012	52,08	4,4	0,5462	4,1	2
U580		14544	0,061	0,059	0,0029	3,451	3,5	0,8172	1,7	2
U581		1008	0,034	0,004	0,00017	24,14	6,3	0,7013	5,0	2
U582		956	0,042	0,004	0,00018	30,02	6,5	0,6766	7,3	2
U583		1008	0,036	0,004	0,00000	24,63	5,2	0,6822	5,5	2
U584		2005	0,055	0,008	0,00000	20,31	4,4	0,7336	4,2	2
U586		1976	0,037	0,008	0,0013	14,06	4,7	0,7426	3,9	2
U587		9765	0,085	0,040	0,00027	6,975	3,6	0,7837	1,9	2
U588		5894	0,069	0,024	0,0011	9,044	3,0	0,7509	2,3	2
U589		2186	0,027	0,009	0,00010	9,913	6,7	0,7714	3,8	2
U590		1732	0,16	0,008	0,00011	52,96	4,5	0,5599	5,2	2
U591		1790	0,043	0,007	0,00013	17,44	5,0	0,7382	4,3	2
RM ₀ (n=24) ^g		544197	37	37	1,01	3,483	0,68	0,9073	0,55	2
RM ₁ (n=22) ^g		18802	3,7	0,17	0,00084	23,29	6,3	0,1016	46	2
RM ₂ (n=12) ^g		29943	15	0,14	0,00003	209,8	98	0,2911	157	2
RM ₃ (n=11) ^g		4157	0,66	0,015	0,00096	82,14	137	0,4338	139	2
RM ₄ (n=12) ^g		38739	0,93	0,14	0,00006	20,24	18	0,7208	2,4	2

^a Within run background-corrected mean ²⁰⁷Pb signal in cps (counts per second).

^b U and Pb concentrations and Th/U ratio were calculated relative to the primary reference material.

^d Corrected for background, within-run Pb/U fractionation (in case of ²⁰⁶Pb/²³⁸U) and subsequently normalised to the primary reference material (ID-TIMS value/measured value).

^g RM_i: Reference material 1.

Accuracy and reproducibility was checked by repeated analyses of secondary reference materials; data given as mean with 2 standard deviation uncertainties.

RM₀										
A001	NIST612	608138	37	36	1,01	3,480	0,47	0,9103	0,45	2
A002	NIST612	613411	37	37	1,01	3,484	0,46	0,9067	0,39	2
A040	NIST612	602124	37	37	1,01	3,505	0,38	0,9083	0,34	2
A041	NIST612	608596	37	37	1,01	3,467	0,48	0,9060	0,35	2
A080	NIST612	597485	37	37	1,01	3,480	0,45	0,9035	0,31	2
A081	NIST612	601124	38	37	1,01	3,481	0,34	0,9075	0,35	2
A130	NIST612	591213	38	38	1,01	3,497	0,31	0,9056	0,30	2
A131	NIST612	581700	37	37	1,02	3,481	0,44	0,9067	0,34	2
A190	NIST612	569105	38	37	1,01	3,488	0,34	0,9096	0,32	2
A191	NIST612	560419	37	37	1,01	3,462	0,36	0,9085	0,28	2
A250	NIST612	545408	37	37	1,01	3,501	0,38	0,9086	0,29	2
A251	NIST612	557930	38	38	1,01	3,483	0,38	0,9058	0,35	2
A310	NIST612	539398	38	38	1,01	3,478	0,40	0,9126	0,28	2
A311	NIST612	548638	38	38	1,01	3,466	0,33	0,9049	0,28	2

A370	NIST612	509863	37	37	1,01	3,505	0,26	0,9068	0,31	2
A371	NIST612	533059	38	38	1,02	3,470	0,36	0,9071	0,27	2
A430	NIST612	507534	38	37	1,01	3,501	0,31	0,9108	0,33	2
A431	NIST612	508273	38	38	1,00	3,477	0,26	0,9023	0,26	2
A490	NIST612	498256	38	38	1,02	3,478	0,33	0,9062	0,21	2
A491	NIST612	495190	38	37	1,01	3,486	0,34	0,9085	0,31	2
A540	NIST612	480940	37	37	1,01	3,476	0,33	0,9027	0,32	2
A541	NIST612	478761	37	37	1,01	3,478	0,35	0,9098	0,27	2
A592	NIST612	457866	36	36	1,01	3,485	0,29	0,9074	0,24	2
A593	NIST612	466294	37	37	1,01	3,488	0,36	0,9090	0,28	2
		544197	37	37	1,01	3,483	0,68	0,9073	0,55	2

RM₁

B003	WC-1	17514	2,5	0,11	0,00049	22,83	2,8	0,1058	15	2
B004	WC-1	20371	4,3	0,19	0,00095	23,39	2,6	0,08058	2,6	2
B042	WC-1	25632	3,4	0,17	0,00034	22,38	2,6	0,1284	1,4	2
B043	WC-1	22092	4,3	0,19	0,0020	23,24	2,6	0,09154	2,6	2
B082	WC-1	16890	2,3	0,12	0,00028	22,41	2,6	0,1286	1,6	2
B083	WC-1	16972	3,7	0,16	0,00091	23,70	2,6	0,08462	1,7	2
B132	WC-1	26196	3,3	0,18	0,00027	22,26	2,6	0,1386	1,4	2
B133	WC-1	17392	3,1	0,14	0,00047	22,79	2,6	0,09871	4,5	2
B192	WC-1	28900	4,8	0,23	0,00093	23,32	2,6	0,1166	1,6	2
B193	WC-1	15481	3,6	0,15	0,0013	23,79	2,6	0,08463	1,4	2
B252	WC-1	11488	2,8	0,12	0,00034	23,76	2,6	0,08272	1,8	2
B253	WC-1	15085	3,6	0,15	0,0019	23,88	2,6	0,08148	2,6	2
B312	WC-1	15200	2,8	0,13	0,00030	23,13	2,6	0,1086	2,3	2
B313	WC-1	13499	3,2	0,14	0,00050	23,55	2,6	0,08415	3,7	2
B372	WC-1	12564	2,8	0,12	0,00018	23,68	2,6	0,09344	2,0	2
B373	WC-1	21868	3,5	0,18	0,0018	22,60	2,7	0,1255	3,2	2
B433	WC-1	12255	3,0	0,13	0,00077	24,00	2,6	0,08923	1,9	2
B493	WC-1	11450	3,8	0,15	0,00042	24,66	2,6	0,07090	2,0	2
B542	WC-1	27656	3,7	0,21	0,00091	21,74	2,6	0,1553	1,1	2
B543	WC-1	12106	3,5	0,15	0,00065	23,83	2,6	0,07870	2,8	2
B594	WC-1	24298	4,3	0,22	0,0017	22,91	2,6	0,1268	1,2	2
B595	WC-1	28743	8,5	0,35	0,0011	24,46	2,6	0,08035	2,6	2
		18802	3,7	0,17	0,00084	23,29	6,3	0,1016	46	2

RM₂

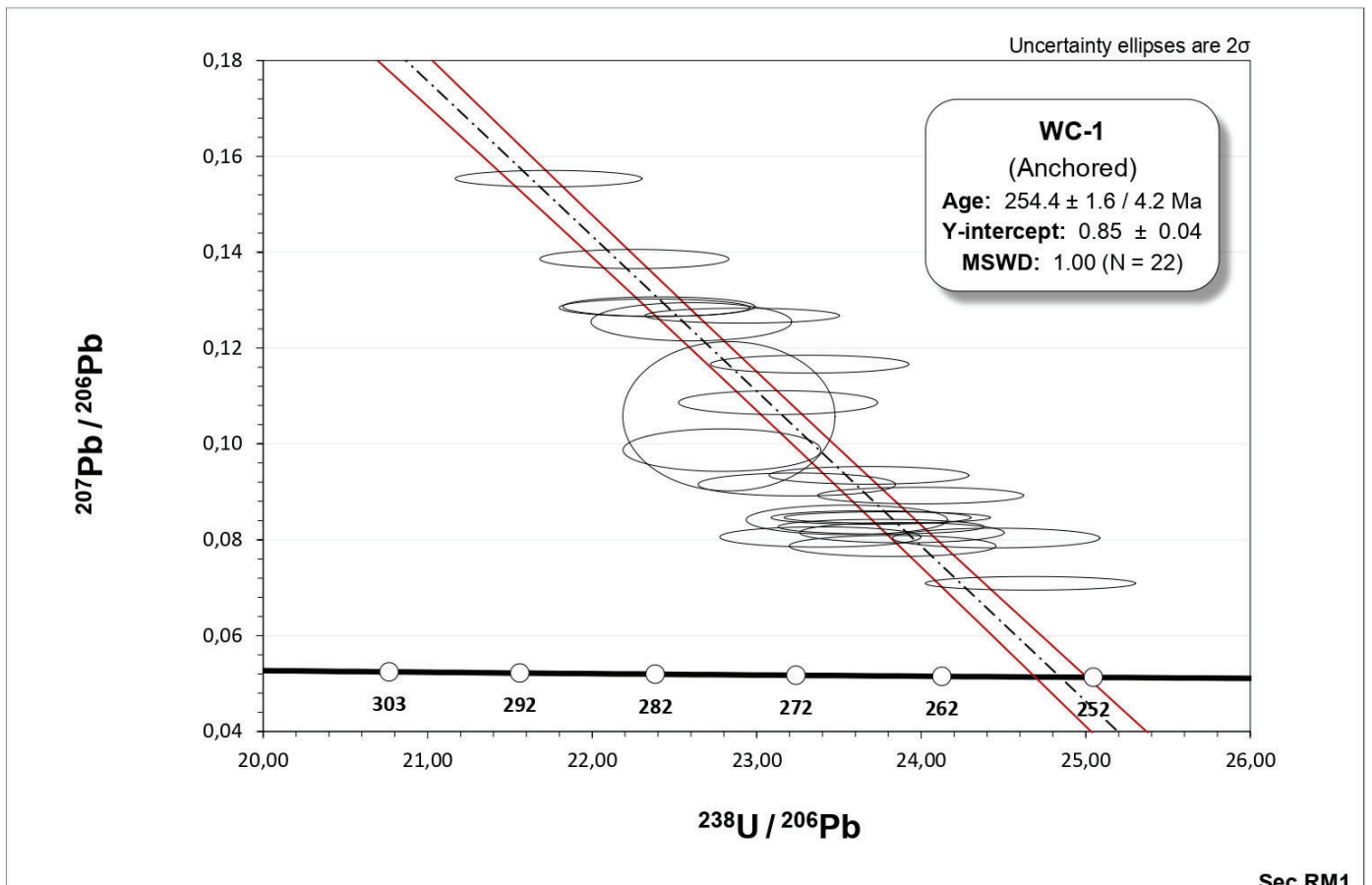
D006	B6	15921	1,9	0,044	0,0011	87,10	9,8	0,3845	18	2
D045	B6	6923	0,44	0,022	0,0011	60,81	7,7	0,5341	8,2	2
D085	B6	777	0,79	0,006	0,00099	148,7	8,6	0,1019	11	2
D135	B6	1500	0,71	0,007	0,0014	136,3	5,0	0,1664	19	2
D195	B6	4127	0,85	0,018	0,0020	92,35	4,1	0,3620	4,2	2
D315	B6	5947	0,030	0,022	0,00081	4,704	4,8	0,8617	2,8	2
D375	B6	1016	0,053	0,004	0,0011	40,18	7,8	0,6833	9,9	2
D435	B6	2190	0,077	0,008	0,00005	27,49	7,0	0,7224	4,7	2
D495	B6	6124	0,098	0,024	0,00031	13,57	5,0	0,7996	3,6	2
D545	B6	809	1,6	0,011	0,00004	149,2	3,1	0,06951	8,6	2
D597	B6	398	0,71	0,005	0,0018	143,1	4,2	0,08655	15	2
		4157	0,66	0,015	0,00096	82,14	137	0,4338	139	2

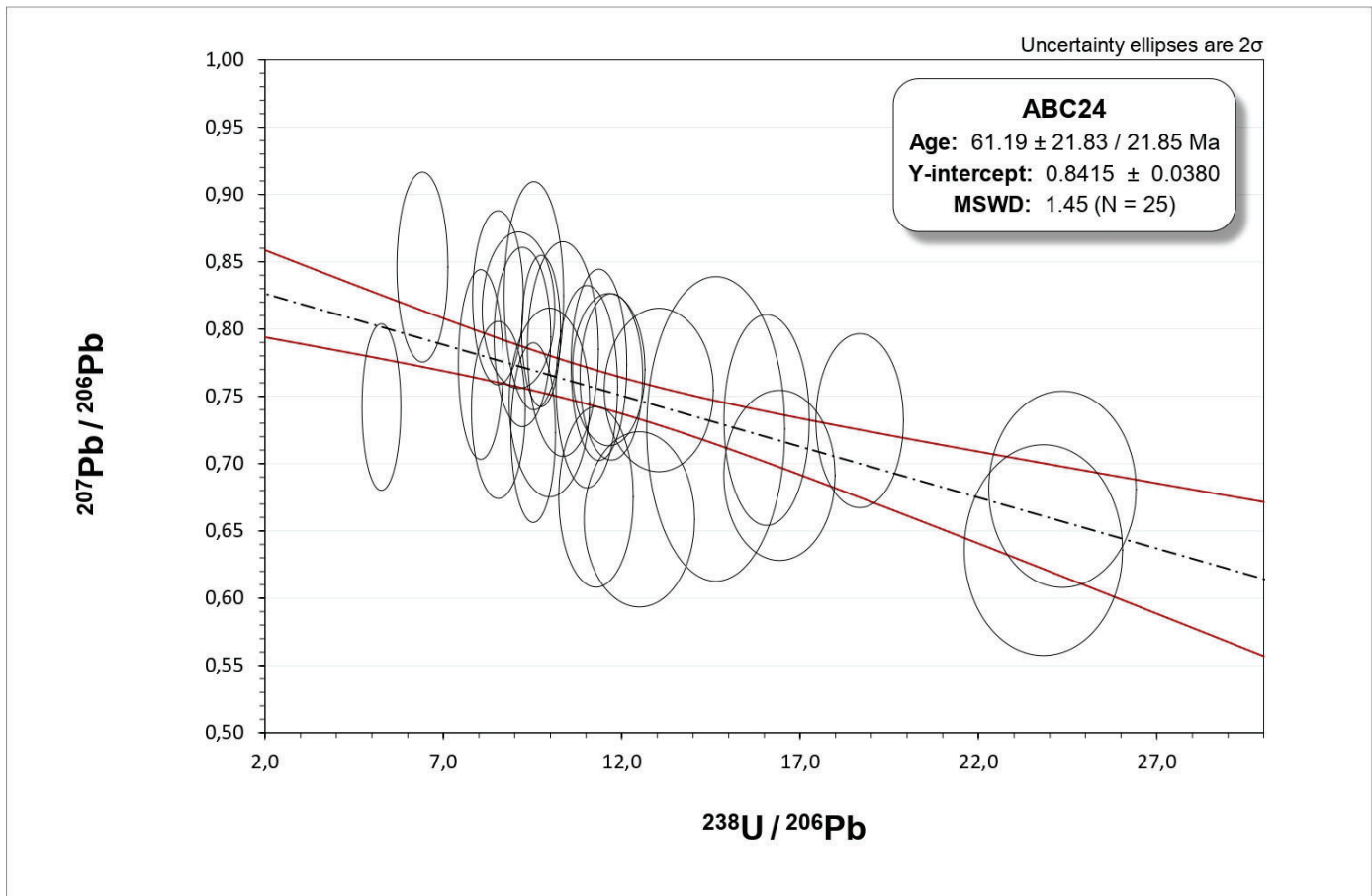
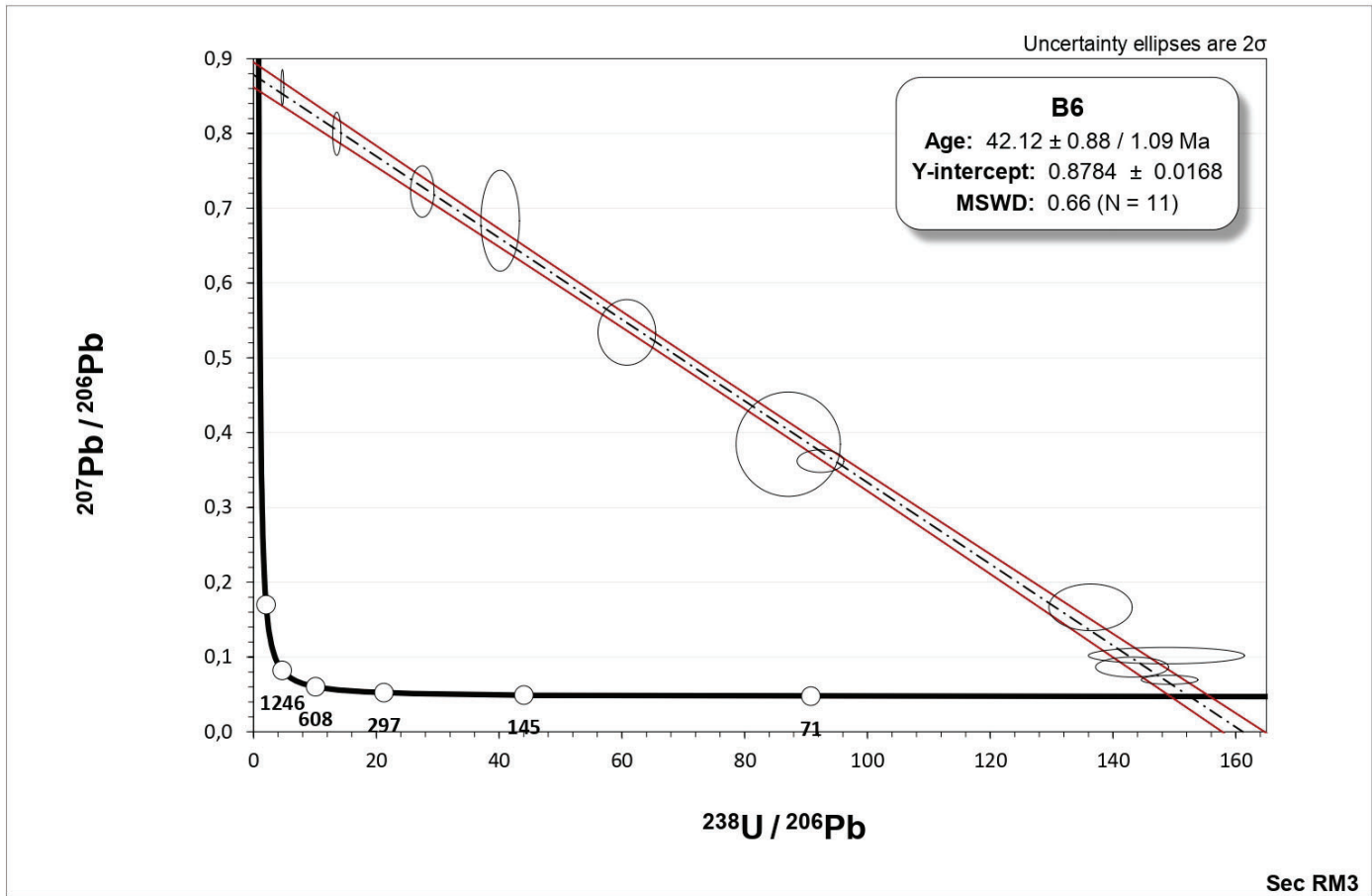
RM₃

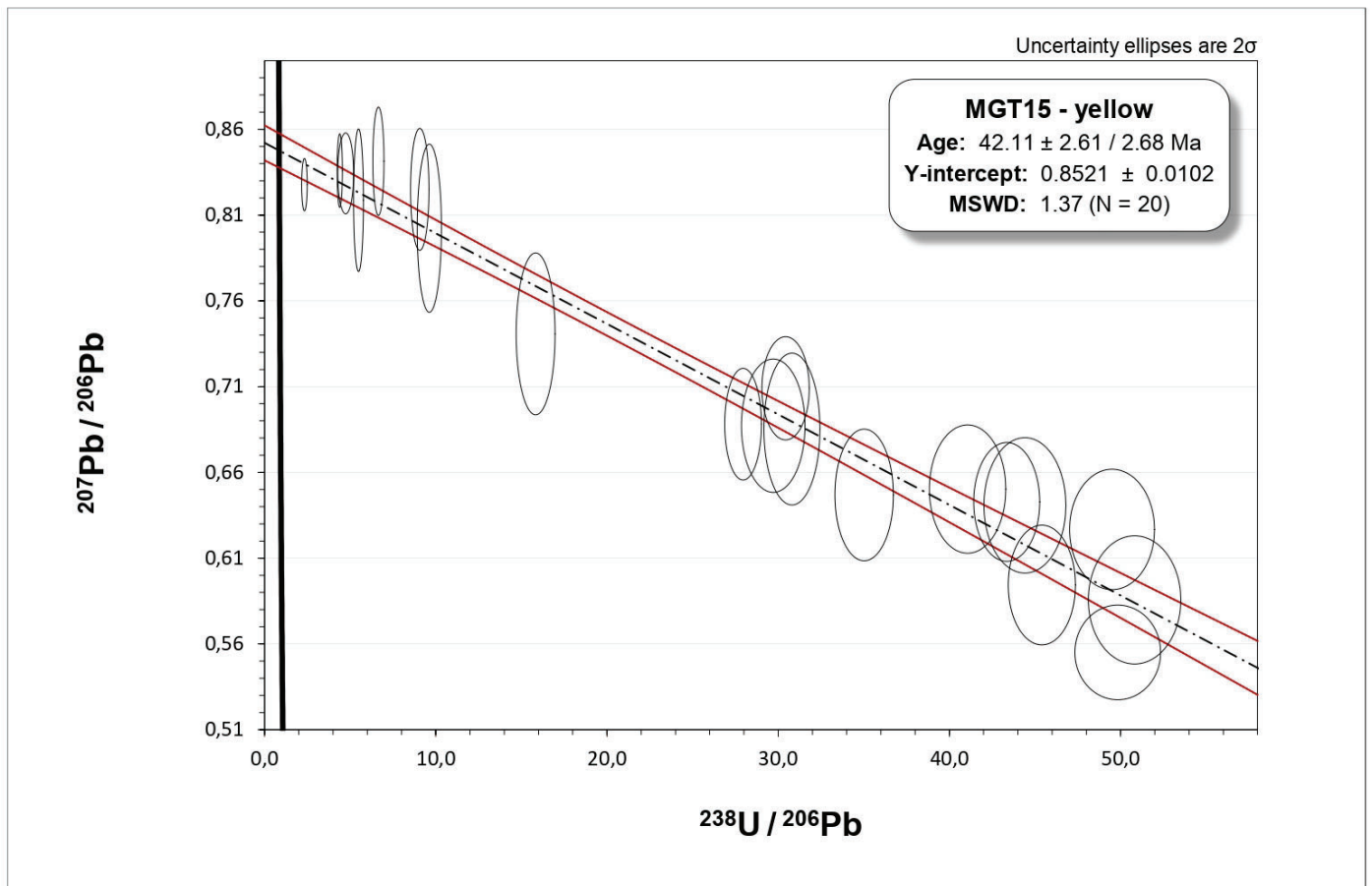
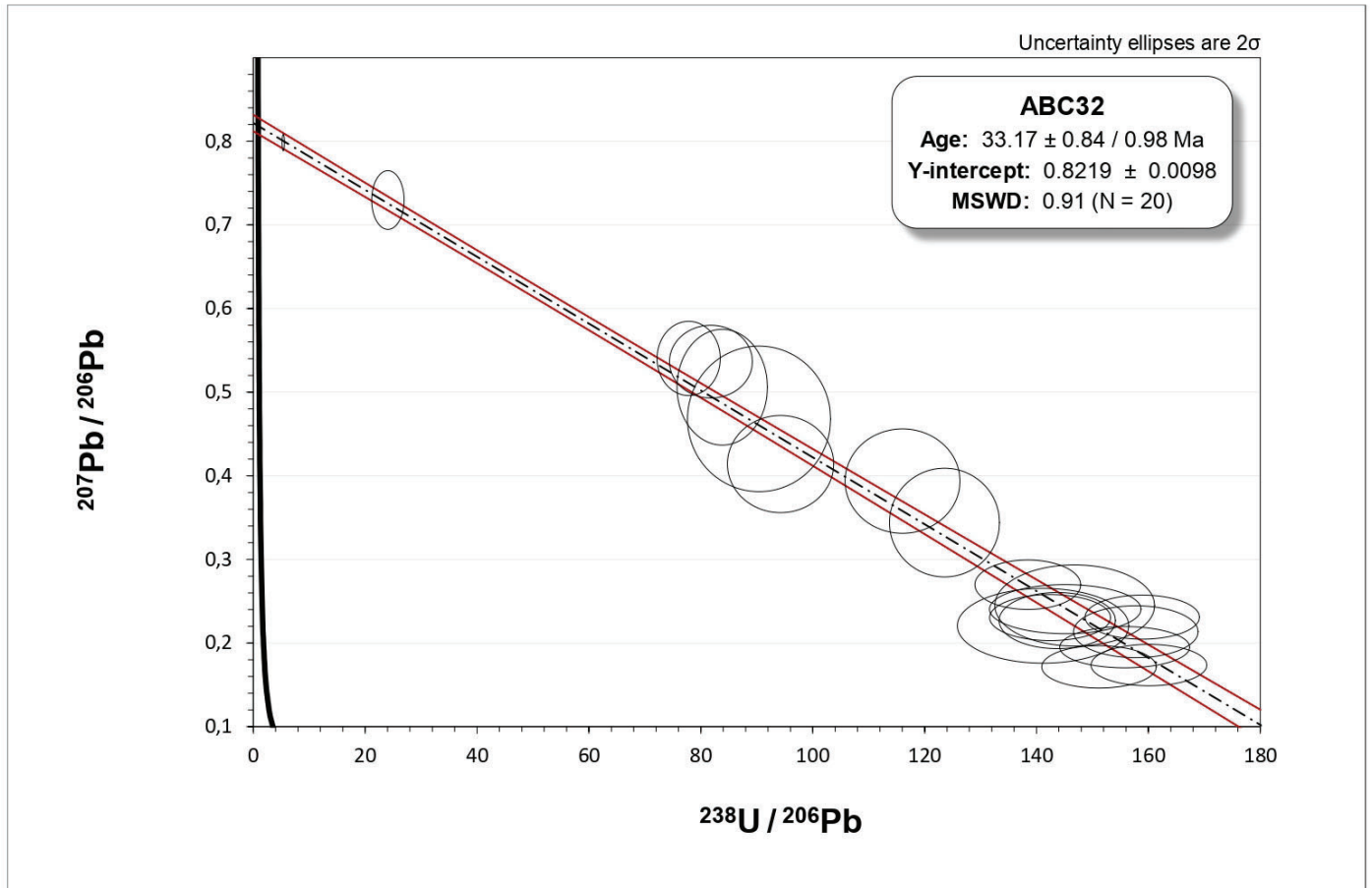
E007	CalGrun	44877	0,81	0,14	0,00010	17,55	2,6	0,7330	1,2	2
E046	CalGrun	43864	0,85	0,14	0,00003	18,25	2,7	0,7280	1,00	2
E086	CalGrun	42139	0,90	0,14	0,00006	19,83	2,7	0,7227	1,2	2

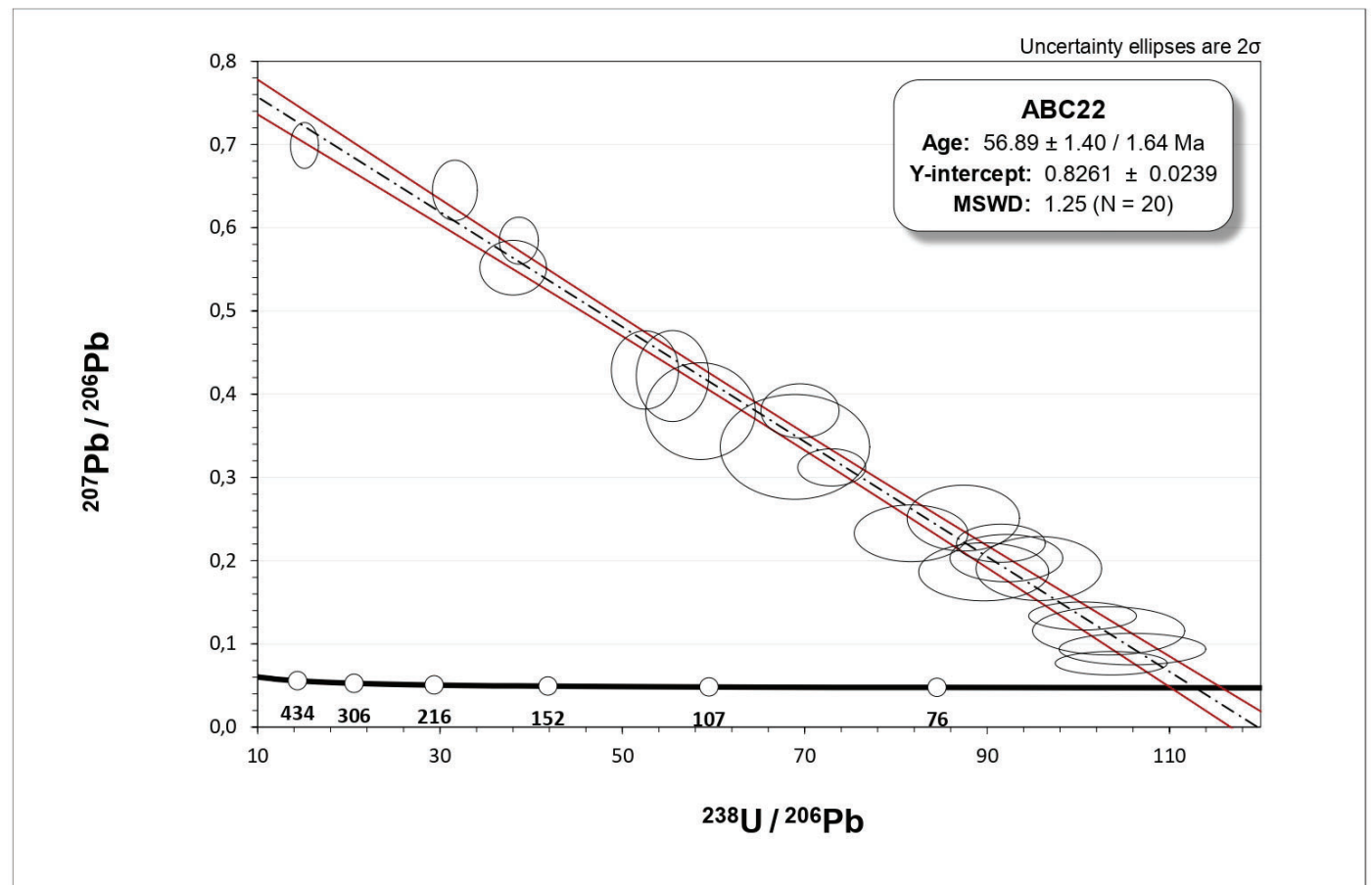
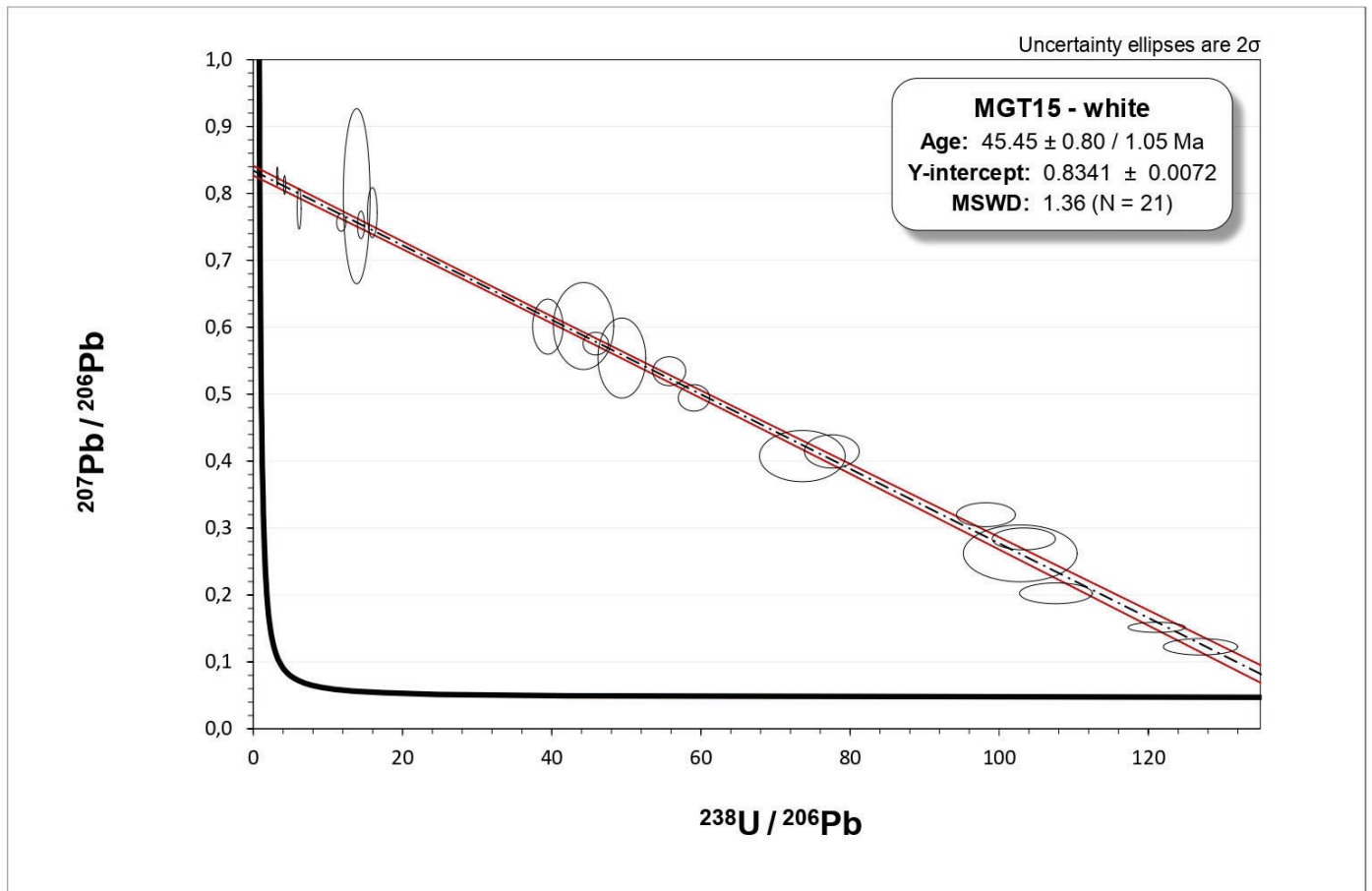
E136	CalGrun	41294	0,92	0,14	0,00006	20,08	2,7	0,7203	1,2	2
E196	CalGrun	39104	0,92	0,14	0,00007	20,31	2,7	0,7151	1,0	2
E256	CalGrun	44983	0,92	0,16	0,00006	17,59	2,6	0,7318	1,0	2
E316	CalGrun	38271	0,93	0,14	0,00006	20,08	2,6	0,7280	1,0	2
E376	CalGrun	34882	0,90	0,13	0,00005	20,43	2,7	0,7086	1,2	2
E436	CalGrun	34546	0,93	0,13	0,00005	20,65	2,7	0,7134	1,3	2
E496	CalGrun	34049	0,99	0,14	0,00007	22,07	2,6	0,7176	1,2	2
E546	CalGrun	34847	1,1	0,14	0,00006	22,89	2,6	0,7229	1,1	2
E598	CalGrun	32007	1,0	0,13	0,00006	23,16	2,7	0,7081	1,3	2
		38739	0,93	0,14	0,00006	20,24	18	0,7208	2,4	2

Concordia graphs 2

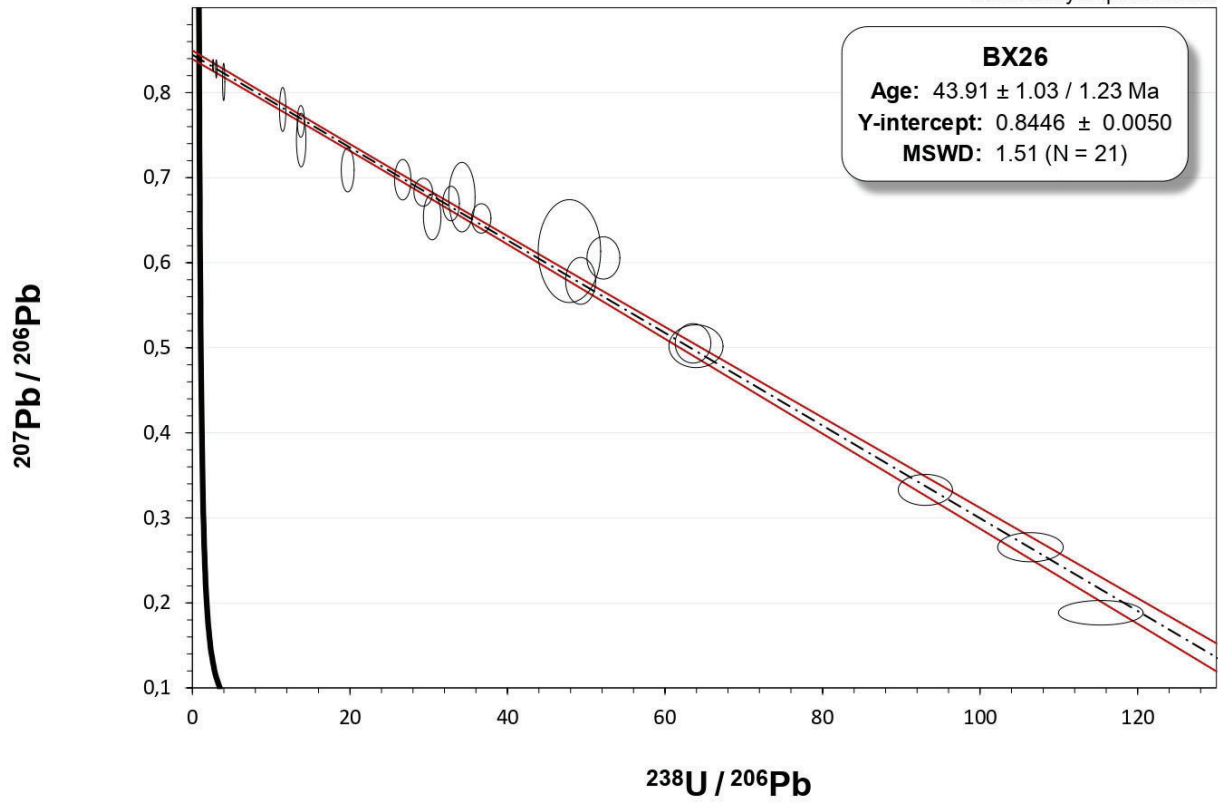




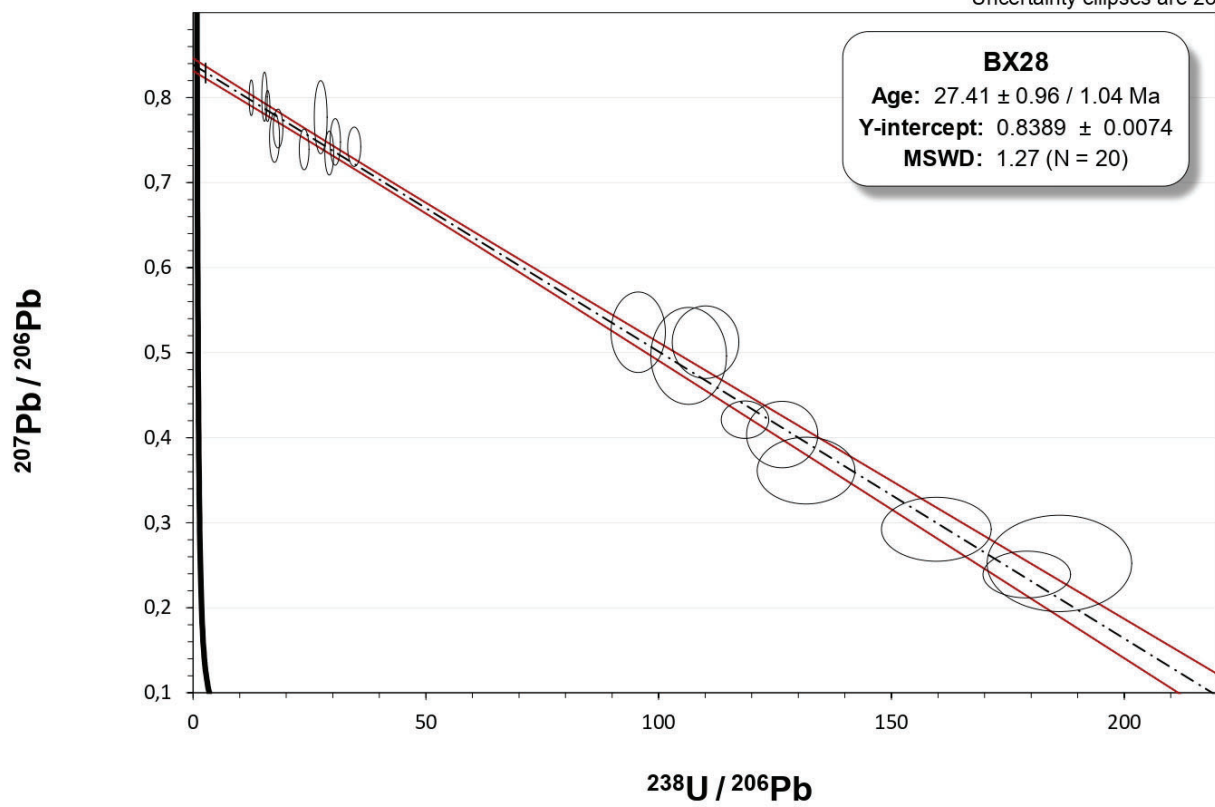


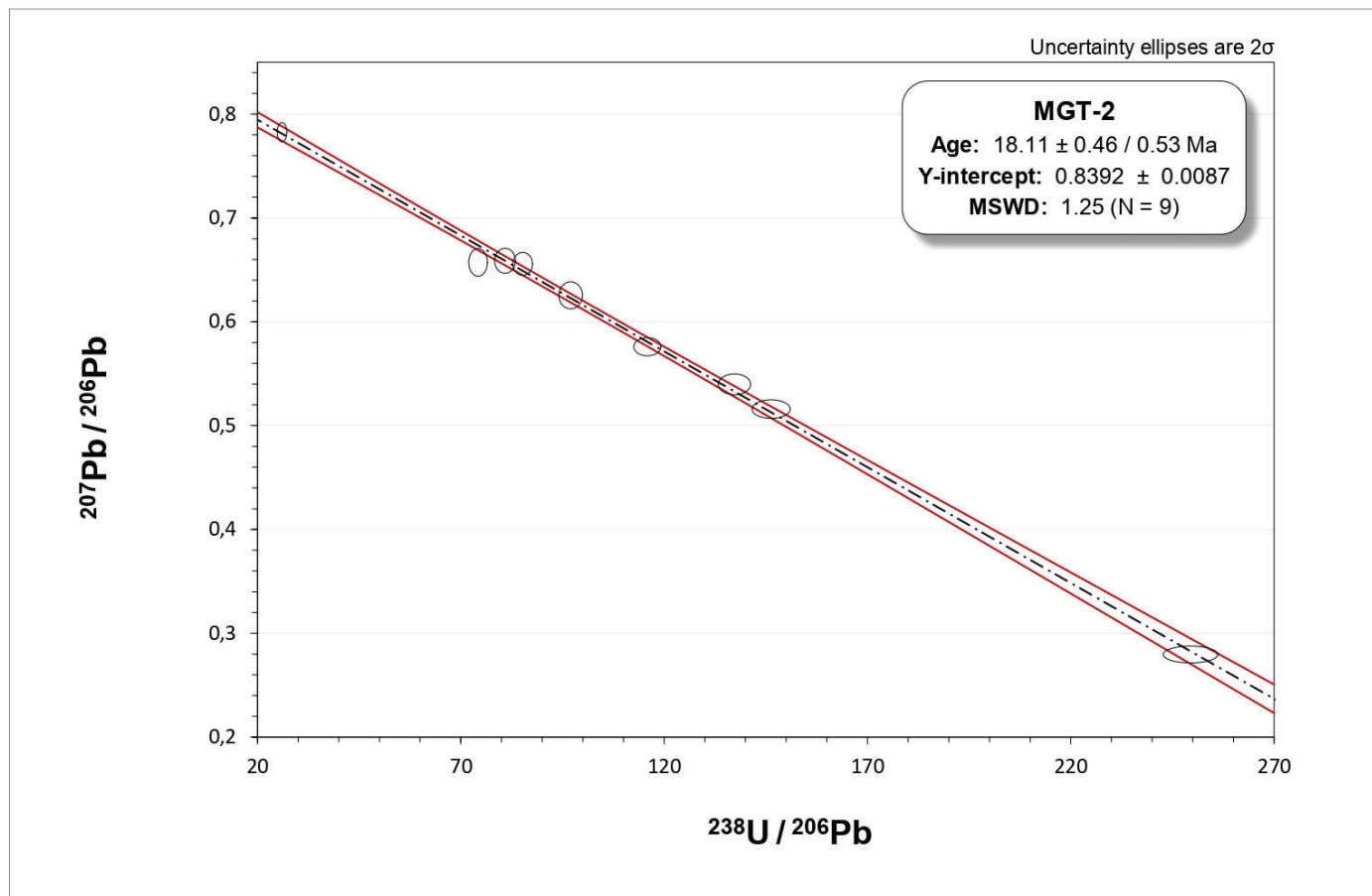
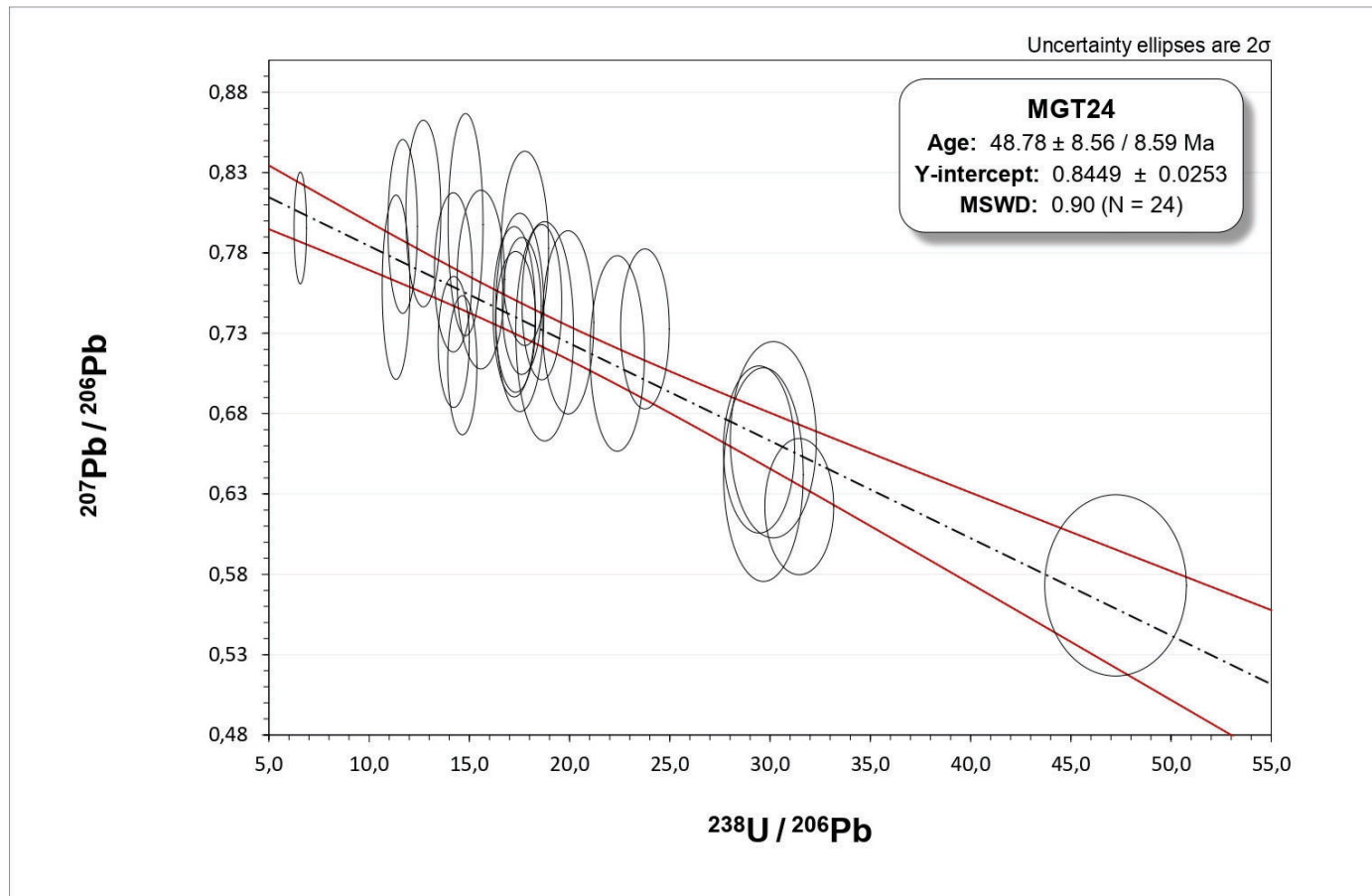


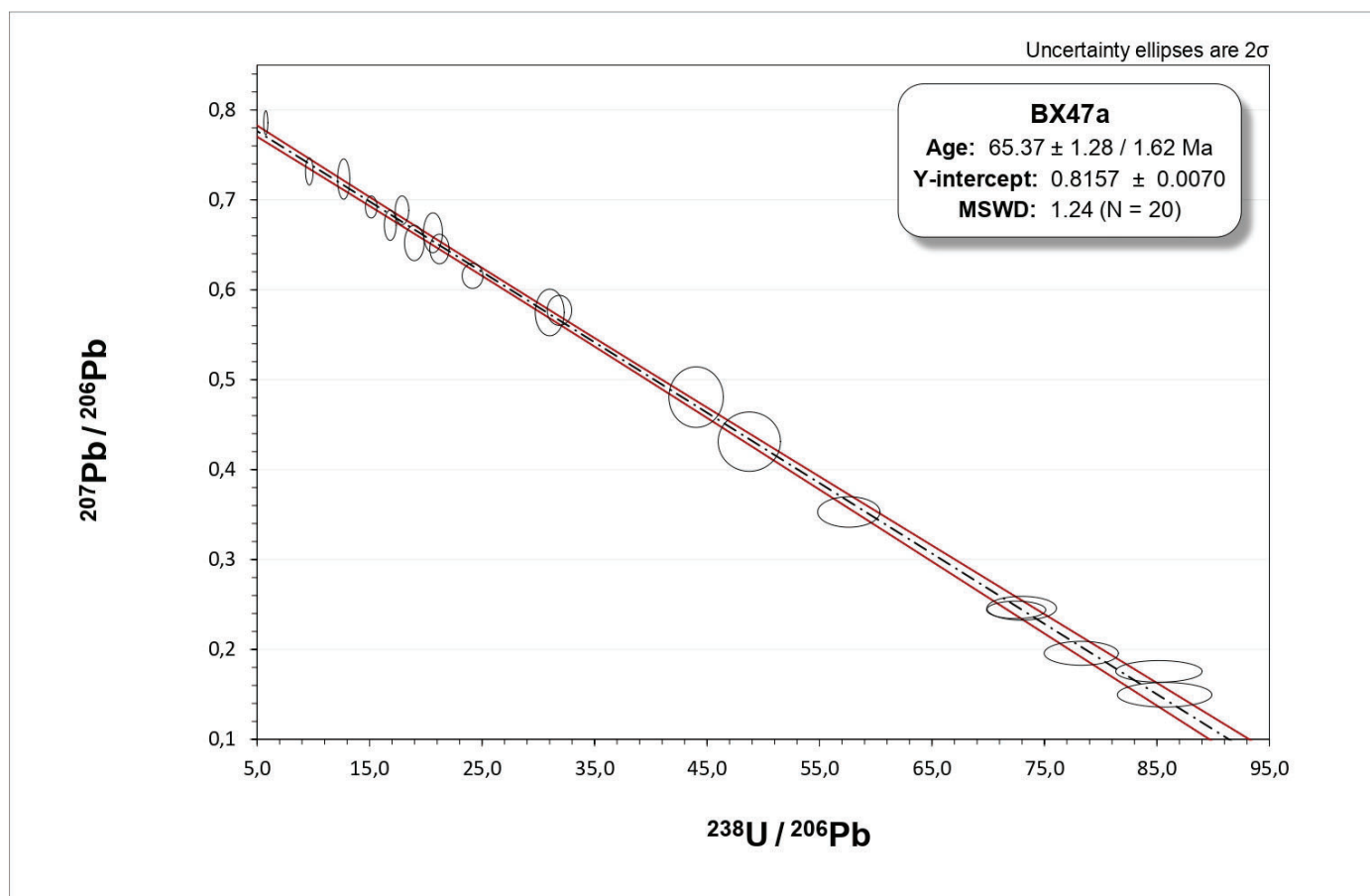
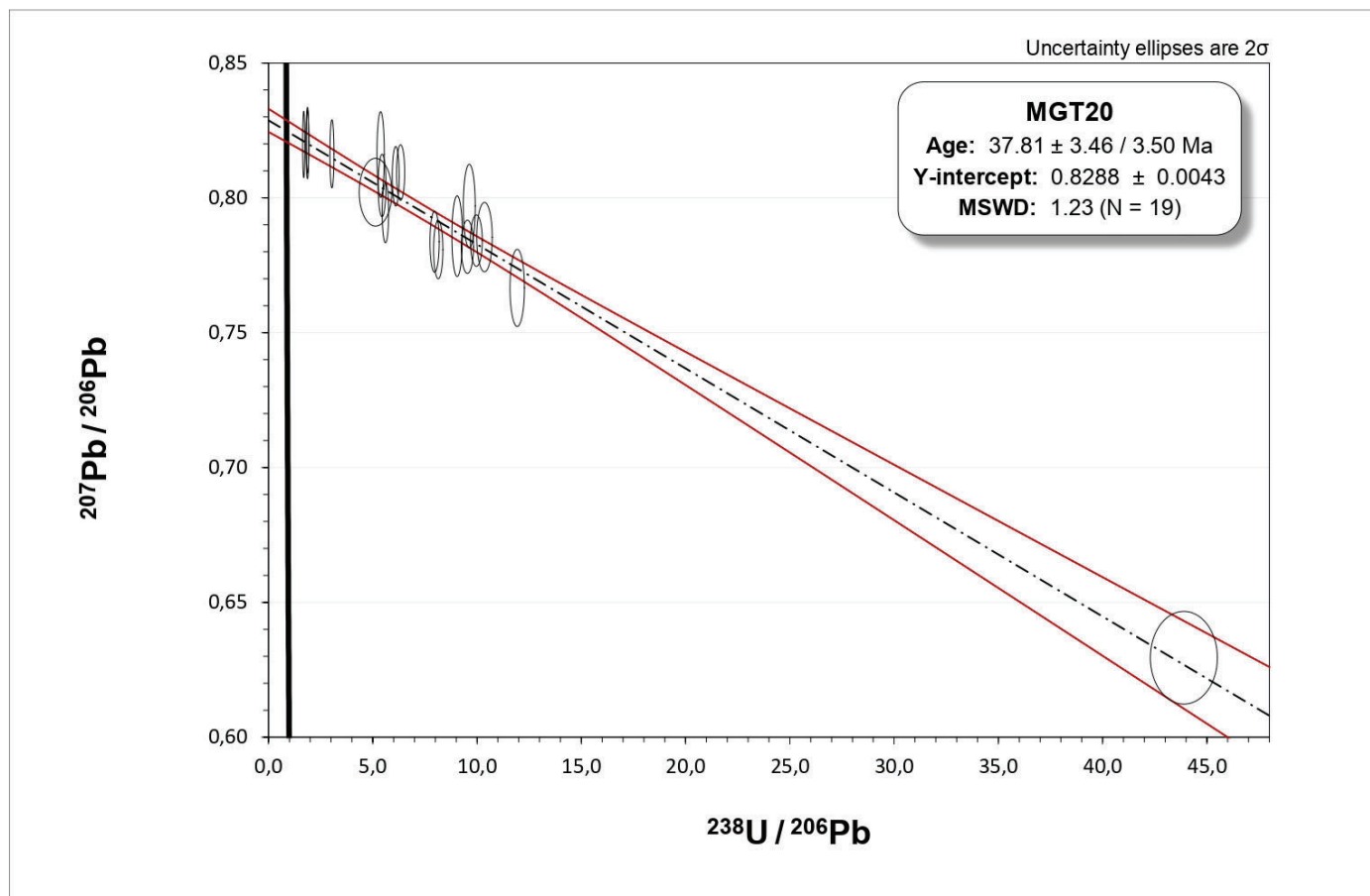
Uncertainty ellipses are 2σ

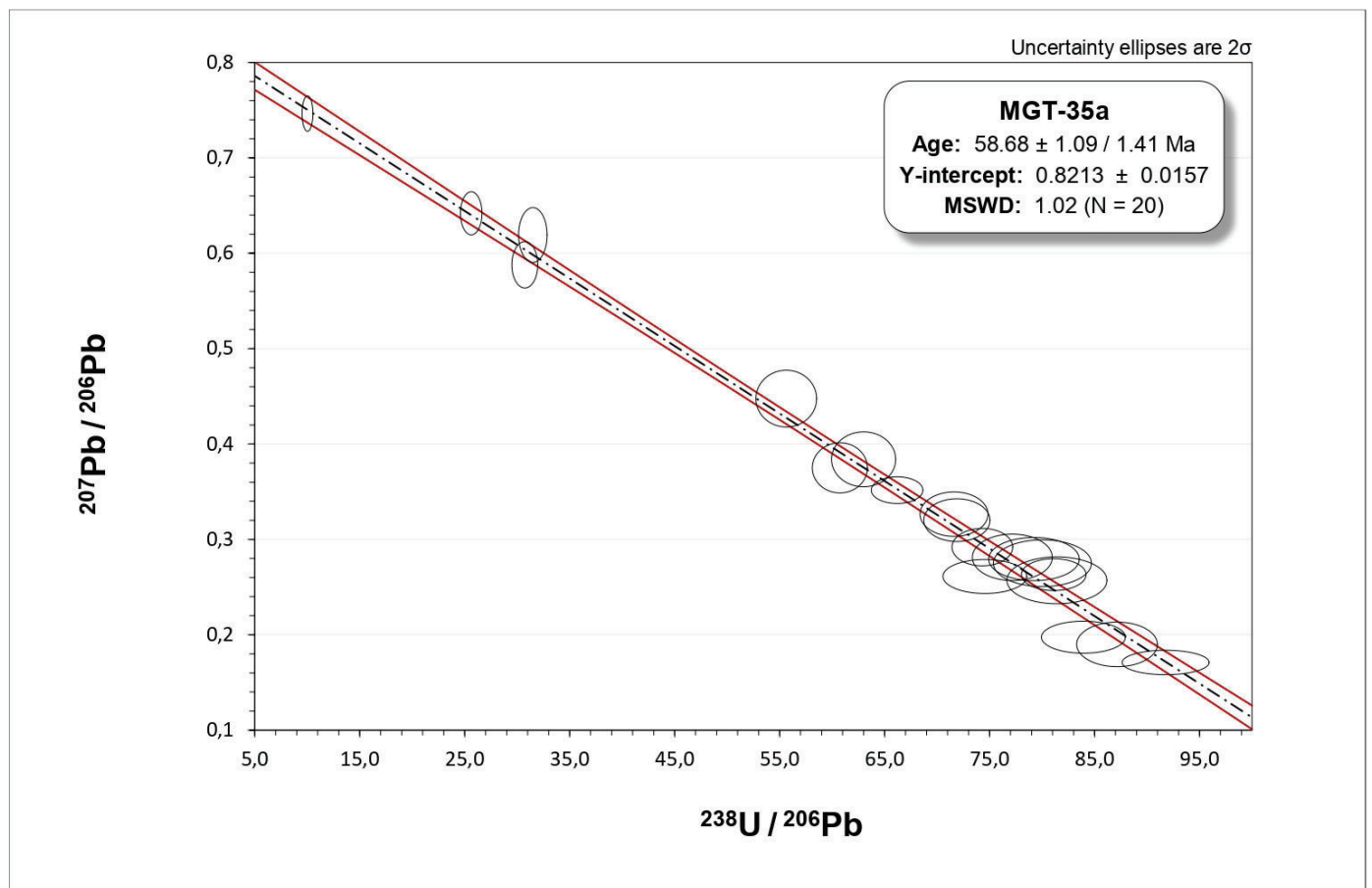
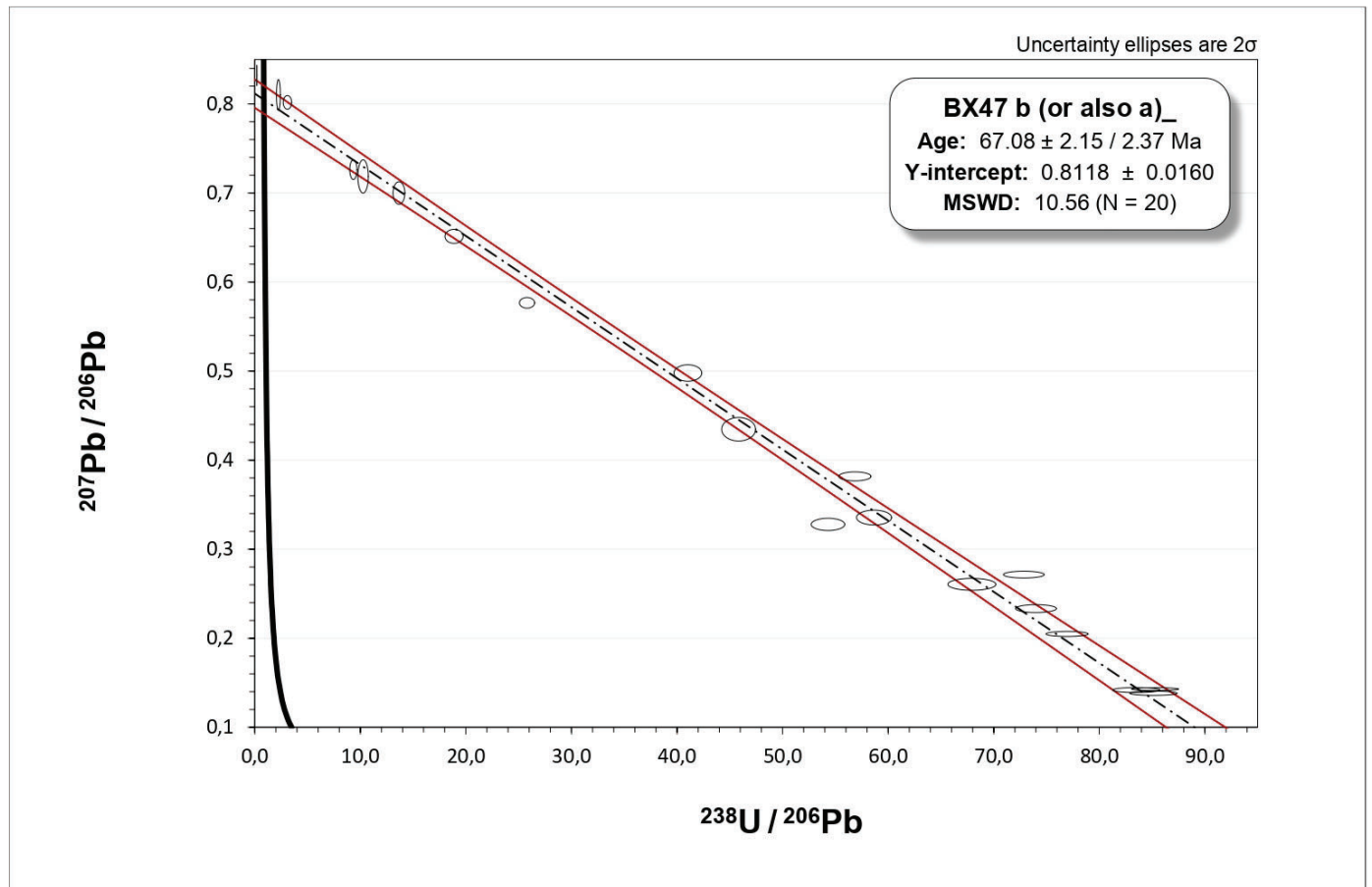


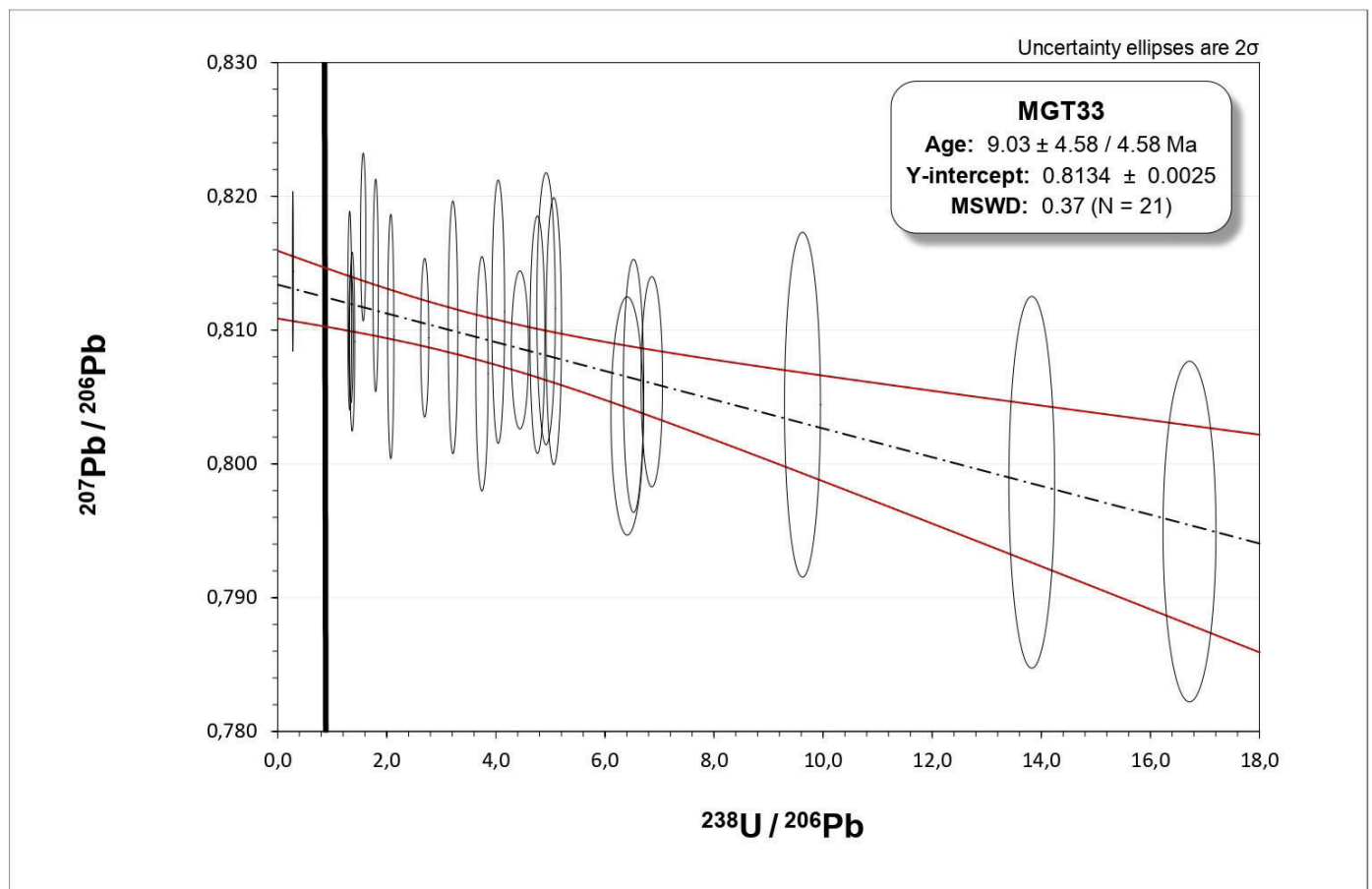
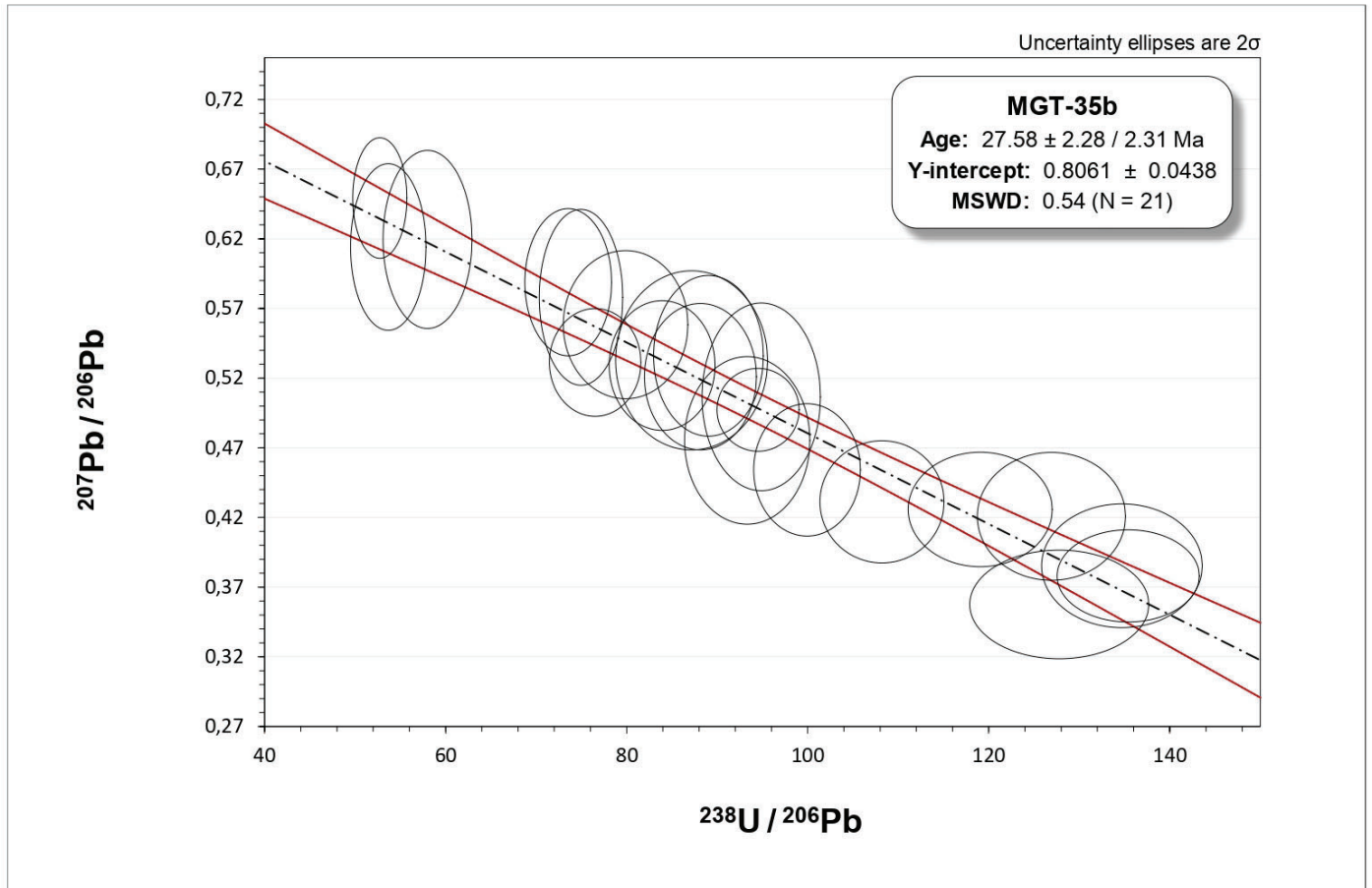
Uncertainty ellipses are 2σ

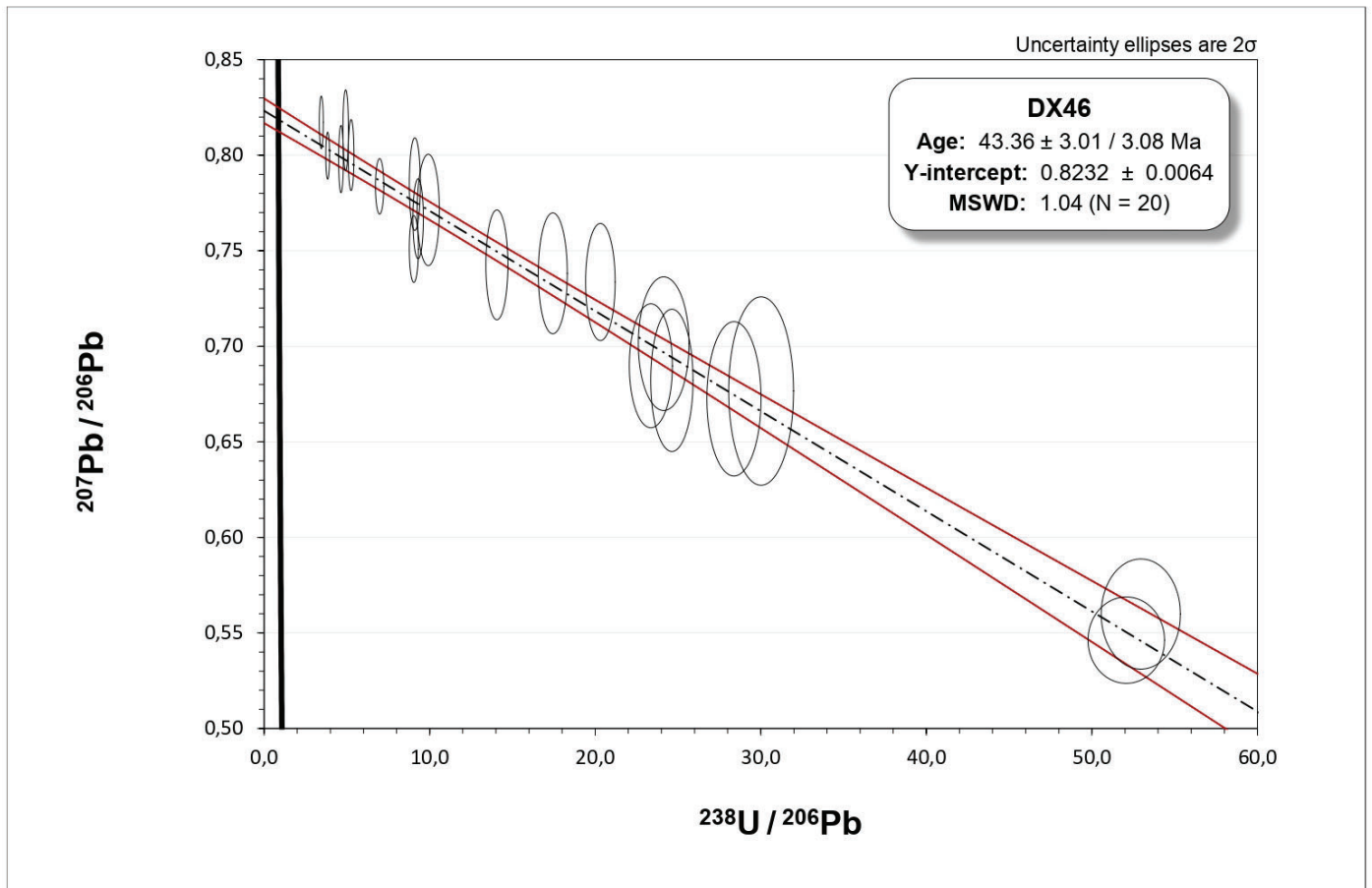
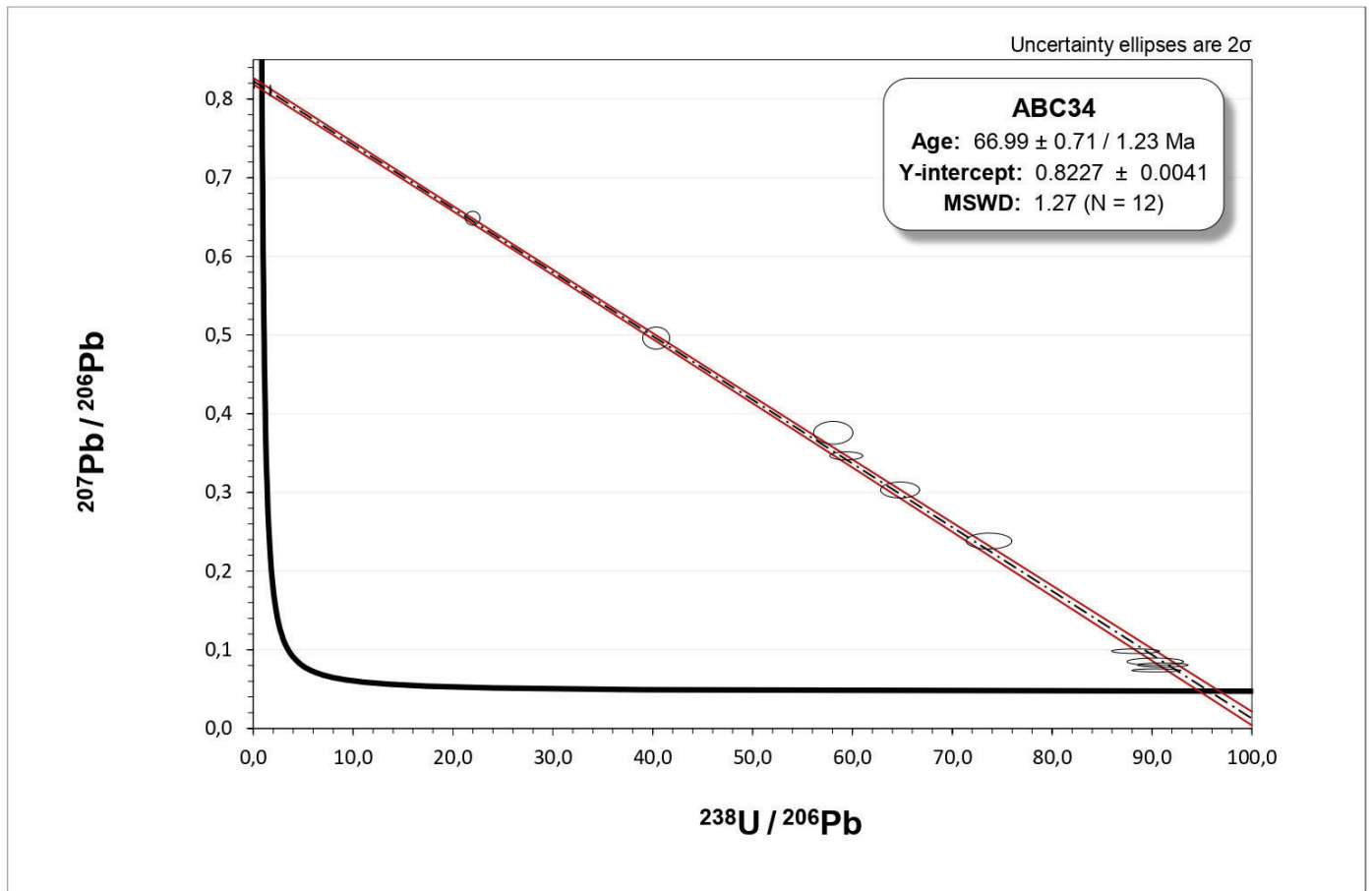












LA-ICP-MS U-Th-Pb data report

Laboratory & Sample Preparation	
Laboratory name	FIERCE, Frankfurt Isotope & Element Research Center Goethe Univesität, Frankfurt am Main
Sample type/mineral	Carbonate
Sample preparation	25 mm polished resin mounts
Imaging	Petrographic microscope & 2400 dpi digital scan
Laser ablation system	
Make, Model & type	RESOLUTION ArF excimer laser (COMpex Pro 102)
Ablation cell	Two-volume ablation cell (Laurin Technic S155)
Laser wavelength	193 nm
Pulse width	20 ns
Fluence	2 J/cm ²
Repetition rate	12 Hz (8 Hz for primary standard)
Pre-ablation	4 pulses (same parameters as main ablation)
Ablation duration	18 s
Ablation rate	~ 0.6 µm/s
Spot shape & size	Circle, 193 µm (diameter), 50 µm for primary standard.
Sampling mode	Static spot ablation
Gasses	Sample cell: He. Funnel: He + Ar. Tubbing: He + Ar + N
Gas flows	He (300 ml/min), Ar (1100 ml/min), N (5 ml/min).
ICP-MS Instrument	
Make, Model & type	ThermoScientific ElementXr sector field ICP-MS
Sample introduction	Ablation aerosol
RF power	1300 W
Detection system	Secondary electron multiplier (with conversion dynode at -8kV). Simultaneous analogue and counting (pulse) modes of detection (conversion factors calculated per mass and applied offline). Magnetic field fixed. Detection by peak jumping with electrostatic analyzer.
Masses measured	206, 207, 208, 232, 238
Dwell times	206: 6.4 ms, 207: 7.5 ms, 208: 3.0 ms, 232: 2.0 ms, 238: 4.6 ms
Samples per peak/integration type	4 for all masses/average
Total time per run	99 ms
Number of runs/total time	370 / 36.6 s
Acquisition mode	Trigger from laser (20 s after pre-ablation), background: 18 s, ablation: 18 s
Dead time	29 ns
Data Processing	
Gas blank	20 s on-peak zero subtracted.
Calibration strategy	NIST SRM-612 as primary RM, WC-1 as offset RM, B6 and CalGrun as validation RM.
Reference Material (RM) information	Soda-lime glass NIST SRM-612, WC-1 (Roberts et al., 2017), B6 (in-house calcite RM), CalGrun (in-house calcite RM).
Data processing / LIEF correction	In-house VBA spreadsheet program (Gerdes and Zeh, 2006, 2009). Intercept method for LIEF correction, assumes cPb corrected WC-1 and samples behave identically.
Mass discrimination	²⁰⁷ Pb/ ²⁰⁶ Pb (0.26%) and ²⁰⁶ Pb/ ²³⁸ U (9%) normalised to primary standard
Common-Pb correction	No common-Pb correction applied to the data.
Uncertainty level & propagation	Uncertainties are quoted at 2δ absolute and are propagated by quadratic addition of the within run precision, counting statistics, the excess of scatter derived from the primary RM and the excess of variance (see below).
Quality control / Validation	
Other information	
	An excess of variance of 1.23 % (1δ), calculated from WC-1, was added quadratically to the ²⁰⁶ Pb/ ²³⁸ U ratios of the secondary RM and unknowns. Long term reproducibility was determined to be 1.5% (2δ) and was added as an expanded uncertainty.